The evolution of morphology and fabric of a sand during shearing

A thesis submitted to the University of London in fulfilment of the requirements for the degree of Doctor of Philosophy

by

Joana Fonseca

April 2011

Department of Civil and Environmental Engineering
Imperial College London

"O caos é uma ordem por decifrar"

("Chaos is merely order waiting to be deciphered")

José Saramago

Declaration

The work presented in this thesis was carried out in the Geotechnics Section of the Department of Civil and Environmental Engineering at Imperial College London. This thesis is the result of my own work and any quotation from, or description of the work of others is acknowledged herein by reference to the sources, whether published or unpublished.

This dissertation is not the same as any that I have submitted for any degree, diploma or other qualification at any other university. No part of this thesis has been or is being concurrently submitted for any such degree, diploma or other qualification.

Joana Fonseca
London, 25/04/2011

Abstract

Over the past 50 years, experimental studies have repeatedly demonstrated that the mechanical behaviour of sand is sensitive to the material fabric, i.e., the arrangement of the grains. Up until now there have been relatively few attempts to describe quantitatively the fabric of sands. In fact, most of our understanding of the link between the particle movements and interactions and the macro-scale response of granular materials, including sand, comes from discrete element modelling (DEM) and experiments on "analogue" sands with simple, idealized shapes. The aim of this study had been to describe quantitatively the particle morphology and fabric of real sand and their evolution under loading.

The material investigated was Reigate sand (from Southeast England), a geologically old sand which, in its intact state, exhibits significant grain interlocking and no bonding. To explore the effects of fabric on the mechanical response of the soil, intact and reconstituted specimens both having similar densities were tested under triaxial compression. The specimens were impregnated with an epoxy resin at three different stages of shear deformation and small cores from each specimen were scanned using X-ray micro-tomography. Different systems and scanning parameters were explored in order to obtain three-dimensional high-resolution images with a voxel size of $5\mu m$ ($0.018d_{50}$) and a quality level required for the identification of the individual particles and the surface defining each particle-particle contact.

The quantification of particle size and shape has shown that breakage of fractured grains, along existing fissures, occurs both during reconstitution and shearing of the intact soil, a phenomenon that cannot be observed using invasive techniques such as sieve analysis. Statistical analyses of the distribution of fabric directional data in terms of particle orientations, contact normals, branch vectors and void orientations were carried out at each loading stage. It has been shown that the initial particle orientation fabric that develops during the deposition of the material tends to persist during shearing, while the contact normals seem to be reorientated along the direction of the major principal stress in the post-peak regime. Different patterns were observed within the shear band as both the particles and the contact normals appeared to rotate towards the direction of the shear plane. The measurements from the tomographic data were complemented with a qualitative description of the morphology and fabric using SEM and optical microscope images of thin sections.

Acknowledgements

This research has been sponsored by the Fundação para a Ciência e a Tecnologia, and the financial support by this Portuguese Government body is gratefully acknowledged. I am deeply grateful to my supervisors Dr. Catherine O'Sullivan and Prof. Matthew Coop for their endless support and guidance throughout this research. The help and advice from numerous people in the Department of Materials, in particular Prof. Peter Lee, Dr. Robert Atwood and Mr. Richard Hamilton is highly appreciated.

I would also like to express my gratitude to Dr. André Egbert from GE phoenix|x-ray for his support and Dr. Gerhard Zacher and Dr. Gennadiy Melnyk for sharing with me their expertise. The discussions with Dr. Clark Fenton about the geology of Reigate sand were very much appreciated. My acknowledgments also go to the laboratory technicians, Mr. Alan Bolsher for his dedication and patience and for making so many experiments possible, Mr. Steve Ackerley and Mr. Graham Keefe for their assistance. I am grateful to Hanson Aggregates for generously allowing the sampling at Park Pit Quarry.

Also appreciated was the contribution of the following people: Mr. Graham Nash from the Department of Earth Science and Engineering, Dr. Richard Abel from the Natural History Museum, Dr. Nick Corps from SkyScan, Mr. Kevin Hanley from University College Dublin, Dr. Robert Bradley from University of Manchester, Dr. Craig Sturrock from the University of Nottingham, Dr. Ajay Limaye from Australian National University, Dr. Mark Tarplee from Queen Mary University of London, Dr. Christoph Rau from Diamond. Thanks also go to Dr. Satoshi Nishimura for helping with the sampling process and Prof. Masanobu Oda for his advice.

Finally, I would like to acknowledge many people I have been privileged to meet in the Skempton Building over the last few years who have contributed, perhaps in a less obvious way, to the work this thesis represents. As was once written by Plutarch, "what we achieve inwardly will change outer reality".

Contents

Declaration **3**

Abstract **4**

Acknowledgements **5**

Contents **6**

List of figures **11**

List of tables **29**

Nomenclature **33**

1 Introduction **36**

1.1 Background 36

1.2 Aims and objectives 38

1.3 Methodology 38

1.4 Outline of the thesis 41

2 Review on soil fabric **43**

2.1 Introduction 43

2.2 Fabric definition 44

2.3 Macro-scale evidence of fabric effects in sand 45

2.3.1 Influence of fabric on strength 45

2.3.2 Influence of fabric on stiffness 46

2.4 Generation of data to quantify fabric 47

2.4.1 Imaging techniques 47

2.4.2 Photoelasticity 48
2.4.3 DEM 49
2.5 Quantifying fabric 49
2.5.1 Scalar quantities 49
2.5.2 Statistical analysis of directional data 51
2.6 Micro-scale observations of fabric effects and its evolution 58
2.6.1 Force chains 58
2.6.2 Quantitative links between measures of fabric and macro-scale response 60
2.7 Fabric in continuum soil mechanics approaches 62
2.7.1 Critical State Soil Mechanics 62
2.7.2 Constitutive modelling 63
2.8 Particle morphology 64
2.8.1 Influence of size and shape on macro scale response 64
2.8.2 Measurement tools 66
2.8.3 Size description 68
2.8.4 Shape description 69
2.9 Concluding remarks 72

3 Soil description **92**
3.1 Introduction 92
3.2 Locked sands 93
3.3 Reigate Sand 94
3.3.1 Local stratigraphy and deposition processes 94
3.3.2 Block sampling 96
3.3.3 Soil description 97
3.4 Concluding remarks 100

4 Laboratory Tests **113**
4.1 Introduction 113
4.2 Previous studies on the behaviour of locked sands 114
4.3 Sample preparation 115

4.3.1 Trimmimg of the intact samples 115
4.3.2 Reconstituted samples 116
4.3.3 Specific volume calculation 117
4.4 Triaxial tests 118
4.4.1 Bishop and Wesley triaxial apparatus 118
4.4.2 Calculations of stress and strain 120
4.4.3 Test description 121
4.4.4 Strain localisation and failure mode analysis 122
4.4.5 Interpretation of test results 125
4.5 Resin impregnation 127
4.5.1 Resin characteristics 128
4.5.2 The use of resin dyes 129
4.5.3 Process description 129
4.6 Specimen preparation for image acquisition 130
4.6.1 Thin sections 130
4.6.2 Core drilling 130

5 X-ray micro-CT **151**
5.1 Introduction 151
5.2 Background 152
5.3 Fundamentals of CT 153
5.3.1 X-ray physics 153
5.3.2 X-ray generation 153
5.3.3 X-ray interaction with matter 154
5.3.4 X-ray detection 156
5.3.5 Reconstruction 157
5.4 Micro-CT setup 157
5.4.1 Configuration of a micro-CT system 158
5.5 Description of the scanning process 160
5.5.1 Data acquisition 160
5.5.2 Micro-CT systems 161
5.5.3 Preliminary inspection 162

5.5.4 Analysis of the scans 163
5.5.5 Scans for image analysis 166
5.6 Summary 167

6 Image processing and analysis **183**
6.1 Introduction 183
6.2 Image processing 184
6.2.1 Image pre-processing 185
6.2.2 Image segmentation 187
6.2.3 Results and discussion 191
6.2.4 Summary 193
6.3 Image Analysis 194
6.3.1 General concept 195
6.3.2 Pre-analysis processes 197
6.3.3 Analysis of the particles 199
6.3.4 Analysis of the contacts 206
6.3.5 Analysis of the voids 213
6.3.6 Validation using a sample of micro-spheres 213
6.3.7 Summary 214
6.4 Concluding remarks 214

7 Results from analysis of morphology **240**
7.1 Introduction 240
7.2 Characterisation of particle morphology 241
7.2.1 Size 241
7.2.2 Shape 242
7.3 Concluding remarks 246

8 Results from analysis of fabric **268**
8.1 Introduction 268
8.2 Fabric quantification using scalar quantities 269
8.2.1 Void ratio 269
8.2.2 Coordination number 270

8.2.3 Contact Index 272
8.2.4 Summary 274
8.3 Fabric quantification using directional data 275
8.3.1 Particle orientation 276
8.3.2 Contact normals 284
8.3.3 Branch vectors 290
8.3.4 Void orientation 295
8.4 Macro-micro correlation 298
8.5 Concluding remarks 301

9 Conclusions **395**
9.1 Summary 395
9.2 Key observations 397
9.3 Recommendations for future research 400

References **402**

List of Figures

1.1 Flow chart of the methodology used in this study 40

2.1 Illustration of possible different arrangements of identical particles at the same relative density (adapted from Kuo, 1994) 73

2.2 Finely dispersed coating of iron oxide on quartz grains of Reigate sand 73

2.3 Effect of deposition on the stress:strain behaviour of sands (from Arthur and Menzies, 1972) 74

2.4 Plot of peak stress ratio against bedding plane angle (from Oda et al., 1982) 74

2.5 Shear wave velocities measured in a dense sand, (a) sample under isotropic stresses (b) sample compressed on path ABCD (modified after Kuwano and Jardine, 2002) 75

2.6 Photoelasticity measurements, (a) images of a disk squeezed between two contacts (b) schematic representation of a circular polarimeter (Howell and Behringer, 1999) 76

2.7 Determination of local void ratio distribution (from Yang, 2005) . . . 76

2.8 Schematic definition of directional data in a granular soil, (a) contact normal (b) branch vector (c) particle major axis orientation 76

2.9 Schematic illustration of doublet vectors (a) nearest neighbour (b) particle interactions (after Wang et al., 2001) 77

2.10 Void cell systems for granular materials proposed by Li and Li (2009) 77

2.11 2D orientation distribution plots, (a) distribution of the preferred orientation of particles from thin section analysis (Oda and Kazama, 1998) (b) density function of the contact normals (Oda et al., 1980) . 77

2.12 Distribution of the 3D contact normals (Wang and Mok, 2008) . . . 78

2.13 Distribution of contact normals from a DEM sample, (a) fitted Fourier series to the distribution (b) variation of the direction of anisotropy (Barreto et al., 2008) 79

2.14 Spherical coordinate system 80

2.15 Two-axis plot of the eigenvalue ratios for shape analysis of the orientation data (Woodcock, 1977) 80

2.16 Example of scanning lines though the pore space in a given direction (from Kuo et al., 1998) 81

2.17 Photoelastic pictures taken at (a) the peak state and (b) the residual stress state (from Oda and Kazama, 1998) 81

2.18 Progressive change of contact normal distribution in a triaxial compression test on sand (Oda, 1993) 82

2.19 Distribution of contact normals at (a) the initial state (b) peak the stress ratio (from Rothenburg and Bathurst, 1989) 82

2.20 Fabric evolution during axial compression for (a) elongated rods, $\theta = 0°$ (b) elongated rods, $\theta = 60°$ (c) circular rods, $\theta = 0°$ (Oda et al., 1985) 83

2.21 Schematic representation of the elongated voids (from Oda et al., 1985) 84

2.22 Evolution of the (a) deviatoric stress and (b) induced structural anisotropy, during axi-symmetric compression (Thornton, 2000) 85

2.23 Evolution of the strength descriptor $(\beta)_1$ of the contact normal vectors with the principal stress ratio for four specimens with different aspect ratios (Ng, 2001) 86

2.24 Definition of state parameters in v:ln(p') space (from Coop, 2005) . . 86

2.25 Effect of sample preparation on the behaviour of Kogyuk sand (from Been and Jefferies, 1985) 87

2.26 Particle shape terminology as defined by Barrett (1980) 87

2.27 Variation of $(e_{max} - e_{min})$ with grain size d_{50} (Miura et al., 1997) . . 88

2.28 Proposed grain contact structures associated with different undrained shearing behaviour (Yamamuro and Wood, 2004) 88

2.29 Particles that meet the definition of "size D" by sieving procedures (Taylor, 2002) 89

2.30 Definition of Feret diameters d_F, d_{Fmax}, d_{Fmin} 89

2.31 2D illustration of the computation of the diameter of a particle (Al-Raoush, 2007) 89

2.32 Outline detection of a sand grain, (a) original image (b) binary image (c) outline of the grain (Fonseca, 2006) 90

2.33 Visual estimation of roundness and sphericity of sand grains (Krumbein and Sloss, 1963) 90

2.34 Classification of form based on the flatness and elongation indices (Zingg, 1935) 90

2.35 Mohr's circle representation of some 3D regular shapes (Taylor, 2002) 91

2.36 2D schematic representation of convexity (from Woldfram Mathworld) 91

2.37 Convex hull obtained for a particle of Reigate sand 91

3.1 Different types of contact often associated with interlocked fabrics (from Dusseault and Morgensten, 1979). 103

3.2 Vertical faces at Park Pit Quarry from where the intact samples of Reigate sand were retrieved 103

3.3 Location of Park Pit Quarry, (a) map (b) general view of the site (from Google). 104

3.4 Geological map of the Wealden Basin, SE England (modified after Blyth and de Freitas, 1984) 104

3.5 Main stages of the block sampling process 105

3.6 PSD curves for Reigate sand obtained by sieving, using QICPIC apparatus and from Cresswell and Powrie (2004) 106

3.7 An example of a sample of sand stained by iron oxide. 106

3.8 EDS spectrum for (a) a sample of white sand (b) a sample of sand stained by iron oxide 107

3.9 Tomographic images showing iron as (a) an iron-rich mineral grain (b) an inclusion in a quartz grain 107

3.10 Micrograph of a thin section under cross-polarised light illustrating monocrystalline and polycrystalline quartz grains. 108

3.11 Micrograph of a thin section under cross-polarised light illustrating a quartz grain with undulose extinction. 108

3.12 SEM image showing the variety of particle morphologies and surface textures in a sample of Reigate sand 109

3.13 X-ray micro-CT image showing highly fractured grains 109

3.14 Micrograph of a thin section under cross-polarised light illustrating highly non-spherical particles, (a) example of an embayment in a grain (b) example of a grain with a long neck 110

3.15 Micrograph of a thin section under cross-polarised light showing grain contacts dominated by straight-to-long and concavo-convex contacts 111

3.16 SEM images on two samples of Reigate sand, (a) white sand showing light cement coating the grains (b) iron stained sand where the cement forms bridges between the grains 112

4.1 Stress-dilatancy relationships for Greensand (Cuccovillo and Coop, 1999) 134

4.2 Typical stress-strain behaviour of Reigate and sheared at low confining pressures (200kPa) (a) intact specimen (b) reconstituted specimen (Cresswell and Powrie, 2004) 134

4.3 Shear modulus G and volumetric strain against axial strain for intact and reconstituted samples of Reigate sand (effective cell pressure of 100 kPa) (Cresswell and Powrie, 2004) 135

4.4 Trimming process of the intact specimens (a)(b)(c) extracting small rectangular blocks from the wooden box (d) mounting the initial sample onto a hand lathe (e) shaping the cylindrical sample (f) trimming the ends of the final sample 136

4.5 Preparation of a reconstituted specimen 137

4.6 Schematic diagram of a typical Bishop & Wesley triaxial apparatus (modified from Qadimi, 2005) 138

4.7 Internal strain measurements, schematic diagrams of (a) an electrolevel inclinometer (b) a radial strain belt (modified after Carrera, 2008) 139

4.8 Instrumentation used for internal axial and radial strain measurements 139

4.9 Modified top cap 139

4.10 Different stages of loading used for morphology and fabric quantification 140

4.11 Evolution of local and external strain measurements during shearing, for the intact specimen representing the final stage of shearing (specimen 295-int) 140

4.12 Evolution of local and external strain measurements during shearing, for the intact specimen representing the stage when the shear band became visible (specimen 293-int) 141

4.13 Evolution of local and external strain measurements during shearing, for the reconstituted specimen representing the final stage of shearing (specimen 290-rec) 141

4.14 Evolution of local and external strain measurements during shearing, for the reconstituted specimen representing the stage when the shear band became visible (specimen 289-rec) 142

4.15 Formation of a shear band (a) intact specimen (b) reconstituted specimen 142

4.16 Shear plane angle, estimated measurements for (a) intact material (b) reconstituted material 143

4.17 Stress:strain plot of the shearing for the intact soil 143

4.18 Volumetric strain plots of the shearing for the intact soil 144

4.19 Stress:strain plot of the shearing for the reconstituted soil 144

4.20 Volumetric strain plots of the shearing for the reconstituted soil . . . 145

4.21 Comparison of the stress:strain and volumetric responses for the intact and reconstituted specimens 145

4.22 Influence of the confining pressure on stress:strain and volumetric behaviour of the intact soil 146

4.23 Stress:dilatancy plots for the intact soil samples at 300kPa 146

4.24 Stress:dilatancy plots for the reconstituted soil samples at 300kPa . . 147

4.25 Influence of the confining pressure on the stress:dilatancy behaviour of the intact soil 147

4.26 Stiffness degradation curves for the intact material 148

4.27 Stiffness degradation curves for the reconstituted material 148

4.28 Influence of the confining pressure on the shear stiffness of the intact soil samples 149

4.29 Resin impregnation process (a) general setup (b) triaxial sample during impregnation 149

4.30 Core drilling process 150

5.1 Object size against spatial resolution (modified from Neuser and Suppes, 2007) 171

5.2 Identification of a shear band in micro-CT images of a sand, (a) section along the vertical axis of the specimen (b) cross-section of the specimen (Desrues et al., 1996) 171

5.3 Schematic illustration of a typical micro-CT setup (from GE, 2010) . 171

5.4 Electromagnetic spectrum (from GE, 2010) 172

5.5 Schematic diagram of X-ray generation (a) electron travelling between the cathode and the anode and the generation of the X-ray radiation upon colliding with the anode (b) similar representation inside an X-ray tube (Larson, 2010) 172

5.6 Schematic diagram of the processes of producing the two components of the X-ray spectrum (a) "Bremsstrahlungand radiation" (b) "characteristic" radiation (Larson, 2010) 172

5.7 Schematic graph of an X-ray energy spectrum (from Oldnall, 2010) . 173

5.8 The three dominant physical processes of X-ray attenuation (a) photoelectric effect (b) Compton scattering (c) pair production (Nave, 2010) 173

5.9 Schematic illustration of X-ray attenuation for (a) an homogeneous object with a monochromatic beam (b) object with two different materials and a monochromatic beam (c) an heterogeneous object with a polychromatic beam (modified from Rivers, 2010) 173

5.10 Schematic illustration of the detection process (modified from Rivers, 2010), (a) from X-ray attenuation to the digital data conversion by a computer (b) signal conversion chain inside the detector (from PerkinElmer) 174

5.11 Illustration of a set of projections through an object at a viewing angle ϕ forming the function P (from Russ, 2007) 174

5.12 An example of a sinogram (a) sinogram (b) 2D slice through the object (modified from Beckmann, 2010) 174

5.13 Schematic illustration of filtered back projection showing that an increase in the number of views also increases the accuracy of the tomographic image to represent the original object (from Smith, 2010) . 175

5.14 Illustration of four experimental approaches to X-ray micro-tomography data collection, (a) pencil beam (b) fan beam (c) parallel beam (d) cone beam, where P is the X-ray source, O is the object being imaged, x_2 is the axis about which sample is rotated to produce different views required for reconstruction and D is the detector (from Stock, 1999) 175

5.15 Main components of a synchrotron, plan view (from Diamond, 2010) 175

5.16 Schematic illustration of the top view of a cone beam set up (from GE, 2010) 176

5.17 Geometric penumbra, (a) simple model of focal spot size and geometrical unsharpness or penumbra (b) example of an unsharp image using a micro-focus of 2-5μm (c) sharp image obtained using a focal spot with <1μm size (modified from GE, 2010). 176

5.18 Schematic illustration of a micro-focus X-ray tube with (a) a transmission target geometry (b) a reflective target geometry (from GE, 2010). 176

5.19 Horizontal cross-sections from the scans on the triaxial specimens using v|tome|x s, (a) top: 295-int, bottom: 297-int (b) top: 2953-int, bottom: 294-int (c) top: 290-rec, bottom: 291-rec (d) scanning parameters. 177

5.20 An example of beam hardening on a 4mm diameter sand sample scanned using the Metris HMX ST (Nikon), (a) 2D cross section, showing the bright shading around the edge (b) grey-level profile across the diametric line showing a significant increase in grey-level around the edges (c) scanning parameters used 178

5.21 Theoretical energy spectra for 420kV X-ray source. The upper is the result of beam filtration using a 3mm aluminum filter, the average X-ray energy is 224kV. The lower curve represents the spectrum after passing through 5cm of quartz; the preferential attenuation of the low-energy X-rays caused the average energy to rise to 178kV (from Ketcham and Carlson, 2001) 178

5.22 Schematic illustration of the beam hardening effect, (a) for low energy (kV) X-rays both long and short paths attenuate the same (b) for high energy (kV) X-rays, longer paths attenuate more than shorter paths (modified from Rivers, 2010) 179

5.23 An example of ring artefacts in a 3mm diameter core sample scanned at $resol = 2.5\mu m$ using v|tome|x s 179

5.24 Iron inclusions in two samples, (a) sample n1 shows "star" artefacts due to iron inclusions (scanned using v|tome|x s) (b) sample n2 shows the inclusions as sharp features (scanned using nanotom) (c) scanning parameters used 180

5.25 A comparison between the level of noise in two samples n1 and n2, scanned with two different nanotom systems, (a) cross-section from sample n1 (b) corresponding intensity profile (across the diamteric line) (c) cross-section from sample n2 (d) corresponding intensity profile (e) scanning parameters used 181

5.26 Cross-section of a 3mm diameter sample scanned at the Advanced Photon Source (Argonne National Laboratory) using phase contrast (using 724 projections) 182

5.27 Intensity profile assessment for a sample scanned with phase contrast using 724 projections 182

6.1 3D visualisation of a tomographic image of a sand sample, (a) 2D section in the xy-plane (b) 2D section in the xz-plane (c) 2D section in the yz-plane (d) 3D view 221

6.2 3D visualisation of a tomographic image of a sample made of resin impregnated glass spheres ($555\mu m$ diameter), (a) 2D section in the xy-plane (b) 2D section in the xz-plane (c) 2D section in the yz-plane (d) 3D view 221

6.3 Image processing flow chart 222

6.4 Calculation of the median value of a pixel on a 3×3 neighbourhood (from Fisher et al., 2010) 222

6.5 The process for threshold value detection, (a) Gaussian fit and finding of the minimum value (b) the minimum value of the combined curves is considered to be the threshold value 223

6.6 Schematic illustration of catchment basins and a watershed lines, (a) original sketch from Beucher and Lantuejoul (1979) (b) sketch from Matworks 223

6.7 2D illustration of two touching features, (a) binary image (b) distance map (c) distance map converted to a height function (from Russ, 2007) 223

6.8 Illustration of the concept of minimum watershed depth. In this case the catchment basin in the right will be merged with the adjacent catchment basin because its watershed depth is lower than the user defined minimum watershed 224

6.9 Intensity histogram for the tomographic images obtained using phase contrast (synchrotron radiation) 224

6.10 Result of the segmentation process on the tomographic images obtained using phase contrast (synchrotron radiation) 224

6.11 Comparison of the histogram for the data before and after filtering, (a) sample 294ph filtered with a 3D median filter, size 3×3×3 (b) sample 295L filtered with 3D adaptive Gaussian filter (from VGStudio Max) *smoothing=1.8* and *edge threshold=0.08* 225

6.12 Binary images of the raw data for (a) sample 294ph (b) sample 295L 226

6.13 Binary image of the filtered data for sample 294ph (xy-plane) 227

6.14 Binary images of sample 295L showing the shear band in the xy-plane at two different z values 227

6.15 2D slices obtained at different stages of the image processing of sample 297ph, (a) filtered image (b) line profile across one grain (c) binary image (d) distance map (e) watershed output of an undersegmented image (t=0.04 and l=0.4) (e) final watershed output (t=0.04 and l=0.2) 228

6.16 2D slice illustrating the final watershed output (using: t=0.04 and l=0.2) of the void analysis of sample 293vd 229

6.17 Image analysis flow chart 230

6.18 Pixel coordinate system used in MATLAB 230

6.19 Three-dimensional connectivities 231

6.20 Spherical coordinates (from Worldfram MathWorld) 231

6.21 Application of the principal component analysis, (a) plot of 50 points in the coordinate system defined by the x_1 and x_2 axes (b) plot of the same 50 points relatively to the principal components z_1 and z_2 (from Jolliffe, 2002) 232

6.22 Schematic representation of particle boundary detection using different connectivities in 2D, (a) face adjacency (b) face plus edge adjacency 232

6.23 Principal axes of inertia of the particle in the global coordinate system233

6.24 Illustration of the three principal orientations for an ellipsoid 233

6.25 Ellipsoid orientated along the direction of its major axis length . . . 234

6.26 Illustration of the identification of the contacts for *particle 1* in 2D (a) *particle 1* in contact with *particle 2*, *particle 3* and *particle 4* (b) contact detection along x direcion (c) contact detection along y direction (d) final contacts 234

6.27 Comparison of contacts between two given particles labeled n_1 and n_2 identified from particle n_1 and from particle n_2 235

6.28 2D illustration of the surface area calculation using the triangulation approach (a) 4 pixels considered (b) triangulated area 235

6.29 Triangulation of a square plane defined by 11×11 voxels (a) surface obtained using delaunay function (b) comparison between the surface area obtained using triangulation and the surface area considering the area of each voxel defining the plane 236

6.30 Illustration of the algorithm for best fit plane and normal vector calculation applied to a set of 3D planar points 236

6.31 Distribution of the length value of the three principal axes for the sample of micro-spheres 237

6.32 Distribution of the elongation index and flatness index for the sample of micro-spheres 237

6.33 Distribution of the convexity index for the sample of micro-spheres . 238

6.34 Distribution of the sphericity index for the sample of micro-spheres . 238

6.35 Comparison between the expected values for the sphericity index and the measured values 239

7.1 Particle size distribution using $d_{effective} = average(a, b, c)$ for the reconstituted samples 250

7.2 Particle size distribution using $d_{effective} = b$ for the reconstituted samples 250

7.3 Particle size distribution using $d_{effective} = b$ for the intact samples . . 251

7.4 Distribution of the mean diameter (d_{50}) for both intact and reconstituted soil at the four load stages 251

7.5 Optical microscope images of thin sections for the specimens analysed 252

7.6 Elongation index distribution for intact samples 297ph and 297L . . . 253

7.7 Flatness index distribution for intact samples 297ph and 297L 253

7.8 Elongation ratio distribution for intact samples 294ph and 294n . . . 253

7.9 Flatness index distribution for intact samples 294ph and 294n 254

7.10 Elongation index distribution for intact samples 293 and 293S 254

7.11 Flatness index distribution for intact samples 293 and 293S 254

7.12 Elongation index distribution for intact samples 295ph and 295L . . . 255

7.13 Flatness index distribution for intact samples 295ph and 295L 255

7.14 Elongation index distribution for reconstituted samples 291ph and 291L255

7.15 Flatness index distribution for intact samples 291ph and 291L 256

7.16 Elongation index distribution for intact samples 289 and 289S 256

7.17 Flatness index distribution for intact samples 289and 289S 256

7.18 Elongation index distribution for intact sample 290 257

7.19 Flatness index distribution for intact sample 290 257

7.20 Evolution of (a) the average elongation index and (b) the average flatness index, of the intact and reconstituted soil at the four stages of loading 258

7.21 Flatness index against elongation index for the intact samples (a) 297ph (b) 293 258

7.22 Flatness index against elongation index for the reconstituted samples (a) 291ph and (b) 289S 259
7.23 Sphericity index distribution for intact sample 297ph 259
7.24 Sphericity index distribution for intact samples 294ph and 294n . . . 259
7.25 Sphericity index distribution for intact samples 293 and 293S 260
7.26 Sphericity index distribution for intact sample 295ph 260
7.27 Sphericity index distribution for reconstituted samples 291ph and 291L260
7.28 Sphericity index distribution for reconstituted samples 289 and 289S . 261
7.29 Sphericity index distribution for reconstituted sample 290 261
7.30 Sphericity index against particle volume for (a) sample 293S (b) sample 289S 261
7.31 Evolution of the average sphericity index for the intact and reconstituted soil at the four stages of loading 262
7.32 Convexity index against particle volume for (a) sample 293 (b) sample 289S 262
7.33 Convexity index distribution for intact sample 297ph 262
7.34 Convexity index distribution for intact samples 294ph and 294n . . . 263
7.35 Convexity index distribution for intact samples 293 and 293S 263
7.36 Convexity index distribution for intact samples 295ph and 295L . . . 263
7.37 Convexity index distribution for reconstituted sample 291ph 264
7.38 Convexity index distribution for reconstituted samples 289 and 289S 264
7.39 Convexity index distribution for reconstituted sample 290 264
7.40 Evolution for average convexity index for intact and reconstituted soil at the four stages of loading 265
7.41 Sphericity against convexity for intact samples (a) 297ph and (b) 294ph 265
7.42 Sphericity against convexity for intact samples (a) 293 and (b) 295ph 265
7.43 Sphericity against convexity for reconstituted samples (a) 291ph and (b) 290 266
7.44 Sphericity against convexity for reconstituted samples (a) 289 and (b) 289S 266
7.45 Aspect ratio distribution, comparison between the 3D measurements and the 2D results from QICPIC 266

7.46 Sphericity distribution, comparison between the 3D measurements and the 2D results from QICPIC 267

7.47 Convexity distribution, comparison between the 3D measurements and the 2D results from QICPIC 267

8.1 3D void ratio measurements (a) from laboratory tests (b) from image analysis (c) comparison of both at the different load stages 327

8.2 2D void ratio distribution from horizontal (z) and vertical (y) slices for sample 297ph 328

8.3 2D void ratio distribution from horizontal (z) and vertical (y) slices for sample 294n 328

8.4 2D void ratio distribution from horizontal (z) and vertical (y) slices for sample 293 329

8.5 2D void ratio distribution from horizontal (z) and vertical (y) slices for sample 293S 329

8.6 2D void ratio distribution from horizontal (z) and vertical (y) slices for sample 289 330

8.7 2D void ratio distribution from horizontal (z) and vertical (y) slices for sample 289S 330

8.8 Coordination number distribution for all samples 331

8.9 Coordination number distribution for samples 297ph and 297L 331

8.10 Coordination number distribution for samples 294ph and 294n 331

8.11 Coordination number distribution for samples 293 and 293S 332

8.12 Coordination number distribution for samples 295ph and 295L 332

8.13 Coordination number distribution for sample 291ph and 291L 332

8.14 Coordination number distribution for samples 289 and 289S 333

8.15 Coordination number distribution for sample 290 333

8.16 Evolution of the average coordination number for intact and reconstituted soil at the four stages of loading 333

8.17 CN plotted against void ratio for (a) intact samples (b) reconstituted samples 334

8.18 CN plotted against particle volume for intact samples (a) 297ph (b) 294ph 334

8.19 CN plotted against particle volume for intact samples (a) 293 (b) 295ph 334

8.20 CN plotted against particle volume for reconstituted samples (a) 291ph (b) 289 335

8.21 CN plotted against particle volume for reconstituted samples (a) 289S (b) 290 335

8.22 CN plotted against sphericity for samples (a) 297ph (b) 291ph 335

8.23 CN plotted against convexity for samples (a) 297ph (b) 291ph 336

8.24 Contact index distribution for all samples 336

8.25 Contact index distribution for samples 297ph and 297L 336

8.26 Contact index distribution for samples 294ph and 294L 337

8.27 Contact index distribution for samples 293 and 293S 337

8.28 Contact index distribution for samples 295ph and 295L 337

8.29 Contact index distribution for samples 291ph and 291L 338

8.30 Contact index distribution for samples 289 and 289S 338

8.31 Contact index distribution for sample 290 338

8.32 Evolution of the average contact index for intact and reconstituted soil at the four stages of loading 339

8.33 CI plotted against void ratio for (a) intact samples (b) reconstituted samples 339

8.34 CI plotted against particle volume for intact samples (a) 297ph and (b) 293 339

8.35 CI plotted against particle volume for reconstituted samples (a) 291 and (b) 289 340

8.36 CN plotted against CI for intact samples (a) 297ph (b) 294ph 340

8.37 CN plotted against CI for intact samples (a) 293 (b) 295ph 340

8.38 CN plotted against CI for reconstituted samples (a) 291ph (b) 289 . . 341

8.39 CN plotted against CI for reconstituted samples (a) 289S (b) 290ph . 341

8.40 Void ratio plotted against CN for (a) intact soil (b) reconstituted soil 341

8.41 Void ratio plotted against CI for (a) intact soil (b) reconstituted soil 342

8.42 Rose diagrams of the particle orientations in the xz-plane: (a) 297ph+297L (b) 291ph+291L, in the yz-plane: (c) 297ph+297L (d) 291ph+291L, in the xy-plane: (e) 297ph+297L (f) 291ph+291L; the shading illustrates the elongation ratio 343

8.43 Rose diagrams of the particle orientations in the xz-plane: (a) 297ph+297L (b) 291ph+291L, in the yz-plane: (c) 297ph+297L (d) 291ph+291L; the shading illustrates the length of the particle major axis (in μm) . 344

8.44 Rose diagrams of the particle orientations in the xz-plane: (a) 294ph (b) 294n, in the yz-plane: (c) 294ph (d) 294n, in the xy-plane: (e) 294ph (f) 294n; the shading illustrates the elongation ratio 345

8.45 Rose diagrams of the particle orientations in the xz-plane: (a) 293 (b) 293S, in the yz-plane: (c) 293 (d) 293S, in the xy-plane: (e) 293 (f) 293S; the shading illustrates the elongation ratio 346

8.46 Rose diagrams of the particle orientations in the xz-plane: (a) 289 (b) 289S, in the yz-plane: (c) 289 (d) 289S, in the xy-plane: (e) 289 (f) 289S; the shading illustrates the elongation ratio 347

8.47 Rose diagrams of the particle orientations in the xz-plane: (a) 295ph (b) 295L, in the yz-plane: (c) 295ph (d) 295L, in the xy-plane: (e) 295ph (f) 295L; the shading illustrates the elongation ratio 348

8.48 Rose diagrams of the particle orientations in the xz-plane: (a) 290, in the yz-plane: (bB) 290, in the xy-plane: (c) 290; the shading illustrates the elongation ratio 349

8.49 Rose diagrams of the particle orientation in one vertical plane (a) 293S (b) 289 (c) 295L (d) 290, the shading illustrates the length of the particle major axis (in μm) 350

8.50 Particle orientation ϕ angle distribution for samples 297ph and 297L . 350

8.51 Particle orientation ϕ angle distribution for samples 294ph and 294n . 351

8.52 Particle orientation ϕ angle distribution for samples 293 and 293S . . 351

8.53 Particle orientation ϕ angle distribution for samples 295ph and 295L . 351

8.54 Particle orientation ϕ angle distribution for samples 291ph and 291L . 352

8.55 Particle orientation ϕ angle distribution for samples 289 and 289S . . 352

8.56 Particle orientation ϕ angle distribution for sample 290 352

8.57 Particle rotation in a shear band (Oda and Kazama, 1998) 353

8.58 Eigenvalue ratios for particle orientation data using (a) Φ^P (b) Φ . . 353

8.59 Evolution of the particle orientation anisotropy at different load stages using the formulations (a) $\Phi_1^P - \Phi_3^P$ (b) Φ_d^P 354

8.60 Evolution of the particle orientation anisotropy at different load stages using the formulations (a) $\Phi_1 - \Phi_3$ (b) Φ_d 355

8.61 Percentage of point contacts at each load stage for intact and reconstituted samples 355

8.62 Contact size distribution of one intact sample (297ph) and one reconstituted sample (291ph) 356

8.63 Rose diagrams of the contact normal orientation for the intact samples prior to loading, in the xz-plane: (a) 297ph (b) 297L, in the yz-plane: (c) 297ph (d) 297L, in the xy-plane: (e) 297ph (f) 297L 357

8.64 Rose diagrams of the contact normal orientation for the intact samples at load stage 2, in the xz-plane: (a) 294ph (b) 294n, in the yz-plane: (c) 294ph (d) 294n, in the xy-plane: (e) 294ph (f) 294n 358

8.65 Rose diagrams of the contact normal orientation for the intact samples at load stage 3, in the xz-plane: (a) 293 (b) 293S, in the yz-plane: (c) 293 (d) 293S, in the xy-plane: (e) 293 (f) 293S 359

8.66 Rose diagrams of the contact normal orientation for the intact samples at load stage 4, in the xz-plane: (a) 295ph (b) 295L, in the yz-plane: (c) 295ph (d) 295L, in the xy-plane: (e) 295ph (f) 295L 360

8.67 Rose diagrams of the contact normal orientation for the reconstituted samples prior to loading, in the xz-plane: (a) 291ph (b) 291L, in the yz-plane: (c) 291ph (d) 291L, in the xy-plane: (e) 291ph (f) 291L . . 361

8.68 Rose diagrams of the contact normal orientation for the reconstituted samples at load stage3, in the xz-plane: (a) 289 (b) 289S, in the yz-plane: (c) 289 (d) 289S, in the xy-plane: (e) 289 (f) 289S 362

8.69 Rose diagrams of the contact normal orientation for the reconstituted sample at load stage 4, in the xz-plane: (a) 290, in the yz-plane: (b) 290, in the xy-plane: (e) 290 363

8.70 Rose diagrams of the contact normal orientation for intact and reconstituted sample at early load stages, in the vertical planes, (a)(b) 297L (c)(d) 291ph (e)(f) 294ph; the shading illustrates the size of the contact (in voxels) 364

8.71 Rose diagrams of the contact normal orientation for the samples outside the shear band, in the vertical planes (a)(b) 293 (c)(d) 289S (e)(f) 295ph; the shading illustrates the size of the contact (in voxels) . . . 365

8.72 Rose diagrams of the contact normal orientation for the samples containing the shear band, in the vertical planes, (a)(b) 293S (c)(d) 289 (e)(f) 295L; the shading illustrates the size of the contact (in voxels) . 366

8.73 Rose diagrams of the contact normal orientation for the reconstituted sample at load satge 4 (containing the shear band), in the vertical planes of sample 290; the shading illustrates the size of the contact (in voxels) 367

8.74 Contact normal angle ϕ distribution for samples 297ph and 297L . . . 367

8.75 Contact normal angle ϕ distribution for samples 294ph and 294n . . . 367

8.76 Contact normal angle ϕ distribution for samples 293 and 293S 368

8.77 Contact normal angle ϕ distribution for samples 295ph and 295L . . . 368

8.78 Contact normal angle ϕ distribution for samples 291ph and 291L . . . 368

8.79 Contact normal angle ϕ distribution for samples 289 and 289S 369

8.80 Contact normal angle ϕ distribution for samples 290 369

8.81 Eigenvalue ratios of the contact normal (CnO) data using (a) Φ (b) Φ^w 370

8.82 Evolution of the contact normal anisotropy at different load stages using (a) Φ_d (b) Φ_d^W 371

8.83 Rose diagrams of the branch vector orientation in the xz-plane: (a) 297ph (b) 294ph, in the yz-plane: (c) 297ph (d) 294ph, in the xy-plane: (e) 297ph (f) 294ph; the shading illustrates the branch vector length (in μm) 372

8.84 Rose diagrams of the branch vector orientation in the xz-plane: (a) 293 (b) 293S, in the yz-plane: (c) 293 (d)293S, in the xy-plane: (e) 293 (f) 293S; the shading illustrates the branch vector length (in μm) 373

8.85 Rose diagrams of the branch vector orientation in the xz-plane: (a) 295ph (b) 295L, in the yz-plane: (c) 295ph (d) 295L, in the xy-plane: (e) 295ph (f) 295L; the shading illustrates the branch vector length (in μm) 374

8.86 Rose diagrams of the branch vector orientation in the xz-plane: (a) 291ph (b) 289, in the yz-plane: (c) 291ph (d) 289, in the xy-plane: (e) 291ph (f) 289; the shading illustrates the branch vector length (in μm) 375

8.87 Rose diagrams of the branch vector orientation in the xz-plane: (a) 289S (b) 290, in the yz-plane: (c) 289S (d) 290, in the xy-plane: (e) 289S (f) 290; the shading illustrates the branch vector length (in μm) 376

8.88 Branch vector angle ϕ distribution for samples 297ph and 297L 377

8.89 Branch vector angle ϕ distribution for samples 294ph and 294n 377

8.90 Branch vector angle ϕ distribution for samples 293 and 293S 377

8.91 Branch vector angle ϕ distribution for samples 295ph and 295L 378

8.92 Branch vector angle ϕ distribution for samples 291ph and 291L 378

8.93 Branch vector angle ϕ distribution for samples 289 and 289S 378

8.94 Branch vector angle ϕ distribution for sample 290 379

8.95 Eigenvalue ratios of the branch vector orientation (bvO) data 379

8.96 Branch vector anisotropy (Φ_d) at different load stages 379

8.97 An example of the relationship between particle orientation and contact orientation and its effect to the branch vector length (bvl) (a) contact approximately orthogonal to the particle minor axis (b) contact approximately orthogonal to the particle major axis 380

8.98 *bvlratio* plotted against particle volume for samples (a) 297ph (b) 291ph380

8.99 Branch vector length distribution for all samples 380

8.100Angle α distribution for (a) intact samples 297ph, 294ph, 293, 295ph (a) reconstituted samples 291ph, 289, 290ph 381

8.101Mean diameter plotted against branch vector length for (a) intact samples (b) reconstituted samples 381

8.102Rose diagrams of α (a) intact sample 293 (b) reconstituted sample 289; the shading illustrates the size of the contact (in voxels) 382

8.103Void size distribution 382

8.104Rose diagrams of the void orientation in the vertical planes (a) 297vd (b) 291vd (c) 293Svd (d) 289Svd; the shading illustrates the major axis length of the void (in μm) 383

8.105Void orientation angle ϕ distribution for samples 297vd and 291vd . . 383

8.106Void orientation angle ϕ distribution for samples 293vd and 293Svd . 384

8.107Void orientation angle ϕ distribution for samples 289vd and 289Svd . 384

8.108Eigenvalue ratios of the void orientation data using (a) Φ^{vd} (b) Φ . . 385

8.109Void orientation anisotropy using (a) Φ^{vd} (b) Φ, at two stages of loading 386

8.110Schematic diagrams of the soil fabric (a) for the intact soil prior to loading (b) for the intact soil in the post-peak regime outside the shear band (c) for the intact soil in the post-peak regime inside the shear band, the dashed lines mark the limits of the shear band (d) for the reconstituted soil prior to loading (e) for the reconstituted soil in the post-peak regime outside the shear band (f) for the reconstituted soil in the post-peak regime inside the shear band 387

8.111Evolution of the deviatoric stress and the contact normal deviatoric fabric for (a) intact samples (b) reconstituted samples 388

8.112Evolution of deviatoric stress and the branch vector deviatoric fabric for (a) the intact samples (b) the reconstituted samples 388

8.113Evolution of the deviatoric stress and the particle orientation deviatoric fabric for intact samples using (a) Φ^P (b) Φ 388

8.114Evolution of the deviatoric stress and particle orientation deviatoric fabric for reconstituted samples using (a) Φ^P (b) Φ 389

8.115Evolution of the deviatoric stress and void orientation deviatoric fabric for (a) intact samples (b) reconstituted samples 389

8.116Evolution of the deviatoric stress and the contact normal ϕ angle for (a) intact samples (b) reconstituted samples 389

8.117Evolution of deviatoric stress and the branch vector ϕ angle for (a) intact samples (b) reconstituted samples 390

8.118Evolution of the deviatoric stress and the particle orientation ϕ angle for intact samples using (a) Φ^P (b) Φ 390

8.119Evolution of the deviatoric stress and the particle orientation ϕ angle for reconstituted samples using (a) Φ^P (b) Φ 390

8.120Evolution of deviatoric stress and the void orientation ϕ angle for (a) intact samples (b) reconstituted samples 391

8.121Evolution of stiffness and (a) CN (b) CI, for the intact samples . . . 391

8.122Evolution of the stiffness with (a) void ratio (b) coordination number (c) contact index, for the intact samples 392

8.123Evolution of stiffness and (a) CN (b) CI, for the reconstituted samples 393

8.124Evolution of the stiffness with (a) void ratio (b) coordination number (c) contact index, for the reconstituted samples 394

List of Tables

3.1 Summary of common characteristics of locked sands(modified after Abdelaziz et al., 2008) 101

3.2 Geological succession at Park Pit (Dines and Edmunds, 1933) 101

3.3 Geological succession deposited above the Folkestone Beds during the Upper Cretaceous (Dines and Edmunds, 1933) 102

3.4 Summary of the specimen composition obtained by EDS analysis . . 102

4.1 Moisture content of the intact soil 131

4.2 Particle density (kg/m^3) obtained by pycnometry 131

4.3 Initial specific volumes for the intact samples used in different studies 131

4.4 Initial specific volumes for the reconstituted samples used in different studies 131

4.5 Characteristics of the tested specimens 132

4.6 Rate of dilation, d, for the intact and reconstituted samples at peak . 133

4.7 Change in specific volume during impregnation 133

5.1 Examples of different types of tomography 169

5.2 Characteristics of two commercial scanners used: v|tome|x s and nanotom (both from GE phoenix|xray) 169

5.3 Characteristics of the additional commercial micro-CT scanners used 169

5.4 Resin impregnated triaxial specimens and the associated samples scanned for image analysis 170

5.5 Scanning parameters used for each scan 170

6.1 Image data types 215

6.2 Size and spatial resolution of the samples analysed, the suffix used is related to the location of the scanner (e.g., 'L' refers to Lees University, 'ph' refers to phoenix|x-ray in Germany, the other samples were scanned at Nottingham University) 215

6.3 Samples for void analysis and the associated samples for particle analysis 215
6.4 Rotation matrices for object rotation 216
6.5 Surface area measurements for a micro-sphere of $555\mu m$ diameter, using different connectivities 216
6.6 Analysis of the fabric tensor obtained using Φ^P, after rotating a systems of ellipsoids (with an initial horizontal position) using different rotation angles 216
6.7 Comparison of the results given by the Φ and Φ^P formulations using three systems of uniformly sized particles, each system containing particles with specific aspect ratios 217
6.8 Comparison of the results given by the Φ and Φ^P formulations for a simple systems of non-uniformly sized particles 218
6.9 Analysis for planes orientated by a given direction 219
6.10 Information of the sample made of micro-spheres 220
6.11 Normal vector to a best fit plane obtained for the data before and after being rotated using the *pc* tensor 220
6.12 Summary of the main functions developed in MATLAB 220

7.1 Information for the tested specimens and the associated samples that were used for morphology and fabric quantification 248
7.2 Statistics for the particles not on the boundary, for each sample . . . 248
7.3 Comparison of some morphological characteristics measured for the particles of two intact samples (297ph and 297L) scanned at different locations with different scanning parameters and pre-processed with a different filter 249

8.1 Information for the tested specimens and the associated samples that were used for morphology and fabric quantification 303
8.2 Void ratio measurements 303
8.3 Comparison between the coordination number (CN) and the mechanical coordination number (CN_m) for all samples 304
8.4 Particle orientation fabric tensor (Φ^P) for the intact samples 297ph and 297L 304
8.5 Particle orientation fabric tensor (Φ^P) for the intact samples 294ph and 294n 305
8.6 Particle orientation fabric tensor (Φ^P) for the intact samples 293 and 293S 305

8.7 Particle orientation fabric tensor (Φ^P) for the intact samples 295ph and 295L 306

8.8 Particle orientation fabric tensor (Φ^P) for the reconstituted samples 291ph and 291L 306

8.9 Particle orientation fabric tensor (Φ^P) for the reconstituted samples 289 and 289S 307

8.10 Particle orientation fabric tensor (Φ^P) for the reconstituted sample 290307

8.11 Particle orientation fabric tensor (Φ) for the intact samples 297ph and 297L 308

8.12 Particle orientation fabric tensor (Φ) for the intact samples 294ph and 294n 308

8.13 Particle orientation fabric tensor (Φ) for the intact samples 293 and 293S 309

8.14 Particle orientation fabric tensor (Φ) for the intact samples 295ph and 295L 309

8.15 Particle orientation fabric tensor (Φ) for the reconstituted samples 291ph and 291L 310

8.16 Particle orientation fabric tensor (Φ) for the reconstituted samples 289 and 289S 310

8.17 Particle orientation fabric tensor (Φ) for the reconstituted sample 290 311

8.18 Direction of the major principal fabric to the horizontal given by the angle Ω_{PO} for Φ and by the angle $\Omega_{PO(P)}$ for Φ^P, for the samples affected by the shear band 311

8.19 Fabric descriptors for the fabric tensors Φ and $\Phi^P$of the particle orientation 311

8.20 Particle orientation anisotropy 312

8.21 Statistics for the total number of contacts for each sample and the number of point contacts and percentage relative to the total number of contacts 312

8.22 Contact normal fabric tensor for the samples 297ph and 297L 313

8.23 Contact normal fabric tensor for the sample 294ph and 294n 313

8.24 Contact normal fabric tensor for the samples 293 and 293S 314

8.25 Contact normal fabric tensor for the samples 295ph and 295L 314

8.26 Contact normal fabric tensor for the samples 291ph and 291L 315

8.27 Contact normal fabric tensor for the samples 289 and 289S 315

8.28 Contact normal fabric tensor for the sample 290 316

8.29 Comparison between the eigenvalues, the eigenvector V_1 and the angle ϕ_1 obtained for the different contact normal fabric tensors, for the intact samples 317

8.30 Comparison between the eigenvalues, the eigenvector V_1 and the angle ϕ_1 obtained for the different contact normal fabric tensors, for the reconstituted samples 318

8.31 Comparison between Ω_{PO} and ϕ_{cnO} for the samples affected by the shear band 319

8.32 Fabric descriptors for the contact normal fabric tensors Φ and Φ^w . . 319

8.33 Contact normal anisotropy 319

8.34 Branch vector fabric tensor for the samples 297ph and 297L 320

8.35 Branch vector fabric tensor for the samples 294ph and 294n 320

8.36 Branch vector fabric tensor for the samples 293 and 293S 321

8.37 Branch vector fabric tensor for the samples 295ph and 295L 321

8.38 Branch vector fabric tensor for the samples 291ph and 291L 322

8.39 Branch vector fabric tensor for the samples 289 and 289S 322

8.40 Branch vector fabric tensor for the sample 290 323

8.41 Fabric descriptors for the branch vector fabric tensor 323

8.42 Branch vector anisotropy 323

8.43 Comparison between Ω_{PO}, ϕ_{CnO} and ϕ_{bvO} for the samples affected by the shear band 324

8.44 Samples used for void space analysis 324

8.45 Comparisons between the d_{50} values obtained for the particles and for the voids for each sample 324

8.46 Void orientation fabric tensor (Φ^{vd}) for the samples 297vd and 291vd 325

8.47 Void orientation fabric tensor (Φ^{vd}) for the samples 293vd and 293Svd 325

8.48 Void orientation fabric tensor (Φ^{vd}) for the samples 289vd and 289Svd 326

8.49 Fabric descriptors for the void orientation fabric tensors Φ and Φ^P . . 326

8.50 Void orientation anisotropy 326

9.1 Comparison of the spatial resolution and source type used in some recent studies using high-resolution tomographic images of sand . . . 397

Nomenclature

Symbol

A_c	current cross-sectional area
A_0	initial cross-sectional area
a	major axis length
b	intermediate axis length
c	minor axis length
C	strength factor
C_U	uniformity coefficient
Cv	convexity index
d	rate of dilation
d_0	initial diameter
$d_{effective}$	effective diameter
d_{50}	mean effective diameter
d_F	Feret diameter
d_{Fmax}	largest Feret diameter
d_{Fmin}	smaller Feret diameter
Dr	relative density
e	void ratio
e_{max}	maximum void ratio
e_{min}	minimum void ratio
F	recorded in the load cell
Fs	size of the radiation source
G	shear modulus
G_s	specific gravity
I_0	incident radiation
I	transmitted radiation
K	shape value
l_0	initial sample length
M_s	mass of the soil

Symbol

N_c	number of contacts
N_p	number of particles
p'	mean effective stress
P	detector pixel size
R	roundness index
S	surface area
t	time
U	unsharpness or penumbra
Z	atomic number
V	volume
V_v	volume of voids
V_s	volume of solid
V_t	total volume of the sample
q	deviatoric stress
η	stress ratio ($= q/p'$)
v	specific volume
ρ_d	dry density
$\rho_{d(intact)}$	intact dry density
$\rho_{d(max)}$	maximum dry density
$\rho_{d(min)}$	minimum dry density
Δd	change in sample diameter
Δl	change in axial length
ε_a	axial strain
ε_r	radial strain
ε_s	shear strain
ε_v	volumetric strain
ϕ	polar angle
ρ_w	density of water
θ	azimuthal angle
μ	linear attenuation coefficient
σ'_c	cell pressure
Ψ	sphericity index
Φ	fabric tensor

Abbreviation

$2D$	two-dimensional
$3D$	three-dimensional
CN	coordination number
CI	contact index
CSL	critical state line
CT	computed tomography
DEM	discrete element modeling
FDD	focus-detector-distance
FOD	focus-object-distance
PCA	principal component analysis
PSD	particle size distribution
SNR	signal to noise ratio
VSD	void size distribution

Chapter 1

Introduction

1.1 Background

The response of granular materials is known to be sensitive to the material fabric, i.e., the topology of the internal structure of the material. This fabric is determined by the particle morphologies, the relative particle positions and the way the particles contact. In particular the responses of intact and reconstituted specimens of the same soils to shearing deformation differ (e.g., Cuccovillo and Coop, 1999; Cresswell and Powrie 2004). These experimental studies that compared the response of intact and reconstituted samples of the same sand, have demonstrated significant differences in the peak strength and dilation for both materials. The intact material also had a markedly higher stiffness than the reconstituted sand. The sensitivity of the mechanical response of sands to fabric can also be observed when the mechanical responses of reconstituted samples formed using different preparation procedures are compared (e.g., Been and Jefferies, 1985; Ibrahim and Kagawa, 1991).

The fact that the measured strength and stiffness depend on the direction in which the soil is deformed relative to the direction of fabric, i.e., the soil anisotropy, has been well established. Oda (1972b) and Arthur and Menzies (1972) were amongst the first to demonstrate the influence of the initial fabric orientation on the strength of sands. Experimental evidence of the effect of fabric anisotropy on soil stiffness was reported by Zdravkovic and Jardine (1997) and Kuwano and Jardine (2002).

Despite the abundant evidence supporting the observation of the fabric effect on the behaviour of granular soils, quantifying fabric and accounting for fabric effects in engineering design and analysis remains a challenge in geotechnical engineering. Various techniques to obtain experimental data to quantify the fabric of sand and describe its evolution during loading have been proposed in the last few decades. A pioneering study was described by Oda (1972b) who made some measurements using two-dimensional images of thin-sections on resin impregnated samples. This approach provided useful insight into the understanding of soil fabric and was later

adopted by other researchers (e.g., Frost and Jang, 2000). The time-consuming nature of the analysis and subjectivity of the results were however important limitations for the use of these two-dimensional imaging techniques.

A significant contribution to advancing our understanding of the link between particle-scale mechanics and the overall response of a granular material has been made using artificial particles to simulate the response of sands under loading. These studies included experiments (mostly 2D) using photoelastic particles (e.g., Oda and Konishi, 1974) and the application of the discrete element modelling, (e.g., Rothenburg and Bathurst, 1989; Thornton, 2000; O'Sullivan et al., 2008). DEM research has advanced understanding of the relationship between the material response and quantitative measures of fabric for relatively simple granular materials, made up of uniform, or close to uniform, spheres or ellipsoids. From a geotechnical perspective the findings of these numerical studies are limited, as real soil particles have complex geometries and contain a range of particle sizes. Therefore, the trends observed in these studies may not apply to real soils.

Recent developments in three-dimensional imaging technologies have enabled observations of the internal features of real sand specimens. High-resolution 3D images of the internal structure of soils can be obtained using X-ray micro-computed tomography (micro-CT). Early applications of micro-CT in the study of sands include the investigation of deformations and failure during shearing (e.g., Desrues et al., 1996; Otani et al., 2000). The spatial resolution in these earlier studies was, however, of the order of 1mm, thus did not permit the individual particles of sand to be identified. More recently, Oda et al. (2004) have shown that high-resolution 3D images of a sand obtained using a micro-focus scanner can achieve a similar level of detail as was previously observed in 2D images from thin sections. Subsequent investigations at a grain-scale have allowed particle-to-particle interactions to be examined (e.g., Al-Raoush, 2007; Hasan and Alshibli, 2010). The work described in this thesis explores further the potential to use 3D imaging techniques in soil mechanics and develops additional image analysis tools to obtain meaningful measurements of the fabric of granular materials which also includes the characterisation of the particle morphology.

1.2 Aims and objectives

The present research aims to advance understanding of the micro-scale behaviour of natural sands by exploiting new methodologies to quantify the initial fabric and to describe the fabric evolution during shear deformation. The following were the key objectives of the research:

1. To develop a methodology to obtain tested samples of sand representing different stages of shearing for subsequent imaging.
2. To carry out an evaluation of various laboratory X-ray micro-CT systems that are commercially available. To investigate the optimal scanning parameters such as image size and image resolution, considering such factors as image quality, cost and time, together with computational limitations.
3. To develop an understanding of the tools available for processing the tomographic images so that an image with meaningful features for subsequent image analysis can be produced.
4. To develop, implement and validate a series of algorithms to quantify particle morphology and fabric using micro-CT data.
5. To analyse critically the statistical measurements of fabric and to evaluate the effectiveness of previously proposed fabric metrics to describe the fabric of real sands.
6. To correlate the macro-scale mechanical response with quantitative measurements of fabric.

1.3 Methodology

Figure 1.1 shows a schematic diagram of the methodology used in this study. The first task was to obtain block samples of the intact soil. Once the soil samples had been retrieved, cylindrical specimens were prepared for testing in the triaxial apparatus. Both intact and reconstituted specimens were used. For the intact specimens, the preparation process consisted of trimming small blocks of soil, cut from the large block samples, to a cylindrical shape 38mm in diameter and 76mm high. The reconstituted specimens were prepared using tamping and vibration with the aim of producing specimens that had similar densities to those of the intact material. The triaxial tests consisted of two main loading stages; an initial isotropic compression stage during which the cell pressure was increased to 300kPa and a subsequent shearing stage with an axial strain rate of 1%/hr. A number of repeated

equivalent tests were performed. Each test was stopped at a different pre-defined value of axial strain and the soil fabric was preserved by impregnation of the specimens with resin while they were in the triaxial cell. Once the resin had set, the specimens were removed from the cell. Small cylindrical cores were extracted from the triaxial specimens in order to be imaged using X-ray micro-CT.

The tomographic images obtained from the micro-CT scans were 3D image data comprising a series of 2D images (slices). In these images the internal structure of the soil was represented by voxels (the 3D equivalent of pixels); all the voxels associated with the sand grains had similar colour intensity value and were distinct from the voxels associated with the void space in the soil. Image processing was carried out to identify meaningful features in the 3D images, i.e., the individual grains and the void space. A series of algorithms was implemented in MATLAB to obtain data for the quantitative description of particle morphology and fabric. A parallel, complementary study was carried out to investigate the particle morphology and fabric qualitatively. In this parallel study, scanning electron microscopy was used to obtain pseudo-3D images to examine the intact specimens prior to testing. Moreover, thin sections were produced from the resin impregnated triaxial specimens and 2D images obtained using an optical microscope under cross-polarised light were analysed.

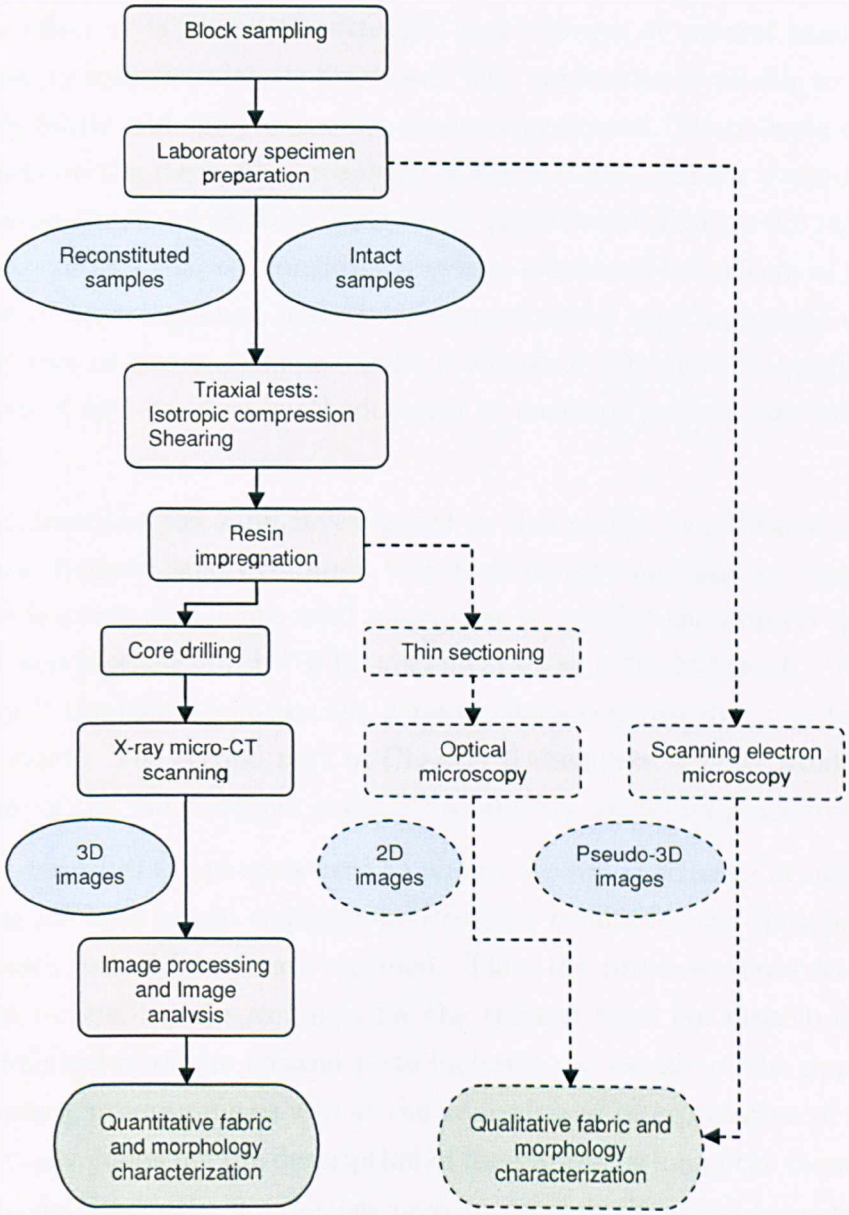

Figure 1.1: Flow chart of the methodology used in this study

1.4 Outline of the thesis

This thesis is organised into nine chapters. This chapter, Chapter 1, gives an introduction to the thesis topic as well as a description of the main objectives of the research.

Chapter 2 presents an overview of our current understanding of the fabric of granular soils. The effect of fabric on the strength and stiffness of natural sand formations and laboratory soil specimens is discussed. The approaches available to obtain data to quantify fabric and the parameters used are presented. Micro-scale observations of the effects on the mechanical response of the material and the evolution of fabric under loading are also described. Fabric and particle morphology are related and so the last part of this chapter considers previous studies of the effects of particle size and shape of coarse grained materials. Experimental and numerical evidence for the importance of size and shape on the mechanical behaviour of granular systems is summarised and previous methodologies to measure particle size and shape are discussed.

Chapter 3 describes the sand investigated in this study, i.e., Reigate sand. In its intact state, Reigate sand exhibits a very high density and has an interlocked fabric. These features of Reigate sand mean that it satisfies the criteria (proposed by Dusseault and Morgensten, 1979) for classification as a "locked sand". The first part of Chapter 3 therefore discusses the general characteristics that can be attributed to locked sands. The second part of Chapter 3 considers Reigate sand specifically; the geology of the sampling site is described and the sampling procedure is outlined

Chapter 4 describes the process used to obtain the soil specimens at different stages of shearing for later image acquisition. Previous results for the shearing behaviour of sands with locked fabrics are outlined. Then the processes used to prepare the intact and reconstituted specimens for the triaxial tests are described. The subsequent description of the triaxial tests includes the details of the apparatus used and the testing programme as well as the analysis and interpretation of the data obtained. Finally, following the description of the impregnation of the tested specimens with resin, details on the approaches used to prepare the small cores for micro-CT scanning and the thin-sections for imaging using optical microscopy, are described.

X-ray micro-CT was used in this study to obtain 3D images of the resin impregnated sand specimens. Chapter 5 introduces X-ray micro-CT imaging techniques from a geotechnical perspective. A brief introduction to the fundamentals of computed tomography is presented. This is followed by a description of the characteristics of modern micro-CT systems including laboratory systems and synchrotron sources. The scanning process is outlined, considering the data acquisition and placing emphasis on the importance of selecting the optimised scan parameters.

Chapter 6 considers the procedures that were used to process and analyse the tomographic images in order to obtain the particle morphologies and material fabric. The process is divided into two main parts. In the first part, the techniques used for image enhancement are discussed, then the image segmentation procedure used to identify the individual grains in the image is described. The second part of Chapter 6 is dedicated to the analysis of the processed images, which consists of the development and application of a series of algorithms that were implemented in MATLAB.

In Chapter 7 the results are presented from the analysis of particle morphology for 13 samples, including both intact and reconstituted samples at different stages of loading, are presented. The particle morphology characterisation is discussed both in terms of size and shape of the grains.

In Chapter 8 the results from fabric quantification of the 13 samples (the same samples analysed in Chapter 7), are presented. The measurements of fabric included both scalar quantities (void ratio, coordination number and contact index) and directional data (particle orientations, contact normal orientations, branch vector orientations and void orientations). The link between the micro-scale characteristics and the overall macro-scale response of the sand during shearing is also presented.

Finally, Chapter 9 presents a summary of the work developed in this study, the key observations and recommendations for future research.

Chapter 2

Review on soil fabric

2.1 Introduction

Sands are composed of discrete particles. When sands are subjected to external loads, the arrangements of the particles are modified as the particles move and rotate under the action of contact forces that transmit the applied load through the material. While there is plenty evidence of the effect of the particulate nature of the material on soil behaviour, e.g., the volume change upon shearing or liquefaction under cyclic loading, the geotechnical analysis of granular soils is carried out primarily using continuum approaches. A poor understanding on the physical particle-scale mechanisms governing soil deformations and the lack of reliable data for quantifying the arrangements of particles is inhibiting a more complete description of the behaviour of these materials.

There has been an awareness of the influence of fabric, i.e., the arrangement of the soil particles, on the macroscopic mechanical response for a long time. The ideas of Reynolds (1885), developed while walking on a wet sand beach, over the apparent whitening and drying up of the sand around his feet, laid down the base for the development of the stress-dilatancy theories, and although lacking in detail regarding the particle kinematics it was certainly a recognition of the micro-scale phenomena.

This chapter aims to present an overview of our current understanding of fabric of granular soils. While special attention is given to the effect of fabric on the strength and stiffness of natural sand formations, examples are presented that show a clear evidence of a directional dependence or anisotropy in the macro-material properties of laboratory soil specimens (primarily considering strength and stiffness). To comprehend how fabric influences the macro-scale response and predict fabric evolution, an understanding the physical mechanisms mobilized in response to the applied external stresses is required. Given the difficulty of analysing the deformation of real soils

at the particle scale, most of our understanding of the link between particle interactions and the macro-scale response comes either from discrete element modelling (DEM) or two-dimensional physical models, often using photoelastic materials.

The load-deformation response of a particulate material is related to the spatial distribution of its particles and the pore space (i.e., the fabric), as well as the load displacement behaviour at the inter-particle contacts. In the most general sense the fabric of a granular material is a measure of the internal "topology", i.e., the arrangements of the particles, the orientation of the contacts, the shape and orientation of the voids. Therefore those quantities are of primary importance in the definition of parameters to quantify fabric. In addition to the geometrical arrangements inside a granular medium, the size and shape of the particles play a key role on the overall behaviour. Evidence of the effects of particle morphology on the response of soil and methodologies to measure and quantify these quantities are presented in the Section 2.8. It is important to recognize that the deformation response of a soil is determined by both the fabric and the load-displacement response at the contacts, but in this study it is restricted to fabric analysis.

2.2 Fabric definition

The term *fabric* refers to the arrangements of particles, particle groups and pore spaces in the soil (Mitchell and Soga, 2005). Figure 2.1 presents a graphical representation of two soil specimens at the same relative density and identical particle shapes but exhibiting different particle arrangements, i.e., different fabrics.

The terms "fabric" and "structure" are often used in an interchangeable way. Referring once more to Mitchell and Soga (2005), structure is considered to account for the combined effects of fabric, composition and interparticle forces (including bonding) on the soil response. In a broader context, in this study it is the micro-structure that is considered, and the above definitions relate to the micro-structure. The macro-structure incorporates larger scale sedimentary features like stratification, bedding and bioturbation (Berg, 1986). Structure in soils arrives as a result of geological history and depends on either depositional or post-depositional mechanisms. In particular, the geological events occurring after deposition, such as a change in the chemical features of the natural pore water due to infiltration or weathering, which can provoke either bonding or destructuration of a soil as well as a change in its fabric. Bonding in sands typically takes the form of inter-particle cementing and can easily be identified by scanning electron microscope (SEM) or optical microscopy. Figure 2.2 shows a SEM image of Reigate sand, the sand investigated in this study, taken from a location where the soil has been stained by iron oxide, the cement can be observed between the grains.

Understanding the changes in fabric that occur over the geological history of a sand, i.e., diagenesis, can be very important when using reconstituted soil samples to reproduce the response of the intact soil. Some of the diagenetic phenomena cannot be reproduced in the laboratory, e.g., the development of a locked fabric as discussed in Chapter 3. This has lead to the differentiation or decomposition of fabric into depositional fabric and diagenetic fabric. Reconstituted sands will only have depositional fabric, while natural sands may have, besides depositional fabric, a diagenetic fabric.

2.3 Macro-scale evidence of fabric effects in sand

This section presents some experimental studies that provide evidence that the strength and stiffness of granular soils are anisotropic, i.e., they are dependent on the direction in which the soil is deformed relative to the material fabric. Anisotropy in soils has been differentiated as inherent and induced (Casagrande and Carrillo, 1944). The inherent anisotropy is the result of the depositional process and although the magnitude of the inherent anisotropy is very sensitive to the particle geometry, even spherical particles can develop anisotropy during deposition (Oda, 1972b). The induced anisotropy is associated with particle contact redistribution due to stresses applied to and strains induced in the soil. In addition, some authors (e.g., Barreto, 2009) have proposed that the term initial anisotropy should include the effect of the processes that have developed over the geological stress history of the deposit.

The main sources of anisotropy are related to the shape of particles, the shape of voids and the contact normal orientation (Oda et al., 1985). This section considers the effect of the soil fabric anisotropy on the mechanical behaviour of the soil. Subsequent sections (Sections 2.4 and 2.5) will deal with the measurement and quantification of the soil fabric and its anisotropy.

2.3.1 Influence of fabric on strength

The effects of fabric anisotropy on the response of reconstituted sands were demonstrated by Arthur and Menzies (1972) and Oda (1972b) by varying the orientation of the samples during particle deposition relative to the direction of subsequent loading. Figure 2.3 shows the stress:strain curves obtained from the cubical tests on a rounded sand carried out by Arthur and Menzies (1972). The authors found a difference of over 200% in the axial strains taken to reach a given stress ratio for sand specimens at the same void ratio and stress level. The results of biaxial tests on circular and elongated rods from Oda et al. (1982) demonstrated the influence of the particle geometry along with the variation of the orientation of deposition

to the direction of loading on the soil strength anisotropy. The specimen that was composed of almost circular rods (aspect ratio 1.1) is referred to as oval I and the specimen composed of more elongated particles (aspect ratio of 1.4) is referred to as oval II. The specimens were prepared with the major axis of the particles lying parallel to the bedding plane and bedding angles (θ) of 0°, 30°, 60° and 90° were used. Figure 2.4 shows the peak stress ratio (σ_1/σ_2) plotted against angle θ. Considering the particle geometry it can be seen that for the assembly of elongated particles the strength anisotropy is more pronounced. There is clear evidence of the effect of fabric anisotropy; the stress ratio at failure shows a maximum value for $\theta = 0°$, i.e., major principal stress perpendicular to the bedding plane and a much lower value for $\theta = 60°$.

Further evidence of the effect of soil fabric on the strength of sands can also be found in laboratory tests where samples of the same sand, with the same void ratio, were made using different specimen preparation methods. Samples prepared by moist tamping tend to have a higher strength than samples prepared by air pluviation (e.g., Ibrahim and Kagawa, 1991).

Although much of modern soil mechanics has been developed from studies on reconstituted soils, the effect of the fabric imparted during the geological depositional process and subsequent stress history of the soil cannot be investigated unless intact specimens are used. The effects of fabric on natural sands is reported by Ventouras and Coop (2009) who completed a series of triaxial compression tests carried out on intact and reconstituted samples of Thanet sand, a sand with no traces of either cementation or locked fabric. Higher peak stress-ratios were observed for the intact soil specimens in comparison with the reconstituted specimens. Additionally, the intact samples appeared to be slightly stiffer than the reconstituted samples at larger strains. Clear evidence of the effect of soil fabric in the response of sands is also demonstrated by triaxial tests on natural interlocked specimens of the Greensand Formation (e.g., Cuccovillo and Coop, 1997; Cresswell and Powrie, 2004). This natural locked sand is the central topic of this study and details relating to earlier studies using this material are given in Chapter 4.

2.3.2 Influence of fabric on stiffness

Experimental evidence of the effect of fabric anisotropy on soil stiffness, can be found in the results reported by Zdravkovic and Jardine (1997) for hollow cylinder tests on a quartzitic silt. The data presented showed that the non-linear stiffness characteristics of the soil are dependent on the stress path direction and the orientation of the major principal stress axis. The directional dependence of shear wave velocities on sand was investigated by Kuwano and Jardine (2002) on air pluviated Ham River sand under various effective stress states. Bender elements mounted on a triaxial

specimen were used to measure three types of shear waves, S_{vh} (vertically propagating horizontally polarised), S_{hh} (horizontally propagating horizontally polarised), and S_{hv} (horizontally propagating vertically polarised). Stiffness anisotropy was seen in freshly formed samples under isotropic confining stresses, reflecting their initially anisotropic (air-pluviated) fabrics as illustrated in Figure 2.5a. This anisotropy could, however, be accentuated or modified considerably by applying anisotropic effective stress conditions as shown in Figure 2.5b. By conducting similar experiments on specimens of pluviated Toyoura sand and specimens made of rice grains (with an aspect ratio 7:2), Wang and Mok (2008) showed that the inherent stiffness anisotropy is much more pronounced for specimens with elongated grains. Also using bender elements, Ventouras and Coop (2009) demonstrated in the triaxial tests on Thanet sand, mentioned earlier, that for large strains the intact soil samples were stiffer than the reconstituted samples.

2.4 Generation of data to quantify fabric

Obtaining experimental data to quantify the packing of sand grains and the evolution of packing during loading is a difficult task. Oda (1972b) carried out pioneering two-dimensional analyse using resin impregnated thin sections. This approach gave a useful insight into the understanding of soil fabric and was adopted by other researchers, e.g., Frost and Jang (2000). The time-consuming nature of the analysis and subjectivity of the results have been identified as limitations in using two-dimensional imaging techniques.

The use of artificial particles to simulate the response of sands, either in model tests using photoelastic particles or in numerical simulations, has made a significant contribution to our understanding of the link between particle scale mechanics and the overall response of a granular material. Recent developments in three-dimensional imaging technology, considering both image acquisition and image processing, have opened a wide range of possible insights into the internal features of a soil specimen. This section presents the main techniques used to obtain data for fabric quantification.

2.4.1 Imaging techniques

Optical microscopy techniques have been used extensively to provide measurements for fabric characterisation. The use of thin sections was reported by Oda (1972b) and Oda (1972c) while polished surfaces of resin impregnated samples were used by Jang (1997). Scanning electron microscopy (SEM) was also be used to provide two-dimensional images of soil (e.g., Alshibli and Alsaleh, 2004). When stereo-

graphic methods are used, two-dimensional images can be the base to extract three-dimensional quantities (e.g., Kanatani, 1984; Kuo, 1994).

Three-dimensional images of the internal structure of soil specimens can be obtained by invasive and non-invasive techniques. Non-invasive techniques include X-ray Computed Tomography (CT) (e.g., Desrues et al., 1996; Otani et al., 2000) and Magnetic Resonance Imaging (MRI) (e.g., Oda and Iwashita, 1999; Ng et al., 2002). The X-ray CT technique is described in detail in Chapter 5. The MRI technique makes use of the magnetic properties of hydrogen and its interaction with an external magnetic field to produce 3D images of the internal features of an object. For practical reasons the use of MRI is limited to the application of artificial particles containing mobile hydrogen molecules. Therefore, application to granular soils is only possible on specimens containing interstitial water. An example of an invasive technique to obtain 3D data is serial sectioning, e.g., Yang (2005). The technique consists of reconstructing a given sample to a 3D volume by stacking together a series of 2D images taken from a surface after successive removal of thin layers of material from the sample.

While three-dimensional images are able to provide much more information from the soil specimen, they also require sophisticated algorithms to interpret the images and extract measurements. This subject is discussed in more detail in Chapter 6 and is only mentioned here to justify the scarce availability of three-dimensional data until now. One example of an image analysis technique, is digital image correlation (DIC). DIC allows displacement and deformation fields to be measured based on the assessment of the spatial transformation between images taken at different moments in time (e.g., Hall et al., 2010; Rechenmacher et al., 2010). This technique can be applied to both 2D and 3D images.

2.4.2 Photoelasticity

When physical models of photoelastic sensitive disks are used, information about the internal stresses or force distributions through particle contacts can be obtained. In photoelastic stress analysis polarized light is passed through a loaded model and the stress fields are interpreted based on the interference fringes that result from the stress-induced optical anisotropy of the material. When polarized light traverses a photoelastic material, there is a polarization-sensitive phase shift (birefringence) in the material along the path of the light which depends on the stress level, Figure 2.6a shows the light and dark fringes formed on a single disk compressed at two contacts. The image was obtained by using a polarimeter as sketched in Figure 2.6b. While the analysis of a photoelastic assembly to generate data on the contact forces was very tedious prior to digital image analysis, and practically limited to 2D analysis, these experiments were key contributions in demonstrating the inhomogeneous nature

of stress transmission network and providing insights into the micro-mechanics of granular material response .

2.4.3 DEM

Since the publication of the distinct element algorithm for particulate materials by Cundall and Strack (1979) discrete element methods (DEM) have been gaining popularity as a numerical means to explore the mechanical behaviour of granular media at a particle scale. In DEM, granular materials are represented and modelled as ideal packing assemblies of rigid particles, e.g., discs, spheres, ellipsoids. Two-dimensional simulations (e.g., Rothenburg and Bathurst, 1989; Nouguier-Lehon et al., 2003) and three-dimensional simulations (e.g., Thornton, 2000; Ng, 2009; Yimsiri and Soga, 2010) can be carried out and information on the particle interactions and contact forces can be obtained. Although ideal packing assemblies cannot fully represent real soil specimens, the development of DEM is highly significant as it provides data on micro-mechanical quantities and parameters that cannot be easily obtained from experimental tests or conventional continuum analyses of granular soils. This is demonstrated by the considerable number of DEM studies referenced in this study. Referring to O'Sullivan (2010), DEM provides us with a tool to develop hypotheses on the particle scale mechanics that drive the overall material response. Models created using DEM are, however, highly idealised.

2.5 Quantifying fabric

2.5.1 Scalar quantities

(a) Void ratio

The void ratio is the most basic measure of fabric and has been traditionally used to quantify the packing density of a granular medium. The void ratio (e) is defined as ratio of the volume of the voids (V_v) to the volume of the solid particles (V_s), as indicated by the following equation:

$$e = \frac{V_v}{V_s} \tag{2.1}$$

Spatial variation of the void ratio can be quantified by considering the distribution map of e within the specimen. This distribution map can be used to describe the specimen heterogeneity and identify localisations during sample deformation. The local void ratio distribution, can be obtained by dividing the image into polygons

that connect the centres of gravity of the soil particles as illustrated in Figure 2.7 (e.g., Kuo, 1994; Li et al., 2005; Yang, 2005).

(b) Coordination Number

The coordination number is a commonly used parameter in DEM and soil micromechanics to measure the packing density based on the average number of contacts per particle. The simplest definition of coordination number (CN) is given by:

$$CN = \frac{2N_c}{N_p} \tag{2.2}$$

where N_c is the number contacts and N_p is the number particles. The total number of contacts is multiplied by 2 as each contact is shared between two particles. Thornton (2000) proposed a modified definition based on the fact that particles that only have one or no contacts do not participate in the stress transmission. This alternative definition is called the mechanical coordination number and is defined by:

$$CN_m = \frac{2N_c - N_1}{N_p - N_0 - N_1} \tag{2.3}$$

where N_0 and N_1 are the number of particles with zero and one contact respectively. These particles are often termed "floaters" (O'Sullivan, 2010). Kuhn (1999) proposed an alternative definition of coordination number, called the effective coordination number, which excludes the particles that have less than two contacts and consequently do not participate in the load transmission framework. Another way of discriminating particles according to their roles in supporting the applied stresses was used by Oda (1977) by introducing what he called "unstable particles", which are particles that have a coordination number less than 4 and can therefore be easily rearranged during the process of deformation. A similar index for quantifying the contact intensity was used by Rothenburg and Bathurst (1989), who defined contact density (m_v) as:

$$m_v = \frac{2N_c}{V} \tag{2.4}$$

where V is the volume of the assembly of particles.

While for a uniform sized packing the average number of contacts is a good indicator of the packing density, for materials with a wide range of particle sizes, such as natural sands the effectiveness of this index is more ambiguous. An example on the influence of the particle size distribution of a granular assembly on its coordination number is given by Summersgill (2009). The author demonstrated that larger sized

particles are more likely to contribute to the stress transmission while smaller particles are often found in a loose or low stressed state. It is also intuitive that a larger particle can form contacts with many small particles which significantly increases its chance of having a high coordination number.

A number of different expressions relating the coordination number to the void ratio have been proposed based on experimental studies on spheres (e.g., Oda, 1977; Chang et al., 1989). A unique relationship between CN and e may only exist for regular packing of rigid and equal sized spheres, and consequently its application to real soil and even DEM packing are limited as it will clearly depend on the particle morphology, both shape and surface roughness, and the particle size distribution. For real sand specimens, Hasan and Alshibli (2010) proposed a different expression relating void ratio and coordination number, based on a regression line from a rather scattered plot of e against CN (as presented in Chapter 8).

The concept of coordination number is based on the assumption that the contacts are represented by a single point or by a very small contact area. This type of contact is, however, restricted to smooth convex particles. In fact, real sands may have rather large contact areas, in particular old sand formations, as demonstrated by previous soil fabric analyse using thin sections (e.g., Palmer and Barton, 1987; Al Asmar, 2006) and discussed in Chapter 8. Therefore, a measure of the contact intensity that considers the contact area may be more appropriate for non-punctual contacts. This consideration leads to the definition of a contact index proposed by Fonseca et al. (2010) as follows:

$$CI = \frac{1}{N_P} \sum_{i=1}^{Np} \frac{1}{Sp_i} \sum_{j=i}^{Nc,i} Sc_j \tag{2.5}$$

where N_P is the number of particles in the assembly, Sp_i is the surface area of particle i, Sc_j is the surface area of the contact j and $N_{c,i}$ is the number of contacts involving particle i.

2.5.2 Statistical analysis of directional data

Oda (1977) introduced the term "orientation fabric" to refer to the magnitude and orientation of the preferred orientation of the major axes of the particles and "packing" to consider the contact normals. In order to describe fabric, Oda et al. (1985) proposed three types of anisotropy considering the distribution of the contact normal orientations, the shapes and orientations of particles and the shape and orientations of the voids.

A schematic diagram in Figure 2.8 illustrates the vector describing the orientation of the contact normal, the orientation of the vector connecting the centroids of contact-

ing particles and the long axis orientation of the particles. The vector connecting the centroids of contacting particles is called the branch vector. Other, less commonly used vectors that can quantify the fabric include the doublet vector and the void vector. The doublet vector is defined as the vector connecting the centroids of a given particle and its nearest neighbours (Christoffersen et al., 1981; Wang et al., 2001). An example of a doublet vector is illustrated in Figure 2.9a. The definition of the nearest particles in a 3D analysis is, however, ambiguous and a cut off distance must be defined. Referring to the void cell systems for granular materials proposed by Li and Li (2009), presented in Figure 2.10, the void vector is defined to be the vector connecting the centre of each void cell to the contacts along the edge of that void cell. These geometrical considerations are, however, of rather complex application to specimens of real sand grains with a diverse range of sizes and shapes.

This orientation data usually comprises a large dataset of vectors, so it must be statistically analysed in order to provide meaningful measures of its distribution. Two approaches can be used to quantify fabric, the fitting of curves to histograms or rose diagrams and the fabric tensor approach. Both approaches are described in the following paragraphs.

(a) Histograms and curve fitting approaches

For a given set of vectors, an effective way to visualise its distribution is by creating histograms or rose diagrams. In these plots the vectors are "binned" into an interval of selected size and represented as a segment whose length is proportional to the number of contacts orientated within the angle defining the bin limits. Figure 2.11a and 2.11b show examples of plots of the 2D vectors. A 3D example of a plot of the contact normal distribution is presented in Figure 2.12.

These plots alone, give only a qualitative description of fabric orientations, and a measure of the preferred orientation of these vectors can be obtained by fitting a probability density function (PDF) $E(n)$ to the data. The PDF function expresses the likelihood that an orientation can be described by a unit vector n. The integral of this function over the domain must be 1, as follows:

$$\int_{\Omega} E(n)\, d\Omega = 1 \tag{2.6}$$

where $d\Omega$ is the differential solid angle in a spherical coordinate system. For a two-dimensional system, Rothenburg and Bathurst (1989) proposed a representation of the probability density function of the contact normal distribution as a Fourier series, as follows:

$$E(\theta) = \frac{1}{2\pi}\{1 + acos2(\theta - \theta_a)\} \tag{2.7}$$

where a is a parameter defining the magnitude of anisotropy and θ_a defines the direction of the fabric anisotropy or the principal fabric.

Barreto et al. (2008) described the procedure to obtain the parameters a and θ_a for a given dataset of contact normal orientation. Each vector is binned into an angular interval $\Delta\theta$, centred around an angle θ_i. The number of contacts in bin i is then given by $\Delta N_c(\theta_i)$ and is normalized by the product $N_c\Delta\theta$, where N_c is the total number of contacts. A discrete least squares approximation is then used to determine the parameters a and θ_a that best fit the following system of linear equations:

$$\frac{\Delta N_c(\theta_i)}{N_c\Delta\theta} = \frac{1}{2\pi}\{1 + acos2(\theta_i - \theta_a)\} \tag{2.8}$$

Figure 2.13a shows a comparison of this approach with the curve given by Equation 2.7. The θ_a values obtained give the major principal fabric direction for $a > 0$ and the minor principal fabric for $a < 0$. As was already mentioned the value of a relates to the degree of anisotropy and takes values between *0* and *1*. Figure 2.13b plots the distribution of the contact normals for diferring preferred orientations.

The Fourier analysis approach can also be applied to three-dimensional datasets. Figure 2.14 illustrates the geometry that must be considered in 3D. In the spherical coordinate system each vector is described in terms of two angles, γ (the zenith angle) and β (the azimuthal angle). Then the PDF can be rewritten as:

$$\int_0^{2\pi}\int_0^{\pi} E(\gamma,\beta)\, sin\gamma\, d\gamma d\beta = 1 \tag{2.9}$$

where $sin\gamma d\gamma d\beta$ is the differential solid angle, and the ranges of γ and β are $0 \leq \gamma \leq \pi$ and $0 \leq \beta \leq 2\pi$.

There have only been a few documented studies using this approach. Most authors using a Fourier series approach in 3D have restricted it to axi-symmetric systems. For example, Chang et al. (1989) considered a cross-anisotropic fabric with its axis of symmetry along z axis (as shown in Figure 2.14), then the function $E(\gamma,\beta)$ is given by:

$$E(\gamma,\beta) = \frac{3(1 + acos2\gamma)}{4\pi(3 - a)} \tag{2.10}$$

where a is the degree of fabric anisotropy, ranging between -1 and 1. This value controls the directional distribution of the contacts (i.e., positive values indicate a

vertical concentration and negative values a horizontal concentration).

(b) Fabric tensor

The fabric tensor is commonly used to describe the preferred orientation of a dataset of vectors and its associated intensity. It takes generally the form of a second order symmetric tensor. Following Satake (1982), the fabric tensor definition used here is:

$$\Phi_{ij} = \frac{1}{N}\sum_{k=1}^{N} n_i^k n_j^k \tag{2.11}$$

where N is the total number of vectors in the system and n_i^k is the unit orientation vector. Higher order fabric tensors can be determined (e.g., Kanatani, 1984), for example the fourth order fabric tensor is defined as following:

$$\Phi_{ijkl} = \frac{1}{N}\sum_{k=1}^{N} n_i^k n_j^k n_k^k n_l^k \tag{2.12}$$

The three-dimensional second rank fabric tensor can be expanded to give the following 3x3 matrix (assuming a Cartesian coordinate system):

$$\begin{bmatrix} \Phi_{xx} & \Phi_{xx} & \Phi_{xx} \\ \Phi_{yx} & \Phi_{yy} & \Phi_{yz} \\ \Phi_{zx} & \Phi_{zy} & \Phi_{zz} \end{bmatrix} = \frac{1}{N}\begin{bmatrix} \sum_1^{N_k} n_x^k n_x^k & \sum_1^{N_k} n_x^k n_y^k & \sum_1^{N} n_x^k n_z^k \\ \sum_1^{N_k} n_y^k n_x^k & \sum_1^{N_k} n_y^k n_y^k & \sum_1^{N} n_y^k n_z^k \\ \sum_1^{N_k} n_z^k n_x^k & \sum_1^{N_k} n_z^k n_y^k & \sum_1^{N} n_z^k n_z^k \end{bmatrix} \tag{2.13}$$

where N is the total number of vectors and n the unit orientation vector.

Referring to Figure 2.14, the probability density function $E(\gamma, \beta)$ can be related to the fabric tensor (Oda, 1972c; Satake, 1982; Rothenburg and Bathurst, 1989), as follows:

$$\Phi_{ij} = \int_0^{2\pi}\int_0^{2\pi} n_i n_j E(\gamma, \beta) sin\gamma d\gamma d\beta \tag{2.14}$$

where the unit vector n is related to the angles β and γ as:

$$n = \begin{pmatrix} sin\gamma cos\beta \\ sin\gamma sin\gamma \\ cos\gamma \end{pmatrix} \tag{2.15}$$

Equation 2.14 is equivalent to the definition of the fabric tensor proposed by Oda (1982) which gives:

$$\Phi_{ij} = \int_{\Omega} n_i n_j E(n) d\Omega \tag{2.16}$$

where n_i is the contact normal in direction i, $E(n)$ is the spatial probability function of n, Ω is the unit sphere and $d\Omega$ is the elementary solid angle.

Referring to Yimsiri and Soga (2010), in the case of axi-symmetric systems, if the distribution of orientation vectors is known, the anisotropy can be quantified by a single parameter a. This parameter can be calculated by equating the fabric tensor obtained using Equation 2.11 with the expression given in Equation 2.17.

$$\begin{bmatrix} \Phi_{xx} & \Phi_{xy} & \Phi_{xz} \\ \Phi_{yx} & \Phi_{yy} & \Phi_{yz} \\ \Phi_{zx} & \Phi_{zy} & \Phi_{zz} \end{bmatrix} = \begin{bmatrix} \frac{3a-5}{5(a-3)} & 0 & 0 \\ 0 & \frac{3a-5}{5(a-3)} & 0 \\ 0 & 0 & \frac{-(5+a)}{5(a-3)} \end{bmatrix} \tag{2.17}$$

Curray (1956), introduced the concept of vector magnitude (Δ) as an index to characterise the intensity of anisotropy of the particle orientations, defining Δ as follows:

$$\Delta = \frac{1}{2N_p}\sqrt{\left(\sum_{k=1}^{2N_p} cos2\alpha_k\right)^2 + \left(\sum_{k=1}^{2N_p} sin2\alpha_k\right)^2} \tag{2.18}$$

where the α_p is the inclination angle of the unit vector defining the orientation of the major axis of particle k measured relative to the horizontal axis and N_p is the number of particles. For an isotropic fabric $\Delta = 0$, and the value of Δ progressively increases with the concentration of the data orientation along a preferable direction up to $\Delta = 1$. The degree of anisotropy, for a transversely anisotropic soil ($\Phi_1 = \Phi_2$), is given by the following expression (Oda and Nakayama, 1989; Yang et al., 2008):

$$\begin{bmatrix} \Phi_{xx} & \Phi_{xy} & \Phi_{xz} \\ \Phi_{yx} & \Phi_{yy} & \Phi_{yz} \\ \Phi_{zx} & \Phi_{zy} & \Phi_{zz} \end{bmatrix} = \frac{1}{3+\Delta} \begin{bmatrix} 1+\Delta & 0 & 0 \\ 0 & 1+\Delta & 0 \\ 0 & 0 & 1-\Delta \end{bmatrix} \tag{2.19}$$

(c) Eigenvalue analysis of the fabric tensor

By analogy with the stress tensor, whose principal stresses and their orientations are given by eigenvalue analysis, information on the principal fabric parameters can also be obtained by eigenvalue decomposition of the fabric tensor (O'Sullivan, 2010). The eigenvectors of the fabric tensor give the orientations of the dominant directions of fabric anisotropy and the eigenvalues (Φ_1,Φ_2, Φ_3) indicate the magnitude or the bias in each of these three directions. Hence, the dominant orientation of the fabric is related to the largest eigenvalue and the corresponding eigenvector gives the direction of the principal fabric.

While it is accepted that the principal components of fabric, Φ_1,Φ_2 and Φ_3 can be used to describe the intensity of the anisotropy, different formulations have been proposed. The difference $\Phi_1 - \Phi_3$ has been adopted by some researchers, e.g., Thornton (2000), while others, e.g., Wan et al. (2005), used the ratio Φ_1/Φ_3. Both definitions of anisotropy are however limited as they neglect the intermediate fabric component (Φ_2) which for non axi-symmetric conditions differs from Φ_1 and Φ_3. Kuo et al. (1998) and Barreto et al. (2009) considered more general formulations to include the second fabric component (Φ_2). Barreto et al. (2009) used a definition of anisotropy or deviator fabric given by:

$$\Phi_d = \frac{1}{\sqrt{2}}\sqrt{(\Phi_1 - \Phi_2)^2 + (\Phi_2 - \Phi_3)^2 + (\Phi_3 - \Phi_1)^2} \tag{2.20}$$

On the basis that the three eigenvalues represent the degree of clustering about the respective eigenvectors, Woodcock (1977) proposed a useful graphical interpretation of the fabric orientation data. Woodcock's approach which has been considered by Ng (2001) and Barreto (2009), uses two fabric descriptors, namely the shape factor (K) and the strength factor (C). These parameters are defined by:

$$K = \frac{ln(S_1/S_2)}{ln(S_2/S_3)} \tag{2.21}$$

$$C = ln(S_1/S_3) \tag{2.22}$$

where the eigenvalues (Φ_1,Φ_2, Φ_3) are designated by (S_1,S_2, S_3). As illustrated in Figure 2.15 the $ln(S_2/S_3)$ values are plotted on the horizontal axis and $ln(S_1/S_2)$ is plotted on the vertical axis. In the case of an isotropic fabric the eigenvalue data are uniformly distributed and plots at the origin. Where the fabric is anisotropic the data plots further from the origin and the shape value (K) determines whether the distribution of orientations are a cluster or a girdle. The extent of the concentration of vectors in the preferred orientation is given by the strength factor (C). Axi-symmetric systems ($S_2 = S_3$) plot along the vertical axis.

(d) Fabric tensor for particle and void orientations

As stated earlier, the previous definition of fabric tensor can be applied to different directional vectors describing the soil packing including the orientation of the particle major axes (e.g., Dafalias et al., 2004; Ng, 2004). However this definition does not account for the shape of the particles. In fact, a particle whose intermediate axis length is only slightly bigger than its minor axis length would have the same contribution to the overall tensor as a particle whose intermediate axis length is

just smaller than its major axis length. A fabric tensor that considers both particle shape and particle orientation was introduced by Oda et al. (1985) and given by:

$$\Phi_{ij}^{particle} = \frac{1}{\lambda}\sum_{k=1}^{Np} T_{ki}^{p} T_{lj}^{p} S_{ij} \tag{2.23}$$

where N_p is the number of particles and T_{ij} is the orientation tensor for particle p that can be understood as follows. For a given point on the particle with coordinates x_i in a Cartesian coordinate system centred at the particle centroid, $x_j'^p = T_{ij}x_i^p$ gives the coordinates of the same point with reference to a local coordinate system centred on the particle centroid with axes aligned with the principal axes of inertia of the particle. The tensor S_{ij}^p is defined as:

$$S_{ij}^{p} = \begin{bmatrix} a^p & 0 & 0 \\ 0 & b^p & 0 \\ 0 & 0 & c^p \end{bmatrix} \tag{2.24}$$

where a^p, b^p, c^p are the major, intermediate and minor half lengths of the particle, respectively. The index λ can be calculated by $\lambda = \sum_{p=1}^{N_p}(a^p + b^p + c^p)$.

Identifying the void orientations in an objective manner is non-trivial. While in two dimensions, individual, closed voids can be identified, this is very rare in 3D. Even if a criterion to separate voids could be decided upon, the void geometries are very complex and difficult to describe. A void orientation fabric tensor was proposed by Oda et al. (1985) based on stereological principles. The two-dimensional approach consists of constructing a series of parallel scan lines through the image at an inclination angle θ, for θ values varying between 0° and 180°. At a given orientation θ, the contribution to the fabric tensor is given by:

$$\begin{bmatrix} l_v^\theta cos^2\theta & l_v^\theta cos\theta sin\theta \\ l_v^\theta cos\theta sin\theta & l_v^\theta sin^2\theta \end{bmatrix} \tag{2.25}$$

where l_v^θ is the total length of scan line obtained by measuring the number of pixels at orientation θ that intersect the void space, so that:

$$\int_0^{180} l_v^\theta d\theta = 1 \tag{2.26}$$

The void fabric tensor is obtained by summing the contribution of each orientation and the ratio of the major and minor fabrics ($\Phi_1^{void}/\Phi_3^{void}$) gives a measure of the void elongation. Stereological principles were also used by Kuo et al. (1998) to obtain a three-dimensional tensor that describes the anisotropy of the voids distribution based on images of thin sections of sands.

2.6 Micro-scale observations of fabric effects and its evolution

2.6.1 Force chains

Perhaps the most striking micro-scale observation of a granular material under external loading is the formation of the strong force chains aligned in the direction of the major principal stress as a consequence of the high heterogeneity of the stress transmission network through the medium. This phenomenon was first reported by means of photoelasticity studies (e.g., Drescher and Josselin De Jong, 1972; Oda et al., 1982). Figure 2.17a shows the stress transmission at the peak state from the experiments of Oda et al. (1982) on photoelastic rods. In the image the more stressed particles are represented as darker colours that form what Oda called the "columns". These chains of forces orientated in the direction of the major principal stress are closely related to the concentration of contact normals along this direction as demonstrated in the pioneering work of Biarez and Wiendieck (1963) who considered the biaxial compression of irregular disc assemblies. This study showed that the contact normals tend to concentrate towards the direction of compression and the distribution of contact normal orientations can be approximated by an ellipse, the orientation of the principal axes of which agree well with those of the principal stresses. As the major principal stress orientation changes from horizontal to the vertical, the major axis of the ellipse turns abruptly to the minor axis. Experimental evidence of the response of contact orientations to the applied stresses in real sands was provided by Oda (1972c) who made observations from thin sections of resin impregnated sands. Figure 2.18 illustrates the progressive orientation of contact normals towards the vertical, i.e., the direction of loading, by a series of rose diagrams along the stress-strain curve. As the axial deformation progresses, the contact normal orientations tend to concentrate around the axial direction (b, Figure 2.18), until a maximum concentration is observed when the peak stress is mobilized (c, Figure 2.18). After the peak, however, the strength of this concentration decreases even though the shear strain is still accumulating (d, Figure 2.18). Oda et al. (1980) described the distribution of the contact normal orientation as "fabric ellipsoid" and demonstrated that it is closely related to the stress ellipsoid. Oda (1972c) observed that the redistribution of the contact normals is restrained in specimens of flatter and elongated sand particles.

Rothenburg and Bathurst (1989) provided a graphical representation of the process both in terms of forces and contact normal distribution, for biaxial simulations of disks using DEM. The resultant contact normal can be visualised on the polar histograms introduced above. Initially, the assembly can be considered to be geometrically isotropic, given that there is no preferential orientation of the con-

tacts as can be seen in Figure 2.19a, hence $a = 0$ and $E(\theta) = 1/2\pi$. When the system is subjected to shear deformations, the contacts orientated along the direction of maximum tensile strain disintegrate more rapidly than contacts in other directions. Consequently, the distribution of contact orientations becomes markedly anisotropic. Figure 2.19b shows the distribution of the contact orientations at the peak stress ratio, with $a = 0.22$ and $E(\theta) \simeq \pi/2$. As can be seen, the anisotropy develops as a result of contact separation occurring along directions which are approximately orthogonal to the direction of the major principal stress. Rothenburg and Bathurst (1989) and Thornton (2000) observed that the normal contact force contributed more significantly to the deviatoric stress than the tangential contact forces, strengthening the evidence of the influence of force chains on the material response.

When one tries to link these micro-scale observations to the macro-scale response of a sand under shearing, the formation of force chains can be associated with the pre-peak strain hardening process and is seen as the major contribution to the induced anisotropy in the specimen. The buckling of the strong force chains has been seen as the key mechanism underlying failure and shear band development in granular materials. This hypothesis has been supported by both DEM simulations (e.g., Iwashita and Oda, 2000; Tordesillas and Walsh, 2002) and by experiments on real sands (e.g., Oda and Kazama, 1998). According to these studies, the buckling occurs with a further increase in axial load after peak as a consequence of the mechanical instability of the strong force chains that are laterally supported by a "weak network" of contacts orientated orthogonally to the major principal stress direction. The buckling process inevitably leads to a strain softening process as the strong force chains carry less stress. Buckling first takes place at random locations and directions but gradually concentrates into shear bands as illustrated in Figure 2.17b. Rechenmacher et al. (2010) applied two-dimensional digital image correlation (DIC) to images of a sand to characterize quantitatively the kinematic features involved on the force chain buckling. By observing the variation of strain in the shear band, the authors proposed that while in the strain softening regime there is a multi force chain buckling, the critical state appears to be governed by the growth and collapse of force chains. The buckling of strong force chains was also demonstrated by Hasan and Alshibli (2010) by identifying arch-like structures of contacting sand particles within a shear band on two-dimensional projections of micro-CT images.

The observations of the contact force network and its evolution in a granular material have given important insights into the understanding of failure in granular materials. Based on the "force chain" theory the soil strength is now thought to depend on the ability of the assembly to develop stable force chains.

2.6.2 Quantitative links between measures of fabric and macro-scale response

An early investigation of the use of fabric tensor eigenvalues to describe anisotropy was described by Oda et al. (1985) who considered photoelastic biaxial experiments on circular and elongated rod samples. The three tensorial quantities considered were the contact normal fabric tensor, the particle orientation fabric tensor and the void shape fabric tensor, whose major and minor eigenvalues are denoted by N_1 and N_2, S_1 and S_2 and V_1 and V_2, respectively. The anisotropy index proposed by Oda was based on the ratio between the major and minor eigenvalues, i.e., N_1/N_2, S_1/S_2 and V_1/V_2. Additional parameters used included the orientation angle for the eigenvectors of each fabric tensor denoted, α, β and γ for the contact normal, particle and void shape orientations respectively. The analyses considered three different specimen types, one made of elongated rods and prepared with the major axes of the particles oriented along the horizontal plane ($\theta = 0°$), specimen two made of elongated rods and prepared with $\theta = 60°$ and specimen three with circular rods and $\theta = 0°$.

The evolution of the anisotropy indices for the three specimens with axial strain (ε_1) are shown in Figure 2.20a, Figure 2.20b and Figure 2.20c for specimens one, two and three respectively. Considering the evolution of the contact normal fabric, the N_1/N_2 ratio curves show a shape similar to the stress ratio, i.e., there is an initial increase up to a maximum value that coincides with the point where the peak stress is mobilized. Oda et al. (1985) proposed that this strain hardening is due to the formation of load paths. After failure, there is a sharp decrease in the N_1/N_2 ratio, analogous to the strain softening as the sample deforms in an unstable manner in the post-peak regime. For the specimen with $\theta = 0°$ the principal fabric orientation is vertical i.e., $\alpha = 90°$, while the specimen with $\theta = 60°$ shows an initial major fabric orientation of $\alpha = 130°$ and this orientation tends to $\alpha = 90°$ as the deformation progresses.

Looking at the evolution of the fabric associated with the preferred orientation of the particles, round circular particles showed no anisotropy while the elongated particles exhibited an almost constant ratio up to failure and then a decrease afterwards. It was assumed that the inherent anisotropy due to particle orientation is preserved until failure of the specimen and therefore contributes to the strength anisotropy. However, according to Oda et al. (1985) the significant strength anisotropy due to the initial alignment of the elongated rods along the bedding plane direction seen in this ideal material is not likely to be observed in natural sands as the inherent soil fabric will be easily destroyed, as shown by for example, Oda (1972a). The major fabric orientation remains constant throughout the tests i.e., $\beta = 0°$ for $\theta = 0°$ and $\beta = 60°$ for $\theta = 60°$.

Considering the void shape, the inherent anisotropy seems to be rather small with values below 1.1. Although no other values have been suggested up to now, this result indicates that the voids tend to have random orientations and that the elongations and aspect ratios are approximately 1. As the deformation progresses, the ratio V_1/V_2 increases, reaching a maximum value at a large axial strain beyond the failure point. The major principal axes tend to orientate along the major principal stress direction, i.e., $\gamma = 90°$. Voids with an elongated shape develop along the direction of axial compression between the stronger force chains. Figure 2.21 illustrates the mechanism of the elongated voids. This structure, composed of particles aligned in an elliptic circle, was later recognized by Maeda et al. (1995) as a unit of micro-structure that can be used to examine mechanical properties of granular media such as deformation anisotropy, dilatancy and non-coaxiality. Maeda et al. (1995) analysed the stability of the chain of particles using shell theory and the theory of micropolar elasticity. The role of particle rotation on the overall deformation was reinforced.

The correlation between the second order fabric tensor (calculated considering the contact normal orientations) and the stress:strain response of the material has been confirmed in numerous DEM simulations. In particular, Rothenburg and Bathurst (1989), Thornton (2000) and Ng (2001), amongst others, have shown that the evolution with strain of the anisotropy calculated by considering the maximum and minimum eigenvalues of the second order fabric tensor correlates closely with the stress:strain response. Referring to the results from the axi-symmetric compression simulations of spherical particles carried out by Thornton (2000), a qualitative agreement can be observed between the evolution of the deviatoric stress, Figure 2.22a, and the evolution of the deviatoric fabric, Figure 2.22b. A similar correlation between the evolution of the principal fabric components and principal stress components, following the contact normal realignment along the axial direction at the loss of contacts in the radial direction, was also observed by Wan et al. (2005). Thornton and Zhang (2005), proposed a correlation between the 4th order fabric tensor (of the contact normal vectors) and the small strain stiffness. This correlation results, however, from mathematical considerations and requires further research. Despite the empirical character of these correlations they represent important insights into the use of parameters describing micro-scale features to reproduce macro-phenomenon of soil behaviour.

The ability of the fabric descriptors proposed by Woodcock, introduced in Section 2.5.2, to describe granular material response was presented by Ng (2001) for simulations of ellipsoids with various aspect ratios. The author found a good agreement between the strength parameter C for the contact normal vector (designated by β_1) and the principal stress ratio (σ_1/σ_3) , as shown in Figure 2.23, and suggested that this descriptor was a good parameter for modelling the behaviour of a granular

material.

DEM simulations have been used to investigate the ability of the coordination number to describe the material fabric by assessing its correlation with the void ratio. Rothenburg and Kruyt (2004) demonstrated by a series of biaxial compression tests that the relation between CN and e is influenced by the degree of anisotropy in contact orientation and so this relationship may not be unique. However, for shearing deformation at large strains, as the sample tends towards a critical state void ratio, a critical coordination number was also observed by Rothenburg and Bathurst (1989) , Thornton (2000) and Rothenburg and Kruyt (2004).

Sliding at the contact points will result in shape changes of the two neighbouring void cells and make a contribution to the macro-strains. The shape change of each void cell can be determined by the void vectors and the displacements at the corresponding contact points. The fabric tensor calculated using the orientations of void length vector was found to be a good index descriptor for dilatancy of granular materials (e.g., Li et al., 2005).

2.7 Fabric in continuum soil mechanics approaches

2.7.1 Critical State Soil Mechanics

Traditionally, accounting for the fabric in soil response, has been limited to the consideration of soil density. Casagrande (1936) introduced the notion of a critical void ratio to which dense samples would expand and loose samples contract as they were sheared. This concept of a critical void ratio as a property of soil was later developed to a critical void ratio line to account for the variation of the critical void ratio with stress (Roscoe et al., 1958). These early concepts lead to the development of the critical state soil mechanics framework in which the key concept is that upon prolonged shearing a soil will tend to an ultimate state where the stresses and volume remain constant. A "critical state locus" or critical state line can be identified, and plotted using axes of specific volume (v) against the logarithm of the mean effective stress and also in $p' : q$ space where q is the deviatoric stress. The mechanical response characteristics of a given soil are determined by the difference between the stress level and the specific volume of the soil at the start of shearing and the critical state. This difference can be quantified by the state parameter ψ, defined as the volumetric distance in terms of specific volume v (or void ratio e) of the current state of the soil from the critical state line (CSL) in the plot against v (or e) against the logarithm of the mean effective stress p'. This state parameter was originally proposed by Wroth and Bassett (1965), however its use in soil mechanics became more widespread following the work of Been and Jefferies (1985). The state

parameter could also be measured in terms of the mean stress distance from the critical state line which is broadly equivalent: one cuts a vertical line through the compression plane, the other cuts a horizontal line, as shown in Figure 2.24.

Referring to Muir Wood (2008) the state parameter is a kind of stress level dependent relative density that has, however, the potential to include other measurable parameters of the current fabric of the soil. The experiments carried out by Been and Jefferies (1985) on Kogyuk sand demonstrated the limitations of a state parameter defined only as a function of the soil void ratio. The samples were prepared to the same density using two different methods, moist tamping and wet pluviation, and subjected to equal confining pressures during the triaxial compression test. As can be seen in Figure 2.25 the difference in the behaviour exhibited by these two samples both in terms of deviator stress:strain curve and volumetric strain can only be attributed to the differences in the initial soil fabric.

2.7.2 Constitutive modelling

Much of our understanding of soil response has been developed using continuum approaches. The particulate nature of granular soils poses real challenges to constitutive modelling as the interactions between individual particles produce unexpectedly complex responses at the macroscopic scale. The fact that, for numerical analysis, continuum descriptions of soil behaviour are necessary, leads to what Muir Wood (2008) calls the particle-continuum duality for soil. Furthermore, as stated by O'Sullivan (2010), micro-scale analyses serve little purpose, and will have little impact on research or practise, if the particulate measurements are not interpreted or translated into continuum mechanics terminology.

While conventional constitutive modelling uses theories largely based in continuum mechanics, an alternative approach is to use the material fabric information to derive constitutive parameters and so account for grain scale mechanisms. This approach is called micro-mechanical continuum modelling or micro-structural continuum modelling (Chang, 1990 and O'Sullivan, 2010). On this basis, various models have been proposed to incorporate fabric measurements. Stress-dilatancy models that incorporate the fabric tensor of the contact normals, were developed by Wan and Guo (2001) and Wan et al. (2005). Oda and Nakayama (1989) formulated a model that considers the fabric tensor for the preferred orientation of the particles, as defined by Equation 2.19, and a good agreement was observed between the proposed yield function and the experimental results for Toyoura sand.

The effect of inherent fabric anisotropy due to preferred particle orientations, on the mechanical response of sands was also taken into consideration in the formulation of constitutive models by Masad and Muhunthan (2000), Dafalias et al. (2004), Abelev et al. (2007), and Yang et al. (2008). Muhunthan et al. (1996) extended the critical

state soil mechanics framework to include the effects of structure in natural soils by accounting for the porosity as a directional measure.

2.8 Particle morphology

Any attempt to describe the fabric of sands would be incomplete without the consideration of the particle morphology, i.e., the size and shape of the sand grains. This section reviews experimental and numerical evidence for the importance of size and shape of granular systems and examines previous methodologies used for their measurement.

It was not until very recently, with the developments in micro-tomography, that three-dimensional information of sand particles became available. However, the data still requires robust techniques for its analysis. In addition, a review of the available literature has revealed only a limited number of existing 3D indices for shape description.

The term form of a particle is considered by many authors to be more accurate to describe the overall shape of the particle as it allows a distinction from a broader definition of shape that also includes roughness and roundness, as shown in Figure 2.26. Roughness and roundness refer to the measure of the surface irregularities at a micro and macro-scale, respectively and they are not considered in this study.

Given the complexity of real granular systems, it is difficult to dissociate the effect of surface irregularities from the effect of form. DEM simulations have been found to provide useful insights into the effect of form by comparing the behaviour of circular or spherical grains with more elongated ones. More recent studies have refined this comparison by using clusters of spheres (e.g., Fu, 2005; Wang et al., 2007), as well as more unusual sand particle shapes such as locked sands (Harkness, 2009). To conclude, there is scope for a three-dimensional characterization of sand particles to provide DEM modellers with the information necessary to approximate the spherical and ellipsoidal particles to real morphologies (e.g., work done by Wang et al. (2007) using aggregates).

2.8.1 Influence of size and shape on macro scale response

Particle size

The assessment of particle size is the most basic soil characterisation; moreover, particle size is the main determinant of soil type. Particle size gradation greatly influences the overall packing and void ratio. The possible range of packing of soil particles is often related to the maximum and minimum void ratios, reflecting

the loosest and densest states respectively. Well graded soils have low void ratios compared with more uniform soils, because the smaller particles fill the large voids enclosed by large particles (Miura et al., 1997). In addition, the void ratio range ($e_{max} - e_{min}$), has been found to be dependent on the grain size distribution (Miura et al., 1997; Cubrinovski and Ishihara, 2002). Figure 2.27 shows that ($e_{max} - e_{min}$) decreases as d_{50} increases.

The distribution of particle sizes influences the soil response, for example at the same relative density a better graded soil may have a larger angle of internal friction (e.g., Holtz and Kovacs, 1981). In addition, previous studies have also suggested the effect of particle size in the compressibility of granular soils. Huffine and Bonilla (1962) showed that finer soils tend to be more compressible. Yamamuro and Wood (2004) demonstrated that soils with a wide range of particle sizes are likely to create a more compressible soil skeleton in comparison with soils with a narrower particle size distribution. The authors attributed this to the occurrence of unstable contacts formed by large-to-small-to-large (L-s-L) grains. As shown in Figure 2.28b these unstable contacts appear to be related to soil liquefaction while contacts formed by large-to-large (L-L) particles were associated with more stable responses (Figure 2.28a).

The properties and characteristic behaviour patterns of granular materials are most often related to the relative density D_R. This quantity indicates the relative position of the current void ratio (e) to the maximum and minimum void ratios, (e_{max}, e_{min}), and is given by:

$$D_R = \frac{e_{max} - e}{e_{max} - e_{min}} \times 100 \tag{2.27}$$

Particle shape

The influence of particle shape on the engineering properties of granular soils is widely reported in the literature. Santamarina and Cho (2004) highlighted the effect of deviations from smooth spherical shapes on the evolution of stress-induced anisotropy as well as the influence of angularity and roughness in decreasing the small-strain stiffness and increasing the large strain strength. Among others, Guo and Su (2007) demonstrated that angularity influences the shear resistance and dilatancy properties of sands. Clayton et al. (2006) attributed the significant differences in response of glass ballotini and Leighton buzzard sand during cyclic triaxial tests to the differences in particle geometry; in contrast to the sand specimens the stiffness of the assembly of ballotini did not degrade with increased cycles of loading.

The range of void ratios ($e_{max} - e_{min}$) tends to decrease with increasing sphericity and roundness (e.g., Cho et al., 2006) and when bulky particles are mixed with

platy ones, the effect is a significant increase in the void ratio accompanied by an increase in compressibility and reduced shear strength (e.g., Clayton et al., 2009). Cho et al. (2006) identified the effect of irregularly-shaped soil particles on micro-scale mechanisms responsible for the observed macro-scale response, e.g hindered rotation, slippage and the capacity for particle rearrangement and increased particle level dilation.

The observations by Rothenburg and Bathurst (1992) based on biaxial simulations using both circular and elliptical particles, showed that circular-shaped particles give much lower strengths than elliptical particles, and the authors suggested that more elongated shapes are better able to reproduce the strength-dilation properties of sands. This phenomenon can be understood by considering the effect that particle shape has on the geometry of the contacts between particles and consequently on the distribution of the stresses at the contact. In the case of disks and spheres, excessive rotation can occur because of their geometry; the branch vector and the contact normal are collinear. This inhibits the transfer of moments to the particles by the normal component of the contact force. For the ellipses and ellipsoids (and any soil particle) the branch vector and contact normal are not collinear, which contributes to a greater resistance to rotation. Contact geometry considerations can also be used to explain that because non-convex particles are more likely to develop a greater number of contacts per particle they will also exhibit higher strength and stiffness in comparison with convex particles, (e.g., O'Sullivan, 2010).

Peña et al. (2007) demonstrated by means of DEM simulations using 2D convex polygons that specimens formed of elongated polygons form a narrower shear band due to the constraints on movement and rotation and exhibit higher values of shear strength when compared to more regular polygons. Also using 2D DEM simulation, Nouguier-Lehon et al. (2003) pointed out the significant effect that the direction of loading relative to the direction of initial fabric has on specimens made of elongated particles. The authors claimed that when the loading direction is perpendicular to the direction of deposition, anisotropy evolves very gradually and a critical state cannot be observed, even for large strains.

2.8.2 Measurement tools

(a) Sieving

Particle size analysis of granular soils has been traditionally carried out by sieving. This method involves determining the percentage by mass of particles passing through sieves within predefined size intervals, according to the applicable standards (e.g., BS-410). The size of particles is therefore, described by a length corresponding to the dimension of the sieve that the particle passes through. The use of a single

value for particle size is, with exception of perfect spheres, an ambiguous description.

The particle size distribution (PSD) of a soil is presented as a curve on a semi logarithmic plot, the ordinates being the percentage by mass of particles smaller than the size given by the abscissa. Qualitative description of the PSD can be achieved by considering the shape of the PSD curve. For example, a flatter curve correspond to a soil with a larger range of particles and is described as *well graded*, while it is *poorly graded* if there are preferred size ranges within the soil, i.e., a uniform soil (Craig, 2002).

The PSD is often used to extract representative sizes. For example the median diameter or d_{50} is defined to be the sieve size such that 50% of the particles by weight pass through. Other sizes such as d_{60} and d_{10}, defined in a similar way, are used to calculate the coefficient of uniformity ($C_U = d_{60}/d_{10}$) that gives a measure of the uniformity of the grading of a soil i.e., its size range. The higher the value of C_U, the larger the range of particle sizes in the soil, for example, a well graded sand will have a C_U>5 to 10 (Mitchell and Soga, 2005).

Standard laboratory sieving analyses are time consuming, require a considerable amount of material and do not provide information about the variation in size between the sieve sizes (e.g., Joudi, 2008). Moreover, Taylor (2002) and Fernlund (1998) pointed out that any definition of size based upon sieves is ambiguous and incapable of providing three-dimensional information, as illustrated in Figure 2.29, sieving does not sufficiently distinguish different grain forms.

(b) Size and shape analysers

Recent developed laboratory instruments, known as size and shape analysers, (e.g., QICPIC (Sympatec) and Camsizer (Retsch)) provide particle size distribution and some shape parameters based on dynamic image analysis. The two-dimensional images are captured while the particles fall and pass between a specially configured light source and a pair of imaging lenses. The main positive aspects are that the analysis can be performed quickly and the shapes of randomly orientated particles that are captured overcome some of the limitations of static image analysis (e.g., particles in a flat surface tend to have a preferred orientation). The drawback is that the measurements are two-dimensional and the spatial resolution is limited.

(c) 2D imaging techniques

There are many available tools to obtain two-dimensional images. The most accessible tool is the use of a conventional digital camera as described in Fonseca and O'Sullivan (2008). Optical microscopy can be used on both thin sections and loose

grains, in addition some devices incorporate extended focus and a better approximation of a 3D view is possible. Scanning electron microscopy (SEM) images can be used to look at the grain surface at high magnification and so to investigate the roughness and the overall shape (e.g., Alshibli and Alsaleh, 2004). To measure the roughness of a surface white light interferometry can be used (e.g., Cavarretta, 2009).

(d) X-ray micro-tomography

High resolution computed tomography or micro-tomography is a powerful technique to obtain 3D images of internal features of a soil and so insights into its constituent particles can be gained. Details about this technique and the way measurements of particle size and shape can be obtained are described in detail in Chapter 5 and Chapter 7, respectively.

2.8.3 Size description

The Feret diameter (d_F) is defined as the distance between two parallel tangents to the particle outline, as illustrated in Figure 2.30. The Feret diameters d_{Fmax} and d_{Fmin} are respectively the largest and the smallest values of d_F for a given outline.

The effective diameter is an approximate particle diameter that can be used for comparison with the particle size from the sieve analysis. Different approaches to determine the effective diameter have been proposed as described here.

Al-Raoush (2007) presented an approach to determine the effective diameter of a particle based on the distance between the centre of gravity of the particle and the voxels on the boundary of the particle. The diameter of the particle is calculated as follows:

$$d_{effective} = 2\prod_{b=1}^{N_b}\left((\overline{x}-x^b)^2+(\overline{y}-y^b)^2+(\overline{z}-z^b)^2\right)^{1/2} \tag{2.28}$$

where N_b is the number of voxels defining the particle boundary and (x^b, y^b, z^b) are the coordinates of a voxel in the boundary. Figure 2.31 illustrates a simplified two-dimensional illustration of the approach. An alternative approach also presented by Al-Raoush (2007) to determine the effective diameter was to calculate the average of the major, intermediate and minor axis lengths, as follows:

$$d_{effective} = average(a, b, c) \tag{2.29}$$

Hasan and Alshibli (2010) used $d_{effective} = PIR(1+AR)$, where PIR is the particle inscribed radius, defined as the radius of the largest sphere that can be inscribed

inside the particle which represents the shortest axis of the particle, and AR is the aspect ratio, defined as $a/2PIR$

2.8.4 Shape description

Traditionally, the soil description has been done in qualitative terms using visual inspection to determine whether the soil is angular, sub-angular, rounded or sub-rounded. This classification has been helped by the use of standard charts against which individual grains could be compared to. An example is the chart proposed by Krumbein and Sloss (1963), as shown in Figure 2.33, which had great impact in the subsequent studies on shape.

Sphericity is commonly used to represent the geometrical proportions of the particle, i.e., form, and is given by the degree of similarity between a particle and a sphere. Roundness or angularity describes the shape of the particle at the scale of its surface features.

Most definitions of particle shape considered in the geomechanics literature to date, are given for two dimensions, e.g., ISO 9276. Two-dimensional shape descriptors are mainly obtained by measurements of projected areas and Feret diameters as described by Cavarretta (2009). Additionally, Fourier descriptors can give a quantitative description of particle shape (e.g., Bowman et al., 2001; Fonseca and O'Sullivan, 2008).

The widespread use of 2D image analysis techniques has greatly contributed to the establishment of methods for quantitative description of shape. Measuring particle shape from image data consists of an analysis of digital images, where each pixel is defined by the spatial coordinates (x, y) and by its intensity value. Many imaging instruments have their own commercial package software for image analysis, and the process consists of the application of a series of algorithms that allow the identification of individual grains in the image. Most shape descriptors require only the outline of each grain to be known (Figure 2.32). The automated process of these algorithms can make the analysis less accurate and sometimes manual corrections are needed. The main drawback of 2D image analysis techniques is that unless dynamic images are used the particles will be invariably imaged in their most stable positions, i.e., with their minor axes vertical.

(a) 3D shape descriptors

The limitations of a two-dimensional characterisation of three-dimensional soil particles is evident, for example a platy and a bulky particle with the same diameter cannot be differentiated unless a 3D description is used. Many of the three dimensional shape descriptors presented here are three-dimensional generalizations of

commonly used two-dimensional parameters. Some formulations are based on 3D image data where each voxel is represented by coordinates (x, y, z) with reference to a given coordinate system.

- **Aspect ratio**

A scalene ellipsoid is an ellipsoid that has three distinct principal axis lengths, designated as a, b and c. These lengths are defined so that $a > b > c$, and a, b and c are the major, intermediate and minor principal axes, respectively. The aspect ratio of the particle based on the three axis lengths is given by the elongation ratio and the flatness ratio:

$$\begin{aligned} elongation &= b/a \\ flatness &= c/b \end{aligned} \tag{2.30}$$

Zingg (1935) proposed a classification of particle form based on the relationship between the flatness and the elongation indices, as presented in Figure 2.34.

While this approach is useful for describing the shape of a regular ellipsoid, determining the true axes lengths for a real 3D sand particle is very challenging, and a variety of approaches have been used to describe shape in 3D. For example, Lin and Miller (2005) propose a methodology to obtain the three principal axes of a particle based on the analysis of moments. The central moment of the particle represented by its voxel coordinates (x,y,z) is defined as:

$$\mu_{p,q,r} = \sum_x \sum_y \sum_z (x - \bar{x})^p (y - \bar{y})^q (z - \bar{z})^r \tag{2.31}$$

where $(\bar{x},\bar{y},\bar{z})$ are the coordinates of the particle centroid. The principal moments of the particle are given by the eigenvalues of the matrix defined by Equation 2.32. These eigenvalues are correlated with the parameters a, b and c of the particle, but their values are only relative and they do not describe the real size of the particle.

$$\begin{bmatrix} \mu_{2,0,0} & -\mu_{1,1,0} & -\mu_{1,0,1} \\ -\mu_{1,1,0} & \mu_{0,2,0} & -\mu_{0,1,1} \\ -\mu_{1,0,1} & -\mu_{0,1,0} & \mu_{0,0,2} \end{bmatrix} \tag{2.32}$$

An alternative approach to determine representative a, b and c values was proposed by Al-Raoush (2007). The approach consists of calculating the eigenvectors of the inertia matrix defined in Equation 2.32, and taking the direction cosines of the rotation matrix. Using this rotation matrix, the particle can be rotated so that its principal axes become parallel to the Cartesian axes and the major, minor and

intermediate lengths of each particle can be computed by searching for the maximum and minimum positions of the rotated particle along the axis of the image.

Taylor (2002) proposed a graphical method of quantifying the shape of particles based on the representation of the second moment of the three principal axis on a Mohr's circle diagram. As illustrated in Figure 2.35 shapes that have three axis of symmetry degenerate to a point and all the other shapes can be approximated to a plate like shape for a≈b>>c, i.e., a measure of flatness (c/b) or a needle like shape when b≈c<<a , i.e., a measure of elongation (b/a).

- **Sphericity**

Sphericity describes how close a particle resembles a sphere or in other terms, it provides a measure of compactness. It was originally defined as S_{sphere}/S , where S is the particle surface area and S_{sphere} is the surface area of a sphere having the same volume as the particle (Wadell, 1932). The sphericity index can be defined as a function of the volume (V) and surface area (S) of the particle, as follows:

$$\psi = \frac{\sqrt[3]{36\pi V^2}}{S} \tag{2.33}$$

Assuming that the data available is a 3D image, and the coordinates of the voxels defining each individual particle are known, the volume and surface area for a given particle, can be determined by the sum of the total voxels and the sum of the exterior voxels representing the particles. Implementation of this idea is, as discussed in Chapter 6, non-trivial. Due to the difficulties associated with the determination of the particle surface areas, simplified formula derived from axis lengths have been proposed. Equation 2.34 gives two expressions to calculate sphericity as a function of a, b and c (Hayakawaa and Oguch, 2005). This approach has, however, limitations as it will not differentiate, for example, an elliptical particle from any other particle with an irregular shape with the same axis length.

$$\begin{gathered}(bc/a^2)^{1/3} \\ (c^2/ab)^{1/3}\end{gathered} \tag{2.34}$$

Al-Raoush (2007) presented a sphericity index as defined by:

$$sphericity = \frac{1}{N_b}\sum_{b=1}^{N_b}\left[\frac{d_b}{c} - \frac{d_b}{a}\right] \tag{2.35}$$

where N_b is the number of voxels defining the particle boundary, d_b is the diameter that originates from boundary voxel b and passes through the centroid of the particle, a and c are the major and minor lengths of the particle.

An alternative definition of sphericity based on the smallest dimension of a scalene ellipsoid with the same volume as a given particle has been proposed by Clayton et al. (2009) and given by Equation 2.36, where M_s is the mass of the specimen, n is the number of particles, G_s specific gravity:

$$SEES = \frac{c}{a} = \frac{(M_s/nG_S)(6/\pi ab)}{a} \tag{2.36}$$

- **Convexity**

The definition of a convex shape is that a straight line joining any two points within the object also remains within the object. When this condition is not satisfied the shape is concave, as illustrated in Figure 2.36 for 2D shapes.

Convexity (Cv) is another measure of compactness of a particle and in three dimensions it can be defined by Equation 2.37, where V_p is the volume of the particle and V_{CH} is the volume of the convex hull defined as the minimum convex volume containing all the points defining the particle, as shown in Figure 2.37.

$$Cv = \frac{V_P}{V_{CH}} \tag{2.37}$$

2.9 Concluding remarks

The overview on fabric presented in this chapter demonstrates the significant contribution given by DEM and photoelastic models to our understanding of the principles governing the micro-mechanics of granular materials. However, the simplifications and assumptions associated with both methods cannot be overlooked when the response of real soil is to be considered. For example, there are limitations associated with the use of circular shapes as well as the deformation characteristics of planar systems to reproduce the strength-dilation properties of sands, as highlighted by Rothenburg and Bathurst (1992). It can be concluded that a more realistic three-dimensional analysis of the morphology and fabric of real soil specimens is needed, for which recently developed imaging techniques such as micro-tomography together with advanced image analysis algorithms can certainly play a major role.

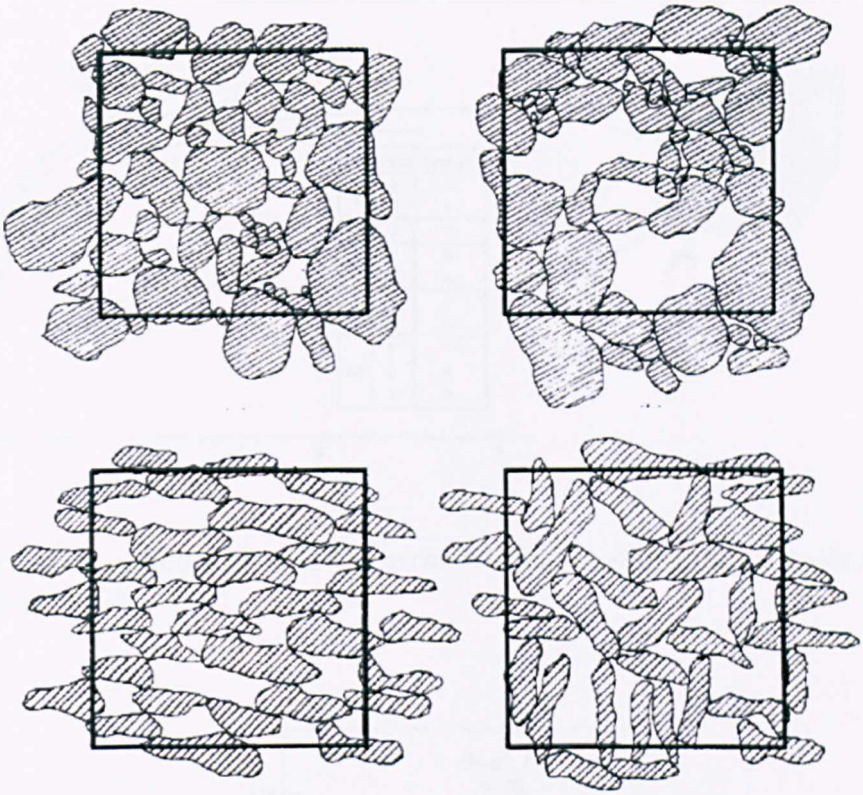

Figure 2.1: Illustration of possible different arrangements of identical particles at the same relative density (adapted from Kuo, 1994)

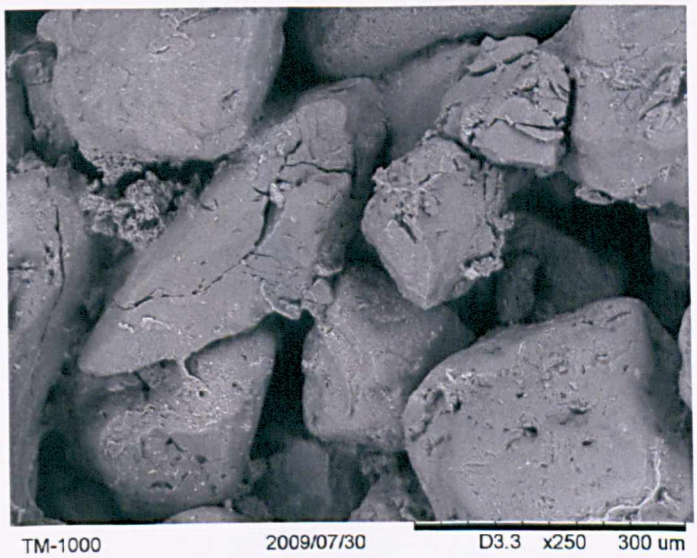

Figure 2.2: Finely dispersed coating of iron oxide on quartz grains of Reigate sand

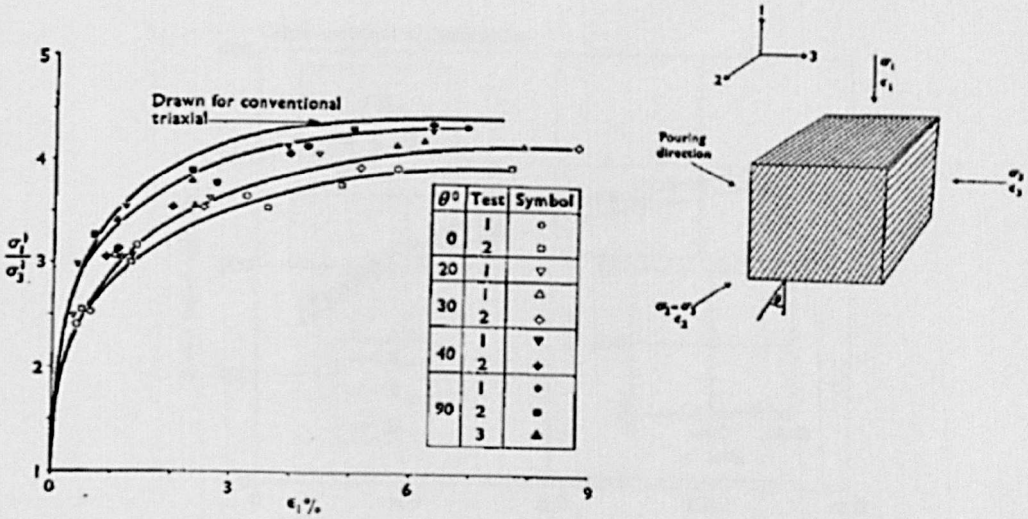

Figure 2.3: Effect of deposition on the stress:strain behaviour of sands (from Arthur and Menzies, 1972)

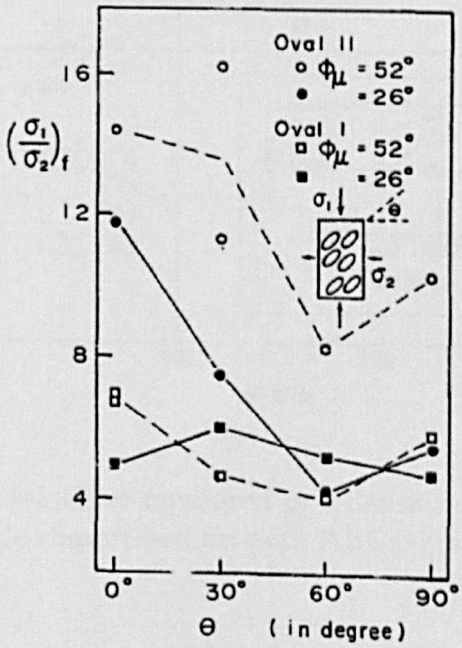

Figure 2.4: Plot of peak stress ratio against bedding plane angle (from Oda et al., 1982)

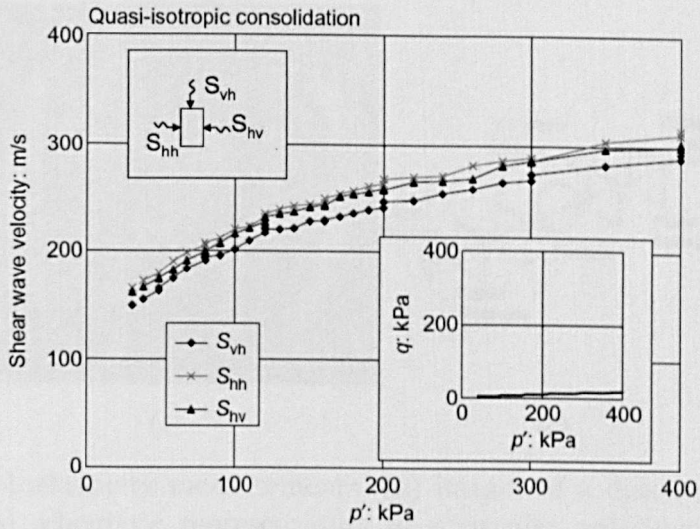

(a)

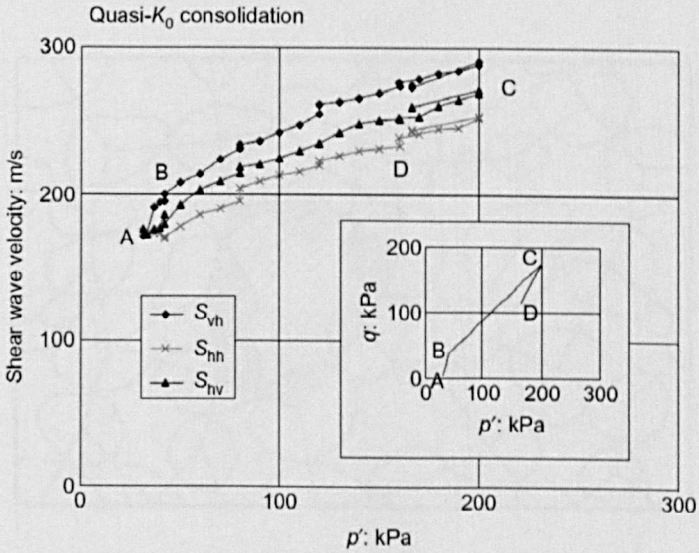

(b)

Figure 2.5: Shear wave velocities measured in a dense sand, (a) sample under isotropic stresses (b) sample compressed on path ABCD (modified after Kuwano and Jardine, 2002)

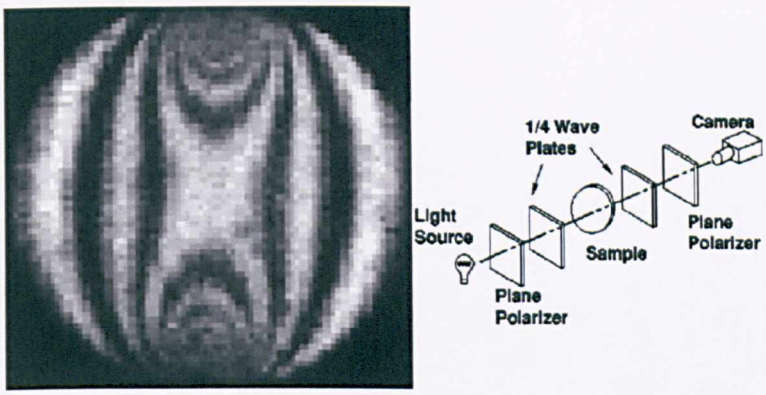

(a) (b)

Figure 2.6: Photoelasticity measurements, (a) images of a disk squeezed between two contacts (b) schematic representation of a circular polarimeter (Howell and Behringer, 1999)

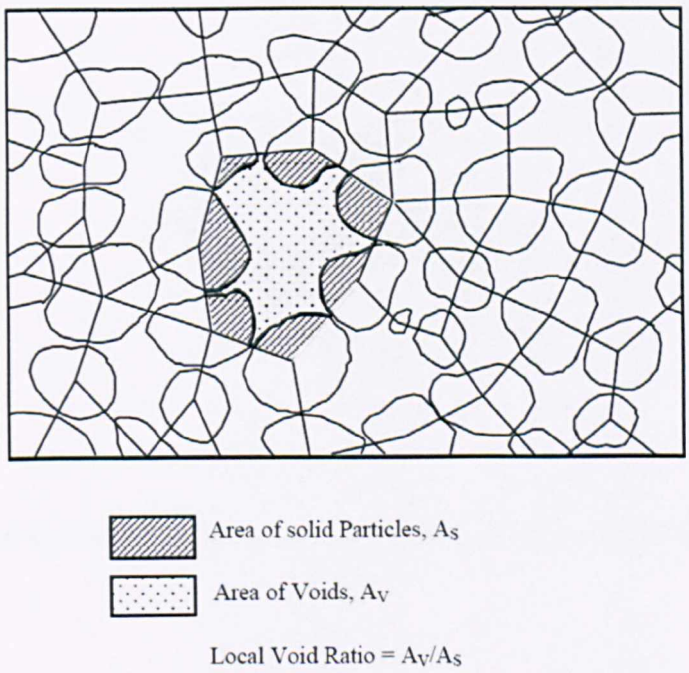

Figure 2.7: Determination of local void ratio distribution (from Yang, 2005)

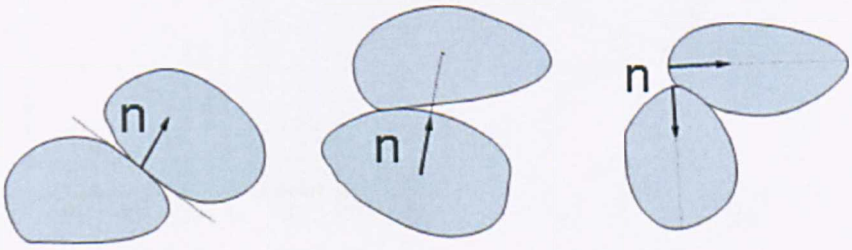

(a) (b) (c)

Figure 2.8: Schematic definition of directional data in a granular soil, (a) contact normal (b) branch vector (c) particle major axis orientation

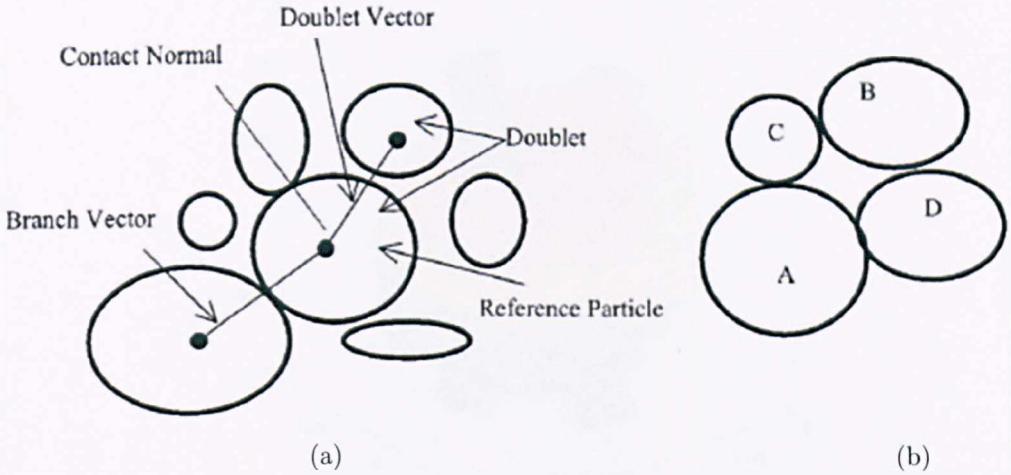

Figure 2.9: Schematic illustration of doublet vectors (a) nearest neighbour (b) particle interactions (after Wang et al., 2001)

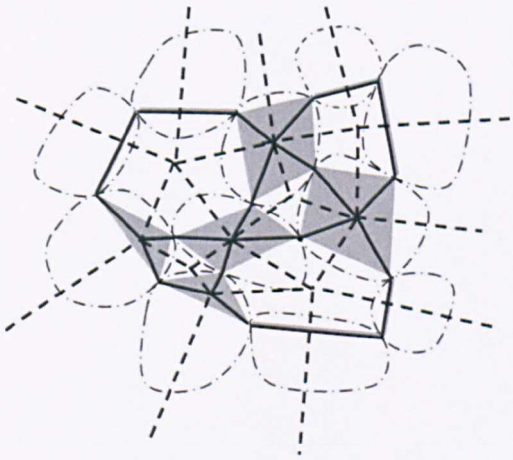

Figure 2.10: Void cell systems for granular materials proposed by Li and Li (2009)

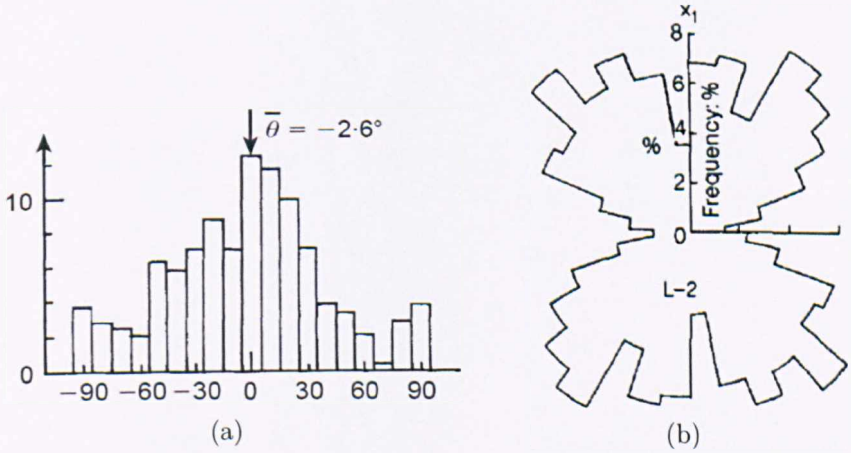

Figure 2.11: 2D orientation distribution plots, (a) distribution of the preferred orientation of particles from thin section analysis (Oda and Kazama, 1998) (b) density function of the contact normals (Oda et al., 1980)

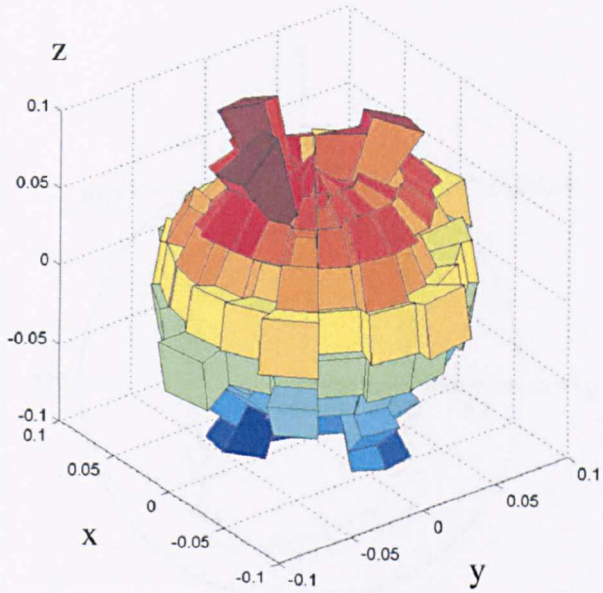

Figure 2.12: Distribution of the 3D contact normals (Wang and Mok, 2008)

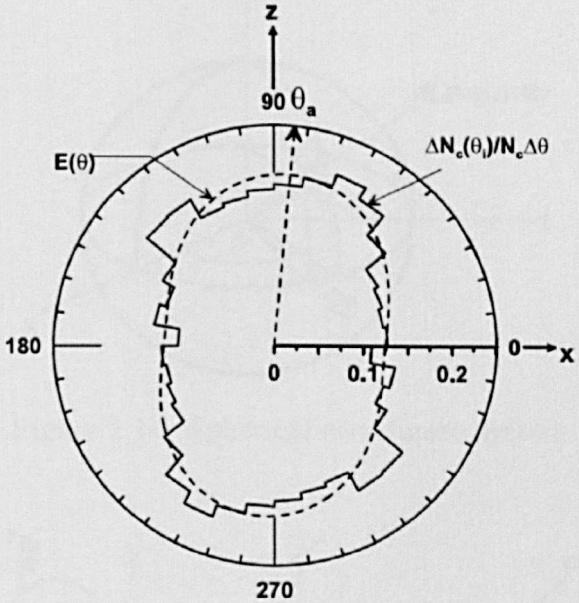

(a)

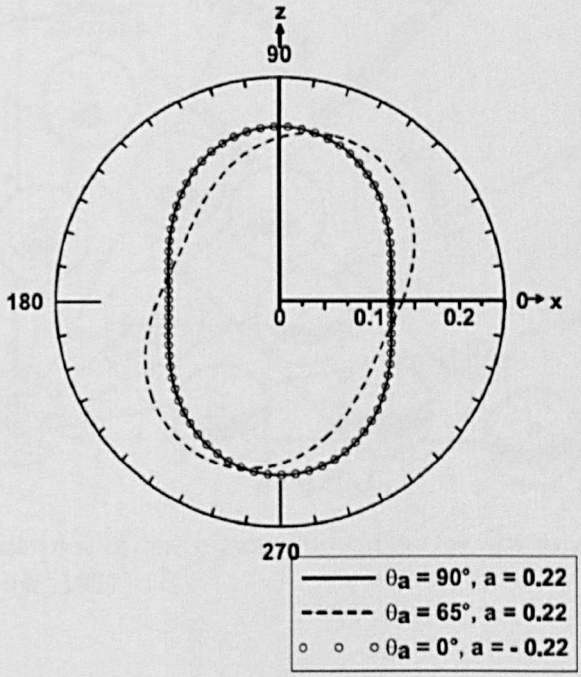

(b)

Figure 2.13: Distribution of contact normals from a DEM sample, (a) fitted Fourier series to the distribution (b) variation of the direction of anisotropy (Barreto et al., 2008)

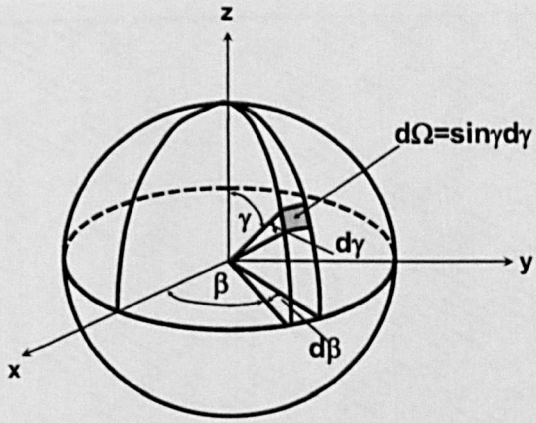

Figure 2.14: Spherical coordinate system

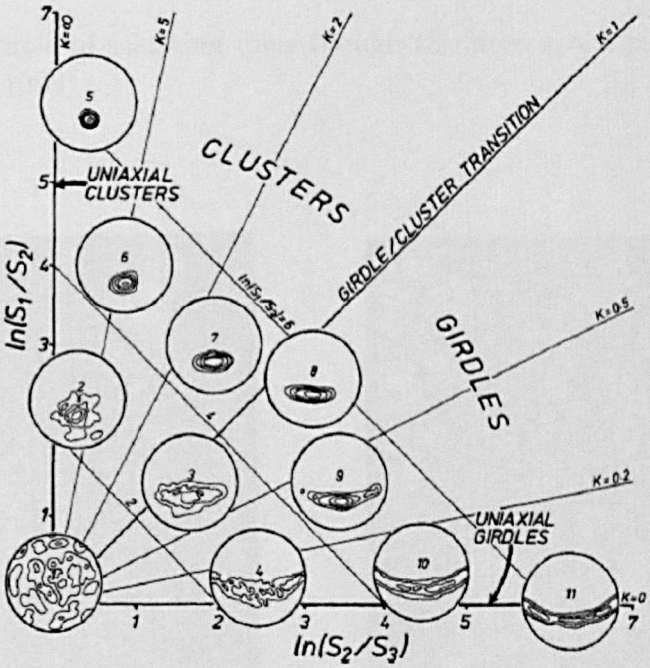

Figure 2.15: Two-axis plot of the eigenvalue ratios for shape analysis of the orientation data (Woodcock, 1977)

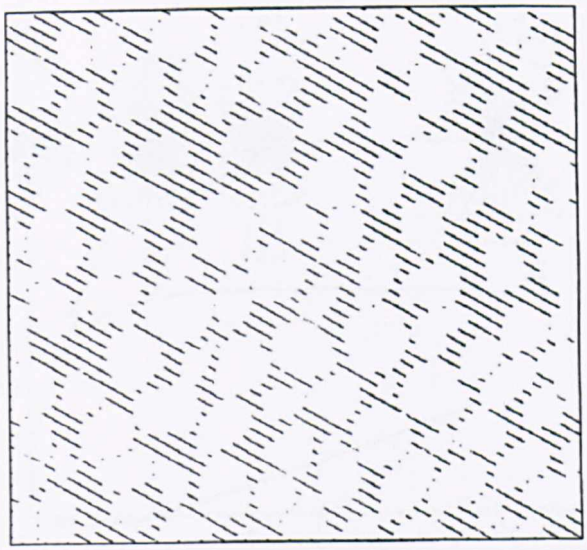

Figure 2.16: Example of scanning lines though the pore space in a given direction (from Kuo et al., 1998)

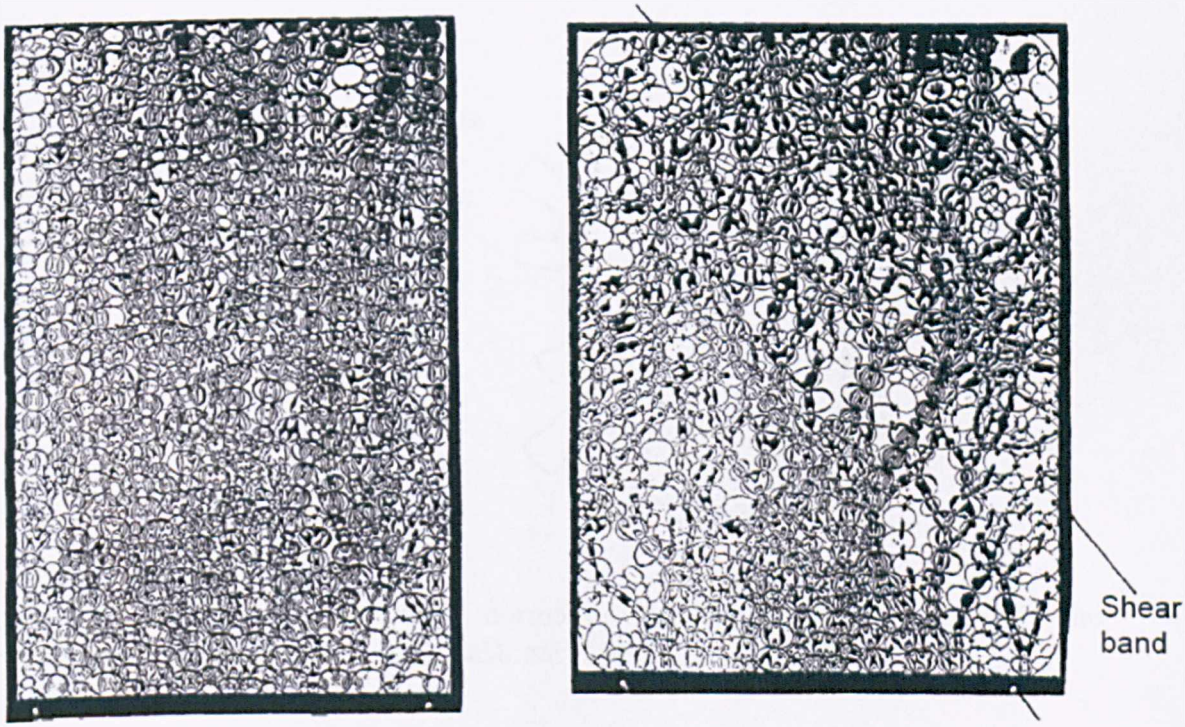

(a) (b)

Figure 2.17: Photoelastic pictures taken at (a) the peak state and (b) the residual stress state (from Oda and Kazama, 1998)

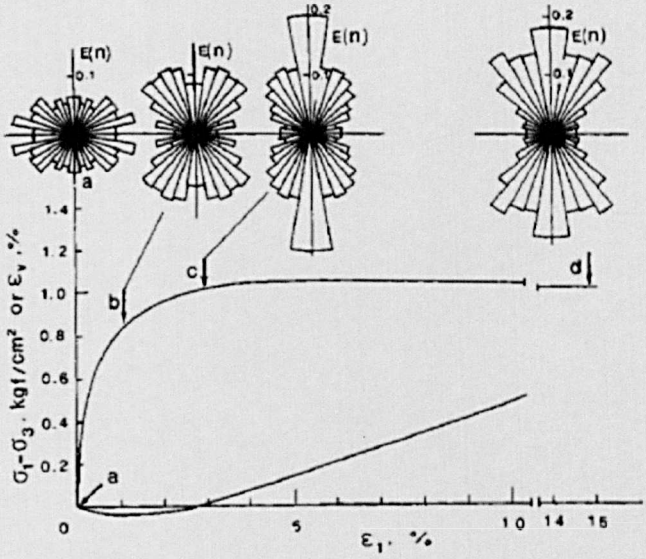

Figure 2.18: Progressive change of contact normal distribution in a triaxial compression test on sand (Oda, 1993)

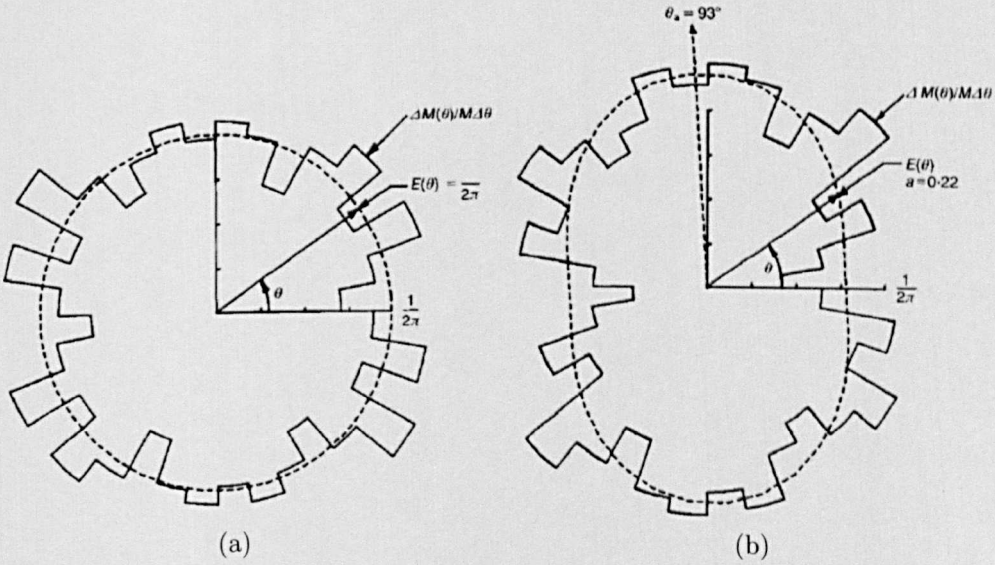

Figure 2.19: Distribution of contact normals at (a) the initial state (b) peak the stress ratio (from Rothenburg and Bathurst, 1989)

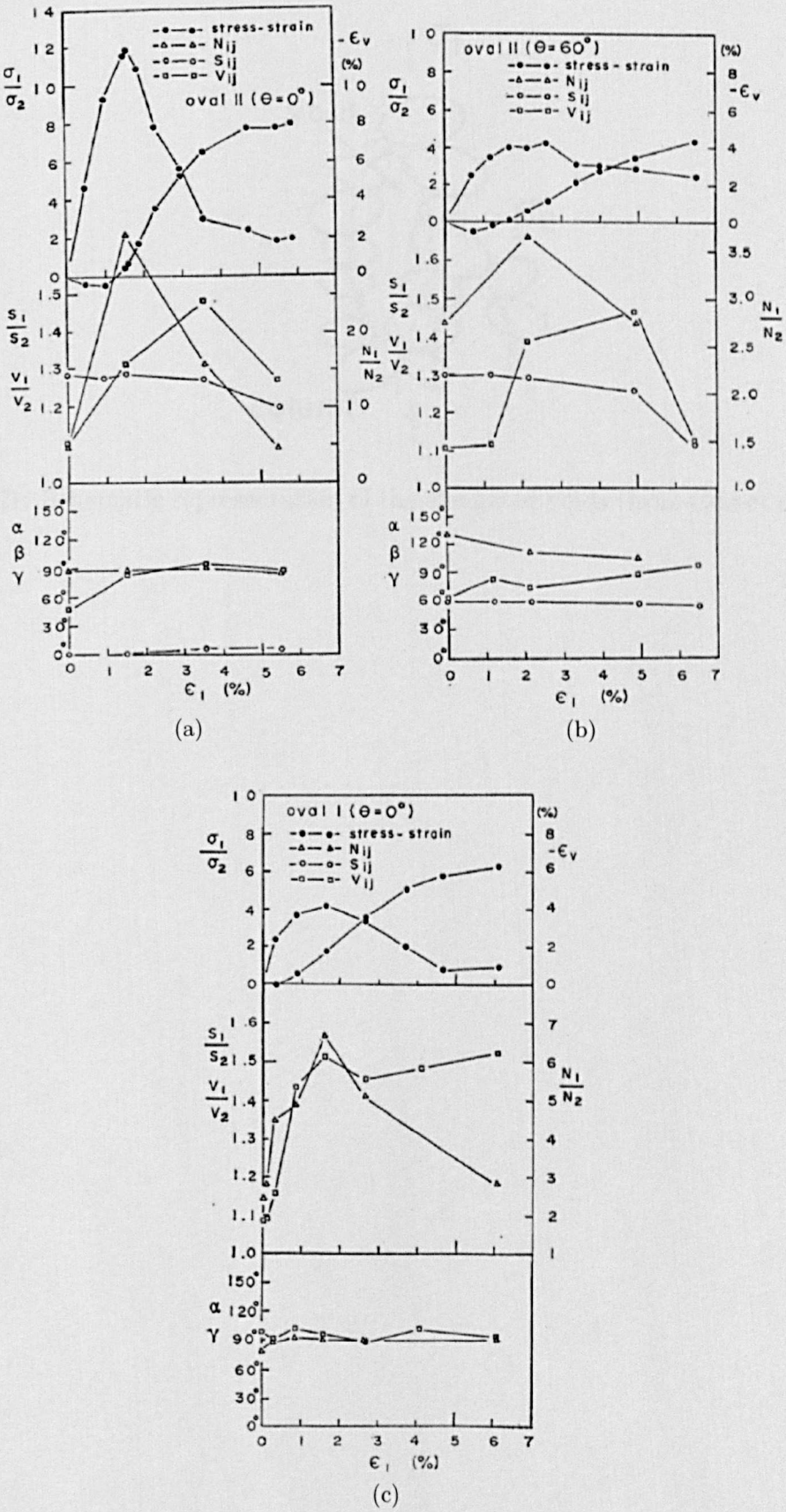

Figure 2.20: Fabric evolution during axial compression for (a) elongated rods, $\theta = 0°$ (b) elongated rods, $\theta = 60°$ (c) circular rods, $\theta = 0°$ (Oda et al., 1985)

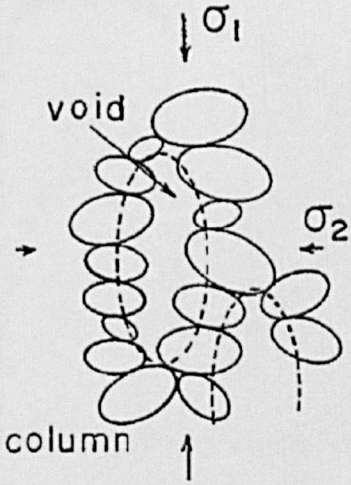

Figure 2.21: Schematic representation of the elongated voids (from Oda et al., 1985)

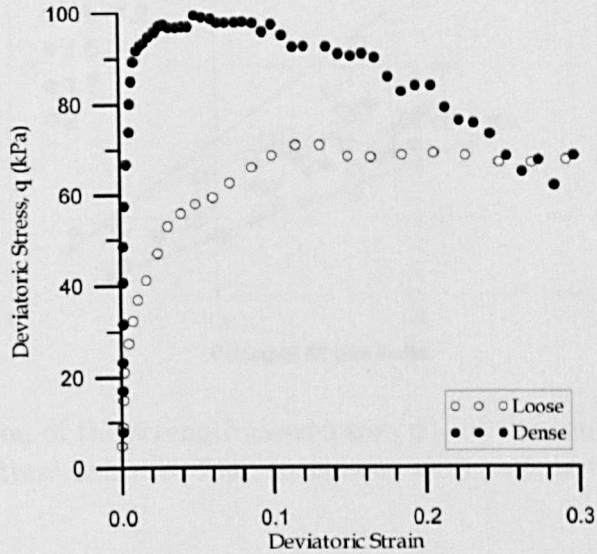

(a)

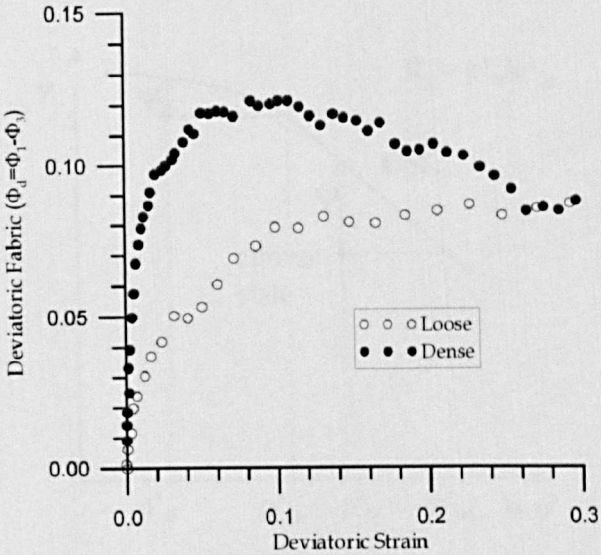

(b)

Figure 2.22: Evolution of the (a) deviatoric stress and (b) induced structural anisotropy, during axi-symmetric compression (Thornton, 2000)

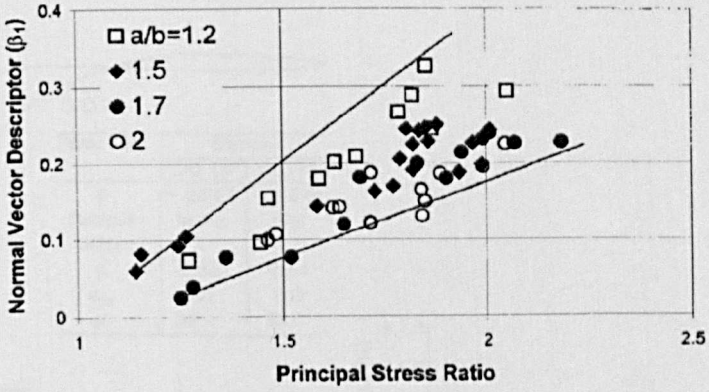

Figure 2.23: Evolution of the strength descriptor $(\beta)_1$ of the contact normal vectors with the principal stress ratio for four specimens with different aspect ratios (Ng, 2001)

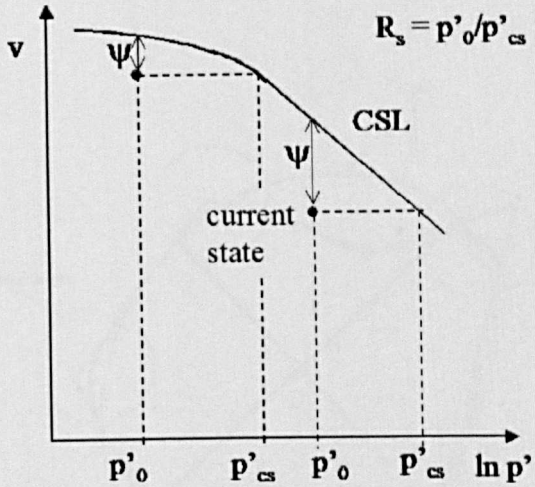

Figure 2.24: Definition of state parameters in v:ln(p') space (from Coop, 2005)

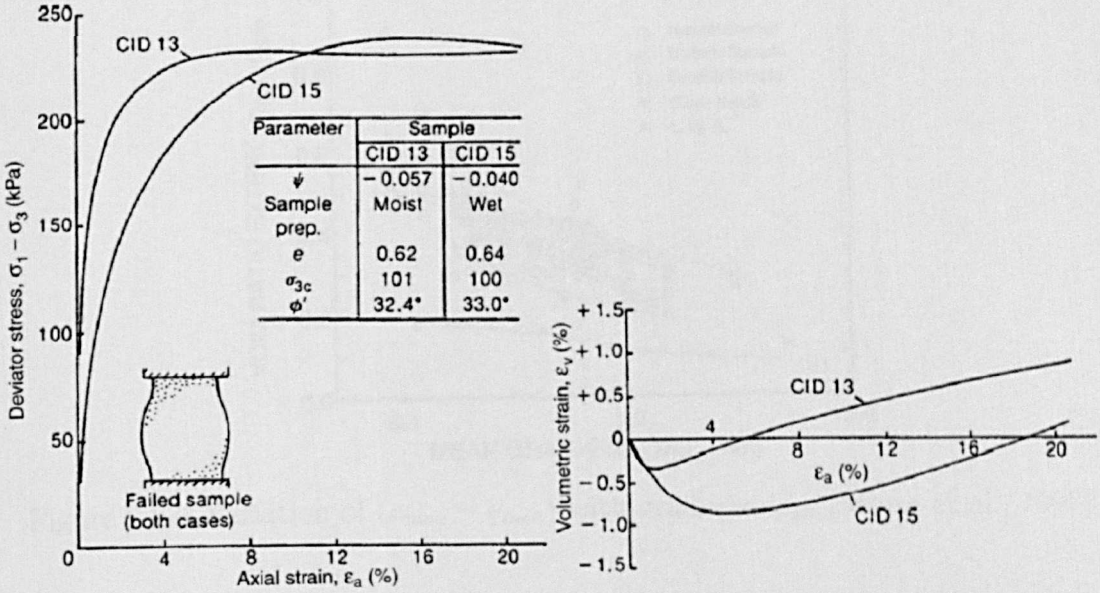

Figure 2.25: Effect of sample preparation on the behaviour of Kogyuk sand (from Been and Jefferies, 1985)

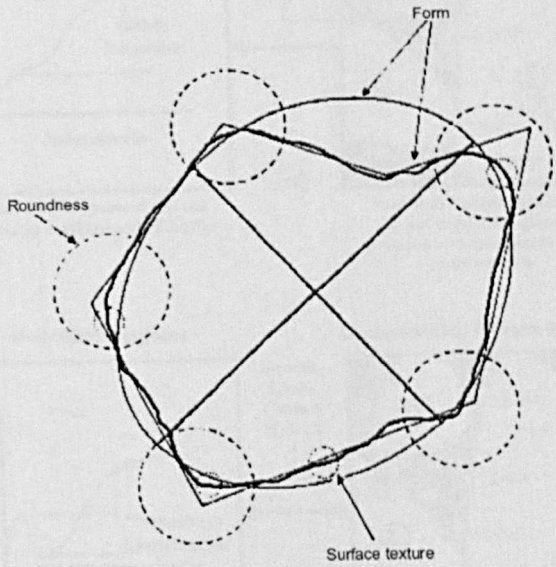

Figure 2.26: Particle shape terminology as defined by Barrett (1980)

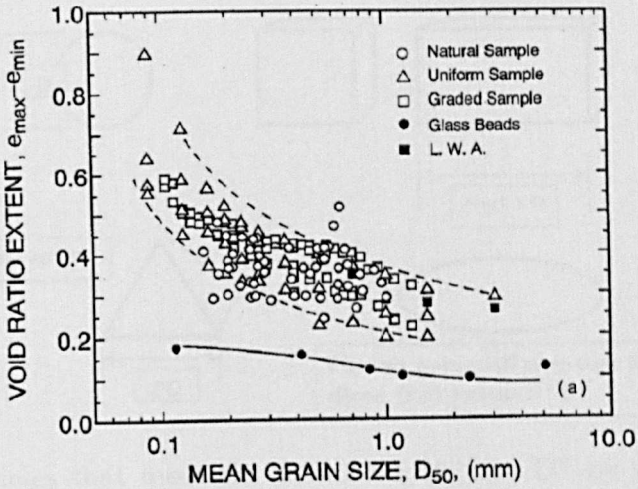

Figure 2.27: Variation of $(e_{max} - e_{min})$ with grain size d_{50} (Miura et al., 1997)

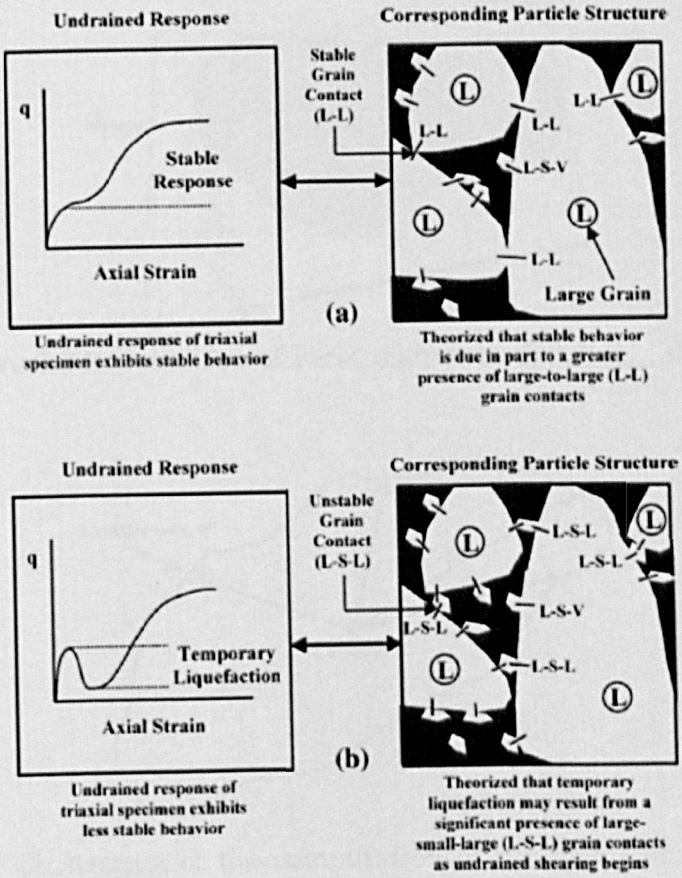

Figure 2.28: Proposed grain contact structures associated with different undrained shearing behaviour (Yamamuro and Wood, 2004)

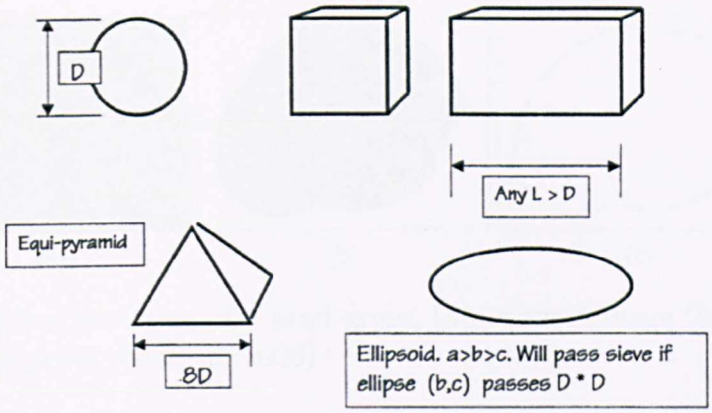

Figure 2.29: Particles that meet the definition of "size D" by sieving procedures (Taylor, 2002)

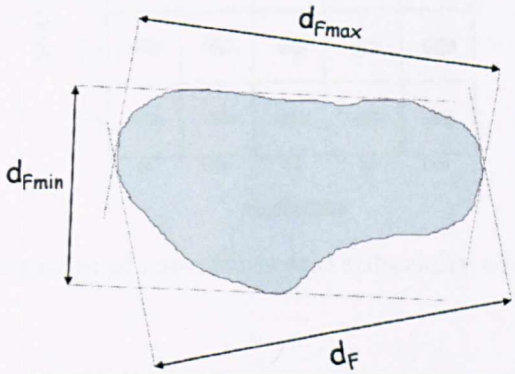

Figure 2.30: Definition of Feret diameters d_F, d_{Fmax}, d_{Fmin}

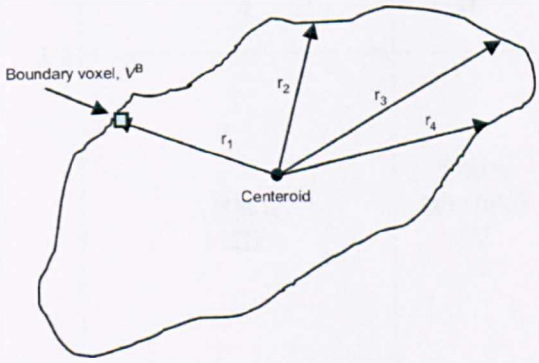

Figure 2.31: 2D illustration of the computation of the diameter of a particle (Al-Raoush, 2007)

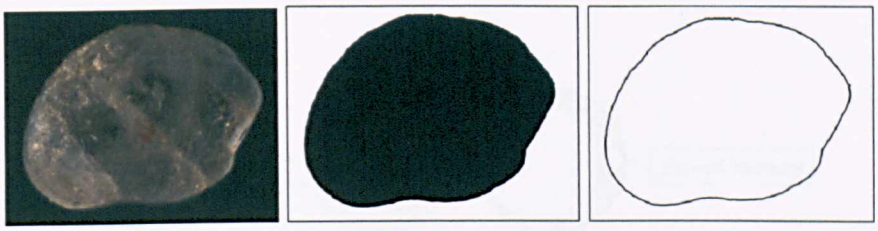

(a) (b) (c)

Figure 2.32: Outline detection of a sand grain, (a) original image (b) binary image (c) outline of the grain (Fonseca, 2006)

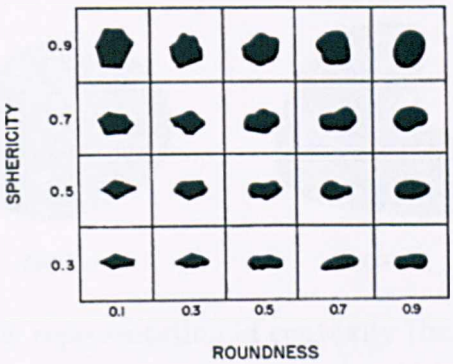

Figure 2.33: Visual estimation of roundness and sphericity of sand grains (Krumbein and Sloss, 1963)

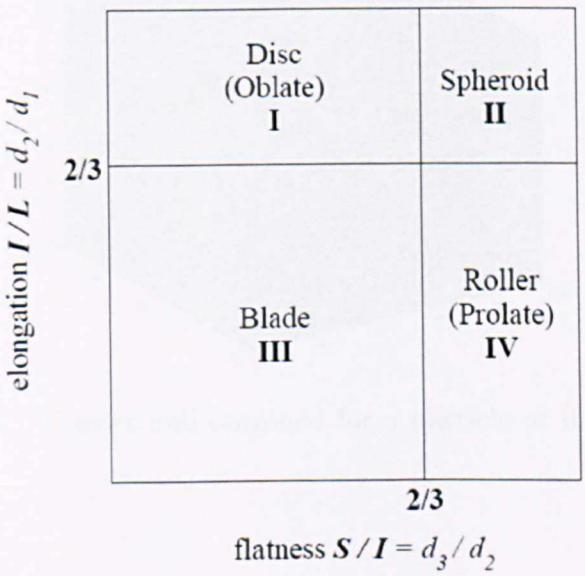

Figure 2.34: Classification of form based on the flatness and elongation indices (Zingg, 1935)

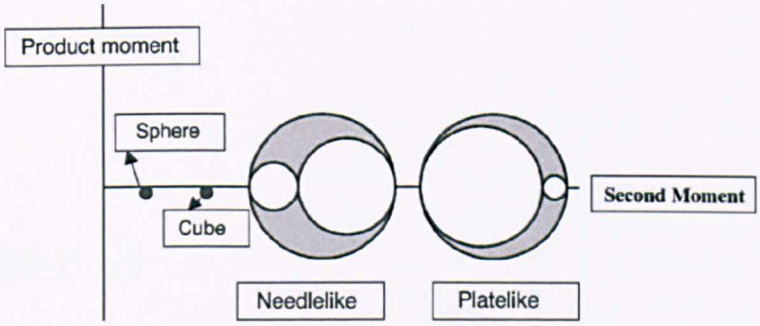

Figure 2.35: Mohr's circle representation of some 3D regular shapes (Taylor, 2002)

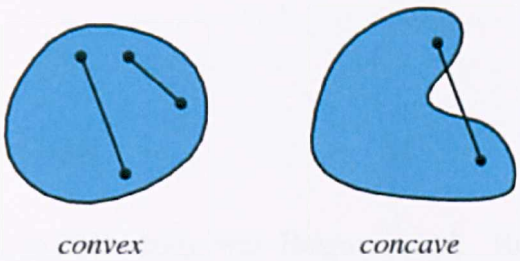

Figure 2.36: 2D schematic representation of convexity (from Woldfram Mathworld)

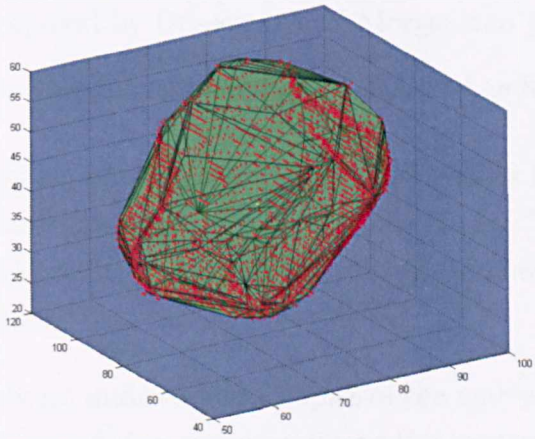

Figure 2.37: Convex hull obtained for a particle of Reigate sand

Chapter 3

Soil description

3.1 Introduction

The sand investigated in this study was Reigate sand. Reigate sand forms part of the Folkestone Beds Formation (Lower Greensand) and the intact samples were retrieved from a quarry near Reigate (Southeast England) where this formation outcrops. Owing to the very high density and the interlocked fabric that the sand presents in its intact state, Reigate sand has been classified as a "locked sand" meeting the criteria proposed by Dusseault and Morgensten (1979).

The motivation for choosing Reigate sand is summarised as follows:

- The sand presents an extreme example of fabric, in its intact state the grains are interlocked and have no bonding between them. Therefore it is a very interesting material to consider when developing a new methodology for soil fabric quantification.
- It is possible to obtain undisturbed samples of the material as it remains intact in the absence of a confining pressure due to the particle interlocking.
- A number of earlier studies (e.g., Cuccovillo and Coop, 1997; Cresswell and Powrie, 2004) have considered the mechanical response of this material and looked at the fabric qualitatively. Thus, there is a well-established context for this research.

This chapter firstly presents the general characteristics attributed to locked sands (Section 3.2). In Section 3.3, the sand used in this study is described, the geology of the sampling site is considered and the sampling procedure is outlined.

3.2 Locked sands

The term locked sand is generally associated with cohesionless sands that were deposited before the Quaternary. During the process of diagenesis, these locked sands developed a particular fabric characterized by grain interlocking and an absence of cementation. The classification was introduced by Dusseault and Morgensten (1979) to differentiate geological materials possessing these characteristics from dense sands and sandstones. The strata in which this type of material was first identified and sampled for investigation were the Athabasca oil sand and the Swan River sandstone of the Lower Cretaceous, and the St. Peter Sandstone of the Ordovician, from Canada. These sands have in common the particular ability to form steep natural slopes and to support considerable loads with small deformations, despite the lack of cohesion suggested by the ability of the sands to be remoulded easily in the hand (e.g.,Dusseault and Morgensten (1979); Dittes and Labuz, 2002; Abdelaziz et al., 2008).

Dusseault and Morgensten (1979) demonstrated that when locked sands are sheared, failure occurs at small strains and is accompanied by extremely high rates of dilation. This peculiar behaviour, when compared to dense sands, was attributed to the interlocked fabric that forms during diagenesis. The different types of contacts often associated with an interlocked fabric, as first proposed by Siever (1959), are illustrated in Figure 3.1. In a typical locked sand there are more straight contacts than tangential contacts, moreover, there is a relatively high frequency of interpenetrative contacts and occasional occurrences of sutured contacts. Conversely, more recent geological formations are dominated by tangential or point contacts.

Following the work of Dusseault and Morgensten (1979), locked sands from different strata have been investigated. Barton et al. (1986) considered two English Hampshire Tertiary sands and found both to have a high in-situ relative density (greater than 100%) and very low cement content. Cuccovillo and Coop (1999), Richards and Barton (1999) and Cresswell and Powrie (2004) considered the Lower Cretacous Folkestone sands from Southeast England (the same formation as Reigate sand) retrieved from various locations, each having a different grading and a different degree of cementation. Dittes and Labuz (2002) investigated St. Peter Sandstone formed in the middle Ordovician age. Abdelaziz et al. (2008) presented an experimental investigation of a sand from Northeastern Alberta (Lower Cretaceous). Referring to these previous investigations, the common characteristics of locked sands are summarised in Table 3.1.

The development of the interlocking fabric is believed to be caused by a combination of different diagenetic processes that can be classified into two main mechanisms. The first mechanism consists of post-depositional grain rearrangement with only elastic deformations as the sand consolidates and its depositional porosity is reduced.

This causes the contact area to increase and the contacts to change from being of a tangential-type to a straight-to-long-type. The second process is responsible for the formation of inter-penetrative and sutured-type contacts and can be associated with different phenomena. As first postulated by Sorby (1908), grain interpenetration can be caused by chemical solution and enhanced by pressure, a phenomenon often called "pressure solution" or "chemical compaction". Therefore, pressure solution of the detrital grains results in the preferential dissolution of stressed material at the grain contact points (Barton, 1993). The material released during pressure solution can also form grain overgrowths. It is possible that these overgrowths may contribute to promote grain interlocking or they may be responsible for rougher grain surfaces (Barton, 1993). On the other hand, Stephenson et al. (1992) argued that the phenomenon of grain interpenetration is an exclusively mechanical phenomenon involving no chemistry, and is a consequence of the inelastic deformations that take place as the sand compacts.

3.3 Reigate Sand

Previous studies on Reigate sand have demonstrated evidence to support the classification of this sand as a locked sand (e.g., Cresswell and Powrie, 2004). At the sample site for the current study, the intact material was able to support steep cliffs and vertical quarry faces (Figure 3.2), these features are a clear manifestation of the interlocked fabric (noting that minimal cement content was observed in the retrieved samples). Cresswell (1999) reported unconfined tensile strengths of less than 5 kPa, indicating the small amount of cohesion or cementation presented. In addition the specimens are eroded easily as individual grains tend to detach by gentle brushing or under a small fingertip pressure.

This section presents an overview of the sedimentation process and the mechanisms that contributed to the development of the interlocked fabric. Block sampling of this uncemented sand is possible due to the interlocked fabric, and the details and challenges of the process are described. The sand characterisation included measurement of the particle size distribution, the identification of the elements presented in the soil samples using energy-dispersive X-ray analysis, and a qualitative description of the soil fabric. This qualitative description was based on the analysis of images from a scanning electron microscope (SEM), optical microscope images of thin sections and X-ray micro-CT images.

3.3.1 Local stratigraphy and deposition processes

The Reigate sand samples considered in this study were retrieved from Park Pit Quarry, located approximately 2km west of Reigate (South East England), OS grid

reference TQ231508, as shown in Figure 3.3a. The quarry is currently used for the extraction of silica sand for glass production and is operated by Hanson Aggregates. A general view of the quarry is presented in Figure 3.3b. This is the same location as the samples investigated by Cresswell (1999) and Cresswell and Powrie (2004).

Reigate sand lies within the Folkestone Beds formation which is the uppermost formation of the Lower Greensand. Stratigraphically it is located at the top of the Lower Cretaceous system and was deposited in the Lower Albian stage. Park Pit Quarry is situated in the outcrop of the Lower Greensand in the Wealden Basin as shown in Figure 3.4.

According to the geological map of the Reigate area (Sheet 286), the Lithological divisions of the Lower Greensand in the region close to Park Pit Quarry comprise the Sandgate Beds, the Hythe Beds and the Atherfield Clay, in addition to the Folkestone Beds, as presented in Table 3.2. These formations were deposited during the Lower Cretaceous period in a shallow marine environment that, according to Casey (1961), marked the beginning of an important cycle of marine sedimentation which took place in Britain during the Aptian and Lower Albian stages.

The Folkestone Beds was the last formation deposited during the Lower Cretaceous, and according to Gossling (1929), the depositional process included the following four stages:

1. The deposition of the Basal Pebbly Band.
2. The deposition of a thick mass of fine sand (Silver sand). This sand was distinguished by the complete absence of glauconite. The aeolian features of the sand apparent on the grains (e.g., rounded grains) suggest the culmination of the silting-up process.
3. The deposition of a Clay Band heavily charged with glauconite above the Silver sand.
4. The deposition of the very coarse and current-bedded Upper Pebbly sands.

During the Upper Cretaceous period, the Folkestone Beds are believed to have been overlain by the Gault Clay, Upper Greensand and Chalk. This geological succession is presented in Table 3.3.

The Folkestone Beds were overconsolidated to different degrees according to the amount of overburden deposited in the various areas and subsequently removed by the erosion which followed tectonic movements. As illustrated in Figure 3.4, the Wealden anticline in the Wealden Basin is a large East-West fold whose limbs dip North and South respectively on either side of the main anticline axis. Erosion has exposed beds of the Lower Cretaceous series in the core of the anticline structure.

Referring to Table 3.3, it would appear that about 450m of overburden was removed from the Folkestone Beds (considering the overlying drift deposits and the Tertiary strata). Therefore, the maximum overburden pressure experienced by the Reigate sand deposit can be estimated to be approximately 9 MPa (a similar value was estimated by Cuccovillo and Coop (1999) for the Maidstone area). Palmer and Barton (1987) reported a maximum depth of burial of 474 m for the Folkestone Beds around West Sussex (20-30 km Southwest Reigate).

Previous studies of the Folkestone Beds from various locations in the Wealden outcrop have shown that this formation is a highly variable sequence of fine, medium and coarse poorly cemented ferruginous sands, and the sand colour is determined by the amount of iron coating and cement. There are detrital grains of iron oxide and glauconite and a trace of feldspar. The high quartz content shows that essentially only this mineral has resisted the transportation and sedimentation processes.

3.3.2 Block sampling

Having identified the Park Pit Quarry near Reigate as a source of sand, the choice of the location for sampling within this quarry was determined based on two criteria. The first was the need to prevent water to ingress during excavation and so the small ponds existing in the quarry were avoided. The second criterion was to obtain sand with minimum cement content, thus it was decided to sample close to the point where Cresswell and Powrie (2004) reported that they retrieved cement free specimens.

Prior to sampling, the horizontal and vertical directions of the sample in the ground were marked. The depth of retrieval was at the quarry excavation surface that was approximately 4 to 5 m below the ground level. At the location of sampling, a small layer of sand (of approximately 20 cm) was removed from the surface as it was considered to have been disturbed by the quarry activities. Two parallel trenches approximately 1m apart were excavated with a heavy excavator in order to define the area that would form the block samples, as shown in Figure 3.5a. The soil around this area was gradually extracted without the use of any heavy equipment that could potentially disturb the soil. Using spades and saws for vertical cutting and scrubbing, the blocks were reduced to the dimensions of the pre-fabricated wooden boxes. These boxes were used to transport and store the soil after sampling and had approximate dimensions of 35×35×25 cm. Initially these boxes had only four sides (the walls), the tops and bottoms of the boxes were added later, as illustrated in Figure 3.5b and Figure 3.5c.

Once the sides and the top surfaces of the blocks of sand had been shaped, they were wrapped in cling-film and waxed (Figure 3.5d). Two layers of cling-film and melted wax were then applied. The wooden box was placed around the block and

polyurethane foam was injected into the void space between the box and the soil (Figure 3.5e). This expansive foam provides a confinement, minimizing the disturbance to the sample during transportation. The top of the box was then closed and the samples were left on site overnight to allow the foam to set. On the following day the base of each block was cut with a wire saw (Figure 3.5f). Each block was then gently turned over and its base was smoothed. It was then again covered with a double layer of cling-film and melted wax, and a layer of polyurethane foam was placed before finally closing the last side of the wooden box.

The difficulties in sampling of natural uncemented sands have been recognised in previous studies (e.g., Cresswell, 2001). The high density of this material in-situ creates great resistance to cutting. The time required and the physical effort, were the main difficulties associated with the sampling process.

3.3.3 Soil description

(a) Particle size distribution

Particle size measurements were obtained using both sieving and the QICPIC apparatus for which $d_{effective} = d_{Fmin}$ was used. For the sieve analysis, 100 g of soil was passed through the following sieve sizes: 0.063, 0.106, 0.150, 0.180, 0.212, 0.300, 0.420, 0.600 and 1.000 mm. The QICPIC analysis was carried out on 20 g of soil. The particle size distributions using both methods are presented in Figure 3.6. Both sieving and the QICPIC curves show good agreement. In addition, the gradation was very similar to that reported by Cresswell and Powrie (2004) for their sand samples extracted from the same site. The sand can be classified as a well-sorted material, a fine to medium sand with a mean grain size of $274\,\mu m$, $C_U = 1.62$ and a percentage of fines <2%.

(b) Composition and mineralogy

Reigate sand is also known as "Silver sand" due to its clean quartzitic character and general whiteness. This characteristic whiteness is, however, locally stained by orange/brown iron oxide ("iron horizons"), as shown in Figure 3.7. According to a geological report by Hanson (2007), percolating iron bearing waters have stained the sand with a coating of limonite (hydrated iron oxide) and chemical weathering, after deposition, resulted in the leaching of certain parts of the deposit creating the lightly stained or "white" sand.

The presence of iron oxide (Fe_2O_3) was confirmed by SEM analysis. Two undisturbed specimens were broken off in order to obtain a fresh surface for scanning electron microscopy. One of the specimens was taken from a region with a high

iron oxide content easily identified due to the orange/brown colour and the second specimen consisted of essentially white sand. An energy dispersive X-Ray analysis (EDS) was carried out to identify the different elements present in the soil. Figure 3.8 shows the EDS spectrum of the energy against relative counts of the detected X-rays, where the counts represent the energy gained by each element, which can then be translated into a percentage of each element in the sample. The composition of each sample is summarised in Table 3.4. The white sand shows a very high quartz content (97.2%) and a trace of aluminium (2.8%) that is believed to be related to clay minerals (kaolinite) and possibly some trace of feldspar grains (silcates of aluminium). The sample of stained sand showed, as it would be expected, a high iron content (35%) and also a slightly higher percentage of aluminium (11.4%) when compared to the sample of white sand.

The iron stained regions are localised in occurrence and can be easily identified by their colour. For the morphology and fabric quantification presented in this study, samples containing the iron staining were not used. The presence of heavy materials such as iron can be detected in the X-ray micro-CT images because of the different attenuation of the X-rays that this element causes when compared to the quartz (as discussed in Chapter 5). As illustrated in Figure 3.9 iron can be identified in the tomographic images owing its very bright colour when compared with other elements in the soil. The white sand samples analysed in this study have shown that iron can appear as iron-rich mineral grains (Figure 3.9a) and as inclusions in the quartz grains (Figure 3.9b).

Thin section inspection under cross-polarized light has shown that the majority of quartz grains are monocrystalline, i.e., grains composed of a single crystal, while only a small percentage of polycrystalline grains (grains composed of two or more crystals) was observed (Figure 3.10). Within the monocrystalline grains, some show undulose extinction, i.e., the crystal is not extinguished uniformly under crossed polars, but the extinction sweeps across the crystal when it is rotated, which reflects strain in the crystal lattice (Figure 3.11). Monocrystalline quartz grains with undulose extinction and polycrystalline quartz grains and commonly of metamorphic origin. These types of grains are strained and less stable than monocrystalline quartz with unit extinction and therefore are more easily weathered.

(c) Qualitative morphology and fabric description

A qualitative morphology and fabric description of the intact samples of Reigate sand is presented based on SEM images, X-ray micro-CT images and optical images of thin sections under cross-polarised light. The interlocking between the grains, as shown in Figure 3.12, is the result of diagenetic processes that reduced the porosity and contributed to a progressive change of contact type and an increase in contact

areas. These phenomena have contributed to the exceptionally dense packing that this sand has in its intact state. The dense packing is also demonstrated by the measured relative density of 140% for the intact soil (Cresswell, 1999). The relative density of the intact sand was calculated by relating the dry density (ρ_d) to the limiting dry densities:

$$Dr = (\rho_{d(intact)} - \rho_{d(min)})/(\rho_{d(max)} - \rho_{d(min)}) \times (\rho_{d(max)}/\rho_{d(intact)}) \qquad (3.1)$$

where $\rho_{d(min)}$ and $\rho_{d(max)}$ are the minimum and maximum dry densities respectively.

Grain fracturing is abundant as shown in Figures 3.12, 3.13 and 3.14a. Quartz grains from metamorphic sources frequently have defects and imperfections and this, associated with high overburden loads, created the fractures in the grains.

The SEM micrograph in Figure 3.12 shows the variety existing in the particle morphologies. The grain morphology varies from highly spherical grains, rounded to angular grains and highly non-spherical grains with embayments (Figure 3.14a). Occasionally, features such as long noses or necks were observed (Figure 3.14b). The particles are essentially characterized by irregular and complex shapes. Considering the significant transport and sorting of the material prior to deposition, grains with more angular features and the presence of interpenetration and micro-suturing are possibly an indication of authigenic alteration of grain morphology. According to Cresswell (1999), pressure solution and recrystallization are not believed to have been the mechanisms responsible for the formation of these features, as overgrowths cannot be observed in the grains and no passive or bonding cement has been deposited. Cresswell (1999) concluded that it is possible that the morphological changes have occurred in the solid state. This is in agreement with the theory presented by Stephenson et al. (1992).

The quartz grains present different surface textures as can be observed in the SEM images (Figure 3.12). Some grains have glassy surfaces while others present more rough surfaces. This is believed to be related to the origins of the materials and the various environmental conditions the grains have been subjected to in the past. As already mentioned, quartz from metamorphic sources is less stable and more susceptible to weathering. Some grains show pitting cavities as a result of chemical dissolution (Figure 3.12). The less spherical particles with concave surfaces contribute more significantly to the interlocked fabric.

Thin section analysis showed that grain contacts are dominated by straight-to-long and concavo-convex contacts, with occasional interpenetrating contacts (Figure 3.15). The contacts between two grains stems from authigenic quartz rather than binding cement. In the stained sand, the cement (iron oxide) can be found either as a bridge between two adjacent grains or in the form of a coating on a single grain

as shown in Figure 3.16b. The white sand shows negligible cement with just some light coating on the grains surfaces as illustrated in Figure 3.16a.

3.4 Concluding remarks

This chapter has described the soil used in this study, i.e., Reigate sand. The key characteristics of Reigate sand, from the perspective of fabric investigation, are the very dense packing along with the considerable contact areas between grains. The investigation of the soil presented here and previous studies on sand from the same location (Cresswell and Powrie, 2004) have shown that Reigate sand has, in general, minimal cement content and its occurrence in the form of iron oxide is restricted to regions easily identified by its orange/brown colour. Therefore, by limiting the analysis to samples of white sand, the bonding could be avoided and an investigation just of fabric could be carried out. The friable character of the sand given the general absence of cement posed difficulties during the preparation of the intact samples for laboratory testing, as discussed in detail in Chapter 4. The low percentage of fines found in the sand specimens (<2 %) was beneficial to the analysis because smaller particle are more likely to be affected by errors associated with the finite size of the voxel in the image (as discussed in Chapter 5). On the other hand, the complex particle shapes, as observed in the thin sections and the highly fractured grains posed challenges for the image processing and analysis as presented in Chapter 6.

Criterion	Description
Geological age	• Older than Quaternary
Physical characteristics	• Friable sands, can easily be reduced to individual grains by gently rubbing • Generally poorly cemented with tendency to disintegrate when immersed in water
Mineralogy	• Quartzose sands • Occasional cross-bedding exists with traces of fines (e.g., iron oxide, kaolinite)
Fabric	• Very low porosity and relative densities greater than 100% • Tangential, straight-to-long and interpenetrative contacts
Shear strength	• Higher rates of dilation and peak strengths when compared to dense sands • High initial shear stiffness

Table 3.1: Summary of common characteristics of locked sands(modified after Abdelaziz et al., 2008)

Formation		Description	Estimated thickness (m)
Lower Greensand	Folkestone Beds	Coarse iron sands	40-80
	Sandgate Beds	Loamy sand and calcareous sandstone	< 20
	Hythe Beds	Sand, sandstone	40 -80
Weald Clay	Atherfield Clay	Sandy mottled clay	< 10
	Weald Clay	Clay and shale	180-210
	Tunbridge Wells Sand	Fine sand and sandstones	30-50

Table 3.2: Geological succession at Park Pit (Dines and Edmunds, 1933)

Formation	Description	Estimated thickness (m)
Upper Chalk	White chalk	170
Middle Chalk	White chalk	40-60
Lower Chalk	Marly chalk	30-50
Upper Greensand	Glauconitic sand	10-20
Gault Clay	Grey clay	40-100

Table 3.3: Geological succession deposited above the Folkestone Beds during the Upper Cretaceous (Dines and Edmunds, 1933)

Element	White sand	Iron oxide stained sand
Aluminum (%)	2.8	11.4
Silicon (%)	97.2	53.3
Iron (%)	-	35.3

Table 3.4: Summary of the specimen composition obtained by EDS analysis

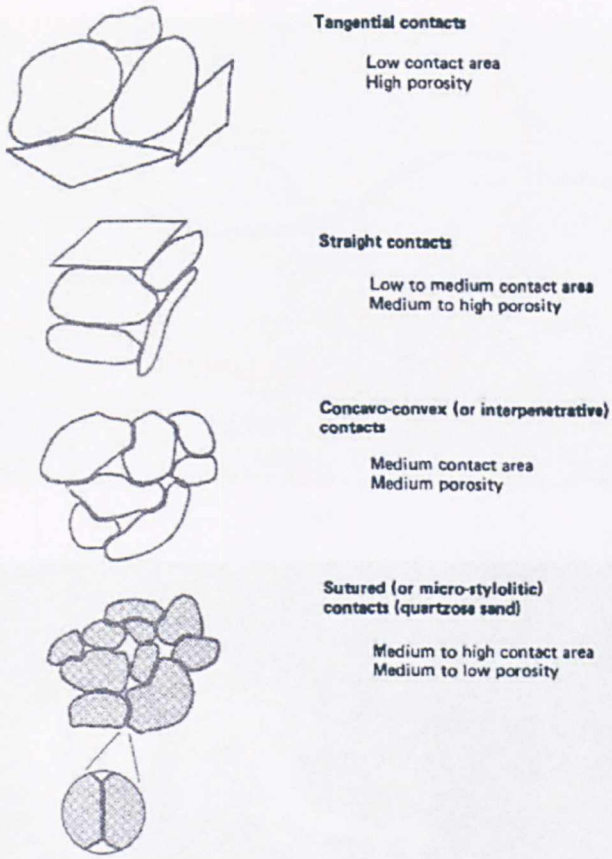

Figure 3.1: Different types of contact often associated with interlocked fabrics (from Dusseault and Morgensten, 1979).

Figure 3.2: Vertical faces at Park Pit Quarry from where the intact samples of Reigate sand were retrieved

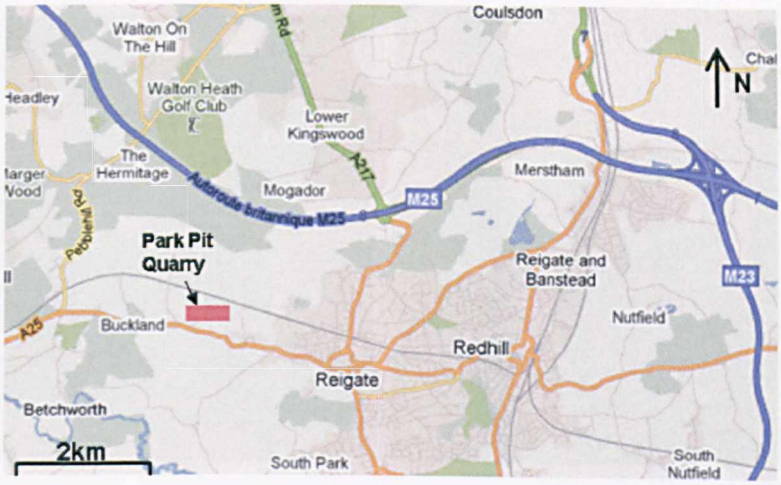

(a)

(b)

Figure 3.3: Location of Park Pit Quarry, (a) map (b) general view of the site (from Google).

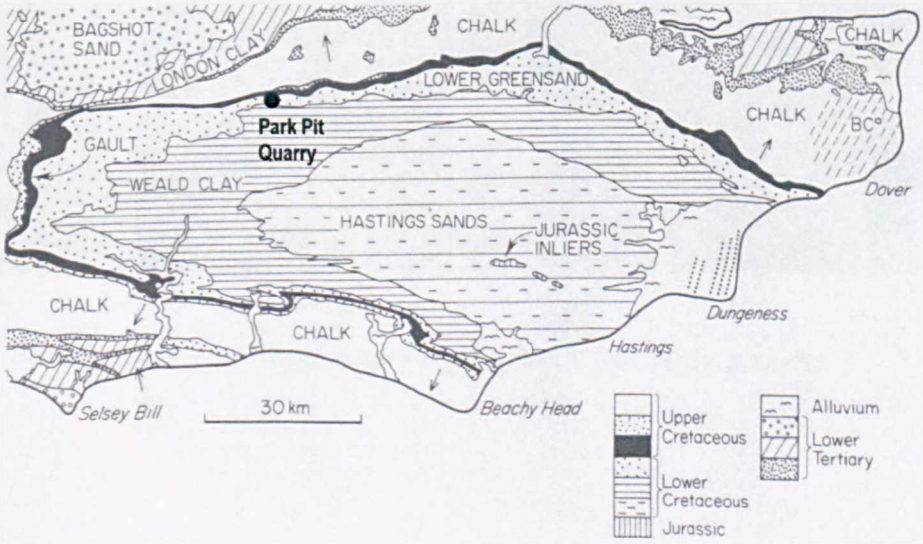

Figure 3.4: Geological map of the Wealden Basin, SE England (modified after Blyth and de Freitas, 1984)

Figure 3.5: Main stages of the block sampling process

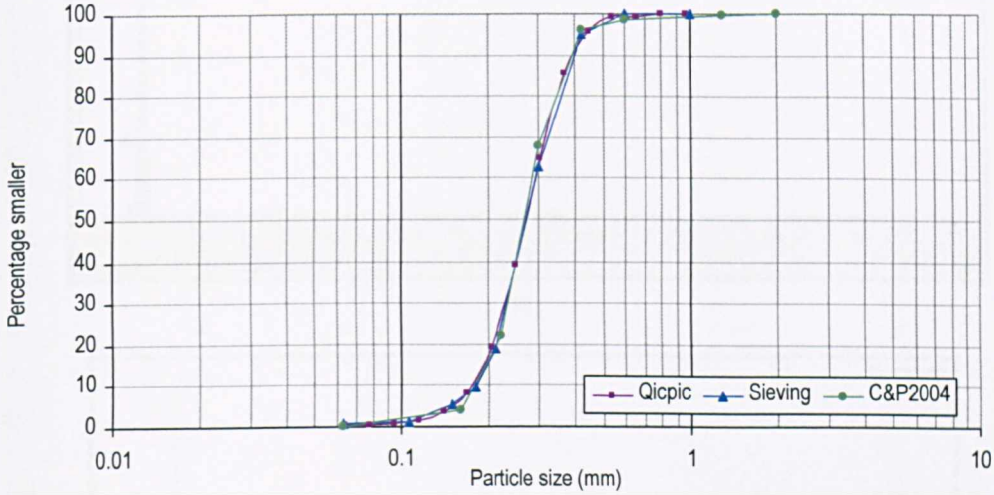

Figure 3.6: PSD curves for Reigate sand obtained by sieving, using QICPIC apparatus and from Cresswell and Powrie (2004)

Figure 3.7: An example of a sample of sand stained by iron oxide.

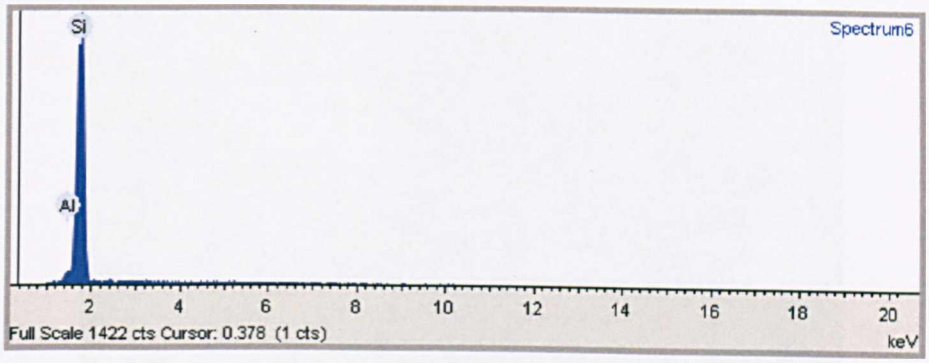

(a)

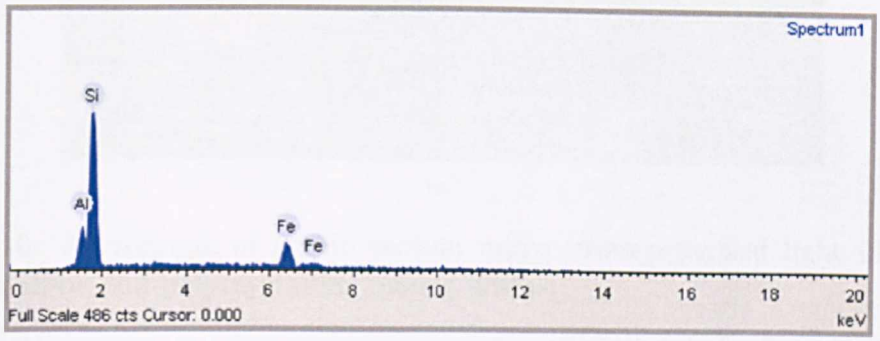

(b)

Figure 3.8: EDS spectrum for (a) a sample of white sand (b) a sample of sand stained by iron oxide

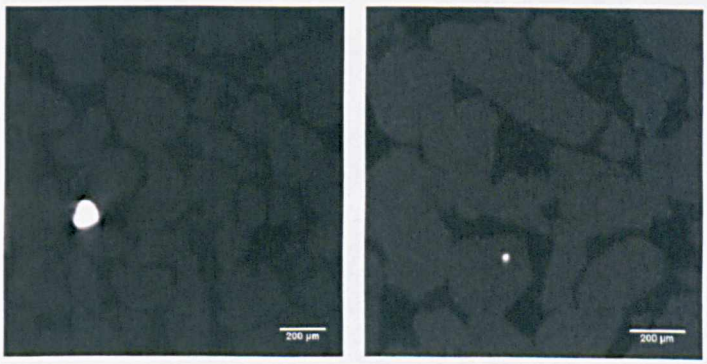

(a) (b)

Figure 3.9: Tomographic images showing iron as (a) an iron-rich mineral grain (b) an inclusion in a quartz grain

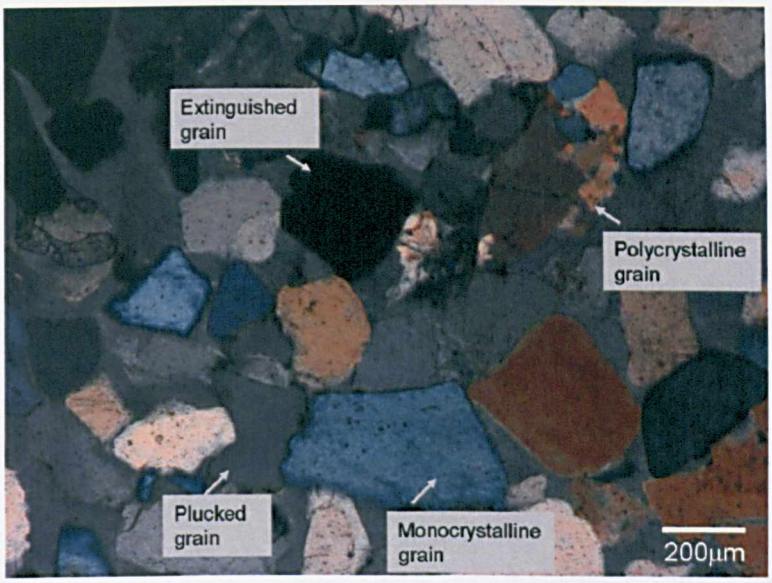

(a)

Figure 3.10: Micrograph of a thin section under cross-polarised light illustrating monocrystalline and polycrystalline quartz grains.

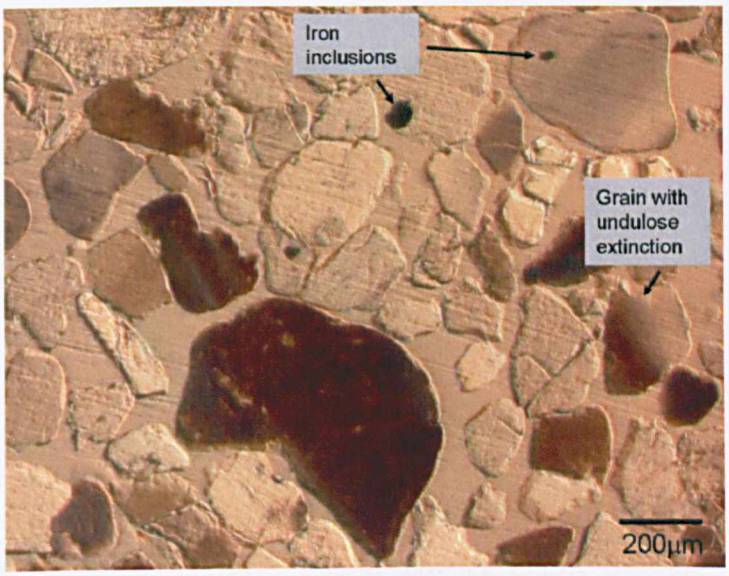

Figure 3.11: Micrograph of a thin section under cross-polarised light illustrating a quartz grain with undulose extinction.

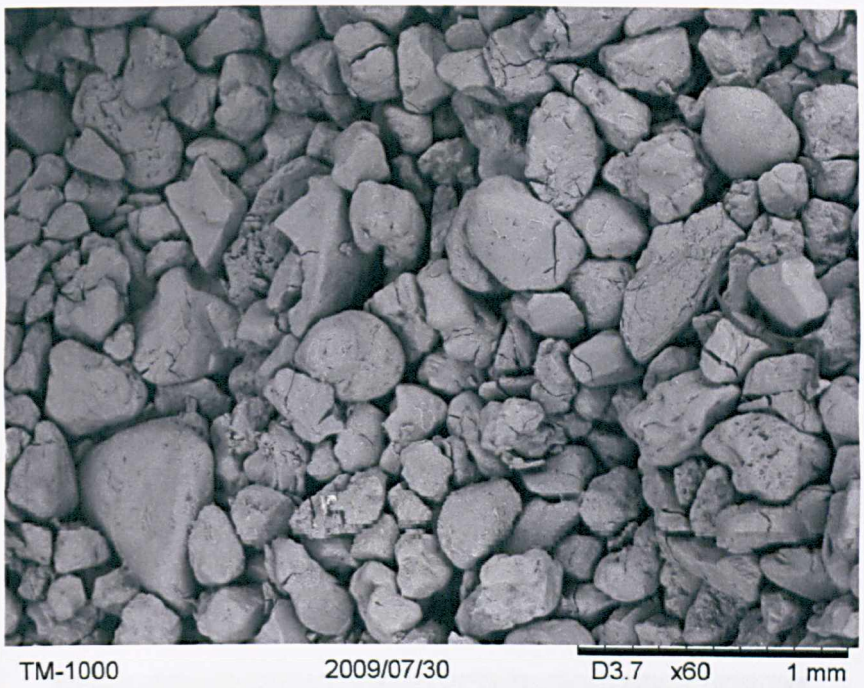

Figure 3.12: SEM image showing the variety of particle morphologies and surface textures in a sample of Reigate sand

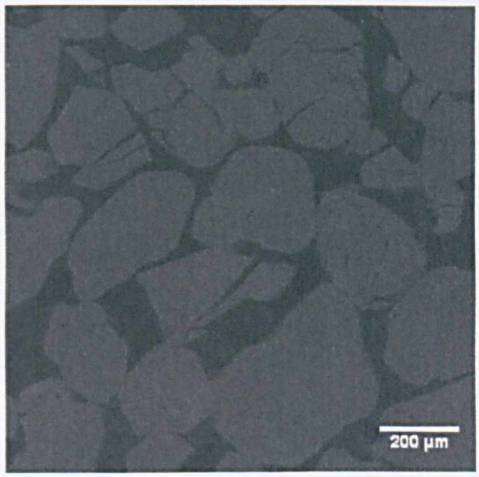

Figure 3.13: X-ray micro-CT image showing highly fractured grains

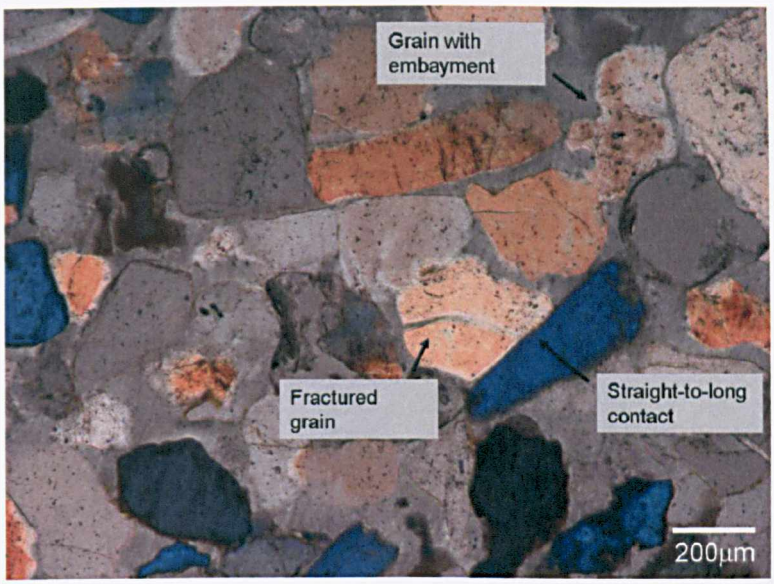

(a)

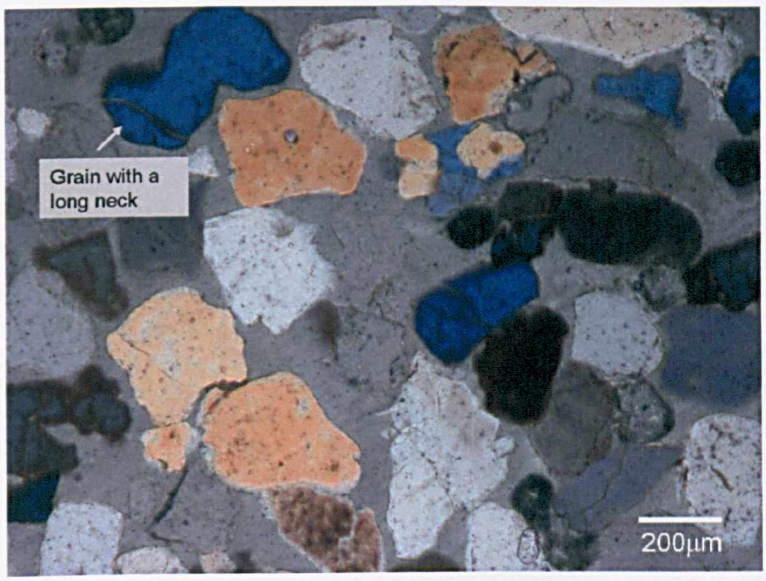

(b)

Figure 3.14: Micrograph of a thin section under cross-polarised light illustrating highly non-spherical particles, (a) example of an embayment in a grain (b) example of a grain with a long neck

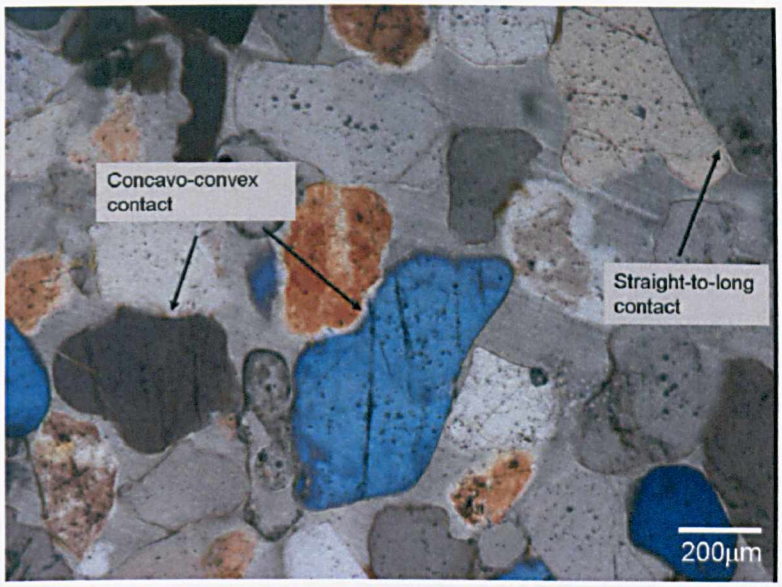

(a)

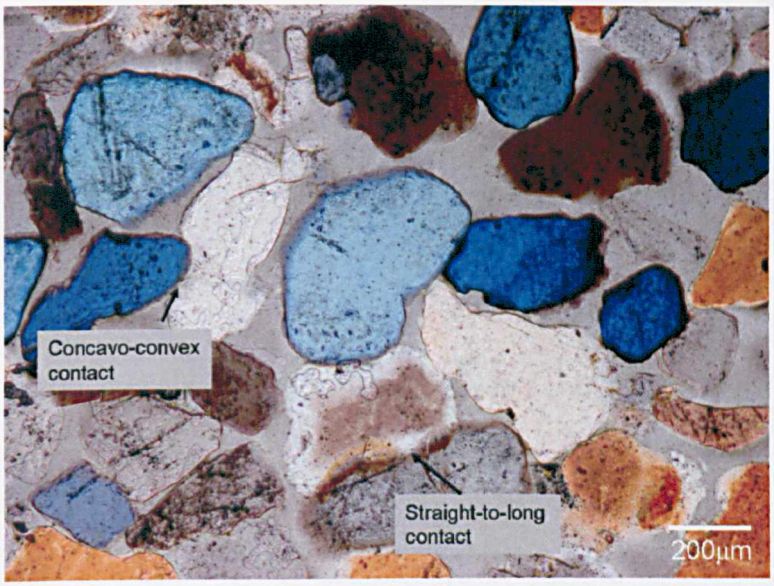

(b)

Figure 3.15: Micrograph of a thin section under cross-polarised light showing grain contacts dominated by straight-to-long and concavo-convex contacts

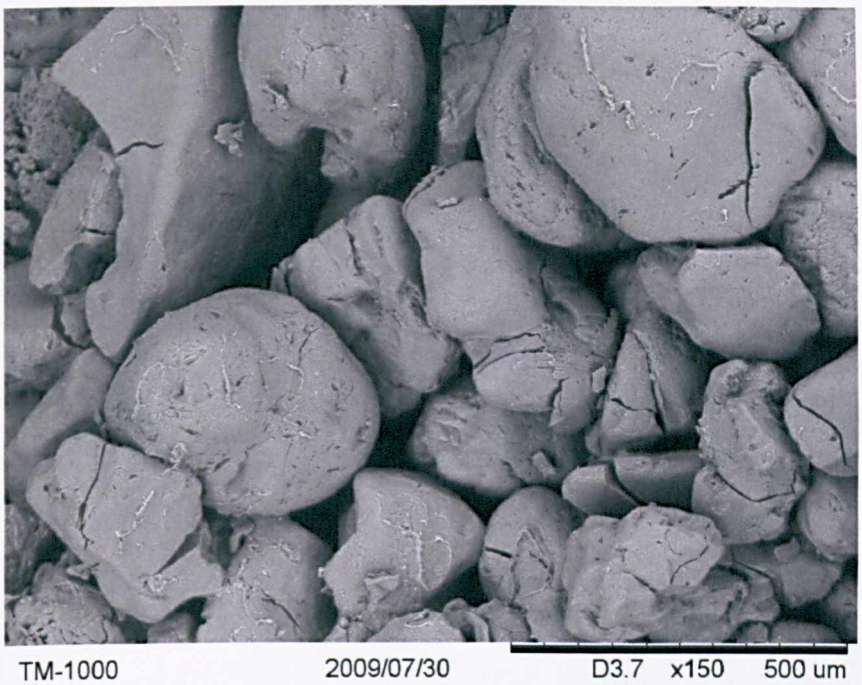

(a)

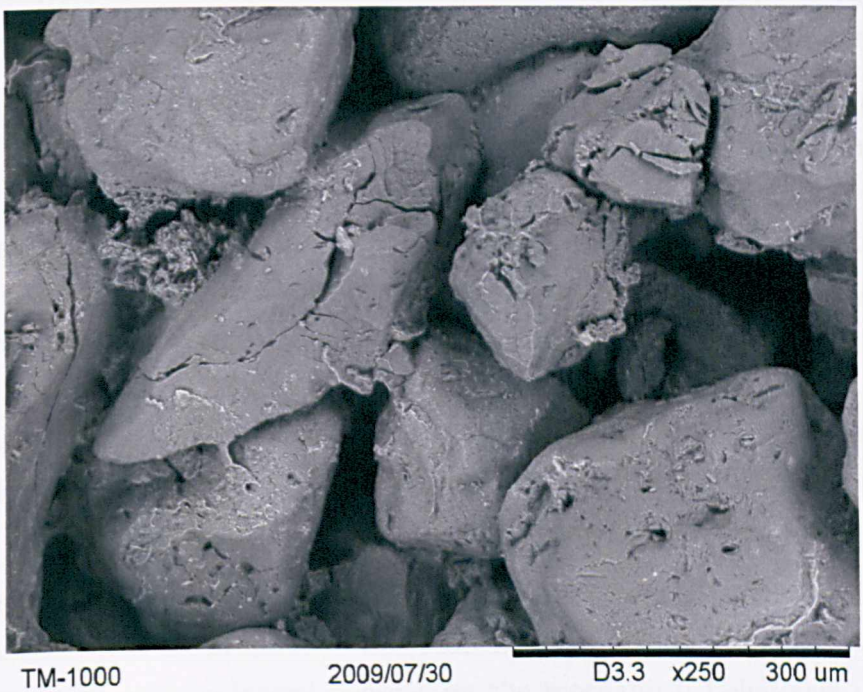

(b)

Figure 3.16: SEM images on two samples of Reigate sand, (a) white sand showing light cement coating the grains (b) iron stained sand where the cement forms bridges between the grains

Chapter 4

Laboratory Tests

4.1 Introduction

This chapter describes the methodology developed to obtain the soil specimens for image acquisition and subsequent morphology and fabric investigation. The primary material used is the natural locked Reigate sand, as described in Chapter 3.

Following the approach commonly used to study the effect of structure in cohesive soils (e.g., Leroueil and Vaughan, 1990), the influence of fabric on the mechanical response of natural sands, can be identified by comparing the response of the intact soil to that of the corresponding reconstituted material. In the current study, a series of triaxial tests was carried out on intact and reconstituted soil samples of Reigate sand at the same confining pressure. The tests were stopped at different strain levels and the soil specimens were impregnated with a resin so that the fabric could be analysed at different stages of deformation. A more extensive series of tests comparing reconstituted and intact samples at various confining pressures is described by Cuccovillo and Coop (1997) and Cresswell and Powrie (2004).

The first section of this chapter discusses previous experimental studies on natural locked sands, which estalishes the effect of diagenic fabric, i.e., fabric developed during deposition and geological history, on the mechanical behaviour of the soil. Section 4.3 describes the trimming process used for the intact samples and the preparation method employed to obtain reconstituted specimens with void ratios similar to the intact state. Section 4.4 includes the description of the triaxial apparatus, outlines the testing programme and presents the macro-scale response observed. The method used to preserved the soil fabric, i.e., the impregnation of the soil with epoxy resin in the triaxial cell, is described in Section 4.5. Finally, Section 4.6 considers specimen preparation prior to image acquisition, including thin section preparation and the drilling of small cores for micro-CT scanning.

4.2 Previous studies on the behaviour of locked sands

Owing to the limited availability of data on the behaviour of natural sands, the response of sands has often been investigated by preparing samples in the laboratory at equivalent relative density. Previous experimental studies on the strength and deformation of natural locked sands, have revealed, not only that this type of fabric cannot be replicated in the laboratory, but also it has a great effect on the strength and stiffness of the material.

Research on the mechanical behaviour of locked sands, has mainly been carried out on formations from the Lower Cretaceous, from South Eastern England, i.e Greensand from Reigate and Maidstone, as well as on an oil sand from North/Northeastern Alberta (Canada).

The Reigate sand used in this project has previously been investigated by means of triaxial compression tests at a range of confining pressures from 12.5-800 kPa (Cresswell, 1999; Cresswell and Powrie, 2004; Bhandari, 2009). The cemented locked sand investigated by Cuccovillo (1995) and Cuccovillo and Coop (1997), comes from the same Lower Greensand outcrop but was sampled at a different location. The oil sands from Alberta were investigated by Dusseault and Morgensten (1979), Wong (2000) and Abdelaziz et al. (2008). Some consistent trends were observed in these experimental studies and the key features are summarised here.

There seems to be a consensus that the locked fabric has the effect of delaying the onset of dilation during shear (Cuccovillo and Coop, 1997). Figure 4.1 compares the stress-dilatancy response for intact and reconstituted samples of the cemented locked sand considered by Cuccovillo and Coop (1997). The data is plotted in $\eta : d$ space, where the stress ratio (q/p') is denoted by η and the rate of dilation by d. While the reconstituted sample follows an almost straight path, the intact samples initially reach much higher stress ratios, with little dilation. This delay is later compensated by a faster dilation that culminated at peak and is believed to be associated with the fabric unlocking. While the studies of Cuccovillo and Coop could not entirely isolate the effect of fabric from that of bonding, the subsequent studies on Reigate sand (a "pure" locked sand, with very little cementation) by Cresswell and Powrie (2004) have confirmed the influence of fabric on the ability of the soil to sustain high stress ratios in the absence of dilation. Figures 4.2a and 4.2b show the plot of the stress ratio (q/p') and average volumetric strain as a function of the axial shortening for intact and reconstituted samples of Reigate sand. For the intact soil, dilation started to occur only just before the peak stress ratio, which is in contrast to what has been traditionally accepted for dense sands, in which any mobilised stress ratio in excess of critical state is associated with dilation (e.g., Casagrande, 1936;

Schofield and Wroth, 1968). High peak strength and dilation rates when compared to reconstituted sands have also been reported by Dusseault and Morgensten (1979), Wong (2000) and Abdelaziz et al. (2008) for the intact oil sands.

The experimental results on Reigate sand, documented by Cresswell and Powrie (2004) have highlighted the effect of the interlocked fabric on the mobilisation of very high initial stiffness when compared with the reconstituted material as shown in Figure 4.3. The reduction and recovery of the stiffness degradation curve at small strains was believed to be associated with rearrangement in the initial fabric, prior to the onset of dilation, as a response to disturbance during sampling.

To summarise, sands with locked fabric are able to mobilise higher rates of dilation and peak strengths than equivalent reconstituted samples at comparable states. In addition, the locked fabric is associated with the high initial shear stiffness of the intact soil.

4.3 Sample preparation

4.3.1 Trimmimg of the intact samples

As was already mentioned in Chapter 3, Reigate silver sand is very friable and samples of this material tend to desintegrate as their size is reduced to the dimensions typically used in element tests. The natural moisture of the soil can generate just enough negative pressure (suction) to prevent small samples from disintegrating. For this reason the time spent during sample preparation was minimized in order to limit the drying of the soil. The cylindrical samples used in the triaxial tests were 76 mm in height and 36 mm in diameter and were obtained by trimming small rectangular blocks, extracted from the wooden box, as illustrated in Figures 4.4a, 4.4b and 4.4c. These blocks were taken from the box prior to each test and the remaining soil in the box was immediately wrapped in cling film and waxed to prevent any moisture loss. The water content of the soil, calculated as the ratio of the mass of water to the mass of solids in the soil, was measured for three samples and the results are presented in Table 4.1. The variation of the moisture content amongst the different samples can be related to the duration of the period they have been exposed to the atmosphere but has little influence on the triaxial tests as further drying out took place during the trimming process.

The trimming process involved mounting the sample onto a hand lathe oriented with the vertical direction maintained the same as in the field (Figure 4.4d). The initial dimensions of the core were first reduced to a diameter of approximately 45mm using a sharp knife, and the required diameter of 38mm was achieved by grain plucking using a very thin wire saw, cutting was avoided at this stage as it would have caused

cracks and the consequent desegregation of the sample. The process was repeated around the perimeter of the sample until the required dimensions were achieved, as shown in Figure 4.4e. Once the correct diameter was achieved, the sample was placed into a cradle where the ends were carefully trimmed and the final geometry of the sample for testing was reached (Figure 4.4f). It was important to ensure that the end faces were perpendicular to the vertical axis of symmetry so the load would be transmitted uniformly along this direction with no stress concentrations. The entire process required gentle handling, and although not all the samples were successfully trimmed, the success of the technique was improved with experience.

Previous researchers documented the challenge of creating lab-sized specimens. Cresswell (2001) used hairspray to create a hard, enclosing shell around the sample, Abdelaziz et al. (2008) used a milling machine to core 63.5 mm diameter samples from a locked sand from Northeastern Alberta and according to the author the sample preparation process typically took more than 6 hours with a 50 % chance of success. The present study has demonstrated that the trimming process of triaxial samples of this sand can be done without additional products that might result in further soil fabric disruption. It is however clear that there is no generally accepted procedure for the preparation of friable soil specimens.

Once the sample had been trimmed to the desired size, it was weighed and its dimensions measured. The membrane was then placed around the sample and finally the sample was mounted on the triaxial cell pedestal.

4.3.2 Reconstituted samples

A key requirement for the reconstituted specimens is that they should have approximately the same void ratio as the intact samples. As discussed already in Chapter 3, Reigate sand in its intact state has very high density due to the interlocked fabric. While previous studies (e.g., Cuccovillo and Coop, 1997) have established that this particular fabric cannot be obtained in laboratory, in the current work different preparation methods were explored with the aim of achieving specimens with an initial density as close as possible to that of the intact soil.

The first method considered was dry pluviation with a drop height of 1m. This method was found to produce samples with a density of approximately 1.60 Mg/m^3 which is much lower than the intact soil (1.79 Mg/m^3). The use of a mechanical vibrator was found to produce very dense samples (1.76 Mg/m^3), however, it was not practical to apply this technique in the triaxial cell. Good results, i.e., a density of approximately 1.75 Mg/m^3 were obtained by using a combination of pouring and tamping and at the same time tapping the mould to produce a vibration effect in the sample. The reconstituted samples were created with sand from the unused trimmings of the intact samples and small crumps were disaggregated.

The setup used for making the samples is described here. A 0.3mm thick latex membrane was placed around the base pedestal and secured by a couple of o-rings. A 38x76 mm brass split mould was then assembled around the latex membrane, which was folded over the top of the mould. The membrane was secured flat against the inner body of the mould by means of a suction line connected to it operating at approximately -20 kPa. Silicon grease was used in order to improve the transmission of the suction around the interior of the mould by eliminating air leaks. A plastic mesh was placed at the base of the sample to prevent the fine sand grains from escaping down the pedestal drainage hole. The soil was then poured into the mould using a tea spoon in layers (6 in total), each layer was compacted by dropping a 1 cm diameter rod weighing 350 g, 20 times from a constant height of 5 cm. After densifying each layer, a tamping rod (32mm diameter and 4.5 kg) was placed on top and approximately 12 blows were applied using a copper mallet (hammer) in order to help to reach a maximum density.

Once the mould was filled with the material, another plastic mesh was placed on top of the sample and the top platen with suction cap was put in place, the membrane was secured with o-rings and a 20 kPa suction was applied to help to hold the sample in place, then the vacuum acting on the membrane was removed (Figure 4.5a). Next, the mould was dismantled, Figure 4.5b, and the sample dimensions were measured. Around six readings were taken of the diameter, equally distributed along the bottom, middle and top of the sample. The average value obtained was reduced by twice the membrane thickness. For the height three measurements were taken and the average value taken as the sample height.

During the positioning of the sample in the triaxial apparatus, the alignment of the sample was checked by using a bubble level placed over the top platen. Once the local instrumentation (as described in Section 4.4.1) was place, the cell was closed and filled with water maintaining the pressure within the cell at atmospheric pressure. After filling the cell, the pressure was increased in 10 kPa steps and the suction reduced in similar steps until it has reduced to zero.

4.3.3 Specific volume calculation

The specific volume (v) is the total volume of soil per unit volume of solids, so that:

$$\nu = 1 + e \tag{4.1}$$

where e is the void ratio defined as the ratio of the volume of voids (V_v) to the volume of solids (V_s):

$$e = \frac{V_v}{V_s} \tag{4.2}$$

The total volume of the sample, V_t is calculated based on the geometry of the sample, then the volume of voids is obtained by $V_v = V_t - V_s$ and V_s can be calculated based on the following expression:

$$V_s = \frac{M_s}{G_s \rho_w} \tag{4.3}$$

where M_s is the mass of the solid, ρ_w is the density of water ($1.00 Mg/m^3$) and G_s is the specific gravity which was determined by the process described below.

(a) Measurement of specific gravity

The particle density measurements were carried out at University College Cork using a pycnometer (model Multivolume Pycnometer 1305 by Micromeritics). This method using an helium pycnometer, has the advantage of giving more accurate and faster measurements when compared to the traditionally used liquid-based techniques, as a gas can easily and thoroughly fill all the pore space in the sample. Three different samples were used and for each sample, three measurements were made for each sample. The measured values are presented in Table 4.2, the mean particle density of $2648\, kg/m^3$ ($2.648\, Mg/m^3$) was used.

(b) Initial specific volume for the intact and reconstituted samples

The initial specific volumes for the samples tested in the current research and in previous studies are presented in Table 4.3 for the intact samples and in Table 4.4 for the reconstituted samples. In the preparation method for the reconstituted samples, Cuccovillo (1995) used tamping of the sand layers during pluviation, while Cresswell (1999) and Bhandari (2009) used a pluviation technique described in Cresswell et al. (1999). The reconstituted samples obtained in this study were denser and so closer to the intact soil. Consequently the mechanical behaviour of the reconstituted samples was somewhat different to that observed in previous studies.

4.4 Triaxial tests

4.4.1 Bishop and Wesley triaxial apparatus

(a) General setup

The triaxial cell used to carry out the tests was a computer controlled hydraulic stress path apparatus, similar to that described by Bishop and Wesley (1975). A general overview of the principles of triaxial testing is given in this section.

The equipment was designed to enable axi-symmetric tests to be carried out on soil samples with a diameter of 38mm and a height to diameter ratio of 2 :1. A schematic diagram of the triaxial cell is shown in Figure 4.6. The cell is equipped with three pressure controllers, for cell pressure, back pressure and axial ram pressure, respectively. These are fed by a main compressed air supply and used together with air-water interfaces to transfer the air pressures to water via a rubber bellofram and then to the apparatus. The cell pressure interface was linked directly into the cell chamber and the ram pressure interface to a pressure chamber below the axial loading piston and pedestal. Two belloframs seal the cell fluid and the water in the ram pressure chamber. As the ram pressure is increased and decreased the piston travels up and down. Axial load can be applied to the sample by increasing the ram pressure, directing the pedestal upwards, pushing the sample top cap against a stationary load cell which records the deviatoric load. Since the samples were tested in a dry condition the drainage and back pressure connections were not used.

(b) Stress and strain measurements

To measure the deviatoric force, a submersible load cell of a maximum capacity of 4.5 kN was used. The load cell was connected to the sample by use of a suction cap. In order to measure the cell pressure a transducer connected to the cell pressure line was used. During the shearing stage, the deformation of the sample was controlled by the axial strain rate using a constant rate of strain pump (CRSP). The CRSP consists of a stepper motor controlled piston that supplies water at a rate defined by the controlling computer.

The external axial displacement was measured with an Linear Variable Differential Transformer (LVDT) and the local axial strain readings were taken by a set of small electrolevel inclinometers attached directly onto the sample in diametrically opposite positions as shown in Figure 4.7a. The radial strain readings were taken with the use of a radial belt, also equipped with an LVDT, that was attached horizontally at the mid-height of the sample (Figure 4.7b). Figure 4.8 shows the instrumentation used to measure the internal axial strain and the radial strain mounted on a sample. All the transducers and instruments were calibrated prior to testing.

The computer control software used was TRIAX, a program written by Dr. David Toll of Durham University. TRIAX monitors pressures and displacements, controls stresses and strains and allows the user to define a fully automated stress path or strain controlled stages.

(c) Load cell connection

The axial loading system was modified to ensure that the axial load was transmitted along the sample vertical axis of symmetry. Achieving the correct allignment is

particularly important for stiff materials such as the intact sand specimens used here. The connection between the sample top platen and the load cell was achieved by a simple contact using a half-ball. As illustrated in Figure 4.9, the half-ball is seated in a spherical notch in the top platen and rotates as the load cell touches the sample, reducing to a minimum the sample disturbance and any non-uniformity during shearing.

(d) Modifications for resin impregnation

To perform resin impregnation on dry soil specimens in the triaxial cell, some modifications to the triaxial apparatus were required. When dealing with resin it is necessary to identify which elements are in contact with the resin as they may not be reusable. The cell components that came into contact with the resin were the pedestal (from where the resin was induced into the specimen), the top cap and plastic tubes connected to the specimen. The tubes used to carry the resin from the container to the specimen have an external diameter of 4.5 mm, i.e., they were larger than the 3 mm generally used. This adjustment was required to allow the resin to flow easily into the sample. The top cap, which is usually made of perspex, was replaced by a brass one, to allow for drilling after resin impregnation. The pedestal was also made of brass. Instead of a porous stone, a nylon mesh was placed at the bottom and top of the soil specimen to stop the material from getting into the holes of the pedestal and the top cap. Only the plastic tubes, the nylon meshes and the resin container were disposable. These modifications do not interfere with the conventional setup and so the specimens could be subjected to conventional triaxial tests.

4.4.2 Calculations of stress and strain

It is important to outline clearly how the various stress and strain values were calculated. The axial strain ε_a, for both local and external axial displacements, was calculated based on the change of axial length Δl over the initial sample length l_0 as follows:

$$\varepsilon_a = \frac{\Delta l}{l_0} \tag{4.4}$$

The average local axial strain measurements were used up to the point where divergences between the LVDTs become significant, as discussed in the next section. After this point the external displacement transducer was used.

The radial strain, ε_r was calculated based on the change in the sample diameter measured by the radial belt Δd divided by the initial diameter d_0 of the sample as follows:

$$\varepsilon_r = \frac{\Delta d}{d_0} \tag{4.5}$$

The shear strain was calculated by the following expression:

$$\varepsilon_s = \frac{2}{3}(\varepsilon_a - \varepsilon_r) \tag{4.6}$$

where ε_a and ε_r are the axial and radial strains obtained from the local instrumentation.

The volumetric strains were also calculated using the following expression, (Klotz and Coop, 2002):

$$\varepsilon_v = \varepsilon_a + 2\varepsilon_r - 2\varepsilon_r\varepsilon_a - \varepsilon_r^2 + \varepsilon_r^2\varepsilon_a \tag{4.7}$$

The deviatoric stress q was calculated based on the force F recorded in the load cell and the current cross-sectional area of the sample A_c, as given by the following expression:

$$q = \frac{F}{A_c} \tag{4.8}$$

The current area, A_c, was calculated by applying a right-cylinder correction, as proposed by Bishop and Henkel (1957), as follows:

$$A_c = A_0 \frac{1 - \varepsilon_v}{1 - \varepsilon_a} \tag{4.9}$$

where A_0 is the initial cross-sectional area of the sample.

Because the tests were drained and with constant cell pressure, the mean effective stress p' is given by $\sigma'_c + q/3$, where σ'_c is the cell pressure.

4.4.3 Test description

(a) Isotropic compression

Prior to the shearing stage, the sample was gradually taken to a specific isotropic effective stress condition, which was 300 kPa for all tests with the exception of one test carried out at 100 kPa. This was done by first connecting the suction cap and then increasing the cell and axial pressure simultaneously, maintaining the deviatoric stress q equal to zero. The isotropic compression rate used was 50 kPa/h. Once the confining pressure value was reached the sample was left for approximately 12 hours to allow creep to take place.

(b) Shearing

Once the required effective stress condition had been achieved the shearing stage was initiated. During the shearing stage the soil was compressed using axial strain control at a constant rate of 1 %/h.

(c) Testing programme

A total of 15 specimens including intact and reconstituted samples were tested. Some specimens were not successfully tested, mainly due to leaks though the membrane and difficulties in connecting the suction cap. In order to characterise the soil fabric prior to loading and the evolution of the fabric upon shearing deformation, 10 specimens, 5 intact and 5 reconstituted, were required. This included one specimen that was impregnated prior to loading and four specimens that were impregnated at the following stages of loading: at the end of isotropic compression, at the onset of dilation, at the start of a visible shear band and the final specimen was impregnated as the soil eventually approaches a critical state. Figure 4.10 illustrates the four stages selected for resin impregnation of the specimens, along a typical stress:strain:volumetric curve.

The initial characteristics of the specimens tested are summarised in Table 4.5. The very similar initial densities (or specific volumes) for all the intact specimens is an indicator of the consistency of the sample preparation technique. For the reconstituted specimens, relatively consistent densities were again achieved, given the difficulty in reproducing specimens with exactly the same density using the proposed method.

4.4.4 Strain localisation and failure mode analysis

It is known that sands subjected to shearing do not undergo uniform deformation (e.g., Desrues et al., 2007; Viggiani and Hall, 2008). The non-uniformity arises because the material is not truly homogeneous at the scale of a laboratory specimen, and the boundary conditions are imperfect. As a consequence, the specimen deformation tends to localise on one or more narrow zones at some point during the test, normally close to the point where the peak deviator stress is mobilised.

As already mentioned, axial strain measurements were obtained using both local transducers and external transducers. Movements that develop during shearing stage, originating from various sources, cause an overestimation of the strain when the external axial strain readings are used. This overestimation is greater in the pre-peak regime. The most important sources of errors are associated with the compliance of the loading device, the tilting of the specimen and the bedding at the

top and bottom of the specimen (Jardine et al., 1984; Goto et al., 1991). The average axial strain measurements obtained from the local transducers are more accurate in the early stages of shearing, prior to the development of major localisations during the post-peak strain softening regime.

The localisation of deformations in a sample during shearing, typically results in the divergence between the two local axial strain measurements, and so, the onset of localisation or strain non-uniformity, can be identified by comparing the axial strain readings. The variation of the instantaneous local and external strain rates ($d\varepsilon/dt$) against the axial strain (calculated as indicated in Section 4.4.2), were investigated for both the intact and reconstituted samples.

As shown in Figure 4.11, for the intact sample tested to a stage near the critical state, after an initial adjustment between the readings from the two local axial strain transducers there was a period of good agreement between both the local and external measurements. Just before the peak deviatoric stress was mobilised the readings started to diverge, this may indicate the onset of localisation or at least the point of an onset of heterogeneity in the strain field. This was followed by a strong divergence that culminated with the development of the shear band. A similar trend can be observed for the other intact sample sheared to this stage just before the shear band became visible (Figure 4.12). The local radial strain rate shows an increase up to the point when the main localisation started to develop and after which volumetric dilation tended to concentrate in the shear plane.

Previous studies on sandstones and locked sands have also demonstrated that the onset of strain localisation and loss of specimen homogeneity, is a pre-peak phenomenon (e.g., Bésuelle et al., 2000; Cresswell and Powrie, 2004). These initial deformations were found to be related to micro-slips and deformation between sand grains. Bhandari (2009) found that the applied confining pressure had a significant influence on the initiation and growth of the localisation.

Figures 4.13 and 4.14 show data for two reconstituted samples, these specimens exhibit a poor agreement between the axial strain readings from the local transducers which may be an indication of the lower degree of homogeneity in these samples when compared to the intact samples. Nonetheless, the point at which the axial strain values started to diverge considerably can be identified to be significantly after the mobilisation of the peak stresses, at an axial strain of approximately 7 % and just before a shear plane became visible in the specimen. For one of the samples this threshold also involved a reversal in the direction of movement of both local inclinometers. The evolution of the radial strain rate showed an increase in the pre-peak regime followed by a constant period until it started to reduce as the shear plane developed.

The localisation of deformation into a thin zone of intense shearing resulted in

the development of a well defined shear plane in both the intact and reconstituted samples. In addition, the samples also underwent considerable barrelling, as the effect of the end restraint became more significant. Figure 4.15 shows images of the intact and reconstituted samples at late stages of shearing. The tests were stopped at axial strain values of 9 % and 12.5 % for the intact and reconstituted samples respectively, as further shearing could have caused the rupture of the membrane.

After the formation of the shear plane the failure mechanism consisted of a sliding of two rigid blocks along the failure surface. This sliding is more evident for the reconstituted sample as can be see by the considerable displacement of the top block in Figure 4.15b. The point of the initiation of this mechanism has been considered by some researchers (e.g., Bésuelle et al., 2000) as the limit after which the measured overall response of the specimen can no longer be considered representative of the material behaviour. In fact, there are many uncertainties associated with the assumptions made for the analysis of the post-localisation data. An alternative to the right cylinder assumption for the cross-sectional area calculation is to use the formulation suggested by Chandler (1966) that considers the shear plane geometry. However, the occurrence of barrelling during strain softening makes the failure mechanism more complex. Therefore, using Chandler's area correction in this case would, predict smaller areas and consequently higher q values when compared to the use of a right cylinder area correction. For similar deformation modes that were observed in dense sands and sandstones Gutierrez (2007) concluded that the use of Chandler's correction would give unrealistic q values.

The orientation of the shear planes was measured based on images of the samples and is presented in Figure 4.16. For the intact soil sample, the shear band is orientated at approximately 63° to the horizontal, which is also the steepest kinematically permissible location for a sample with a height to diameter ratio of 2 : 1. However, triaxial tests carried out by Cresswell (1999) on samples with greater height to diameter ratio showed approximately the same shear band orientation. The reconstituted soil exhibited a less steep shear band, with an inclination of about 57° to the horizontal plane.

The shear plane that formed in the reconstituted soil specimen was thicker that those observed in the intact soil. Assuming that shear band thickness measurements from visual inspection are never precise, approximate values of $7 \times d_{50}$ for the intact specimen and $11 \times d_{50}$ for the reconstituted were observed. Cresswell (1999) reported slightly lower typical thickness values, of $4 \times d_{50}$ for the intact soil and $10 \times d_{50}$ for the reconstituted material.

4.4.5 Interpretation of test results

(a) Stress strain behaviour

The stress-strain plots for all the three intact specimens that were sheared are shown in Figure 4.17 and the corresponding volumetric responses are presented in Figure 4.18. The plot of the volumetric changes showed an initial contracting behaviour followed by a main dilation stage. In the early stages of shearing, the soil was able to mobilise high stress ratios, in excess of that at the critical stage, before the onset of dilation. Following previous studies, this "less conventional" strain-hardening regime can be explained by the locked fabric of the soil. Just after the dilation started the stress-strain responses showed an extended peak followed by a drop in the mobilised stress. This marked reduction in stress is associated with the development of the localisations in the soil and coincides with the formation of a visible shear plane. At the end of shearing the stress ratio seems to have stabilised and this indicates that the soil must had been close to reaching a critical state although localised on a discrete shear plane. It was not possible to confirm that a critical state was achieved as the volumetric strains continued to increase showing a unrealistic behaviour that can be explained based on the limitations in measuring the volumetric changes, where the LVDT data cannot be relied upon after the development of strain localisations. While the true volumetric strains will be restricted to the shear plane, the rigid body deformation mechanism gives unrealistically high negative radial strains and hence dilation (Klotz and Coop, 2002) Where the strain levels overlap, the stress:strain curves for the intact samples show good agreement which is an indicator of the soil homogeneity as well as consistency of the testing procedures.

Figure 4.19 shows the stress-strain responses of the three reconstituted samples, followed by the volumetric curves in Figure 4.20. The volumetric response shows a slight initial contraction prior to the onset of dilation, just as for the intact soil. As before, the volumetric measurements after the shear band forms are clearly not reliable. The differences in the stress-strain behaviour between the intact and the reconstituted samples are significant as can also be observed in the comparative plots presented in Figure 4.21. For the same confining pressure, the intact soil shows a peak strength that is significantly higher than the reconstituted soil. While the reconstituted soil was unable to reach the same high stress ratios, it also exhibited a much less pronounced drop in the soil strength during the strain softening regime. The formation of a visible rupture occured in the intact sample at an axial strain level of about 4 % while in the reconstituted soil a visible shear band occured at about 9% axial strain. Again, is difficult to say if the sample taken to an axial strain of 12 % have reached the critical state.

The influence of the effective confining stress on the response of the intact soil can be seen by a comparison of the stress:strain curves for two specimens tested at

confining pressures of 100 kPa and 300 kPa, as shown in Figure 4.22. The specimen tested at a lower confining pressure (100 kPa) mobilised higher peak stress ratios than the sample tested at 300 kPa. It can be observed that for a cell pressure of 300 kPa the stress:strain curve of the material exhibited a considerable plastic plateau and much less pronounced strain softening. As the volumetric curves show, both samples developed major strain localisation at similar axial strains, but the sample tested at 100 kPa reached higher volumetric strains at this stage when compared to the reconstituted sample. These findings were in accordance with the results from previous studies carried out at different cell pressures (Cresswell and Powrie, 2004; Bhandari, 2009), which also demonstrated the role of confining pressure in controlling the localisation characteristics.

(b) Stress dilatancy analysis

In the stress:dilatancy analysis, the dilatancy or rate of dilation (d), is defined as $d = -\delta\varepsilon_v/\delta\varepsilon_s$, where $\delta\varepsilon_v$ is the volumetric strain and $\delta\varepsilon_s$ is the shear strain. Figures 4.23 and 4.24 show the stress-dilatancy plots for the intact and reconstituted samples, respectively. As already mentioned above, at the onset of dilation the intact soil shows higher stress ratios of about 1.7 when compared to those mobilised by the reconstituted samples, where a value of 1.35 was observed. This shows that the work required to overcome the deformation resistance provided by the locked fabric mobilises additional strength.

In the case of the intact soil, the peak stress ratio $(q/p')_{peak}$ was mobilised at an earlier stage of dilation and occurred before the maximum dilation rate was achieved, as shown in Table 4.6, where d_{peak} is the dilatancy observed at peak stress and d_{max} is the maximum rate of dilation. In contrast to the intact soil, for the reconstituted samples the peak stress ratio was mobilized at the maximum rate of dilation. The intact samples also exhibited higher dilation rates compared to the reconstituted samples.

The stress:dilatancy curves for the two intact samples tested at 100 kPa and 300 kPa are compared in Figure 4.25. As expected, the sample sheared at 100 kPa exhibited higher rates of dilation, which shows that the maximum rate of dilation decreases with increasing confining pressure, as also demonstrated in Figure 4.1 from Cuccovillo and Coop (1999).

(c) Stiffness degradation curves

The data from the shearing stage was analysed in terms of tangent stiffness ($\delta q/3\delta\varepsilon_s$) by a simple 30 point linear regression and plotted against the logarithm of the shear strain (ε_s). Figures 4.26 and 4.27 present the shear stiffness degradation

curves for the intact and for the reconstituted samples, respectively. At very low strains, the intact specimens, show a decrease in the shear modulus, during the initial compression of the sample. An acceleration in the rate of compression is associated with a recovery of stiffness back to its initial value. The initial drop and subsequent rise in the stiffness may be due to the arrangements of the grains as they respond to the imposed stress. Associated with the start of dilation the sample stiffness starts to reduce dramatically. The intact material shows higher initial shear stiffness values and a more abrupt stiffness degradation when compared to the reconstituted soil.

The magnitudes of the initial values of the shear stiffness decreased as the initial confining pressure decreased from 300 kPa to 100 kPa, as shown in Figure 4.28. Bhandari (2009) also observed the decrease of the shear stiffness as the confining pressure decreases.

(d) Discussion

Cresswell and Powrie (2004) hypothesised that for sands with locked fabric, dilation is the mechanism by which the soil becomes destructured and its strength is reduced towards that of an unstructured material. In these early studies, the extent of this destructurisation was, however, not established. It is therefore unclear whether at the final stage of shearing the intact material retains any of the initial locked fabric, as the opening of fabric may only occur in the localisations and not throughout the specimen.

This uncertainty led to the existance of a unique critical state line for both the intact locked soil and the reconstituted material (as discussed in Cuccovillo and Coop, 1999). Desrues et al. (1996) showed that for unstructured soils, the void ratio reached inside the shear bands is independent of the initial density of the soil, suggesting the existance of a critical void ratio. Oda and Kazama (1998) have shown that outside the shear band the void ratio is very close to the initial one. The assumption that there exists a unique critical-state line for a soil is based on the hypothesis that the soil has a unique structure at the critical state, which is essentially independent of the soil initial fabric and the loading history and so it is expected that a large shear deformation that the sample fabric does not resemble the initial fabric. The fabric investigation presented in Chapter 8 aims to give a better understanding into the micro-scale deformation of both structured and unstructured soils.

4.5 Resin impregnation

Preservation of the fabric in sand specimens by impregnating the specimen with resin and allowing the resin to cure has been used in a number of previous studies

(e.g., Palmer and Barton, 1986; Jang et al., 1999; Masad and Muhunthan, 2000). An alternative technique for soil preservation involves saturating the specimen with water and freezing it (e.g., Mimura, 2003; Frydman et al., 2007). Resin impregnation has, however, the great advantage of being more practical, allowing for thin sections to be made, while frozen samples are susceptible to thawing and require the imaging process to be carried out under controlled environmental conditions. In additon, freezing is often associated to changes of volume.

4.5.1 Resin characteristics

The success of any resin impregnation technique is greatly dependent on the resin characteristics. The most critical requirement for a resin is that it should not cause disturbance to the soil fabric. Disturbance can happen due to the viscosity of the resin, or if there is significant shrinkage during curing. Many epoxy resins have a viscosity that is too high to achieve satisfactory impregnation. Typical epoxy viscosity values can be higher than 300 cps at room temperature, compared to the viscosity of water of 1 cps. Low-viscosity resins are in general thermo-curing, and consequently differential thermal stresses and volume changes of the specimen can occur due to temperature changes resulting in soil disturbance. The curing of epoxy can also disturb the soil structure since all epoxy resins incur some shrinkage during curing, even in the absence of heating. This shrinkage of most epoxy resins can be attributed to the high solvent content, and so the resin should ideally have little or no solvent content.

The properties of an ideal resin suitable for impregnating sand specimens were summarized by Jang et al. (1999) to be as follows:

- Low viscosity
- Can cure at room temperature
- Exhibit low shrinkage during curing
- Have a high hardness value and high bonding strength on curing
- Have a short curing time
- Non-toxic
- Non-reactive both with the soil and the test equipment

Previous studies on the impregnation of sands (e.g., Palmer and Barton, 1986 and Jang et al., 1999), have suggested EPO-TEK 301 (by Epoxy Technology Inc.) as a suitable resin that meets the above criteria. EPO-TEK 301 resin and hardener, is a

two-part epoxy resin that cures at room temperature within about 12 hr after mixing and has a relatively low viscosity (100 cps at 25 °C). As noted by Jang et al. (1999) the linear shrinkage of this resin is relatively low when compared with other epoxy resins and additionally it has an excellent bonding strength and medium hardness, when cured, which allows small cores to be drilled and thin sections be made. As like most epoxy resins, EPO-TEK 301 does not cure well in moist environments.

4.5.2 The use of resin dyes

Coloured dyes are commonly used to increase the contrast between grains and void space in thin section analysis. However, adding colorant to the epoxy resin is likely to change the mixture viscosity and consequently cause fabric disruption as reported by Palmer and Barton (1986). Given the limited amount of information available on the use of resin dyes in friable uncemented sands, no colorant was used in this study.

4.5.3 Process description

The resin and the hardener mixed by weight with a ratio of 4:1, according to the EPO-TEK 301 Data Sheet (1998). Both parts were poured into a disposable glass container and stirred for a few minutes until the they were mixed together.

Impregnation was carried out by introducing the mixture into the specimen through the hole in the pedestal, under a initial suction of approximately 20 kPa, applied at the top of the sample. Once the resin became visible inside the sample the suction was reduced to 10 kPa, this suction was found to be sufficient to allow the full sample impregnation.

The velocity of the resin flow was controlled by the suction value applied to the specimen. While the velocity should be kept as low as possible to minimise fabric disruption, the duration of the impregnation process is limited by the resin pot life, i.e., the time when the viscosity of the resin reaches twice the viscosity immediately after mixing. The pot life for EPO-TEK 301 is 1-2 hours. The pot life can be slightly extended by keeping the epoxy resin in a fridge prior to use and a careful monitoring of the impregnation velocity is required to make sure that the sample is fully impregnated before the resin viscosity increases too much.

The full impregnation of the specimens took in general 1 to 1.5 hours. Once the resin reached the top of the sample the suction valve was closed and the sample was left overnight to set. The global sample disturbance during impregnation with epoxy resin was monitored by means of true LVDT instrumentation and was found to be negligible, as shown in Table 4.7.

4.6 Specimen preparation for image acquisition

4.6.1 Thin sections

Vertical thin sections from the central part of each impregnated sample were produced at Royal Holloway (University of London) for image analysis using optical microscopy. The thin sections had a thickness of $30\,\mu m$ and a size equivalent to the cross-section of the triaxial specimens, approximately 38 mm wide and 76 mm in height. The thin sections were used for a qualitative description of the particle morphology and fabric.

4.6.2 Core drilling

Cylindrical samples of diameters between 5 and 9 mm and approximately 10 mm high were cored at the Earth Science laboratory at Imperial College from the impregnated samples, for X-ray micro-CT scanning, as illustrated in Figure 4.30. The locations for the core extraction are discussed in Chapter 5.

Sample ref.	Soil mass (g) initial	final	moisture content (%)
RS1	35.10	34.54	1.61
RS2	20.50	20.19	1.54
RS3	38.19	37.70	1.32

Table 4.1: Moisture content of the intact soil

Sample ref.	Particle Density (kg/m^3)		
	Measurement 1	Measurement 2	Measurement 3
A	2682.51	2684.87	2642.01
B	2678.52	2640.34	2687.76
C	2582.61	2548.73	2689.01

Table 4.2: Particle density (kg/m^3) obtained by pycnometry

Initial specific volume (intact specimens)			
Cuccovillo (1995)*	Cresswell (1999)	Bhandari (2009)	This study
1.44	1.46	1.44	1.47-1.48

*soil with inter-granular cement

Table 4.3: Initial specific volumes for the intact samples used in different studies

Initial specific volume (reconstituted specimens)			
Cuccovillo (1995)*	Cresswell (1999)	Bhandari (2009)	This study
1.66	1.56-1.59	1.65	1.49-1.53

*soil with inter-granular cement in intact state

Table 4.4: Initial specific volumes for the reconstituted samples used in different studies

Sample ref.	Material	Sample mass (g)	Sample diameter (mm)	Sample height (mm)	Initial Density (Mg/m^3)	Initial specific volume	Stage of investigation
297-int	intact	154.00	38.00	76.00	1.787	1.48	prior to loading
296-int	intact	154.00	38.00	76.00	1.787	1.48	end of iso. comp.
294-int	intact	153.98	38.00	76.00	1.786	1.48	onset of dilation
293-int	intact	154.78	38.00	76.00	1.796	1.47	start visible shear band
295-int	intact	154.62	38.00	76.00	1.794	1.48	approaching CS
291-rec	reconstituted	144.59	38.25	71.20	1.767	1.50	prior to loading
292-rec	reconstituted	149.07	38.49	73.3	1.748	1.52	end of iso. comp.
288-rec	reconstituted	146.00	38.27	72.5	1.751	1.51	onset of dilation
289-rec	reconstituted	146.47	38.54	72.62	1.729	1.53	start visible shear band
290-rec	reconstituted	146.18	38.04	72.5	1.774	1.49	approaching CS

Table 4.5: Characteristics of the tested specimens

Sample ref.	$(q/p')_{peak}$	d_{peak}	d_{max}
293-int	2.06	1.45	1.71
295-int	2.05	1.40	1.83
289-rec	1.68	1.25	1.25
290-rec	1.75	1.26	1.26

Table 4.6: Rate of dilation, d, for the intact and reconstituted samples at peak

Sample ref.	Specific volume measured at	
	the end of test	the end of impregnation
294-int	1.462	1.463
293-int	1.625	1.633
295-int	1.667	1.668
288-rec	1.501	1.500
289-rec	1.872	1.870
290-rec	1.698	1.696

Table 4.7: Change in specific volume during impregnation

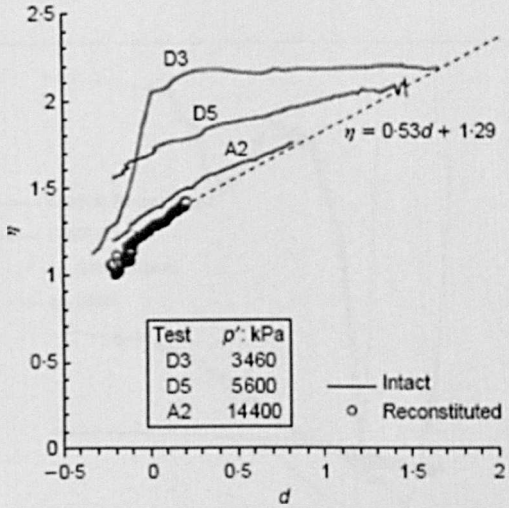

Figure 4.1: Stress-dilatancy relationships for Greensand (Cuccovillo and Coop, 1999)

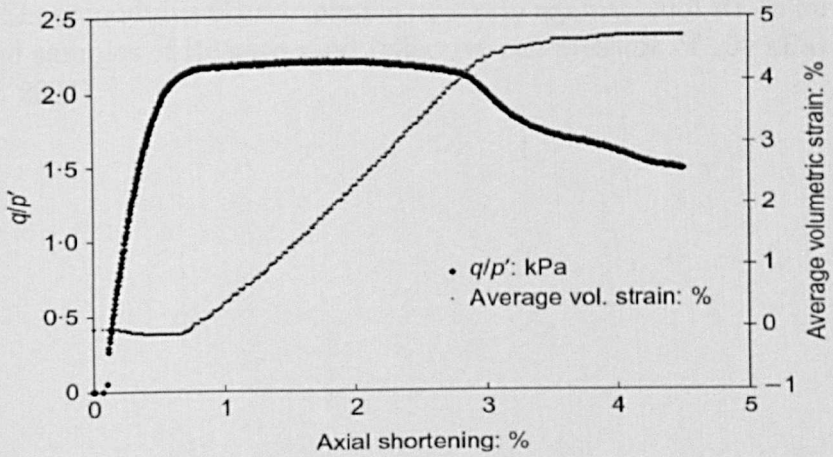

(a)

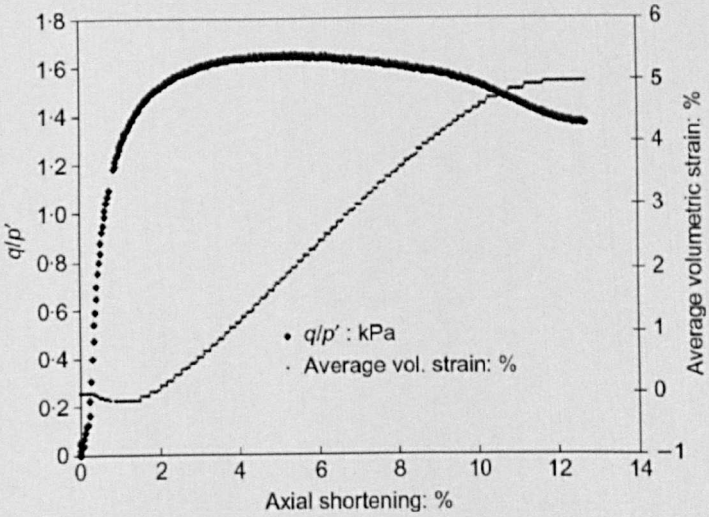

(b)

Figure 4.2: Typical stress-strain behaviour of Reigate and sheared at low confining pressures (200kPa) (a) intact specimen (b) reconstituted specimen (Cresswell and Powrie, 2004)

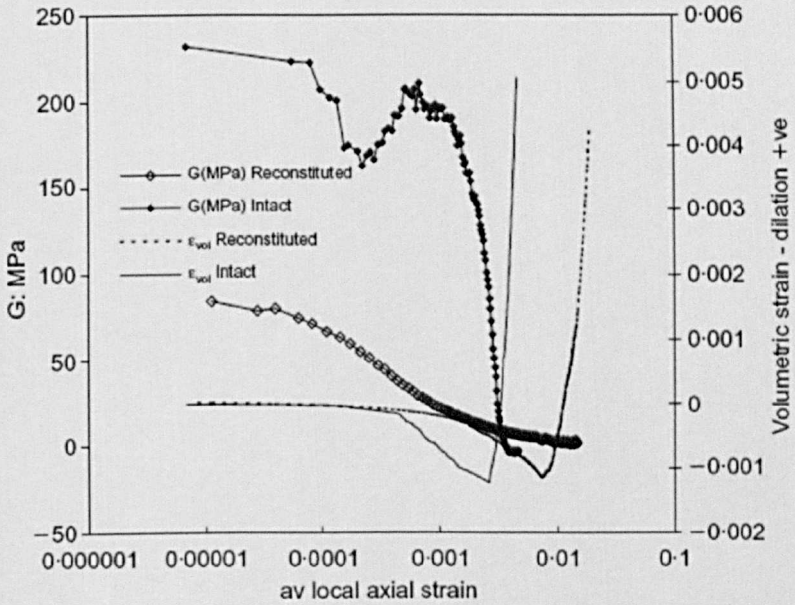

Figure 4.3: Shear modulus G and volumetric strain against axial strain for intact and reconstituted samples of Reigate sand (effective cell pressure of 100 kPa) (Cresswell and Powrie, 2004)

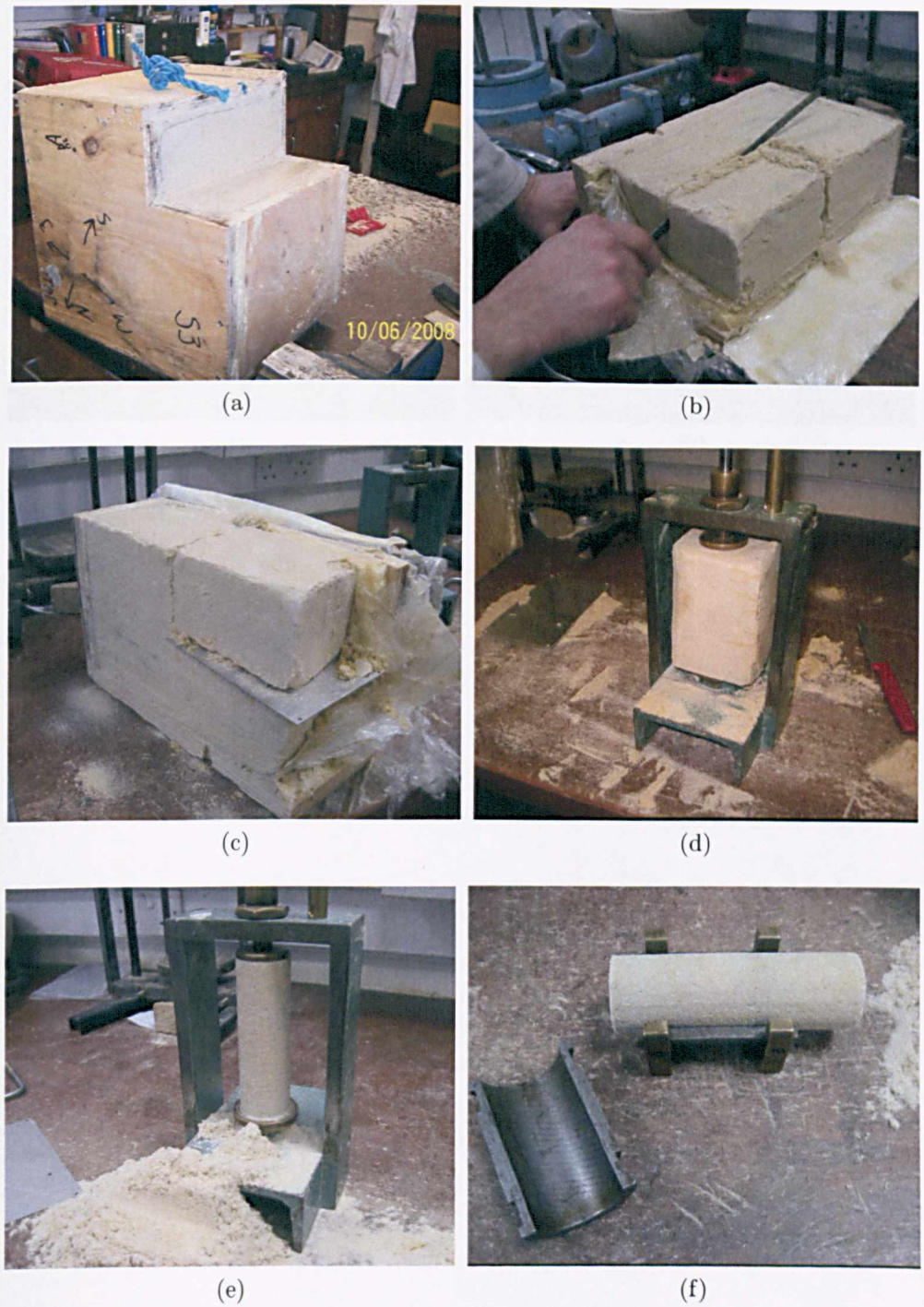

(a) (b) (c) (d) (e) (f)

Figure 4.4: Trimming process of the intact specimens (a)(b)(c) extracting small rectangular blocks from the wooden box (d) mounting the initial sample onto a hand lathe (e) shaping the cylindrical sample (f) trimming the ends of the final sample

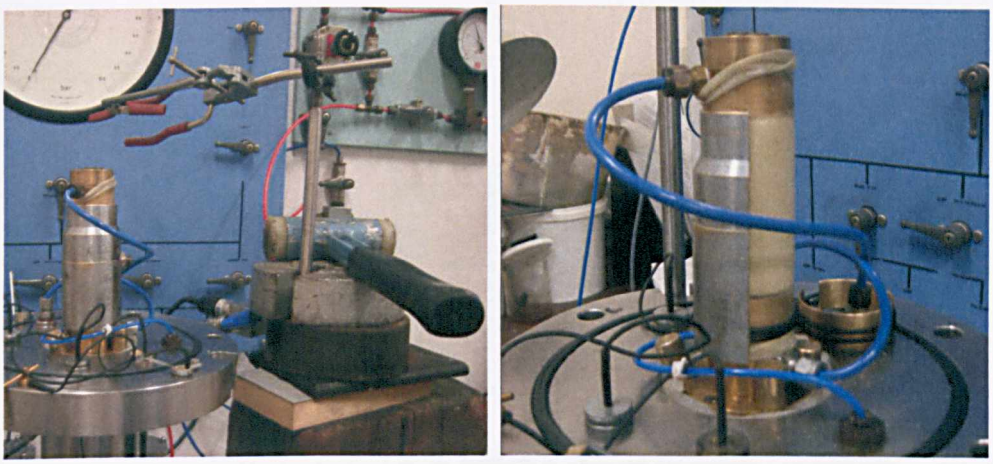

(a) (b)

Figure 4.5: Preparation of a reconstituted specimen

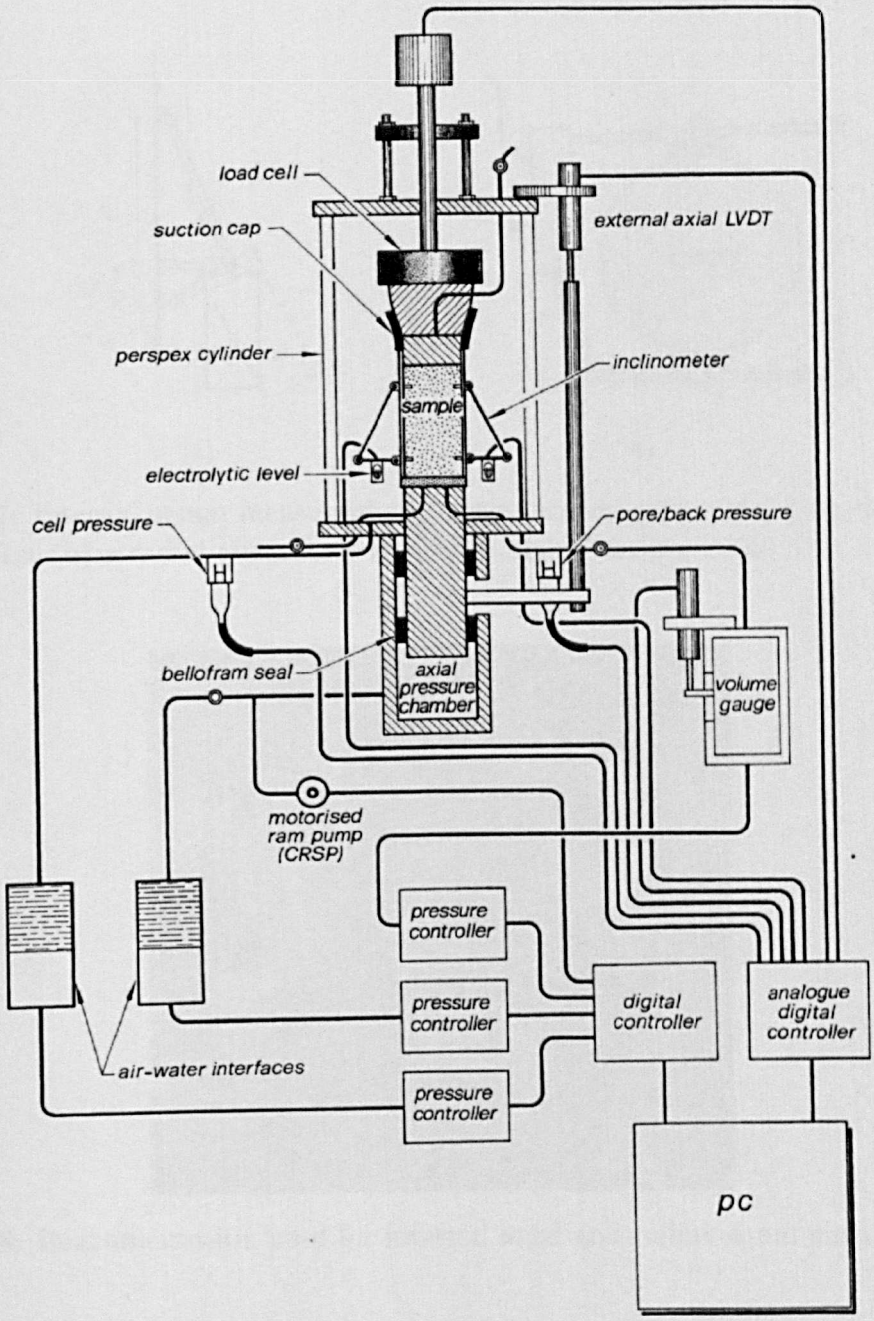

Figure 4.6: Schematic diagram of a typical Bishop & Wesley triaxial apparatus (modified from Qadimi, 2005)

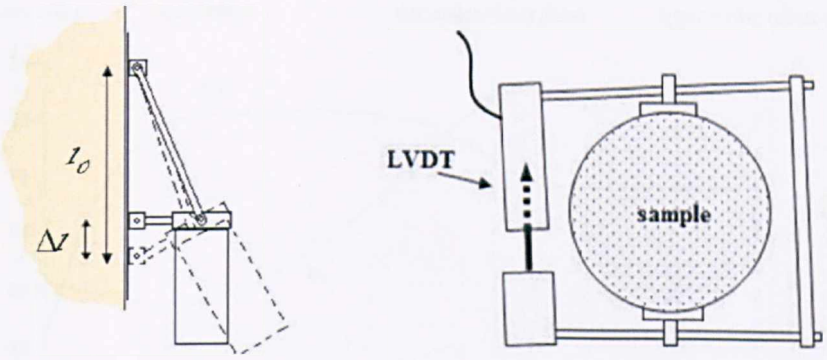

(a) (b)

Figure 4.7: Internal strain measurements, schematic diagrams of (a) an electrolevel inclinometer (b) a radial strain belt (modified after Carrera, 2008)

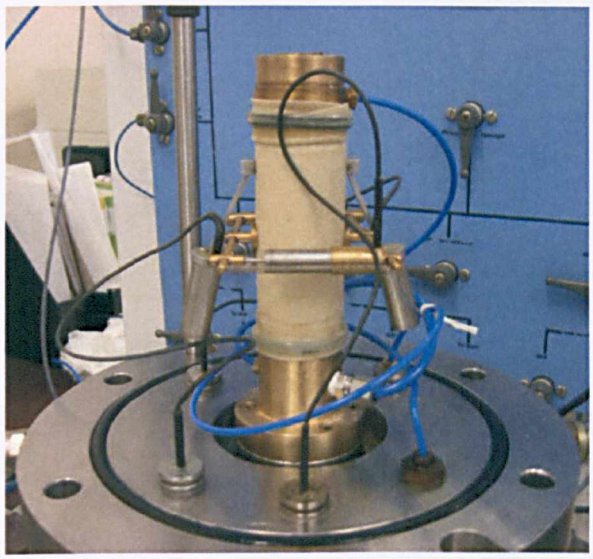

Figure 4.8: Instrumentation used for internal axial and radial strain measurements

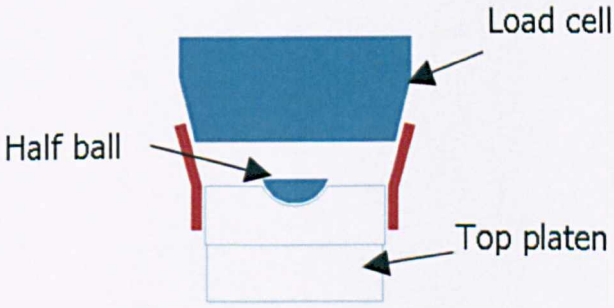

Figure 4.9: Modified top cap

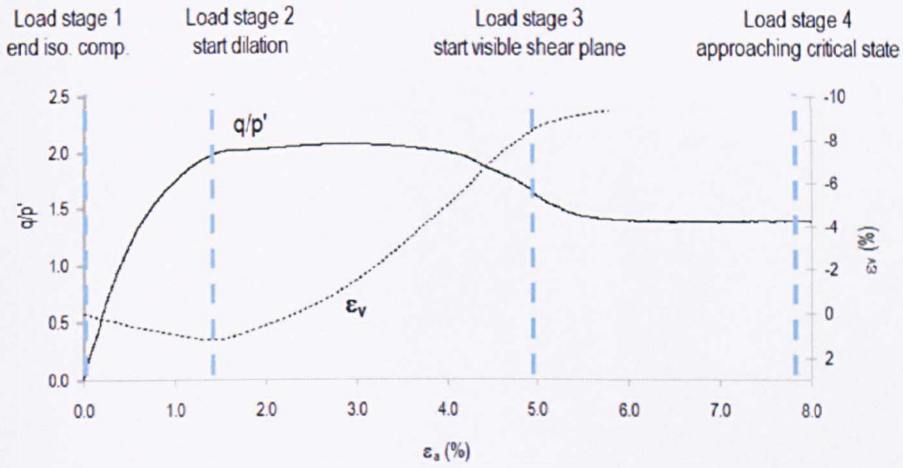

Figure 4.10: Different stages of loading used for morphology and fabric quantification

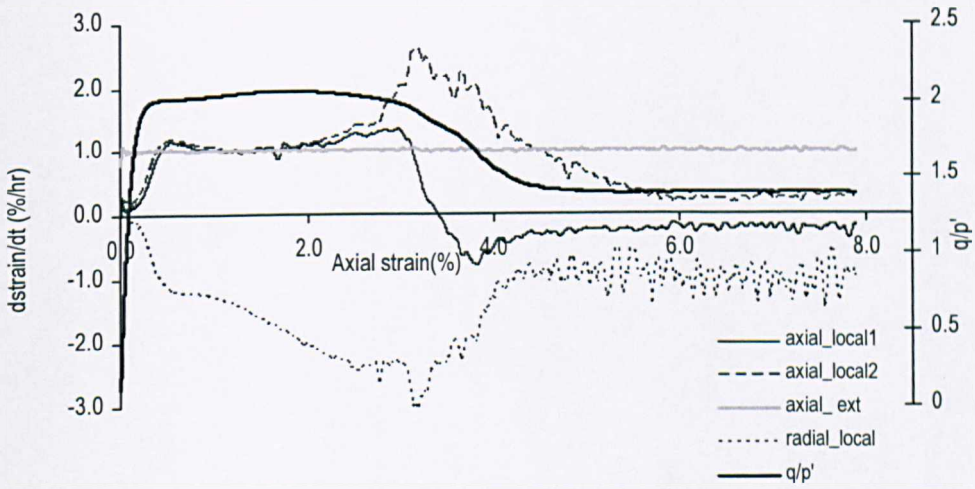

Figure 4.11: Evolution of local and external strain measurements during shearing, for the intact specimen representing the final stage of shearing (specimen 295-int)

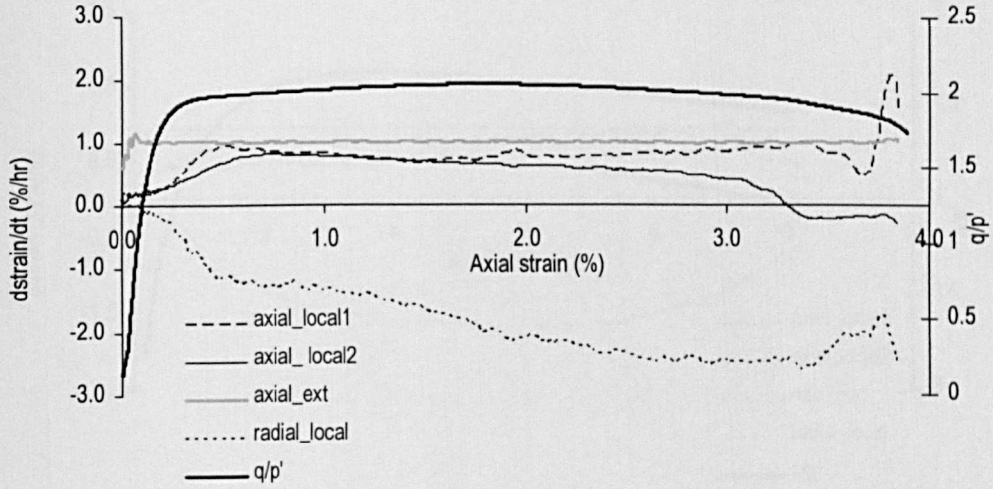

Figure 4.12: Evolution of local and external strain measurements during shearing, for the intact specimen representing the stage when the shear band became visible (specimen 293-int)

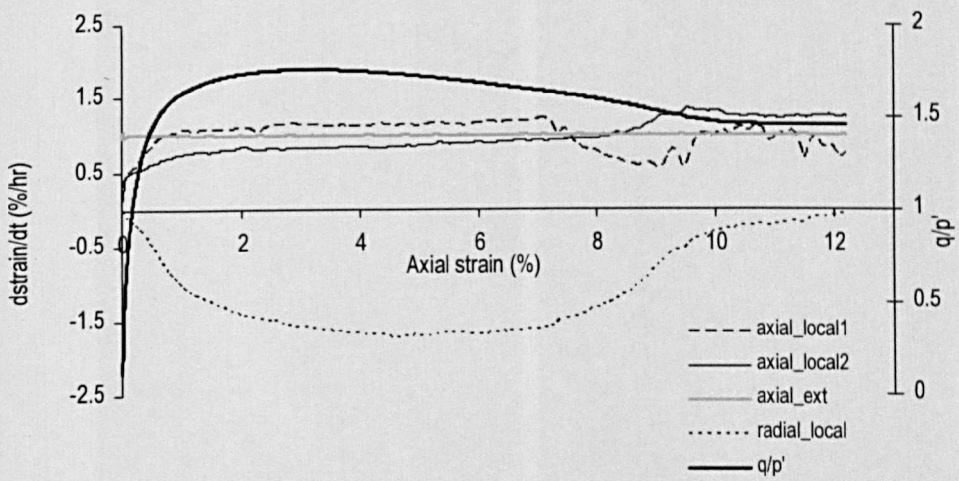

Figure 4.13: Evolution of local and external strain measurements during shearing, for the reconstituted specimen representing the final stage of shearing (specimen 290-rec)

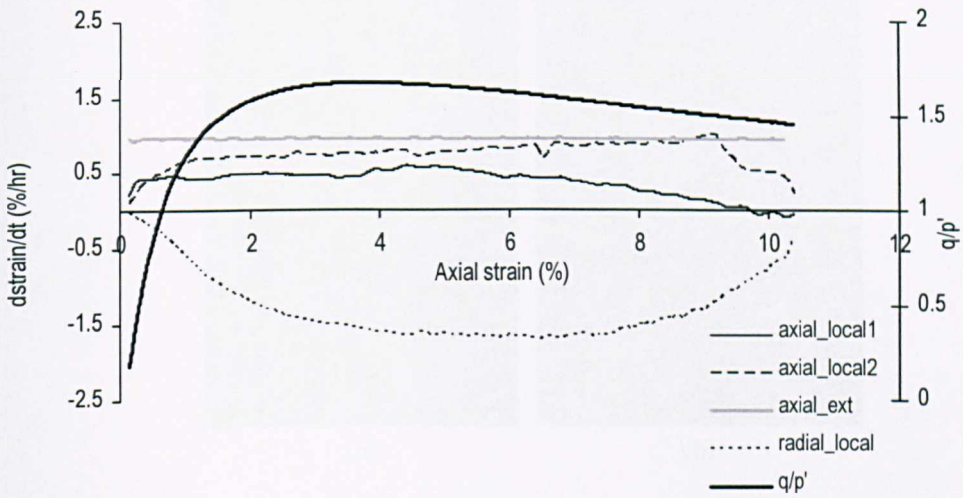

Figure 4.14: Evolution of local and external strain measurements during shearing, for the reconstituted specimen representing the stage when the shear band became visible (specimen 289-rec)

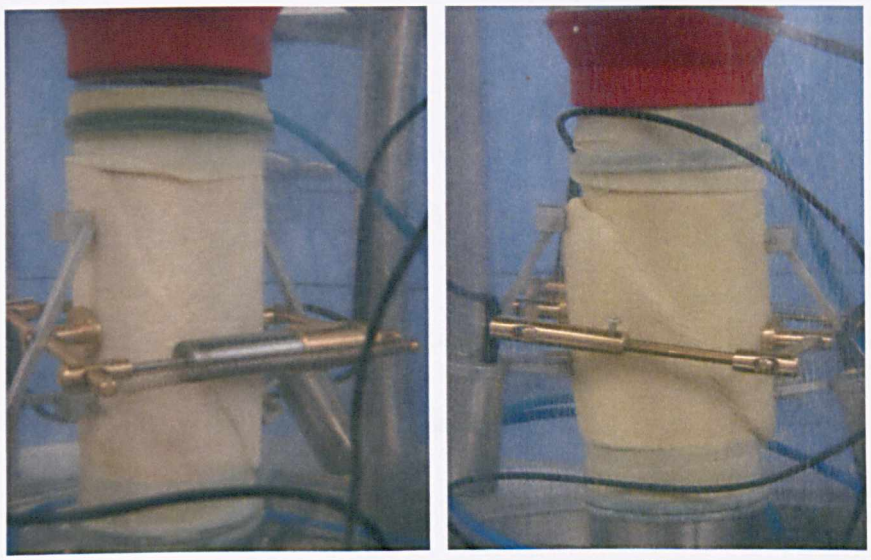

(a) (b)

Figure 4.15: Formation of a shear band (a) intact specimen (b) reconstituted specimen

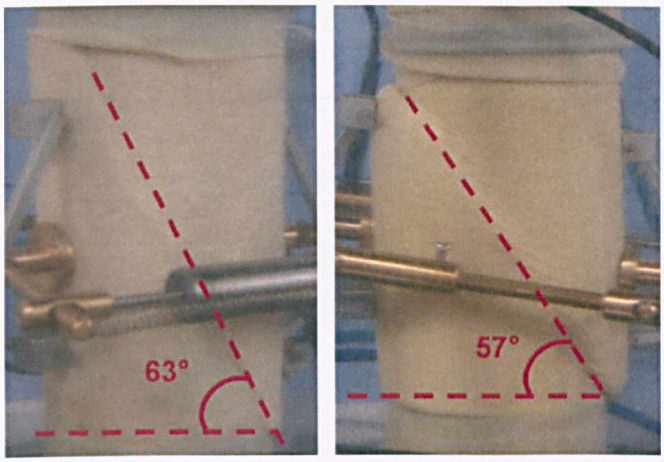

(a) (b)

Figure 4.16: Shear plane angle, estimated measurements for (a) intact material (b) reconstituted material

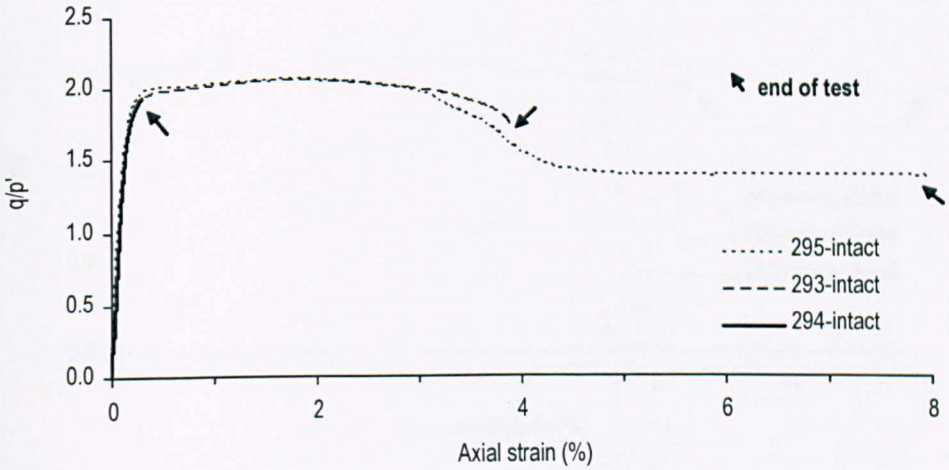

Figure 4.17: Stress:strain plot of the shearing for the intact soil

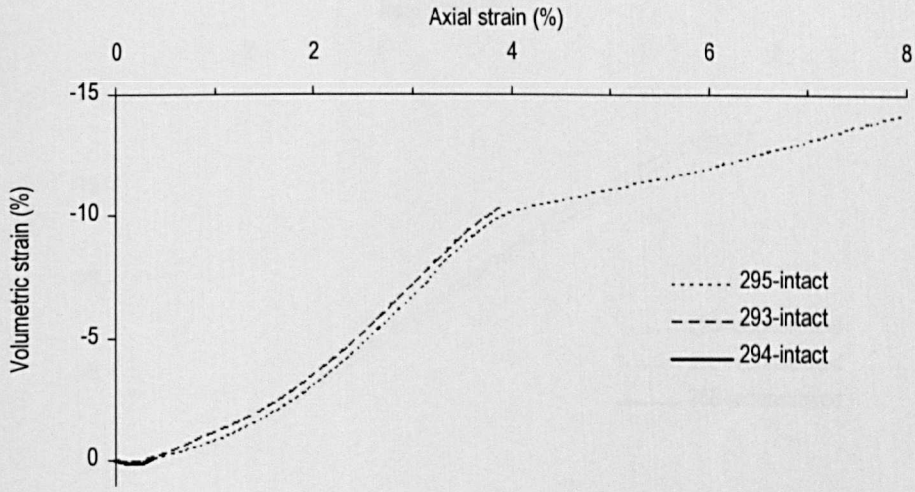

Figure 4.18: Volumetric strain plots of the shearing for the intact soil

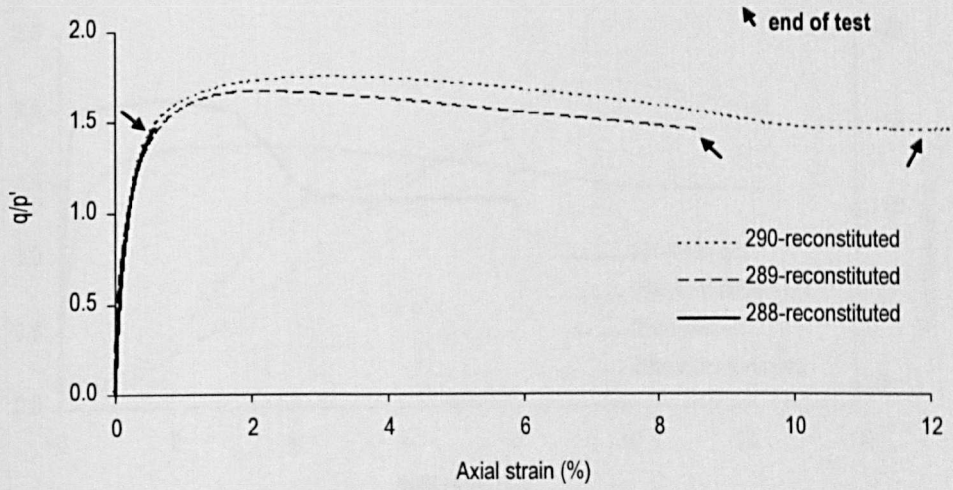

Figure 4.19: Stress:strain plot of the shearing for the reconstituted soil

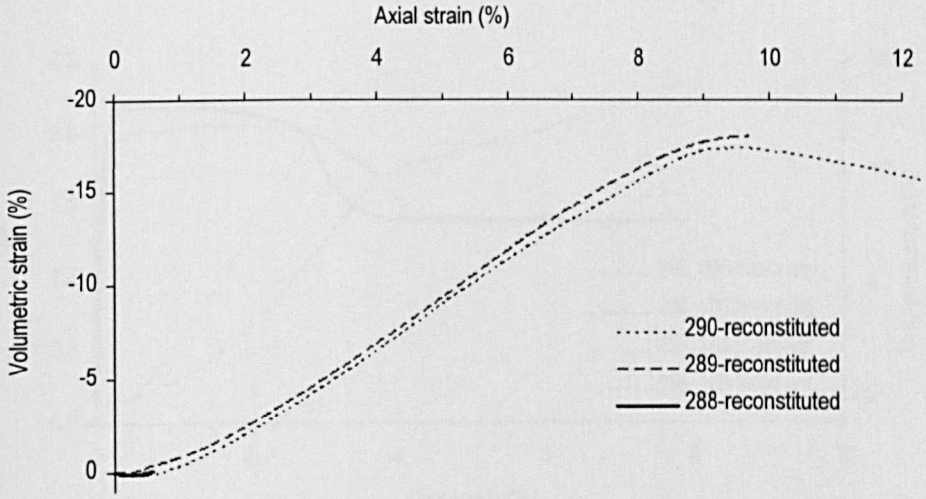

Figure 4.20: Volumetric strain plots of the shearing for the reconstituted soil

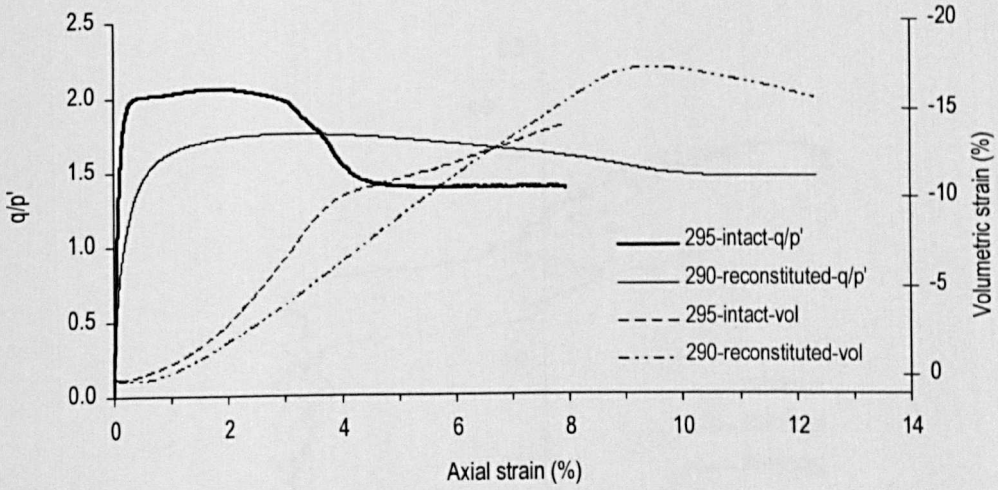

Figure 4.21: Comparison of the stress:strain and volumetric responses for the intact and reconstituted specimens

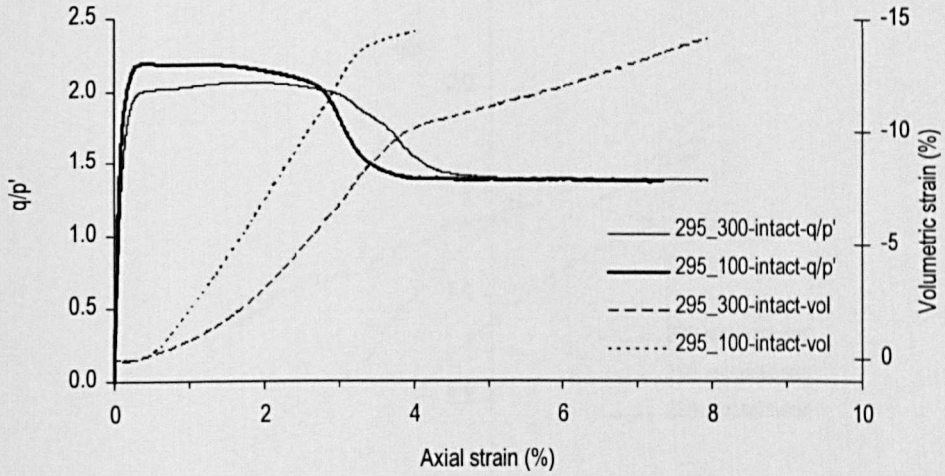

Figure 4.22: Influence of the confining pressure on stress:strain and volumetric behaviour of the intact soil

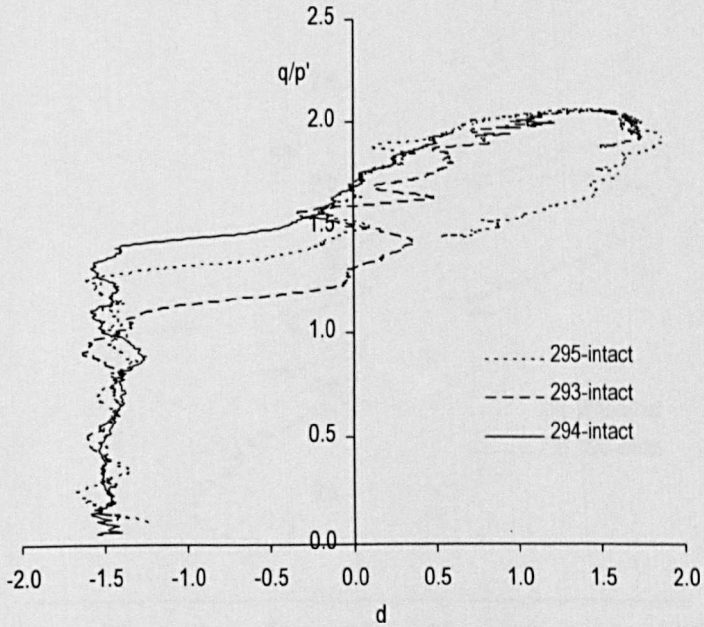

Figure 4.23: Stress:dilatancy plots for the intact soil samples at 300kPa

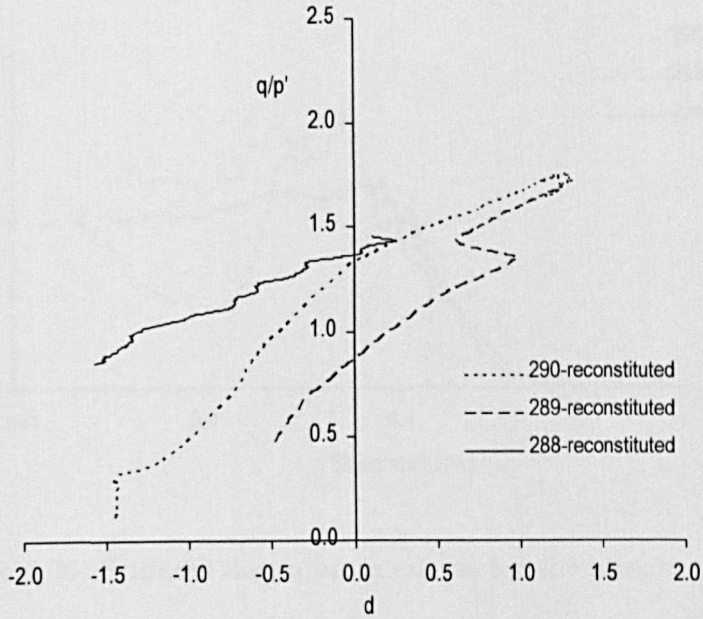

Figure 4.24: Stress:dilatancy plots for the reconstituted soil samples at 300kPa

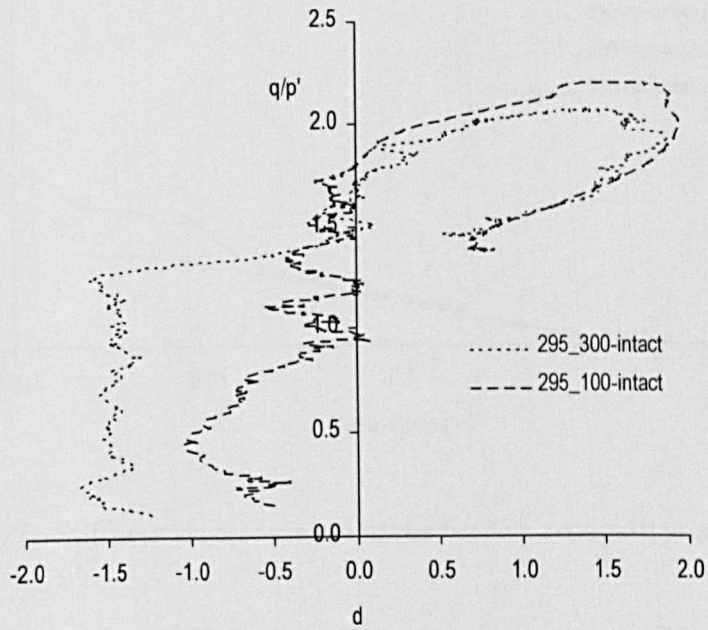

Figure 4.25: Influence of the confining pressure on the stress:dilatancy behaviour of the intact soil

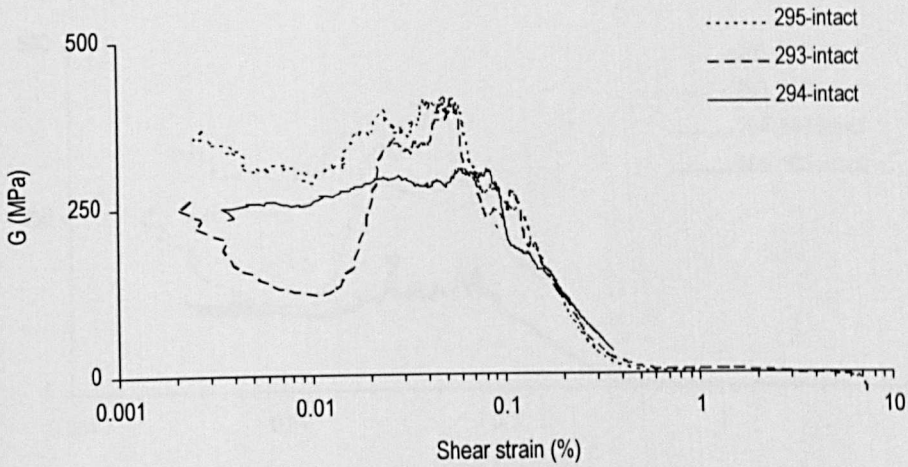

Figure 4.26: Stiffness degradation curves for the intact material

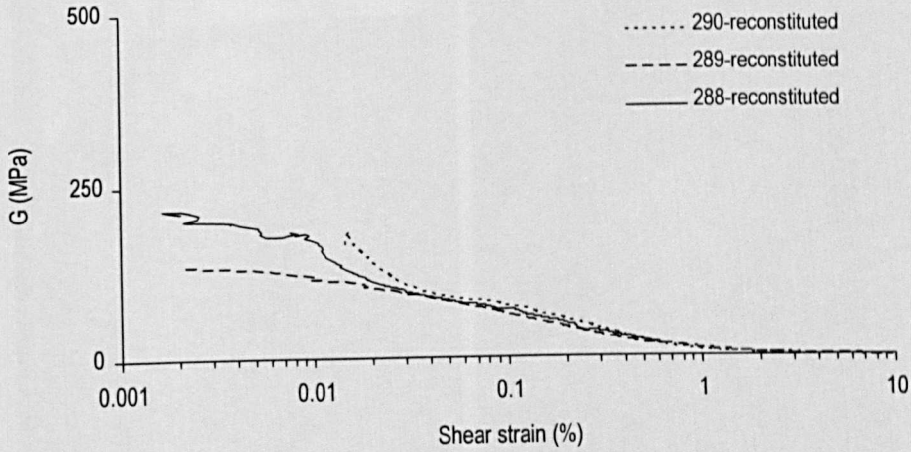

Figure 4.27: Stiffness degradation curves for the reconstituted material

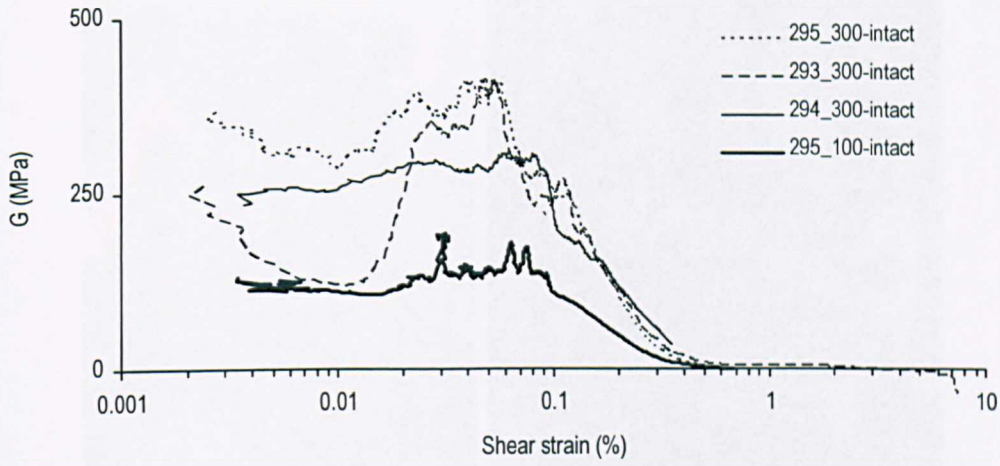

Figure 4.28: Influence of the confining pressure on the shear stiffness of the intact soil samples

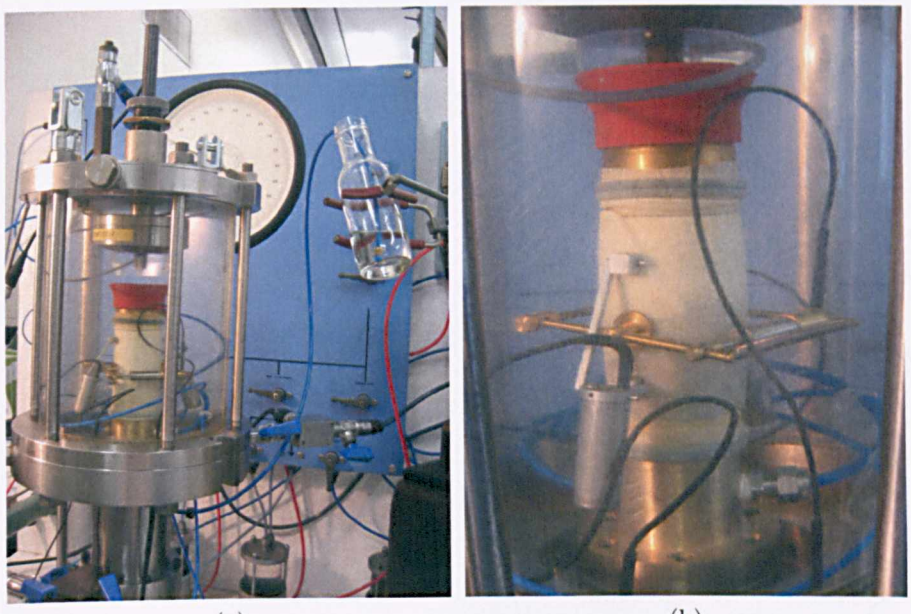

(a) (b)

Figure 4.29: Resin impregnation process (a) general setup (b) triaxial sample during impregnation

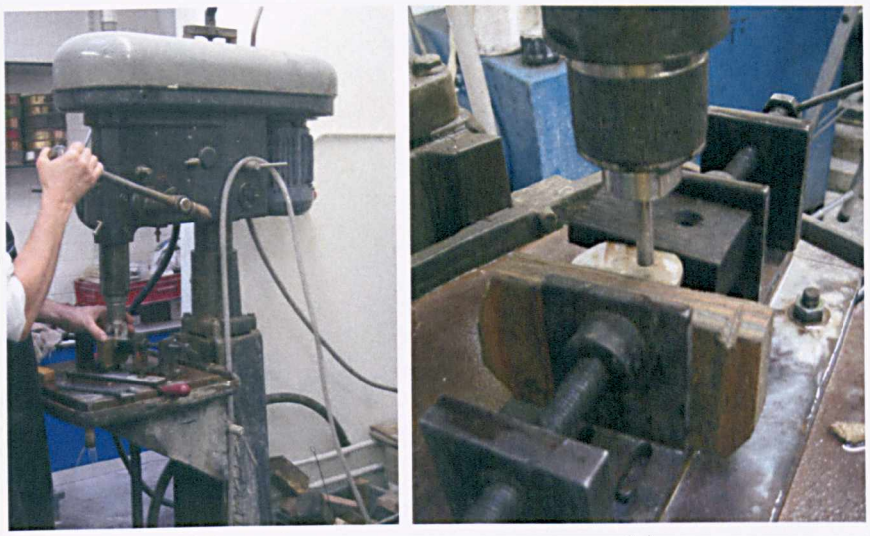

(a) (b)

Figure 4.30: Core drilling process

Chapter 5

X-ray micro-CT

5.1 Introduction

X-ray micro-CT is a non-destructive, 3D high resolution imaging method that allows the internal structure of objects to be investigated. Since its early development in the 1970s as a medical imaging technique, micro-CT has progressed significantly and its potential is today recognised in various areas from material science to engineering.

The use of micro-CT in the geotechnical field has continuously grown in the last decade. Early studies using micro-CT in granular soils investigation were related to the development of deformations (e.g., Desrues et al., 1996) and the spatial resolution used was in the order of a few millimetres. It was not until very recently that imaging at a particle scale, i.e., of a few microns, started to be used (e.g., Al-Raoush, 2007; Hall et al., 2010; Hasan and Alshibli, 2010).

Micro-CT has been used in this study in order to obtain 3D images of the resin impregnated sand specimens (as described in Chapter 4). The images obtained were analysed for fabric quantification and because the accuracy of the results is highly dependent of the quality of the images, an optimisation of the image acquisition process was attempted and is described in this chapter. A brief introduction to tomography is given in Section 5.2. Section 5.3 describes the fundamentals of absorption contrast micro-CT. The images produced by micro-CT are maps of the attenuation of the X-rays as they go through the object to be imaged. The main aspects of the physics of X-ray radiation, i.e., X-ray generation and the process of X-ray interaction with matter, are described. The process of detecting the X-ray radiation and the reconstruction approach used to obtain the 3D images are also described. The different systems and setup used for imaging are described in Section 5.4. Finally, in Section 5.5, the parameters to be employed in the data acquisition process and the micro-CT systems used in this study, are described. Examples of artefacts and noise in tomographic images are also presented.

5.2 Background

Tomography is the process of generating cross-sections of an object in a non-invasive way and the name derives from the Greek words *tomi* for "slice" with *grapho* meaning "to write". Tomography refers to the imaging of an object from either transmission or reflection and the data is collected by illuminating the object from many different directions (Kak and Slaney, 2001). The different types of tomography can be classified based on the type of excitation used. A few examples are presented in Table 5.1.

This study considers X-ray tomography, which is often, and perhaps abusively, just called Computed Tomography. The term "Computed Tomography" is historically associated with the development of computers, which have been applied to the field of image reconstruction since 1960s.

The mathematical basis for CT was first discovered by Radon in 1971 and one year later, the first CT scanner was invented, for which G.N. Hounsfield and Alan McCormack received the Nobel Prize in 1979. Since then, many advances have been made in scanner technology as well as in the algorithms used for CT reconstruction. High resolution computed tomography (micro-CT) has evolved from the CT methods introduced in the early 1970s for clinical practice. Micro-CT creates images that map the variation of X-ray attenuation within objects, based on the composition and density of the object and in the energy of the beam. Today CT scanners are used extensively in many applications (e.g., medicine, material science, astronomy, non-destructive testing) to carry out 3D volume visualisation of objects.

In computerized tomography, spatial resolution and object size are generally linked to each other, the higher the resolution the smaller the object size can be. Figure 5.1 shows a schematic illustration of the variation of the object size with the resolution using different types of X-ray sources (or focus). Conventional medical CT is associated with objects larger than 100 mm and a resolution of a few millimetres and using a macro-focus. Micro-CT includes resolutions of the order of a few microns as well as submicron resolutions using both micro-focus and nano-focus. An example of early research in the geotechnical field using micro-CT was the work carried out by Desrues et al. (1996) to investigate the void ratio evolution inside a shear band. As shown in Figure 5.2 the images used by Desrues et al. (1996) allow the identification of the shear band (shown as a darker region) but the resolution of 2 mm was not sufficient for the grains to be recognized. In order to identify the individual grains of a sand, a particle scale analysis is required for which higher spatial resolutions need to be achieved. The present study considers samples of a few millimetres in size so that high resolutions of a few microns can be attained.

5.3 Fundamentals of CT

This sections deals with the physical principles of X-ray absorption tomography. Absorption CT is based on the process that the intensity of an X-ray beam is reduced as it passes through an object. The X-rays are absorbed according to the density and composition of the material that constitutes the object. The intensity is reduced according to the linear attenuation of the material and the image obtained maps this attenuation.

The imaging process can be summarised as follows. The object is placed on a turntable stage whose rotation can be accurately controlled. An X-ray source generates a continuous beam of X-rays, the beam passes through the object and casts an X-ray shadow onto the detector (Figure 5.3). The radiation that hits the detector is converted into an electronic charge that is subsequently passed to a computer to create a digital image. A series of images is acquired while rotating the object step by step through 360° (or 180°) at a pre-defined angular increment. These projections contain information on the position and density of the absorbing features within the sample. The data obtained is used for the numerical reconstruction of the final 3D image.

5.3.1 X-ray physics

X-rays are electromagnetic radiation, i.e., a form of energy which is carried by waves of photons, that has the ability to penetrate optically opaque objects. X-ray radiation is located at the high-energy end of the electromagnetic spectrum as shown in Figure 5.4. Their location in the energy distribution is measured by either the wavelength value λ (m) or the frequency value ν (Hz) of the radiation. As the energy of the radiation increases, the wavelength decreases and frequency increases.

5.3.2 X-ray generation

There are three main requirements to generate X-radiation which include a source of electrons, a means of acceleration and a target for interaction. The first step to generate X-rays is to create the electron source. Matter is made up of atoms, which have electrons that orbit around the nucleus in shells. Therefore, to get the electron free of its orbit a current is passed through a conductive wire (or filament); once the filament is heated up, it emits electrons. Because the energy that the electron possesses and can transfer is dependent on its velocity, the second step is to accelerate the electrons. The higher the velocity of the electron when it interacts with an atom, the greater the energy of the radiation produced (Larson, 2010). The principle used to propelling the electrons is to place a piece of positively charged metal (the anode) a short distance from the filament (the cathode) which will attract the negatively charged electron. By increasing the voltage applied to the anode we can increase the

speed of the electrons. Finally, a target material for the electrons to interact with, is required. The target material is usually embedded into the anode. The X-rays are then produced when the high velocity electrons suddenly decelerate upon colliding with a solid metal anode (Figure 5.5). The radiation energy depends on the energy gained by the electron and is equal to the potential difference (voltage) between the anode and cathode. The electron energy is typically expressed in kilovolts (kV). The generation of X-rays produces a great amount of heat; for that reason the anode is typically made from materials with good thermal properties to dissipate heat, such as copper and tungsten (Larson, 2010). Another important characteristic of the target material is its density. The material must be of high atomic mass for electron interaction; low density materials do not provide sufficient density for interaction.

The X-rays are produced in parcels of energy called photons. There are two different atomic processes that can produce X-ray photons. The first process produces the "Bremsstrahlungand radiation" (German for "braking radiation") that is the continuous component of the X-ray spectrum (Figure 5.6a). The highest energy in the spectrum, i.e., the shortest wave length, corresponds to the maximum acceleration potential of the electrons. The higher the tube voltage, the higher energy of the photons and so their capability to pass through material. X-rays can also be produced when excited electrons interact with the electrons of the target atoms and so the electrons make transitions between lower atomic energy levels in heavy elements (Figure 5.6b). X-rays produced in this way are called "characteristic" X-rays since they have specific energies determined by the atomic energy levels.

The lower energy X-rays are absorbed within the X-ray tube, which reduces the number of lower energy X-rays in the resultant spectrum. The resulting X-ray spectrum energy, as illustrated in Figure 5.7 is a mixture of the characteristic and bremsstrahlung radiation, but without the primarily low energy X-rays that are absorbed by the X-ray tube. The maximum energy of the X-rays produced is dependent on the maximum potential applied across the X-ray tube. The peak X-ray energy is used to describe the beam energy.

5.3.3 X-ray interaction with matter

When the photons hit the object only part of the photons go through the material. The rate of removal of photons from the original X-ray is a function of the linear attenuation coefficient (μ) which depends on characteristics of the material, such as density and composition, and also on the X-ray energy. X-ray interaction with matter is a function of the material density, the material thickness, and the X-ray energy. Dense materials (i.e., materials with high atomic numbers) attenuate more the X-ray beam energy than less dense materials and this difference in attenuation provides the contrast that forms the image. The capacity of X-rays to penetrate an object is highly material dependent. The number of photons, i.e., the radia-

tion intensity along the incident direction, decreases exponentially while the X-ray passes through the object along the incident direction, as each photon is removed individually from the incident beam by an interaction. This attenuation is due to both absorption and scattering, as discussed in the following paragraphs.

The three dominant physical processes responsible for the attenuation of an X-ray are the photoelectric effect, Compton scattering and pair production. Photoelectric absorption occurs when the total energy of the X-ray photon is transferred to an inner electron, causing the electron to be emitted (Figure 5.8a). In Compton scattering the X-ray photon interacts with a free or loosely bound electron and ejects the electron; as a result, the photon is deflected to move in a different direction losing part of its own energy (Figure 5.8b). In pair production, the photon interacts with a nucleus and is transformed into a positron-electron pair (Figure 5.8c).

For geomaterials, photoelectric absorption is generally the dominant attenuation mechanism at low energies (up to 100 kV), while at higher energies (up to 10 MV) Compton scattering dominants (Ketcham and Carlson, 2001). Furthermore, photoelectric absorption is proportional to $Z^4 - Z^5$ (where Z is the atomic number), whereas Compton scattering is proportional to Z. Consequently low energy X-rays are more sensitive to variations in composition than higher energy X-rays (Ketcham and Carlson, 2001). When materials with similar Z are imaged, a contrast agent, usually made of heavy elements, can be used to improve the contrast, such as Iodine (Z=53) or Barium (Z=56). For example, when resin impregnated materials are used, the heavy elements are added to the resin prior to impregnation.

The distinction between absorption and scattering is important as each of these attenuation mechanisms affects the final image in a different way. Barrett and Swindell (1981) highlight the negative impact that scattered photons can have on the quality of the obtained image. In fact, a scattered photon has lost its "memory" regarding its direction of travel and therefore cannot be expected to cast a sharp shadow image on the detector, instead they form a broad, diffuse distribution on the detector; impairing the image contrast.

X-ray attenuation

As the X-rays pass through the object, the signal is attenuated. The equation for the attenuation of a mono-energetic beam going through a homogeneous material is given by Bee's law as follows:

$$I = I_0 exp(-\mu x) \tag{5.1}$$

where I_0 is the initial or incident radiation, μ is the linear attenuation coefficient of the material, x is the length of the X-ray path though the object and I is the

transmitted radiation. Figure 5.9a shows a schematic illustration of photons passing through an object of thickness x with a constant attenuation coefficient μ.

For an object composed of different materials, the equation becomes:

$$I = I_0 exp\left(\sum_{i=1}^{N}(-\mu_i x_i)\right) \tag{5.2}$$

where μ_i and x_i represent the attenuation coefficients and the linear extents of the materials, for a total number of N materials (Figure 5.9b).

To take into consideration the fact that the attenuation coefficient is also a function of the X-ray energy (Figure 5.9c), the complete solution would require to solve the equation over the range of the effective X-ray spectrum (Ketcham and Carlson, 2001), as follows:

$$I = \int I_0(E) exp\left(\sum_{i=1}^{N}(-\mu_i(E)x_i)\right) \tag{5.3}$$

Reconstruction algorithms can only solve Equation 5.2 and so the variations in the X-ray energy spectrum can cause artefacts as will be discussed in Section 5.5.4.

5.3.4 X-ray detection

The general idea behind X-ray detection is that the number of photons that go through the object, along a certain ray-path, are counted at the detector array. Modern micro-CT systems are equipped with scintillator detectors that consist of two main components which are a scintillator medium (luminescent material) and a photodiode (diode array). Upon entering the detector the short-wave X-ray radiation is converted into light (long-radiation) inside the scintillator medium; the photodiode converts this light into an electrical charge and passes it on to the computer where is converted into digital data (Figure 5.10a). A schematic illustration of the signal conversion chain inside the detector is presented in Figure 5.10b for a PerkinElmer detector used in the system v|tome|x s (GE phoenix|x-ray) used in this study.

The quality of the images obtained is influenced by the characteristics of the detector. The size of the pixel in the detector determines the amount of an object that is averaged into a single intensity reading and so is one of the parameters controlling the spatial resolution of the image. The total number of pixels determines how large the object can be for a given resolution. The efficiency of scintillation detectors varies with X-ray energy; higher-energy X-rays are more penetrative than lower-energy ones. Ideally, detectors should be made of materials with a high mass density in order to increase the effective absorption of the signal and so improve the acquisition

at lower signals (suitable for low density materials). For very low input signals, the output signal is dominated by noise and does not represent the object features. Depending on the characteristics of the detector, the noise level can be reduced by longer detector integration times or by averaging subsequent measurements of the same input signal, as discussed in Section 5.5.1.

5.3.5 Reconstruction

Knowing the transmitted intensity (I), the ratio I/I_0 can be obtained for each detector pixel for each projection. At any point this ratio is the sum of the absorption values along a single X-ray path (in the x direction). It is called the ray-integral and is defined by the following expression:

$$ln\frac{I}{I_0} = -\int_x \mu(x)dx \tag{5.4}$$

By combining a series of ray-paths at a given rotation of the object that is being imaged, a profile of intensity is obtained, which is called a view, as illustrated in Figure 5.11. Each view, measured along a row of pixels on the detector, is a 1D profile of the measured attenuation as a function of position corresponding to the current rotation angle. A series of views can be combined and presented as a 2D image in which the position along the detector row is given in one axis and the other axis gives the angle ϕ. This image is called a sinogram or the random transform of a 2D slice (Figure 5.12a). As discussed in Section 5.4, the micro-CT systems considered in this study use cone beam sources but for simplicity the examples in Figures 5.11 and 5.12 consider a paralell beam.

Reconstruction is the mathematical process of converting sinograms into two dimensional images (slices), i.e., taking data from Figure 5.12a to create Figure 5.12b. The filtered back projection or the Feldkamp algorithm (Feldkamp et al., 1984) is commonly used for cone beam data. Back projection derives its name from the fact that the data is back projected uniformly over the original planes. The filtered back projection algorithm consists firstly of filtering the data in the frequency domain and secondly each view is successively superimposed over a square grid at an angle corresponding to its acquisition angle (Ketcham and Carlson, 2001). The superposition of the attenuation values will correspond to the features presented in the object (Figure 5.13).

5.4 Micro-CT setup

Figure 5.14 shows the different types of X-ray beam that are used in micro-tomography. Figure 5.14a refers to the pencil beam ("First generation") and Figure 5.14b to the

fan beam ("Third generation"). In modern micro-tomography, there are two important types of X-ray beam which is the parallel beam (which is obtain in synchrotrons) as illustrated in Figure 5.14c and cone beam (typical of laboratory sources), shown in Figure 5.14d.

Laboratory sources use a beam originated from a focal point and describing a conical shape. The X-radiation is generated as described in Section 5.3.2.

In synchrotron sources, the electrons are generated in an electron gun, much like the cathode ray tube used for the laboratory sources. The electrons are then accelerated up to very high speeds through a series of three particle accelerators, which are the linear accelerator (or linac) the booster synchrotron and the large storage ring, as shown in Figure 5.15 (Diamond, 2010). When synchrotron radiation is used, the light is well collimated, making the X-rays nearly parallel. The use of synchrotron radiation has some advantages when compared to laboratory sources as summarised below:

- The light is bright and intense, i.e., has a high flux of photons which allows a high signal-to-noise ratio in a short time step
- The beam is monochromatic which reduces some artefacts
- The light is partially coherent and so phase contrast imaging can be used
- The X-rays are linearly polarized, which minimizes the scattered background radiation and improves sensitivity

Access to synchrotron radiation facilities is limited despite the increase globally in the number of synchrotrons. Today there are more than 70 facilities worldwide, a list can be found in *lightsources.org*.

Laboratory sources offer more flexibility in terms of access to beam time and data can be obtained at a much reduced cost. The increasing interest in laboratory micro-CT scanning has seen a number of commercial companies providing high resolution laboratory systems, e.g., phoenix x-ray (Germany), Nikon (UK), SkyScan (Belgium), Xradia (US) and North Star Imaging Inc. (US). Previous studies have shown that the image quality obtained using recently developed laboratory systems, e.g., nanotom (phoenix|x-ray) can compete with synchrotron radiation (e.g., Brunke et al., 2008; Kastner et al., 2010).

5.4.1 Configuration of a micro-CT system

The basic components of micro-CT scanners are the X-ray source, the detector and the rotational stage (Figure 5.16). The X-ray source or focal spot emits the radiation

that goes through the object that is placed on a rotary stage. The detector measures the extent to which the X-ray signal has been attenuated by the object.

The object is magnified in the detector and referring to Figure 5.16, the geometrical magnification (M) is defined as the ratio of the focus-detector-distance (FDD) and the focus-object-distance (FOD), i.e., $M = FDD/FOD$. The parameters affecting geometric magnification are the sample diameter (d) and the size of the effective detector surface D, i.e., $M_{max} = D/d$. The resolution in the image equals the voxel size of the reconstructed volume dataset and can be calculated by dividing the detector pixel size (P) by the geometric magnification, as $resol = P/M$.

The smallest voxel size possible, and therefore the best resolution obtainable, is defined as $resol_{max} = P \times diam/D$. For small objects, very high magnifications can be obtained, making the size of the radiation source, Fs, the only limiting factor for geometric magnification. Rivers (2010) proposed the following expression to obtain the maximum resolution taking into account the focal spot size, $resol_{max} = P/M + (1 - 1/M) \times Fs$. The effect of the focal spot is discussed in the following paragraphs.

The focal spot can be defined as the area of the target where the X-radiation is generated. The size of the focal spot and the detector pixel size determine the number of possible source-detector paths that can intersect a given point in the object being scanned, and hence these two factors determine the image resolution (Ketcham and Carlson, 2001). The greater the number of these paths, the more blurred the image features will appear. The loss of definition in an image occurs when the radiation is originated over an area rather than a single point, this is called geometric unsharpness or penumbra (U), as illustrated in Figure 5.17a. The width of the penumbra can be calculated as $U = Fs \times (M - 1)$.

Figure 5.17b illustrates schematically the extent of the blurring for a focal spot that is $10\,\mu m$ in size and for a focal spot that has a sub-micron diameter. As the size of the focal spot decreases, the image sharpness increases because the penumbra is reduced. Therefore an ideal point-like X-ray source will produce a sharp image. Reducing the size of the focal spot has however, the drawback of reducing the flux and consequently the signal available for detection.

Most of the micro-focus X-ray sources use transmission targets while industrial X-ray sources use reflection targets. Reflection targets use, in general, higher voltage and are particularly suited to inspection of larger samples. When a transmission target is used, the X-ray source is located very close to the outer wall of the micro-focus X-ray tube, this allows the sample to be positioned closer to the source and consequently higher magnifications can be obtained.

Some micro-CT configurations (e.g., Xradia) use optical components, which have the advantage that they do not require a small focal spot and consequently the flux

of the X-rays does not have to be limited. Therefore, larger samples can be imaged when compared to the setup that uses a strictly geometrical magnification where high resolutions require the object to be very close to the source which limits the size of the object to be imaged.

5.5 Description of the scanning process

5.5.1 Data acquisition

The micro-CT inspection of the core samples was carried out using different systems and parameters as will be discussed in the following paragraphs. In all cases, the sample was glued on the top of a brass pedestal on the rotary stage, ensuring that the part of the object to be imaged was inside the field of view for all the rotation positions. The main considerations and parameters of a micro-CT scan are discussed in the following paragraphs.

The number of projections acquired and the exposure time (and frame averaging) have a great influence on the quality of the reconstructed images. Selecting adequate scanning parameters is a compromise between the quality required for the subsequent analysis and the time available (and its associated cost). For the number of projections, even if a "the more the better" criterion could be applied, a rule of thumb is to use $\frac{\pi}{2}N$ projections, where N is the number of pixels in the image in the direction perpendicular to the rotation axis. According to some manufacturers, e.g., phoenix|x-ray, for high resolution systems $1.2N$ projections are generally enough to obtain good quality images.

The exposure time is the time period over which the input signal is sampled on the detector. Acquiring the same image more than once and averaging the results, i.e., frame averaging, is a good compromise between reducing noise and keeping scan time down. In addition, increasing the number of frames can be more effective than extending the exposure time, because it prevents the detector from saturating. Increasing the number of averaged frames will produce images that have less noise but the length of the scan will also increase significantly. The radiographs are in general collected from 0 to 360° (full rotation); some manufacturers, e.g., Xradia systems often consider 0 to 180°.

The X-ray source settings are the tube voltage and the tube current. The tube voltage is the difference in potential between filament and anode in the X-ray tube and its value controls the speed at which the electrons travel from cathode to anode. For example at a tube voltage of 100 kV, the electrons travel at approximately one third of the speed of light (GE, 2010). The tube voltage determines the maximum energy of the X-ray spectrum and consequently controls the X-ray penetration and the signal to noise ratio. The X-ray photon energy is generally adjusted in order to

achieve an optimal energy-dependent attenuation of the specimen and so maximizing the signal to noise ratio (as defined below). High energy X-rays penetrate more effectively than lower energy X-rays and produce images with less noise, but they are less sensitive to changes in material density and composition. Low energy X-rays produce images that have better contrast and so are able to discriminate between different materials. In the X-ray tube, the flux of electrons travelling from the cathode to the anode, due to the differences in voltage, is the tube current. The filament temperature controls the intensity of the X-ray output, the higher the temperature of the filament, the larger the number of electrons emitted. An increase in tube current results in a proportional increase in electron intensity. High X-ray flux reduces image noise as more photons improve the counting statistics.

Ideally the shape of the object that is to be scanned, should be cylindrical (or circular in cross-section) so the amount of material that the X-rays pass through for each angular interval is constant. This aspect is important as differences in the lengths of the X-ray paths will affect the measured attenuation values.

There are two important concepts in tomographic images, the spatial resolution and the contrast resolution. Spatial resolution is the ability to resolve close and high contrast features in the image. Two objects will not be separable in an image if the spatial resolution of the image is larger than the distance between them. As discussed above, the potential resolution can be limited by the penumbra blurring factor. Contrast resolution is the ability to distinguish between objects with small contrast differences (attenuation coefficient). Contrast is often defined in terms of the ratio of the divergence in signal between a feature and the background to the background signal i.e., $contrast = \frac{|sig_f - sig_b|}{sig_b}$, where sig is the signal or intensity level of each voxel in the image and the subscripts f and b denote the feature and the background respectively (Stock, 1999). The level of contrast in a reconstructed slice is determined by the X-ray intensity flux through the specimen and the exposure time is determined by the total number of photons incident per image pixel, provided the detector is not saturated by light photons (Stock, 2008).

Another parameter that is important in CT data is the *signal to noise ratio* (SNR) defined as the ratio of the contrast that is due to the structural differences represented by the image to the noise level (Russ, 2007). A feature is visible in an image only if its contrast is large enough to overcome the random image noise, when the SNR is too low the feature becomes invisible to the observer.

5.5.2 Micro-CT systems

The two primary micro-CT systems used in this study were the v|tome|x s and nanotom both from phoenix|r-xay. The v|tome|x s used was located in the Department of Materials (Imperial College) and the nanotom systems were at the phoenix|x-ray

laboratories (Germany), Nottingham University, Leeds University and Waterford Institute of Technology (Ireland). The characteristics of both systems are compared in Table 5.2. The nanotom is a more recently developed system and the main differences when compared to the v|tome|x s are the nanofocus X-ray tube, which has a focal spot that is minimized by means of a special setup consisting of lenses and diaphragms and a more advanced detector which allows better quality images to be obtained.

The x|tome|x s system uses a digital flat panel detector manufactured by PerkinElmer that is based on a solid state amorphous silicon sensor (aSi) and has the characteristics specified in Table 5.2. The nanotom system uses a Hamamatsu detector made of gadolinium oxysulphide scintillator (GOS); this detector has the possibility of binning 2×2 or 4×4 pixels. Binning is used to increase the signal to noise ratio at the cost of reducing image resolution. Both detectors can be shifted during acquisition for a "virtual" increase in the effective detector width to increase the available magnification.

Other commercial systems were considered, the Metris HMX ST (Nikon, formerly X-tek) located at Natural History Museum London, the microXCT (Xradia) at Manchester University and the SkyScan 1172 at SkyScan laboratories in Belgium. Some of the systems characteristics are presented in Table 5.3.

The feasibility of using synchrotron radiation for phase contrast imaging instead of absorption were considered. Two samples were scanned at the Advanced Photon Source (APS) at the Argonne National Laboratory (USA).

5.5.3 Preliminary inspection

A preliminary inspection of the impregnated triaxial specimens was carried out with the objective of detecting localisations and macro-scale fabric variations throughout the specimen. The micro-CT scans were carried out on a longitudinal half of each cylindrical specimen, which allowed two specimens to be scanned at a time thus limiting the number of scans. The system used was the v|tome|x s. The spatial resolution used was of 45 μm, which is approximately $d_{50}/6$ and so individual grains could be identified although not very clearly. In total, six specimens were imaged; the intact specimens 297-int, 294-int, 293-int and 295-int and the reconstituted specimens 291-rec and 290-rec (Table 5.4). The sample diameters were approximately 38 mm for the specimens in the initial stages of loading (297-int, 294-int and 290-rec) and slightly higher (approximately 42 mm) for the samples after dilation (293-int, 295-int and 290-rec). A representative horizontal cross-section through each specimen is presented in Figure 5.19 together with the parameters used for the scans (Figure 5.19d). The darker voxels represent the void spaces filled with resin and the sand particles are associated with voxels that have higher intensity values and thus are brighter in colour. Occasional, very bright voxels (almost white) can be

observed in the images; they represent a material that is able to attenuate the X-ray more than the quartz grains which is thought to be iron.

An inspection of the 3D images showed that intact specimens are more homogeneous than the reconstituted samples. A shear band could be clearly identified in specimen 295-int, as shown in the top left corner of Figure 5.19a, which is defined as a region with a greater number of dark voxels, indicating a higher void ratio. A more subtle indication of the presence of a shear band can be identified in specimen 293-int, as shown in the top left corner of Figure 5.19b. A diffuse shear band is evident in specimen 290-rec (top of Figure 5.19c). What appear to be regions of higher void ratio can however be observed in other locations of specimen 290-rec and also in specimen 291-rec prior to loading which shows the heterogeneity of the reconstituted specimens.

5.5.4 Analysis of the scans

Having identified the main localisations in the triaxial specimens, numerous core samples were extracted at various positions. Core sample diameters of 9 mm, 6 mm, 5 mm, 4 mm, 3 mm and 1.8 mm were used. The data obtained from the various scans allowed an investigation of the most appropriate spatial resolution, sample size and scanning parameters for this study.

Computer memory constraints play a major role in limiting the maximum number of voxels that an image volume can have for subsequent analysis, as discussed in Chapter 6. Therefore the optimum spatial resolution is a compromise between the level of detail required for the image analysis and the minimum number of particles that make the volume representative. Considering the available commercial micro-CT systems, the influence of the source settings (voltage and current), the number of projections and the exposure time were investigated to optimise the acquisition conditions for the samples to be used for quantitative image analysis.

(a) Artefacts and other sources of error

Kak and Slaney (2001) identified two main types of reconstruction errors. These are: the errors that are fundamental to the projection process and depend upon the interaction of object inhomogeneities with the form of energy used (and cannot be minimised by simply increasing the total number of projections) and the errors caused either by a lack of sufficient data or by the presence of random noise in the measurements. If the X-ray flux detected is too low, or if insufficient projections are recorded, there may be a lack of sufficient data.

The imperfections or defects resulting from the scanning process are often called artefacts. Artefacts, when presented in the projection sets are likely to propagate errors back to the reconstructed images. Scanning artefacts can obscure details

of interest or cause the intensity values associated with a single material to vary according to the location in the image.

The beam hardening artefact is the most common artefact in CT (e.g., Ketcham and Carlson, 2001). The typical manifestation of beam hardening artefact is that the edges of the image will appear brighter than the centre. Figure 5.20a shows an example of beam hardening in a 2D tomographic image from a scan on a 4mm diameter sample. The grey-level profile (across the diametric line) given in Figure 5.20b shows a great increase in the grey-level values at the edge. This effect is produced by the preferential absorption of the lower energy in a polychromatic beam as it passes through an object, which increases the average X-ray energy so "hardening" the X-ray beam. As the beam passes through an object the effective attenuation of any material diminishes thus making short ray-paths proportionally more attenuating than long ray paths (Figure 5.21).

One possible solution to alleviate the beam hardening effect is to use an X-ray beam that has sufficient energy to negate or minimise this effect (Figure 5.22). However when the object scanned is made of a relatively low density material as it is the case of most geomaterials (when compared to metals), increasing the X-ray energy will create images with poor contrast between different features. Another simple way to reduce beam hardening artefacts is to "pre-harden" the X-ray beam by passing it through an attenuating filter before it passes through the object. Filters are normally flat pieces of metal such as aluminium or copper that have the effect of absorbing the low energy part of the X-ray beam. The disadvantage of this approach is the reduction of the X-ray beam flux that leads to a lower signal to noise ratio unless longer acquisition times are used. In addition, most reconstruction software has a beam hardening correction that is applied. For the cases where the effects of beam hardening cannot be completely eliminated, one solution is to remove the outer edges of the image (where the problem is generally more severe) prior to its analysis.

Ring artefacts are caused by defective detector pixels as well as by defects or impurities on the scintillator crystals (e.g., Davis and Elliott, 2006). They appear as a circle centred on the rotational axis; the pixels with anomalous values have the same position in all the projections and they appear as ring patterns as the projections are summed, with the level of intensity greater in the centre. Figure 5.23 gives an example of ring artefacts in a 3 mm core sample. Following scanning, correction of the data is possible as these anomalous readings appear on a sinogram as vertical lines and consequently they can be detected and removed prior to reconstruction.

When the scanned object includes features that have a much higher density than the surrounding material, as is the case of the iron inclusions found in the samples of Reigate sand, a "star" artefact can form. As shown in Figure 5.24a it is called a star artefact because bright streaks emanate from the inclusion into the nearby soil

material. Figure 5.24b shows that optimising the scanning parameters, for which the number of projections seems to play a key rule, can produce images where highly dense features appear as a sharp feature.

Other sources of error include motion artefacts owing to movement of the X-ray source and the object caused by the heat produced during generation of the X-rays. When X-rays are generated, only a small fraction of the energy imparted by the decelerating electrons is converted into X-rays, and the remaining energy is converted to heat. This phenomenon is particularly important for very high resolution images, not only because the object is closer to the source (and so more susceptible to being affected) but also small variations in position will be more pronounced (Salaberger et al., 2010). Recently developed mechanical systems provide long term stability against thermally induced drift effects. Motion artefacts have the overall effect of degrading the quality of the image by blurring feature edges and/or increasing the noise in the image.

In tomographic images, noise appears as a fluctuation in the intensity values within a uniform material. These fluctuations appear as variations in the grey-levels of the shading in the images. Such noise in the images is usually related to either a low photon flux, scatter radiation or possibly electronic noise, or a combination of these effects (Kak and Slaney, 2001). The detector pixel width has also an effect on the image noise as the flux detected is a function of the pixel size. The greater the pixel width, the greater the flux detected and so less significant the noise. However, the spatial resolution is compromised by an increase in the detector pixel size. Therefore for high spatial resolution the reduction in pixel width has to be compensated with an increase in the exposure time. In general, different detectors are appropriate for different energy spectra.

Figure 5.25 compares two images affected by different degrees of noise presented along with the scanning parameters for each image. Grey-scale images are presented in Figures 5.25a and 5.25c while the intensity profiles are given in Figures 5.25b and 5.25d. Figure 5.25b (sample n1) shows a great variation in the intensity level for both the grain and the void space and more importantly, the intensity values for both phases overlap. Figure 5.25d (sample n2) shows a much clearer distinction between grain and void space, with only slight variation within each phase. The poor quality of the images from sample n1, when compared to sample n2, can be attributed both to the lower photon flux and to thermal effects, as the nanotom used to scan sample n1 did not have any device for temperature control.

The images from sample n2 are a good example of sharpness in a tomographic image, as shown by the almost vertical lines in the intensity profile at the grain edges (Figure 5.25d). This example shows that visual observation does not always permit an assessment of the image quality. In fact, significant differences in the SNR can exist between two slices that at a first glance look comparable (e.g., Figures 5.25a

and 5.25c).

In an X-ray CT image each voxel represents the attenuation properties of a specific finite volume and so, when the volume of the voxel overlaps more than one material, the intensity of the voxel represents some form of average attenuation for those materials. This is called the partial-volume effect and because of resolution limitations, it will be to some extent inherent in every image. The greater the image resolution, the smaller the voxel size and so the lower this effect will be. The partial volume effect results in the blurring of the feature edges and an effective way of assessing this effect is by looking at the image histogram, i.e., the frequency distribution of the intensity values in the image, as discussed in Chapter 6.

(b) Phase contrast images

Phase contrast imaging takes advantage of the fact that different materials have different refractive indices. Therefore, variations in the refractive index across the sample result in wave effects which influence the propagation and phase of the X-ray beam traversing the sample (Davis et al., 1995). For a low-absorption material, quantifying the deformation of wave front in addition to beam attenuation by absorption can be particularly advantageous.

The use of phase contrast to enhance the edges can be seen in Figure 5.26 where the edges of the particles are defined by a black and white fringe. The intensity profile (Figure 5.26b) shows a significant contrast enhancement at the edges due to phase-shift effects. Because the object to detector distance has to be large enough to resolve phase contrast effects, the flux of photons that reach the detector was insufficient to provide good contrast by absorption attenuation, which explains the small difference between the intensity values for the grain and for the void space. Further analysis of these images is presented in Chapter 6.

5.5.5 Scans for image analysis

In this study, a total of 13 core samples that had been imaged were judged to have adequate quality for subsequent image analysis. Approximately 20 scans were discarded. The scans were carried out using the nanotom (from phoenix|x-ray) at the University of Nottingham, the University of Leeds (referred to as *L samples), and at the phoenix|x-ray facilities in Germany (referred to *ph samples). Table 5.4 summarises the sample references and the triaxial specimen from which each sample was retrieved. Note that the terms "specimen" is used to refer to the specimen tested in the triaxial apparatus, while the term "sample" is used to refer to the core that was imaged. With the exception of specimen 290-rec, for all cases at least two samples from the same triaxial specimen were used. For the specimens representing

stages prior to the formation of visible localisations (297-int, 294-int and 291-rec), the corresponding samples were retrieved from random locations, simply avoiding locations near to the boundaries where the soil is more susceptible to being disturbed during specimen preparation. For the two intact specimens where the shear band was identified (293-int and 295-int) one sample was retrieved from a region containing part of the shear band (293S and 295L) and the other sample from a region away from the shear band. For the reconstituted samples from the post-peak regime, sample 290ph was retrieved from a region containing part of the shear band from the 290-rec specimen, while for the specimen 289-rec a shear band could not be clearly identified. The settings used for most of the scans were the same as defined by the "general case" with the exception of samples 297L, 295L and 291L that have specific sample sizes and parameters. The settings for all the cases are summarised in Table 5.5. These images were essentially free from artefacts and further analysis is presented in Chapter 6.

5.6 Summary

Micro-CT systems have developed significantly over the past decade and good quality, high resolution 3D images (of a few microns) can be obtained using either laboratory souces or synchrotron radiation. There clearly is potential for the technique to be used for accurate quantification of the internal structure of the most diverse materials.

The use of micro-CT in geomaterials appears to have started in petroleum research in the late 1980s and has grown significantly since as the third international workshop on "X-ray CT for geomaterials" (Alshibli and Reed, 2010), confirms. In other areas of research such as material science and biomedicine, micro-CT is a well established technique and soil disciplines will certainly have much to gain from "borrowing" knowledge from these fields. The potential of micro-CT to investigate the internal structure of geomaterials is large. A basic knowledge of the process is however required for a correct interpretation of the results. The examples presented in Section 5.5 have shown that artefacts and noise can obscure and in some cases modify the original object features if scanning conditions are not optimised.

When laboratory sources are used, the polychromatic nature of the source, limited photon flux, cone beam artefacts and temperature instability, all lead to restrictions on the image quality and the limitations are particularly pronounced for very high resolutions. The selection of the system and settings for the micro-CT scans will be a compromise between image quality, cost and the overall time of the imaging processing and must take account of the objective of the scan, subsequent analysis methods and the material. When noise in the tomographic image is not severe it can

also be reduced by processing filters (Chapter 6). Sharpness, contrast and SNR were the main parameters considered for the assessment of the image quality, considering that beam hardening and ring artefacts had essentially been removed. While both contrast and SNR are important to distinguish the different elements in the image (the grains from the void space in this particular case), image sharpness can make a significant difference when it comes to define the grain edges.

Above all, this study shows that good quality, high resolution, images can be obtained using commercial laboratory sources and with reasonable time/cost. This will of particular importance if in the future, the investigation of soil deformation at the particle scale using micro-CT is to become a common practice in geotechnics.

Physical excitation	Process
X-rays	X-ray Computed Tomography or CT
Magnetic fields	Magnetic Resonance Imaging (MRI) or (NMRI)
Electrons	Electron Tomography
Electric fields	Electrical Resistance Tomography (ERT)
Gamma rays	Positron Emission Tomography (PET) Gama-Ray Tomography (GRT)
Ultrasonics	Photo Acoustic Tomography (PAT)

Table 5.1: Examples of different types of tomography

	v|tome|x s (phoenix)	nanotom (phoenix)
focal spot size (μm)	3	< 1
max acceleration voltage (kV)	100	180
detector pixel size *(μm)	400	50
detector array	512 × 512 (shift 2×)	2300 × 2300 (shift 3×)
detector type	PerkinElmer	Hamamatsu
detector field of view (mm)	200 × 200	110 × 110
max resolution (μm)	2-3	0.5
max sample diameter (mm)	25	10

*uses optical magnification

Table 5.2: Characteristics of two commercial scanners used: v|tome|x s and nanotom (both from GE phoenix|xray)

	Metris HMX ST (Nikon)	micro XCT (Xradia)	SkysScan 1172 (SkyScan)
focal spot size (μm)	2	7*	< 5
max acceleration voltage (kv)	180**	150	100
max resolution (μm)	3.7	–	0.8
max sample diameter (mm)	>100mm	–	27/50

**180kV for transmission and 225kV for reflection target

Table 5.3: Characteristics of the additional commercial micro-CT scanners used

Specimen ref. & loading stage	Sample ref.	Sample diam. (mm)	Scanner location	Scan settings
297-int	297ph	5	phoenix G.	general case
(prior to loading)	297L	6	Leeds	*
294-int	294ph	5	phoenix G.	general case
(pre-peak regime)	294n	5	Nott.	general case
293-int	293	5	Nott.	general case
(post-peak regime)	293S	5	Nott.	general case
295-int	295ph	5	phoenix G.	general case
(post-peak regime)	295L	6	Leeds	*
291-rec	291ph	5	phoenix G.	general case
(prior to loading)	291L	6	Leeds	*
289-rec	289	5	Nott.	general case
(post-peak regime)	289S	5	Nott.	general case
290-rec	290ph	5	phoenix G.	general case
(post-peak regime)				

* see Table 5.5

Table 5.4: Resin impregnated triaxial specimens and the associated samples scanned for image analysis

Settings	General case	291L	297L	295L
Magnification	20	16.7	12.5	12.5
Voxel size (μm)	2.5	3	4	4
FOD (mm)	10	15	20	20
FDD (mm)	200	250	250	250
No. projections	1440	1440	1440	1440
Total rotation (°)	360	360	360	360
Exposure time (s)	0.5	1.0	1.0	1.0
Frame averaging	4	1	1	1
Voltage (kV)	90	100	100	110
Current (W)	116	80	80	80

Table 5.5: Scanning parameters used for each scan

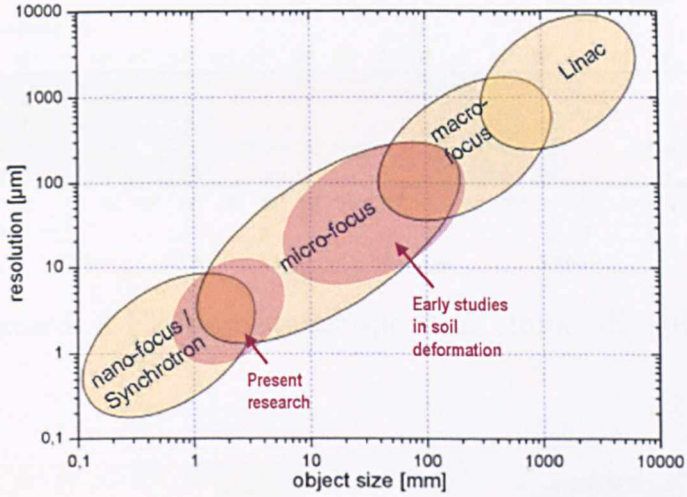

Figure 5.1: Object size against spatial resolution (modified from Neuser and Suppes, 2007)

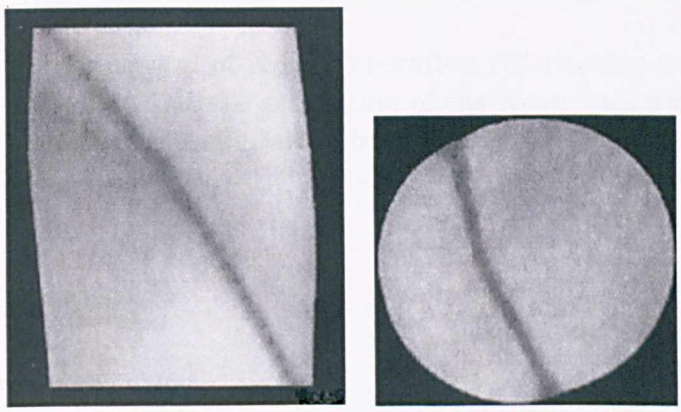

(a) (b)

Figure 5.2: Identification of a shear band in micro-CT images of a sand, (a) section along the vertical axis of the specimen (b) cross-section of the specimen (Desrues et al., 1996)

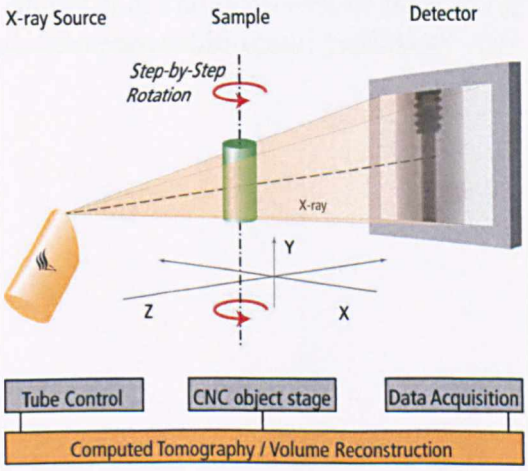

Figure 5.3: Schematic illustration of a typical micro-CT setup (from GE, 2010)

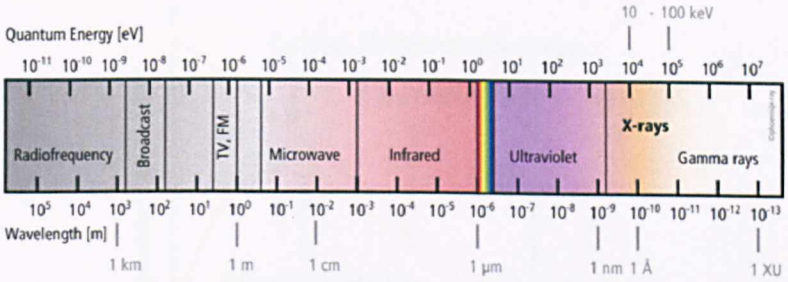

Figure 5.4: Electromagnetic spectrum (from GE, 2010)

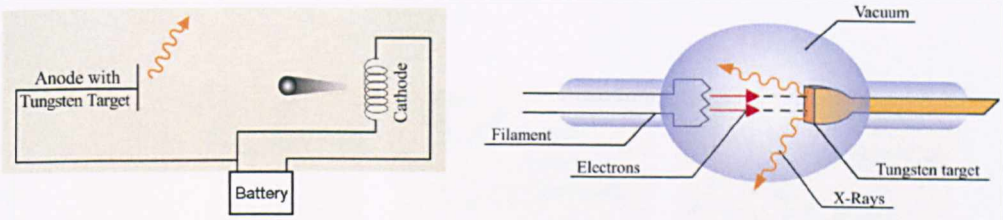

(a) (b)

Figure 5.5: Schematic diagram of X-ray generation (a) electron travelling between the cathode and the anode and the generation of the X-ray radiation upon colliding with the anode (b) similar representation inside an X-ray tube (Larson, 2010)

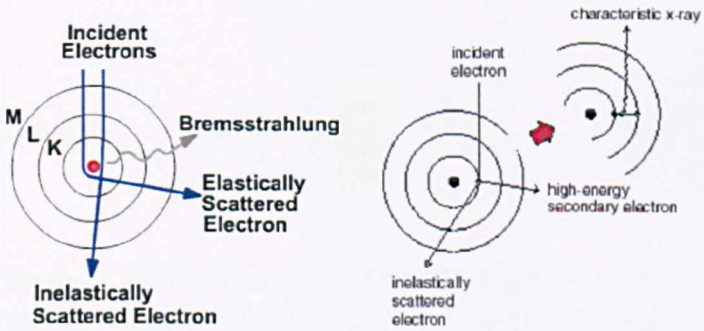

(a) (b)

Figure 5.6: Schematic diagram of the processes of producing the two components of the X-ray spectrum (a) "Bremsstrahlungand radiation" (b) "characteristic" radiation (Larson, 2010)

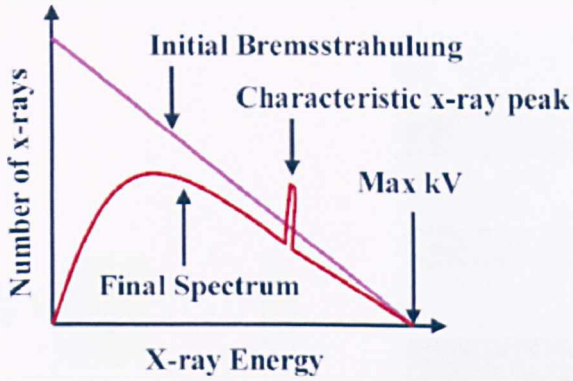

Figure 5.7: Schematic graph of an X-ray energy spectrum (from Oldnall, 2010)

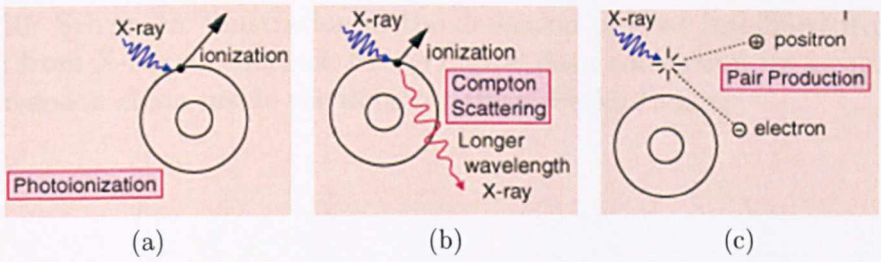

Figure 5.8: The three dominant physical processes of X-ray attenuation (a) photoelectric effect (b) Compton scattering (c) pair production (Nave, 2010)

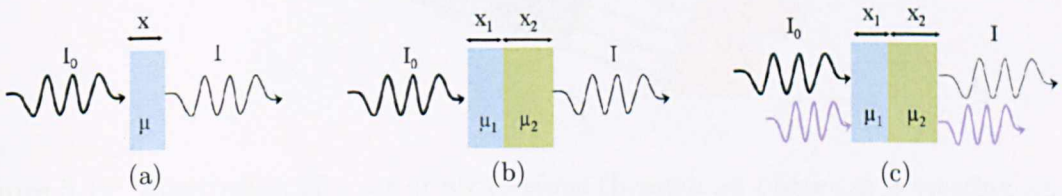

Figure 5.9: Schematic illustration of X-ray attenuation for (a) an homogeneous object with a monochromatic beam (b) object with two different materials and a monochromatic beam (c) an heterogeneous object with a polychromatic beam (modified from Rivers, 2010)

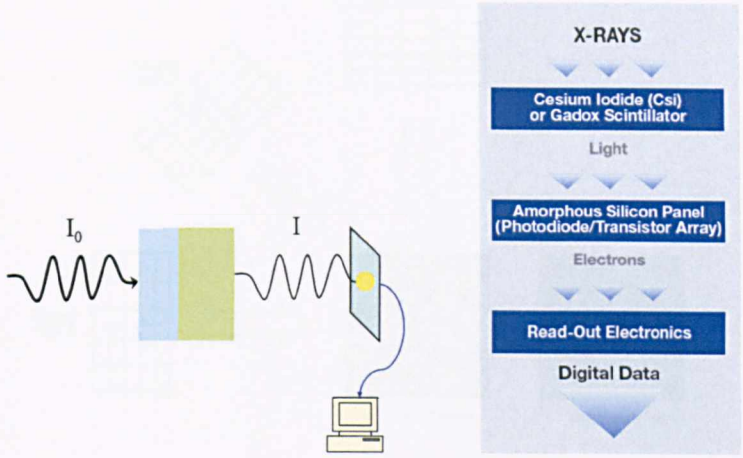

(a) (b)

Figure 5.10: Schematic illustration of the detection process (modified from Rivers, 2010), (a) from X-ray attenuation to the digital data conversion by a computer (b) signal conversion chain inside the detector (from PerkinElmer)

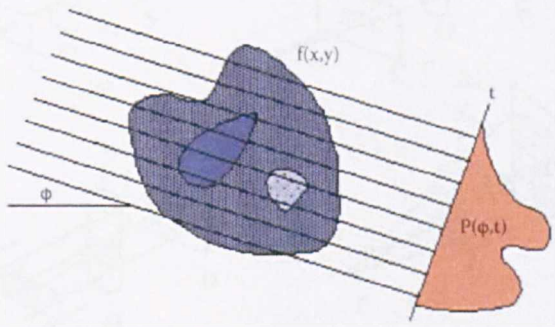

Figure 5.11: Illustration of a set of projections through an object at a viewing angle ϕ forming the function P (from Russ, 2007)

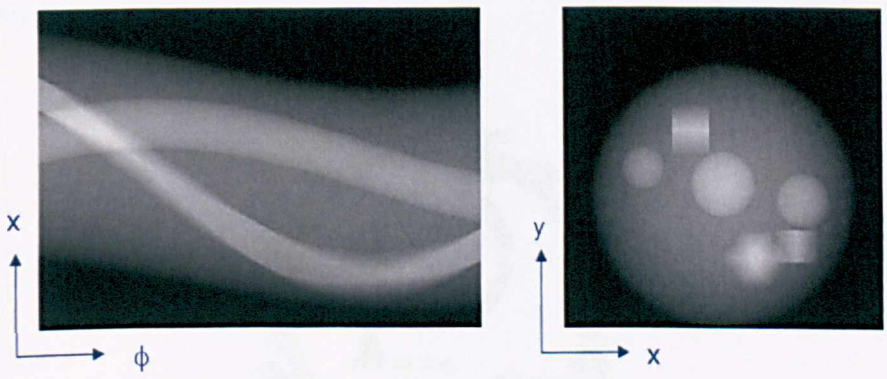

(a) (b)

Figure 5.12: An example of a sinogram (a) sinogram (b) 2D slice through the object (modified from Beckmann, 2010)

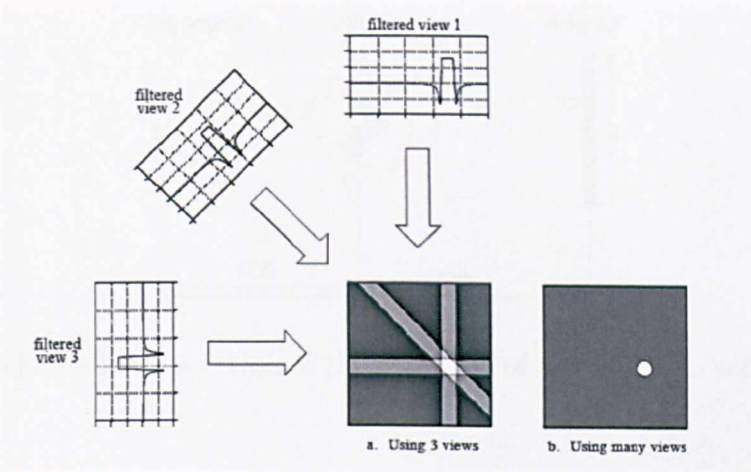

Figure 5.13: Schematic illustration of filtered back projection showing that an increase in the number of views also increases the accuracy of the tomographic image to represent the original object (from Smith, 2010)

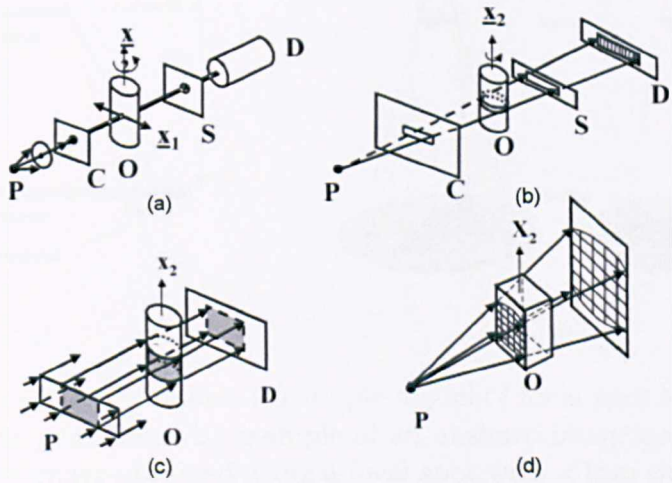

Figure 5.14: Illustration of four experimental approaches to X-ray micro-tomography data collection, (a) pencil beam (b) fan beam (c) parallel beam (d) cone beam, where P is the X-ray source, O is the object being imaged, x_2 is the axis about which sample is rotated to produce different views required for reconstruction and D is the detector (from Stock, 1999)

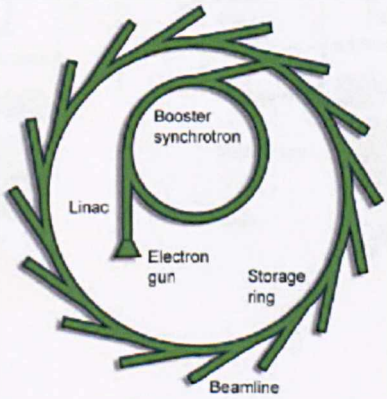

Figure 5.15: Main components of a synchrotron, plan view (from Diamond, 2010)

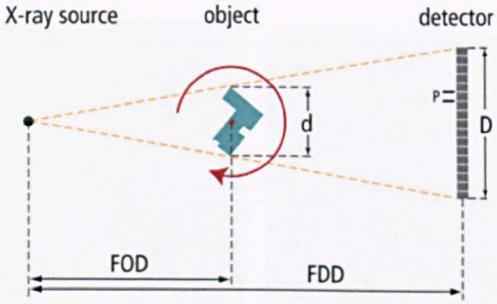

Figure 5.16: Schematic illustration of the top view of a cone beam set up (from GE, 2010)

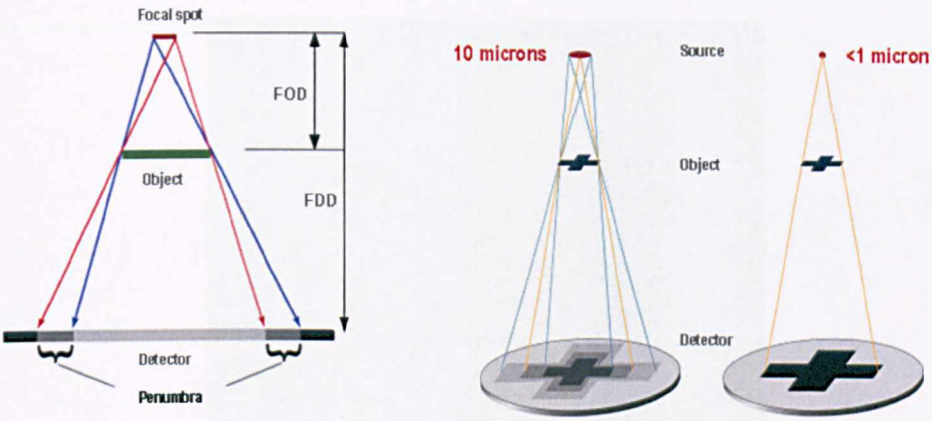

(a) (b)

Figure 5.17: Geometric penumbra, (a) simple model of focal spot size and geometrical unsharpness or penumbra (b) example of an unsharp image using a micro-focus of 2-5μm (c) sharp image obtained using a focal spot with <1μm size (modified from GE, 2010).

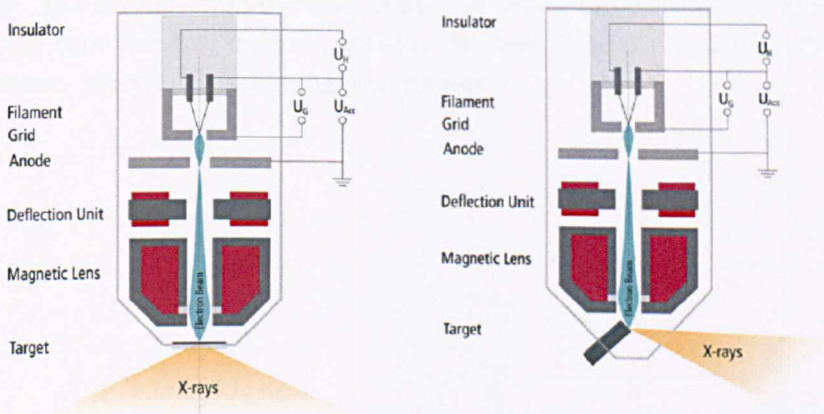

(a) (b)

Figure 5.18: Schematic illustration of a micro-focus X-ray tube with (a) a transmission target geometry (b) a reflective target geometry (from GE, 2010).

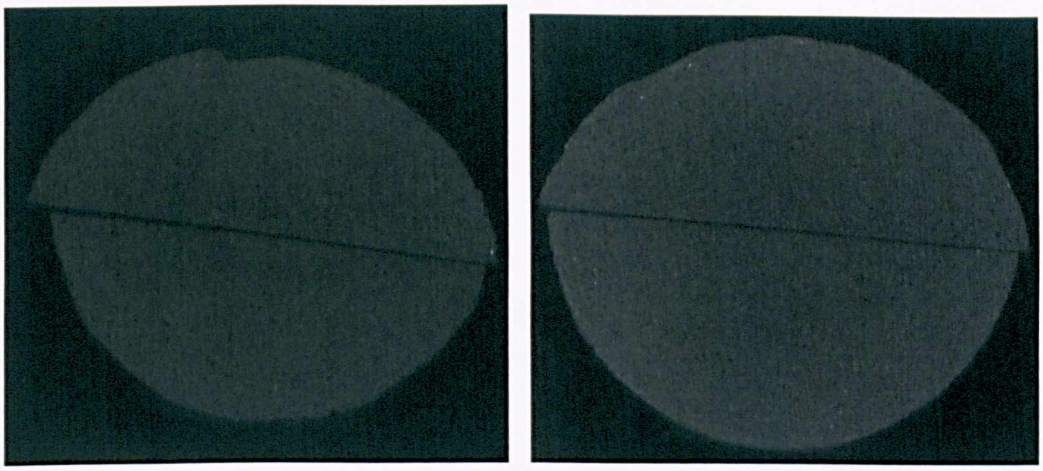

(a) (b)

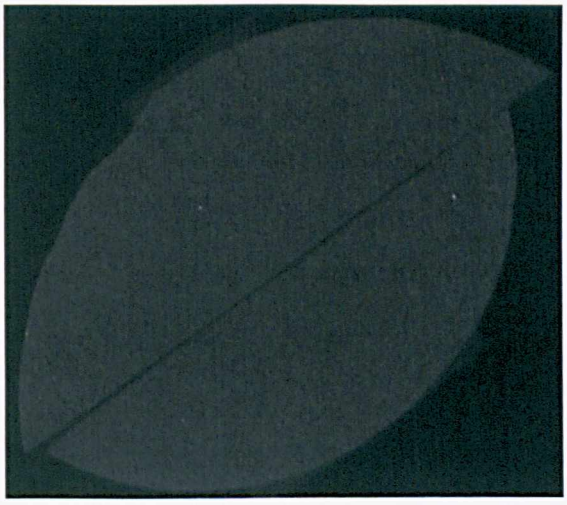

(c)

Voltage (kV)	Current (μA)	No. proj.	Resol. (μm)	Exp. time (s)	Averaging
100	70	720	45	1.6	3

(d)

Figure 5.19: Horizontal cross-sections from the scans on the triaxial specimens using v|tome|x s, (a) top: 295-int, bottom: 297-int (b) top: 2953-int, bottom: 294-int (c) top: 290-rec, bottom: 291-rec (d) scanning parameters.

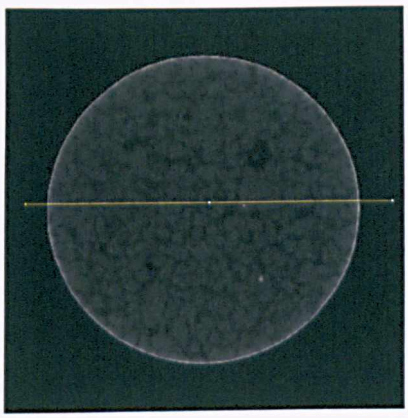

(a)

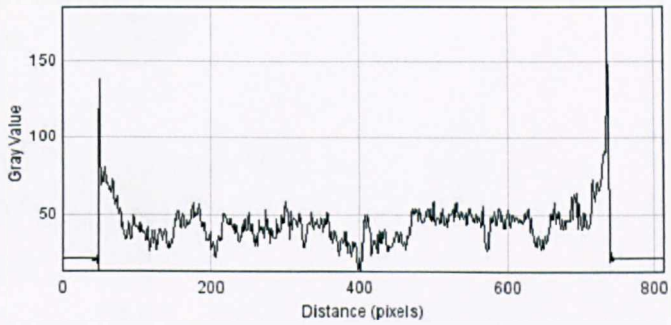

(b)

Voltage (kV)	Current (μA)	No. proj.	Resol. (μm)
180	123	3142	3.7

(c)

Figure 5.20: An example of beam hardening on a 4mm diameter sand sample scanned using the Metris HMX ST (Nikon), (a) 2D cross section, showing the bright shading around the edge (b) grey-level profile across the diametric line showing a significant increase in grey-level around the edges (c) scanning parameters used

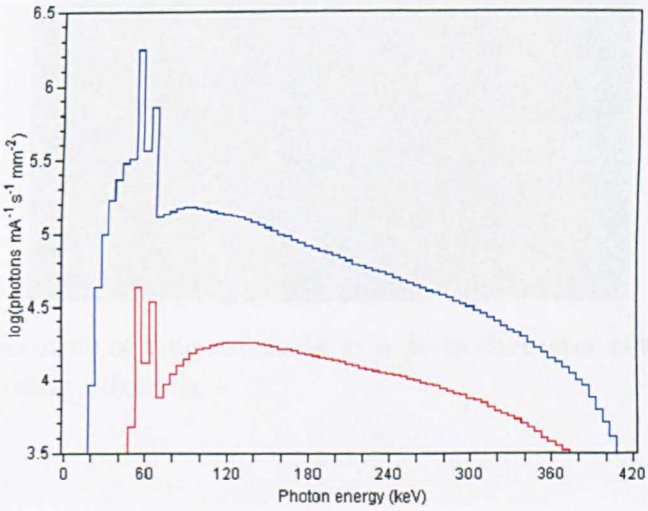

Figure 5.21: Theoretical energy spectra for 420kV X-ray source. The upper is the result of beam filtration using a 3mm aluminum filter, the average X-ray energy is 224kV. The lower curve represents the spectrum after passing through 5cm of quartz; the preferential attenuation of the low-energy X-rays caused the average energy to rise to 178kV (from Ketcham and Carlson, 2001)

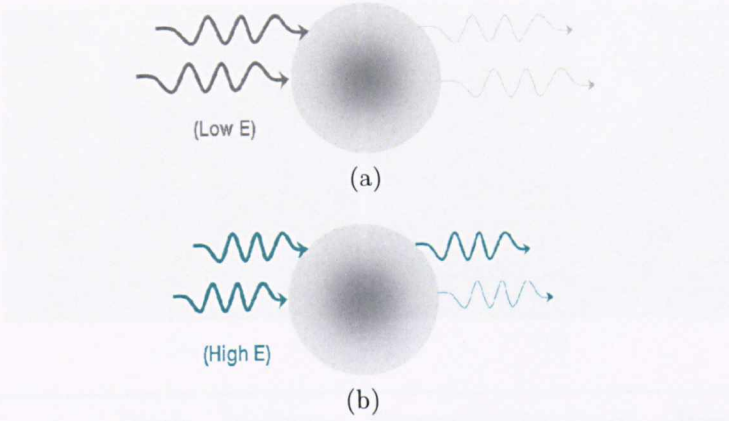

Figure 5.22: Schematic illustration of the beam hardening effect, (a) for low energy (kV) X-rays both long and short paths attenuate the same (b) for high energy (kV) X-rays, longer paths attenuate more than shorter paths (modified from Rivers, 2010)

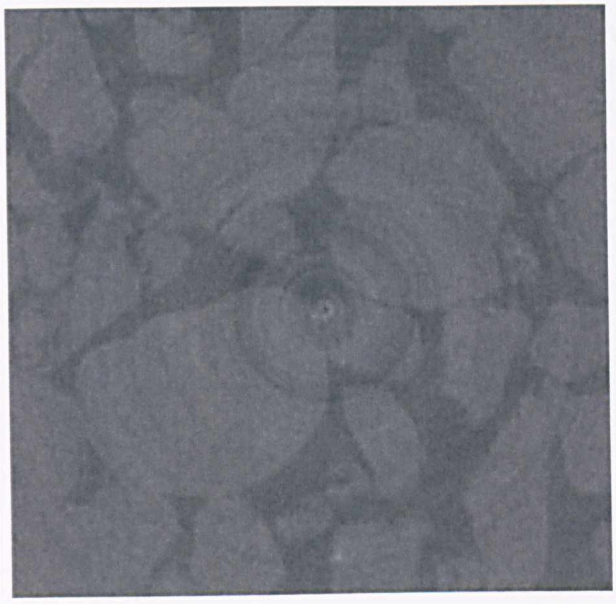

Figure 5.23: An example of ring artefacts in a 3mm diameter core sample scanned at $resol = 2.5\mu m$ using v|tome|x s

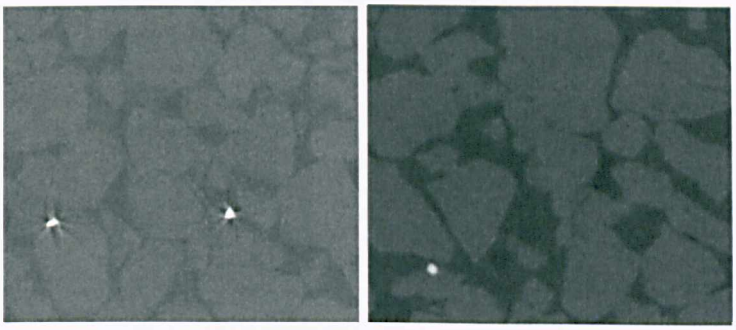

(a) (b)

	Diam. (mm)	Voltage (kV)	Current (μA)	No. proj.	Resol. (μm)
sample s1	1.8	100	180	720	2.5
sample s2	4	120	50	1800	1.2

(c)

Figure 5.24: Iron inclusions in two samples, (a) sample n1 shows "star" artefacts due to iron inclusions (scanned using v|tome|x s) (b) sample n2 shows the inclusions as sharp features (scanned using nanotom) (c) scanning parameters used

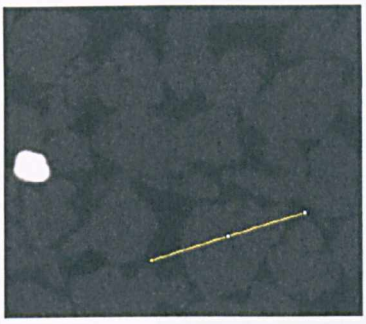

(a)

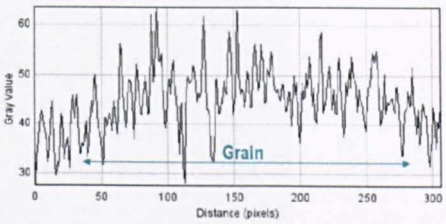

(b)

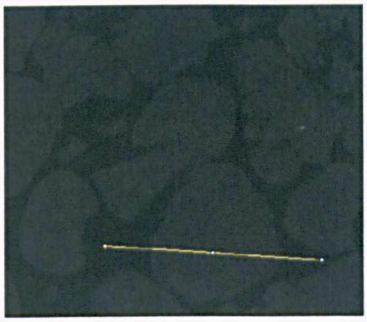

(c)

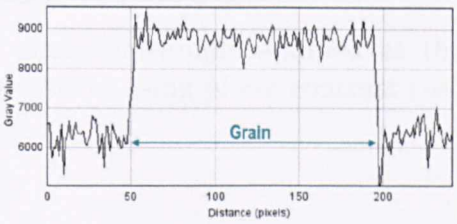

(d)

	Diam. (mm)	**Voltage** (kV)	**Current** (μA)	**No. proj.**	**Resol.** (μm)
sample n1	6	120	60	1800	1.4
sample n2	4	80	180	1800	0.8

(e)

Figure 5.25: A comparison between the level of noise in two samples n1 and n2, scanned with two different nanotom systems, (a) cross-section from sample n1 (b) corresponding intensity profile (across the diamteric line) (c) cross-section from sample n2 (d) corresponding intensity profile (e) scanning parameters used

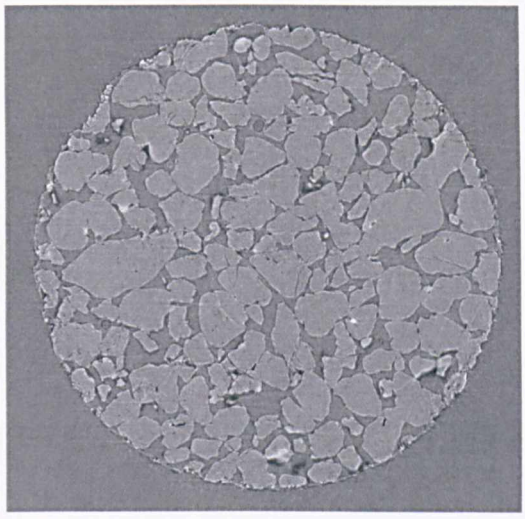

Figure 5.26: Cross-section of a 3mm diameter sample scanned at the Advanced Photon Source (Argonne National Laboratory) using phase contrast (using 724 projections)

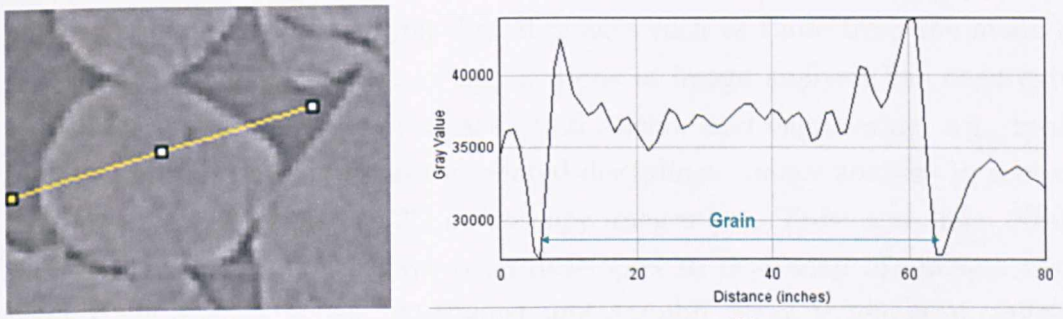

(a) (b)

Figure 5.27: Intensity profile assessment for a sample scanned with phase contrast using 724 projections

Chapter 6

Image processing and analysis

6.1 Introduction

The use of computer-based image processing and analysis began in the late 1960s with the acquisition of the first digital images such as those from the moon exploration. Since then the range of applications of image analysis has been extended to include a diverse range of areas within science and engineering, e.g., medicine, biology, materials science and soil related disciplines. Image analysis in geotechnics has already been applied to 2D microscopy images (e.g., Frost and Jang, 2000) and more recently, techniques have been developed to deal with 3D images obtained from X-ray micro-CT (e.g., Al-Raoush and Alshibli, 2006; Videla et al., 2006).

This chapter is divided into two main parts, the first part is related to image processing of micro-CT data and the second describes the algorithms developed for the subsequent image analysis. Although no general agreement exists regarding where image processing stops and image analysis starts, in the context of this study, image processing is seen as a series of algorithms in which both the input and output are images, while image analysis has images as input and the extracted measurements as output.

Section 6.2 describes the image processing methodology. Image filtering is considered in a first stage prior to image enhancement and noise reduction. The main objective of the image processing is to perform the segmentation of the image, i.e., the partitioning of the image into regions or objects of interest. Image segmentation by thersholding and by morphological watershed is discussed. Finally the images obtained at different stages of the image process are presented and discussed.

Section 6.3 is dedicated to the image analysis stage. It starts with the description of general concepts and the main body is the methodology developed to obtain the measurements required for morphology and fabric quantification. While for morphology quantification only the individual particles are taken into consideration, for

fabric quantification the contacts between the particles and the voids are also considered, in addition to the particles. The fabric measurements were of two main types, scalar and directional. The scalar quantities include the void ratio, the particle size distribution, the void size distribution, the particle surface areas and contact surface areas. The directional data comprise the orientation of the three principal axes of the particle and the voids, the orientations of the normal to the contact and the branch vectors. For every image analysis routine or function developed, synthetic data was used for validation. Additional validation used tomographic images of a sample of resin impregnated micro-spheres.

6.2 Image processing

Image processing is used here with the main purpose of preparing the images for the subsequent measurements to quantify morphology and fabric. The input is the tomographic images as presented in Table 5.4 (Chapter 5). At this stage is convenient to introduce some concepts regarding digital imaging.

A 3D digital image can be defined as a function $f(x,y,z)$ where x, y and z are the spatial coordinates and the amplitude of f is the intensity or grey-level of the image at that point. In 2D the function will be $f(x,y)$. A digital image is composed of a finite number of elements called pixels (picture elements) or voxels (volume elements). Pixels are associated with 2D images, while voxels are associated with 3D images. Digital images are bit mapped images in which the colour or intensity level of a single pixel is represented by a number of bits given by the bit depth. This concept is also known as bits per pixel (bpp), particularly when specified along with the number of bits used. A higher colour depth gives a broader range of distinct colours.

The number of intensity levels (L) is typically an integer power of 2, i.e., $L=2^k$. An image having 2^k intensity levels is referred to as a k-bit image. The images considered in this study were of 8-bit, 16-bit or 32-bit type as shown in Table 6.1. The prefix unsigned means that the integer number, containing k bits, can have a value between 0 and $2^k - 1$, while signed integers have values between -2^{k-1} and $+(2^{k-1} - 1)$.

The number of bits (b) required to store a digitized image is $b=R\times C\times Z$, where R, C and Z are the size of the image along the x, y and z directions respectively. Therefore, the file size (in bytes) is obtained by multiplying b by the number of bytes per element, as shown in Table 6.1.

The reconstructed images were of 16-bit type. The output images from the segmentation process were of 32-bit type. Prior to the image analysis stage the images were converted to 16-bit type as it reduces considerably the size of the file (to half of the original value) without compromising the image quality. The preservation of quality

is achieved because the segmented images have a range of voxel values between *0* and the maximum number of particles and the number of particles in any sample never exceeded *65535*.

The samples used for image processing are summarised in Table 6.2. The samples imaged at a resolution of 2.5 μm were re-sampled to 5 μm; this allowed a reduction in the file size from 3.4 Gb to 0.4 Gb and so the volume could be analysed as a whole. Volumes over 1 Gb in size needed to be divided into smaller sub-volumes for analysis due to computer memory limitations. While investigating sub-volumes is computationally more efficient, the sub-volumes must be merged again prior to image analysis, as discussed in Section 6.3.2. To allow for this merging, an overlapping zone of a few voxels was allowed.

The void analysis was carried out for six of the samples. Table 6.3 presents the list of the images (samples) considered for void analysis and the corresponding samples used for particle analysis. The image filtering and thresholding of the volume image was the same for both analyses and the differences in the application of the watershed process in each case are discussed in detail in Section 6.2.2.

The primary commercial software used for the image processing was Avizo (Visualization Science Group). In addition, ImageJ (National Institute of Health, US), VGStudio Max (Volume Graphics GmbH) and Drishti (ANU Vizlab) were also used. An example of a 3D inspection of the tomographic images is shown in Figure 6.1 for a sample of sand and in Figure 6.2 on a sample made of resin impregnated glass spheres (555 μm diameter).

This section includes the description of the methodology employed in the processing of the images. The main steps of this process are summarised in Figure 6.3. A discussion of the results obtained at each stage of the process is presented in the last part of the section.

6.2.1 Image pre-processing

As discussed in Chapter 5, micro-CT images have some noise, which arises from the image acquisition and reconstruction processes. Noise alters the intensity of the voxels and this can make difficult the process of interpreting and extracting information from an image. Image filtering is commonly used prior to segmentation to reduce noise and enhance the image quality. The filters used in this study are described in the following paragraphs.

A 3D median filter, of size 3×3×3 (from Avizo) was applied to almost all the samples with the exception of 297L, 295L and 291L. A median filter is a non-linear spatial filter, which, as its name implies, replaces the value of a voxel intensity by the median of the intensity values in the neighbourhood of that voxel (Gonzalez and Woods,

2008). The 2D process of calculating the median value of a pixel is illustrated in Figure 6.4 and the 3D process is analogous. In Figure 6.4 the central pixel of a 3×3 square neighbourhood has value 150 which is unrepresentative of the surrounding pixels, but after applying the median value to this pixel its intensity is replaced to take the value of 124, i.e., the median of the 9 values.

The median filter is particularly effective in reducing noise while causing considerably less blurring than other linear smoothing filters of similar size, e.g., the mean filter (Gonzalez and Woods, 2008). In fact, because the median value will always be the value of one of the pixels in the neighbourhood, the median filter does not create new unrealistic pixel values and so it is believed to be relatively efficient at preserving edges and so preserving details in an image.

As already mentioned, a different filter was applied to samples 297L, 295L and 291L. These samples were imaged using different scanning parameters (see Table 5.5, Chapter 5) and the use of the median filter size 3×3×3 did not achieve sufficient smoothing in the images. One option to increase the smoothing was to use a larger neighbourhood for the median filter but this could affect the edges of the features. A commonly used de-noising filter is the Gaussian filter. A Gaussian filter is applied in the frequency domain using a kernel with a Gaussian shape (i.e., bell-shaped). This filter is efficient in removing noise, but it has the drawback that the blurring can also remove some detail from the image and in addition it can give rise to edge position displacement or even removal of edges (Deng and Cahil, 2002). A more refined version of the standard Gaussian is the adaptive Gaussian filter that adapts the blurring of the image according to the frequencies, i.e., the blurring will be lower at sharp edges (e.g., Hodson et al., 1981; Deng and Cahil, 2002). A 3D adaptive Gaussian filter (from VGStudio Max) was applied to these three samples with the following parameters: *smoothing=1.8* and *edge threshold=0.08*. Those settings were found to produce good results. For the reduction of more severe noise, the smoothing parameter can be increased but it also increases the overall blurring of the image. The edge threshold value specifies to what extent edges are protected from the smoothing process, and it can be decreased in order to preserve weak edges (i.e., unclear edges). The memory requirements for this filter are considerable; it can be up to five times the size of the original dataset.

Any digital filter should be used with caution and an understanding of the technique is required. Significant information can be lost or altered during the filtering process. The filter design chosen should be optimized to the particular needs of the data being processed.

6.2.2 Image segmentation

Image segmentation is used here with the objective of identifying the individual particles in the image and the individual voids in the case of the void analysis. Thesholding segmentation is a technique that allows the separation of the features of interest (particles or voids) from the background based on the intensity value of the voxels. In order to separate features that were touching into individual features, a more sophisticated segmentation technique known as a morphological watershed algorithm was employed.

The distribution of the number of voxels as a function of their intensity level, known as an intensity histogram, or simply histogram, is a widely used tool in image processing. Histograms can have different shapes according to the features present in the images that they represent. For the images considered in this study there are two main phases, the solid phase formed by voxels representing the particles and the void phase associated with the voxels that represent the void space. For the tomographic images obtained by absorption contrast, the void voxels have lower intensity values and so they look darker than the solid voxels. Therefore the typical histogram for these images takes the form of a bi-modal distribution in which the voxel intensities are clustered around two well-separated values (see Figure 6.5a). The cluster located at lower intensity values is thus associated with the void voxels while the cluster located at the higher intensity is associated with the solid phase. There are a smaller number of voxels associated with the void phase, which is in agreement with the measured porosity value of approximately 30%, calculated as the ratio of volume of voids to the total volume of the whole triaxial specimen. Moreover, for these images where there are two distinct populations of voxels, the size of the gap, often called a valley, between the two peaks can be used as an indicator of the image quality. The number of voxels located in the gap between two peaks can be associated with the partial volume effect caused by voxels whose intensity is an average of the attenuation of the two main materials in the soil samples (soil and resin) due to the finite resolution of the images. Also noise caused by voxels with random intensity can contribute to increasing the number of voxels located at this specific region of the histogram.

The effect of filtering can be observed in the change in the histogram shape by making the valley between the two peaks deeper i.e., the number of voxels with intermediate intensity is reduced. Therefore the allocation of voxels to one of the two phases can be achieved more straightforwardly.

(a) Thresholding

Thresholding is the simplest method of image segmentation and consists of labelling each voxel according to its intensity value relative to a reference parameter known as

the intensity threshold. The key parameter in the thresholding process is the choice of the threshold value; some approaches use more than one threshold value (e.g., Oh and Lindquist, 1999). Different methods exist for finding the threshold value. A simple approach might be to use the lowest point in the valley of the histogram. However, even after filtering, finding the minimum between the two peaks can be difficult.

Therefore a more sophisticated approach, also based on the histogram shape was developed and implemented in MATLAB. This approach fits a Gaussian curve to the two peaks of the histogram to determine the minimum point between them. Because the histogram obtained from the micro-CT data is generally a bi-modal smooth distribution with to clear peaks, the maximum associated with each phase can be identified by calculating the gradient of the histogram. Knowing the two maximum points, two Gaussian curves are fitted to each phase distribution. In the next step the curves are combined into a new curve for which the minimum value was calculated, which is used as the threshold value (Figure 6.5a). This method has the drawback that the best fit Gaussian curve is selected by visual inspection with the standard deviation value as the input.

In addition, the implementation in ImageJ of Otsu's thresholding method (Otsu, 1979) was used. In this algorithm, the histogram is divided into two classes and the inter-class variance is minimized. The process involves iterating through all the possible threshold values and calculating the inter-class variance, i.e., the sum of the variances for the two phases (class) multiplied by their associated weights. Otsu's method is one of the most cited thresholding methods in image processing and according to Sezgin and Sankur (2004) more satisfactory results are often associated with similar number of voxels within each phase. The threshold value applied to each sample was based on the results obtained from Otsu's method and the Gaussian curve-fitting, as well as visual inspection.

The threshold value is commonly used to generate a binary image, in which voxels belonging to the particles have value *1* and voxels in the void space have value *0*. The fabric measurements possible from a binary image are however limited because individual particles are not dissociated and so only the void ratio can be obtained. In order to separate touching particles and to identify individual particles, a more sophisticated segmentation technique using a watershed algorithm was used.

Morphological watershed

The watershed algorithm was first proposed by Beucher and Lantuejoul (1979) as a geophysical model of rainfall on a terrain. The principle behind it was that a raindrop falling on a surface will trickle down the path of steepest descent to a minimum. The set of points on the surface that lead to the same minimum can

be defined as a catchment basin and the borders between catchment basins are defined as watershed lines (Figure 6.6). By analogy, if an image is considered as a terrain surface and divided into catchment basins, each of the regions defined by a catchment basin can be associated with an object of interest in the image.

The principle in which regions in an image can be segmented into catchment basins requires the image to be defined as a continuous height function f. The assumption is that the lowest values of f indicate the presence of boundaries in the original image; therefore watershed can be seen as a step of a hybrid segmentation process where the initial segmentation by threshold is the generation of the edge feature map.

For the current analysis the original image was converted into a surface where the physical elevation was given by a distance map. While other criteria for the function f are relevant, the distance function is particularly suitable for segmentation based on the shape of the image features. Distance maps can be obtained by applying a distance transform that calculates the distance between two adjoining voxels (e.g., Danielsson, 1980 and Borgefors, 1996) however the 3D application of these algorithms to large datasets is computationally expensive.

The distance map was obtained by applying an in-house code (Atwood et al., 2004) based on morphological dilation (Gonzalez and Woods, 2008). Starting from the solid phase boundary, the number of iterations required to fill the region completely (solid phase for the particle analysis and void phase for the void analysis) was calculated and the distance measure function was generated. As shown in Figure 6.7b, different grey-levels indicate different distance values, and greater distances (at the centre of the particles) can be associated with a mountain peak.

Prior to the watershed segmentation, the distance map was filtered to reduce noise and to smooth homogeneous regions. The filtering consisted of an edge-preserving, smoothing technique known as anisotropic diffusion (Ibanez et al., 2005). The parameters used were a $time.step = 0.0625$ and $no.iterations = 10$. This smoothing step is believed to reduce the computation time by decreasing sensitivity to small-scale features and additionally to improve the quality of the final segmentation by removing noise and enhancing edges (Cates et al., 2005).

The watershed algorithm was applied to the inverse of the distance map, where the topography is inverted and peaks are replaced by minima. A catchment basin can therefore be defined as the set of points whose path of steepest descent terminates at the same local minimum in the inverse distance map.

There are two algorithms commonly used to implement the watershed transform: the immersion algorithm (top-down) and the bottom up approach. The immersion algorithm (Vincent and Soille, 1991), consists of flooding the regions surrounding the minima from the bottom up and looking for the places where the flooded regions

touch. The top-down approach (Mangan and Whitaker, 1999), associates each voxel with a catchment basin by identifying a preferential downhill flow path towards a minimum. The top-down approach, as implemented by Ibanez et al. (2005), was used in this study and the main steps of the methodology are described in the following paragraphs.

The first step is the classification of all the voxels into catchment basin regions. The downhill, or gradient direction, of a voxel is usually computed by examining the connected neighbours (6-connectivity for 3D analysis, as discussed in Section 6.3.1). Because watershed segmentation produces a region for each local minimum, in practice too many regions or oversegmentation of the image can occur. To alleviate this, a minimum watershed depth, can be specified. The watershed depth is defined as the difference in height between the watershed minimum and the lowest boundary point (Figure 6.8). This value is the maximum depth of water a region could hold without flowing into any of its neighbours. And so, regions whose depth falls below the minimum are merged or combined as shown in Figure 6.8.

The watershed process is controlled by two input parameters: the threshold (t) and the level (l), both set as a fraction between *0* and *1* of the maximum flood level. The flood level is defined as the value that reflects the amount of metaphorical precipitation that is rained into the catchment basins. In this case the maximum flood level is given by the highest distance measured in the image, i.e., approximately the radius of the largest grain. The threshold parameter t value controls the lower thresholding of the input, i.e., it is used to remove shallow background regions. Raising this threshold percentage effectively decreases the number of local minima in the input, resulting in an initial segmentation with fewer regions. The assumption is that the shallow regions removed by thresholding are of less interest.

The level parameter l controls the watershed depth, i.e., the depth of metaphorical flooding of the image. Raising and lowering l, influences the number of regions that are merged to produce the final output. A level of l=0.0 produces the basic segmentation, which will typically be very oversegmented, while l=1.0 will generate very few regions. According to Ibanez et al. (2005), l values of interest are typically low (i.e., less than about 0.40 or 40%), since higher values quickly start to undersegment the image.

In order to decide which values for t and l parameters produce better results, the watershed algorithm was carried out just for one slice considering different possible combinations of t and l parameters. The output was a series of colour images and by visual inspection the parameters of t and l were selected. An initial selection was done by inspection of the slices but because the 2D images are not representative of the 3D features, the 3D volume was also investigated for a more refined parameter selection. The next step was to run the watershed algorithm for the whole volume using the selected input parameters. For all the samples the parameters used were

t=0.04 and l=0.2.

Segmentation by edge detection

An alternative segmentation method was used for the tomographic images obtained by phase contrast using synchrotron radiation. This technique falls into the edge detection classification. As shown in Figure 6.9 the histogram of these images is uni-modal and no distinct phases can be identified, and so the images are not suitable for thresholding segmentation. An alternative approach to segment the images was found in the Drishti software. The method used was based on an occlusion spectrum technique (Correa and Ma, 2009), which separates structures according to the distribution of intensities in the neighbourhood. This methodology makes use of the ability of value-gradient magnitude, based on 2D transfer functions, to identify material boundaries. The segmented image is shown in Figure 6.10. This technique is presented here as an alternative to the thresholding and watershed approaches. The segmented images obtained were not used for fabric quantification because of a deficient reconstruction of the tomographic slices, which resulted in different ranges of intensity for different slices.

6.2.3 Results and discussion

The ability of filtering to enhance the quality of the image is shown by comparing the data prior to the application of the filter (raw data) and the filtered data. While filtering is a powerful tool in image processing, its use requires caution and understanding in order to avoid losing or changing information in an image.

The change in the shape of the intensity histogram due to image filtering is presented in Figure 6.11. The results for sample 294ph filtered with the 3D median filter (Figure 6.11a) are representative of the majority of the samples scanned using the same settings (see Table 5.4, Chapter 5). This plot shows that the overall trend is an increase in the number of voxels with an intensity that is close to the peak value of each cluster, while the number of voxels with intensity values lying in between the peaks decreases. Figure 6.11b refers to sample 295L which was filtered with a 3D adaptive Gaussian filter. A similar trend was observed as for sample 294ph. However, these histograms show that the quality of these images is not as good as the majority of the samples. In fact, for sample 295L, there is a significant number of voxels with intermediate intensity, shown by the fact that the height of the distribution curve at the valley is about one third of the height at the peak for the solid phase, considerably greater than the ratio observed in Figure 6.11a. Sample 295L is shown here as an example of an image with significant noise. Both samples 297L and 291L showed histograms with deeper valleys when compared with the histogram of 295L .

Binary images were also used to evaluate the degree of enhancement required prior to segmentation. Because they are easier to visualise, 2D slices along the xy-plane are presented instead of the 3D image. Figure 6.12a shows a binary image of sample 294ph prior to filtering. There are some white voxels in the dark background and some dark voxels in the solid phase represented with the white colour. For Figure 6.12b the effect of misclassified voxels is more severe. This noise is randomly distributed throughout the image. In addition, the binary image revealed that this sample was affected by a beam hardening artefact, as can be observed in the corners of the image. Beam hardening was not observed in the other samples and the occurrence of this artefact in this image can be explained by the larger size of this sample, i.e., 9mm diameter (see Table 5.5, Chapter 5). By removing a slice of approximately 40 voxels from each boundary of the xy-plane the effect was eliminated.

An example of a binary image obtained using the threshold selected on the pre-filtered image is presented in Figure 6.13. The differences with Figure 6.12a are evident; the grain edges have been smoothed and the noise has been reduced. Both grains and void space are shown in the binary filtered image as homogeneous regions contrasting to what is shown in Figure 6.12a. Some black regions can be found in the grain (shown as white pixels) in the filtered image; this is often associated to concavities of the particles. Knowledge of the features represented in the image and an awareness of the limitations of a 2D representation of 3D objects are required for interpretation of these output images. Significant improvements can also be observed for the filtered binary images from sample 295L (Figure 6.14), when compared to Figure 6.12b. As already mentioned, sample 295L contains part of the shear band developed in the triaxial specimen 295-int. The two cross-sections in Figure 6.14 correspond to top views of the triaxial specimen at different heights. As shown in Figure 6.14a and 6.14b, the region associated with the shear band develops from the top left corner to the lower right corner of the images and can be easily identified by the greater amount of black pixels which indicate the increase in the void ratio in that region.

An overview of the process used to create the segmented image is exemplified here by considering 2D sections obtained at different stages during the image processing of sample 297ph (Figure 6.15). The filtered image is shown in Figure 6.15a, while Figure 6.15b shows the line profile giving the grey-levels (intensity levels) across a grain surrounded by both resin (on the left) and an air bubble (on the right). There is a slightly higher contrast between the particle and the air as the air has a lower liner attenuation coefficient than the resin. The small air bubbles observed in the samples, result from the air being trapped in the resin during the impregnation process. The voxels associated with these air bubbles are located at the region of the lowest intensity level in the histogram. Both the resin and air regions are considered to be part of the void space in this study and they are not differentiated.

The binary image is shown in Figure 6.15c. The distance map (Figure 6.15d) is displayed using a colour-map that uses white colour to represent distances equal to zero and darker colour to represent greater distances. Figure 6.15e shows the output of the watershed result using the parameters t=0.04 and l=0.4, which results in an undersegmented image as some touching grains are considered to be single grains, i.e., they share the same colour and consequently their voxels have the same label. The final output of the application of the watershed algorithm using the parameters t=0.04 and l=0.2 (Figure 6.15f) shows a segmentation where touching particles are considered to be unique, individual particles.

For the void space analysis, the process to obtain segmented voids is common up to the selection of the threshold value and generation of the binary image. The major difference is that the distance map was calculated in the void space rather than in the solid phase. The final output of the watershed using the parameters t=0.04 and l=0.2 is illustrated in Figure 6.16, where each individual void is illustrated with a different label and colour.

6.2.4 Summary

This section summarises the key points of the image processing stage. It has been found that void ratio measurements are sensitive to the selection of the threshold value as a change in the threshold has a direct effect on the number of voxels allocated to each phase. The voxels affected by the partial volume effect are likely to be located along the boundaries of the particles and again uncertainty on the threshold selection can affect the particle size and the size of the contact between two particles. However the high resolution of the image with a voxel size equal to $0.018d_{50}$, and the general sharpness of the images are believed to have minimised this effect.

The watershed transforms the original image into a labeled image such that all points in a given catchment basin have the same unique label. Two scenarios can often occur when the partitioning of particles touching is carried out. A single grain can be divided into more than one grain which results in an oversegmented image, or two touching grains may not be separated into individual features, which results in the number of labeled regions being lower than the features they represent (undersegmentation).

One way to assess the success of the algorithms is to apply them to a "simple" system. The sample of micro-spheres analysed show good segmentation results but the regular and convex particle shapes and point contacts are not representative of the main challenges the locked sand represent, i.e., the highly complex and concave shapes, the great variation in the particle size and large contact areas. The accuracy

of the algorithm is difficult to evaluate given the interlocked fabric, and the identification of individual grains can be challenging even for a human expert. By plotting the surface of each individual particle (using the code described in Section 6.3.3), one inaccuracy observed was the case of a large particle that was in contact with a very small particle being considered as one. The implications of this specific error when the size difference between the two particles is significant, is not likely to affect the fabric quantification. The watershed level parameter appears to be efficient in avoiding oversegmentation but again this evaluation is not straightforward.

Based on the fundamental assumption of the watershed algorithm that each regional minimum in the distance map represents the centre of a distinct object, irregularities and variations along the surfaces of particles will cause the same particle to be divided into multiple parts. This can happen for concave particle morphologies and concave regions may be associated with a watershed line. Similarly for very elongated shapes, irregularities along the edge will be interpreted as indicators of limits of the zone of influence and so partitioning the grain or void into smaller particles or voids may occur. Pre-filtering the distance map with a smoothing filter alleviates the errors caused by small irregularities and prevents small minor regional minima being associated with different particles.

The individual voids were generated by locating the interconnects that were narrower than their surroundings. While particles are physical features in the image, the definition of individual voids is more abstract or subjective. Pore or void space characterisation has been widely investigated in material science and the use of watershed segmentation to identify individual pores is well documented (e.g., Atwood et al., 2004).

Finally it can be concluded that an adequate segmentation presents several challenges mainly due to the irregular shape and irregular size of the particles and image quality limitations. No single method can give the right answer. The tools available should be creatively combined in a constructive process to achieve the designed purpose.

6.3 Image Analysis

This section describes a series of algorithms that were developed and implemented in MATLAB (Mathworks, Natick, MA, USA). MATLAB stands for matrix laboratory. It is a high-level matrix/array language that has as its basic data structure the array. This fact makes MATLAB particularly suited to the representation of images as each single voxel in the image will correspond to an element of the matrix. Therefore, 3D images are represented as 3D arrays while 2D images are represented as 2D arrays. MATLAB allows for numerical computation and data visualisation using

both built-in functions, referred to in this study as "mfunctions", and new functions developed by users. Many of the functions used in this study were found in the Image Processing and Statistic Toolboxes, rather than in the basic MATLAB software.

Some general concepts regarding representation of digital images in MATLAB, including pixel connectivity as well as more general concepts used throughout this section are first introduced. This is followed by the description of the procedures employed to obtain the measurements for fabric quantification. The methodology for this analysis is organised as follows: pre-analysis processes, analysis of the particles, analysis of the contacts and analysis of the voids. A summary of the methodology is illustrated schematically in Figure 6.17. The primary objects of the analysis are the particles, the voids and the contacts between particles. The algorithms developed for measuring micro-quantities of the soil samples are described and validated with synthetic datasets for ideal-shaped objects. Finally, some of the routines developed are validated using tomographic images of a resin impregnated sample of micro-spheres.

6.3.1 General concept

Some concepts are here introduced to allow the reader to understand better the procedures described in this section. The concepts are diverse and can be summarised as follows: defining images as matrices, voxel connectivity, spherical coordinates, rotation matrices and principal component analysis.

(a) Images as matrices

A given three-dimensional digital image defined as $f(x, y, z)$ in the Cartesian coordinates, for $1 \leq x \leq R$, $1 \leq y \leq C$, $1 \leq z \leq Z$, can be represented as a MATLAB matrix as follows:

$$\begin{bmatrix} f(1,1,z) & f(1,2,z) & \cdots & f(1,C,z) \\ f(2,1,z) & f(2,2,z) & \cdots & f(2,C,z) \\ \vdots & \vdots & \ddots & \vdots \\ f(R,1,z) & f(R,2,z) & \cdots & f(R,C,z) \end{bmatrix} \tag{6.1}$$

This matrix can be seen as a grid of discrete elements defined with the first component x giving the row number, the second component y giving the column number and the third component z is the slice number, as illustrated in Figure 6.18. For example the voxel represented in dark can be described as $f(2, 3, 1) = 1$, for z coordinates increasing from top downwards.

(b) Voxel connectivity

The concept of voxel connectivity is of major importance for many operations in image analysis. There are three typical connectivities or neighbourhood relations between voxels in three-dimensions. The terms 6-, 18- and 26-connectivity are used according to the number of voxels that have common face, common edge (including the case of common face as well) and common vertex (also including all the edge-neighbours) with a given voxel, respectively (Figure 6.19).

(c) Spherical coordinates

A spherical coordinate system is useful to quantify orientations in 3D. As illustrated in Figure 6.20, the quantities necessary for the polar representation of a given vector are the azimuthal angle θ, measured in the xy-plane from the y-axis, the polar angle ϕ (also known as the zenith angle) measured from the positive z-axis, and the magnitude of the vector, the radius r. For a unit vector defined by its projections (n_x, n_y, n_z) relative to the Cartesian coordinate system (x, y, z), r is equal to *1* and the angles θ and ϕ can be obtained by the following expressions:

$$\phi = acos\,(n_z) \tag{6.2}$$

$$\theta = atan2\,(n_y, n_x) \tag{6.3}$$

where $\phi \in [0, \pi/2]$ and $\theta \in [-\pi, \pi]$ and the inverse tangent is defined by the function $atan2$ that takes the correct quadrant into account.

(d) Rotation matrices

In order to assess the ability of an algorithm to compute the orientation of a certain object as its direction varies, rotation matrices can be used. The rotation of a given object by a counter clockwise angle (when looking towards the origin) in a fixed coordinate system can be obtained using the rotation matrices presented in Table 6.4, for a rotation of angle α about the x axis, a rotation of angle β about the y axis and a rotation of angle γ about the z axis.

(e) Principal Component Analysis

Principal component analysis (PCA) is a mathematical tool that can be used to reduce the dimensionality (number of variables) of a dataset while retaining most of the original variability in the data. This can be achieved by transforming the original

correlated variables into a new set of uncorrelated variables called the principal components. The first principal component accounts for as much of the variability in the data as possible, and each succeeding component accounts for as much of the remaining variability as possible. It can be viewed as a rotation of the existing axes to new positions in the space defined by the original variables. Figure 6.21 shows an example of the application of principal component analysis in two-dimensions. Figure 6.21a shows the plot of 50 points relative to two highly correlated variables x_1 and x_2. There is considerable variation in both variables, particularly in the direction x_2. By calculating the principal components of the cloud of points, given by z_1 and z_2, the plot in Figure 6.21b can be obtained. The first principal component is z_1 as can be seen by the greater variation along z_1 direction, little variation can be observed along z_2 direction, the second principal component.

6.3.2 Pre-analysis processes

The processes described in the pre-analysis step have the purpose of preparing the images for the subsequent analysis, i.e., the extraction of the information from the images. The processes are summarised as follows: loading images into MATLAB, re-labelling images and merging images.

(a) Loading images into MATLAB

The 3D segmented images were imported into the MATLAB environment using the function *loadimage* that stores the image as a 3D array. This function has as input the name of the file, the size of the file and the data type. The output is the 3D array designed by A_{inital} that stores the intensity of each voxel given by $f(x, y, z)$ as $f(rows, columns, slices)$. The z direction, defined in Figure 6.18, was made to be coincident with the vertical direction of the initial cylindrical specimen (vertical direction of the triaxial specimen).

(b) Re-labelling particles

The segmented images (obtained from the watershed algorithm) had an integer associated to each feature in the image and stored in each cell of the array, e.g., all the voxels in the void space had value *1*. The individual particles were labelled with integer numbers greater than *1* in a sequential way if the images had not been previously cropped.

To apply the algorithms described in this section, the voxels belonging to the void space should have the value *0* and the voxels defining the particles, should have values between *1* and the total number of particles in the image (N_{part}). When the

original image did not satisfy these requirements the voxels were re-labelled using the user defined function `labelpart`. This function takes as input the 3D array with the original labels ($A_{initial}$), for both the void space and particles, and the original value of the background (bc). The output is the 3D array with the required labels (A).

(c) Merging images

As discussed in Section 6.2, due to computational limitations some samples had to be divided into smaller sub-volumes for image processing. In order to perform a rigorous analysis of fabric the sample must be analysed as a single volume, so an algorithm that takes into consideration the particles on the boundaries of two sub-volumes should be developed.

To facilitate a sub-volume based analysis, the particles belonging to more than one sub-volume were assigned the same index. Indices could not be repeated in different sub-volumes and followed a sequential order within each sub-volume. Considering two sub-volumes A_1 and A_2, to perform the analysis:

1. The size of the two images was adjusted to achieve an overlapping of one voxel along the y direction, i.e., $A_1(R, C, Z)$ and $A_2(R, C+1, Z)$.

2. This overlapping layer was used to identify the particles common to both sub-volumes. The overlap is a 2D image given by either the last column along all the slices of A_1 or the first column of A_2.

3. Particles in volume A_1 were relabelled from *1* to $Npart_{A1}$.

4. Particles in volume A_2 were relabelled from $N_{partA1}+1$ to $N_{partA1}+1+N_{partA2}$ to make sure that there were no repeated indices.

5. The centroids of the particles cross-section in the common slice (CS) were calculated using mfunction `Centroid.regionprops` (see explanation below).

6. The particles in image A_2 that participated in the common slice were re-labelled to take the indices used in image A_1 that have the same centroid.

7. All the other particles in image A_2 which did not intercept the common slice were relabelled from $N_{partA1}+1$ to $N_{partA1}+1+N_{partA2}-N_{partCS}$.

8. A similar procedure was repeated for the cases that the original sample was divided into more than two sub-volumes.

6.3.3 Analysis of the particles

The analysis of the particles was carried out to obtain the vector defining their orientation as well as size and shape, i.e., information for morphological characterization. As the particles in the boundary of the image were not complete, only the inner particles of the image were considered for this analysis. The process is divided into eight parts, which include the identification of the indices of the particles that intercept the image boundary (boundary particles) and the determination of the following information relative to the particles: coordinates of the voxels and centroids, volume and surface areas, an alternative calculation of volume and surface area for convex particles, orientation, dimensions, particle size distribution and the fabric tensor for the particle orientation.

(a) Identification of the boundary particles

A 3D volume image is a parallelepiped bounded by six rectangles. Any particle located at the boundaries of the image will be intercepted by at least one of these planes. The function `removepartboundary` identifies the label of the voxels along each of these six planes and stores the integers in 1D array called *bp*. For example, referring to Figure 6.18 for the top plane the z coordinate has the constant value of *1*, and so in a nested loop considering x values between *1* and R and y values between *1* and C, the indices of the particles intercepting this boundary were identified and stored. By repeating this procedure for the other planes, a single array (bp) storing the boundary particles was created.

(b) Coordinates of voxels and centroids

In a 3D image each particle is essentially given by a "cloud of points". The coordinates in (x, y, z) of these points or voxels can be obtained by using the intrinsic mfunction `PixelList.regionprops`. This specific measurement (i.e., the coordinates of the pixels) is one of the various properties that the function `regionprops` is able to provide. The measures available include shape properties and pixel value properties and can be performed for each region in an image, where each region is defined by pixels sharing a common value.

The function `PixelList.regionprops` returns a structure array with length N_{part} that can be converted into a cell array designated by *pp*. The cell array data structure available in MATLAB allows arrays, integers and real numbers to be stored together as an array of information. This means that the entry $pp\{1, n\}$ is itself an array giving the voxel coordinates for particle n as is outlined in Equation 6.4 where ctx_i, cty_i, ctz_i, are the x, y and z coordinates, respectively of the ith voxel coordinate making up particle n, for $i \in [1, N_{vox}]$.

In a similar way, the centroid of each particle can be obtained by calling the intrinsic mfunction `Centroid.regionprops`. This function returns again a cell structure array where each cell stores a 1×3 array with the (x, y, z) coordinates of the particle centroid, i.e., $(ccx,\ ccy,\ ccz)$ as given by Equation 6.5.

$$pp\{1,n\} = \begin{bmatrix} ctx_1 & cty_1 & ctz_1 \\ ctx_2 & cty_2 & ctz_2 \\ \vdots & \vdots & \vdots \\ ctx_{Nvox} & cty_{Nvox} & ctz_{Nvox} \end{bmatrix} \tag{6.4}$$

$$cc\{1,n\} = \begin{bmatrix} ccx & ccy & ccz \end{bmatrix} \tag{6.5}$$

(c) Volume and surface area

The volume of each particle was calculated by simply counting the number of voxels defining each particle, which is given by the size of the matrix in Equation 6.4. The volume in μm^3 was obtained by multiplying the number of voxels by the size n of each voxel, i.e., $resol^3$, where $resol$ is the spatial resolution of the image.

In a similar way, the surface of a particle was obtained by counting the number of voxels defining the 3D boundary of the particles. The surface area in μm^2 was obtained by multiplying the number of voxels by the area of a voxel face, i.e., $resol^2$. The identification of the voxels in the particle boundary is however not trivial, the user defined function `surfarea` was developed for this purpose and is described in the following paragraphs.

The function `surfarea` makes use of the intrinsic mfunction `bwperim`, which returns the perimeter voxels of the objects in the binary image taken as input. Because in the binary version of image A, the particles were not differentiated as they all have the same value *1*, the outline obtained was of the solid phase and not specifically of each individual grain. For this reason, function `bwperim` was applied sequentially to each individual particle rather than to the entire image. To determine the boundary of particle n, all the voxels in A were changed to *0* with the exception of the voxels belonging to particle label n that were changed to *1*. This binary image was then used as input to obtain the 3D outline of particle n. The number of voxels in the outline ($N_{vox,surface}$) was obtained by determining the size of the cell array output using the intrinsic function.

The mfunction `bwperim` considers a given voxel as part of the perimeter if this voxel is non-zero and it is connected to at least one zero-valued pixel. The process of assigning the voxels is therefore based on the type of connectivity considered. A 6-connected neighbourhood was chosen as, given the complex and irregular shapes

of the sand grains, higher order connectivities will return boundaries defined by a much larger number of voxels.

A simple way of understanding the effect of the pixel connectivity on the definition of the boundary of an object is by considering the cross-section of an object in 2D. Figure 6.22a shows a 2D schematic representation of a particle boundary using face adjacency, the equivalent 6-connectivity in 3D and Figure 6.22b shows the boundary detection for the same outline using face and edge adjacency, the equivalent to 18-connectivity in 3D. As can be seen the presence of irregularities on the surface can contribute to a significant increase in the number of voxels defining the outline when edge connectivities are used.

To assess the effect of voxel connectivity and the ability of this algorithm to calculate the surface area of objects, the function `surfarea` was applied to an image of microspheres of $555\mu m$ diameter. The surface area of a sphere of $555\mu m$ diameter is $967689\mu m^2$. Table 6.5 shows the values for the surface area obtained using 6-, 18- and 26-connectivities. The spheres were not perfect and therefore some error was expected. The smaller error was found for the 6-connectivity, in average 15% lower than the expected value. Both 18- and 26-connectivity showed higher values with errors of 30% and 50% respectively.

(d) Volume and surface area for convex particles

An alternative algorithm was developed to calculate the volume and the surface area of the particles. The code makes use of the intrinsic function `delaunay3`. This function computes the triangulation of the points defining the boundary of the particle with the particle centroid, in a way that the tetrahedrons obtained have three vertices on the surface and the fourth is the particle centroid. In other words, it is a 3D Delaunay tessellation which returns the array *tri* where each row contains the indices of the points in (x,y,z) that make up a tetrahedron.

The volume for each tetrahedron was calculated using the user defined function `volumetetrahedron` which has as input the coordinates of the points defining the particle boundary and the centroid coordinates. The grain volume is equal to the sum of volumes of the tetrahedrons forming the particle multiplied by the spatial resolution. For a tetrahedron with vertices v_1, v_2, v_3, v_4, the volume is given by the following formula:

$$V = \frac{|(v_1 - v_4) \cdot ((v_2 - v_4) \times (v_3 - v_4))|}{6} . \tag{6.6}$$

The volume of the particles is the sum of the volume of all tetrahedrons. The surface area can be calculated by using the exterior face of the tetrahedron which can easily be identified as this tetrahedron face is unique, in the way that is not common to any

other tetrahedron. This triangulation-based algorithm cannot be applied to concave particles but it is effective if convex shapes are to be used.

The convex hull, or convex envelope, of a particle can also be obtained using the intrinsic function `convhulln` that takes as input the array *pp* with the coordinates of the voxels defining the particles. The function returns the volume and the indices K of the points in *pp*{i,1} that comprise the facets of the convex hull of *pp*{i,1}. For a 3D object, the convex hull has p facets and K has size $p \times 3$.

(e) Orientation

The orientations of the principal axes of inertia of each particle were determined using a principal component analysis (PCA) based method. These orientations can be described by three unit vectors that define a local coordinate system for the particle. To describe any point on the surface of the particle in this local system, the coordinates of the point in a Cartesian coordinate system centred on the particle centroid have to be calculated first. One can describe any point on the surface of the particle in a local Cartesian coordinate system centred on the centre of the body by a simple translation. This local Cartesian coordinate system (which axes are parallel to the global Cartesian axes) is defined by axes (x_p, y_p, z_p). This means that if the coordinates of a point on the surface of the particle are (x^b, y^b, z^b) in the global coordinate system, in this local Cartesian coordinate system the coordinates ($x^b{}_p$, $y^b{}_p$, $z^b{}_p$) are equal to ($x_p - x_c$, $y_p - y_c$, $z_p - z_c$), where the particle centroid is (x_c, y_c, z_c) in the global coordinate system. Three vectors that describe the orientation of the particle centroid in the local coordinate system can then be obtained from PCA. The application of PCA in MATLAB (using the intrinsic functions described below) takes as input the coordinates of the particle voxels and returns a 3×3 matrix as follows:

$$P = \begin{bmatrix} n_{x'^b x^b} & n_{y'^b x^b} & n_{z'^b x^b} \\ n_{x'^b y^b} & n_{y'^b y^b} & n_{z'^b y^b} \\ n_{x'^b z^b} & n_{y'^b z x^b} & n_{z'^b z^b} \end{bmatrix} \tag{6.7}$$

The principal axes of inertia of the particle in the global coordinate system are presented in Figure 6.23.

This vector P is an orthogonal matrix, so that the inverse of P equals the transpose of $P^{-1} = P^T$. Furthermore P defines an orthogonal or rigid body rotation as the matrix product PP^{-1}returns the identity matrix. Just as was the case for the rotation matrices defined in Table 6.4, the matrix P is orthogonal. If a vector defined in 3D in the local Cartesian coordinate system is multiplied by this matrix a rigid body rotation is performed. This means the vector length is preserved as its orientation changes. By extension, having a series of coordinates in the local coordinate

system defining a particle, the same particle can be rotated by multiplying all the coordinates by this vector, without changing its shape or volume. The coordinates of the point ($x^b{}_p$, $y^b{}_p$, $z^b{}_p$) can be calculated in the transformed coordinate system, i.e., the coordinates of that point relative to the principal axes, as follows:

$$\begin{aligned} x^b_{p'} &= n_{x'^b x^b} x^b_p + n_{x'^b y^b} y^b_p + n_{x'^b z^b} z^b_p \\ y^b_{p'} &= n_{y'^b x^b} x^b_p + n_{y x'^b y^b} y^b_p + n_{y'^b z^b} z^b_p \\ z^b_{p'} &= n_{z' x^b} x^b_p + n_{z'^b y^b} y^b_p + n_{z'^b z^b} z^b_p \end{aligned} \tag{6.8}$$

The components of the normal vectors are sometimes called the direction cosines, i.e., the direction cosine between the $x^{b'}$axis and the x^b axis. Typically when applying an orthogonal rotation to a column vector, it is pre-multiplied by the rotation matrix, as follows:

$$\begin{bmatrix} x^b_{p'} \\ y^b_{p'} \\ z^b_{p'} \end{bmatrix} = \begin{bmatrix} a_{11} & a_{12} & a_{13} \\ a_{21} & a_{22} & a_{23} \\ a_{131} & a_{32} & a_{33} \end{bmatrix} \begin{bmatrix} x^b_p \\ y^b_p \\ z^b_p \end{bmatrix} \tag{6.9}$$

In the present case the direction cosines for the transformation are given directly by the PCA analysis in columns rather than rows (i.e., the PCA gives us the inverse of the conventional rotation matrix). In order to rotate a large data set of coordinates into the local coordinate system, and taking advantage of efficiencies in vector calculations in MATLAB it is preferable to obtain the coordinates of the points defining the particle coordinates by expressing the rotation operation in the following format:

$$\begin{bmatrix} x^b_{p1'} & y^b_{p1'} & z^b_{p1'} \\ x^b_{p2'} & y^b_{p2'} & z^b_{p2'} \\ \vdots & \vdots & \vdots \\ \vdots & \vdots & \vdots \\ x^b_{pNvox'} & y^b_{pNvox'} & z^b_{pNvox'} \end{bmatrix} = \begin{bmatrix} x^b_{p1} & y^b_{p1} & z^b_{p1} \\ x^b_{p2} & y^b_{p2} & z^b_{p2} \\ \vdots & \vdots & \vdots \\ \vdots & \vdots & \vdots \\ x^b_{pNvox} & y^b_{pNvox} & z^b_{pNvox} \end{bmatrix} \begin{bmatrix} n_{x'^b x^b} & n_{y'^b x^b} & n_{z'^b x^b} \\ n_{x'^b y^b} & n_{y'^b y^b} & n_{z'^b y^b} \\ n_{x'^b z^b} & n_{y'^b z x^b} & n_{z'^b z^b} \end{bmatrix} \tag{6.10}$$

where (x^b_{pj} ,y^b_{pj}, z^b_{pj}) are the coordinates of the point j on the particle outline in the local Cartesian coordinate system, and ($x^b_{pj'}$,$y^b_{pj'}$, $z^b_{pj'}$) are the coordinates in the local rotated coordinate system for the N_{vox} points defining the particle.

The user defined function `orientationpart` was developed to compute the three unit vectors that define the orientations of the particles, as given by the PCA analysis. This function considers each particle sequentially; to carry out PCA analysis in MATLAB the intrinsic function `pcacov` can be applied to the covariance matrix of the matrix containing the particle coordinates or alternatively the intrinsic function

`princomp` can be applied directly to the coordinates. In either case, the result is the principal component tensor, pc that stores in each column the vector defining each of the principal component directions, with the first column storing the vector defining the major axis orientation (maximum variability), the second column storing the orientation of the intermediate axis and the third column storing the orientation of the minor axis. These axes are mutually orthogonal to each other. Figure 6.24 illustrates the vectors along the three principal directions determined following the application of the code developed to a synthetic ellipsoidal-shaped particle.

(f) Dimensions

The three principal axes lengths, i.e., the major axis length (a), the intermediate axis length (b) and the minor axis length (c), were obtained from the PCA algorithm presented above. The user defined function created for this purpose was named `partdiameter`. This function takes as input the voxel coordinates for a single particle. The particle was rotated using the rotation matrix pc and the coordinates of the particle voxels in the local rotated coordinate system were obtained. Figure 6.25 shows the ellipsoidal particle presented previously, now orientated along the local rotated coordinate system. The three principal dimensions of the particle can be obtained as the difference between the maximum and minimum x^b_{pj} values, and the same for the other two orthogonal directions, as follows:

$$\begin{aligned} a &= (x^b_{pj})_{max} - (x^b_{pj})_{min} \\ b &= (y^b_{pj})_{max} - (y^b_{pj})_{min} \\ c &= (z^b_{pj})_{max} - (z^b_{pj})_{min} \end{aligned} \tag{6.11}$$

The diameter in μm is obtained by multiplying the length given in voxels by the size of each voxel ($resol$).

(g) Particle size distribution

The user defined function `plotPSD` was created to plot the particle size distribution (PSD) curve. The function considers the sieves apertures of 1000, 600, 420, 300, 212, 180, 150, 106, 63 microns. The input of this function is the most representative length of the particle dimensions ($d_{effective}$), taken in this study as the intermediate axis length (b). The percentages finer than these dimensions, i.e., the percentage passing was calculated by volume as follows:

$$\%Passing = \frac{Cumulative\,Vol\,of\,soil\,passing}{Total\,Vol\,soil}$$

(h) Fabric tensor

The fabric tensor for the orientation of the particles was calculated using two formulations. The first formulation considers the orientation of the three principal axes of the particle (given by the rotation tensor pc) and its associated length (given by a, b and c) and is designated by Φ^p (Equation 2.23). The second formulation takes into account the orientation of the particle major axis and is designated by Φ (Equation 2.11). For both cases the respective eingenvalues and eigenvectors were obtained using the intrinsic function `eig`.

The accuracy of the MATLAB functions described above in measuring the orientation and the dimensions of the particles was assessed by applying them to a group of synthetically created ellipsoids for which the geometrical characteristics were previously known. The following three examples serve to give a better understanding of the information given by the fabric tensor and the associated eigenvalues and eigenvectors applied to simple systems.

The first example considers a synthetic sample made of 64 uniformly sized ellipsoids for which the semi-axis dimensions (in voxels) were a=40, b=32 and c=24, giving aspect ratios equivalent to that of a typical grain of Reigate sand. The ellipsoids were rotated from their initial horizontal position (with their major axis parallel to the x axis) about the y axis by an angle β and about the z axis by γ. Table 6.6 shows the results obtained for the fabric tensor and the respective eigenvalues and the principal eigenvector and its orientation in terms of the angles ϕ and θ. The eigenvalues are related to the aspect ratio of the particle, i.e., $\frac{S_1}{S_2} = \frac{a}{b}$ and $\frac{S_2}{S_3} = \frac{b}{c}$, and so their values are invariant upon rotation. The angle θ obtained is based on the principal orientation of the fabric tensor, i.e., the eigenvector V_1 is able to measure the variation of the particle orientation with an error <1°. The angle β is measured from the y axis which explains the 90° difference between β and ϕ angles.

The second example compares the results obtained using the two fabric tensor formulations Φ and Φ^p applied to three systems of uniformly sized and shaped ellipsoids but with very distinct shapes within the systems (Table 6.7). Each synthetic dataset considered contained 64 particles. The first sample was formed of nail-like particles with an aspect ratio $c/a = 0.08$. In the second sample the particles were platy shaped with a ratio $b/a \simeq 1$ and in the third sample the particles had aspect ratios closer to a typical grain of Reigate sand. In all the three samples the ellipsoids had the principal axes parallel to the x direction (length a), an intermediate length b parallel to the y direction and the minor length c parallel to the z direction. Despite the differences in the packing between the different samples (as a consequence of the particle shapes), the fabric tensor based only on the particle orientations (Φ) gave exactly the same answer for all cases. The results given by the eigenvalues of the fabric tensor that considers the size and the shape of the particles (Φ^p) were better

able to differentiate the fabric of the different samples. Both formulations returned the same eigenvectors. Since all the particles have the major axis orientated along the x direction both ϕ and θ are equal to 90° for the three cases.

The following example serves to illustrate the capabilities of the two fabric tensor formulations (i.e., Φ and Φ^P) to capture the anisotropy imparted by the larger particles in a system constituted of particles with different sizes. The demonstration considers two systems of ellipsoids, A_1 and A_2 each containing 64 uniformly sized ellipsoids (Table 6.8). System A_2 had larger ellipsoids than system A_1 but for both systems the aspect ratios were the same and equal to $b/a = 0.5$ and $c/b = 0.5$. In system A_1 the particles were orientated with their major axes along the x axis, their intermediate axes along y and their minor axes along the z axis, while in system A_2 the ellipsoids had their major axes along y, intermediate along z and their minor axes along the x axis. Therefore the principal fabric was horizontal ($\phi_{V_1} = 90°$) for A_1 and vertical ($\phi_{V_1} = 0°$) for A_2. When the two systems were merged, the fabric tensor formulation Φ returned a principal fabric orientated at 45° while the formulation Φ^P returned an orientation of 8°, which is closer to the 0° of the sample with the larger ellipsoids. These results show that the fabric tensor that takes into account the associated axis length for each orientation is better able to capture the anisotropy imparted to the granular system by the larger particles.

6.3.4 Analysis of the contacts

As already mentioned, a given voxel can be associated with a feature in the image depending on the value it holds, i.e., value *0* corresponds to a void space voxel and any other integer ≥ 1 is associated with a specific grain. A new voxel classification is introduced here, that is the contact. The concept of contact is however different from the particle or void space as a contact is not a "physical" feature of the image but a rather conceptual one. It is assumed that the voxels defining a contact are voxels that belong to one of the particles in contact. The contact analysis process is divided into six parts, starting with the description of the contact detection process. The contact classification and surface area calculation are followed by the description of the algorithm used to obtain the contact normal. Planar objects were used to validate the process to obtain the directional data and the fabric tensor. Finally, the algorithms used to obtain the branch vector orientation and the branch vector length are described.

(a) Contact detection

Considering two contacting particles (*particle 1* with label n_1 and *particle 2* labeled n_2), each particle is defined as a cloud of voxels that share the same common intensity value and so three possible classifications for each of these voxels are can be

determined based on its its neighbourhood. Voxels with an intensity given as an index n_1 are inner voxels if they are only connected to voxels indexed n_1, they are edge voxels if they are connected both to voxels with value *0* and to voxels with a value index of the same value n_1. They are "contact voxels" if they are connected with voxels with a different non-zero index, i.e., if they are in connection with voxels with indices n_1 and n_2, where n_2 is the index associated with voxels of another particle. Using this concept, the user defined function `identifcontcoord` was developed. This function takes as input the 3D array A with all the particles, including the ones along the image boundary. The algorithm underlying this function is explained in the following paragraphs.

The voxel contact classification is based on a 6-connectivity voxel neighbouhood relation, and requires a total of six "passes" through the data along the three principal directions x, y and z. For example there are two "passes" along x. The first pass forward, identifies the contact voxel $(x+1, y, z)$ for a given voxel (x, y, z), and the second pass backward considers the neighbourhood $(x-1, y, z)$. A similar process is repeated for direction y and z for detection based on the its neighbourhoods $(x, y \pm 1, z)$ and $(x, y, z \pm 1)$, respectively.

This procedure was applied to each individual particle separately, and so for a particle labelled n_1 the contact voxels were stored in the 3D array called $contc.n_1$. Array $contc.n_1$ has the same size as array A and initially all voxels had values equal to *0* and so as the contact voxels are detected the voxels with coordinates (x, y, z) were changed in value from *0* to n_2, with n_2 being the index of the adjacent contacting particle.

Figure 6.26 illustrates the contact detection process in two dimensions, as it is easier to visualise than the 3D process and uses the same principle. Figure 6.26a shows *Particle 1* in contact with P*articles 2*, *3* and *4*. In order to obtain the contacts between *Particle 1* and the other particles, the contact voxels were first identified along direction x, as shown in Figure 6.26b. The integer value correspondent to the label of the second particle in the contact, i.e., n_2, is attributed to these voxels defining the contact. In the same way, the contacts are identified along the y direction, as shown in Figure 6.26c. The contact voxels identified along both x and y directions are then combined as shown in Figure 6.26d.

This algorithm assumes that the contact between particle n_k and particle n_h is defined in two different ways, when the contact is detected for particle n_k and when the contact is detected for particle n_h. There are slight differences in the contact voxels identified, depending on which particle is considered. Figure 6.27 illustrates the resulting differences in two dimensions. Considering the small voxel size used in this study $(3-5\mu m)$ compared with the size of the particles $(d_{50} = 270\mu m)$ the differences are not expected to be significant.

Once the contacts were identified for each particle in the image, the coordinates of the voxels defining the contacts were obtained and stored in a cell array called *contactcoord,* which has size $N_{part}\times 2$ where in the first column the label n_1 is stored and in the second column there is a cell array that has the length of the maximum value of n_2. Just as was the case for the particles, the intrinsic function `PixelList.regionprops` was used and the output was the array *ppc.*

The *neigbarray* array was created to store the labels of the particles in contact. The array has size $N_{part}\times$ 2; the first column stores the index n_1 and the second column stores the indices n_2 of all the particles in contact with n_1. Therefore the number of different integer value indices corresponds to the coordination number (CN) of the particle under consideration.

(b) Contact classification

The contacts were classified as either "point contacts" for contacts defined by 6 voxels or less and "finite contacts" for contacts larger than 6 voxels. For the contact normal calculations, only finite contacts were considered, as less than 6 voxels were not considered sufficient to define clearly the orientation of a plane and so it would be associated with a bias that could be significant.

(c) Contact surface area

The surface area of the contacts was calculated by multiplying the number of voxels defining each contact by the area of each voxel ($resol^2$) to give the result in μm^2. The number of voxels is given by the size of the matrix in Equation 6.15.

An alternative method for calculating the contact surface area was to consider a surface defining the outline of each particle. Once the coordinates of the voxels defining the contact were known, as described above, the surface could be obtained by triangulating these voxels using the mfunction *delaunay.* The function *delaunay* returns the matrix *tri* with the indices of the triangle vertices, i.e., the number of rows is the number of triangles. Each row of the m×3 matrix *tri* defines one such triangle. The coordinates in (x, y, z) for vertex i, (for $i = 1, 2, 3$) are given by:

$$(ctx(tri(1,i)),\ cty(tri(1,i)),\ ctz(tri(1,i))) \tag{6.12}$$

The surface area was obtained by summing the area of all the triangles on the surface. For each triangle the area was calculated using Heron's formula, given the lengths of the sides l_1, l_2 and l_3 and the semi-perimeter s, as follows:

$$s = \frac{1}{2}(l_1 + l_2 + l_3) \tag{6.13}$$

$$Area\ \Delta = \sqrt{s(s-l_1)(s-l_2)(s-l_3)} \tag{6.14}$$

To illustrate the results using this algorithm, it was applied to a square plane with 11×11 voxels, making 121 voxels in total and so a surface area of $121\mu m^2$ considering $resol = 1$. Using the triangulation approach, for this particular case where all the triangles have equal dimensions and so an area of 0.5 and the matrix *tri* with size 200×3, the surface area obtained was $100\mu m^2$. The different values obtained using the two approaches is due to the fact that the triangulation approach considers the voxel as a *0*-dimensional object, i.e., a point defined on the 3D cubic grid and so triangles between these points will "cover" a smaller area than the area associated with the cubic voxels centred on these points. Figure 6.28a illustrates a simple 2D example of a surface defined by 4 pixels and with an area of $4\mu m^2$ considering the unit square area of each pixel. Figure 6.28b shows that the surface area using the triangulation approach will be equal to $1\mu m^2$, i.e., 25% less than the actual area defined by the pixels. In the same way, Figure 6.29a illustrates the triangulated surface of the square plane and Figure 6.29b compares the areas obtained by considering the triangulation approach and by taking into account the area of each voxel defining the plane. It can be concluded that the differences between both approaches are more significant for small surfaces and become less significant as the size of the surface increases. For consistency with the methodology used to calculate the surface area of the particles, the triangulation approach was not used to calculate the surface area of the contacts.

(d) Contact normals

The process developed to obtain the contact normals consists of two main tasks, firstly the best-fitting plane was calculated for the cloud of voxels defining the contact and secondly the normal to that plane was obtained. The user defined function `contnormallsq` was created for this purpose as described in the following paragraphs.

When dealing with complex-shaped soil grains, the same two particles can be in contact through more than one contact region. Consequently the cloud of voxels that has been identified as defining the contact between two particles in some cases comprises discrete regions that required to be identified and analysed individually.

The intrinsic function `bwlabeln` was used to identify the unconnected regions of the contacts and re-label them with distinct labels. This function takes as input a binary image, i.e., a 3D array where voxels associated with features have value *1* and background voxels value *0*. Therefore, a loop was developed that for each m value, created a 3D array called Bm where m is the label of each contact for $m \in [1, Ncont]$

and so the coordinates of each contact $(ctx, cty, ctz)_m$ were represented as voxels labelled *1*. In the mfunction *bwlabeln* a 26-connectivity was considered, i.e., voxels were assigned to the same region if there were adjacent to a face, edge or corner of another voxel in the region. For individual regions with more than 6 voxels the best fit plane was calculated.

The cloud of points defining each contact region is approximated to the best fit plane using a least square approach. The coordinates of the voxels defining each region are stored in the array *ppc*, defined as:

$$ppc\{1, m\} = \begin{bmatrix} ctx_1 & cty_1 & ctz_1 \\ ctx_2 & cty_2 & ctz_2 \\ \vdots & \vdots & \vdots \\ ctx_{Nvox} & cty_{Nvox} & ctz_{Nvox} \end{bmatrix} \tag{6.15}$$

The plane that best fits the data was determined by considering the equation of the plane in the following format:

$$z = b_1 x + b_2 y + b_4 \tag{6.16}$$

where b_1, b_2 and b_3 are constants.

The values b_1, b_2 and b_3 that give the plane that best fits the data was obtained by solving the following set of linear equations in MATLAB:

$$\begin{aligned} b_1 ctx_1 + b_2 cty_1 + b_3 &= ctz_1 \\ b_{1ct} x_2 + b_2 cty_2 + b_3 &= ctz_2 \\ &\vdots \\ b_1 ctx_n + b_2 cty_n + b_3 &= ctz_n \end{aligned} \tag{6.17}$$

where (ctx_i, cty_i, ctz_i) gives the coordinates of voxel i.

These equations can be expressed in a matrix form as:

$$\begin{bmatrix} ctx_1 & cty_1 & 1 \\ ctx_2 & cty_2 & 1 \\ \vdots & \vdots & \vdots \\ ctx_n & cty_n & 1 \end{bmatrix} \begin{bmatrix} b_1 \\ b_2 \\ b_3 \end{bmatrix} = \begin{bmatrix} ctz_1 \\ ctz_2 \\ \vdots \\ ctz_n \end{bmatrix} \tag{6.18}$$

or $X \cdot b = ctz$.

Given the array X and the vector ctz, the least squares solution, i.e., the array b can be obtained by the command `b=X\ctz` in MATLAB.

The normal vector to the best fitting plane is given by:

$$n = \begin{bmatrix} b_1 \\ b_2 \\ -1 \end{bmatrix} \tag{6.19}$$

The unit normal can be obtained by dividing each component of the vector by the vector magnitude, given by the intrinsic function `norm`.

The plane defining the surface can be visualised by calling the intrinsic function `delaunay` which triangulates the set of points defined by the coordinates (*ctx, cty,M*) where M represents the best fitting along the z direction, i.e., $M = X \cdot b$. The intrinsic function `delaunay` returns an m×3 matrix *tri* with the indices of the vertices of each triangle, m being the number of triangles. Each row of *tri* defines a single face by indexing into the matrices that contain the *ctx, cty* and M vertices. The coordinates in (x, y, z) for vertex i, (for $i = 1, 2, 3$) are given by:

$$(ctx(tri(1,i)),\ cty(tri(1,i)),\ M(tri(1,i))) \tag{6.20}$$

The surface can be displayed using the intrinsic function `trisurf` which shows the triangles defined by *tri*.

Collinear points, i.e., distinct voxels with the same x and y coordinates and different z, are not detected by the triangulation function and this leads to errors in the final surface. One way of avoiding collinearity is to rotate the points defining the contact by multiplying it by the rotation matrix *pc* from the PCA analysis. Once the contact points were in the new position, the planar regression was carried out and the normal vector was obtained. The normal vector of the contact in the original position was obtained by multiplying by the inverse of the *pc* matrix.

Table 6.11 shows the normal vector obtained by applying the algorithm described above for an ideal contact defined by a planar set of 3D points in the xy-plane and so with an expected normal in the z direction. As can be seen, the rotation of the data using the *pc* rotation tensor does not affect the final result. Figure 6.30a illustrates the second example presented in Table 6.11 (for $\alpha = 30°$); the vector normal at the original position (n_{org}) for the set of planar points is represented by the line orientated upwards and the final normal vector obtained by multiplying n_{org} by the inverse of the *pc* tensor (i.e., n_{final}) although it is being orientated upwards, it has the same line of action as n_{org}. Figure 6.30b shows the best-fit plane of the data after being rotated using *pc* and the corresponding normal vector.

(e) Fabric tensor

The fabric tensor was obtained using the user developed function `fabrictensor` that users Equation 2.11 applied to the unit normal vectors given by [*nx,ny,nz*].

A 3D image containing 10 planar surfaces defined by 121voxels (11×11) each was used to validate the algorithm described above (i.e., the normal to a surface). All the planar surfaces were initially orientated along the xy-plane. Using the rotation matrices defined in Section 6.3.1, the planes were all rotated to four different positions. For the first two cases, the planes were rotated relative to the axis x by an angle $\alpha = 30°$ and $\alpha = 45°$. In the third case the planes were rotated relative to axis y by $\beta = 95°$ and in the last case, the planes were rotated relative to axis z by $\gamma = 40°$ (Table 6.9). For each position the unit normal vector, common to every plane, was determined. The angle ϕ and angle θ associated with the normal vector were calculated. The fabric tensor of the dataset of normal vectors was also calculated as well as the ϕ and θ angles of the principal fabric given by the eigenvector V_1. As the inital positions of the planes were horizontal, both the normal vector and V_1 were given by a vertical vector. The error measured, designated by ω, was less than e^{-15} and so can be considered insignificant. It was found that the normal vector wich the routine returns can point upwards or downwards. Therefore the absolute values of n_z should be used for the calculation of the angle ϕ of the dataset. Whether the vectores are pointing upwards or downwards seems to have no effect on the fabric tensor calculations.

(f) Branch vector

The branch vector connecting the centroids of two particles in contact (with labels n_1 and n_2) was obtained using the following equation:

$$\begin{aligned} nx &= cc\{1, n_1\}(1,1) - cc\{1, neigbarray\{n_1, 2\}(d)\}(1,1) \\ ny &= cc\{1, n_1\}(1,2) - cc\{1, neigbarray\{n_1, 2\}(d)\}(1,2) \\ nz &= cc\{1, n_1\}(1,3) - cc\{1, neigbarray\{n_1, 2\}(d)\}(1,3) \end{aligned} \tag{6.21}$$

where cc is the array that stores the coordinates of the centroid of each particle in the image, *neigbarray* is the array that stores the label of the particles in contact, n_1 is the label of the first particle in the contact and d takes values from *1* to the maximum number of particles in contact with particle n_1.

The calculation of the branch vector used all the particles in the volume just as the contact detection process did. There was a minor error associated with the determination of the centroid for the particles in the boundary, but this is thought to have an insignificant influence on the final results. The fabric tensor of the unit branch vector was calculated in a similar way as used for the contact normal vectors. While for the fabric tensor based on the contact normal only the finite contacts were used, for the branch vector fabric tensor all the contacts were taken into consideration. The length of the branch vector is given by the value of its

magnitude. The length in μm was obtained by multiplying the vector magnitude by the spatial resolution of the image.

6.3.5 Analysis of the voids

The analysis of the void space was carried out in a similar way to the analysis of the particles. The measured quantities were the orientations of the voids and the sizes of the voids.

The void ratio was calculated from binary images, where the solid phase has value *1* and voxels assigned to the void spaces have value *0*, by a simple count of the voxels of the solid and void phases. The total number of voxels in the image (*nvoxel total*) was equal to the volume of the image, i.e., R×C×Z, and the number of voxels assigned to the solid phase (*nvoxel solid*) was equal to the number of voxels with label *1*. The void ratio was obtained from the following expression:

$$voidratio = \frac{(nvoxel\ total - nvoxel\ solid)}{nvoxel\ solid} \tag{6.22}$$

6.3.6 Validation using a sample of micro-spheres

The algorithms described in this chapter for both image processing and analysis were applied to images of glass micro-spheres (from Whitehouse Scientific) with $555\mu m$ diameter, i.e., approximately twice the mean diameter (d_{50}) of Reigate sand. The samples were prepared in a dense state (void ratio=0.604) and impregnated with epoxy resin just as the soil samples. Table 6.10 summarises the information of the 3D image of the sample made of micro-spheres.

The algorithm developed to obtain the dimensions of the particles as a function of the major, intermediate and minor axis lengths (a, b and c, respectively) was applied to the image of micro-spheres. The results are presented in Figure 6.31. Some scatter can be observed and the average values of the three lengths are also slightly different from the expected $555\mu m$. These differences are related to the limited precision of the spheres. Better results were obtained for the aspect ratios of the particles, calculated as defined in Equation 2.30, illustrated in Figure 6.32. Despite the small scatter, the average elongation value is 0.966 and the average flatness is 1.052, only differing slightly from the expected value of 1 for a perfect sphere. The average convexity index, obtained using Equation 2.37, was 1.00 as expected (Figure 6.33). As illustrated in Figure 6.34, the average sphericity index obtained using a 6-connectivity was of 1.179. As discussed in Section 6.3.3, using a 6-connectivity produced lower surface areas than expected and consequently the sphericity index, as defined in Equation 2.33, was greater than 1. Figure 6.35 shows

the comparison between the measured and the expected values for the sphericity index. The results show that the expected value is equal to 0.83×measured value. The algorithm developed for the analysis of the contacts could not be tested using regular convex particles as they are likely to form point contacts.

6.3.7 Summary

Table 6.12 summarises the main functions developed in order to measure the fabric quantities for images of granular materials. The validations carried out using both synthetic data and tomographic images of micro-spheres have demonstrated the capability and accurancy of the routines.

6.4 Concluding remarks

This chapter has presented a methodology that can be applied to 3D images of granular materials for quantification of the morphology and fabric of the system of particles. The procedures described here have shown to provide a powerful tool for the identification of the individual grains that is believed to be the main challenge associated with the image analysis of a sand with interlocked fabric. Most of the tasks are, however, computationally expensive and require a balance between speed and the size of the data.

Data type	Bytes per element	Max. value	output range
Unsigned 8-bit	1	2^8	0 to 255
Unsigned 16-bit	2	2^{16}	0 to 65 535
Unsigned 32-bit	4	2^{32}	0 to 4 294 967 295

Table 6.1: Image data types

Sample ref.	volume size (voxels)	Total no. of voxels	Resolution (μm)	File size (Gb)
297ph	600x600x600	216 E+06	5	0.4
297L	880x880x1000	774.4 E+06	4	1.5
294ph	600x600x600	216 E+06	5	0.4
294n	600x600x600	216 E+06	5	0.4
293	600x600x600	216 E+06	5	0.4
293S	600x600x600	216 E+06	5	0.4
295ph	600x600x600	216 E+06	5	0.4
295L	1460x1460x400	852.64 E+06	4	1.7
291ph	600x600x600	216 E+06	5	0.4
291L	1100x1100x700	847 E+06	3	1.7
289	600x600x600	216 E+06	5	0.4
289S	600x600x600	216 E+06	5	0.4
290ph	600x600x600	216 E+06	5	0.4

Table 6.2: Size and spatial resolution of the samples analysed, the suffix used is related to the location of the scanner (e.g., 'L' refers to Lees University, 'ph' refers to phoenix|x-ray in Germany, the other samples were scanned at Nottingham University)

Sample ref. (for void analysis)	Sample ref. (for particle analysis)
297vd	297ph
293vd	293
293Svd	293S
291vd	291ph
289vd	289
289Svd	289S

Table 6.3: Samples for void analysis and the associated samples for particle analysis

$R_x(\alpha)$	$R_y(\beta)$	$R_z(\gamma)$
$\begin{bmatrix} 1 & 0 & 0 \\ 0 & cos\alpha & -sin\alpha \\ 0 & sin\alpha & cos\alpha \end{bmatrix}$	$\begin{bmatrix} cos\beta & 0 & sin\beta \\ 0 & 1 & 0 \\ -sin\beta & 0 & cos\beta \end{bmatrix}$	$\begin{bmatrix} cos\gamma & -sin\gamma & 0 \\ sin\gamma & cos\gamma & 0 \\ 0 & 0 & 1 \end{bmatrix}$

Table 6.4: Rotation matrices for object rotation

Connectivity	**Surface area** (μm^2)	**error** (%)
6	822 629	-15
18	1 253 903	+30
26	1 455 617	+50
real value	967 689	0

Table 6.5: Surface area measurements for a micro-sphere of $555\mu m$ diameter, using different connectivities

Applied rotation	**Fabric Tensor** Φ^P	**Eigenvalues** $S1$ $S2$ $S3$	**Eigenvector** (V_1)	ϕ_{V1} (°)	θ_{V1} (°)	**error** (°)
–	$\begin{bmatrix} 0.416 & 0 & -0.071 \\ 0 & 0.333 & 0 \\ -0.071 & 0 & 0.250 \end{bmatrix}$	0.416 0.33 0.25	$\begin{bmatrix} 1 \\ 0 \\ 0 \end{bmatrix}$	90	0	0
$\beta = 30°$	$\begin{bmatrix} 0.375 & 0 & -0.071 \\ 0 & 0.333 & 0 \\ -0.071 & 0 & 0.290 \end{bmatrix}$	0.416 0.33 0.25	$\begin{bmatrix} -0.869 \\ 0 \\ 0.494 \end{bmatrix}$	60.37	180	0.37
$\beta = 85°$	$\begin{bmatrix} 0.251 & 0 & -0.013 \\ 0 & 0.333 & 0 \\ -0.013 & 0 & 0.415 \end{bmatrix}$	0.416 0.33 0.25	$\begin{bmatrix} -0.081 \\ 5e-17 \\ 0.996 \end{bmatrix}$	4.67	180	0.67
$\beta = 90°$	$\begin{bmatrix} 0.251 & 0 & -0.013 \\ 0 & 0.333 & 0 \\ -0.013 & 0 & 0.416 \end{bmatrix}$	0.416 0.33 0.25	$\begin{bmatrix} 0 \\ 0 \\ 1 \end{bmatrix}$	0	0	0
$\beta = 100°$	$\begin{bmatrix} 0.255 & 0 & -0.028 \\ 0 & 0.333 & 0 \\ -0.028 & 0 & 0.411 \end{bmatrix}$	0.416 0.33 0.25	$\begin{bmatrix} -0.175 \\ 0 \\ 0.984 \end{bmatrix}$	10.08	180	0.08
$\gamma = 40°$	$\begin{bmatrix} 0.382 & 0 & -0 \\ -0.04 & 0.367 & 0 \\ 0 & 0 & 0.25 \end{bmatrix}$	0.416 0.33 0.25	$\begin{bmatrix} -0.768 \\ 0.64 \\ 0 \end{bmatrix}$	90	140.19	0

Table 6.6: Analysis of the fabric tensor obtained using Φ^P, after rotating a systems of ellipsoids (with an initial horizontal position) using different rotation angles

Particles dimensions	Fabric Tensor Φ	Fabric Tensor Φ^p	Eigenvalues Φ	Eigenvalues Φ^p	Eigenvector (V_1) Φ	Eigenvector (V_1) Φ^p
$a = 60$ $b = 10$ $c = 5$	$\begin{bmatrix} 1 & 0 & 0 \\ 0 & 0 & 0 \\ 0 & 0 & 0 \end{bmatrix}$	$\begin{bmatrix} 0.8 & 0 & 0 \\ 0 & 0.133 & 0 \\ 0 & 0 & 0.066 \end{bmatrix}$	$S1 = 1$ $S2 = 0$ $S3 = 0$	$S1 = 0.800$ $S2 = 0.133$ $S3 = 0.066$	$\begin{bmatrix} 1 \\ 0 \\ 0 \end{bmatrix}$	$\begin{bmatrix} 1 \\ 0 \\ 0 \end{bmatrix}$
$a = 60$ $b = 55$ $c = 10$	$\begin{bmatrix} 0 & 0 & 0 \\ 0 & 0 & 0 \\ 0 & 0 & 1 \end{bmatrix}$	$\begin{bmatrix} 0.521 & 0 & 0 \\ 0 & 0.391 & 0 \\ 0 & 0 & 0.087 \end{bmatrix}$	$S1 = 1$ $S2 = 0$ $S3 = 0$	$S1 = 0.521$ $S2 = 0.391$ $S3 = 0.087$	$\begin{bmatrix} 1 \\ 0 \\ 0 \end{bmatrix}$	$\begin{bmatrix} 1 \\ 0 \\ 0 \end{bmatrix}$
$a = 40$ $b = 32$ $c = 24$	$\begin{bmatrix} 1 & 0 & 0 \\ 0 & 0 & 0 \\ 0 & 0 & 0 \end{bmatrix}$	$\begin{bmatrix} 0.416 & 0 & 0 \\ 0 & 0.333 & 0 \\ 0 & 0 & 0.250 \end{bmatrix}$	$S1 = 1$ $S2 = 0$ $S3 = 0$	$S1 = 0.416$ $S2 = 0.333$ $S3 = 0.250$	$\begin{bmatrix} 1 \\ 0 \\ 0 \end{bmatrix}$	$\begin{bmatrix} 1 \\ 0 \\ 0 \end{bmatrix}$

Table 6.7: Comparison of the results given by the Φ and Φ^P formulations using three systems of uniformly sized particles, each system containing particles with specific aspect ratios

System ref.	Particle dimensions	Fabric Tensor Φ	Fabric Tensor Φ^p	Eigenvalues Φ	Eigenvalues Φ^p	Eigenvector (V_1) Φ	Eigenvector (V_1) Φ^p	ϕ_{V1} (°) Φ	ϕ_{V1} (°) Φ^p
A_1 (64*part*)	$a = 20$ $b = 10$ $c = 5$	$\begin{bmatrix} 1 & 0 & 0 \\ 0 & 0 & 0 \\ 0 & 0 & 0 \end{bmatrix}$	$\begin{bmatrix} 0.57 & 0 & 0 \\ 0 & 0.29 & 0 \\ 0 & 0 & 0.14 \end{bmatrix}$	$S1 = 1$ $S2 = 0$ $S3 = 0$	$S1 = 0.57$ $S2 = 0.29$ $S3 = 0.14$	$V_1 = \begin{bmatrix} 1 \\ 0 \\ 0 \end{bmatrix}$ $V_2 = \begin{bmatrix} 0 \\ 1 \\ 0 \end{bmatrix}$ $V_3 = \begin{bmatrix} 0 \\ 0 \\ 1 \end{bmatrix}$	$V_1 = \begin{bmatrix} 1 \\ 0 \\ 0 \end{bmatrix}$ $V_2 = \begin{bmatrix} 0 \\ 1 \\ 0 \end{bmatrix}$ $V_3 = \begin{bmatrix} 0 \\ 0 \\ 1 \end{bmatrix}$	90	90
A_2 (64*part*)	$a = 30$ $b = 15$ $c = 7.5$	$\begin{bmatrix} 0 & 0 & 0 \\ 0 & 0 & 0 \\ 0 & 0 & 1 \end{bmatrix}$	$\begin{bmatrix} 0.14 & 0 & 0 \\ 0 & 0.29 & 0 \\ 0 & 0 & 0.57 \end{bmatrix}$	$S1 = 1$ $S2 = 0$ $S3 = 0$	$S1 = 0.57$ $S2 = 0.29$ $S3 = 0.14$	$V_1 = \begin{bmatrix} 0 \\ 0 \\ 1 \end{bmatrix}$ $V_2 = \begin{bmatrix} 0 \\ 1 \\ 0 \end{bmatrix}$ $V_3 = \begin{bmatrix} 1 \\ 0 \\ 0 \end{bmatrix}$	$V_1 = \begin{bmatrix} 0 \\ 0 \\ 1 \end{bmatrix}$ $V_2 = \begin{bmatrix} 0 \\ 1 \\ 0 \end{bmatrix}$ $V_3 = \begin{bmatrix} 1 \\ 0 \\ 0 \end{bmatrix}$	0	0
$A_1 + A_2$ (128*part*)		$\begin{bmatrix} 0.50 & 0 & -0.01 \\ 0 & 0 & 0 \\ -0.01 & 0 & 0.50 \end{bmatrix}$	$\begin{bmatrix} 0.31 & 0 & -0.01 \\ 0 & 0.29 & 0 \\ -0.01 & 0 & 0.40 \end{bmatrix}$	$S1 = 0.51$ $S2 = 0.49$ $S3 = 0$	$S1 = 0.40$ $S2 = 0.31$ $S3 = 0.29$	$V_1 = \begin{bmatrix} -0.72 \\ 0 \\ 0.70 \end{bmatrix}$ $V_2 = \begin{bmatrix} -0.70 \\ 0 \\ -0.72 \end{bmatrix}$ $V_3 = \begin{bmatrix} 0 \\ 1 \\ 0 \end{bmatrix}$	$V_1 = \begin{bmatrix} -0.08 \\ w \\ 0.99 \end{bmatrix}$ $V_2 = \begin{bmatrix} 0.99 \\ w \\ -0.08 \end{bmatrix}$ $V_3 = \begin{bmatrix} w \\ 1.00 \\ w \end{bmatrix}$	45.5	8.1

Table 6.8: Comparison of the results given by the Φ and Φ^P formulations for a simple systems of non-uniformly sized particles

Rx α (°)	Ry β (°)	Rz γ (°)	Unit normal vector	ϕ (°)	θ (°)	Fabric tensor	V_1	ϕ_{V1} (°)	θ_{V1} (°)	Error (ω)
0	0	0	$\begin{bmatrix} \omega \\ \omega \\ -1 \end{bmatrix}$	0	random	$\begin{bmatrix} \omega & \omega & \omega \\ \omega & \omega & \omega \\ \omega & \omega & 1 \end{bmatrix}$	$\begin{bmatrix} \omega \\ \omega \\ 1 \end{bmatrix}$	0	47.7	$< e-15$
30	0	0	$\begin{bmatrix} \omega \\ 0.5 \\ 0.866 \end{bmatrix}$	30	90	$\begin{bmatrix} \omega & \omega & \omega \\ \omega & 0.25 & 0.433 \\ \omega & 0.433 & 0.75 \end{bmatrix}$	$\begin{bmatrix} \omega \\ 0.5 \\ 0.866 \end{bmatrix}$	30	90	$< e-15$
-45	0	0	$\begin{bmatrix} \omega \\ -0.707 \\ 0.707 \end{bmatrix} \& \begin{bmatrix} \omega \\ 0.707 \\ -0.707 \end{bmatrix}$	45	90 & -90	$\begin{bmatrix} \omega & \omega & \omega \\ \omega & 0.5 & 0.5 \\ \omega & -0.5 & 0.5 \end{bmatrix}$	$\begin{bmatrix} \omega \\ -0.707 \\ 0.707 \end{bmatrix}$	45	-90	$< e-15$
0	95	0	$\begin{bmatrix} -0.996 \\ \omega \\ -0.087 \end{bmatrix} \& \begin{bmatrix} 0.996 \\ \omega \\ 0.087 \end{bmatrix}$	85	-180 & ω	$\begin{bmatrix} 0.992 & \omega & 0.086 \\ \omega & \omega & \omega \\ 0.086 & \omega & 0.007 \end{bmatrix}$	$\begin{bmatrix} 0.996 \\ \omega \\ 0.087 \end{bmatrix}$	85	ω	$< e-15$
0	0	40	$\begin{bmatrix} \omega \\ \omega \\ -1 \end{bmatrix} \& \begin{bmatrix} 0 \\ 0 \\ -1 \end{bmatrix}$	0	random & 0	$\begin{bmatrix} \omega & \omega & \omega \\ \omega & \omega & \omega \\ \omega & \omega & 1 \end{bmatrix}$	$\begin{bmatrix} \omega \\ \omega \\ 1 \end{bmatrix}$	0	168	$< e-15$

Table 6.9: Analysis for planes orientated by a given direction

No. part.	No. particles (inner)	Resolution scan	Resolution image analysis	Size (voxels)	Size (Mb)
821	388	$5\mu m$	$10\mu m$	400×400×600	192

Table 6.10: Information of the sample made of micro-spheres

Rx α (°)	rotation tensor pc	n at original position n_{org}	n rotated nrot	nrot*inv(pc) n_{final}	error (ω)
0	$\begin{bmatrix} 1 & 0 & 0 \\ 0 & 1 & 0 \\ 0 & 0 & 1 \end{bmatrix}$	$\begin{bmatrix} \omega \\ \omega \\ -1 \end{bmatrix}$	$\begin{bmatrix} \omega \\ \omega \\ -1 \end{bmatrix}$	$\begin{bmatrix} \omega \\ \omega \\ -1 \end{bmatrix}$	$< e-15$
30	$\begin{bmatrix} 0 & 1 & 0 \\ -0.866 & 0 & -0.5 \\ 0.5 & 0 & -0.866 \end{bmatrix}$	$\begin{bmatrix} \omega \\ -0.5 \\ -0.866 \end{bmatrix}$	$\begin{bmatrix} \omega \\ \omega \\ -1 \end{bmatrix}$	$\begin{bmatrix} \omega \\ 0.5 \\ 0.866 \end{bmatrix}$	$< e-15$
100	$\begin{bmatrix} 1 & 0 & 0 \\ 0 & 0.173 & -0.984 \\ 0 & 0.984 & 0.173 \end{bmatrix}$	$\begin{bmatrix} \omega \\ 0.985 \\ -0.173 \end{bmatrix}$	$\begin{bmatrix} \omega \\ \omega \\ -1 \end{bmatrix}$	$\begin{bmatrix} \omega \\ 0.985 \\ -0.173 \end{bmatrix}$	$< e-15$

Table 6.11: Normal vector to a best fit plane obtained for the data before and after being rotated using the *pc* tensor

Function	Input	Output
loadimage	filename, filesize, data type	A_{inital}
labelpart	$A_{initial}$, bc	A
removepartboundary	A	bp
surfarea	A	$N_{vox,surface}$
orientationpart	pp, cc	pc
particlesize	pp, cc, $Npart$	a,b,c
plotPSD	$deff$	PSD
particleFT	$Qcell$, a, b, c	FTp, Ep, Vp
identifcontcoord	A	neigbarray, contactcoord
contnormallsq	contactcoord	normal vector
fabrictensor	unit normal vector	FT, E, V

Table 6.12: Summary of the main functions developed in MATLAB

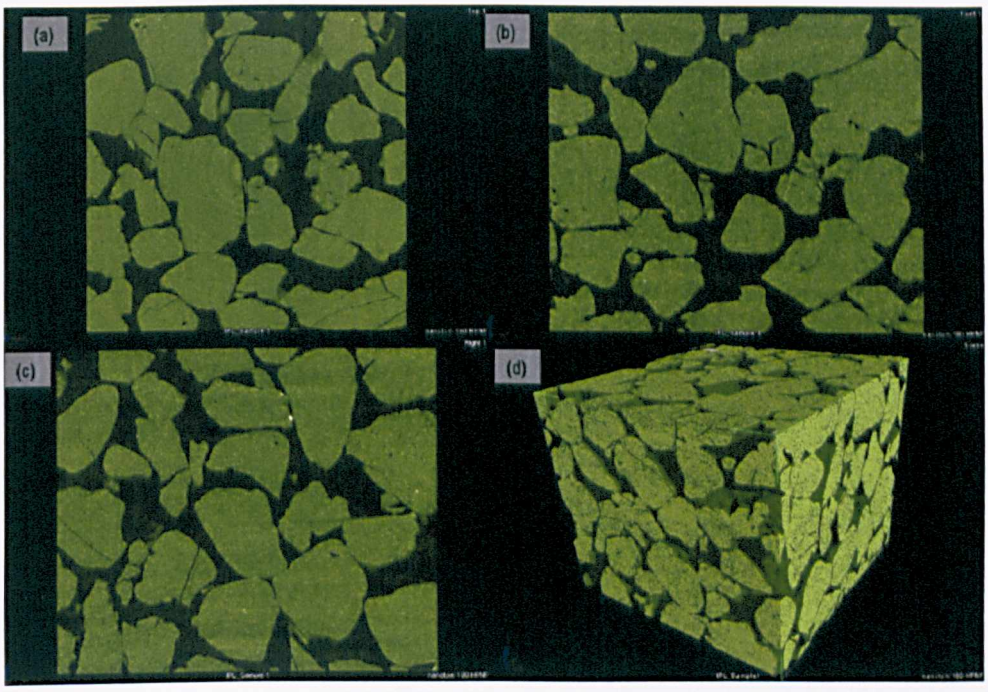

Figure 6.1: 3D visualisation of a tomographic image of a sand sample, (a) 2D section in the xy-plane (b) 2D section in the xz-plane (c) 2D section in the yz-plane (d) 3D view

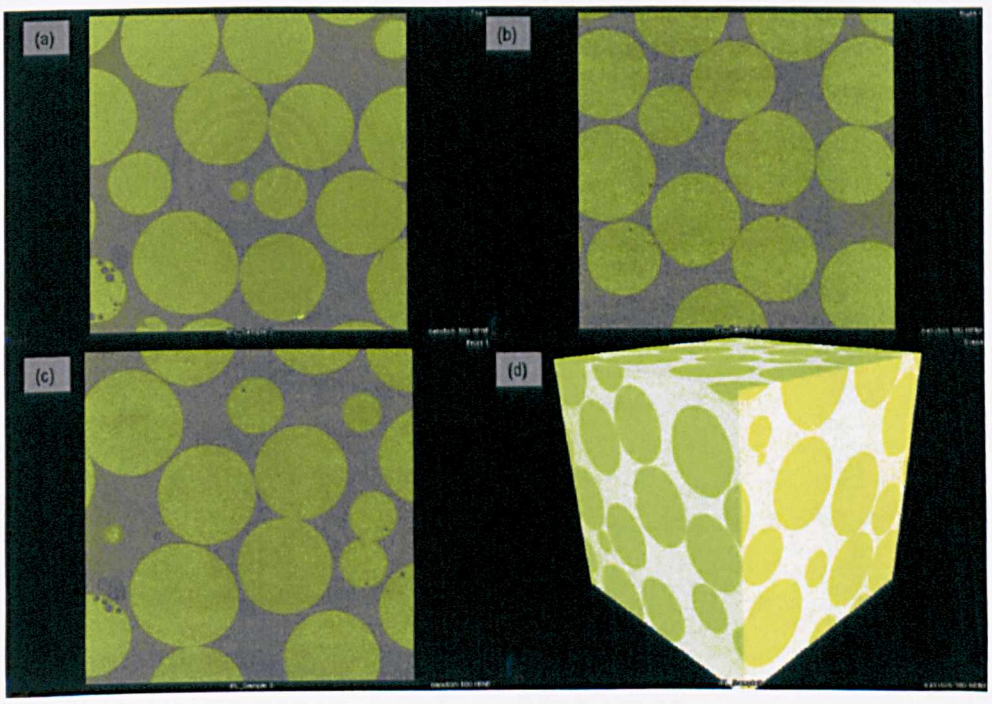

Figure 6.2: 3D visualisation of a tomographic image of a sample made of resin impregnated glass spheres ($555\mu m$ diameter), (a) 2D section in the xy-plane (b) 2D section in the xz-plane (c) 2D section in the yz-plane (d) 3D view

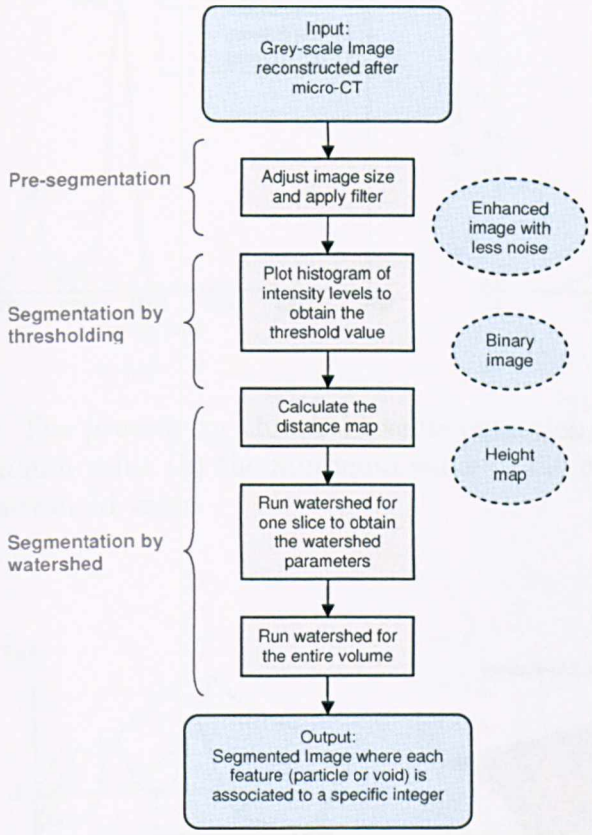

Figure 6.3: Image processing flow chart

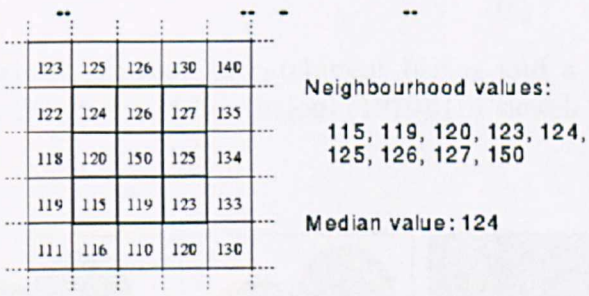

Figure 6.4: Calculation of the median value of a pixel on a 3×3 neighbourhood (from Fisher et al., 2010)

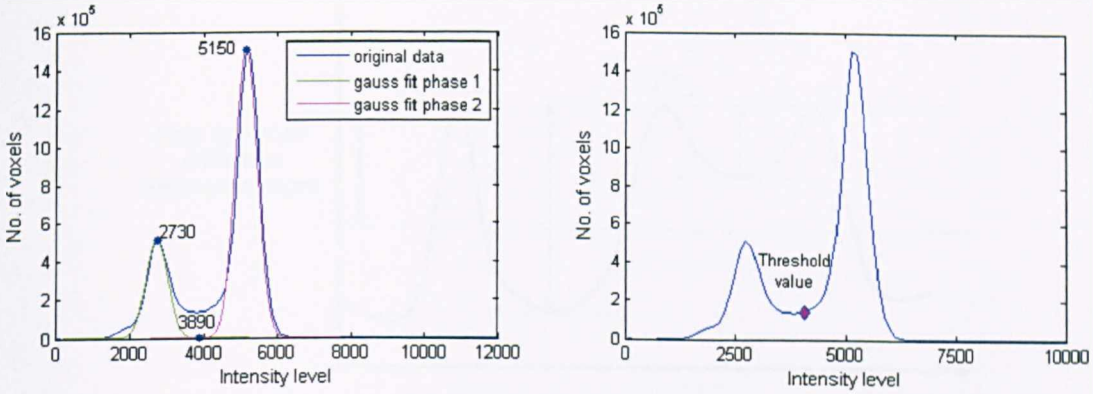

(a) (b)

Figure 6.5: The process for threshold value detection, (a) Gaussian fit and finding of the minimum value (b) the minimum value of the combined curves is considered to be the threshold value

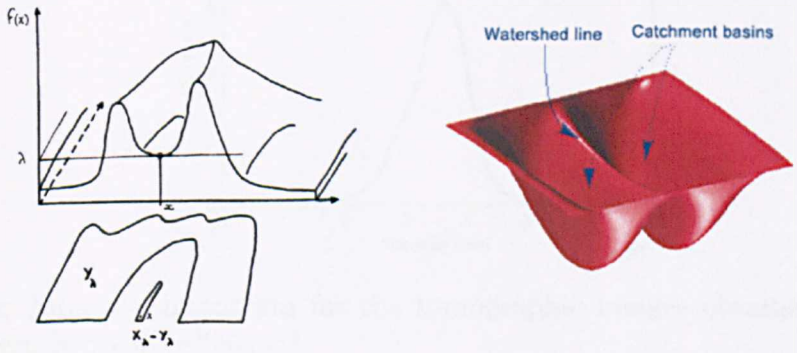

(a) (b)

Figure 6.6: Schematic illustration of catchment basins and a watershed lines, (a) original sketch from Beucher and Lantuejoul (1979) (b) sketch from Matworks

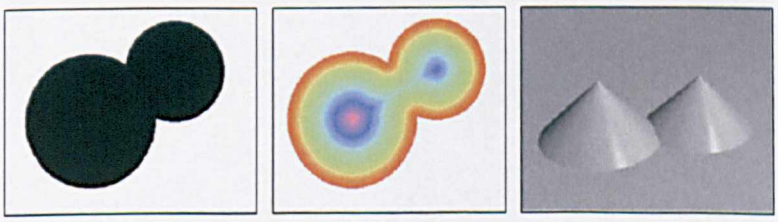

(a) (b) (c)

Figure 6.7: 2D illustration of two touching features, (a) binary image (b) distance map (c) distance map converted to a height function (from Russ, 2007)

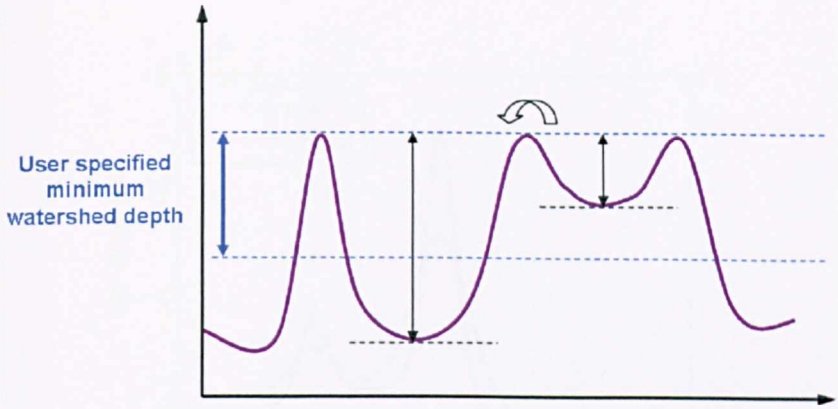

Figure 6.8: Illustration of the concept of minimum watershed depth. In this case the catchment basin in the right will be merged with the adjacent catchment basin because its watershed depth is lower than the user defined minimum watershed

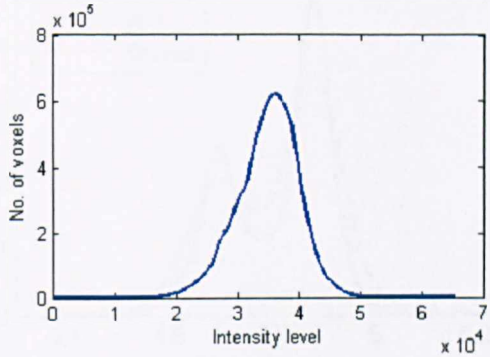

Figure 6.9: Intensity histogram for the tomographic images obtained using phase contrast (synchrotron radiation)

Figure 6.10: Result of the segmentation process on the tomographic images obtained using phase contrast (synchrotron radiation)

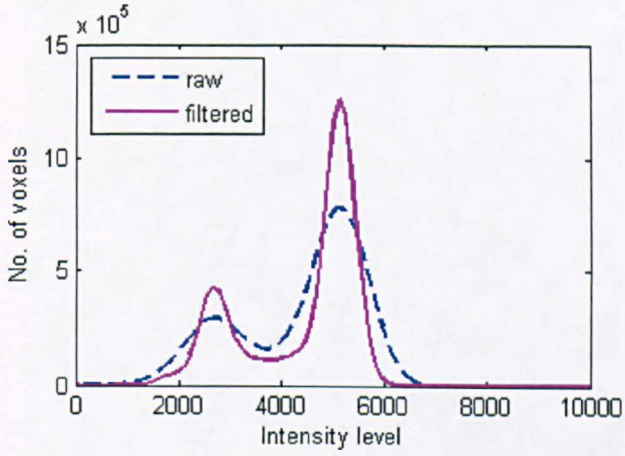

(a)

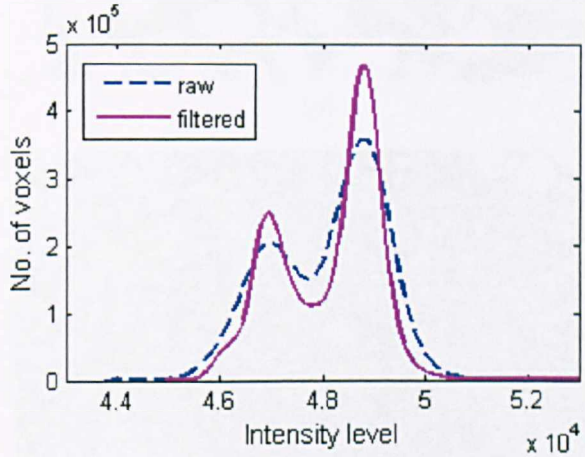

(b)

Figure 6.11: Comparison of the histogram for the data before and after filtering, (a) sample 294ph filtered with a 3D median filter, size 3×3×3 (b) sample 295L filtered with 3D adaptive Gaussian filter (from VGStudio Max) *smoothing=1.8* and *edge threshold=0.08*

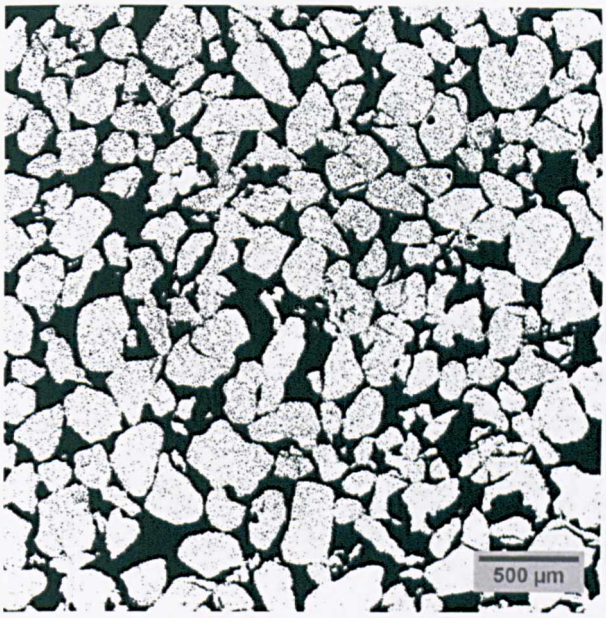

(a)

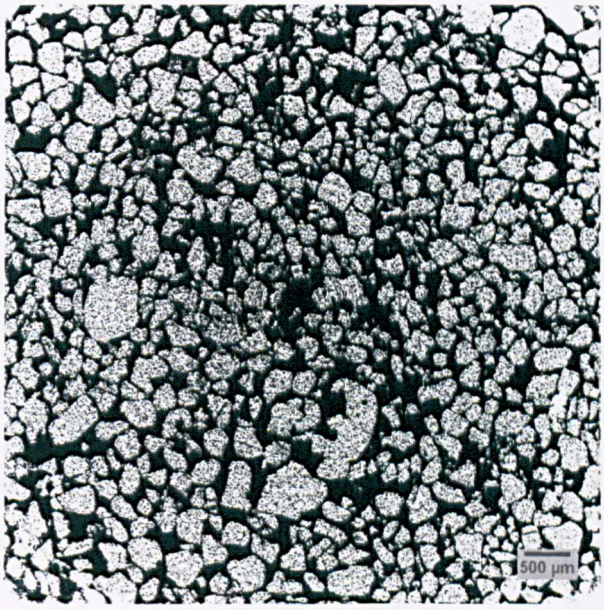

(b)

Figure 6.12: Binary images of the raw data for (a) sample 294ph (b) sample 295L

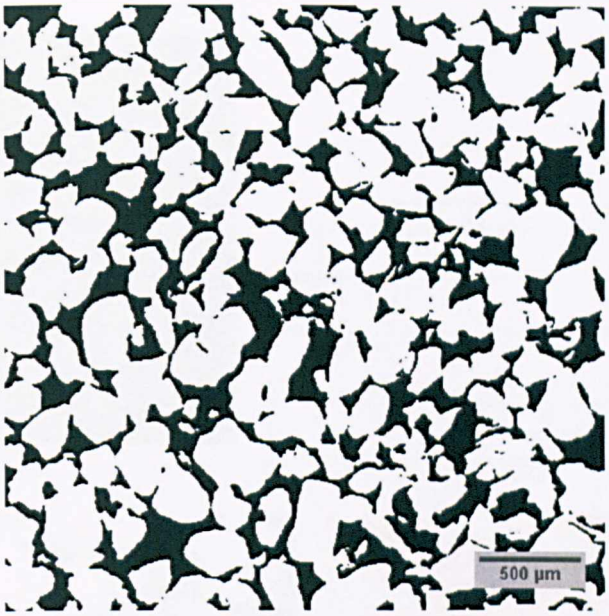

Figure 6.13: Binary image of the filtered data for sample 294ph (xy-plane)

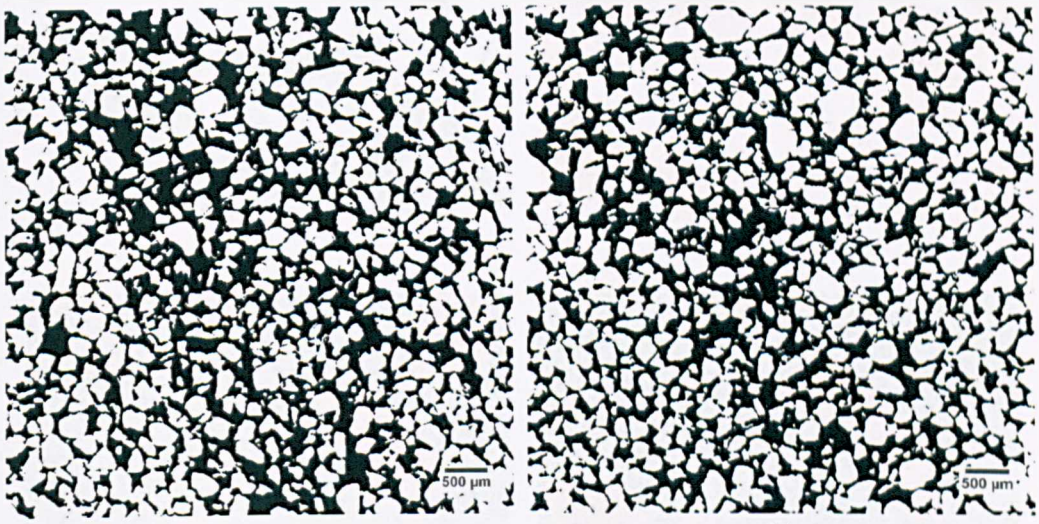

(a) (b)

Figure 6.14: Binary images of sample 295L showing the shear band in the xy-plane at two different z values

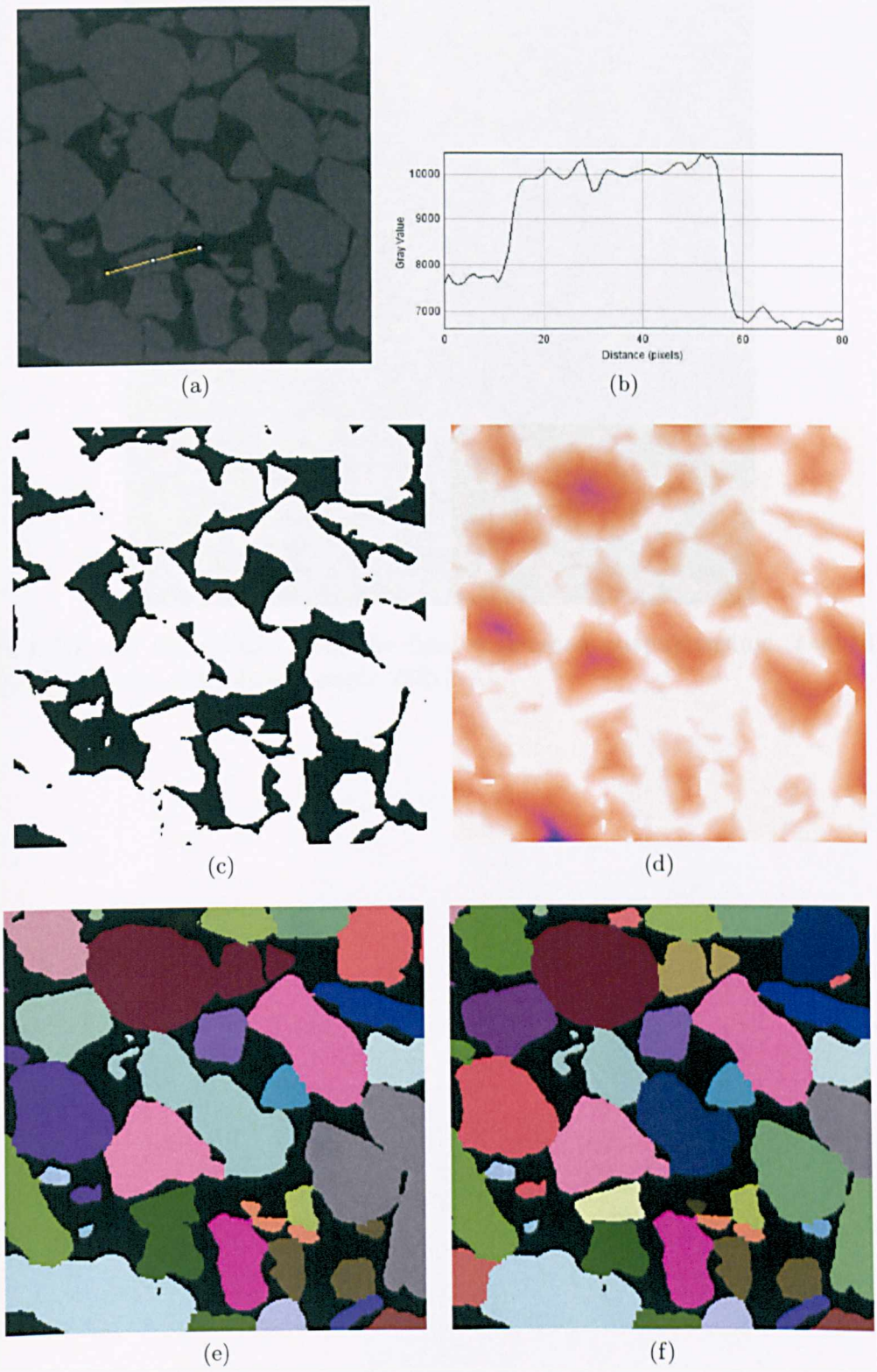

Figure 6.15: 2D slices obtained at different stages of the image processing of sample 297ph, (a) filtered image (b) line profile across one grain (c) binary image (d) distance map (e) watershed output of an undersegmented image (t=0.04 and l=0.4) (e) final watershed output (t=0.04 and l=0.2)

Figure 6.16: 2D slice illustrating the final watershed output (using: t=0.04 and l=0.2) of the void analysis of sample 293vd

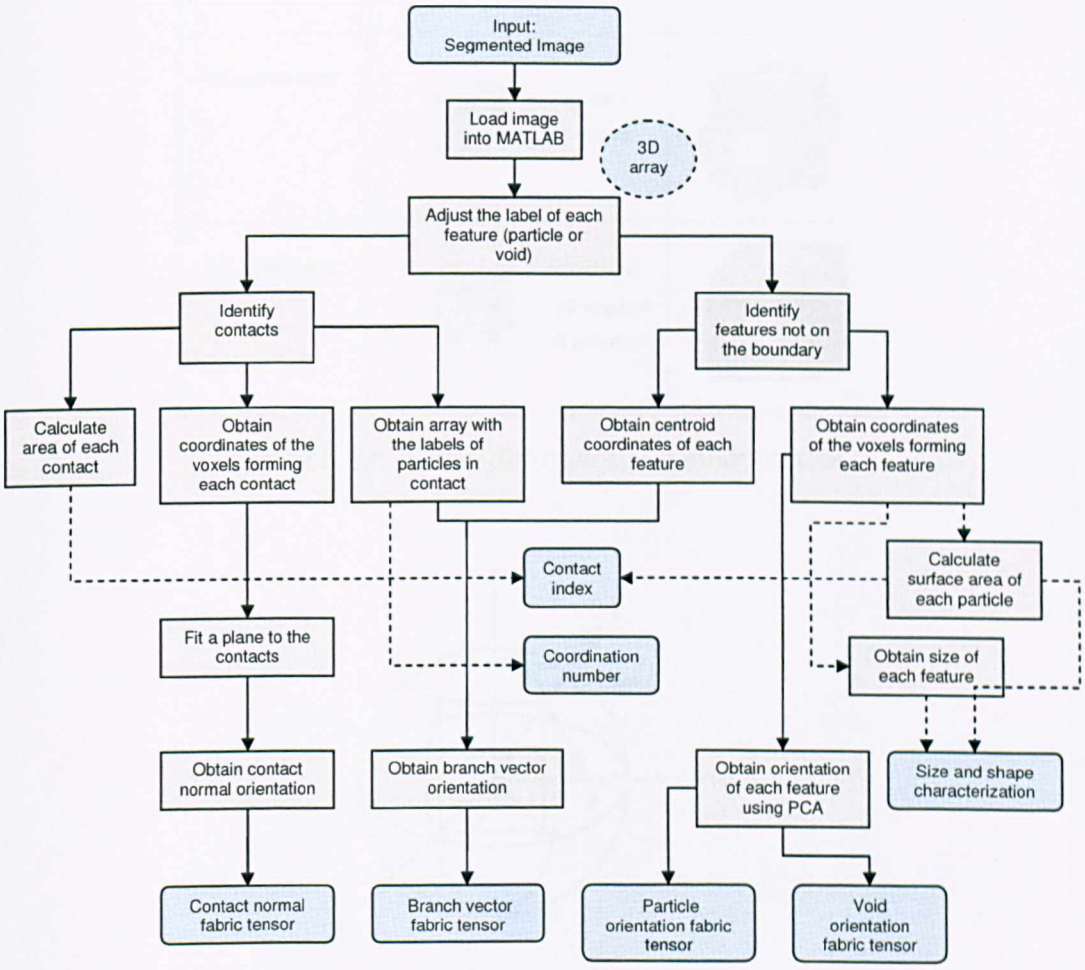

Figure 6.17: Image analysis flow chart

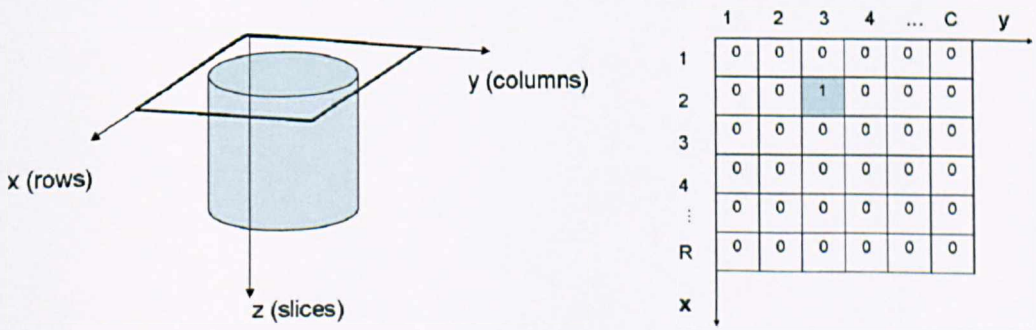

(a) (b)

Figure 6.18: Pixel coordinate system used in MATLAB

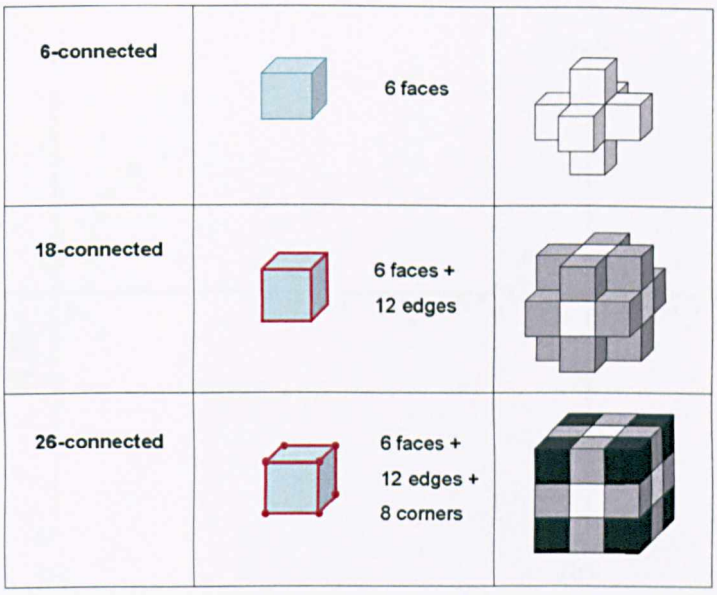

Figure 6.19: Three-dimensional connectivities

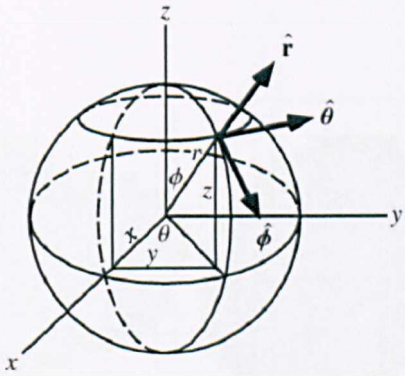

Figure 6.20: Spherical coordinates (from Worldfram MathWorld)

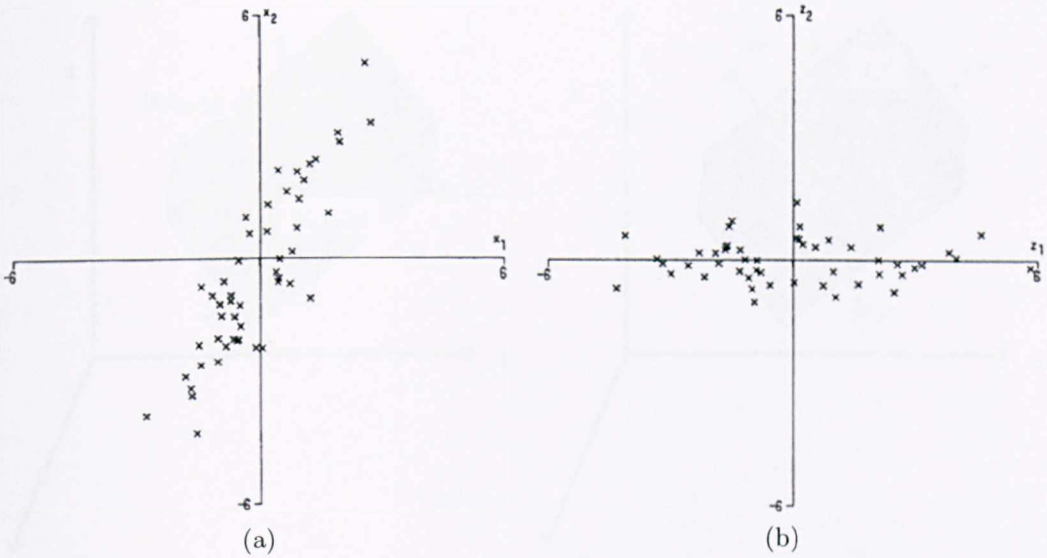

Figure 6.21: Application of the principal component analysis, (a) plot of 50 points in the coordinate system defined by the x_1 and x_2 axes (b) plot of the same 50 points relatively to the principal components z_1 and z_2 (from Jolliffe, 2002)

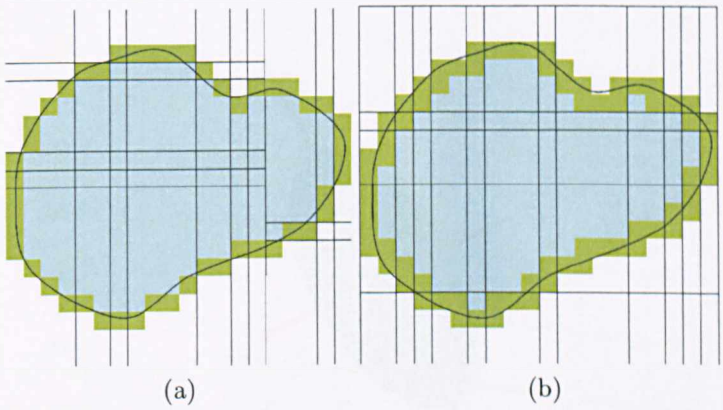

Figure 6.22: Schematic representation of particle boundary detection using different connectivities in 2D, (a) face adjacency (b) face plus edge adjacency

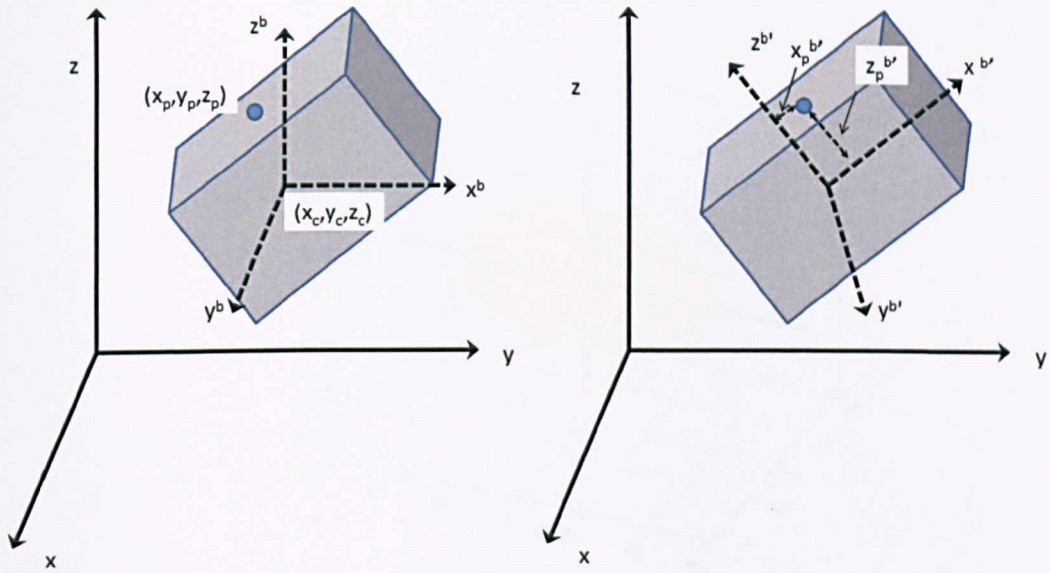

(a) (b)

Figure 6.23: Principal axes of inertia of the particle in the global coordinate system

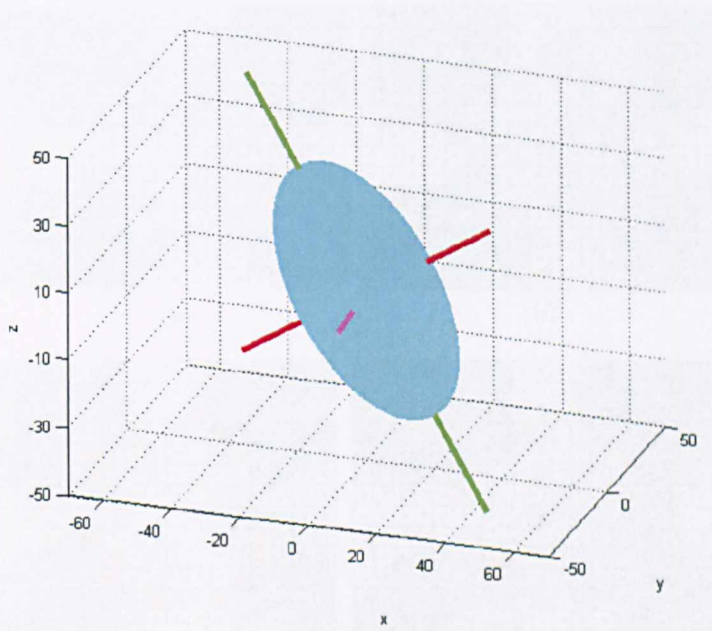

Figure 6.24: Illustration of the three principal orientations for an ellipsoid

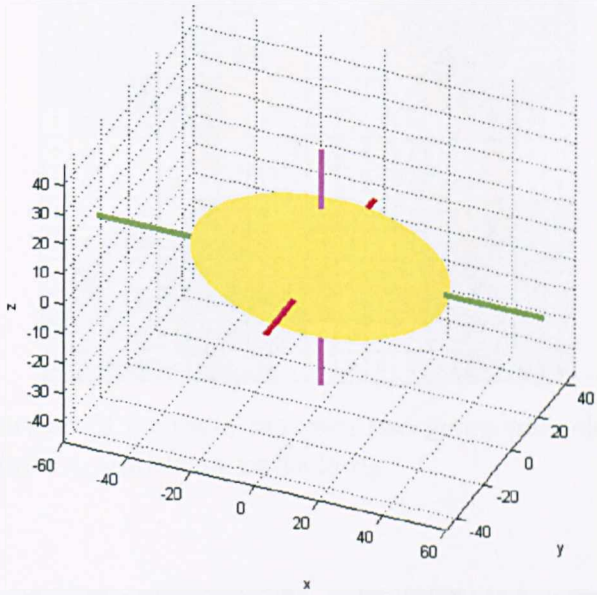

Figure 6.25: Ellipsoid orientated along the direction of its major axis length

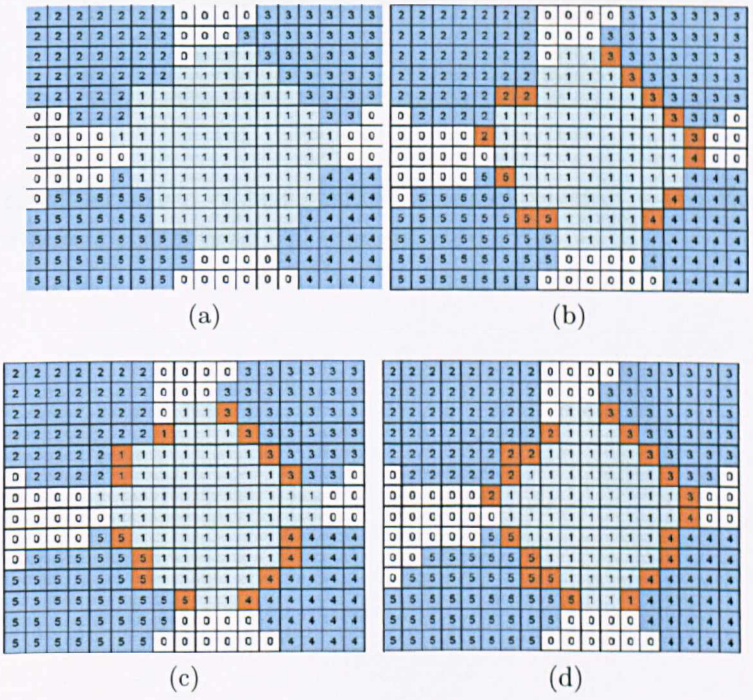

Figure 6.26: Illustration of the identification of the contacts for *particle 1* in 2D (a) *particle 1* in contact with *particle 2*, *particle 3* and *particle 4* (b) contact detection along x direcion (c) contact detection along y direction (d) final contacts

2	2	2	2	2	2	2	2	0	0	0	0	3	3	3	3	3	3
2	2	2	2	2	2	2	2	0	0	0	1	3	3	3	3	3	3
2	2	2	2	2	2	2	2	0	1	1	3	1	3	3	3	3	3
2	2	2	2	2	2	1	1	2	1	1	1	3	1	3	3	3	3
2	2	2	2	2	1	2	2	1	1	1	1	1	3	1	3	3	3
0	2	2	2	2	1	2	1	1	1	1	1	1	1	3	1	3	0
0	0	0	0	0	2	1	1	1	1	1	1	1	1	1	3	0	0
0	0	0	0	0	0	1	1	1	1	1	1	1	1	1	4	0	0
0	0	0	0	0	1	5	1	1	1	1	1	1	1	4	1	4	4
0	0	5	5	5	5	1	5	1	1	1	1	1	1	4	1	4	4
0	5	5	5	5	5	1	5	5	1	1	1	1	4	1	4	4	4
5	5	5	5	5	5	5	1	1	5	1	1	1	1	4	4	4	4
5	5	5	5	5	5	5	5	5	0	0	0	0	4	4	4	4	4
5	5	5	5	5	5	5	5	0	0	0	0	0	0	4	4	4	4

Figure 6.27: Comparison of contacts between two given particles labeled n_1 and n_2 identified from particle n_1 and from particle n_2

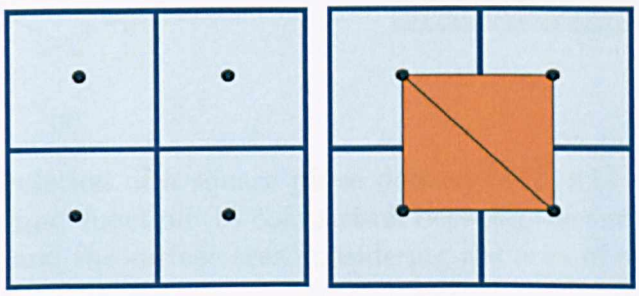

(a) (b)

Figure 6.28: 2D illustration of the surface area calculation using the triangulation approach (a) 4 pixels considered (b) triangulated area

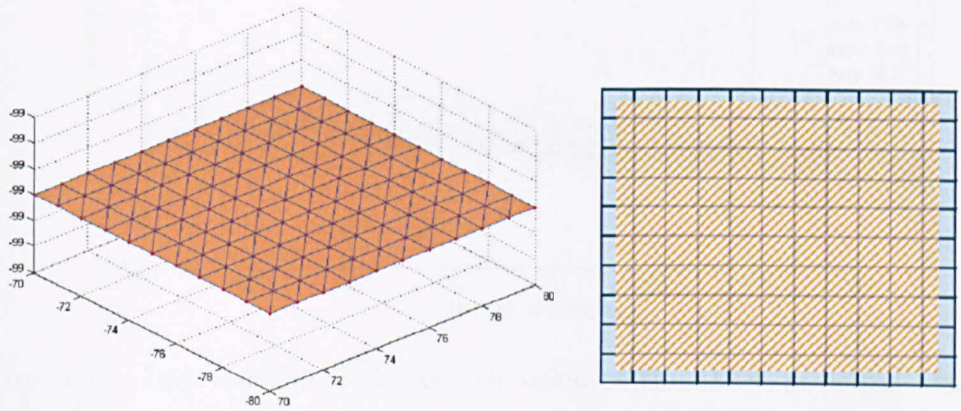

(a) (b)

Figure 6.29: Triangulation of a square plane defined by 11×11 voxels (a) surface obtained using delaunay function (b) comparison between the surface area obtained using triangulation and the surface area considering the area of each voxel defining the plane

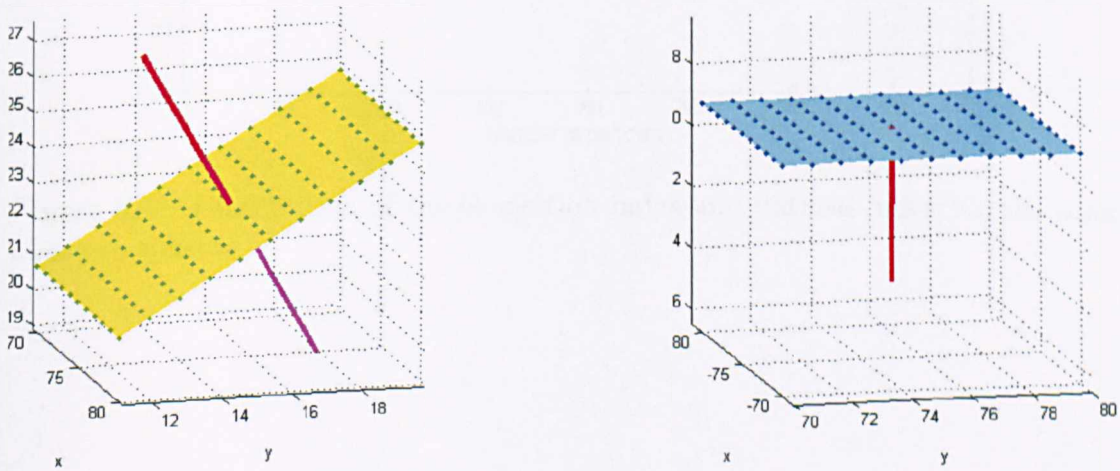

(a) (b)

Figure 6.30: Illustration of the algorithm for best fit plane and normal vector calculation applied to a set of 3D planar points

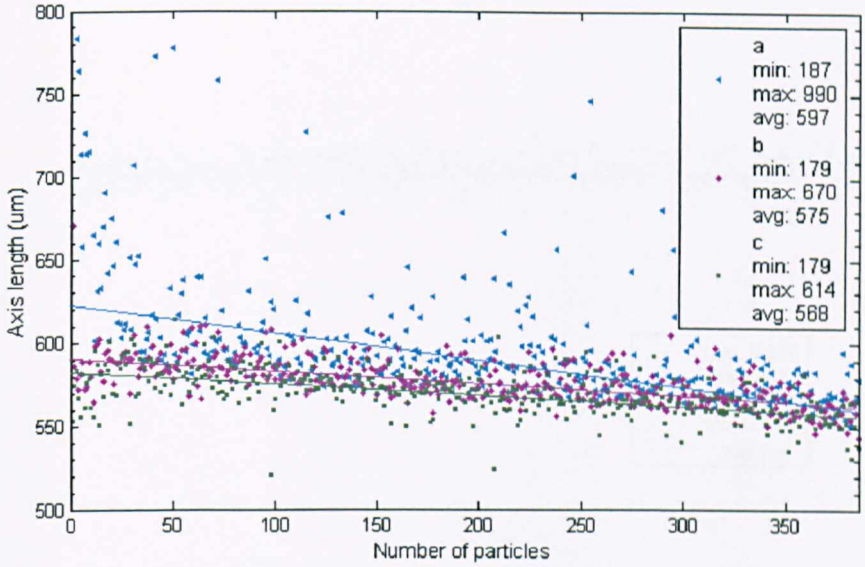

Figure 6.31: Distribution of the length value of the three principal axes for the sample of micro-spheres

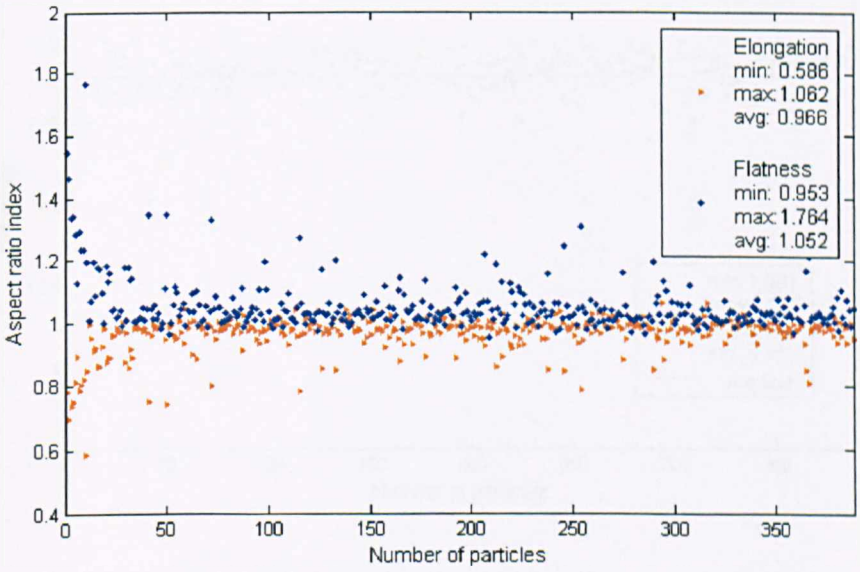

Figure 6.32: Distribution of the elongation index and flatness index for the sample of micro-spheres

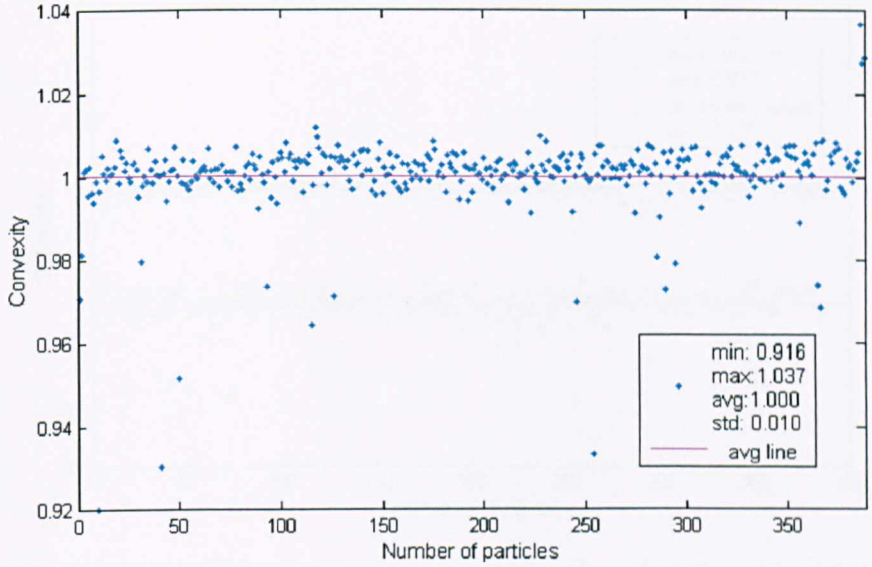

Figure 6.33: Distribution of the convexity index for the sample of micro-spheres

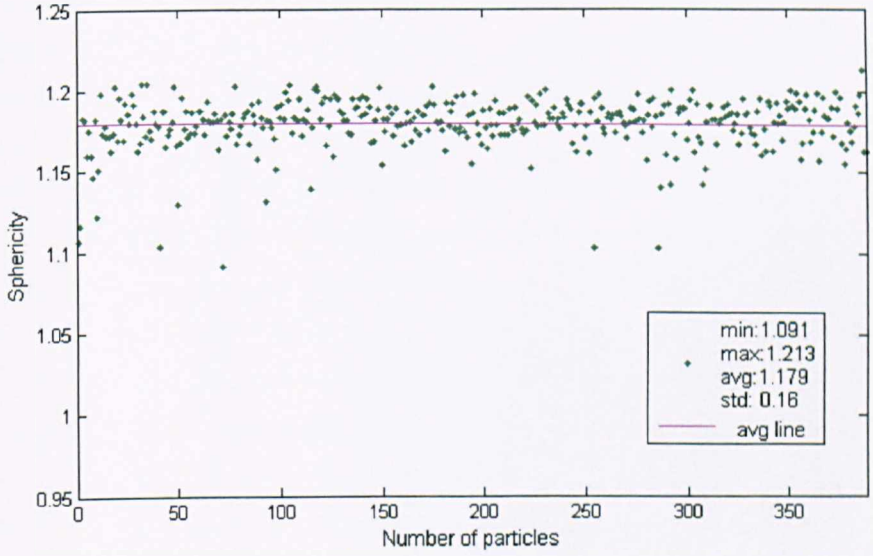

Figure 6.34: Distribution of the sphericity index for the sample of micro-spheres

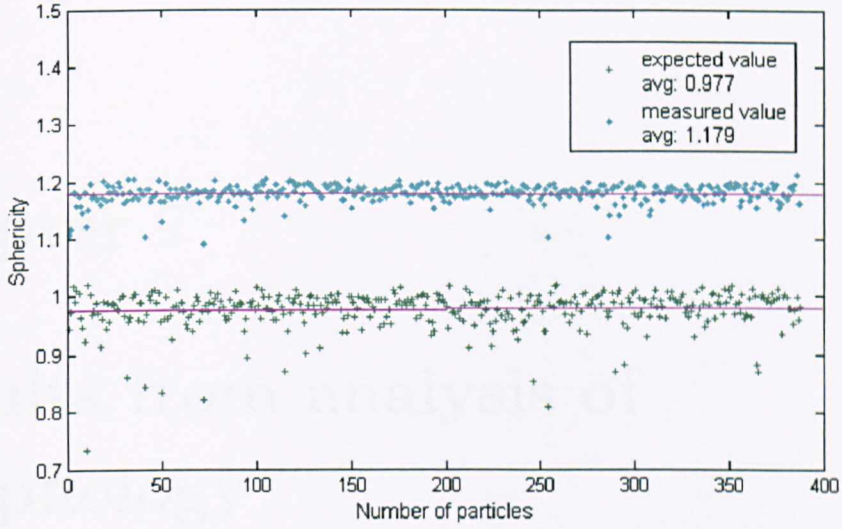

Figure 6.35: Comparison between the expected values for the sphericity index and the measured values

Chapter 7

Results from analysis of morphology

7.1 Introduction

This chapter presents the quantification of particle morphology of Reigate sand at the initial state and at three stages during shearing deformation for both the intact and reconstituted material. As discussed in Chapter 4, the specimens for fabric investigation were tested and resin impregnated at four loading stages. However, due to time constraints and limitations in the number of scans, the isotropic compression stage (load stage 1) has not been included in this analysis. The initial condition, prior to loading, is referred to as load stage 0, load stage 2 refers to the onset of dilation, load stage 3 represents the strain softening regime when the shear band becomes visible and load stage 4 refers to the final shearing stage as the sample approaches the critical state (Table 7.1). In total 13 samples were analysed, which included 8 intact and 5 reconstituted samples. In general, two samples were used to represent each triaxial specimen, but again, due to limitations in the number of scans, the reconstituted specimen at load stage 2 was not investigated and just one sample from the specimen 290-rec was analysed. Table 7.1 summarises the details of the loading stage that each sample represents.

The characterisation of the particle morphology in terms of size and shape is described. The size analysis includes the calculation of the particle size distribution curves for all the samples and its comparison with the sieve analysis data. For the shape characterisation, the elongation, flatness, sphericity and convexity indices of all samples were assessed and the results were compared with 2D measurements obtained using a size and shape analyser.

7.2 Characterisation of particle morphology

For the characterisation of the particle morphology, particles intercepting the boundary of the image were excluded from the analysis. Table 7.2 summarises the total number of particles and the number and percentage of particles that were not in the boundary, for each sample. As shown, between 30% and 40% of the particles in each sample were not used for the particle characterisation. Statistics for the number of voxels defining each particle (full particles only) for each sample is also presented. These statistics serve to demonstrate that given the high number of voxels in each particle, the calculations are not likely to be affected by the voxel size. A rule of thumb of 10 pixels as the minimum size for the diagonal of each feature in the image is often used (e.g., QICPIC).

7.2.1 Size

(a) Particle size distribution

The $d_{effective}$ used for the particle size distribution (PSD) curves was calculated for the reconstituted samples based on two approaches. The first approach used the intermediate axis length (b) while the second approach took the average value of the three lengths of the particle (Equation 2.29). Figure 7.1 shows the PSD using $d_{effective} = average(a, b, c)$ for the five reconstituted samples and compares this data with the PSD obtained from the sieve analysis. Figure 7.2 refers to the same data but uses $d_{effective} = b$. Both plots show just a small deviation from the sieve curve with the curves obtained using the $d_{effective} = b$ showing a better agreement with the results from the laboratory measurements. The mean diameter (d_{50}) and the coefficient of uniformity ($C_U = d_{60}/d_{10}$) for the five reconstituted samples are presented in Figure 7.2. The C_U values obtained from the micro-CT data are in general close to the sieve value ($C_U = 1.62$) and the d_{50} values were slightly higher than the $274\mu m$ obtained by sieving.

Figure 7.3 shows the particle size distribution using $d_{effective} = b$ for the intact samples compared to the sieve curve, together with information regarding the d_{50} and C_U values for each sample. The curves of the two intact samples prior to loading (297ph and 297L) show good agreement between, with d_{50} values of $324\mu m$ and $325\mu m$, respectively. These results deviate significantly from the sieve data. In addition, there are differences between the PSDs for the intact and the reconstituted material ($d_{50} = 284\mu m$). For the intact samples at load stage 2 (samples 294ph and 294n) a slight decrease in d_{50} in comparison with samples 297ph and 297L, can be observed, as the curves move towards the sieve curve. As shearing progresses this trend becomes more pronounced as the intact sample at load stage 3 (located outside

the shear band, sample 293), shows very good agreement with the sieving curve. At the last stage of shearing (samples 295ph and 295L) the PSD curves move again away from the sieve curve to positions closer to the intact curves. The C_U values are slightly lower than the sieve value and the values obtained for the reconstituted samples

The change of the intact soil grading upon shearing is due to the disintegration of the larger particles at early stages of loading along existing fissures. For the reconstituted samples, these fissures break during the reconstitution process changing the PSD.

Figure 7.4 summarises the distribution of the mean diameter values (d_{50}) for both the intact and reconstituted soil at the four load stages. The d_{50} of the reconstituted soil is consistently lower than that of the intact material at the initial state (load stage 0) and it does not change significantly during shearing. The d_{50} for the intact soil decreases as shearing progresses and approaches values similar to the reconstituted soil at load stage 3 and at load stage 4 d_{50} increases slightly again. This reversal in the trend for d_{50} to decrease during load stage 4 can be understood by assuming that some small fragments may become attached to other grains which seems to support the theory proposed by Wong (2003) that at the last stages of shearing some grains deform in groups instead of individual grains. These groups of small grains (or grain fragments) may have been identified as individual grains by the segmentation algorithm, discussed in Chapter 6.

The differences in grading between the intact and reconstituted material and for the intact soil at different stages of loading can be confirmed by the optical microscope images of thin sections presented in Figure 7.5. Figure 7.5a and Figure 7.5b show a "clean" void space for specimens 297 and 294, which contrasts with the specimens after the onset of dilation, where small fragments are apparent in the void space (Figures 7.5c, 7.5d and 7.5e). At load stages 3 and 4, the differentiation between the intact and the reconstituted specimens become less evident. Images from outside and inside the shear band for the intact specimen at load stage 4 are presented in 7.5d and 7.5e, respectively. While both samples exhibit very similar grading, the difference in their void ratios is significant as discussed below.

7.2.2 Shape

(a) Aspect ratio

The aspect ratio of the particles was characterised using the elongation index and flatness index. Both these indices are functions of the three principal axis lengths a, b and c as defined in Equation 2.30. Figures 7.6 to 7.19 show the distributions of the elongation and flatness indices for all the intact and the reconstituted samples.

Each plot compares the samples from the same triaxial specimen. The bin size used was 0.04 and because the number of particles was different in each sample (see Table 7.2), the frequencies observed are presented as percentages of the total number of particles in the sample.

The statistical information in terms of minimum, maximum and average values as well as the standard deviation for each sample is presented. The shape of the distribution curves for the samples from the same triaxial specimen are in good agreement (e.g., compare 297ph and 297L, Figure 7.6), but slight differences can be observed for samples with localisations, when the material containing the shear band is compared to the material away from the shear band (e.g., compare 293 and 293S, Figure 7.10). While the plots show a wide range of elongation and flatness values varying from 0.4 to 1.0, the higher frequencies are in general associated with indices between 0.7 and 0.9.

Figure 7.20a shows the distribution of the average elongation index for the intact and the reconstituted samples at the four stages of loading. The reconstituted samples contain more elongated and more flatter particles when compared with the intact samples, as illustrated in Figure 7.20b, which is likely to be due to breakage during reconstitution. Similarities can be found in the evolution of the aspect ratio indices as the shearing progresses and with the equivalent d_{50} plot (Figure 7.4) which may suggest that the changes in particle shape are related to changes in the grading of the soil.

Figures 7.21 and 7.22 show the flatness index plotted against the elongation index for two intact and two reconstituted samples at load stage 0 and load stage 3, respectively. Referring to Figure 2.34 (Chapter 2) the majority of the particles are located in sector II which according to Zingg (1935) classifies them as spheroids. The samples at load stage 3 show an increase in the number of particles located in sectors I (disc-shaped particles) and IV (roller-shaped particles) compared with the initial stage. This observation is in accordance with the slight decrease in the elongation and flatness indices observed in Figure 7.20 for the samples at load stage 3.

(b) Sphericity

The sphericity index (Ψ) was calculated based on the formulation proposed by Wadell (1932) that account for the volume (V) and the surface area (S) of the particle, as defined in Equation 2.33. This formulation returns a maximum value of 1 for a perfect sphere. All the sphericity values presented here have been corrected by a factor of 0.83, as discussed in Chapter 6, to take into consideration the effect of the voxel connectivity in the calculation of the surface area.

Figures 7.23 to 7.29 show the distribution of the sphericity index for different samples. The bin size used was 0.04 and the frequency distribution is presented as a percentage of the total number of particles in the sample. Information for the minimum, maximum and average values is included. For the samples analysed, higher frequencies are associated with Ψ values between 0.7 and 0.9. The intact sample prior to loading shows lower Ψ index values with an average value of 0.75 (Figure 7.23), when compared with the other intact samples that show averages greater than 0.79 (Figures 7.24, 7.25 and 7.26). The reconstituted samples show average sphericity values between 0.79 to 0.82 (Figures 7.27, 7.28 and 7.29). With the exception of the intact samples at early stages of loading, all the other samples show maximum sphericity values greater than 1, which in theory should not be possible and the reason for this anomaly is discussed in the following paragraph.

Figure 7.30 illustrates the distribution of the sphericity index as a function of the particle volume for one intact (293) and one reconstituted sample (289S). Both plots show that $\Psi > 1$ is associated with particles with very small volumes. By taking a closer look at each sample distribution, it can be concluded that the particles with $\Psi > 1$ are defined by less than 2000 voxels which may affect the surface area calculations due to voxel size effects, as discussed in Chapter 6. This effect on the sphericity calculations is not likely to be significant as, for example, for sample 289S, which shows the smallest average number of voxels per particle (Table 7.2), the particles with less than 2000 voxels represent less than 10% of the total number of particles in the sample (and just part of the particle with less than 2000 voxels show $\Psi > 1$). The intact sample 297ph, for example, has no particles with less than 2000 voxels.

Figure 7.31 shows the evolution of the average sphericity for the intact and reconstituted soil at the four stages of loading. The intact soil samples show lower Ψ values when compared to the reconstituted soil. The lowest Ψ value was observed for the intact soil prior to loading. For both materials Ψ seems to increase with shearing deformation up to load stage 3 and then decrease at load stage 4. When compared to Figure 7.4 it appears that the number of particles with higher sphericity increases with the decrease of the mean diameter of the particles (as a consequence of the disintegration of the fractured grains). This observation is likely to be related to the less accurate sphericity values obtained for the smaller particles (often with $\Psi > 1$) which contribute to the increase in the average sphericity value of the sample.

(c) Convexity

The convexity index (Cv) was calculated as the ratio between the particle volume (V_p) and the volume of the particle convex hull (V_{CH}) as defined in Equation 2.37. A convex shaped grain will have $Cv = 1$. The approach used to calculate V_{CH}, as

discussed in Chapter 6, will underestimate the volume of the grain when compared with the approach used to calculate V_P, specially for small particles. For this reason, the convexity index obtained for very small particles was greater than 1, as shown in Figure 7.32. As was the case for sphericity index, particles with less than 2000 voxels may have convexity indices very close to 1 or above.

Figures 7.33 to 7.39 show the distribution of the convexity index for all samples with information for the minimum, maximum and average values. The intact sample prior to loading exhibits lower convexity indices with an average value of 0.79 (Figure 7.33) when compared to the other samples, which show average values greater than 0.81 (Figure 7.34, 7.35 and 7.36). Samples 289 and 289S show a significant number of particles with $Cv > 1$ and this affects their average convexity values of 0.84 and 0.86 (Figure 7.38); which are higher when compared with the average convexity of approximately 0.82 for the other reconstituted samples (Figures 7.37 and 7.39). These observations are also shown in the plot of the average convexity for the intact and reconstituted soil at the four stages of loading as illustrated in Figure 7.40. Similarly to what was observed for Ψ, Cv seems to increase with shearing deformation up to load stage 3 and then decrease at load stage 4. Again a correlation between the average particle size and the particle convexity can be made, i.e., the overall convexity seems to increase with the increase in the number of small grains in the sample. The variation of the convexity index with flatness and elongation indices showed no clear trend. Also the variation of the sphericity index with flatness and elongation indices showed a great amount of scater.

(d) Sphericity compared to Convexity

The variation of the sphericity index against the convexity index is shown in Figures 7.41 to 7.44 for some of the intact and reconstituted samples. As can be observed, Ψ increases with Cv for all cases. The relationship between Ψ and Cv can be expressed by a linear regression with a slope of approximately 0.91-0.94 for the intact soil and a slightly higher slope of approximately 1.1-1.4 for the reconstituted soil.

(e) 3D vs 2D measurements

The 3D shape indices were compared with the 2D equivalent parameters obtained using the size and shape analyser QICPIC. The analysis using the QICPIC apparatus was carried out on 15g of dry Reigate sand and the image acquisition process took approximately 12min with a rate of feeding of 20%. The shape measurements obtained were the cumulative distributions of the aspect ratio, sphericity and convexity.

Figure 7.45 shows the cumulative distribution curves for three 3D aspect ratios (b/a, c/b and c/a) for one of the reconstituted samples (291ph) and the 2D aspect ratio

(d_{Fmin}/d_{Fmax}) measured using the QICPIC analyser. The 2D aspect ratio data has a median value (r_{50}) equal to 0.73. The 2D data gives an aspect ratio that is consistently lower than the 3D elongation ratio (b/a) and flatness ratio (c/b) that gives an $r_{50} = 0.78$ and overestimates 3D the ratio c/a that gives an $r_{50} = 0.62$; but it appears to be a good approximation to the average value given by the three 3D measurements.

Figure 7.46 shows that the QICPIC 2D measurements tend to overestimate the sphericity index. The 3D distribution gives an $r_{50} = 0.78$ and the 2D curve has a significantly higher $r_{50} = 0.89$. A similar trend can be observed for the convexity results presented in Figure 7.47 where the QICPIC distribution (with an $r_{50} = 0.94$) plots to the right of the 3D curve (with an $r_{50} = 0.80$).

7.3 Concluding remarks

The potential of using micro-CT data for 3D particle morphology quantification has been demonstrated here. High-resolution good quality images are, however, required for a detail and accurate examination of the size and form of irregular particles. Less accurate sphericity and convexity measurements were obtained for particles defined by less than 2000 voxels; demonstrating that the voxel size effect restricts the applicability of morphology analysis, based on micro-CT data, to soils with a very low proportion of fines, unless very high resolutions are used. Increasing the image resolution would, due to computer memory restrictions, lead to a reduction on the number of particles analysed, which is not desirable. The challenges associated with providing a correct particle surface area for irregular non-convex grains can be overcome using alternative definitions for the sphericity index; the method proposed by Clayton et al. (2009) and defined in Equation 2.36 is an example.

The repeatability of the methodology when applied to samples of the same specimen but imaged with different scanning parameters and pre-processed with different filters was investigated. Some morphology measures were compared for the two samples (297ph and 297L) extracted from the intact specimen prior to loading. As the intact material is likely to be homogeneous it was expected both samples to produce comparable results. As presented in Table 7.3, the size quantities as d_{50} and C_U and the aspect ratios (elongation and flatness) obtained for both samples showed very similar values. It can be concluded that for good quality high-resolution images, using different scanning parameters or different pre-processing filters do not affect the data measurements.

While it can be argued that the size of the sample and the number of particles is much smaller when compared with the samples used in laboratory measurements and therefore may not be representative, this investigation showed that 3000 particles

seem to provide reliable results (referring to Table 7.3). Previous 3D analyses of particle size and shape have reported data using 1060 full particles (Clayton et al., 2009). Hasan and Alshibli (2010) used data for 5857 particles but this number included the grains on the boundary of the sample.

Three-dimensional particle morphology measurements reported in the literature are still rare. Moreover, the use of different approaches does not always allow a direct comparison to be made. Clayton et al. (2009) reported an average true sphericity for Leighton Buzzard sand of 0.72 (using Equation 2.36 which gives values also between 0 and 1) and this is slightly lower that the average Ψ measured for Reigate sand. Al-Raoush (2007) reported an average sphericity of 0.30 for a natural sand (using Equation 2.35), but the results from the formulation used were not in the range of 0 to 1. The comparison with the QICPIC measurements showed that the 2D aspect ratio was close to an average value between the two 3D aspect ratio values given by the elongation and the flatness indices. Another soil type with a different grading may require a different correlation. For both convexity and sphericity, the 2D measurements were higher than the 3D values.

The particle morphology characterisation presented here has revealed differences in particle size and shape between the intact and the reconstituted soil. This is the result of the breakage of the fractured grains, along existing fissures, into small fragments as the original fabric is destroyed during loading. The change in grading, which would also occur during reconstitution, may have been partially responsible for the high densities achieved for the reconstituted specimens. Further, even if the interlocked fabric could not be produced artificially, densities closer to the intact soil were obtained to which the small fragments may have contributed by filling the pore space more effectively. This analysis highlighs the benefits of using non-invasive techniques the describe the particle size distribution of natural sands with friable grain that are broken during reconstitution.

Specimen ref.	Loading stage ref.	ε_a(%)	q/p'	ν	Sample ref.	Observations
297-int	0	-	-	1.48	297*ph* 297*L*	prior to loading
294-int	2	0.30	1.96	1.46	294*ph* 294*n*	onset of dilation
293-int	3	3.88	1.73	1.63	293 293*S*	start visible shear band 293*S* incl. shear band
295-int	4	9.00	1.38	1.67	295*ph* 295*L*	approaching CS 295*L* incl. shear band
291-rec	0	-	-	1.50	291*ph* 291*L*	prior to loading
289-rec	3	8.62	1.46	1.87	289 289*S*	start visible shear band
290-rec	4	12.5	1.46	1.70	290*ph*	approaching CS

Table 7.1: Information for the tested specimens and the associated samples that were used for morphology and fabric quantification

Sample ref.	Total no. of particles	Particles not in boundary		No. voxels per particle		
		No.	%	min	max	mean
297ph	2329	1438	62	5730	470 249	74 059
297L	4078	2849	70	20	141 4251	138 600
294ph	3004	1930	64	616	1 119 239	55 936
294n	2633	1635	62	2703	3 719 477	66 254
293	3959	2574	65	537	515 324	40 513
293S	3082	1912	62	538	550 184	47 200
295ph	2618	1598	61	1051	755 154	61 486
295L	5324	3247	61	256	7 621 329	104 570
291ph	3845	2513	65	512	524 952	39 893
291L	3385	2110	62	686	1 485 001	169 740
289	4142	2704	65	433	465 414	35 977
289S	4907	3387	69	229	567 276	27 504
290ph	3906	2591	66	340	769 829	35 070

Table 7.2: Statistics for the particles not on the boundary, for each sample

	Scanner location	Resolution (μm)	Pre-processing filter	d_{50} (μm)	C_U	Aspect ratio (average) Elongation	Flatness
sample 297ph	phoenix G.	5	Median	324	1.54	0.787	0.784
sample 297L	Leeds	4	Adaptive Gaussian	325	1.52	0.784	0.789

Table 7.3: Comparison of some morphological characteristics measured for the particles of two intact samples (297ph and 297L) scanned at different locations with different scanning parameters and pre-processed with a different filter

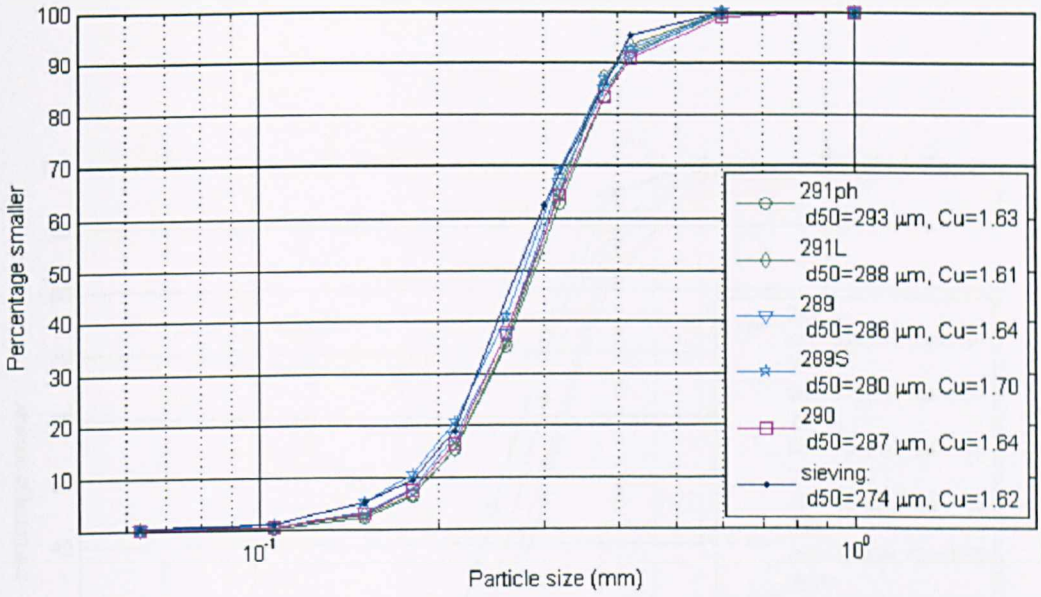

Figure 7.1: Particle size distribution using $d_{effective} = average(a, b, c)$ for the reconstituted samples

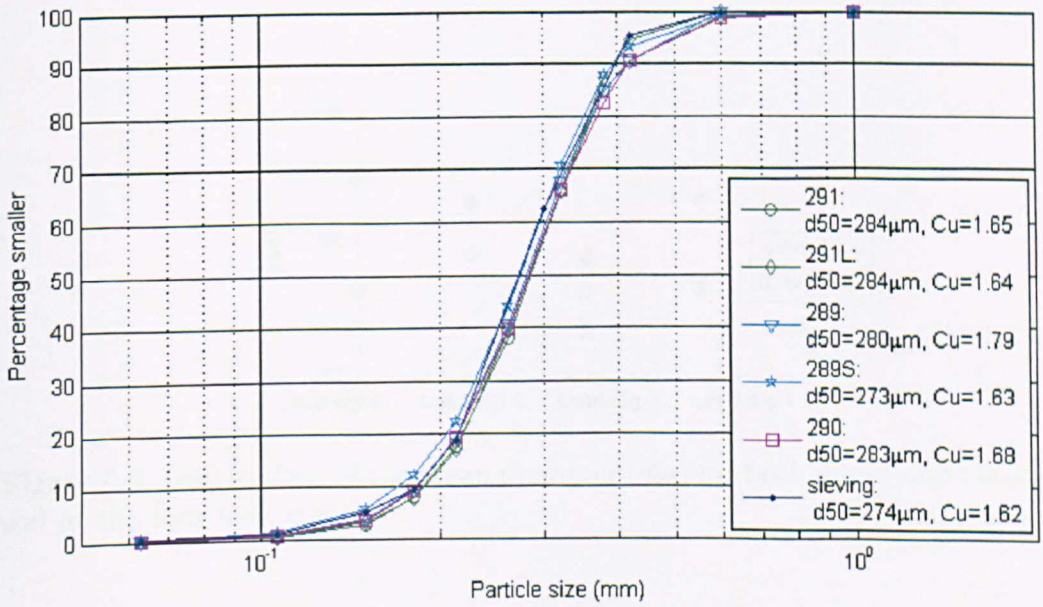

Figure 7.2: Particle size distribution using $d_{effective} = b$ for the reconstituted samples

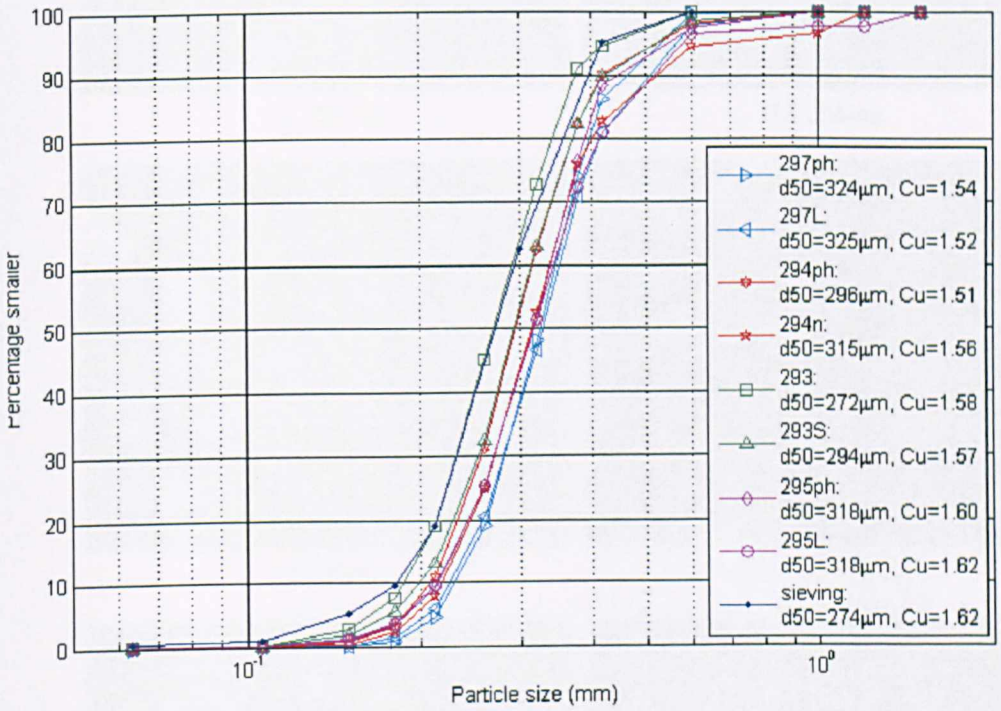

Figure 7.3: Particle size distribution using $d_{effective} = b$ for the intact samples

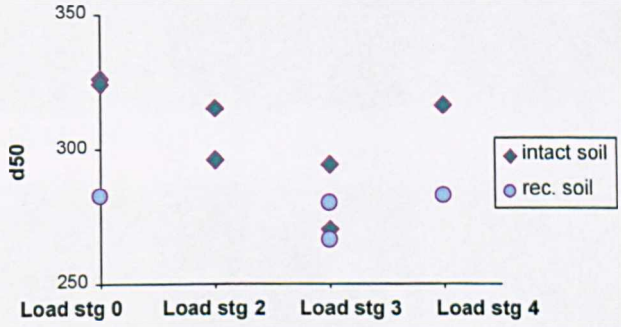

Figure 7.4: Distribution of the mean diameter (d_{50}) for both intact and reconstituted soil at the four load stages

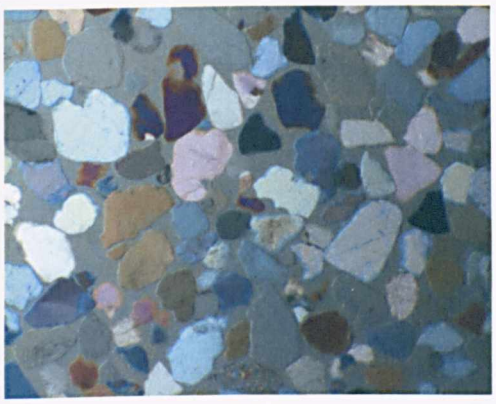

(a) 297-int

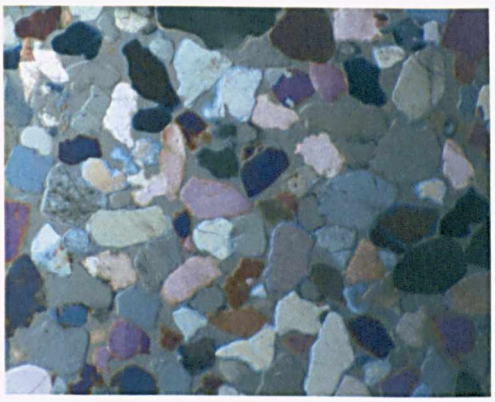

(b) 294-int

(c) 293-int

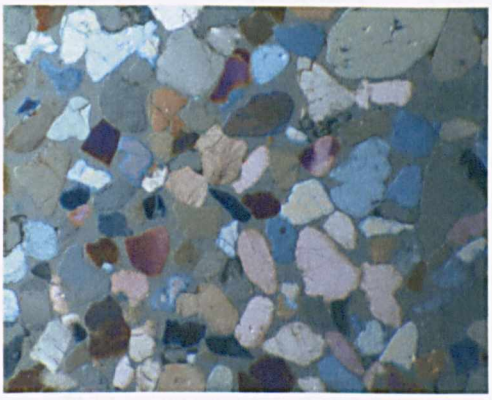

(d) 295-int (bottom)

(e) 295-int (middle)

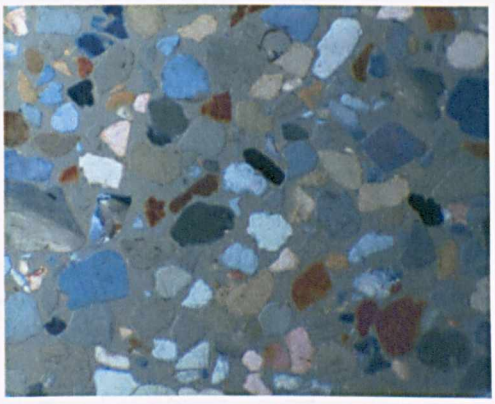

(f) 291-rec

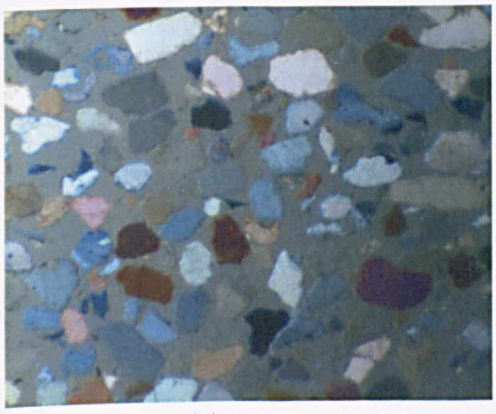

(g) 289-rec

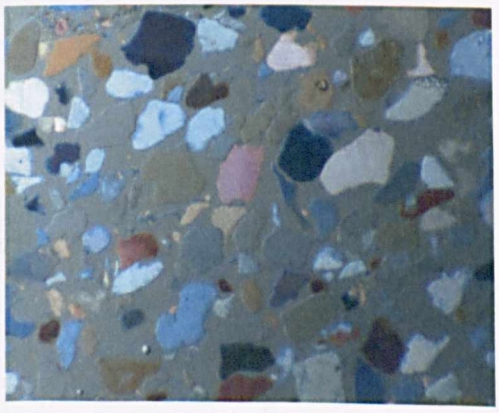

(h) 290-rec (middle)

Figure 7.5: Optical microscope images of thin sections for the specimens analysed

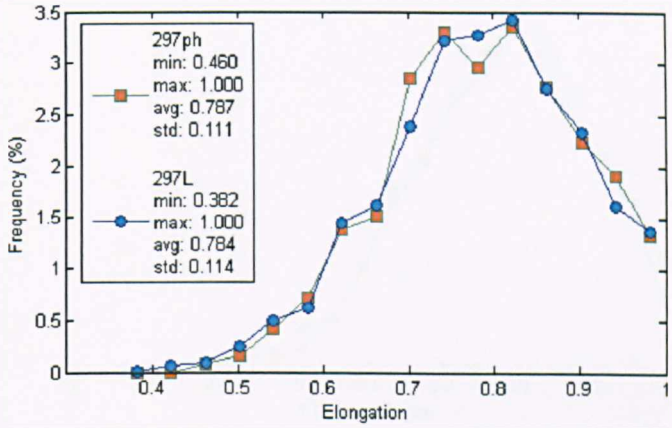

Figure 7.6: Elongation index distribution for intact samples 297ph and 297L

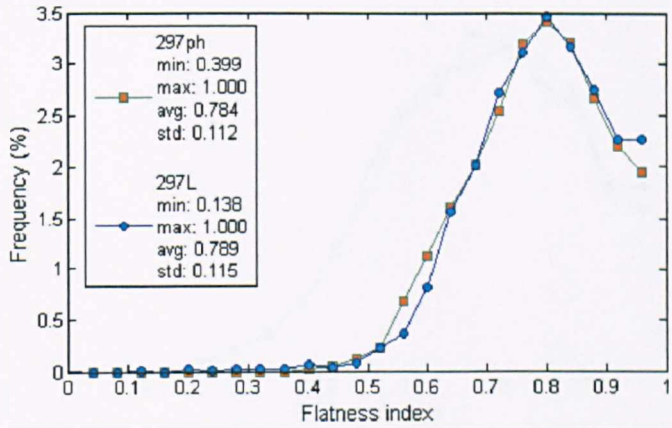

Figure 7.7: Flatness index distribution for intact samples 297ph and 297L

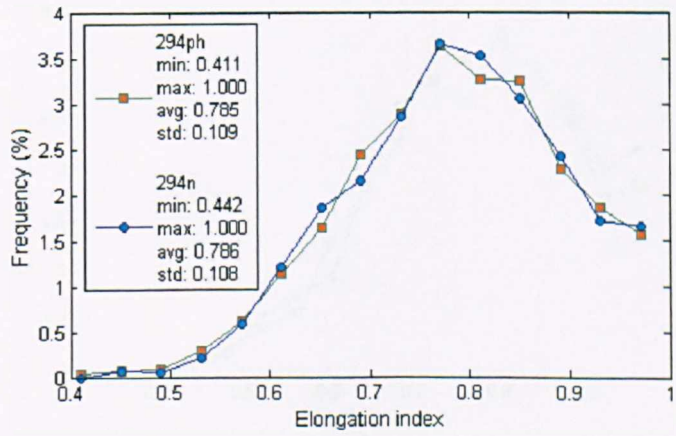

Figure 7.8: Elongation ratio distribution for intact samples 294ph and 294n

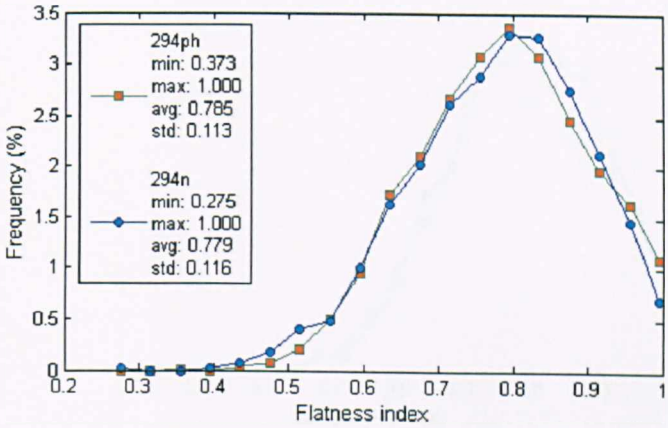

Figure 7.9: Flatness index distribution for intact samples 294ph and 294n

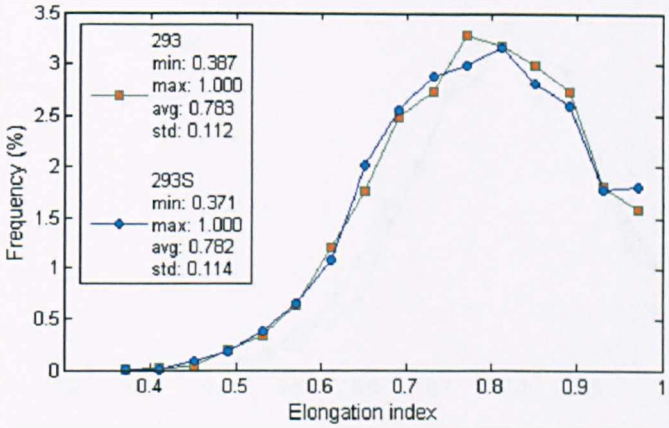

Figure 7.10: Elongation index distribution for intact samples 293 and 293S

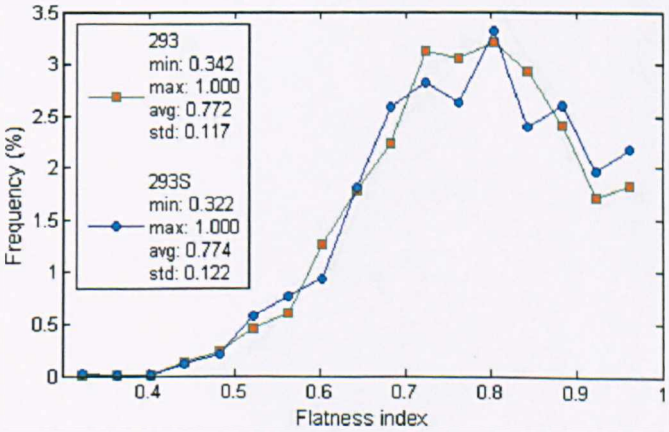

Figure 7.11: Flatness index distribution for intact samples 293 and 293S

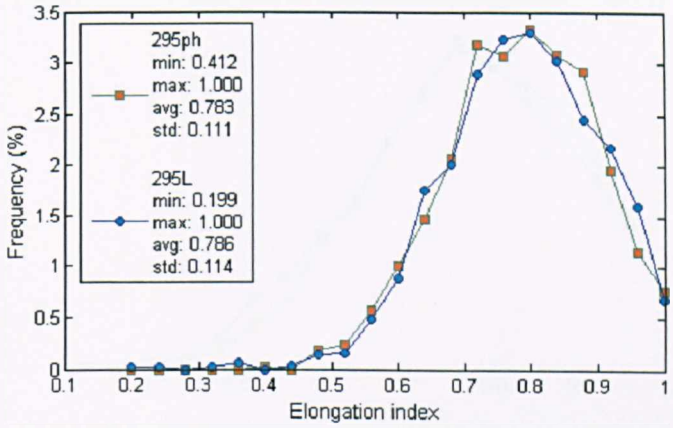

Figure 7.12: Elongation index distribution for intact samples 295ph and 295L

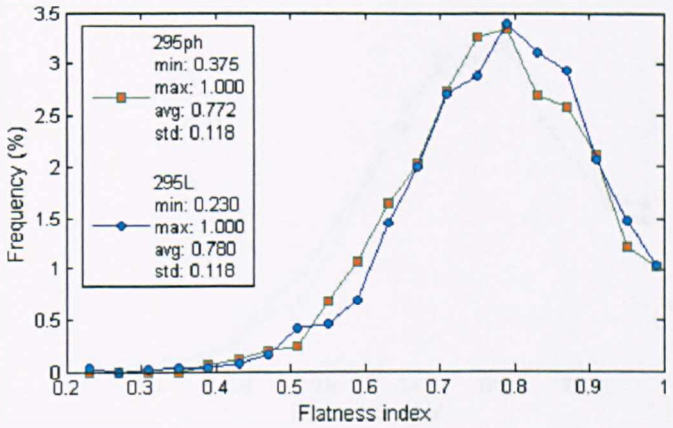

Figure 7.13: Flatness index distribution for intact samples 295ph and 295L

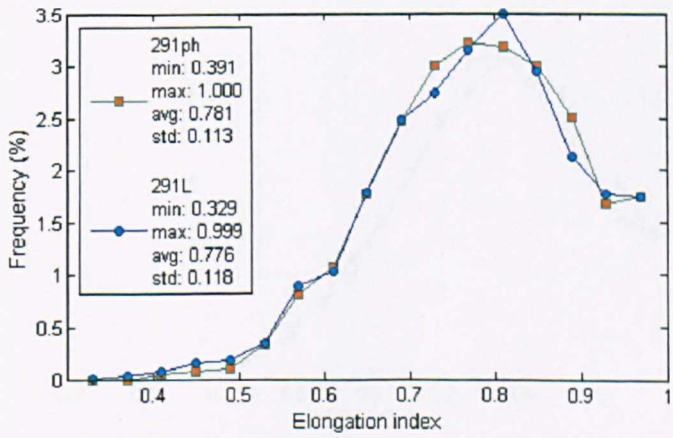

Figure 7.14: Elongation index distribution for reconstituted samples 291ph and 291L

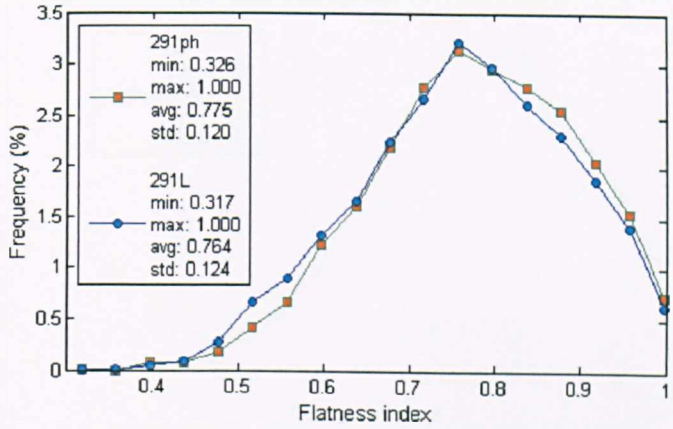

Figure 7.15: Flatness index distribution for intact samples 291ph and 291L

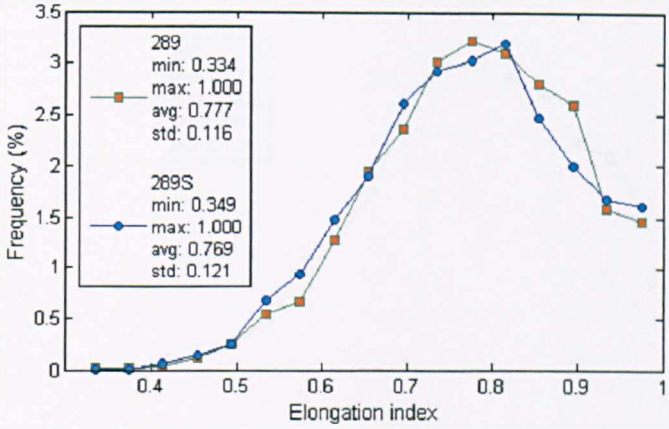

Figure 7.16: Elongation index distribution for intact samples 289 and 289S

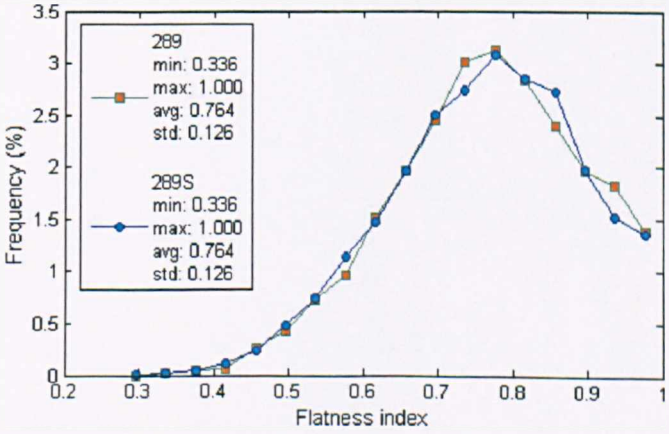

Figure 7.17: Flatness index distribution for intact samples 289and 289S

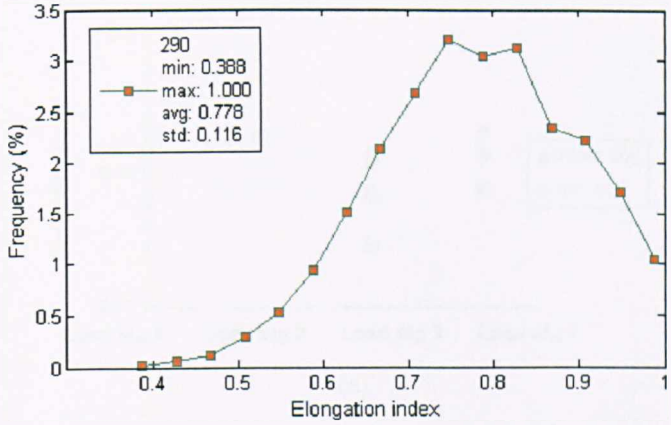

Figure 7.18: Elongation index distribution for intact sample 290

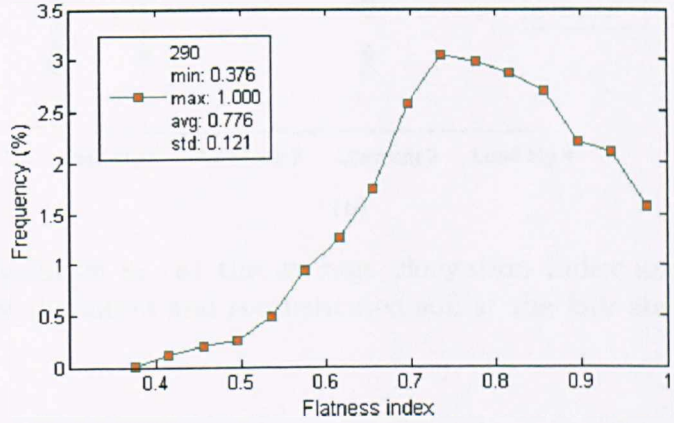

Figure 7.19: Flatness index distribution for intact sample 290

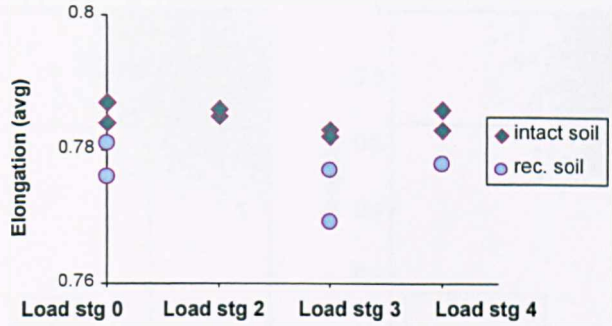

(a)

(b)

Figure 7.20: Evolution of (a) the average elongation index and (b) the average flatness index, of the intact and reconstituted soil at the four stages of loading

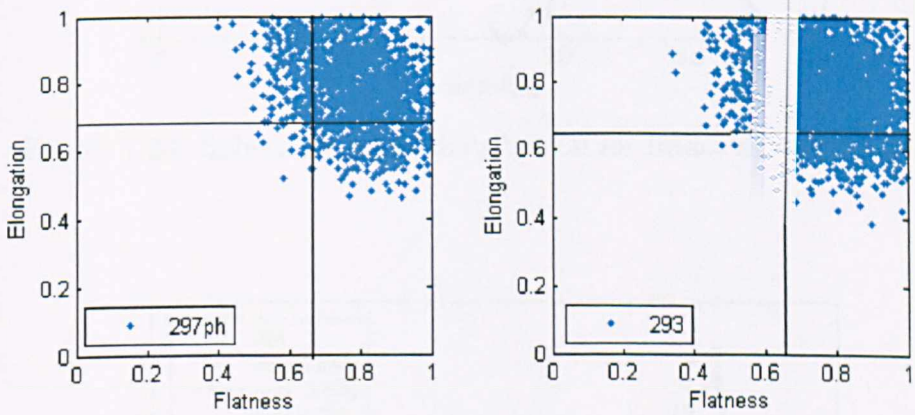

(a) (b)

Figure 7.21: Flatness index against elongation index for the intact samples (a) 297ph (b) 293

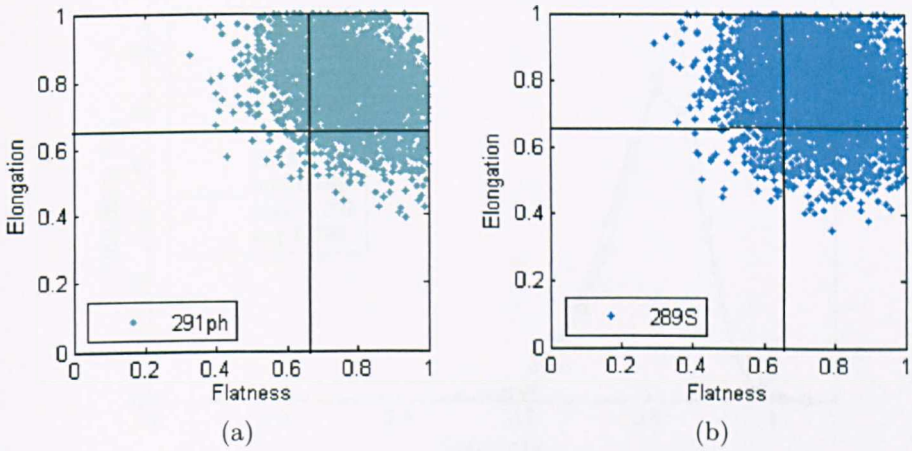

Figure 7.22: Flatness index against elongation index for the reconstituted samples (a) 291ph and (b) 289S

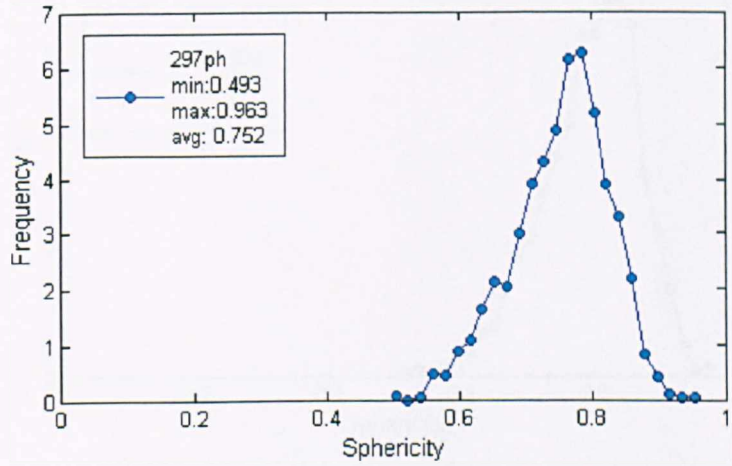

Figure 7.23: Sphericity index distribution for intact sample 297ph

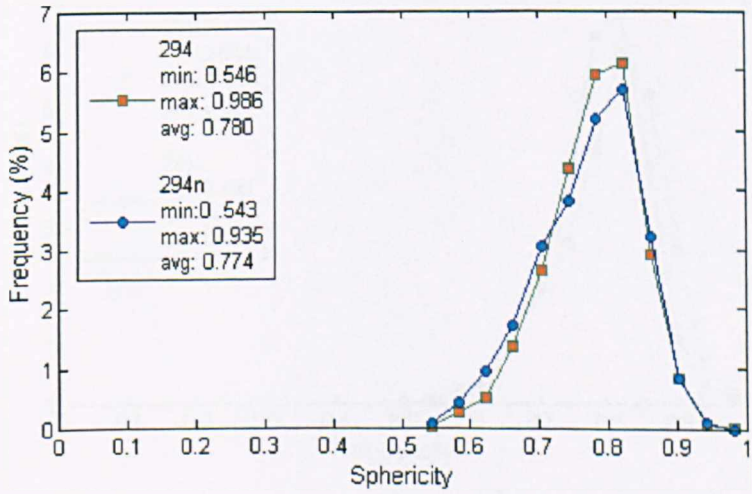

Figure 7.24: Sphericity index distribution for intact samples 294ph and 294n

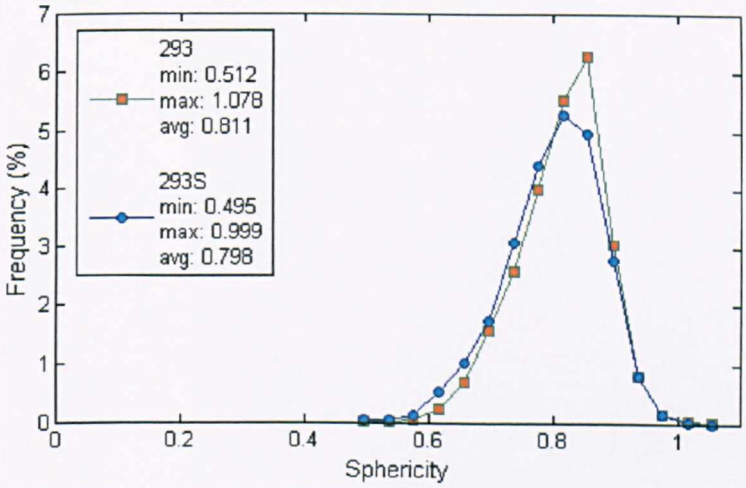

Figure 7.25: Sphericity index distribution for intact samples 293 and 293S

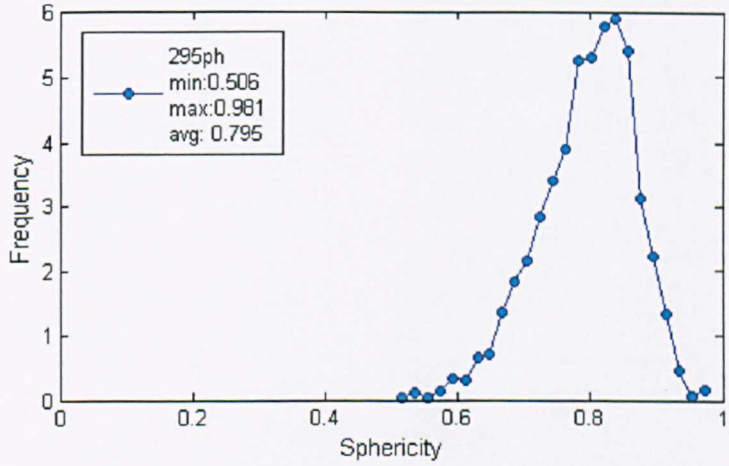

Figure 7.26: Sphericity index distribution for intact sample 295ph

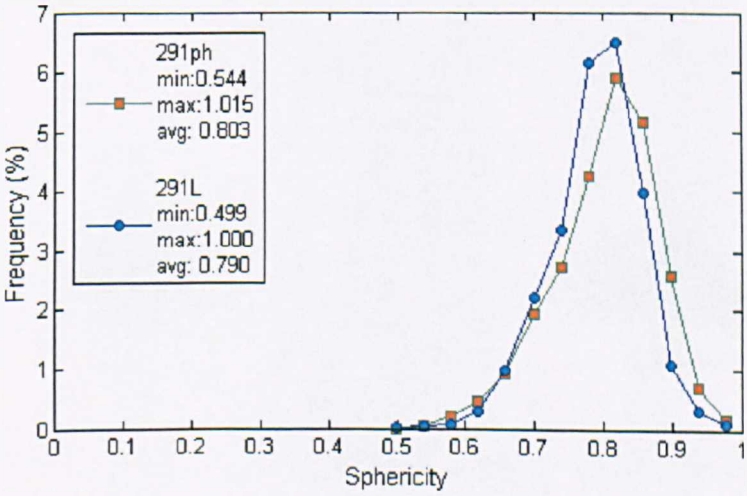

Figure 7.27: Sphericity index distribution for reconstituted samples 291ph and 291L

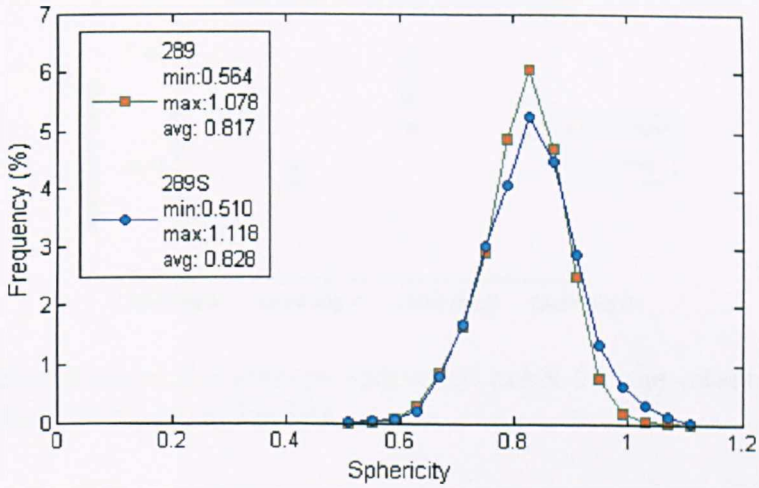

Figure 7.28: Sphericity index distribution for reconstituted samples 289 and 289S

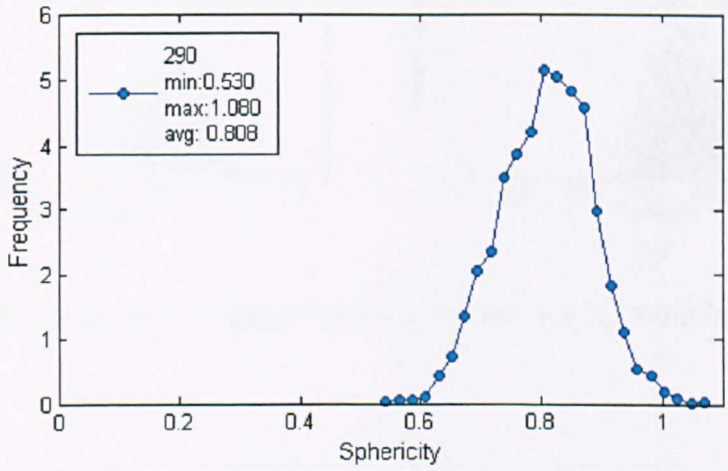

Figure 7.29: Sphericity index distribution for reconstituted sample 290

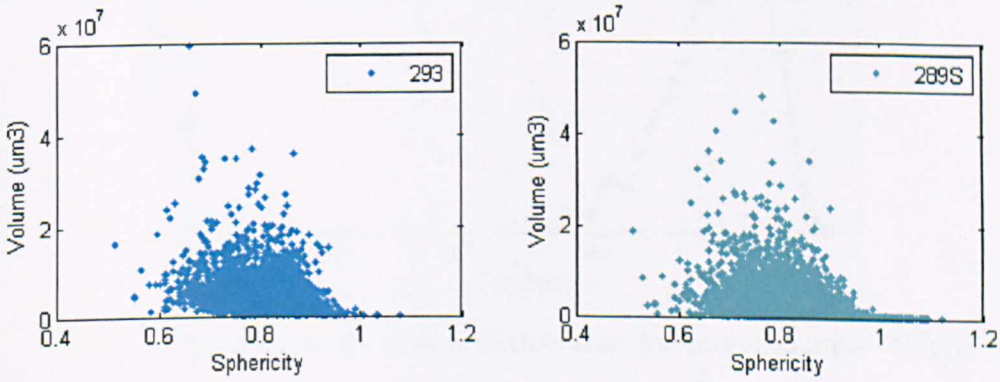

(a) (b)

Figure 7.30: Sphericity index against particle volume for (a) sample 293S (b) sample 289S

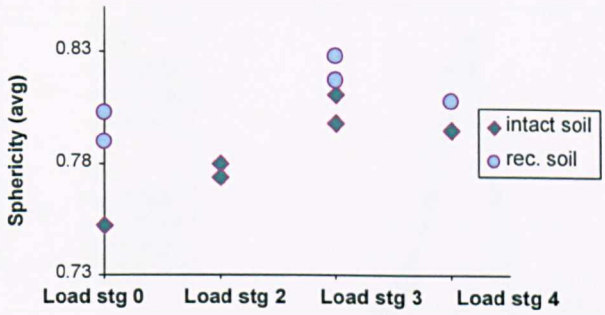

Figure 7.31: Evolution of the average sphericity index for the intact and reconstituted soil at the four stages of loading

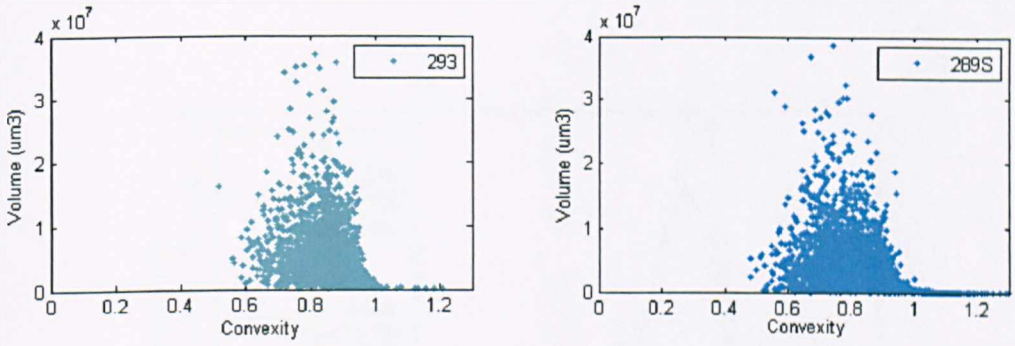

(a) (b)

Figure 7.32: Convexity index against particle volume for (a) sample 293 (b) sample 289S

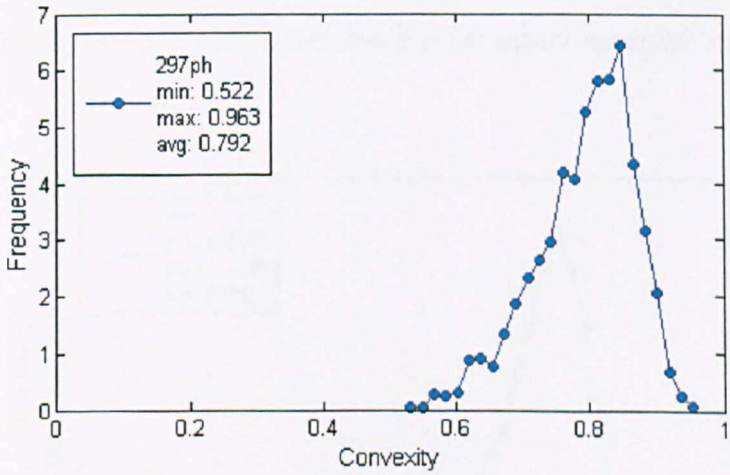

Figure 7.33: Convexity index distribution for intact sample 297ph

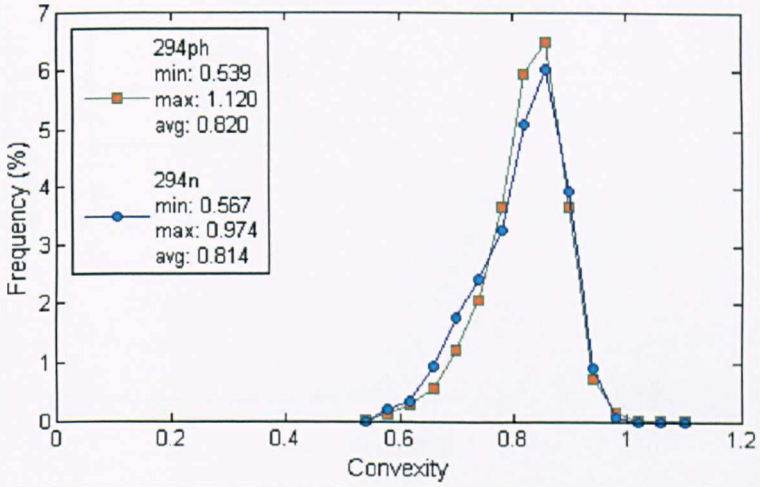

Figure 7.34: Convexity index distribution for intact samples 294ph and 294n

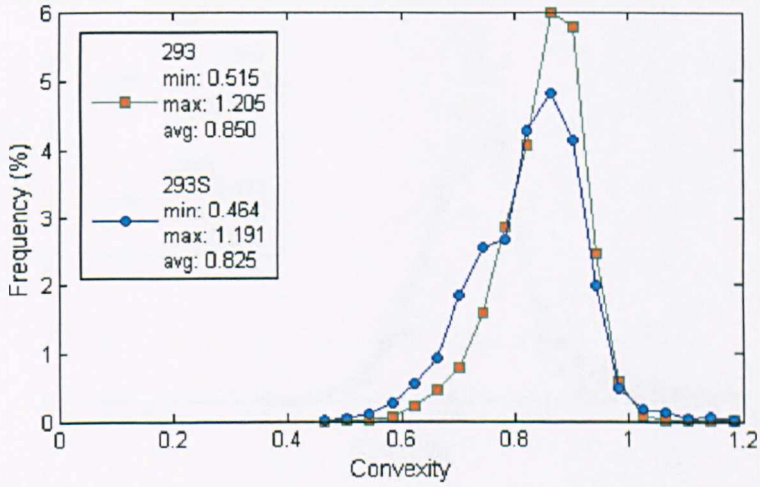

Figure 7.35: Convexity index distribution for intact samples 293 and 293S

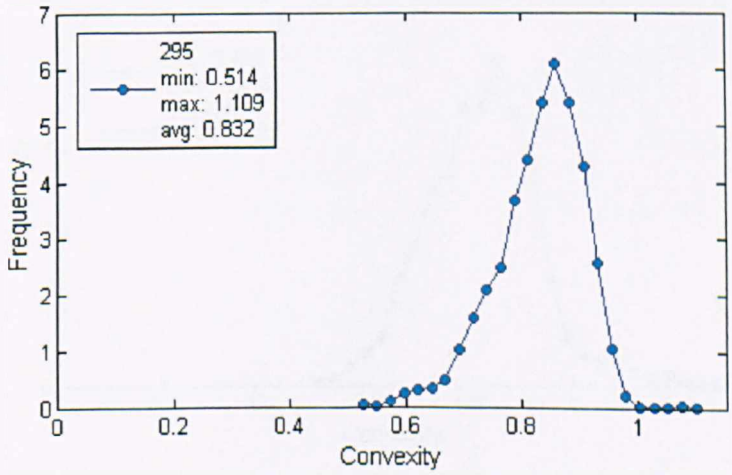

Figure 7.36: Convexity index distribution for intact samples 295ph and 295L

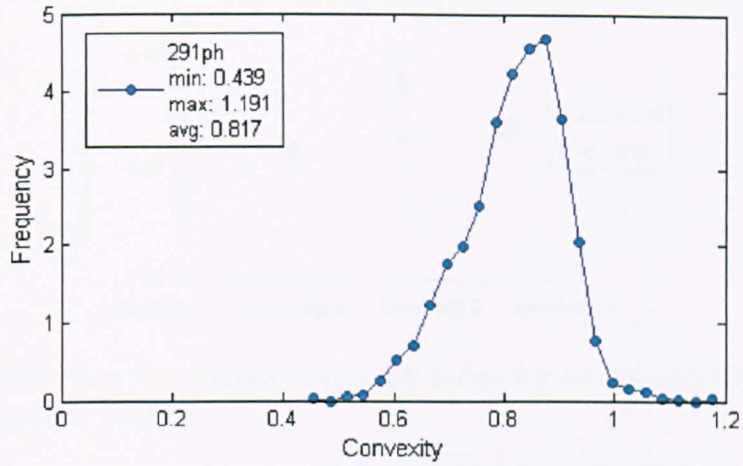

Figure 7.37: Convexity index distribution for reconstituted sample 291ph

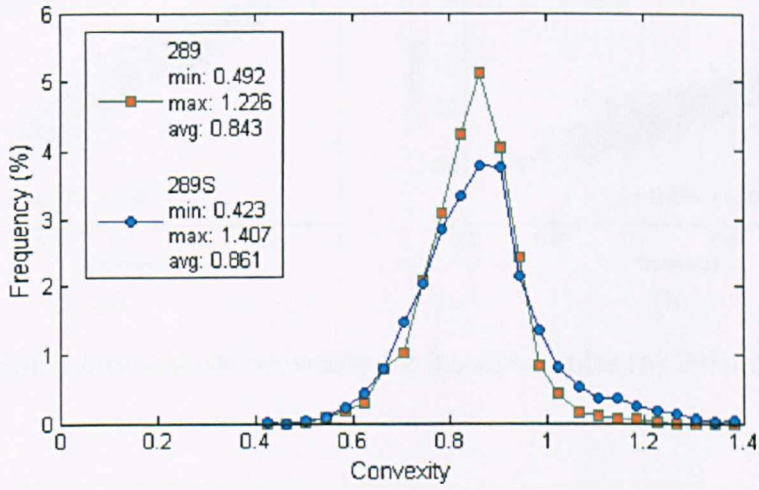

Figure 7.38: Convexity index distribution for reconstituted samples 289 and 289S

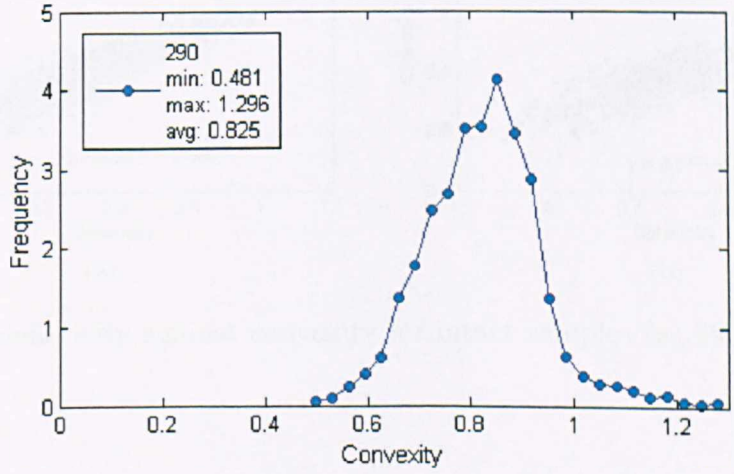

Figure 7.39: Convexity index distribution for reconstituted sample 290

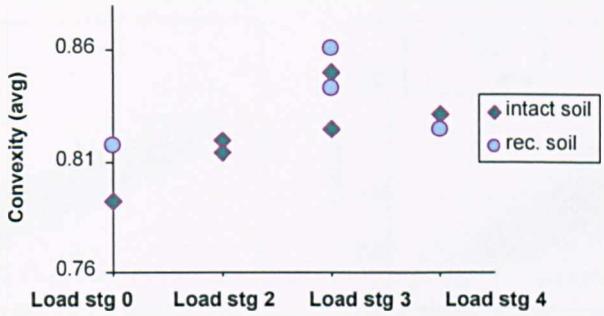

Figure 7.40: Evolution for average convexity index for intact and reconstituted soil at the four stages of loading

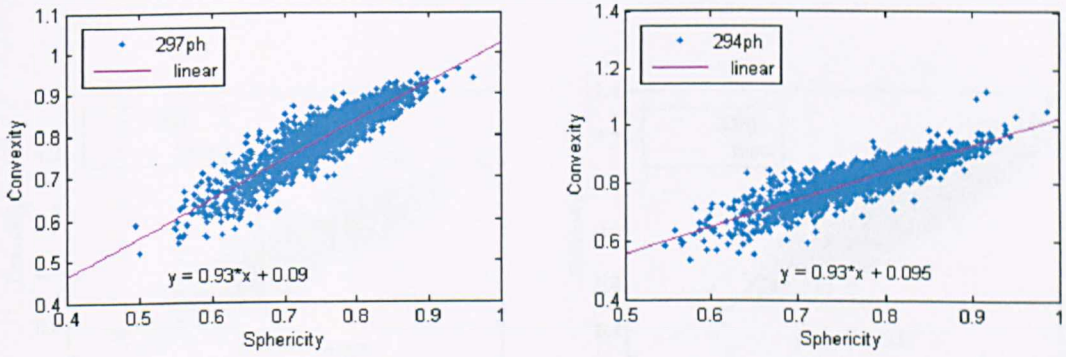

(a) (b)

Figure 7.41: Sphericity against convexity for intact samples (a) 297ph and (b) 294ph

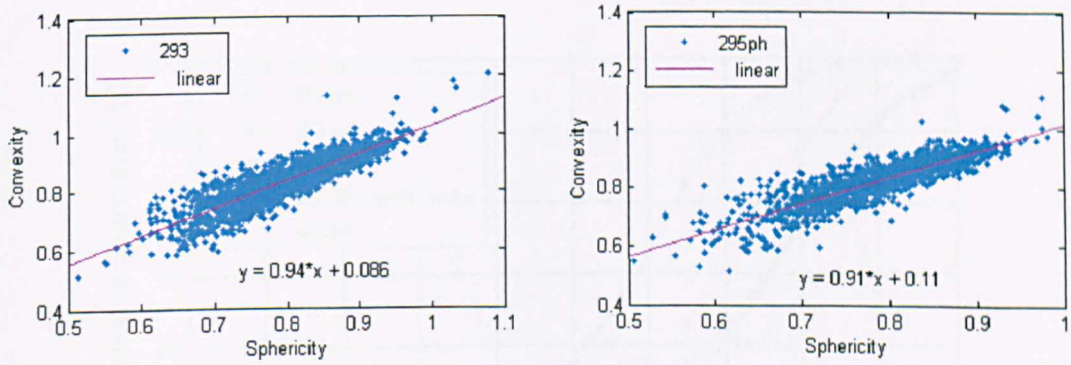

(a) (b)

Figure 7.42: Sphericity against convexity for intact samples (a) 293 and (b) 295ph

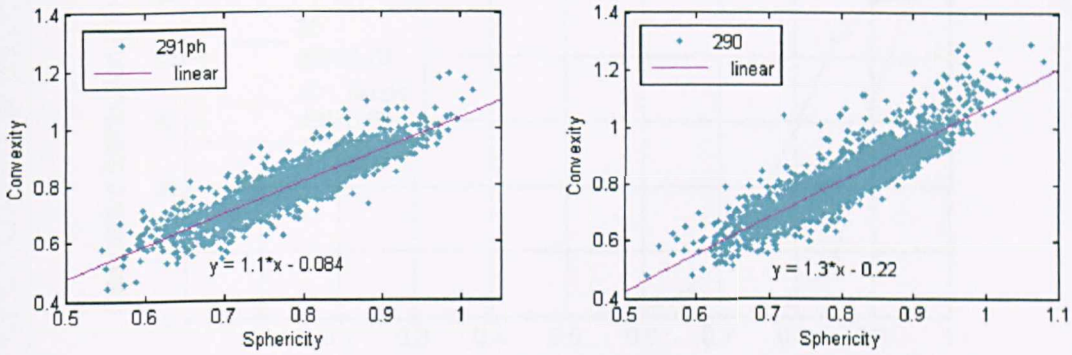

(a) (b)

Figure 7.43: Sphericity against convexity for reconstituted samples (a) 291ph and (b) 290

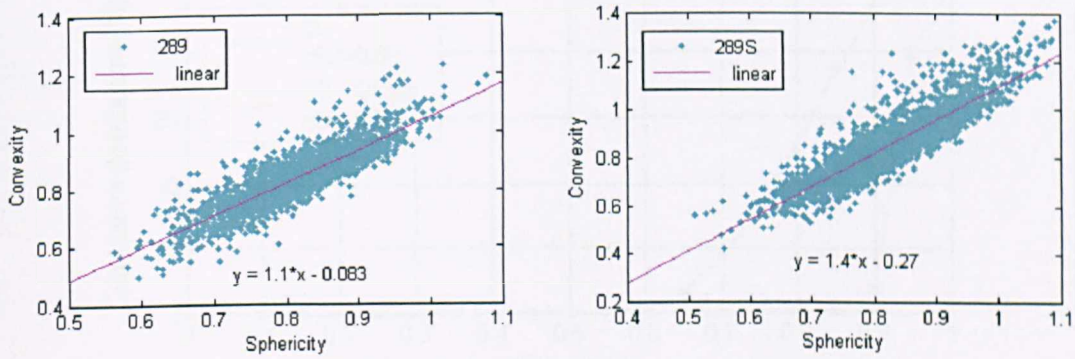

(a) (b)

Figure 7.44: Sphericity against convexity for reconstituted samples (a) 289 and (b) 289S

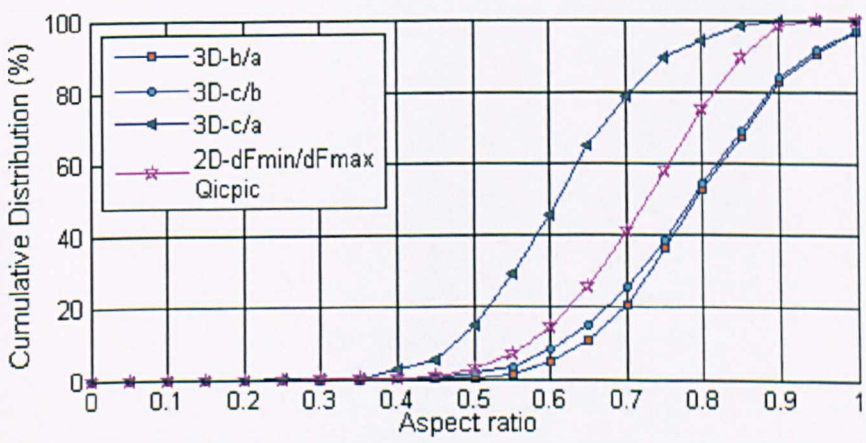

Figure 7.45: Aspect ratio distribution, comparison between the 3D measurements and the 2D results from QICPIC

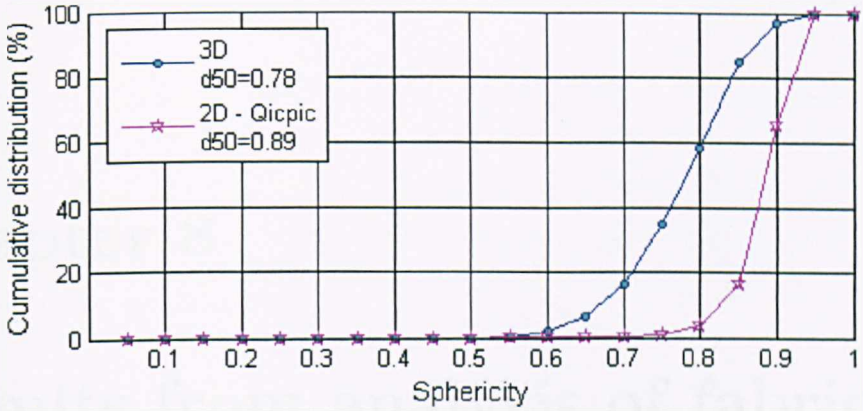

Figure 7.46: Sphericity distribution, comparison between the 3D measurements and the 2D results from QICPIC

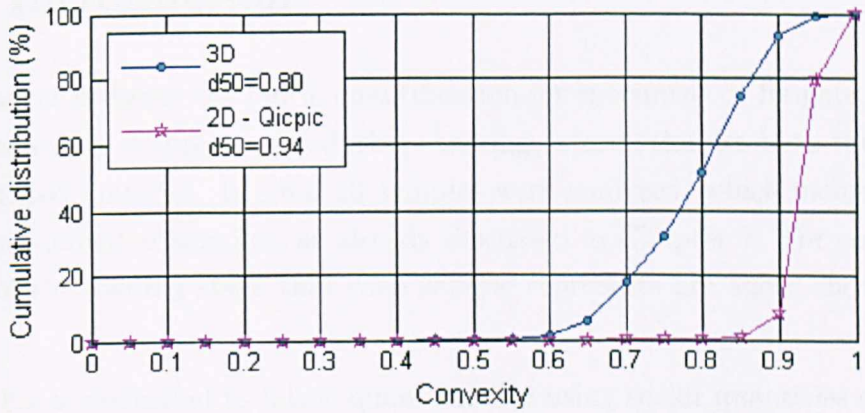

Figure 7.47: Convexity distribution, comparison between the 3D measurements and the 2D results from QICPIC

Chapter 8

Results from analysis of fabric

8.1 Introduction

This chapter presents the fabric quantification for specimens of Reigate sand at the initial state and at three stages during shearing deformation for both the intact and reconstituted material. In total 13 samples were analysed, which included 8 intact and 5 reconstituted samples, as already discussed in Chapter 7. For completeness, details of the loading stage that each sample represents are again shown in Table 8.1.

Section 8.2 is dedicated to fabric quantification using scalar quantities such as void ratio, coordination number and contact index. The laboratory void ratio measurements are compared with the 3D results from the micro-CT data. In addition to the 3D void ratio, 2D measurements were obtained using horizontal and vertical slices from the tomographic images. The ability of the coordination number and contact index to describe the interlocked fabric and its evolution with shearing deformation is discussed.

Section 8.3 presents the statistical analysis of the directional data using particle orientations, contact normals, branch vectors and void orientation. For each case, the angular distribution of the vectors is quantified by means of rose diagrams and histograms of the polar angle ϕ (in spherical coordinates). The fabric tensor and the corresponding eigenvalues and eigenvectors are presented.

Finally, in Section 8.4, the link between micro-scale measurements and the overall macro-scale response of the soil and how these micro-scale measurements evolve during loading is examined. The stress:strain evolution and the stiffness:strain evolution are compared with the evolution of fabric measurements including the deviatoric fabric, the orientation of the principal fabric to the z axis (angle ϕ), the coordination number, the contact index and the void ratio.

8.2 Fabric quantification using scalar quantities

The fabric quantification using three scalar quantities is presented in this section. The quantities are the void ratio, the coordination number and the contact index. The relationship between the different indices is then investigated. Both 3D and 2D void ratio measurements from the micro-CT data are presented; in addition those measures are compared with the laboratory measured void ratio and with the results using QICPIC.

8.2.1 Void ratio

Table 8.2 shows the void ratio measurements from the laboratory data (e_{exp}) and from the micro-CT data (e_{IA}). The shortcomings associated with each approach are discussed here. The experimental measurements are global and so do not capture the variations of void ratio within the specimen which is particularly relevant when, for example, a shear band develops in the specimen. The e_{exp} was calculated using the volume of the specimen based on the LVDT readings which, as discussed in Chapter 4, were not accurate after the development of the shear band. On the other hand, the void ratio obtained by voxel counting (as discussed in Chapter 6), is very sensitive to the threshold value selected during the image binarization process and also to errors associated with the finite voxel size. The differences between e_{exp} and e_{IA}, calculated as a percentage of the e_{IA} value, are presented in Table 8.2. The average difference is 14% and the maximum difference observed is 36%.

Figure 8.1a shows the e_{exp} data for the four stages of loading. Both the intact and the reconstituted specimens show very similar void ratios at the initial and final stages. At load stage 3 the reconstituted specimen shows a higher e value as a consequence of the more significant dilation of this material when compared to the intact soil. The evolution of e_{IA} is illustrated in Figure 8.1b; the two intact samples prior to loading show the same e value while the two reconstituted samples present different values which confirms the heterogeneity of the reconstituted samples when compared with the intact sample, as was observed in the preliminary micro-CT scans (Chapter 5). The difference between the e_{IA} values for the intact samples at load stages 3 and 4 is related to effect of the shear bands in sample 293S and 295L. The e values for the samples that contain part of the shear band are larger than the values for the samples outside the shear band. Figure 8.1c compares the e_{exp} and e_{IA} for all the samples. In general, e_{exp} is higher than e_{IA}; and the best agreement is observed for the intact samples containing part of the shear band (samples 293S and 295L) probably because for these sample e_{IA} is also an average value of the void ratio inside and outside the shear band.

(a) 2D vs 3D void ratio

2D void ratio calculations were carried out on horizontal slices (slices of constant z) and vertical slices of constant y, using the same approach as for the 3D measurements, i.e., by voxel counting. Figures 8.2 to 8.7 show the void ratio measurements in each slice (600 slices were used) for the following samples: an intact sample prior to loading, an intact sample at load stage 2, two intact samples at load stage 3 and two reconstituted samples at load stage 3. In addition the figures provide information on the minimum, maximum and average e values. A significant variation around the mean value can be observed for all samples. Figure 8.5 clearly illustrates the effect of the shear band, the first 180 vertical slices show a void ratio value below the mean value while slices 350 to 550 show values above the mean value. All the other samples show a more uniform spatial distribution around the mean value. Sample 293 shows the greatest difference between the minimum and maximum void ratio measured in the vertical samples, i.e., 0.454 and 0.632 (Figure 8.4). These plots demonstrate that when a 2D analysis, using for example thin sections, is used to calculate the void ratio, taking into account an average value from various sections is likely to reduce the potential error. No significant differences were observed between the vertical and the horizontal slices.

8.2.2 Coordination number

Figure 8.8 shows the frequency distribution of the coordination number (CN) for all samples. The curves for the intact samples at load stages 0 and 2 (297ph, 297L, 294ph and 294n) are located slightly to the right (higher CN) when compared with the reconstituted samples (291ph, 291L, 289, 289S and 290), which are associated with lower CN values, but this trend is not obvious as the distribution curves for different samples cannot be clearly differentiated.

The coordination number distribution for the intact samples is shown in Figures 8.9 to 8.12, together with statistical information for the minimum, maximum and average values. As illustrated in Figure 8.9, the frequency distribution curves for the two intact samples at load stage 0 (297ph and 297L) show very good agreement and the same average CN of 10.0. A similar average value of 9.6 was observed for the intact samples at load stage 2 (294ph and 294n, Figure 8.10). At these initial stages only an insignificant number of particles have CN values higher than 20. The average CN reduces as the shearing progresses, with the intact samples at load stage 3 (293 and 293S, Figure 8.11) showing values of 7.8 and 6.7 with the lower CN value being associated with the sample that includes part of the shear band (293S). The samples at load stage 4 show average values of 7.5 and 7.6 (295ph and 295L, Figure 8.12). For the load stages 3 and 4, CN values greater than 15 are associated with very low

frequencies. For all intact samples, CN values greater than 20 are associated with some exceptional geometrical configurations and are not representative. Only sample 293 has floating particles, i.e., particles with no contacts; all the other samples have particles with at least one contact. It is believed that the resin have caused these particles to float.

Figures 8.13 to 8.15 illustrate the CN distribution for the reconstituted samples. When compared to the intact soil, the reconstituted specimens show higher frequencies associated with lower CN indices. As illustrated in Figure 8.13, the samples prior to loading (291ph and 291L) show average CN values of 7.2 and 8.3 while the samples at load stage 3 (289 and 289S, Figure 8.14) show values of 7.0 and 5.8. At load stage 4 (290, Figure 8.15) the average CN is 7.0. For reconstituted samples in general, CN values greater than 15 can only be observed for a very small number of particles.

Figure 8.16 shows to the evolution of the average CN value at the four stages of loading. It can be observed that CN decreases with shearing deformation up to load stage 3 as a consequence of the dilation of the soil. From stage 3 to stage 4 no significant changes can be observed which may be an indicator that a critical coordination number was reached, as observed in previous studies (e.g., Thornton, 2000).

The correlation between the average CN and void ratio is shown in Figures 8.17a and 8.17b for the intact and reconstituted samples, respectively. The trend observed indicates an increase in the number of contacts as e decreases and the relationships obtained were $e = 1.73e^{-0.14CN}$ and $e = 1.33e^{-0.10CN}$ for the intact and reconstituted soil, respectively. For a dense silica sand prepared in the laboratory and sheared under plain strain conditions, Hasan and Alshibli (2010) reported a relationship defined as $e = 2.23e^{-0.13CN}$ with a R^2 of 0.68 which is slightly lower that the value of 0.88 obtained here. Despite the number of formulations proposed in the literature that relate CN to void ratio, the plots here presented indicate that for real sands a clear correlation may not exist. In fact, real sands are made of particles with various sizes and shapes and the number of contacts alone may not be an indicator of the density of the soil.

Figures 8.18 to 8.21 show the variation of the CN with particle volume for the intact and the reconstituted samples at the four stages of loading. CN increases with volume in all cases and the relationship between CN and the volume can be expressed by a quadratic line. As would be expected these observations indicate that the larger particles can potentially form more contacts than small particles.

Figure 8.22 shows the variation of the CN with sphericity index for just one intact and one reconstituted sample as all the other samples show similar trends. Despite the scatter, the CN values seem to increase with the reduction in particle sphericity.

Particles with sphericity closer to one have lower CN value while particles with more irregular shapes can more easily form contacts with neighbouring grains. This can be demonstrated based on the results presented by Al-Raoush (2007) comparing the CN values of a system of random mono-sized spheres and a sample of sand. The author have found that for the sand the CN values vary between 2 and 16 with an average of 7.3 while for the spheres the CN values range from 2 to 11 with an average of 6.83. The present study shows that a sand with interlocked fabric can exhibit CN values between 1 and 23 (the higher values shown in Figure 8.9 are not believed to be representative) with an average of 10.0. While after the disruption of the initial fabric the CN values observed were between 1 and 18.

The variation of CN with convexity for one intact and one reconstituted sample is illustrated in Figure 8.23. Just as was the case for the sphericity data, there seems to be an increase in the CN as the convexity decreases. There is however some scatter in the data but it shows that a decrease in convexity does not necessarily lead to an increase in CN.

No trend was found between the aspect ratio and CN. Because the particles do not deviate significantly from a spheroid, the increase in CN with elongation as observed by Ng (1999) in a system of ellipsoids could not be confirmed.

The mechanical coordination number (CN_m), as defined in Equation 2.3, which takes into account the number of particles with one contact (N_1) and the number of particles with zero contacts (N_0) was compared with CN and presented in Table 8.3. A small number of floating particles (with zero contacts) was found in the reconstituted samples and in the intact samples at load stages 3 and 4 which is an indicator that they were likely to be small fragments that got detached from the large particles. As already mentioned, the resin may have caused these small fragments to float. There is no variation between CN and CN_m as expected, given the very small number of particles with one or no contacts.

8.2.3 Contact Index

The contact index (CI) was calculated based on the ratio between the contact area and the particle surface as defined in Equation 2.5. Figure 8.24 shows the distribution of CI the for all samples. In contrast to what was observed in the analysis of CN, the CI curves show a clear distinction between the intact (samples 297ph and 297L) and the reconstituted (samples 291ph and 291L) materials prior to loading. The intact soil is associated with higher CI values while the reconstituted samples are located in the region of lower CI values. The curves for the intact soil at load stage 3 (in particular the sample outside the shear band, 293) are located in the same region (lower CI values) as the reconstituted samples at the same load stage (samples 289 and 289S).

The contact index distribution for the intact samples is shown in Figures 8.25 to 8.28, together with the statistical information for the minimum, maximum and average values. As illustrated in Figure 8.25, the samples at load stage 0 show very high CI average values of around 0.30; which means that on average approximately one third of each particle is "covered" with contact surfaces. The values of CI greater than 0.5 observed for some particles in sample 297L seem rather unrealistic and are likely to be related to inaccuracies in measuring the surface area for either the particle or the contact. These erroneous measurements are, in total, associated with less than 1% of the particles in the sample. At load stage 2 the two intact samples (294ph and 294n) also show high average CI values of around 0.25, as illustrated in Figure 8.26. The effect of dilation can be observed in Figure 8.27 where there is a drop in the average CI value at load stage 3 to a value of approximately 0.11 for sample 293 located outside the shear band. This reduction in CI as the shearing progresses is believed to be associated to the formation of new contacts with smaller contact areas and the opening up of the original contacts as a consequence of disruption of the soil fabric. Referring to Figure 8.28, at load stage 4 the samples show CI values of 0.15 and 0.17. It is interesting to note that the samples inside the shear band at load stages 3 and 4 show higher CI values compared with the samples outside the shear band. This was also observed by Wong (2003) in his study of shear bands in an oil sand (with a similar interlocked fabric). Wong (2003) suggested that some original contacts were still preserved inside the shear band which infers that some sand grains deform in interlocked groups instead of individual grains. Also, this feature was not observed for reconstituted sands.

Figures 8.29, 8.30 and 8.31 show the contact index distribution for the reconstituted samples. For this material, the maximum CI values do not exceed by much a value of 0.2 and the average is approximately 0.1.

Figure 8.32 shows the evolution of the average CI value at the four stages of loading. There is a clear differentiation between the CI values for the intact and for the reconstituted samples prior to the onset of dilation, which confirms the ability of the CI index to differentiate between the intact interlocked fabric and the fabric produced in the laboratory. There is no significant change in CI for the reconstituted soil while for the intact soil CI clearly decreases with shearing deformation up to load stage 3. Just as was the case for the CN data, the CI values do not change significantly at the last stage of shearing.

The correlation between the average CI and void ratio is displayed in Figure 8.33a for the intact samples and 8.33b for the reconstituted samples. The trend indicates an increase in CI as e decreases and the relationships obtained were $e = 0.84e^{-2.42CI}$ with $R^2 = 0.79$ $e = 1.18e^{-5.53CI}$ with $R^2 = 0.44$ for the intact and the reconstituted soil respectively.

Figures 8.34 and 8.35 show the evolution of the CI values with particle volume. No

clear trend can be observed. For the intact soil prior to loading, higher CI values are observed for a wide range of particle volume. For this material at load stage 3 and for the reconstituted soil, the maximum CI value can only be found for the smaller particles. These observations show that CI is size insensitive, which reinforces its potential to be used in fabric description. No significant trend was found between CI and sphericity index, or CI and convexity index.

(a) CI compared to CN

The relationship between the coordination number and the contact index was investigated. Figures 8.36 and 8.39 show the plots of CN versus CI at each of the four loading stages for both the intact and the reconstituted samples. The plots show significant scatter and no clear trend can be observed. Low CN values are associated with a wide range of CI values and as CN increases (along the straight line fitted to the data) this range of CI values reduces towards the CI average value. The data for the reconstituted samples show a greater concentration of CI and CN values close the origin when compared to the intact soil, especially at the early stages of loading.

The fact that little correlation can be observed between CN and CI is not surprising given the fact that the indices measure different characteristics. An increase in the number of contacts may indicate a denser packing but if the contacts are mainly of point-like type they will not contribute to an increase of the CI values. In fact, a high number of contacts per particle may limit the possible surface area of each contact. There is also a particle size effect. A large grain may be surrounded by smaller grains and in this case, the CN value is high because of the number contacts, but the CI can be low as the contact area in each case will be small relative to the size of the large grain. On the other hand, a small grain can potentially have a higher CI given its small surface area.

(b) Void ratio compared to CI and CN

Plots of void ratio against coordination number are presented in Figure 8.40a for the intact soil and Figure 8.40b for the reconstituted soil. Both materials show an almost liner reduction of CN as the void ratio increases. A similar trend can be observed for the variation of void ratio with contact index for the intact soil, as shown in Figure 8.41a. The reconstituted soil shows slight fluctuations in the contact index as the void ratio increases.

8.2.4 Summary

The void ratio measurements presented here highlight the fact that despite void ratio being the most basic measure of soil fabric, its correct measurement is not

simple to obtain. Laboratory measurements can only provide a global value for the void ratio. Using micro-CT data to measure void ratio requires very good quality images in order to minimize the uncertainty in selecting the threshold for the binarization process and to minimise the voxel size effect. Additionally, it has been demonstrated that 2D void ratio measurements are not representative of the 3D value, and therefore if 2D measurements are to be used, using an average value obtained from different sections is likely to reduce the potential error.

It has been demonstrated that when dealing with real sands specimens in which contacts may be surfaces rather than points, the use of the contact index, which takes into account the size of the contact, presents a clear advantage when compared with the coordination number. Despite many formulations have been proposed in the literature which relate CN to void ratio, no clear correlation was found in this study. Natural sands, given their wide range of particle sizes and shapes, may require more refined parameters for fabric quantification when compared with the ones commonly used for DEM simulations.

Comparison of the fabric measures presented here with previous studies can be made by referring to the study by Richards and Barton (1999) carried out on specimens of Reigate sand retrieved from the same location. The authors reported an average coordination number of 1.8 and 35% of tangential contacts relative to the total number of contacts, measured with optical microscope images of thin sections. The average coordination number measured in this study for the intact samples was of 10.0 and the proportion of tangential contacts was of 98.8%. The differences in the results highlight the limitations of a 2D analysis in which only the contacts intercepted by the image plane are taken into consideration and a contact can be erroneously classified as point like when it develops out of the image plane.

8.3 Fabric quantification using directional data

This section presents the analysis of the directional data of the soil fabric by means of four types of vectors given by the particle orientation, the contact normal, the branch vector and the void orientation, respectively. Each dataset of vectors is examined using rose diagrams, the frequency distribution of the angle ϕ that each vector forms with the z axis and the fabric tensor. The fabric tensor eigenvalues are used to calculate the fabric descriptors and to obtain the anisotropy.

8.3.1 Particle orientation

(a) Rose diagrams

An assessment of the particle orientation may be achieved using polar histograms or rose diagrams of the projections of the vectors onto the xz-plane, yz-plane and xy-plane, as presented in Figures 8.42 to 8.46. Each bin in the rose diagram has been shaded and the degree of shading indicates the average elongation index for the particles which are orientated within the limits defined by that bin. Therefore, these plots give an indication of both the orientation of the particles in the sample as well as the average elongation of the particles in each direction. In the plots relative to the vertical planes, the z-axis is always shown as the vertical axis and x and y as the horizontal.

Figure 8.42 is for the intact and reconstituted samples prior to loading. As there was a limited number of full particles in each sample, samples 297ph and 297L were merged together and samples 291ph and 291L were also combined. By increasing the number of particles the scatter should be reduced and any trends in the data should become clearer. As would be expected, the distribution of the particle orientations for the intact soil shows a greater concentration around the horizontal plane, i.e., perpendicular to the direction of deposition as shown in Figures 8.42a and 8.42c for the xz- and yz-planes respectively. The more elongated particles, represented with the darker shading, appear to be mainly orientated along the horizontal direction while the less elongated particles appear to be orientated in a less "stable" positions. The reconstituted sample shows a similar trend, as can be seen in Figures 8.42b and 8.42d. However, for this material the relationship between orientation and particle elongation index seems to be less clear. The distribution in the xy-plane for the intact soil shows a reasonable amount of axi-symmetry (noting the almost circular plot illustrated in Figure 8.42e) while the reconstituted sample shows a bias that may possibly relate to the small number of particles analysed. A similar analysis was done using the major axis length instead of the elongation index and the rose diagrams are presented in Figure 8.43 for the vertical planes only. The intact samples (297ph and 297L) are shown in Figures 8.43a and 8.43b while the reconstituted samples (291ph and 291L) as illustrated in Figures 8.43c and 8.43d. In both cases the particles with the larger major axis (represented by the lighter shading) seem to lie in the horizontal plane.

Figure 8.44 presents the results for the two intact samples obtained at load stage 2 (294ph and 294n). Figures 8.44a, 8.44c and 8.44e show that for sample 294ph, the particle orientations have not changed significantly from the previous stage as they still show a preferred horizontal orientation and a relatively uniform distribution in the xy-plane. A less expected distribution can be found for the particles in sample 294n; this data shows a strong bias in the horizontal plane as illustrated in Figure

8.44f, which affects the distribution in the vertical planes as shown in Figure 8.44b and 8.44d.

Figure 8.45 is for the intact soil at load stage 3. In comparison with the data for load stage 0 presented in Figure 8.43, sample 293 shows an increase in the number of particles orientated closer to the vertical direction which results in a more uniform distribution in the vertical projections (Figures 8.45a and 8.45c). Sample 293S, which contains part of the shear band shows a strong preferred orientation of approximately 30° to the x-axis in the vertical projection. This is related to the reorientation of the particles caused by the shear plane movement (Figure 8.45b). The data in the yz-plane (Figure 8.45c) show a decrease in the number of particles orientated between angles 220° and 320° also related to the effect of the shear plane.

For the reconstituted soil at load stage 3, the data for sample 289 (Figures 8.46a and 8.46c) show a similar distribution pattern to that for the sample 293S, i.e., the particle orientation seems to be affected by the proximity of a shear plane. Sample 289S (Figures 8.46b and 8.46d) shows that the majority of particles are aligned along the horizontal plane as was the case for load stage 0.

The intact samples at load stage 4 are shown in Figure 8.47. Sample 295L shows the effect of the shear plane with the particles mainly orientated at 30° to the x-axis (Figure 8.47a) for which the more elongated particles (darker shading) appear to give a significant contribution. Sample 295ph, extracted from a region outside the shear band (Figure 8.47b and 8.47d), does not show major changes when compared to sample 293 from the previous stage. Figure 8.48 shows the reconstituted sample at load stage 4. The effect of the shear plane can be observed by the 20° deviation from the horizontal plane (Figures 8.48a and 8.48b). The shear plane also affects the distribution in the horizontal plane (Figure 8.48c).

The relationship between preferred orientation and major axis length for the samples affected by the movement inside the shear band was investigated. Rose diagrams with shading related to the length of the particle major axis are presented in Figure 8.49 for the intact samples 293S and 295L and for the reconstituted samples 289 and 290. The plots show that the greater contribution to the preferred orientation observed at this stage of loading is given by the particles with longer axes, for both the intact and reconstituted samples.

It is worth noting that some rose diagrams present distributions that do not seem clear; this is mainly related to the small number of vectors. For the samples affected by the shear band there are two main factors to take into consideration. Firstly the sample contain just part of the shear plane and so the distribution will reflect not only the orientations in the localisation but also in the regions outside the shear band. Furthermore the planes representing the projection of the vectors are not likely to be orthogonal to the shear band which makes the interpretation of the

plots more complex.

(b) Frequency distribution of ϕ

The orientation of the principal fabric to the positive z-axis given by the angle ϕ, as described in Chapter 6, was calculated for each vector and the frequency distribution of the angles obtained is presented in Figures 8.50 to 8.56. Figure 8.50 is for the intact samples at load stage 0, compared with the distribution of an isotropic system. Although the data for the samples 297ph and 297L have been merged for the rose diagram analysis, they where analysed individually in the ϕ plots to demonstrate that both samples show similar distribution patterns. Both samples show frequencies greater than the isotropic distribution for ϕ>1rad (60°) which demonstrates the concentration of the particle orientations in a region that is within 0.52rad (30°) of the horizontal plane. The intact samples at load stage 2, are presented in Figure 8.51 and just as for the previous stage, the preferred orientation is closer to the horizontal direction. However for this load stage the plots intercept the isotropic line at $\phi \approx$0.87rad (50°), indicating that the concentration of particle orientations is more diffuse than for the soil prior to loading. At load stage 3, sample 293 shows an almost isotropic distribution while the samples affected by the shear band show a bias at 0.52rad (30°) to the horizontal, as shown in Figure 8.52. Referring to Figure 8.53, sample 295ph shows a preferred orientation at $\phi \approx$1.1rad (63°) but both samples show distributions very close to the isotropic curve.

Referring to the reconstituted samples, Figure 8.54 presents the data for the samples prior to loading and Figures 8.55 and 8.56 give data for the samples at load stages 3 and 4, respectively. There is no apparent evolution in the ϕ angle distribution with shearing with all the plots showing a similar degree of concentration along the horizontal direction as opposed to the vertical direction. These plots confirm the previous observations from the rose diagrams.

(c) Fabric tensor

The particle orientation fabric tensor was calculated based on the formulation that takes into account the shape of the particles in addition to the orientation vectors (Φ^P) as defined in Equation 2.23 and using the general formulation (Φ) as presented in Equation 2.11. The results of Φ^P are presented in Tables 8.4 to 8.10 and the results of Φ in Tables 8.11 to 8.17 for all the samples analysed. The corresponding eigenvalues and eigenvectors of each fabric tensor as well as the ϕ and θ angles calculated for the vector representing the orientation of the major principal fabric (V_1), are also presented. For all the samples the off diagonal terms of the fabric tensor are small which indicates that the principal values are aligned along the Cartesian axes.

For the intact soil prior to loading (297 and 297L, Tables 8.4 and 8.11) both V_1^P and V_1 and V_2^P and V_2 confirm the previous observation that the particles are essentially lying in the "most stable" position with the major and intermediate axes orientated in the horizontal plane. The results from the eigenvalue analysis of Φ^P and Φ, showed that taking into account the size and shape of the particles (i.e., using Φ^P), markedly changes the fabric tensor data. While the eigenvalues for Φ, i.e., S_1, S_2 and S_3 have similar values, indicating a rather uniform distribution of the particle orientation vectors; for Φ^P, S_1^P and S_2^P are significantly higher than S_3^P which shows the contribution of the larger particles to the preferred concentration of the vectors in the horizontal plane. This observation is in accordance with Figures 8.43a and 8.43c that shows that the orientations closer to the vertical are associated with small particles. Similar observations can be made for the reconstituted soil before loading. In this case the differences between both fabric tensor formulations are less significant, i.e., 3° between the ϕ angles for V_1^P and $V_1$and 10° between the ϕ angles for V_2^P and V_2. This means that the distribution of the orientation vectors for the reconstituted material is less affected by the size of the particles than is the case for the intact material.

Tables 8.5 and 8.12 show the fabric tensor results for the intact soil at load stage 2. The orientation of the principal and intermediate fabrics for the intact soil does not differ from the previous stage. However the differences between Φ and Φ^P are more significant; this means that larger particles are less prone to change their orientations at the beginning of shearing.

The intact soil at load stage 3 is presented in Tables 8.6 and 8.13. For the region away from the shear band (sample 293) a major change in the fabric orientation can be observed. The principal fabric given by V_1^P is still essentially horizontal and is orientated within 10° of the horizontal plane. However the ϕ angle for V_2^P has rotated by about 80° and become vertical while the minor fabric given by V_3^P is horizontal. Referring to Figures 8.45a and 8.45c the orientation vectors are rather uniformly distributed and this explains the difference between ϕ_1^P and ϕ_1 which take values of 98° and 79°, respectively. The sample containing part of the shear band shows a change in particle orientations with deviations from the horizontal plane of 9° and 23° that might be explained by the reorientation of particles along the shear band direction as illustrated in Figure 8.45b. The difference between ϕ_1^P and ϕ_1 shows again that the particles with longer major axes are more likely to change their orientation (Figure 8.49).

The reconstituted soil at the same load stage is presented in Tables 8.9 and 8.16. While sample 289S did not show a significant change from the previous stage (load stage 0), as also shown in Figures 8.46b and 8.46d, sample 289 shows V_1^P orientated in the horizontal plane and V_1 showing a 25° deviation from the horizontal plane, which is in accordance with Figure 8.46b and shows the effect of the proximity to

the shear band.

At load stage 4, for the intact sample outside the shear band the fabric ellipsoid given by Φ^P preserves essentially the shape initiated at the previous load stage with its major and minor axis horizontal and its intermediate axis vertical. Moreover the data do not differ significantly from the results given by Φ, as shown in Tables 8.7 and 8.10. The intact sample that contains part of the shear band shows a 30° deviation from the horizontal plane given by V_1 which is in accordance with Figure 8.47a but again this deviation is not completely captured by the V_1^P orientation, which is within 5° of the horizontal plane. The reconstituted soil shows a preferential deviation of 20° from the horizontal plane given by V_1 as also illustrated in Figure 8.48a and V_1^P deviates only 6°, as shown in Tables 8.10 and 8.17.

The significant difference shown between ϕ_{V1}^P and ϕ_{V1} for the samples at load stages 3 and 4 can be explained by the observation that the particles with larger major axis, despite being more affected by the shear band movement, still exhibit little deviation from the horizontal plane (Figure 8.49). This can be confirmed by investigating the deviation from the horizontal measured for the vectors V_1 and V_1^P, for the samples affected by the shear band, i.e., Ω_{PO} and $\Omega_{PO(P)}$, respectively. As presented in Table 8.18 for both intact and reconstituted samples, the effect of particles with a larger major axis (captured by Φ^P) is to attenuate this deviation as shown by the significantly lower values of $\Omega_{PO(P)}$ when compared with Ω_{PO}.

As hypothesised by Oda and Kazama (1998), the preferred orientation of particles does not coincide with the general direction of shear band as illustrated in Figure 8.57. The authors reported Ω_{PO} values of 44° and 24° measured in vertical thin sections of Toyoura sand and Ticino sand, respectively, for shear bands inclined respectively at 70° and 67° to the horizontal. Table 8.18 shows that the values of Ω_{PO} measured for the major principal fabric (for fabric tensor Φ) are also lower than the inclinations measured for the shear band, i.e., 63° and 57° for the intact and reconstituted specimens respectively, at load stage 4.

(d) Fabric descriptors

The eigenvalue based approach to assess the shape of the orientation data, as proposed by Woodcock (1977), is presented in Figure 8.58a using the Φ^P formulation. For completeness, the fabric descriptors C and K are summarised in Table 8.19. For the samples prior to loading the intact data (samples 297*) is more like a cluster shaped (K>1) while the reconstituted material (sample 291*) fabric is more girdle-like (K<1) but none of the samples deviates significantly from the K=1 line. For load stage 4 (samples 295* and 290) both materials are clusters with a strength factor of 0.05 for the intact soil and 0.08 for the reconstituted soil. For load stages 2 and 3, the shape of the fabric is not very clear as the samples scatter around the

K=1 line. The strength factor C gives the extent of the concentration of the vectors in the preferred orientation and the highest factor is associated with the reconstituted sample 289S at load stage 3 (C=0.1) while the intact sample 294n exhibits the lowest value (C=0.02).

The equivalent plot using the eigenvalues of Φ is presented in Figure 8.58b. All the distributions are clusters except sample 294n, which is in agreement with the unexpected distribution seen already in Figure 8.44f. The almost isotropic distribution of samples 293* and 295* can be confirmed, as they plot very close to the origin of the graph. The samples prior to loading (297* and 291*) all have K values of approximately 0.45 and at load stage 3 the intact samples (293*) moves towards K=1 (as the concentration around horizontal is being lost) while the reconstituted samples at the same load stage (289*) move in the opposite direction. Ng (2001) demonstrated that for a system of ellipsoids, K increases with strain, but while this trend may be replicated for the intact sample up to load stage 3 it was not observed for the reconstituted soil.

(e) Anisotropy

The intensity of the anisotropy or deviatoric fabric was calculated using two approaches. The first approach uses the difference between the principal and minor eigenvalues of the fabric tensor, i.e., $\Phi_1 - \Phi_3$; and the second approach, denoted by Φ_d takes into account the second fabric component (Φ_2) as presented in Equation 2.20. The values obtained for the fabric tensors Φ and $\Phi^P$are summarised in Table 8.20 and plots of their evolution for the four loading stages are used for a more comprehensive analysis.

Figures 8.59a and 8.59b show that the deviatoric fabric values obtained using $\Phi_1^P - \Phi_3^P$ are slightly higher than the ones obtained using Φ_d^P but the distributions are very similar. The same observation is valid for the comparison of the results using $\Phi_1 - \Phi_3$ and Φ_d, as illustrated in Figures 8.60a and 8.60b. The most significant observation is however the comparison between the anisotropy calculated using Φ and Φ^P, as discussed in the following paragraphs.

As shown in Figure 8.59b, using Φ_d^P the inherent anisotropy obtained for the reconstituted soil is 0.023 and for the intact is on average 0.022. At load stage 2 the scatter between the two samples is high and so no clear trend can be observed. At load stage 3 the anisotropy values seem to be similar to the initial ones and this is followed by a slightly decrease up to load stage 4. Both samples affected by the shear plane (293S and 295L, see Table 8.20) show higher anisotropies when compared to the samples away from the shear band at equivalent load stages. For the reconstituted soil, the anisotropy seems to reach its maximum value at load stage 3 and to decrease slightly towards the final stage of shearing.

A different trend in the evolution can be observed in 8.60b when Φ_d is used. The inherent anisotropy is still similar for the intact and reconstituted soil, being on average 0.11. Small variation is observed for the intact soil from load stage 0 to load stage 2; from load stage 2 on, two main trends can be observed. For the samples not affected by the shear band (293 and 295ph, see Table 8.20), the anisotropy decreases considerably until the final stage of shearing. However, for the two samples that contain part of the shear band (293S and 295L), the anisotropy does not seem to vary significantly from its initial value. This observation is in accordance with the rose diagrams for sample 293 and 293S. Figure 8.45a shows an almost uniform angular distribution and so $\Phi_d = 0.038$, while Figure 8.45b shows a strongly preferred orientation of the vectors and so $\Phi_d = 0.123$. Also the almost isotropic particle orientation can be confirmed by the proximity of the ϕ distribution to the isotropic case as presented in Figure 8.52. Similarly, sample 295 has $\Phi_d = 0.016$ and the sample within the shear band has $\Phi_d = 0.104$. For the reconstituted soil the anisotropy remains high thoughtout all the stages, which is in agreement with the rose diagrams that show a strong concentration of the particle orientation along the horizontal. Also the ϕ distributions presented in Figures 8.54 to 8.56 show that the divergences from the isotropic case do not vary significantly throughout the three stages of loading.

Based on photoelastic biaxial experiments on samples of elongated rods with aspect ratio 1.4 (see Chapter 2), Oda et al. (1985) have reported an inherent anisotropy of $\Phi_1/\Phi_2 = 1.3$ which tend to decrease slightly with axial deformation, i.e., at the end of compression the anisotropy were of $\Phi_1/\Phi_2 = 1.2$ (for $\theta = 0°$) and $\Phi_1/\Phi_2 = 1.1$ (for $\theta = 60°$). Those values are higher when compared with the anisotropy obtained in this study, as shown in Table 8.20, the large aspect ratio of the rods is likely to be responsible for this difference.

(f) Summary and discussion

The distribution of the particle orientations for the intact soil showed a significant concentration around the horizontal plane, i.e., perpendicular to the direction of deposition as would be expected given that no evident dip was observed in the soil strata and there were no obvious depositional features such as cross-bedding. A similar trend was observed for the reconstituted samples. The results also indicated similar inherent anisotropy for both materials.

This initial preferred orientation of the particle orientation vectors is captured by both the fabric tensor formulations Φ and Φ^P. However, following the onset of dilation (load stage 2) the divergence between the results from both formulations becomes clear for the intact soil. Formulation Φ indicates a decrease in the soil anisotropy as a result of the increase in the number of vectors orientated along more

vertical directions, which is in accordance with the observations from the rose diagrams for load stages 3 and 4 for the samples outside the shear band. Formulation Φ^P, however, indicates an almost constant concentration of the vectors in the horizontal plane (with a greater contribution from the larger particles) and consequently no major change in the anisotropy. For the reconstituted soil, the agreement between both fabric tensor formulations is better and it confirms which was observed in the rose diagrams and in the histograms of the ϕ angle that the initial horizontal concentration of the vectors is preserved throughout shearing.

The differences observed between Φ or Φ^P for the intact soil are believed to be related to the small fragments that become detached from fractured grains as the soil dilates, as discussed in Section 7.2 (illustrated in Figures 7.5c and 7.5d, and shown in the PSD curves, Figure 7.3). The small fragments will have random orientations which explains the rather isotropic distribution at load stage 3. This also explains the major differences observed between the intact and the reconstituted soil because for the reconstituted material the small fragments were already individual particles at the time of the sample preparation and so they were orientated along the horizontal during the sample preparation along with the larger grains. Based on these observations, it can be concluded that the fabric tensor Φ^P, because of its ability to capture the effect that larger particles have in the soil anisotropy, provides a more complete description of the soil fabric when compared to the Φ formulation.

Some results found in the literature are presented here. Hasan and Alshibli (2010) have examined the distribution of the particle orientations for a pluviated sand under plain strain compression (with a final axial strain of 5%), also based on micro-CT data, and reported a preferred angle of 60-80° to the z-axis inside the shear band and a preferred angle with the z-axis of 30-60° outside the shear band. Comparing with the results obtained here, the major principal fabric of the intact sample at load stage 4, $\phi_{V1} = 60°$ for the samples that included the shear band and $\phi_{V1} = 85°$ outside the shear band; similarly for the reconstituted sample at load stage 3, $\phi_{V1} = 65°$ for the sample that included the shear band and $\phi_{V1} = 83°$ outside the shear band. While there seems to be a good agreement for the orientation inside the shear band, more significant differences can be observed for orientation outside the shear band between the study presented here and analysis carried out by Hasan and Alshibli. Also worth mentioning is the study on the orientation of clay particles after isotropic consolidation reported by Hattab and Fleureau (2010), where the angular plot presented in the horizontal plane showed very few particles orientated between 45-90° and 225-270° for a case where an isotropic distribution would be expected, at least in the case of a coarse grained material. Both Oda et al. (1985) and Arthur and Menzies (1972) have suggested that for a natural sand the inherent anisotropy could easily be destroyed under triaxial stress conditions, but this is contrary to what has been observed, i.e., the persistence of fabric even after a critical state

has apparently been reached. DEM analyses of irregularly shaped particles carried out by Nougier-Lehon et al. (2005) have shown that the fabric effects persist long after the volume and stresses were constant, which is in agrement to what has been observed here.

8.3.2 Contact normals

Statistical information relative to the number and characteristics of the contacts in each sample is presented in Table 8.21. As discussed in Chapter 6, in many cases the contact surface between two particles may be formed by a number of non-connecting regions. It can be observed that despite the tendency for the size of the contacts to decrease as the shearing deformation progresses, the proportion of the total number of particle-particle contacts relative to the total number of regions remains essentially constant (of approximately 70%). The evolution of the percentage of point contacts relative to the total number of contacts (particle-particle) in each sample at the four load stages is presented in Figure 8.61. As can be observed, the number of point contacts is very small compared with the overall number of contacts. Both the intact and the reconstituted materials exhibit an increase in the number of point contacts as dilation progresses, up to load stage 3, followed by a slight decrease. The percentage of point contacts for the reconstituted soil is significantly higher, compared to the intact soil, for all stages.

The size of the contacts was already investigated by means of the parameter CI and it has been shown that the long contacts typically associated with an interlocked fabric are destroyed once the dilation starts. Figure 8.62 compares the frequency distribution of the contact size between an intact and a reconstituted sample prior to loading. While for reconstituted samples high frequencies are associated with contacts with sizes less than 200 voxels, the intact samples show high frequencies for contact size up to 600 voxels. This confirms the significantly larger contacts present in the intact locked soil.

(a) Rose diagrams

Figures 8.63 to 8.69 show the angular distribution of the contact normals, using the orientation vector of each individual contact region, in the xz-plane, yz-plane and xy-plane. For all plots a small bias can be observed along the x, y and z axes. This is related to the 6-connectivity algorithm used to detect the contacts (see Chapter 6), which preferentially identifies features located along the three principal axes. Figures 8.63a to 8.63d show the distribution of the vectors in the vertical planes for the two intact samples prior to loading (297ph and 297L). In the plots relative to the vertical planes, the z-axis is always shown in the vertical axis and x and y

in the horizontal. The distributions are essentially uniform and do not show any clear preferred orientation. Referring to Figures 8.63e to 8.63f the contact normal distribution effectively shows axi-symmetry relative to the z-axis. The angular distributions at load stage 2 for the intact samples (294ph and 294n), presented in Figures 8.64a to 8.64f do not show any significant evolution from the previous stage.

Considerable changes can be observed for the intact samples at the load stage 3 (293 and 293S). As illustrated in Figures 8.65a, 8.65c and 8.65e sample 293 shows a strong concentration along the vertical axis and axi-symmetry in the horizontal plane (i.e., an almost circular plot in the xy-plane). The distributions of the contact normal orientation are affected by the shear plane as shown in Figures 8.65b, 8.65d and 8.65f. At load stage 4, the intact samples (295ph and 295L) show similar patterns to the previous stage, as illustrated in Figures 8.66a to 8.66f.

The data for the reconstituted samples prior to loading generates similar distributions to those observed in the equivalent intact samples. As illustrated in Figures 8.67a to 8.67f, the distributions are almost uniform in the three planes for samples 291ph and 291L. Just as was the case for the intact soil, at load stage 3 (289 and 289S) the contact normal distribution shows a strong concentration along the z-axis, as presented in Figures 8.68a to 8.68f. Sample 289 seems to be affected by the shear plane (as already observed for the particle orientation analysis) as shown by the slight deviation from the z-axis and no axi-symmetry in the horizontal plane. At load stage 4 (290) the angular distribution also shows the effect of the shear band (Figures 8.69a to 8.69c).

In order to investigate the influence of the contact size on the preferred orientation of the contact normal distribution rose diagrams using a single normal vector per particle-particle contact are shown in Figures 8.70 to 8.73 for the xy- and yz-planes, where the shading represents the size of the contacts (measured in voxels). Figure 8.70 is for samples 297L, 291ph and 294ph, and no clear correlation between the normal vector orientation and the contact size can be observed. Figure 8.71 is for the sample outside the shear band for load stages 3 and 4 (293, 289S and 295ph), and a tendency of the larger contacts (brighter shading) to become orientated along the vertical direction, coincident with the major principal stress direction, can be observed. In Figure 8.72 for the samples inside the shear band (293S, 289 and 295L), the larger contacts appear to give a major contribution to the preferred orientation, i.e., a small deviation from the vertical direction as a result of the buckling of the force chains. A similar observation applies to sample 290 in Figure 8.73, also affected by the shear band. No major differences in the shape of the angular plots were found between the distribution using one normal vector per region (Figures 8.63 to 8.69) or just one single normal per particle-particle contact (Figures 8.70 to 8.73).

(b) Frequency distribution of ϕ

The distribution of the polar angle ϕ, i.e., the angle between the normal to each contact and the z-axis, is illustrated in Figures 8.74 to 8.69. Figure 8.74 is for the two intact samples prior to loading, compared to the distribution of an isotropic system. There is good agreement between the curves for both samples. The deviation from the isotropic curve can be attributed to the 6-connectivity voxels used for the contact identification algorithm. A similar trend can be observed for the intact soil at load stage 2 as shown in Figure 8.75. The distribution for the two samples at load stage 3, changes significantly as the contact normals tend to become concentrated mainly in the vertical direction in a region of approximately 0.52rad (30°) from the z-axis (Figure 8.76). This preferred orientation along the vertical direction is also observed for load stage 4 (Figure 8.77).

Referring to the reconstituted samples, the two samples prior to loading (Figure 8.78) show a distribution that is very close to the isotropic case. At load stage 3, just as was the case for the intact soil, the contact normals show a strong concentration along the vertical direction as shown in Figure 8.79. Finally, at load stage 4, the vertical preferred orientation persists but is less pronounced (Figure 8.80). These observations are in agreement with the rose diagrams.

(c) Fabric tensor

The fabric tensor of the contact normal orientations, using one normal vector per region (Φ), was calculated based on Equation 2.11 and is presented, together with the corresponding eigenvalues and eigenvectors, in Tables 8.22 to 8.28, for all the samples. The ϕ and θ angles associated with the vector representing the major orientation of the fabric tensor (V_1), are also presented for each sample. At load stages 0 and 2, there is no clear orientation of the principal fabric as the ϕ value varies between 27° and 43° to the z-axis for both intact and reconstituted samples.

Both the intact samples at load stage 3 have contact normal sthat are mainly orientated in the vertical direction with $\phi_{V1} = 8°$ for sample 293 and $\phi_{V1} = 18°$ for sample 293S which includes part of the shear band. In a similar way, at load stage 4, both samples show a preferred vertical orientation. The sample outside the shear band (295ph) has $\phi_{V1} = 1°$ and shows an almost perfect axi-symmetry relatively to z axis, noting that the S_2 and S_3 values are very close and much lower than the value given by S_1. The sample that includes part of the shear band (295L) shows $\phi_{V1} = 15°$ and no axi-symmetry is observed in the horizontal plane, given the significant difference between S_2 and S_3.

The reconstituted samples at load stage 3 show the major principal fabric preferentially vertically orientated with sample 289S having $\phi_{V1} = 4°$ and showing axi-

symmetry relative to the z-axis, i.e., the difference between S_2 and S_3 is very small, while sample 289 shows $\phi_{V1} = 14°$ and no axi-symmetry in the xy-plane. These observations confirm the hypothesis that sample 289 is affected by the shear band. Finally, sample 290 at load stage 4 has $\phi_{V1} = 22°$ and does not have an axi-symmetric distribution in the horizontal plane, which also confirms the effect of the shear band in the contact normal orientations.

Large contacts are better able to transmit moments and provide greater rotational resistance. Based on the importance of the contact size for load transmission, three alternative fabric tensors for the contact normals were taken into consideration. In the first case, just one vector was used for each particle-particle contact (Φ^{p-p}), and the resultant vector was given by the major eigenvector of the set of vectors from each region in the contact. For the second case, a greater contribution to the fabric tensor given by the larger contacts was considered. In this formulation, similarly to the previous case, just one vector per particle-particle contact was used and in addition each vector was weighted by a size factor that represents the size of the corresponding particle-particle contact, designated by Φ^{w}. The size factor was given by the ratio of the contact size in voxels divided by the sum of the size of all contacts. For the third case the same size factor was used in the fabric tensor calculations, but in this case just the 500 largest contacts were used ($\Phi^{w}_{(500)}$).

Tables 8.29 and 8.30 present the comparison of these three fabric tensors with the fabric tensor calculated using one vector for each region (Φ) in terms of the three eigenvalues, the principal eigenvector (V_1) and its corresponding angle to the z-axis (ϕ_{V1}). Comparing the results obtained using Φ and Φ^{p-p}, a significant difference can be observed in the orientation of the principal fabric for the intact samples 297ph, 297L, 294ph and 294n and in the case of sample 297ph there is also a difference in the anisotropy, as shown in Table 8.21 and discussed later in this section. As the shearing progresses, the large contacts are destroyed in the intact soil and the fabric tensors obtained for both formulations do not differ significantly, which is in accordance with the contact index analysis. This happens despite the number of regions remaining significantly greater than the number of particle-particle contacts (Table 8.21). For the reconstituted samples, no significant change in the major principal fabric orientation can be seen, with the exception of sample 291ph for which a reorientation of approximately 8° can be observed. The difference between the two fabric tensor formulations is thought to be related to the shapes of the particle-particle contact surfaces. For example, in the case of a planar contact formed by non-connecting regions, all the regions will have the same normal vector and so the same resultant vector. Large contacts with complex shapes are likely to be formed by non-connecting regions of distinct orientations and in these cases the formulation used is more likely to affect the results.

The comparison between the results obtained using Φ^{p-p} and Φ^{w} formulations for

samples 297ph, 297L and 294n, shows that the effect of taking into account the size of the contact is to rotate V_1 to orientations closer to the horizontal plane. Therefore, it appears that the largest contacts (at the initial stages) are mainly vertical, with the normal vectors being horizontal. With the exception of sample 297L, using just the 500 largest contacts ($\Phi^{w}_{(500)}$) has no significant effect on the orientation of the major principal fabric. For the reconstituted samples, only sample 291L (which shows an exceptionally high average contact size) shows some influence on the direction of the major principal fabric when the size factor is taken into consideration. The tendency is for the vector V_1 to move away from the vertical axis and this is more pronounced when only the 500 largest contacts are used. The major result of weighting the unit contact normal vectors by the contact size is the change of the anisotropy as discussed later in the section.

Referring again to Figure 8.57, the force chains are aligned in an almost perpendicular position to the particle orientation. The relationship between the angle of the particle orientation measured from the horizontal Ω_{PO} and the angle of the contact normal orientation to the vertical ϕ_{cnO} was therefore investigated (Table 8.31). The value of the angle ϕ_{cnO} is in general slightly lower than Ω_{PO} with the exception of sample 290 for which both angles show similar values. In a situation of perpendicularity, both angles would show similar magnitudes for a 2D analysis as shown in Figure 8.57. However, the 3D case is more complex as not only the angle value but also the quadrant where the vector is located is required, and for this reason a conclusive observation could not be made.

(d) Fabric descriptors

Figure 8.81a shows the plot of the eigenvalue ratios for the shape analysis of the contact normal data and for completeness, the fabric descriptors C and K are presented in Table 8.32. Both intact and reconstituted samples at load stage 0 and 2 show uniform distributions as they plot close to the origin while the samples at load stage 3 and 4 show a cluster of data. The extent of the concentration of the vectors in the preferred orientation is given by the strength factor C and four lines of constant C can be identified to describe the load stages. The uniform distributions show very low strength factors;. a line of $C \approx 0.11$ can be identified for load stage 0 and $C \approx 0.07$ for load stage 2. The highest C factor is reached for samples at load stage 3 with $C \approx 0.42$ and the strength factor that decreases again as the samples reach the final stages of shearing, with a $C \approx 0.28$ identified at load stage 4. Sample 289S (load stage 3) exhibits the greatest degree of clustering and an almost perfect axi-symmetry given its proximity to the vertical axis of the plot. The degree of preferred orientation increases with strain from load stage 2 to load stage 3 and slightly decreases from stage 3 to stage 4. Similar observations were reported by Ng

(2001) for simulations of systems of ellipsoids under triaxial compression.

Figure 8.81b shows the plot of the fabric descriptors using the fabric tensor Φ^w and C and K are also presented in Table 8.32. When compared to Figure 8.81a the distribution remains essentially the same with the exception of the location of the intact samples at load stages 0 and 2 for which the strength factor is significantly larger than using the Φ formulation (given the large size of the contacts found in these samples). This approach has the advantage of allowing differentiation between the intact and the reconstituted samples.

(e) Anisotropy

Table 8.33 summarises the anisotropy values obtained using the eigenvalues of the fabric tensors Φ, Φ^{p-p} and Φ^w using the formulation $\Phi_1 - \Phi_3$ and Φ_d (from Equation 2.20). In the case of the intact sample 297ph, the anisotropy given by the fabric tensor Φ^{p-p} is significantly greater than the anisotropy given by the fabric tensor Φ. For the other intact samples the difference appears to be random with no clear trend observed. All the reconstituted samples show slightly higher anisotropy for the fabric tensor that uses one normal vector per region (Φ). The anisotropy associated with the fabric tensor Φ^w is generally (with exception of sample 297ph) higher than the anisotropy obtained for the fabric tensor Φ^{p-p}.

The evolution of the anisotropy (Φ_d) at the different load stages is presented in Figure 8.82a. Both intact and reconstituted samples show a similar inherent anisotropy of approximately 0.035. This value slightly decreases at load stage 2, reaching a value of approximately 0.020. The maximum anisotropy is attained at load stage 3 with a value of 0.129 for the reconstituted and intact samples including the shear band (289 and 293S) and slightly lower values of 0.083 and 0.123 for samples 293 and 289S respectively. A slight decrease is observed from load stage 3 to load stage 4 for both intact and reconstituted samples.

The evolution of the deviatoric fabric Φ_d^w (Figure 8.82b) shows greater anisotropy for load stage 0 and load stage 2 when compared with the previous plot. However, after load stage 2, the progress is similar to Φ_d which confirms that the initial contacts are destroyed after the onset of dilation. Referring to Figure 2.22b, Thornton (2000) reported $(\Phi_1 - \Phi_3)_{peak} = 0.12$ and $(\Phi_1 - \Phi_3)_{CS} = 0.085$ based on the contact normal fabric tensor (Φ) obtained from simulations using a system of spheres under axi-symmetric compression.

(f) Summary

At the initial stage, no clear preferential orientation can be found on the contact normal vector distributions. In the post-peak regime, a clear redistribution of the

contact normals can be observed, with the vectors associated with the largest contacts becoming parallel with the direction of the major principal stress. This would be expected based on the force chain theory and will contribute to provide a more anisotropic fabric. The buckling of these chains may explain the deviation from the z-axis found in the samples inside the shear band and can be related to the reduction in the number of contact normal vectors providing lateral support. Using a fabric tensor formulation that takes into consideration the size of each contact is useful to describe the inherent anisotropy of the intact soil at the initial state.

8.3.3 Branch vectors

(a) Rose diagrams

The rose diagrams of the branch vectors relative to the xz-plane, yz-plane and xy-plane are presented in Figures 8.83 to 8.87. For each bin in the rose diagram the degree of shading indicates the average length of the branch vector (in μm) the orientation of which is within that bin. Therefore, these diagrams give an indication of both the orientation of the branch vector in the sample and the average length of the branch vector in each direction. In the plots relative to the vertical planes the z-axis is always shown as the vertical axis and the x or y axes are horizontal.

Figures 8.83a, 8.83c and 8.83e are for one intact sample (297ph) prior to loading. For this sample, the distributions in the xz- and yz-planes show a small concentration of orientations around the horizontal plane for which the vectors with a greater length appear to give a more significant contribution. In addition, the distribution exhibits axi-symmetry relative to the z-axis. No major changes can be observed for the intact sample (294ph) at load stage 2 (Figures 8.83b, 8.83d and 8.83f). The intact samples at load stage 3 are presented in Figure 8.84. A concentration of the branch vectors around the z-axis can be observed, and the vectors of higher magnitude tend to be preferentially orientated vertically when compared to the branch vectors of lower magnitude. This trend is not clear for sample 293S due to the influence of the shear band movement. Similar observations can be made for the intact sample at load stage 4, as shown in Figure 8.85. The sample that is not affected by the shear band shows a stronger concentration of the larger branch vectors around the vertical while the effect of the shear band in sample 295L seems to be to rotate the shorter length vectors to take up more horizontal positions.

As shown in Figures 8.86a, 8.86c and 8.86e for the reconstituted soil prior to loading, the branch vector distribution is similar to the intact soil, i.e., there is a strong concentration of vectors distributed around the horizontal plane, and these vectors tend to have larger lengths (brighter shading). The distributions for the reconstituted samples at load stage 3 are presented in Figures 8.86a, 8.86c and 8.86e for

sample 289 and in Figures 8.87b, 8.87d and 8.87f for sample 289S. There seems to be a slight concentration of vectors around the z-axis for both samples despite the scattering. Finally, at load stage 4, the data presented in Figures 8.87b, 8.87d and 8.87f for the reconstituted sample 290, no clear preferred orientation or trend can be observed.

(b) Frequency distribution of ϕ

The distribution of the polar angle ϕ between each branch vector and the z-axis is illustrated in Figures 8.88 to 8.94. Figure 8.88 is for the two intact samples at load stage 0, comparing with the distribution that would be observed for an isotropic system. There is a notable difference between the curves of both samples. Sample 297ph shows a distribution that is very close to the isotropic case, while in sample 297L there are fewer vectors that are orientated close to the vertical direction. This can be related to the difference also observed in Figure 8.50 in which sample 297ph shows a greater concentration of particle orientations in the horizontal direction when compared with sample 297L. For load stage 2, the curves of the two samples show very good agreement between each other and the plots do not show significant divergence from the isotropic curve (Figure 8.89). The distribution for the two samples at load stage 3, show a decrease in the number of vectors with horizontal orientations (Figure 8.90). This pattern is also observed for load stage 4, as presented Figure 8.91 in particular for the sample not affected by the shear band. For both samples 293S and 295L that contain part of the shear plane this trend is attenuated. As presented in Figure 8.92, 8.93 and 8.94, the reconstituted samples show distributions very close to the isotropic case with a slight concentration around the horizontal direction for the samples prior to loading.

(c) Fabric tensor

The fabric tensor for the branch vector was calculated based on Equation 2.11 and the corresponding eigenvalues and eigenvectors are presented in Tables 8.34 to 8.40, for all samples. The ϕ and θ angles calculated for the major eigenvector (V_1), are also presented for each sample. The intact sample prior to loading shows a preferred orientation that is almost horizontal (within 20° of the horizontal plane). There is no significant change at load stage 2 and the preferred orientation is still horizontal with a 10° deviation. At load stage 3 the principal fabric becomes essentially vertical with $\phi_{V1} = 6°$ for the sample outside the shear band, and $\phi_{V1} = 26°$ for sample 293S which contained the shear zone. For load stage 4, the sample outside the shear band preserves the preferential vertical orientation with $\phi_{V1} = 3°$ while the effect of the shear band is to rotate the principal fabric further to a more horizontal position $\phi_{V1} = 76°$.

For the reconstituted samples prior to loading the principal fabric is essentially horizontal as presented in Table 8.38. For load stage 3, sample 289 shows a preferred orientation closer to the vertical with $\phi_{V1} = 27°$ while sample 289S appears to be closer to the horizontal with $\phi_{V1} = 67°$ (Table 8.39). At load stage 4, the principal fabric shows a 20° deviation from the horizontal, as seen in Table 8.40

For this analysis, all the contacts were used. The comparisons with the fabric tensors calculated using just the contacts with more than 6 voxels, as was the case for the analysis of the contact normal, show no significant differences. This can be justified by the small number of point contacts for all samples, as can be seen in Table 8.21.

(d) Fabric descriptors

The shape of the fabric ellipsoid of the branch vectors was investigated by plotting the eigenvalue ratios, as presented in Figure 8.95. For completeness, the fabric descriptors C and K are presented in Table 8.41. The majority of the distributions of the branch vectors are girdles (K<1). The intact samples prior to loading have $C \approx 0.11$, while the corresponding reconstituted ones show $C \approx 0.17$. The degree of preferred orientation seems to decrease with strain for the reconstituted samples but no clear trend can be observed for the intact specimens. The degree of clustering is the highest for the intact sample outside the shear band at load stage 4.

(e) Anisotropy

The intensityies of the deviator fabric using the formulations $\Phi_1 - \Phi_3$ and Φ_d (from Equation 2.20) are presented in Table 8.42 and the evolution of Φ_d at the four stages of loading is presented in Figure 8.96. The reconstituted soil shows slightly higher inherent anisotropy $\Phi_d \approx 0.05$ when compared to the intact soil $\Phi_d \approx 0.03$. For the intact soil, the induced anisotropy seems to increase for the samples outside the shear band. At load stages 3 and 4, both reconstituted samples show anisotropy closer to the intact samples that contain part of the shear band.

(f) Branch vector length

The magnitude of the vectors or branch vector length (*bvl*) can be used to obtain additional information regarding the particle packings as discussed in the following paragraphs. As shown in Figure 8.97 two given particles in contact can have different *bvl* depending on how the direction of the contact relates to the orientation of the particles. The *bvl* is given by the sum of the semi-axis length of the particles along the branch vector direction assuming that the particles are touching along the direction of the branch vector. In order to investigate the relative position of

the particles in contact, a new parameter designated by *bvlratio* was calculated as follows:

$$bvlratio = bvl/(b_1/2 + b_2/2) \tag{8.1}$$

where *bvl* is the branch vector length and b_1 and b_2 the intermediate axis lengths of particles in the contact

When *bvl* is equal to 1 the particles are in contact with each other orthogonally to the intermediate axis of the particle while for values lower than *1*, the particles are forming a contact orthogonal to the direction of the particle major axis (8.97b) while for values greater than 1 the contact is orthogonal (or close to orthogonal) to the direction of the particle minor axis (8.97a). Figure 8.98a shows the plot of *bvlratio* against the size of the contact (in voxels) for one intact sample and Figure 8.98b shows a similar plot for a reconstituted sample. As can be observed in both cases, for the largest contacts, *bvlratio* takes only values lower than 1 which means that for the long contacts the particles are likely to be in contact in a direction orthogonal to its minor semi-axis length. This would be expected as referring to Figure 8.97b when the branch vector is aligned with the particle major axis the particle surface available to form contact is lower than in the case shown in Figure 8.97a.

Figure 8.99 shows the distribution of the branch vector length for all the samples. The curves for the intact soil at the initial state are located in the region of higher *bvl* values when compared to the reconstituted samples at the same stage. As shearing progresses the curves associated with the intact samples appear to move closer to those of the reconstituted soil (i.e., shifting to the left side of the plot). The average *bvl* values presented for each sample confirm the previous observation, i.e., the intact sample 297ph has a $bvl = 276\mu m$ while for example the reconstituted sample 289S has a $bvl = 213\mu m$.

The plots of the median particle diameter (d_{50}) against *bvl* are presented in Figure 8.101 for both the intact and the reconstituted soil. As shown in Figure 8.101a, the intact samples show a good correlation between d_{50} and *bvl*, i.e., *bvl* increases with the particle size. For the reconstituted samples (Figure 8.101b) no clear trend can be observed which may indicate that the particles tend to form contacts more randomly.

Correlations between branch vector length and a number of other parameters were investigated but no conclusive relationships were found. When the soil dilates and the grains move apart, the *bvl* parameter cannot be used to describe this phenomenon as the contacts are lost and the branch vector is no longer a branch vector. This highlights the advantage of using doublet vectors (as discussed in Chapter 2) to describe the changes in fabric for small deformations, as the change in the magnitude of doublet vectors can be related to micro-strains. The concept of nearest particle in a 3D analysis is very ambiguous and so this approach was not considered

in this study.

(g) Branch vector compared to contact normal vector

The relationship between the branch vector and the contact normal was investigated by means of the angle between the two vectors, denoted by α. The distribution of α is plotted in Figure 8.100a for the intact samples (297ph, 294ph, 293 and 295ph) and in Figure 8.100b for the reconstituted samples (291ph, 289 and 290ph). With the exception of a few cases the maximum value of α is 60° and the most frequent value of α is approximately 20° for both intact and reconstituted samples. No significant variation can be seen for samples at different load stages, which is in agreement with the observation made by Ng (1999) in a system of ellipsoids with different aspect ratios. Ng reported, however, a significantly narrower range of α values, i.e., a maximum value of 13° for the system with an elongation of 0.5 and 5° for the system with an elongation 0.67. This non-collinearity of the branch vectors and contact normal means that the line of action of the normal force does not pass through the particle centroid and so the contact normal force can impart a moment to the particle, which contributes to the rotational resistance at the particle contact.

Given the little information provided by the distribution plots of α, the correlation between α and the size of the contact was investigated. It has been found that, in general, α decreases with the increase of the contact size. This trend is very clear for the samples at load stage 3 as shown in the rose diagrams of angle α presented in Figure 8.102 (for the intact sample 293 and the reconstituted sample 289), where the shading illustrates the size of the contact in voxels. For the larger contacts (brighter shading) α is closer to 0° and α increases for smaller contact surfaces for both intact and reconstituted samples.

The angles of the major principal fabric of the branch vector to the vertical (ϕ_{bvO}) for the samples that contain part of the shear band are presented in Table 8.43. For comparison, the angles Ω_{PO} and ϕ_{CnO} (as defined in Sections 8.3.1 and 8.3.2, respectively) are also presented. The samples at load stage 3 (293S and 289) show similar ϕ_{bvO} values which are considerably lower when compared to the ϕ_{bvO} of the samples at load stage 4 (295L and 290). No clear correlation can be observed between ϕ_{bvO} and Ω_{PO} or between ϕ_{bvO} and ϕ_{CnO}.

(h) Summary

At the initial state, while the contact normal distributions were found to be effectively isotropic, the distribution of the branch vectors shows some concentration towards the horizontal which may be related to the initial arrangement of the particles. In a similar way to what has been observed for the contact normals, a reorientation of the branch vectors towards the direction of the major principal stress

can be observed. This is particularly evident for the intact sample at load stage 3. It is interesting to note the way the buckling of the force chains affects the branch vector distribution, the concentration towards the z-axis becoming less pronounced but no clear rotation of the principal fabric in the vertical planes (as was seen for the particle orientations and contact normals) can be observed. Instead the distribution appears to be rather uniform. While the use of the branch vectors may not be as effective as the vectors associated with the particle orientation and the contact normals to describe the evolution of the fabric with loading, the indices *bvl*, *bvlratio* and angle α have been shown to provide important information on the description of the packing of irregular particles.

8.3.4 Void orientation

(a) General information

The void analysis was carried out for six samples at load stages 0 and 3. The samples for void analysis and the corresponding samples for particle analysis, as discussed in Chapter 6, are summarised in Table 8.44, together with the number of full voids (i.e., voids not crossing the image boundary) in each sample. All the samples have the same volume and so the comparison of the number of voids in each sample gives already an idea of the difference in void size in each case, e.g., sample 293Svd has one third of number of voids in sample 291vd.

Similar to the approach used in the particle size analysis, the void size distribution (VSD) curves were calculated for $d_{effective} = b$ where b is the length of the intermediate axis of the void. The distribution is presented in Figure 8.103 together with the mean effective diameter (d_{50}) for each sample. The sieve curve of the grains is used for comparison. The VSD curve for the intact sample prior to loading (297) plots close to the sieve curve and at load stage 3 the curves tend to shift to the right as the void sizes increase. This trend is very clear for the sample containing the shear band where the voids are substantially larger (293S), while outside the shear band the increase in the size of the voids is not so significant (293). For the reconstituted soil prior to loading (291), the VSD curve shows very good agreement with the PSD from the sieve analysis and as shearing progresses there is a clear increase in the void size for both samples (289 and 289S). These observations confirm previous hypotheses from Oda and Kazama (1998) that very large voids are generated inside the shear band. In addition, they appear to indicate that the dilation is effectively concentrated in the shear band for the intact sample, while for the reconstituted soil it is more diffuse throughout the sample.

The comparison between the d_{50} for the particles and for the voids in the same samples is presented in Table 8.45. Only at load stage 0 are the voids smaller than

the particles.

(b) Rose diagrams

The rose diagrams of the void orientation show more scatter than the distributions for the particle or contact orientations. For this reason, just a few representative examples are presented in Figure 8.104 where the shading indicates the length of the void major axis. The two samples prior to loading show a strong concentration of void orientation in the horizontal direction and while for the intact sample this seems to be the preferred orientation of the voids with longer major axes (Figure 8.104a), for the reconstituted sample this trend is not so clear (Figure 8.104b). At load stage 3, as illustrated in Figures 8.104c and 8.104d, no clear preferred orientation can be observed, which means that the initial horizontal concentration has been lost.

(c) Frequency distribution of ϕ

Figure 8.105 shows the distribution of the ϕ angle of the void orientation for the intact and reconstituted samples prior to loading compared with the curve of an isotropic distribution. The curves show a preferred orientation around the horizontal in a similar way to what was observed for the particle orientation. For the intact samples at load stage 3 the distribution shows a slight concentration for values of ϕ in the range 0 to 0.52rad (30°) and some scatter closer to the horizontal direction, as illustrated in Figure 8.106. At the same stage the reconstituted soil shows a distribution close to the isotropic case, as presented in Figure 8.107.

(d) Fabric tensor

The void orientation fabric tensor was calculated based on the formulation that takes into consideration the shape of the voids in addition to the orientation vectors (Φ^{vd}) as defined in Equation 2.23 and the results for the six samples are presented in Tables 8.46, 8.47 and 8.48. The general formulation (Φ) as presented in Equation 2.11 was also used and the analysis of the eigenvalues obtained is presented below. The samples prior to loading show both the major and intermediate fabric orientated in the horizontal plane just as was the case for the particle orientations. For load stage 3 the most significant change is the rotation of the intermediate fabric to more vertical positions while the principal fabric remains essentially horizontal.

(e) Fabric descriptors

The shape of the fabric was investigated for the eigenvalues of the fabric tensors Φ^{vd} and Φ. The plot of the fabric descriptors of Φ^{vd} is shown in Figure 8.108a and

for completeness the C and K values are presented in Table 8.49. The two samples prior to loading show a similar initial cluster like shape with S_1 significantly greater than S_2 and S_3 and as shearing progresses the shape of the fabric becomes more girdle like, i.e S_2 approximates to S_1 and S_3 is significantly smaller. This coincides with the rotation of V_2 from the horizontal to close to the vertical.

The plot of the fabric descriptors of Φ is presented in Figure 8.108b, which shows a slightly different distribution when compared to Figure 8.108a. The strength factor C is greater for the samples prior to loading, which show a girdle shaped fabric with the major fabric essentially horizontal and also for sample 293, which is also of girdle type but with the major axis closer to vertical.

(f) Anisotropy

The deviatoric fabrics associated with the fabric tensors Φ^{vd} and Φ are presented in Table 8.50 and the values Φ_d^{vd} and Φ_d are plotted in Figure 8.109a and 8.109b, respectively. In both plots the samples prior to loading show similar inherent anisotropy and despite the limited data the induced anisotropy appears to decrease in the post-peak regime (with the exception of sample 293vd).

(g) Summary

The void size distribution curves showed that prior to deformation the voids are small and their size increases as deformation progresses, in particular inside the shear band. It was observed that at the beginning of the test the voids were mainly horizontally orientated, in a similar way to the grains. In the post-peak regime the distribution of the void orientations becomes more uniform and the anisotropy decreases slightly.

Based on photoelastic images of biaxial tests on rods, Oda et al. (1985) suggested that as shearing progresses the voids connect with each other to form elongated voids the longest dimensions of which grow nearly parallel to the direction of major principal stress. This cannot be verified because the watershed algorithm used to divide the void space into individual voids will, in theory, subdivide a very elongated and slim feature into more than one domain at the points where irregularities in the boundary are to be found.

The hypothesis that large voids form in the shear band was confirmed, and the different orientations of the fabric tensor Φ for the sample at load stage 3 inside and outside the shear band, $\phi_{V1} = 10°$ and $\phi_{V1} = 53°$ respectively, may be an indicator of the buckling of voids following their prior alignment parallel to the direction of the major principal stress.

This analysis has demonstrated that taking into consideration the characteristics of the voids in terms of size and orientation can provide insightful information that the scalar void ratio index alone cannot quantify. The ambiguity associated with the partitioning of the individual voids in 3D images of real soil is probably the main constraint on the use of void space analysis to characterize the fabric.

8.4 Macro-micro correlation

Various DEM studies (e.g., Rothenburg and Bathurst, 1989; Thornton, 2000; Cui and O'Sullivan, 2006) have demonstrated a correlation between the deviatoric fabric evolution and the overall stress:strain response. Ng (2009) has considered branch vector orientation and particle orientation using DEM simulations on ellipsoidal particles. The link between the macro-scale soil response and the micro-scale characteristics was investigated. Firstly, the evolution of the deviatoric stress was compared to the evolution of the deviatoric fabric and to the evolution of the angle ϕ (the orientation of the principal fabric to the z axis). Secondly, the evolution of the stiffness was compared to the scalar fabric quantities, coordination number, contact index and void ratio.

(a) Deviatoric stress compared to deviatoric fabric

To explore whether any correlation exists between the fabric tensor and macro-scale response for a real sand, the second order fabric tensors were calculated for the particle orientation, contact normal orientation, branch vector and void orientation. Just as the deviatoric stress is calculated, i.e., by the difference between the major and the minor stresses ($\sigma_1 - \sigma_3$), the deviatoric fabric was defined to be the difference between the major and the minor eigenvalues of the fabric tensor ($\Phi_1 - \Phi_3$).

Figures 8.111a and 8.111b compare the evolution of the deviatoric stress with the deviatoric fabric for the contact normal orientation (CnO) of the intact and reconstituted samples, respectively. Given the limited data for the deviatoric fabric, the scale of the axes in the plots was chosen in a way to find a possible correlation between the stress:strain curve and the deviatoric fabric values. In contrast to the data presented by Thornton (2000) for DEM simulations on isotropic samples, where the anisotropy increased with shearing, Figure 8.111a shows an initial decrease in anisotropy caused by the destruction of the inherent fabric upon shearing. While no information about the fabric at the peak deviatoric stress is available, after the initial destructuration an anisotropy is induced, and in the post-peak regime there seems to be some agreement between the stress:strain response and the evolution of the deviatoric fabric. The samples containing the shear band show higher anisotropy. It is difficult to established a correlation between deviatoric stress and deviatoric fabric

for the reconstituted samples in the post-peak regime (Figure 8.111b), although the deviatoric fabric seems to decrease with decreasing deviatoric stress.

Figures 8.112a and 8.112b show the evolution of the deviatoric fabric for the branch vector orientation (bvO), for the intact and reconstituted samples, respectively. The intact soil at early stages of shearing, shows an induced anisotropy slightly higher than the inherent anisotropy and there appears to be a correlation between the deviatoric stress and the deviatoric fabric in the post-peak regime. Lower anisotropy is seen for the sample containing the shear band. For the reconstituted soil the induced anisotropy in the post-peak regime seems to be lower than the inherent anisotropy (approximately half the initial value).

The evolution of the deviatoric fabric based on the particle orientation (PO) for the intact samples is presented in Figure 8.113a and 8.113b for the fabric tensor Φ and Φ^P, respectively, where Φ and Φ^P for the particle orientations are defined in Section 8.3.1 (note that Φ^P includes consideration of particle form). Comparing the differences between the two plots is it observed in the post-peak regime that the Φ^P gives similar anisotropy values for the samples whether they are affected or not by the shear band, while the results given by Φ seem to indicate that the material outside the shear plane has a lower anisotropy (as confirmed by Figure 8.45a). Both plots show small decreases in anisotropy in the post-peak regime. For the reconstituted samples the equivalent plots are presented in Figures 8.114a (for Φ^P) and 8.114b (for Φ). In this case the formulation used to calculate the fabric tensor does not seem to have an influence on the qualitative evolution of the deviatoric fabric, and as observed for the intact soil, in the post-peak regime both the deviatoric stress and the deviatoric fabric seem to decrease. The anisotropy given by Φ gives much higher values when compared with Φ^P.

The evolution of the deviatoric fabric due to the void orientation (vdO) is shown in Figures 8.115a and 8.115b for the intact and reconstituted samples, respectively. However, no conclusions can be drawn from the limited data available.

(b) Deviatoric stress compared to ϕ angle

For the contact normal fabric tensor, in the post-peak regime, the angle ϕ decreases towards a value of 0° for the sample extracted outside the shear band (as the principal fabric is reorientated towards the direction of the major principal stress) and for the sample affected by the shear band the deviation from the vertical axis is greater (due to buckling of the force chains). In the case of the intact soil (Figure 8.116a) some correlation can be found with the stress:strain curve for the two last stages of shearing, while for the reconstituted soil the plot shows more scatter (Figure 8.116b). A similar trend can be observed for the orientation of the branch vector

fabric tensor for the intact samples (Figure 8.117a) and for the reconstituted soil (Figure 8.117b).

The orientation of the principal fabric based on the particle orientation (using the Φ^P formulation) appears to remain essentially horizontal ($\phi = 90°$) at the four stages of deformation investigated and so no clear correlation is observed with the deviatoric stress (Figure 8.118a). In the case of the Φ formulation, the most significant deviations of the principal fabric from the horizontal are associated with the shear band (Figure 8.118b) but no correlation with the deviatoric fabric is observed. A similar trend is observed for the reconstituted soil as shown in Figures 8.119a and 8.119b for the Φ^P and Φ formulations respectively. In the case of the void orientation fabric tensor the insufficient data does not allow conclusive observations for either the intact soil (Figure 8.120a) or reconstituted soil (Figure 8.120b).

(c) Stiffness compared to scalar fabric quantities

Figure 8.121a compares the evolution of stiffness (G) with the evolution of CN for the intact soil. In the same way, Figure 8.121b presents the evolution of CI compared with the evolution of stiffness. In both plots measurable drops in CI and CN occur with the degradation of the stiffness. Plots of stiffness variation with void ratio, coordination number and contact index for the intact soil are illustrated in Figure 8.122. The variation of G with e, Figure 8.122a, shows no measurable variation in the void ratio prior to the complete stiffness degradation, i.e., the stiffness degradation appears to occur at constant void ratio, and just after the G value becomes close to zero the e value starts to increase. A similar observation can be made for the plot of G against CN in Figure 8.122b, where a very small change in CN occurs prior to the G values becoming close to zero. Referring to Figure 8.122c, the evolution of G with CI show a measurable variations in CI during stiffnes degradation. These observations indicate that stiffness is sensitive to very small changes in contacts, which is not clear from the plots of e against G or CN against G but is better illustrated by the decrease in CI as the high initial stiffness values become close to zero.

For the reconstituted soil, the comparison of the evolution of stiffness with the evolution of CN and CI is presented in Figure 8.123a and Figure 8.123b respectively. No clear trend can be observed as the soil samples exhibit similar CI and CN values prior to and following the stiffness degradation. The plot of G against e is shown in Figure 8.124a, the plot of G against CN is shown in Figure 8.124b) and Figure 8.124c illustrates the plot of G against CI. The heterogeneity of the reconstituted samples and the limited number of load stages considered for this material do not allow clear observations to be made regarding the effect of the micro-scale measures in the stiffness degradation.

(d) Summary

While earlier numerical and photoelastic studies have shown that the evolution of the anisotropy with strain calculated using the maximum and minimum eigenvalues of the second order fabric tensor (based on the contact normals) correlates closely with the stress:strain response, no such observation can be made here. Even if the fact that the limited number of load stages investigated does not allow a detailed analysis, these data seem to show that some observations from numerical simulations may not hold true for real soils.

8.5 Concluding remarks

This investigation has provided insights into the particle-particle contact geometries, not previously reported for a natural sand. As a result of the irregular and non-convex particles morphology, natural sands typically form contact surfaces with a finite area. A measure of the contact intensity that considers the contact area, rather than simply the number of contacts, has been found to provide a more complete description of both the initial fabric and the fabric evolution during shearing.

The observations from the analysis of the soil fabric are summarised in schematic diagrams illustrated in Figure 8.110. Six diagrams are presented. Figure 8.110a shows the intact soil prior to loading, the majority of the particles have horizontal orientation and similar trend is observed for the voids. Both the contact normal vectors and the branch vectors show an isotropic distribution. For the intact soil in the post-peak regime, the larger particles are essentially horizontal while the detached fragments exhibit random orientations (Figure 8.110b). At this stage the voids show an increase in size as a consequence of the dilation and their orientations are more random compared with the previous stage. Outside the shear band, the soil exhibits contact normals with a strong concentration along the vertical and the branch vectors show a slight concentration also along the vertical direction. For the same stage, the movement along the shear band causes the particles to rotate towards the direction of the shear plane (Figure 8.110c). Therefore, inside the shear band, the contact normal vectors and the branch vectors show a deviation from the vertical plane towards the direction of the shear plane. For the reconstituted soil prior to loading, the small fragments have been detached from the large particles during reconstitution and the majority of the particles, regardless their size, show an horizontal orientation (Figure 8.110d). The distribution of the branch vectors and the voids show a slight concentration along the horizontal direction while the contact normals exhibit an isotropic distribution. In the post-peak regime, the particles remain essentially horizontal outside the shear band, while the contact normals show a strong concentration along the vertical direction and a similar, yet

less pronounced, trend is observed for the branch vectors (Figure 8.110e). At the same stage, the movement caused by the shear band makes the particles to rotate towards the direction of the shear plane and the contact normal and branch vectors also tend to deviate from the vertical direction inside the shear band (Figure 8.110f).

Specimen ref.	Loading stage ref.	ε_a(%)	q/p'	ν	Sample ref.	Observations
297-int	0	-	-	1.48	297*ph* 297*L*	prior to loading
294-int	2	0.30	1.96	1.46	294*ph* 294*n*	onset of dilation
293-int	3	3.88	1.73	1.63	293 293*S*	start visible shear band 293*S* incl. shear band
295-int	4	9.00	1.38	1.67	295*ph* 295*L*	approaching CS 295*L* incl. shear band
291-rec	0	-	-	1.50	291*ph* 291*L*	prior to loading
289-rec	3	8.62	1.46	1.87	289 289*S*	start visible shear band
290-rec	4	12.5	1.46	1.70	290*ph*	approaching CS

Table 8.1: Information for the tested specimens and the associated samples that were used for morphology and fabric quantification

Sample ref.	Void ratio e_{exp}	e_{IA}	Divergence $\%e_{IA}$	Observations
297ph	0.482	0.425	+13	
297L	0.482	0.432	+12	
294ph	0.463	0.439	+5	
294n	0.463	0.430	+8	
293	0.633	0.515	+23	
293S	0.633	0.680	-7	including shear band
295ph	0.668	0.556	+20	
295L	0.668	0.665	0	including shear band
291ph	0.494	0.545	-9	
291L	0.494	0.642	+23	
289	0.868	0.637	+36	
289S	0.868	0.708	+23	
290ph	0.696	0.677	+3	

Table 8.2: Void ratio measurements

Sample ref.	N_1	N_0	CN	CN_m
297ph	0	0	10.00	9.97
297L	6	0	10.06	10.05
294ph	1	0	9.52	9.48
294n	0	0	9.60	9.60
293	5	3	7.81	7.81
293S	27	13	6.75	6.75
295ph	4	1	7.66	7.63
295L	28	22	7.51	7.45
291ph	13	11	8.32	8.28
291L	15	14	7.21	7.07
289	39	18	7.00	7.00
289S	171	166	5.81	5.81
290ph	71	66	7.00	6.80

Table 8.3: Comparison between the coordination number (CN) and the mechanical coordination number (CN_m) for all samples

Sample ref.	FT	Eigenvalues	Eigenvectors	ϕ (°)	θ (°)
297ph	$\begin{bmatrix} 0.343 & -0.008 & 0.001 \\ -0.008 & 0.337 & 0.001 \\ 0.001 & 0.001 & 0.319 \end{bmatrix}$	$S_1 = 0.349$	$V_1 = \begin{bmatrix} -0.816 \\ 0.578 \\ -0.002 \end{bmatrix}$	90	145
		$S_2 = 0.332$	$V_2 = \begin{bmatrix} 0.575 \\ 0.812 \\ 0.101 \end{bmatrix}$	84	55
		$S_3 = 0.319$	$V_3 = \begin{bmatrix} -0.059 \\ -0.081 \\ 0.995 \end{bmatrix}$	6	-126
297L	$\begin{bmatrix} 0.337 & -0.008 & -0.001 \\ -0.008 & 0.337 & -0.001 \\ -0.001 & 0.001 & 0.326 \end{bmatrix}$	$S_1 = 0.345$	$V_1 = \begin{bmatrix} -0.701 \\ 0.713 \\ 0.022 \end{bmatrix}$	89	135
		$S_2 = 0.329$	$V_2 = \begin{bmatrix} 0.626 \\ 0.631 \\ -0.458 \end{bmatrix}$	63	45
		$S_3 = 0.326$	$V_3 = \begin{bmatrix} 0.341 \\ 0.307 \\ 0.889 \end{bmatrix}$	27	42

Table 8.4: Particle orientation fabric tensor (Φ^P) for the intact samples 297ph and 297L

Sample ref.	FT	Eigenvalues	Eigenvectors	ϕ (°)	θ (°)
294ph	$\begin{bmatrix} 0.341 & -0.008 & 0.000 \\ -0.008 & 0.333 & 0.002 \\ 0.000 & 0.002 & 0.325 \end{bmatrix}$	$S_1 = 0.346$	$V_1 = \begin{bmatrix} -0.848 \\ 0.528 \\ 0.035 \end{bmatrix}$	88	148
		$S_2 = 0.329$	$V_2 = \begin{bmatrix} 0.509 \\ 0.796 \\ 0.329 \end{bmatrix}$	71	57
		$S_3 = 0.325$	$V_3 = \begin{bmatrix} -0.146 \\ -0.297 \\ 0.944 \end{bmatrix}$	19	-116
294n	$\begin{bmatrix} 0.335 & -0.001 & -0.001 \\ 0.001 & 0.336 & 0.000 \\ -0.001 & 0.000 & 0.329 \end{bmatrix}$	$S_1 = 0.337$	$V_1 = \begin{bmatrix} 0.681 \\ -0.730 \\ -0.066 \end{bmatrix}$	86	-47
		$S_2 = 0.334$	$V_2 = \begin{bmatrix} -0.724 \\ -0.684 \\ 0.092 \end{bmatrix}$	85	-137
		$S_3 = 0.329$	$V_3 = \begin{bmatrix} 0.112 \\ 0.015 \\ 0.994 \end{bmatrix}$	6	7

Table 8.5: Particle orientation fabric tensor (Φ^P) for the intact samples 294ph and 294n

Sample ref.	FT	Eigenvalues	Eigenvectors	ϕ (°)	θ (°)
293	$\begin{bmatrix} 0.330 & -0.011 & 0.001 \\ -0.011 & 0.334 & -0.001 \\ 0.001 & -0.001 & 0.335 \end{bmatrix}$	$S_1 = 0.344$	$V_1 = \begin{bmatrix} -0.633 \\ 0.760 \\ -0.143 \end{bmatrix}$	82	130
		$S_2 = 0.335$	$V_2 = \begin{bmatrix} 0.087 \\ -0.114 \\ -0.990 \end{bmatrix}$	8	-53
		$S_3 = 0.321$	$V_3 = \begin{bmatrix} 0.769 \\ 0.639 \\ -0.006 \end{bmatrix}$	90	40
293S	$\begin{bmatrix} 0.342 & -0.009 & 0.004 \\ -0.009 & 0.336 & -0.001 \\ 0.004 & -0.001 & 0.322 \end{bmatrix}$	$S_1 = 0.349$	$V_1 = \begin{bmatrix} 0.816 \\ -0.558 \\ 0.150 \end{bmatrix}$	81	-34
		$S_2 = 0.329$	$V_2 = \begin{bmatrix} -0.540 \\ -0.829 \\ -0.148 \end{bmatrix}$	81	-123
		$S_3 = 0.321$	$V_3 = \begin{bmatrix} -0.207 \\ -0.040 \\ 0.978 \end{bmatrix}$	12	-169

Table 8.6: Particle orientation fabric tensor (Φ^P) for the intact samples 293 and 293S

Sample ref.	FT	Eigenvalues	Eigenvectors	ϕ (°)	θ (°)
		$S_1 = 0.341$	$V_1 = \begin{bmatrix} 0.635 \\ -0.770 \\ 0.063 \end{bmatrix}$	86	-50
295ph	$\begin{bmatrix} 0.333 & -0.007 & 0.001 \\ -0.007 & 0.336 & 0.000 \\ 0.001 & 0.000 & 0.332 \end{bmatrix}$	$S_2 = 0.332$	$V_2 = \begin{bmatrix} 0.027 \\ 0.103 \\ 0.994 \end{bmatrix}$	6	76
		$S_3 = 0.327$	$V_3 = \begin{bmatrix} 0.772 \\ 0.630 \\ -0.086 \end{bmatrix}$	85	39
		$S_1 = 0.343$	$V_1 = \begin{bmatrix} -0.780 \\ 0.620 \\ 0.089 \end{bmatrix}$	85	142
295L	$\begin{bmatrix} 0.338 & -0.006 & -0.003 \\ -0.006 & 0.336 & -0.001 \\ -0.003 & -0.001 & 0.326 \end{bmatrix}$	$S_2 = 0.332$	$V_2 = \begin{bmatrix} 0.559 \\ 0.754 \\ -0.345 \end{bmatrix}$	70	53
		$S_3 = 0.325$	$V_3 = \begin{bmatrix} 0.281 \\ 0.219 \\ 0.934 \end{bmatrix}$	21	38

Table 8.7: Particle orientation fabric tensor (Φ^P) for the intact samples 295ph and 295L

Sample ref.	FT	Eigenvalues	Eigenvectors	ϕ (°)	θ (°)
		$S_1 = 0.346$	$V_1 = \begin{bmatrix} -0.805 \\ 0.593 \\ 0.02 \end{bmatrix}$	89	144
291ph	$\begin{bmatrix} 0.342 & -0.005 & -0.001 \\ -0.005 & 0.339 & -0.001 \\ -0.001 & -0.001 & 0.320 \end{bmatrix}$	$S_2 = 0.335$	$V_2 = \begin{bmatrix} 0.591 \\ 0.803 \\ -0.077 \end{bmatrix}$	86	54
		$S_3 = 0.319$	$V_3 = \begin{bmatrix} 0.062 \\ 0.051 \\ 0.997 \end{bmatrix}$	5	39
		$S_1 = 0.345$	$V_1 = \begin{bmatrix} -0.702 \\ 0.712 \\ -0.013 \end{bmatrix}$	89	135
291L	$\begin{bmatrix} 0.340 & -0.004 & 0.001 \\ -0.004 & 0.340 & 0.000 \\ 0.001 & 0.000 & 0.319 \end{bmatrix}$	$S_2 = 0.336$	$V_2 = \begin{bmatrix} 0.711 \\ 0.702 \\ 0.051 \end{bmatrix}$	87	45
		$S_3 = 0.319$	$V_3 = \begin{bmatrix} -0.046 \\ -0.026 \\ 0.999 \end{bmatrix}$	3	-150

Table 8.8: Particle orientation fabric tensor (Φ^P) for the reconstituted samples 291ph and 291L

Sample ref.	FT	Eigenvalues	Eigenvectors	ϕ (°)	θ (°)
		$S_1 = 0.346$	$V_1 = \begin{bmatrix} -0.733 \\ 0.680 \\ 0.025 \end{bmatrix}$	89	66
289	$\begin{bmatrix} 0.341 & -0.009 & 0.002 \\ 0.008 & 0.339 & 0.003 \\ 0.002 & 0.003 & 0.320 \end{bmatrix}$	$S_2 = 0.329$	$V_2 = \begin{bmatrix} 0.656 \\ 0.697 \\ 0.289 \end{bmatrix}$	73	-23
		$S_3 = 0.325$	$V_3 = \begin{bmatrix} -0.179 \\ -0.228 \\ 0.957 \end{bmatrix}$	17	-128
		$S_1 = 0.337$	$V_1 = \begin{bmatrix} -0.835 \\ 0.549 \\ -0.028 \end{bmatrix}$	88	147
289S	$\begin{bmatrix} 0.345 & -0.007 & 0.000 \\ -0.007 & 0.339 & -0.001 \\ 0.000 & -0.001 & 0.317 \end{bmatrix}$	$S_2 = 0.334$	$V_2 = \begin{bmatrix} 0.550 \\ 0.835 \\ -0.033 \end{bmatrix}$	88	57
		$S_3 = 0.329$	$V_3 = \begin{bmatrix} -0.3005 \\ 0.043 \\ 0.999 \end{bmatrix}$	2	97

Table 8.9: Particle orientation fabric tensor (Φ^P) for the reconstituted samples 289 and 289S

Sample ref.	FT	Eigenvalues	Eigenvectors	ϕ (°)	θ (°)
		$S_1 = 0.337$	$V_1 = \begin{bmatrix} 0.853 \\ -0.510 \\ -0.113 \end{bmatrix}$	84	-31
290ph	$\begin{bmatrix} 0.343 & -0.008 & -0.003 \\ & 0.335 & 0.001 \\ & & 0.321 \end{bmatrix}$	$S_2 = 0.334$	$V_2 = \begin{bmatrix} -0.509 \\ -0.860 \\ 0.036 \end{bmatrix}$	88	59
		$S_3 = 0.329$	$V_3 = \begin{bmatrix} 0.116 \\ -0.027 \\ 0.993 \end{bmatrix}$	7	-13

Table 8.10: Particle orientation fabric tensor (Φ^P) for the reconstituted sample 290

Sample ref.	FT	Eigenvalues	Eigenvectors	ϕ (°)	θ (°)
297ph	$\begin{bmatrix} 0.376 & 0.023 & 0.009 \\ 0.023 & 0.357 & 0.028 \\ 0.009 & 0.028 & 0.266 \end{bmatrix}$	$S_1 = 0.396$	$V_1 = \begin{bmatrix} -0.776 \\ 0.602 \\ -0.187 \end{bmatrix}$	79	-142
		$S_2 = 0.345$	$V_2 = \begin{bmatrix} -0.630 \\ 0.751 \\ 0.197 \end{bmatrix}$	79	130
		$S_3 = 0.258$	$V_3 = \begin{bmatrix} -0.022 \\ -0.271 \\ 0.962 \end{bmatrix}$	16	-95
297L	$\begin{bmatrix} 0.342 & 0.000 & -0.018 \\ 0.000 & 0.357 & -0.036 \\ -0.018 & 0.036 & 0.301 \end{bmatrix}$	$S_1 = 0.376$	$V_1 = \begin{bmatrix} -0.237 \\ -0.856 \\ 0.460 \end{bmatrix}$	63	-105
		$S_2 = 0.345$	$V_2 = \begin{bmatrix} -0.940 \\ 0.322 \\ 0.116 \end{bmatrix}$	83	161
		$S_3 = 0.279$	$V_3 = \begin{bmatrix} 0.247 \\ 0.405 \\ 0.880 \end{bmatrix}$	28	59

Table 8.11: Particle orientation fabric tensor (Φ) for the intact samples 297ph and 297L

Sample ref.	FT	Eigenvalues	Eigenvectors	ϕ (°)	θ (°)
294ph	$\begin{bmatrix} 0.363 & -0.013 & -0.014 \\ -0.013 & 0.350 & 0.009 \\ -0.014 & 0.009 & 0.287 \end{bmatrix}$	$S_1 = 0.375$	$V_1 = \begin{bmatrix} 0.837 \\ -0.513 \\ -0.189 \end{bmatrix}$	79	-32
		$S_2 = 0.342$	$V_2 = \begin{bmatrix} -0.523 \\ -0.852 \\ -0.004 \end{bmatrix}$	90	-122
		$S_3 = 0.283$	$V_3 = \begin{bmatrix} -0.159 \\ -0.103 \\ 0.982 \end{bmatrix}$	11	-33
294n	$\begin{bmatrix} 0.330 & -0.062 & -0.007 \\ -0.062 & 0.356 & 0.018 \\ -0.007 & 0.018 & 0.314 \end{bmatrix}$	$S_1 = 0.409$	$V_1 = \begin{bmatrix} -0.612 \\ 0.769 \\ 0.187 \end{bmatrix}$	79	129
		$S_2 = 0.311$	$V_2 = \begin{bmatrix} -0.251 \\ 0.036 \\ -0.967 \end{bmatrix}$	15	172
		$S_3 = 0.279$	$V_3 = \begin{bmatrix} 0.750 \\ 0.639 \\ -0.171 \end{bmatrix}$	80	40

Table 8.12: Particle orientation fabric tensor (Φ) for the intact samples 294ph and 294n

Sample ref.	FT	Eigenvalues	Eigenvectors	ϕ (°)	θ (°)
		$S_1 = 0.355$	$V_1 = \begin{bmatrix} 0.341 \\ 0.922 \\ 0.184 \end{bmatrix}$	79	70
293	$\begin{bmatrix} 0.316 & 0.014 & 0.002 \\ 0.014 & 0.349 & 0.003 \\ 0.002 & 0.003 & 0.335 \end{bmatrix}$	$S_2 = 0.334$	$V_2 = \begin{bmatrix} 0.067 \\ 0.183 \\ -0.983 \end{bmatrix}$	11	79
		$S_3 = 0.311$	$V_3 = \begin{bmatrix} 0.939 \\ -0.342 \\ -0.030 \end{bmatrix}$	88	-20
		$S_1 = 0.405$	$V_1 = \begin{bmatrix} 0.867 \\ 0.318 \\ 0.383 \end{bmatrix}$	67	20
293S	$\begin{bmatrix} 0.375 & 0.020 & 0.050 \\ 0.020 & 0.340 & 0.008 \\ 0.050 & 0.008 & 0.285 \end{bmatrix}$	$S_2 = 0.333$	$V_2 = \begin{bmatrix} 0.283 \\ -0.948 \\ 0.145 \end{bmatrix}$	82	-73
		$S_3 = 0.263$	$V_3 = \begin{bmatrix} -0.410 \\ 0.017 \\ 0.912 \end{bmatrix}$	24	178

Table 8.13: Particle orientation fabric tensor (Φ) for the intact samples 293 and 293S

Sample ref.	FT	Eigenvalues	Eigenvectors	ϕ (°)	θ (°)
		$S_1 = 0.339$	$V_1 = \begin{bmatrix} -0.826 \\ 0.558 \\ 0.080 \end{bmatrix}$	85	146
295ph	$\begin{bmatrix} 0.334 & -0.007 & -0.003 \\ -0.007 & 0.329 & -0.004 \\ -0.003 & -0.004 & 0.337 \end{bmatrix}$	$S_2 = 0.338$	$V_2 = \begin{bmatrix} -0.110 \\ -0.299 \\ 0.948 \end{bmatrix}$	19	-110
		$S_3 = 0.323$	$V_3 = \begin{bmatrix} 0.553 \\ 0.774 \\ 0.309 \end{bmatrix}$	72	54
		$S_1 = 0.387$	$V_1 = \begin{bmatrix} 0.791 \\ -0.350 \\ -0.503 \end{bmatrix}$	60	-24
295L	$\begin{bmatrix} 0.350 & -0.010 & -0.051 \\ -0.010 & 0.351 & 0.009 \\ -0.051 & 0.009 & 0.300 \end{bmatrix}$	$S_2 = 0.346$	$V_2 = \begin{bmatrix} -0.313 \\ -0.936 \\ 0.160 \end{bmatrix}$	81	-108
		$S_3 = 0.268$	$V_3 = \begin{bmatrix} 0.526 \\ -0.031 \\ 0.850 \end{bmatrix}$	32	-3

Table 8.14: Particle orientation fabric tensor (Φ) for the intact samples 295ph and 295L

Sample ref.	FT	Eigenvalues	Eigenvectors	ϕ (°)	θ (°)
		$S_1 = 0.401$	$V_1 = \begin{bmatrix} -0.237 \\ 0.971 \\ -0.030 \end{bmatrix}$	98	104
291ph	$\begin{bmatrix} 0.348 & -0.013 & -0.014 \\ -0.013 & 0.398 & -0.008 \\ -0.014 & -0.008 & 0.255 \end{bmatrix}$	$S_2 = 0.347$	$V_2 = \begin{bmatrix} 0.9591 \\ 0.229 \\ -0166 \end{bmatrix}$	80	13
		$S_3 = 0.252$	$V_3 = \begin{bmatrix} 0.154 \\ 0.068 \\ 0.986 \end{bmatrix}$	10	24
		$S_1 = 0.385$	$V_1 = \begin{bmatrix} -0.397 \\ 0.917 \\ 0.046 \end{bmatrix}$	87	113
291L	$\begin{bmatrix} 0.346 & -0.016 & -0.016 \\ -0.016 & 0.378 & -0.002 \\ -0.016 & -0.002 & 0.276 \end{bmatrix}$	$S_2 = 0.343$	$V_2 = \begin{bmatrix} 0.890 \\ 0.396 \\ -0.226 \end{bmatrix}$	77	24
		$S_3 = 0.272$	$V_3 = \begin{bmatrix} 0.225 \\ 0.048 \\ 0.973 \end{bmatrix}$	13	12

Table 8.15: Particle orientation fabric tensor (Φ) for the reconstituted samples 291ph and 291L

Sample ref.	FT	Eigenvalues	Eigenvectors	ϕ (°)	θ (°)
		$S_1 = 0.398$	$V_1 = \begin{bmatrix} -0.361 \\ 0.828 \\ -0.430 \end{bmatrix}$	65	-114
289	$\begin{bmatrix} 0.356 & 0.008 & 0.020 \\ 0.008 & 0.367 & 0.054 \\ 0.020 & 0.054 & 0.278 \end{bmatrix}$	$S_2 = 0.352$	$V_2 = \begin{bmatrix} -0.922 \\ 0.385 \\ 0.032 \end{bmatrix}$	88	157
		$S_3 = 0.251$	$V_3 = \begin{bmatrix} -0.139 \\ -0.408 \\ 0.902 \end{bmatrix}$	26	-109
		$S_1 = 0.386$	$V_1 = \begin{bmatrix} -0.265 \\ -0.957 \\ -0.118 \end{bmatrix}$	83	-106
289S	$\begin{bmatrix} 0.363 & 0.005 & -0.011 \\ 0.005 & 0.383 & -0.013 \\ -0.011 & -0.013 & 0.253 \end{bmatrix}$	$S_2 = 0.363$	$V_2 = \begin{bmatrix} -0.959 \\ 0.274 \\ 0.065 \end{bmatrix}$	86	164
		$S_3 = 0.251$	$V_3 = \begin{bmatrix} 0.095 \\ 0.096 \\ 0.991 \end{bmatrix}$	8	45

Table 8.16: Particle orientation fabric tensor (Φ) for the reconstituted samples 289 and 289S

Sample ref.	FT	Eigenvalues	Eigenvectors	ϕ (°)	θ (°)
		$S_1 = 0.387$	$V_1 = \begin{bmatrix} 0.777 \\ -0.532 \\ -0.336 \end{bmatrix}$	70	-34
290ph	$\begin{bmatrix} 0.366 & -0.008 & -0.003 \\ -0.008 & 0.335 & 0.020 \\ -0.003 & 0.020 & 0.321 \end{bmatrix}$	$S_2 = 0.357$	$V_2 = \begin{bmatrix} -0.554 \\ -0.832 \\ 0.034 \end{bmatrix}$	88	-124
		$S_3 = 0.257$	$V_3 = \begin{bmatrix} 0.298 \\ -0.160 \\ 0.941 \end{bmatrix}$	20	-28

Table 8.17: Particle orientation fabric tensor (Φ) for the reconstituted sample 290

Sample ref.	Ω_{PO} (°)	$\Omega_{PO(P)}$ (°)
293S	23	9
295L	30	5
289	25	1
290	20	6

Table 8.18: Direction of the major principal fabric to the horizontal given by the angle Ω_{PO} for Φ and by the angle $\Omega_{PO(P)}$ for Φ^P, for the samples affected by the shear band

Sample ref.	C for Φ^P	K for Φ^P	C for Φ	K for Φ
297ph	0.09	1.35	0.43	0.47
297L	0.06	4.05	0.30	0.42
294ph	0.07	3.73	0.28	0.49
294n	0.02	0.43	0.38	2.52
293	0.07	0.64	0.13	0.84
293S	0.08	2.35	0.43	0.82
295ph	0.04	1.95	0.05	0.09
295L	0.06	1.46	0.37	0.44
291ph	0.08	0.70	0.47	0.45
291L	0.08	0.50	0.35	0.51
289	0.09	1.11	0.46	0.37
289S	0.10	0.76	0.43	0.17
290ph	0.08	1.75	0.41	0.25

Table 8.19: Fabric descriptors for the fabric tensors Φ and $\Phi^P$of the particle orientation

Sample ref.	$\Phi_1^P - \Phi_3^P$	Φ_d^P	Φ_1^P/Φ_3^P	$\Phi_1 - \Phi_3$	Φ_d
297ph	0.030	0.026	1.09	0.138	0.121
297L	0.019	0.018	1.06	0.097	0.086
294ph	0.022	0.020	1.07	0.092	0.080
294n	0.008	0.007	1.02	0.130	0.118
293	0.022	0.019	1.07	0.044	0.038
293S	0.028	0.025	1.09	0.142	0.123
295ph	0.015	0.013	1.04	0.017	0.016
295L	0.019	0.016	1.06	0.119	0.104
291ph	0.026	0.023	1.08	0.149	0.131
291L	0.036	0.023	1.08	0.112	0.098
289	0.030	0.026	1.09	0.147	0.131
289S	0.032	0.028	1.10	0.135	0.125
290ph	0.027	0.024	1.09	0.130	0.118

Table 8.20: Particle orientation anisotropy

Sample ref.	Avg. contact size (voxels)	Total No. of contacts			Point contacts	
		part-part	all regions	%(part-part)	No.	%
297ph	256	14339	20543	70	172	1.20
297L	443	28635	40549	71	335	1.17
294ph	199	18304	24328	75	331	1.70
294n	207	15696	22044	71	192	1.22
293	117	20096	26222	77	652	3.24
293S	99	12906	18053	71	441	3.42
295ph	139	12200	17009	72	314	2.57
295L	264	24192	35158	69	516	2.13
291ph	84	20816	29197	71	937	4.50
291L	205	14925	21846	68	296	1.98
289	80	18924	24510	77	964	5.01
289S	74	19674	24896	79	1360	6.91
290ph	90	17630	24180	73	859	4.87

Table 8.21: Statistics for the total number of contacts for each sample and the number of point contacts and percentage relative to the total number of contacts

Sample ref.	FT	Eigenvalues	Eigenvectors	ϕ (°)	θ (°)
297ph	$\begin{bmatrix} 0.338 & -0.009 & -0.008 \\ -0.009 & 0.315 & 0.001 \\ -0.008 & 0.001 & 0.347 \end{bmatrix}$	$S_1 = 0.352$	$V_1 = \begin{bmatrix} -0.553 \\ 0.152 \\ 0.819 \end{bmatrix}$	35	165
		$S_2 = 0.336$	$V_2 = \begin{bmatrix} -0.761 \\ 0.309 \\ -0.570 \end{bmatrix}$	55	158
		$S_3 = 0.312$	$V_3 = \begin{bmatrix} -0.340 \\ 0.939 \\ 0.056 \end{bmatrix}$	87	70
297L	$\begin{bmatrix} 0.321 & 0.006 & 0.013 \\ 0.006 & 0.330 & 0.008 \\ 0.013 & 0.008 & 0.349 \end{bmatrix}$	$S_1 = 0.357$	$V_1 = \begin{bmatrix} 0.361 \\ 0.321 \\ 0.876 \end{bmatrix}$	29	42
		$S_2 = 0.327$	$V_2 = \begin{bmatrix} -0.074 \\ -0.926 \\ 0.370 \end{bmatrix}$	68	-95
		$S_3 = 0.316$	$V_3 = \begin{bmatrix} -0.930 \\ 0.198 \\ 0.310 \end{bmatrix}$	72	168

Table 8.22: Contact normal fabric tensor for the samples 297ph and 297L

Sample ref.	FT	Eigenvalues	Eigenvectors	ϕ (°)	θ (°)
294ph	$\begin{bmatrix} 0.328 & 0.006 & -0.003 \\ 0.006 & 0.335 & 0.005 \\ -0.003 & 0.005 & 0.337 \end{bmatrix}$	$S_1 = 0.341$	$V_1 = \begin{bmatrix} -0.156 \\ -0.719 \\ -0.677 \end{bmatrix}$	47	-102
		$S_2 = 0.336$	$V_2 = \begin{bmatrix} 0.626 \\ 0.458 \\ -0.613 \end{bmatrix}$	51	36
		$S_3 = 0.323$	$V_3 = \begin{bmatrix} 0.764 \\ -0.522 \\ 0.379 \end{bmatrix}$	68	-34
294n	$\begin{bmatrix} 0.335 & 0.009 & -0.001 \\ 0.009 & 0.324 & 0.005 \\ -0.001 & 0.005 & 0.341 \end{bmatrix}$	$S_1 = 0.343$	$V_1 = \begin{bmatrix} -0.318 \\ -0.349 \\ -0.881 \end{bmatrix}$	28	-132
		$S_2 = 0.339$	$V_2 = \begin{bmatrix} 0.832 \\ 0.344 \\ -0.436 \end{bmatrix}$	64	22
		$S_3 = 0.318$	$V_3 = \begin{bmatrix} 0.455 \\ -0.872 \\ 0.181 \end{bmatrix}$	80	-62

Table 8.23: Contact normal fabric tensor for the sample 294ph and 294n

Sample ref.	FT	Eigenvalues	Eigenvectors	ϕ (°)	θ (°)
293	$\begin{bmatrix} 0.304 & 0.006 & -0.003 \\ 0.006 & 0.309 & -0.010 \\ -0.003 & -0.010 & 0.387 \end{bmatrix}$	$S_1 = 0.388$	$V_1 = \begin{bmatrix} -0.046 \\ -0.124 \\ 0.991 \end{bmatrix}$	8	-110
		$S_2 = 0.312$	$V_2 = \begin{bmatrix} 0.596 \\ 0.793 \\ 0.127 \end{bmatrix}$	83	53
		$S_3 = 0.300$	$V_3 = \begin{bmatrix} 0.802 \\ -0.597 \\ -0.038 \end{bmatrix}$	88	-37
293S	$\begin{bmatrix} 0.320 & -0.015 & -0.007 \\ -0.015 & 0.282 & -0.043 \\ -0.007 & -0.043 & 0.398 \end{bmatrix}$	$S_1 = 0.412$	$V_1 = \begin{bmatrix} -0.019 \\ -0.312 \\ 0.950 \end{bmatrix}$	18	-94
		$S_2 = 0.325$	$V_2 = \begin{bmatrix} 0.960 \\ -0.273 \\ -0.070 \end{bmatrix}$	86	-16
		$S_3 = 0.263$	$V_3 = \begin{bmatrix} 0.281 \\ 0.910 \\ 0.305 \end{bmatrix}$	72	73

Table 8.24: Contact normal fabric tensor for the samples 293 and 293S

Sample ref.	FT	Eigenvalues	Eigenvectors	ϕ (°)	θ (°)
295ph	$\begin{bmatrix} 0.304 & 0.005 & -0.001 \\ 0.005 & 0.313 & 0.002 \\ -0.001 & -0.002 & 0.383 \end{bmatrix}$	$S_1 = 0.383$	$V_1 = \begin{bmatrix} -0.010 \\ 0.023 \\ 1.000 \end{bmatrix}$	1	113
		$S_2 = 0.315$	$V_2 = \begin{bmatrix} 0.418 \\ 0.908 \\ -0.017 \end{bmatrix}$	89	65
		$S_3 = 0.302$	$V_3 = \begin{bmatrix} -0.908 \\ 0.418 \\ -0.019 \end{bmatrix}$	89	155
295L	$\begin{bmatrix} 0.324 & 0.012 & -0.005 \\ 0.012 & 0.296 & 0.024 \\ -0.005 & -0.024 & 0.380 \end{bmatrix}$	$S_1 = 0.387$	$V_1 = \begin{bmatrix} -0.037 \\ 0.252 \\ 0.967 \end{bmatrix}$	15	98
		$S_2 = 0.328$	$V_2 = \begin{bmatrix} 0.949 \\ 0.313 \\ -0.045 \end{bmatrix}$	87	18
		$S_3 = 0.285$	$V_3 = \begin{bmatrix} -0.314 \\ 0.916 \\ -0.250 \end{bmatrix}$	76	109

Table 8.25: Contact normal fabric tensor for the samples 295ph and 295L

Sample ref.	FT	Eigenvalues	Eigenvectors	ϕ (°)	θ (°)
		$S_1 = 0.352$	$V_1 = \begin{bmatrix} 0.077 \\ 0.682 \\ 0.727 \end{bmatrix}$	43	84
291ph	$\begin{bmatrix} 0.315 & -0.001 & 0.005 \\ -0.001 & 0.342 & 0.009 \\ 0.005 & 0.009 & 0.343 \end{bmatrix}$	$S_2 = 0.335$	$V_2 = \begin{bmatrix} -0.222 \\ 0.723 \\ -0.654 \end{bmatrix}$	49	107
		$S_3 = 0.314$	$V_3 = \begin{bmatrix} 0.972 \\ 0.111 \\ -0.207 \end{bmatrix}$	78	7
		$S_1 = 0.356$	$V_1 = \begin{bmatrix} 0.446 \\ -0.081 \\ 0.891 \end{bmatrix}$	27	-10
291L	$\begin{bmatrix} 0.329 & 0.002 & 0.014 \\ 0.002 & 0.322 & -0.004 \\ 0.014 & -0.004 & 0.349 \end{bmatrix}$	$S_2 = 0.326$	$V_2 = \begin{bmatrix} -0.688 \\ -0.668 \\ 0.283 \end{bmatrix}$	74	-136
		$S_3 = 0.318$	$V_3 = \begin{bmatrix} 0.572 \\ -0.740 \\ -0.354 \end{bmatrix}$	69	-52

Table 8.26: Contact normal fabric tensor for the samples 291ph and 291L

Sample ref.	FT	Eigenvalues	Eigenvectors	ϕ (°)	θ (°)
		$S_1 = 0.416$	$V_1 = \begin{bmatrix} -0.214 \\ -0.101 \\ 0.972 \end{bmatrix}$	14	-155
289	$\begin{bmatrix} 0.285 & -0.010 & -0.030 \\ -0.010 & 0.307 & -0.013 \\ 0.030 & -0.013 & 0.408 \end{bmatrix}$	$S_2 = 0.311$	$V_2 = \begin{bmatrix} 0.365 \\ -0.931 \\ -0.017 \end{bmatrix}$	89	-69
		$S_3 = 0.273$	$V_3 = \begin{bmatrix} 0.906 \\ 0.351 \\ 0.236 \end{bmatrix}$	76	21
		$S_1 = 0.415$	$V_1 = \begin{bmatrix} 0.020 \\ 0.070 \\ 0.997 \end{bmatrix}$	4	74
289S	$\begin{bmatrix} 0.290 & 0.001 & 0.002 \\ 0.001 & 0.295 & 0.008 \\ 0.002 & 0.008 & 0.415 \end{bmatrix}$	$S_2 = 0.295$	$V_2 = \begin{bmatrix} 0.189 \\ 0.979 \\ -0.072 \end{bmatrix}$	86	79
		$S_3 = 0.290$	$V_3 = \begin{bmatrix} 0.982 \\ -0.190 \\ -0.006 \end{bmatrix}$	90	-11

Table 8.27: Contact normal fabric tensor for the samples 289 and 289S

Sample ref.	FT	Eigenvalues	Eigenvectors	ϕ (°)	θ (°)
290	$\begin{bmatrix} 0.318 & 0.010 & -0.024 \\ 0.010 & 0.310 & 0.022 \\ -0.024 & 0.022 & 0.372 \end{bmatrix}$	$S_1 = 0.385$	$V_1 = \begin{bmatrix} -0.289 \\ 0.233 \\ 0.929 \end{bmatrix}$	22	141
		$S_2 = 0.324$	$V_2 = \begin{bmatrix} 0.757 \\ 0.649 \\ 0.073 \end{bmatrix}$	86	41
		$S_3 = 0.290$	$V_3 = \begin{bmatrix} -0.586 \\ 0.724 \\ -0.364 \end{bmatrix}$	69	129

Table 8.28: Contact normal fabric tensor for the sample 290

Sample ref.	Φ Eigenvelues	Φ V_1	ϕ_{V1}	Φ^{p-p} Eigenvelues	Φ^{p-p} V_1	ϕ_{V1}	Φ^{w} Eigenvelues	Φ^{w} V_1	ϕ_{V1}	$\Phi^{w}_{(500)}$ Eigenvelues	$\Phi^{w}_{(500)}$ V_1	ϕ_{V1}
297ph	$S_1 = 0.352$ $S_2 = 0.336$ $S_3 = 0.312$	$\begin{bmatrix} -0.553 \\ 0.152 \\ 0.819 \end{bmatrix}$	35	$S_1 = 0.528$ $S_2 = 0.311$ $S_3 = 0.161$	$\begin{bmatrix} 0.521 \\ -0.672 \\ 0.526 \end{bmatrix}$	51	$S_1 = 0.420$ $S_2 = 0.338$ $S_3 = 0.242$	$\begin{bmatrix} 0.484 \\ -0.657 \\ 0.578 \end{bmatrix}$	55	$S_1 = 0.408$ $S_2 = 0.345$ $S_3 = 0.246$	$\begin{bmatrix} -0.349 \\ 0.676 \\ -0.649 \end{bmatrix}$	50
297L	$S_1 = 0.357$ $S_2 = 0.327$ $S_3 = 0.316$	$\begin{bmatrix} 0.361 \\ 0.321 \\ 0.876 \end{bmatrix}$	55	$S_1 = 0.356$ $S_2 = 0.328$ $S_3 = 0.316$	$\begin{bmatrix} 0.507 \\ 0.424 \\ 0.750 \end{bmatrix}$	41	$S_1 = 0.392$ $S_2 = 0.315$ $S_3 = 0.293$	$\begin{bmatrix} 0.741 \\ 0.556 \\ 0.377 \end{bmatrix}$	68	$S_1 = 0.442$ $S_2 = 0.313$ $S_3 = 0.246$	$\begin{bmatrix} -0.803 \\ -0.589 \\ -0.088 \end{bmatrix}$	85
294ph	$S_1 = 0.341$ $S_2 = 0.336$ $S_3 = 0.323$	$\begin{bmatrix} -0.156 \\ -0.719 \\ -0.677 \end{bmatrix}$	47	$S_1 = 0.346$ $S_2 = 0.331$ $S_3 = 0.322$	$\begin{bmatrix} -0.535 \\ -0.845 \\ -0.015 \end{bmatrix}$	89	$S_1 = 0.399$ $S_2 = 0.309$ $S_3 = 0.292$	$\begin{bmatrix} -0.490 \\ -0.871 \\ -0.036 \end{bmatrix}$	88	$S_1 = 0.472$ $S_2 = 0.287$ $S_3 = 0.242$	$\begin{bmatrix} -0.449 \\ -0.887 \\ -0.106 \end{bmatrix}$	84
294n	$S_1 = 0.343$ $S_2 = 0.339$ $S_3 = 0.318$	$\begin{bmatrix} -0.318 \\ -0.349 \\ -0.881 \end{bmatrix}$	28	$S_1 = 0.342$ $S_2 = 0.336$ $S_3 = 0.322$	$\begin{bmatrix} -0.867 \\ -0.303 \\ -0.396 \end{bmatrix}$	67	$S_1 = 0.392$ $S_2 = 0.311$ $S_3 = 0.297$	$\begin{bmatrix} -0.974 \\ 0.221 \\ -0.056 \end{bmatrix}$	87	$S_1 = 0.464$ $S_2 = 0.289$ $S_3 = 0.247$	$\begin{bmatrix} -0.971 \\ 0.236 \\ -0.049 \end{bmatrix}$	87
293	$S_1 = 0.388$ $S_2 = 0.312$ $S_3 = 0.300$	$\begin{bmatrix} -0.046 \\ -0.124 \\ 0.991 \end{bmatrix}$	8	$S_1 = 0.390$ $S_2 = 0.313$ $S_3 = 0.296$	$\begin{bmatrix} -0.048 \\ -0.119 \\ -0.992 \end{bmatrix}$	7	$S_1 = 0.401$ $S_2 = 0.323$ $S_3 = 0.276$	$\begin{bmatrix} -0.053 \\ -0.093 \\ 0.994 \end{bmatrix}$	6	$S_1 = 0.395$ $S_2 = 0.330$ $S_3 = 0.275$	$\begin{bmatrix} -0.091 \\ -0.062 \\ 0.994 \end{bmatrix}$	6
293S	$S_1 = 0.412$ $S_2 = 0.325$ $S_3 = 0.263$	$\begin{bmatrix} -0.019 \\ -0.312 \\ 0.950 \end{bmatrix}$	18	$S_1 = 0.411$ $S_2 = 0.321$ $S_3 = 0.268$	$\begin{bmatrix} -0.017 \\ -0.289 \\ 0.957 \end{bmatrix}$	17	$S_1 = 0.441$ $S_2 = 0.314$ $S_3 = 0.245$	$\begin{bmatrix} -0.024 \\ -0.296 \\ 0.955 \end{bmatrix}$	17	$S_1 = 0.442$ $S_2 = 0.330$ $S_3 = 0.228$	$\begin{bmatrix} 0.017 \\ -0.356 \\ 0.934 \end{bmatrix}$	21
295ph	$S_1 = 0.383$ $S_2 = 0.315$ $S_3 = 0.302$	$\begin{bmatrix} -0.010 \\ 0.023 \\ 1.000 \end{bmatrix}$	1	$S_1 = 0.387$ $S_2 = 0.311$ $S_3 = 0.302$	$\begin{bmatrix} -0.004 \\ 0.005 \\ 1.000 \end{bmatrix}$	0	$S_1 = 0.395$ $S_2 = 0.314$ $S_3 = 0.291$	$\begin{bmatrix} 0.012 \\ 0.049 \\ 0.999 \end{bmatrix}$	3	$S_1 = 0.376$ $S_2 = 0.342$ $S_3 = 0.282$	$\begin{bmatrix} 0.207 \\ -0.164 \\ 0.965 \end{bmatrix}$	15
295L	$S_1 = 0.387$ $S_2 = 0.328$ $S_3 = 0.285$	$\begin{bmatrix} -0.037 \\ 0.252 \\ 0.967 \end{bmatrix}$	15	$S_1 = 0.386$ $S_2 = 0.329$ $S_3 = 0.285$	$\begin{bmatrix} -0.055 \\ 0.224 \\ 0.973 \end{bmatrix}$	13	$S_1 = 0.415$ $S_2 = 0.315$ $S_3 = 0.269$	$\begin{bmatrix} -0.014 \\ 0.207 \\ 0.978 \end{bmatrix}$	12	$S_1 = 0.413$ $S_2 = 0.305$ $S_3 = 0.283$	$\begin{bmatrix} -0.018 \\ 0.166 \\ 0.986 \end{bmatrix}$	10

Table 8.29: Comparison between the eigenvalues, the eigenvector V_1 and the angle ϕ_1 obtained for the different contact normal fabric tensors, for the intact samples

Sample ref.	Φ Eigenvalues	Φ V_1	ϕ_{V1}	Φ^{p-p} Eigenvalues	Φ^{p-p} V_1	ϕ_{V1}	Φ^{w} Eigenvalues	Φ^{w} V_1	ϕ_{V1}	$\Phi^{w}_{(500)}$ Eigenvalues	$\Phi^{w}_{(500)}$ V_1	ϕ_{V1}
291ph	$S_1 = 0.352$ $S_2 = 0.335$ $S_3 = 0.314$	$\begin{bmatrix} 0.077 \\ 0.682 \\ 0.727 \end{bmatrix}$	43	$S_1 = 0.348$ $S_2 = 0.335$ $S_3 = 0.316$	$\begin{bmatrix} 0.018 \\ 0.781 \\ 0.624 \end{bmatrix}$	51	$S_1 = 0.361$ $S_2 = 0.332$ $S_3 = 0.306$	$\begin{bmatrix} -0.006 \\ 0.790 \\ 0.613 \end{bmatrix}$	52	$S_1 = 0.390$ $S_2 = 0.322$ $S_3 = 0.288$	$\begin{bmatrix} -0.084 \\ 0.796 \\ 0.599 \end{bmatrix}$	53
291L	$S_1 = 0.356$ $S_2 = 0.326$ $S_3 = 0.318$	$\begin{bmatrix} 0.446 \\ -0.081 \\ 0.891 \end{bmatrix}$	27	$S_1 = 0.354$ $S_2 = 0.325$ $S_3 = 0.321$	$\begin{bmatrix} 0.404 \\ -0.042 \\ 0.914 \end{bmatrix}$	24	$S_1 = 0.365$ $S_2 = 0.326$ $S_3 = 0.309$	$\begin{bmatrix} 0.565 \\ 0.059 \\ 0.823 \end{bmatrix}$	35	$S_1 = 0.407$ $S_2 = 0.322$ $S_3 = 0.270$	$\begin{bmatrix} 0.899 \\ 0.241 \\ 0.366 \end{bmatrix}$	69
289	$S_1 = 0.416$ $S_2 = 0.311$ $S_3 = 0.273$	$\begin{bmatrix} -0.214 \\ -0.101 \\ 0.972 \end{bmatrix}$	14	$S_1 = 0.412$ $S_2 = 0.313$ $S_3 = 0.275$	$\begin{bmatrix} -0.194 \\ -0.092 \\ 0.977 \end{bmatrix}$	12	$S_1 = 0.455$ $S_2 = 0.292$ $S_3 = 0.253$	$\begin{bmatrix} -0.186 \\ -0.082 \\ 0.979 \end{bmatrix}$	12	$S_1 = 0.466$ $S_2 = 0.299$ $S_3 = 0.235$	$\begin{bmatrix} -0.180 \\ -0.071 \\ 0.981 \end{bmatrix}$	11
289S	$S_1 = 0.415$ $S_2 = 0.295$ $S_3 = 0.290$	$\begin{bmatrix} 0.020 \\ 0.070 \\ 0.997 \end{bmatrix}$	4	$S_1 = 0.408$ $S_2 = 0.299$ $S_3 = 0.293$	$\begin{bmatrix} 0.017 \\ 0.091 \\ 0.996 \end{bmatrix}$	5	$S_1 = 0.457$ $S_2 = 0.275$ $S_3 = 0.268$	$\begin{bmatrix} 0.023 \\ 0.080 \\ 0.997 \end{bmatrix}$	5	$S_1 = 0.498$ $S_2 = 0.275$ $S_3 = 0.227$	$\begin{bmatrix} -0.034 \\ 0.088 \\ 0.996 \end{bmatrix}$	5
290ph	$S_1 = 0.385$ $S_2 = 0.324$ $S_3 = 0.290$	$\begin{bmatrix} -0.289 \\ 0.233 \\ 0.929 \end{bmatrix}$	22	$S_1 = 0.381$ $S_2 = 0.324$ $S_3 = 0.295$	$\begin{bmatrix} -0.284 \\ 0.198 \\ 0.938 \end{bmatrix}$	20	$S_1 = 0.419$ $S_2 = 0.312$ $S_3 = 0.268$	$\begin{bmatrix} -0.301 \\ 0.236 \\ 0.924 \end{bmatrix}$	22	$S_1 = 0.497$ $S_2 = 0.297$ $S_3 = 0.206$	$\begin{bmatrix} -0.338 \\ 0.304 \\ 0.891 \end{bmatrix}$	27

Table 8.30: Comparison between the eigenvalues, the eigenvector V_1 and the angle ϕ_1 obtained for the different contact normal fabric tensors, for the reconstituted samples

Sample ref.	Ω_{PO} (°)	ϕ_{cnO} (°)
293S	23	18
295L	30	15
289	25	14
290	20	22

Table 8.31: Comparison between Ω_{PO} and ϕ_{cnO} for the samples affected by the shear band

Sample ref.	C (for Φ)	K (for Φ)	C (for Φ^w)	K (for Φ^w)
297ph	0.12	0.65	0.55	0.66
297L	0.12	2.55	0.29	3.11
294ph	0.06	0.41	0.31	4.72
294n	0.08	0.19	0.23	5.35
293	0.26	5.70	0.37	1.40
293S	0.45	1.13	0.59	1.35
295ph	0.24	4.38	0.30	3.09
295L	0.31	1.16	0.43	1.76
291ph	0.11	0.75	0.17	1.99
291L	0.11	3.84	0.17	0.06
289	0.42	2.26	0.58	3.12
289S	0.36	19.07	0.53	21.50
290ph	0.28	1.54	0.45	1.92

Table 8.32: Fabric descriptors for the contact normal fabric tensors Φ and Φ^w

Sample ref.	$\Phi_1 - \Phi_3$	Φ_d	$\Phi_1^{p-p} - \Phi_3^{p-p}$	Φ_d^{p-p}	$\Phi_1^w - \Phi_3^w$	Φ_d^w
297ph	0.041	0.035	0.368	0.320	0.177	0.154
297L	0.042	0.037	0.040	0.035	0.099	0.090
294ph	0.019	0.017	0.024	0.021	0.107	0.100
294n	0.025	0.023	0.020	0.018	0.077	0.072
293	0.088	0.083	0.094	0.087	0.126	0.110
293S	0.148	0.129	0.143	0.126	0.196	0.172
295ph	0.081	0.075	0.085	0.081	0.104	0.094
295L	0.102	0.089	0.100	0.087	0.146	0.129
291ph	0.038	0.033	0.032	0.028	0.056	0.048
291L	0.038	0.035	0.033	0.031	0.056	0.050
289	0.143	0.129	0.137	0.123	0.201	0.185
289S	0.125	0.123	0.115	0.112	0.189	0.186
290ph	0.095	0.084	0.086	0.076	0.151	0.135

Table 8.33: Contact normal anisotropy

Sample ref.	FT	Eigenvalues	Eigenvectors	ϕ (°)	θ (°)
297ph	$\begin{bmatrix} 0.343 & 0.003 & 0.004 \\ 0.003 & 0.346 & 0.008 \\ 0.004 & 0.008 & 0.311 \end{bmatrix}$	$S_1 = 0.350$	$V_1 = \begin{bmatrix} -0.453 \\ -0.864 \\ -0.219 \end{bmatrix}$	77	-118
		$S_2 = 0.341$	$V_2 = \begin{bmatrix} -0.887 \\ 0.461 \\ 0.019 \end{bmatrix}$	89	153
		$S_3 = 0.309$	$V_3 = \begin{bmatrix} -0.085 \\ -0.202 \\ 0.976 \end{bmatrix}$	13	-113
297L	$\begin{bmatrix} 0.335 & 0.003 & -0.005 \\ 0.003 & 0.341 & -0.010 \\ -0.005 & -0.010 & 0.324 \end{bmatrix}$	$S_1 = 0.347$	$V_1 = \begin{bmatrix} -0.344 \\ -0.841 \\ 0.418 \end{bmatrix}$	65	-112
		$S_2 = 0.334$	$V_2 = \begin{bmatrix} -0.919 \\ 0.392 \\ 0.031 \end{bmatrix}$	88	157
		$S_3 = 0.319$	$V_3 = \begin{bmatrix} 0.190 \\ 0.373 \\ 0.908 \end{bmatrix}$	25	63

Table 8.34: Branch vector fabric tensor for the samples 297ph and 297L

Sample ref.	FT	Eigenvalues	Eigenvectors	ϕ (°)	θ (°)
294ph	$\begin{bmatrix} 0.345 & 0.002 & -0.008 \\ 0.002 & 0.339 & 0.001 \\ -0.008 & 0.001 & 0.316 \end{bmatrix}$	$S_1 = 0.348$	$V_1 = \begin{bmatrix} 0.950 \\ 0.220 \\ -0.222 \end{bmatrix}$	77	13
		$S_2 = 0.338$	$V_2 = \begin{bmatrix} 0.210 \\ -0.974 \\ -0.105 \end{bmatrix}$	84	-78
		$S_3 = 0.314$	$V_3 = \begin{bmatrix} 0.240 \\ -0.055 \\ 0.969 \end{bmatrix}$	14	-13
294n	$\begin{bmatrix} 0.333 & -0.021 & -0.003 \\ -0.021 & 0.341 & 0.006 \\ -0.003 & 0.006 & 0.324 \end{bmatrix}$	$S_1 = 0.360$	$V_1 = \begin{bmatrix} -0.609 \\ 0.774 \\ 0.174 \end{bmatrix}$	80	128
		$S_2 = 0.323$	$V_2 = \begin{bmatrix} -0.251 \\ 0.020 \\ -0.968 \end{bmatrix}$	15	175
		$S_3 = 0.316$	$V_3 = \begin{bmatrix} 0.752 \\ 0.633 \\ -0.182 \end{bmatrix}$	80	40

Table 8.35: Branch vector fabric tensor for the samples 294ph and 294n

Sample ref.	FT	Eigenvalues	Eigenvectors	ϕ (°)	θ (°)
293	$\begin{bmatrix} 0.311 & 0.012 & -0.001 \\ 0.012 & 0.325 & -0.004 \\ -0.001 & -0.004 & 0.364 \end{bmatrix}$	$S_1 = 0.365$	$V_1 = \begin{bmatrix} -0.033 \\ -0.101 \\ 0.994 \end{bmatrix}$	6	-108
		$S_2 = 0.332$	$V_2 = \begin{bmatrix} 0.502 \\ 0.859 \\ 0.103 \end{bmatrix}$	84	60
		$S_3 = 0.303$	$V_3 = \begin{bmatrix} 0.864 \\ -0.503 \\ -0.022 \end{bmatrix}$	89	-30
293S	$\begin{bmatrix} 0.320 & -0.005 & -0.007 \\ -0.005 & 0.340 & -0.003 \\ -0.007 & -0.003 & 0.341 \end{bmatrix}$	$S_1 = 0.343$	$V_1 = \begin{bmatrix} -0.157 \\ -0.412 \\ 0.897 \end{bmatrix}$	26	-111
		$S_2 = 0.341$	$V_2 = \begin{bmatrix} 0.335 \\ -0.877 \\ -0.345 \end{bmatrix}$	70	-69
		$S_3 = 0.316$	$V_3 = \begin{bmatrix} 0.929 \\ 0.246 \\ 0.276 \end{bmatrix}$	74	15

Table 8.36: Branch vector fabric tensor for the samples 293 and 293S

Sample ref.	FT	Eigenvalues	Eigenvectors	ϕ (°)	θ (°)
295	$\begin{bmatrix} 0.319 & -0.001 & -0.002 \\ -0.001 & 0.315 & -0.002 \\ -0.002 & -0.002 & 0.366 \end{bmatrix}$	$S_1 = 0.366$	$V_1 = \begin{bmatrix} -0.038 \\ -0.041 \\ 0.998 \end{bmatrix}$	3	-133
		$S_2 = 0.319$	$V_2 = \begin{bmatrix} 0.962 \\ -0.272 \\ 0.026 \end{bmatrix}$	89	-16
		$S_3 = 0.314$	$V_3 = \begin{bmatrix} 0.270 \\ 0.961 \\ 0.049 \end{bmatrix}$	87	74
295L	$\begin{bmatrix} 0.322 & 0.007 & -0.003 \\ 0.007 & 0.345 & -0.003 \\ -0.003 & -0.003 & 0.333 \end{bmatrix}$	$S_1 = 0.348$	$V_1 = \begin{bmatrix} -0.275 \\ -0.931 \\ 0.239 \end{bmatrix}$	76	-106
		$S_2 = 0.333$	$V_2 = \begin{bmatrix} -0.085 \\ 0.272 \\ 0.959 \end{bmatrix}$	17	107
		$S_3 = 0.320$	$V_3 = \begin{bmatrix} 0.958 \\ -0.244 \\ 0.154 \end{bmatrix}$	81	-14

Table 8.37: Branch vector fabric tensor for the samples 295ph and 295L

Sample ref.	FT	Eigenvalues	Eigenvectors	ϕ (°)	θ (°)
291	$\begin{bmatrix} 0.348 & -0.005 & -0.005 \\ -0.005 & 0.353 & 0.000 \\ -0.005 & 0.000 & 0.299 \end{bmatrix}$	$S_1 = 0.356$	$V_1 = \begin{bmatrix} -0.513 \\ 0.857 \\ 0.046 \end{bmatrix}$	87	121
		$S_2 = 0.345$	$V_2 = \begin{bmatrix} 0.851 \\ 0.515 \\ -0.102 \end{bmatrix}$	84	31
		$S_3 = 0.299$	$V_3 = \begin{bmatrix} 0.111 \\ 0.013 \\ 0.994 \end{bmatrix}$	6	7
291L	$\begin{bmatrix} 0.343 & -0.007 & -0.006 \\ -0.007 & 0.352 & -0.002 \\ -0.006 & -0.002 & 0.304 \end{bmatrix}$	$S_1 = 0.356$	$V_1 = \begin{bmatrix} -0.496 \\ 0.868 \\ 0.026 \end{bmatrix}$	89	120
		$S_2 = 0.340$	$V_2 = \begin{bmatrix} 0.853 \\ 0.492 \\ -0.175 \end{bmatrix}$	80	30
		$S_3 = 0.303$	$V_3 = \begin{bmatrix} -0.165 \\ 0.065 \\ 0.984 \end{bmatrix}$	10	21

Table 8.38: Branch vector fabric tensor for the samples 291ph and 291L

Sample ref.	FT	Eigenvalues	Eigenvectors	ϕ (°)	θ (°)
289	$\begin{bmatrix} 0.336 & -0.005 & 0.003 \\ -0.005 & 0.327 & 0.008 \\ 0.003 & 0.008 & 0.337 \end{bmatrix}$	$S_1 = 0.342$	$V_1 = \begin{bmatrix} 0.137 \\ 0.439 \\ 0.888 \end{bmatrix}$	27	73
		$S_2 = 0.338$	$V_2 = \begin{bmatrix} 0.926 \\ -0.376 \\ 0.043 \end{bmatrix}$	88	-22
		$S_3 = 0.320$	$V_3 = \begin{bmatrix} -0.353 \\ -0.816 \\ 0.458 \end{bmatrix}$	63	-113
289S	$\begin{bmatrix} 0.338 & 0.002 & 0.002 \\ 0.002 & 0.343 & -0.012 \\ 0.002 & -0.012 & 0.304 \end{bmatrix}$	$S_1 = 0.348$	$V_1 = \begin{bmatrix} -0.086 \\ -0.918 \\ 0.386 \end{bmatrix}$	67	-95
		$S_2 = 0.338$	$V_2 = \begin{bmatrix} -0.992 \\ 0.041 \\ -0.122 \end{bmatrix}$	83	178
		$S_3 = 0.314$	$V_3 = \begin{bmatrix} -0.096 \\ 0.393 \\ 0.914 \end{bmatrix}$	24	104

Table 8.39: Branch vector fabric tensor for the samples 289 and 289S

Sample ref.	FT	Eigenvalues	Eigenvectors	ϕ (°)	θ (°)
290	$\begin{bmatrix} 0.341 & 0.004 & -0.008 \\ 0.004 & 0.338 & -0.006 \\ -0.008 & -0.006 & 0.321 \end{bmatrix}$	$S_1 = 0.347$	$V_1 = \begin{bmatrix} -0.754 \\ -0.551 \\ 0.358 \end{bmatrix}$	69	-144
		$S_2 = 0.335$	$V_2 = \begin{bmatrix} -0.593 \\ 0.805 \\ -0.010 \end{bmatrix}$	89	126
		$S_3 = 0.317$	$V_3 = \begin{bmatrix} 0.283 \\ 0.220 \\ 0.934 \end{bmatrix}$	21	38

Table 8.40: Branch vector fabric tensor for the sample 290

Sample ref.	C	K
297ph	0.12	0.27
297L	0.09	0.84
294ph	0.10	0.38
294n	0.63	3
293	0.36	1.00
293S	0.66	0.79
295ph	0.15	8.88
295L	0.08	1.12
291ph	0.18	0.21
291L	0.16	0.40
289	0.69	1.82
289S	0.78	3.16
290ph	0.09	0.65

Table 8.41: Fabric descriptors for the branch vector fabric tensor

Sample ref.	$\Phi_1 - \Phi_3$	Φ_d
297ph	0.041	0.037
297L	0.029	0.025
294ph	0.034	0.030
294n	0.044	0.041
293	0.061	0.053
293S	0.027	0.026
295ph	0.052	0.050
295L	0.028	0.024
291ph	0.058	0.053
291L	0.053	0.047
289	0.022	0.020
289S	0.034	0.030
290ph	0.030	0.026

Table 8.42: Branch vector anisotropy

Sample ref.	Ω_{PO} (°)	ϕ_{cnO} (°)	ϕ_{bvO} (°)
293S	23	18	26
295L	30	15	76
289	25	14	27
290	20	22	69

Table 8.43: Comparison between Ω_{PO}, ϕ_{CnO} and ϕ_{bvO} for the samples affected by the shear band

Material	Sample ref. (particle)	Sample ref. (void)	Load stage	No. full voids	Observations
Intact	297ph	297vd	0	2335	
Intact	293	293vd	3	2322	
Intact	293S	293Svd	3	1056	incl. shear band
Rec.	291ph	291vd	0	3151	
Rec.	289	289vd	3	1688	
Rec.	289S	289Svd	3	1518	

Table 8.44: Samples used for void space analysis

Sample ref.		$d_{50}(\mu m)$	
(particle)	(void)	particles	voids
297ph	297vd	324	288
293	293vd	272	298
293S	293Svd	294	430
291ph	291vd	284	276
289	289vd	280	338
289S	289Svd	273	360

Table 8.45: Comparisons between the d_{50} values obtained for the particles and for the voids for each sample

Sample ref.	FT	Eigenvalues	Eigenvectors	ϕ (°)	θ (°)
297vd	$\begin{bmatrix} 0.336 & -0.007 & -0.000 \\ -0.007 & 0.337 & 0.001 \\ 0.000 & 0.001 & 0.327 \end{bmatrix}$	$S_1 = 0.343$	$V_1 = \begin{bmatrix} -0.689 \\ 0.724 \\ 0.029 \end{bmatrix}$	88	134
		$S_2 = 0.330$	$V_2 = \begin{bmatrix} 0.671 \\ 0.623 \\ 0.401 \end{bmatrix}$	66	43
		$S_3 = 0.327$	$V_3 = \begin{bmatrix} -0.272 \\ -0.296 \\ 0.916 \end{bmatrix}$	24	-133
291vd	$\begin{bmatrix} 0.339 & -0.007 & -0.001 \\ -0.007 & 0.337 & 0.002 \\ -0.001 & 0.002 & 0.324 \end{bmatrix}$	$S_1 = 0.345$	$V_1 = \begin{bmatrix} -0.746 \\ 0.660 \\ 0.084 \end{bmatrix}$	85	138
		$S_2 = 0.331$	$V_2 = \begin{bmatrix} 0.665 \\ 0.744 \\ 0.066 \end{bmatrix}$	86	48
		$S_3 = 0.324$	$V_3 = \begin{bmatrix} 0.019 \\ -0.066 \\ 0.998 \end{bmatrix}$	6	-80

Table 8.46: Void orientation fabric tensor (Φ^{vd}) for the samples 297vd and 291vd

Sample ref.	FT	Eigenvalues	Eigenvectors	ϕ (°)	θ (°)
293vd	$\begin{bmatrix} 0.330 & -0.009 & 0.001 \\ -0.009 & 0.332 & -0.001 \\ 0.001 & 0.001 & 0.338 \end{bmatrix}$	$S_1 = 0.341$	$V_1 = \begin{bmatrix} -0.597 \\ 0.679 \\ -0.427 \end{bmatrix}$	65	131
		$S_2 = 0.338$	$V_2 = \begin{bmatrix} 0.266 \\ -0.335 \\ -0.904 \end{bmatrix}$	25	-52
		$S_3 = 0.322$	$V_3 = \begin{bmatrix} 0.757 \\ 0.653 \\ -0.020 \end{bmatrix}$	89	41
293Svd	$\begin{bmatrix} 0.332 & -0.007 & 0.000 \\ -0.007 & 0.334 & 0.001 \\ 0.000 & 0.001 & 0.335 \end{bmatrix}$	$S_1 = 0.339$	$V_1 = \begin{bmatrix} -0.649 \\ 0.760 \\ 0.031 \end{bmatrix}$	88	-50
		$S_2 = 0.335$	$V_2 = \begin{bmatrix} 0.076 \\ 0.024 \\ 0.997 \end{bmatrix}$	4	18
		$S_3 = 0.326$	$V_3 = \begin{bmatrix} -0.757 \\ 0.649 \\ -0.074 \end{bmatrix}$	86	41

Table 8.47: Void orientation fabric tensor (Φ^{vd}) for the samples 293vd and 293Svd

Sample ref.	FT	Eigenvalues	Eigenvectors	ϕ (°)	θ (°)
289vd	$\begin{bmatrix} 0.336 & -0.007 & -0.001 \\ -0.007 & 0.334 & 0.002 \\ 0.001 & 0.002 & 0.331 \end{bmatrix}$	$S_1 = 0.342$	$V_1 = \begin{bmatrix} -0.744 \\ 0.636 \\ 0.206 \end{bmatrix}$	78	139
		$S_2 = 0.330$	$V_2 = \begin{bmatrix} -0.356 \\ -0.117 \\ -0.927 \end{bmatrix}$	22	-162
		$S_3 = 0.328$	$V_3 = \begin{bmatrix} 0.565 \\ 0.763 \\ -0.314 \end{bmatrix}$	72	53
289Svd	$\begin{bmatrix} 0.334 & -0.007 & -0.001 \\ -0.007 & 0.332 & 0.001 \\ -0.001 & 0.001 & 0.333 \end{bmatrix}$	$S_1 = 0.341$	$V_1 = \begin{bmatrix} -0.748 \\ 0.657 \\ 0.093 \end{bmatrix}$	85	139
		$S_2 = 0.334$	$V_2 = \begin{bmatrix} -0.054 \\ -0.200 \\ 0.978 \end{bmatrix}$	12	-105
		$S_3 = 0.326$	$V_3 = \begin{bmatrix} 0.661 \\ 0.727 \\ 0.185 \end{bmatrix}$	79	48

Table 8.48: Void orientation fabric tensor (Φ^{vd}) for the samples 289vd and 289Svd

Sample ref.	C for Φ	K for Φ	C for Φ^{vd}	K for Φ^{vd}
297vd	0.23	0.67	0.05	4.61
293vd	0.22	0.09	0.06	0.19
293Svd	0.12	2.38	0.04	0.49
291vd	0.23	0.29	0.06	1.95
289vd	0.18	0.55	0.04	4.73
289Svd	0.13	4.05	0.04	0.88

Table 8.49: Fabric descriptors for the void orientation fabric tensors Φ and Φ^P

Sample ref.	$\Phi_1^{vd} - \Phi_3^{vd}$	Φ_d^{vd}	$\Phi_1 - \Phi_3$	Φ_d
297vd	0.017	0.015	0.076	0.066
293vd	0.019	0.018	0.097	0.086
293Svd	0.014	0.012	0.039	0.035
291vd	0.021	0.019	0.076	0.069
289vd	0.014	0.013	0.059	0.052
289Svd	0.015	0.013	0.044	0.040

Table 8.50: Void orientation anisotropy

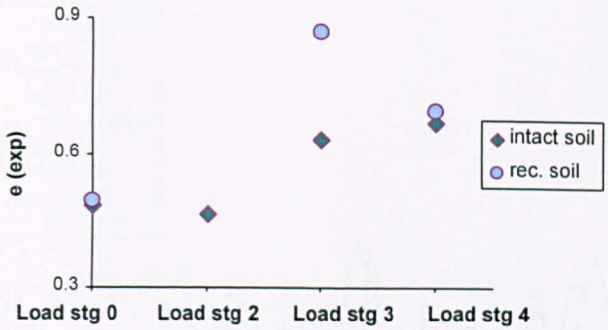

(a)

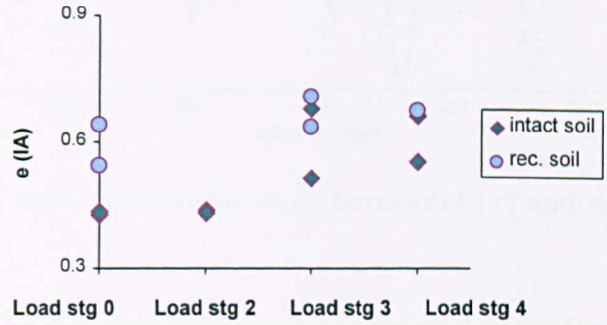

(b)

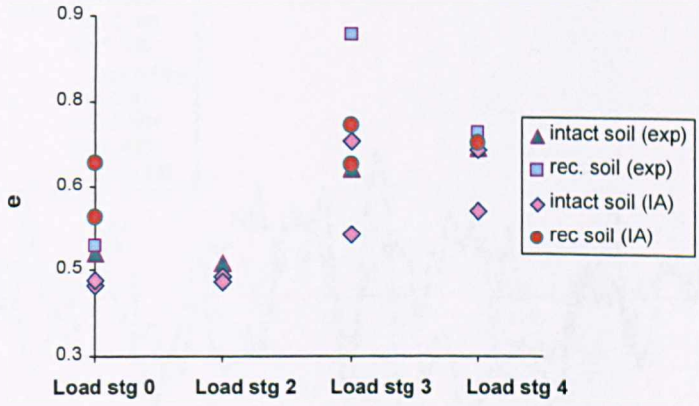

(c)

Figure 8.1: 3D void ratio measurements (a) from laboratory tests (b) from image analysis (c) comparison of both at the different load stages

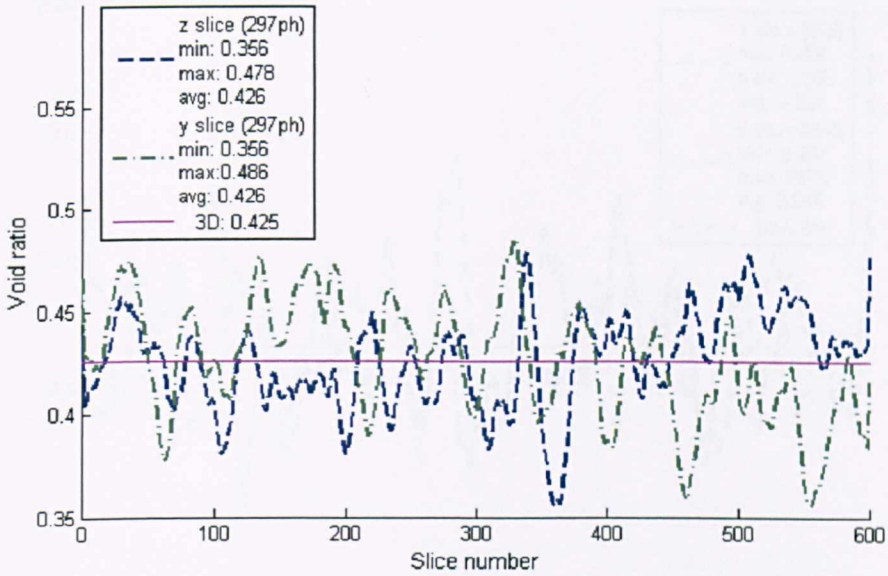

Figure 8.2: 2D void ratio distribution from horizontal (z) and vertical (y) slices for sample 297ph

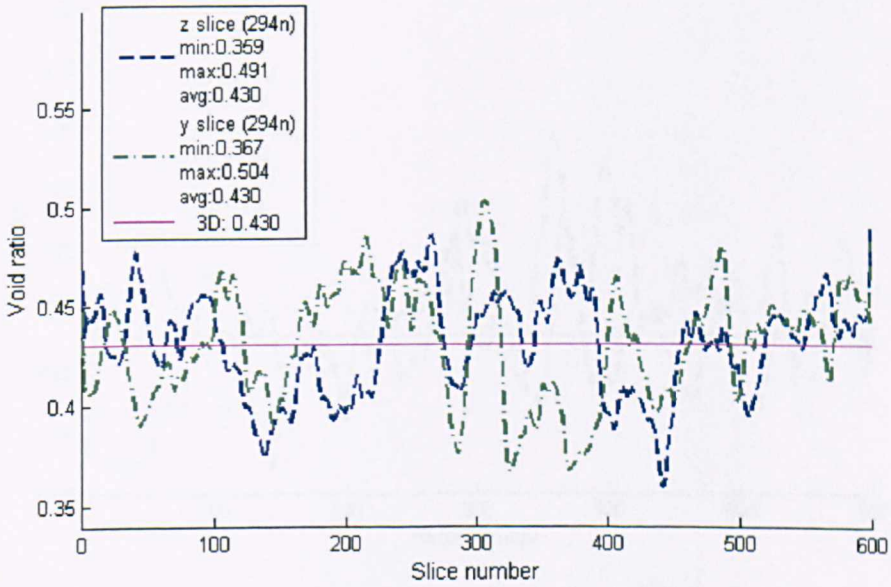

Figure 8.3: 2D void ratio distribution from horizontal (z) and vertical (y) slices for sample 294n

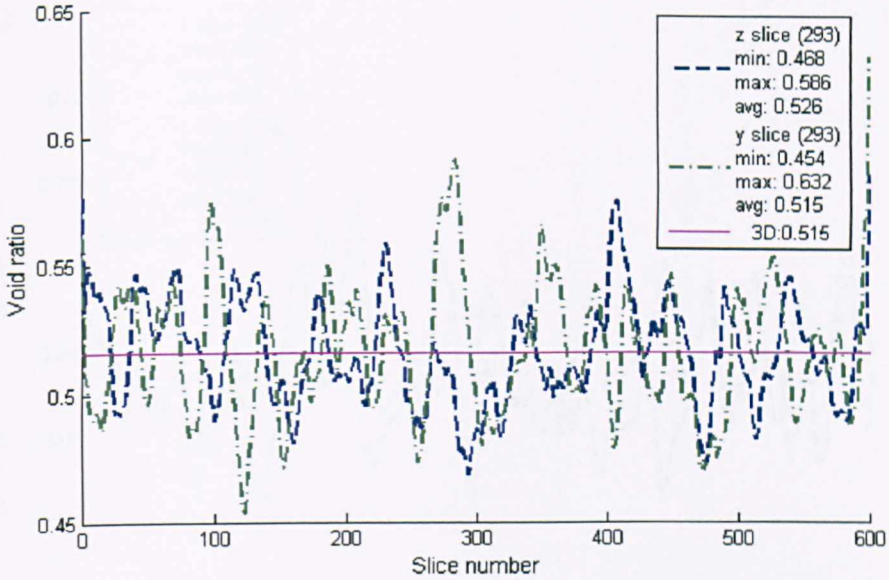

Figure 8.4: 2D void ratio distribution from horizontal (z) and vertical (y) slices for sample 293

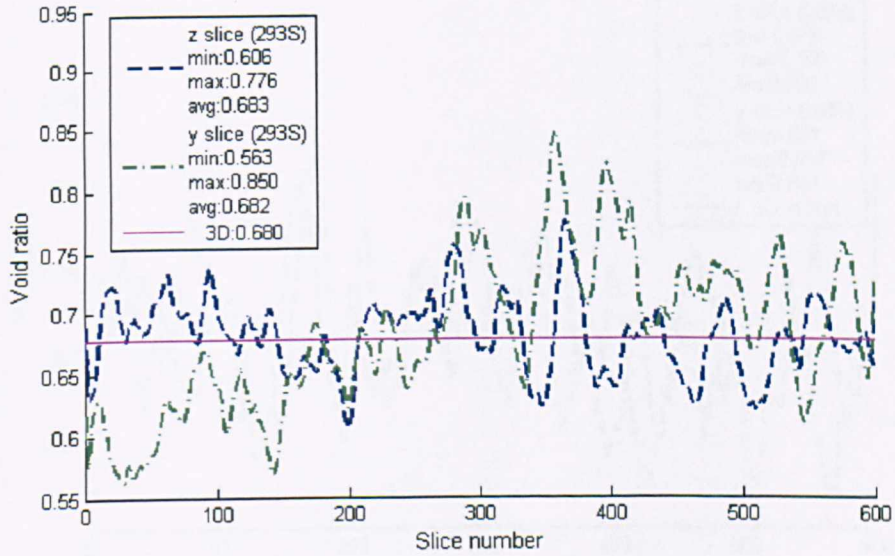

Figure 8.5: 2D void ratio distribution from horizontal (z) and vertical (y) slices for sample 293S

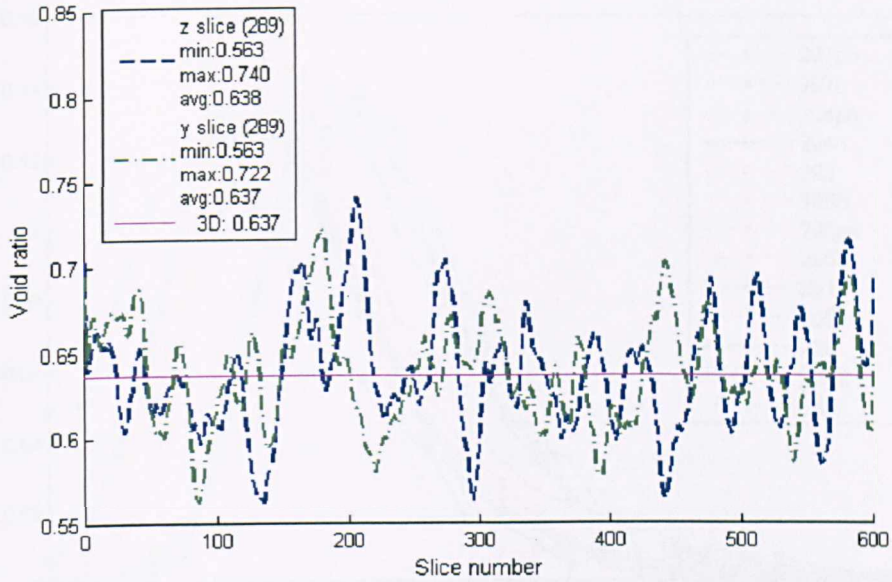

Figure 8.6: 2D void ratio distribution from horizontal (z) and vertical (y) slices for sample 289

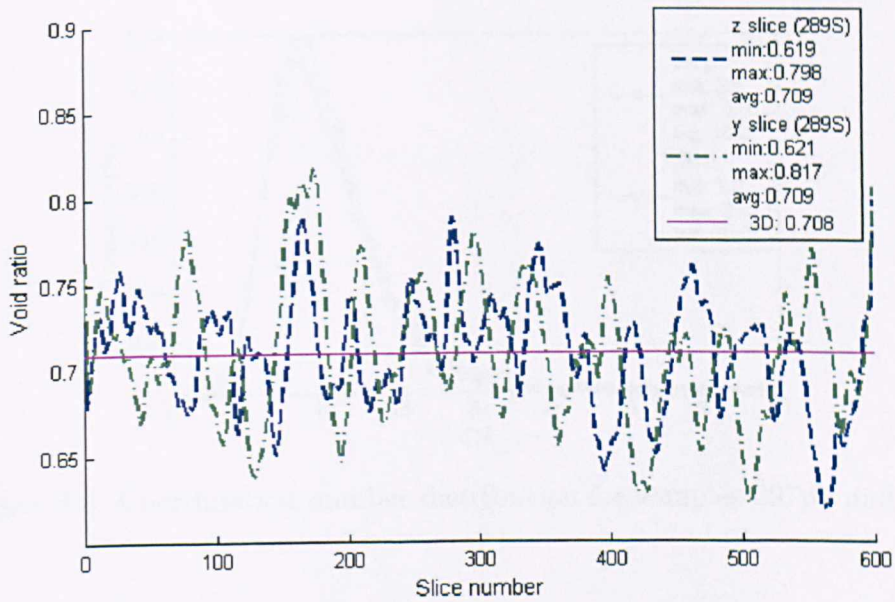

Figure 8.7: 2D void ratio distribution from horizontal (z) and vertical (y) slices for sample 289S

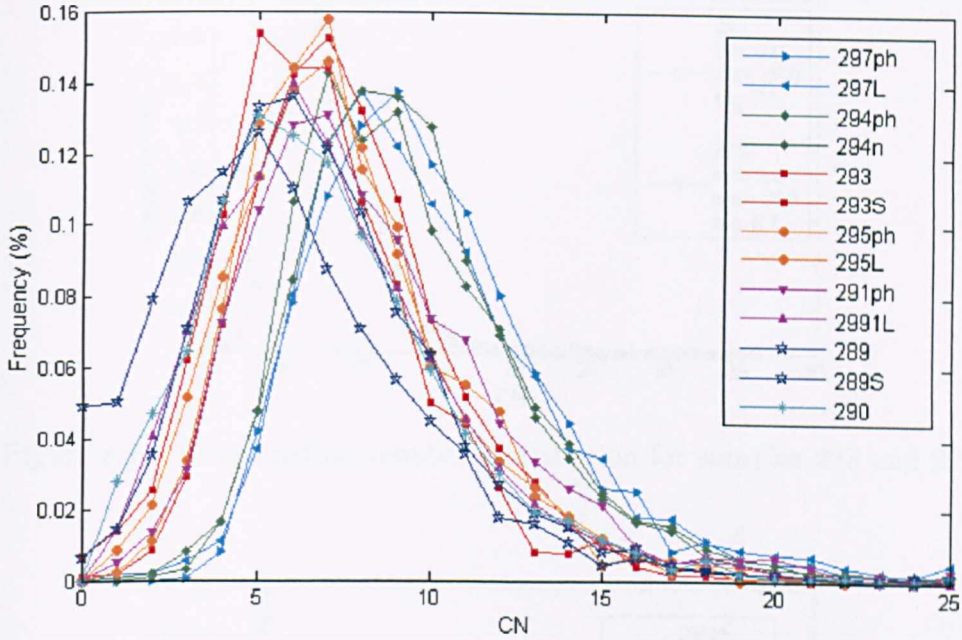

Figure 8.8: Coordination number distribution for all samples

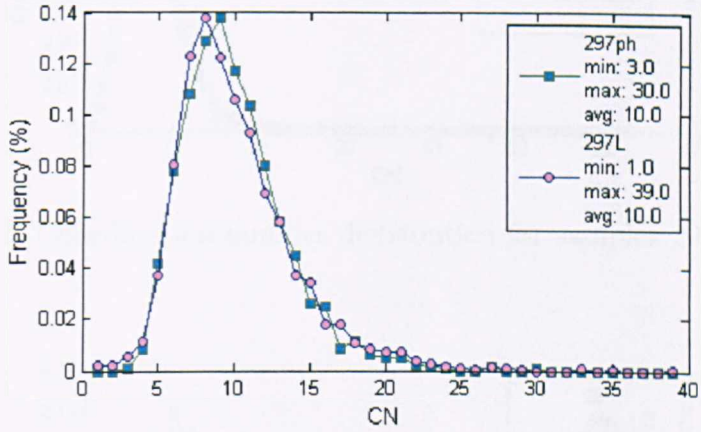

Figure 8.9: Coordination number distribution for samples 297ph and 297L

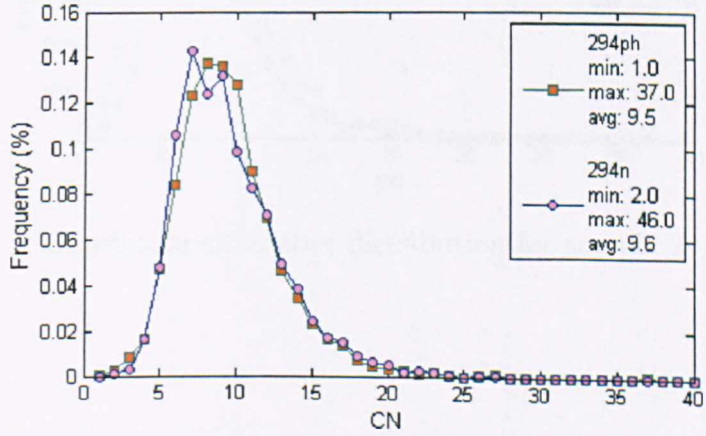

Figure 8.10: Coordination number distribution for samples 294ph and 294n

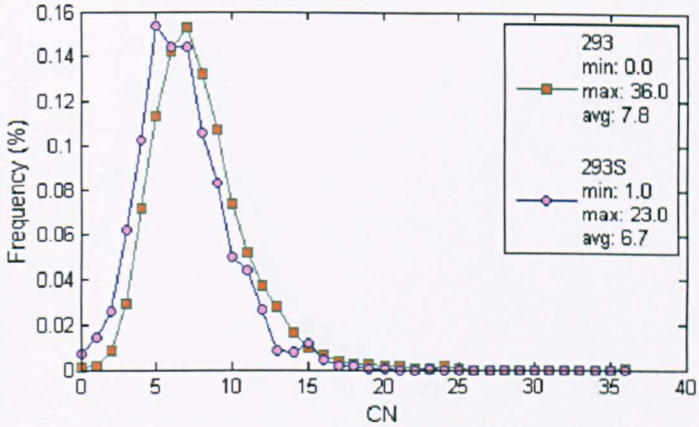

Figure 8.11: Coordination number distribution for samples 293 and 293S

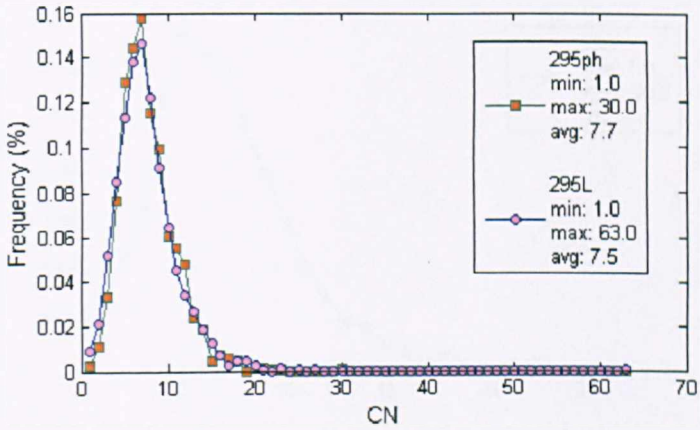

Figure 8.12: Coordination number distribution for samples 295ph and 295L

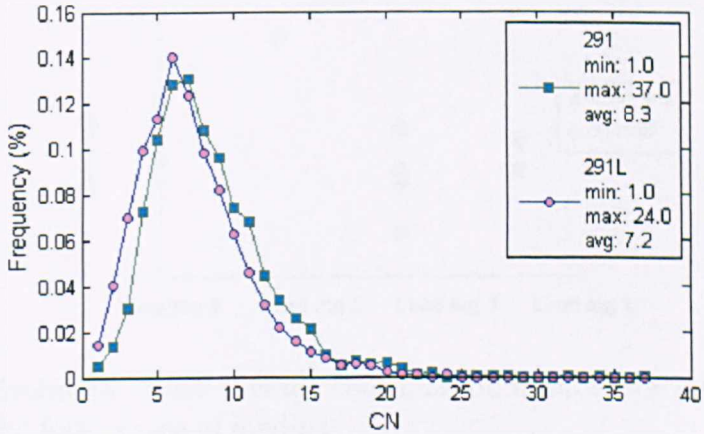

Figure 8.13: Coordination number distribution for sample 291ph and 291L

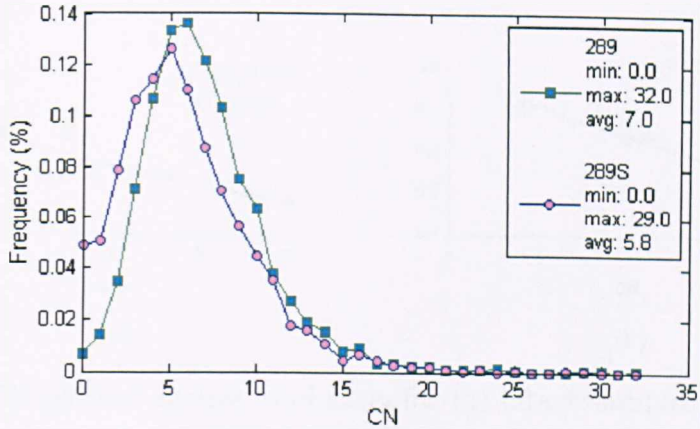

Figure 8.14: Coordination number distribution for samples 289 and 289S

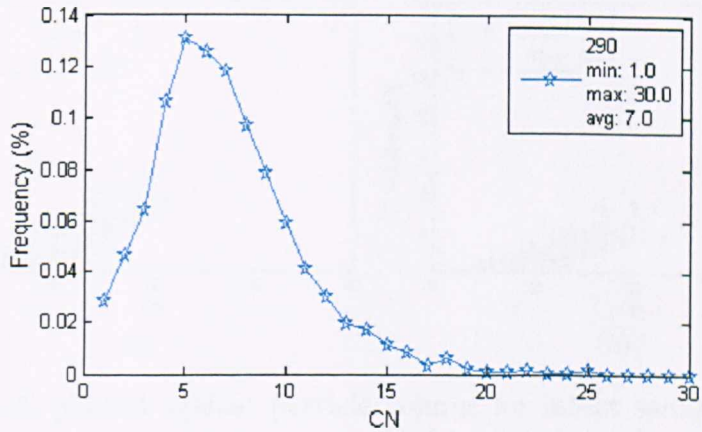

Figure 8.15: Coordination number distribution for sample 290

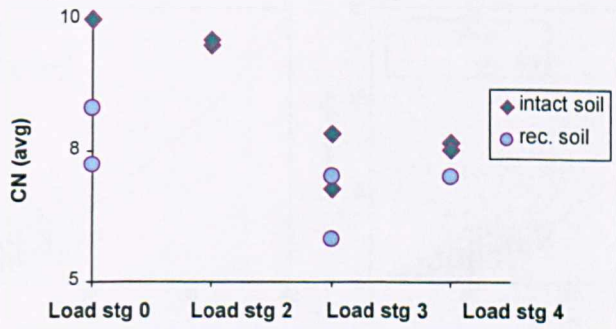

Figure 8.16: Evolution of the average coordination number for intact and reconstituted soil at the four stages of loading

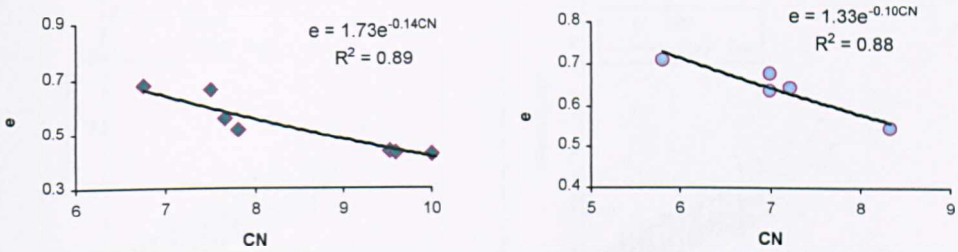

(a) (b)

Figure 8.17: CN plotted against void ratio for (a) intact samples (b) reconstituted samples

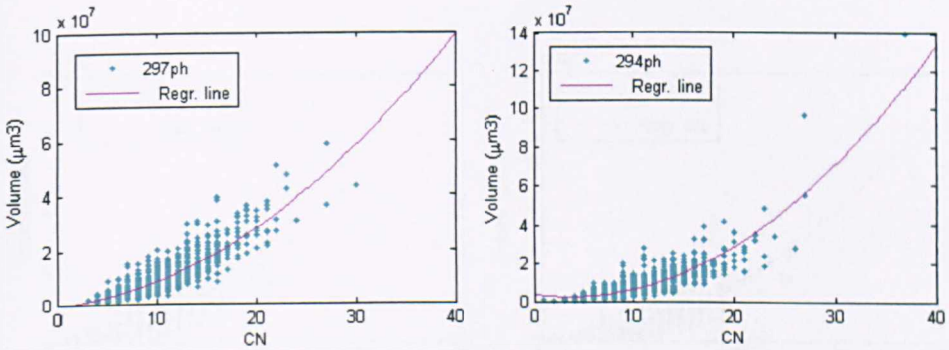

(a) (b)

Figure 8.18: CN plotted against particle volume for intact samples (a) 297ph (b) 294ph

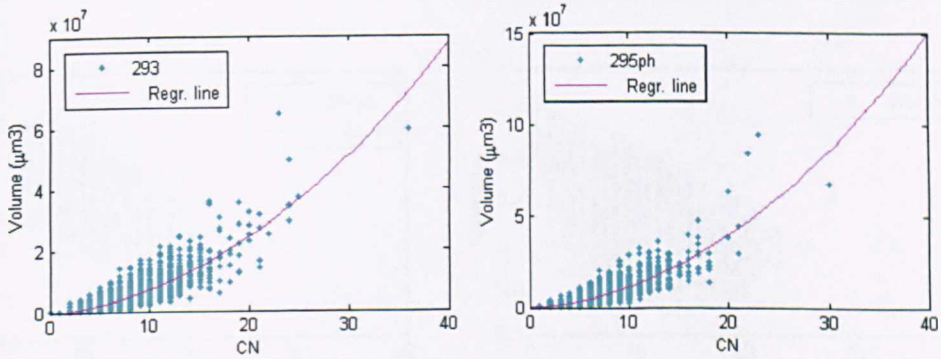

(a) (b)

Figure 8.19: CN plotted against particle volume for intact samples (a) 293 (b) 295ph

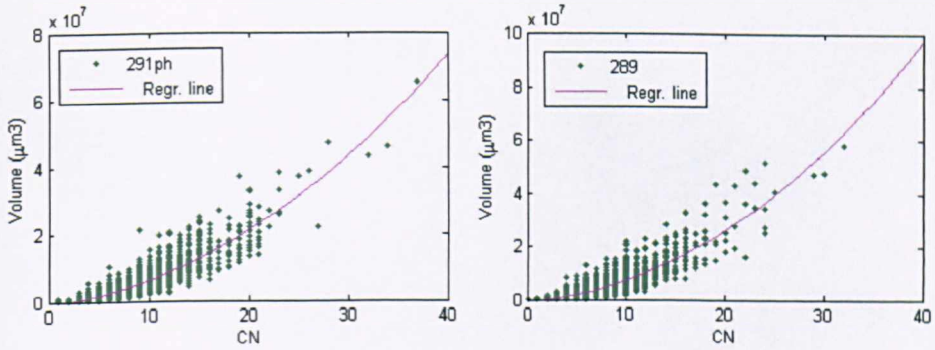

(a) (b)

Figure 8.20: CN plotted against particle volume for reconstituted samples (a) 291ph (b) 289

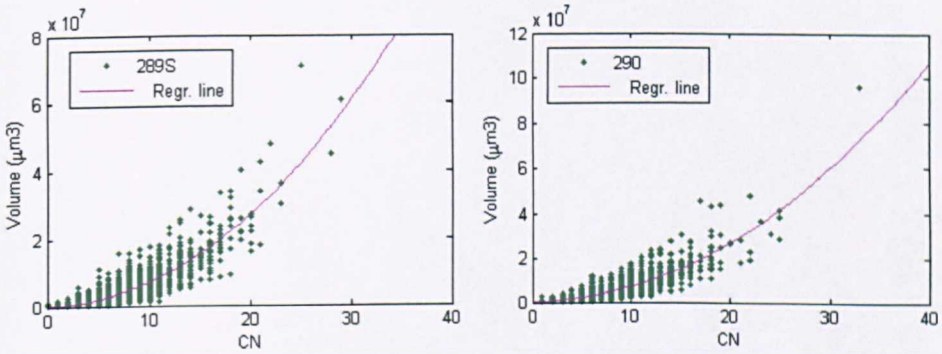

(a) (b)

Figure 8.21: CN plotted against particle volume for reconstituted samples (a) 289S (b) 290

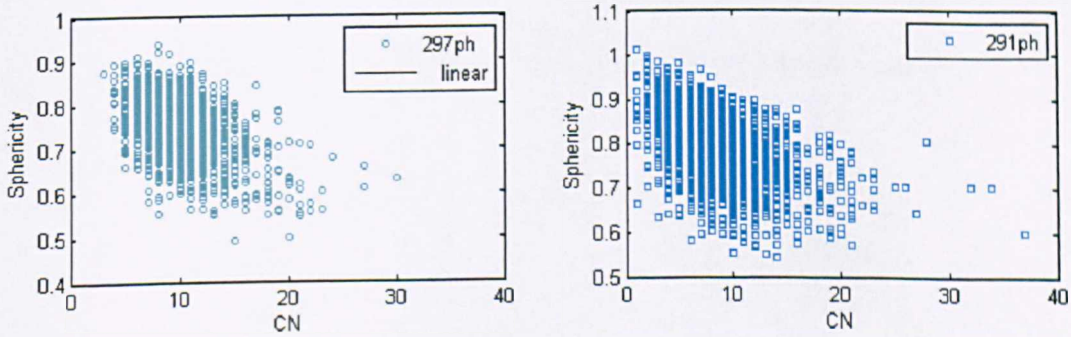

(a) (b)

Figure 8.22: CN plotted against sphericity for samples (a) 297ph (b) 291ph

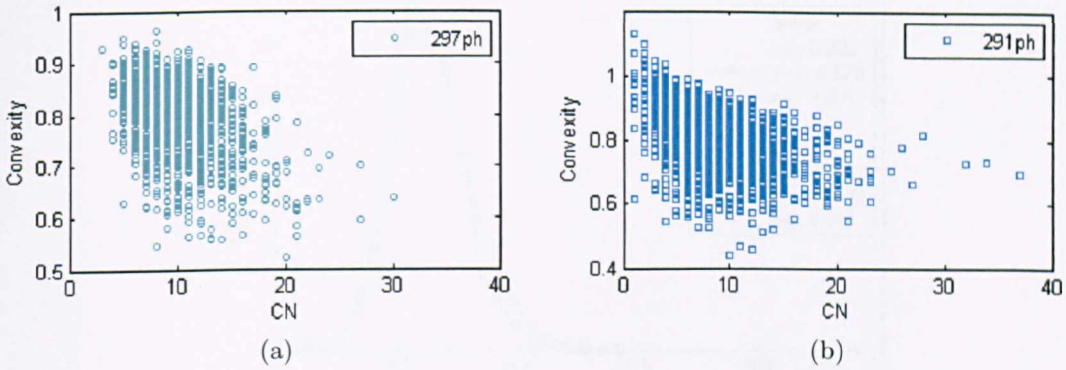

(a) (b)

Figure 8.23: CN plotted against convexity for samples (a) 297ph (b) 291ph

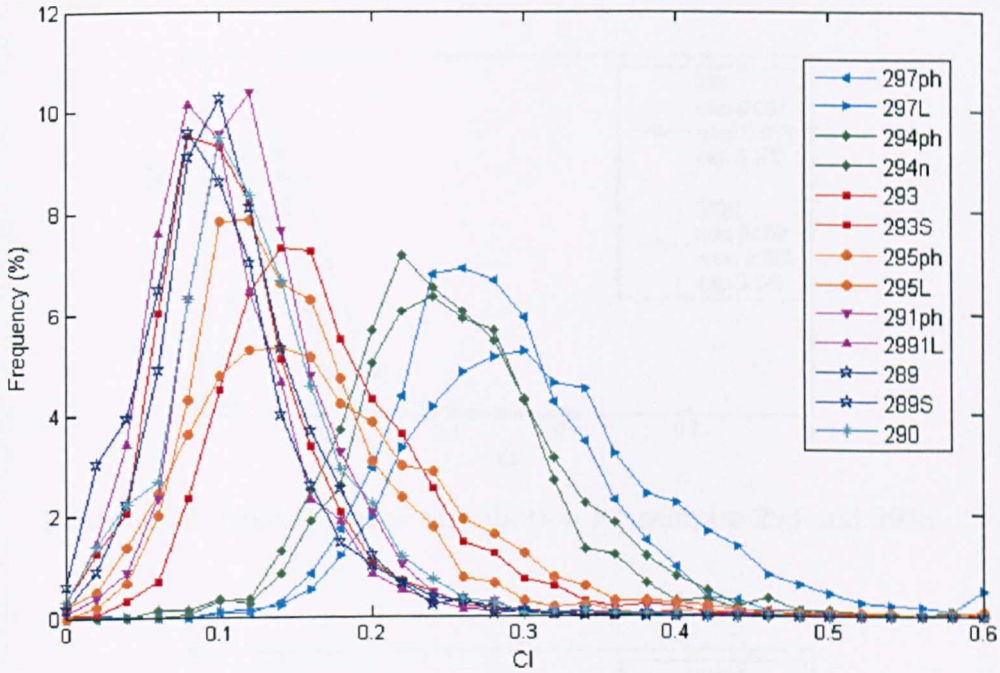

Figure 8.24: Contact index distribution for all samples

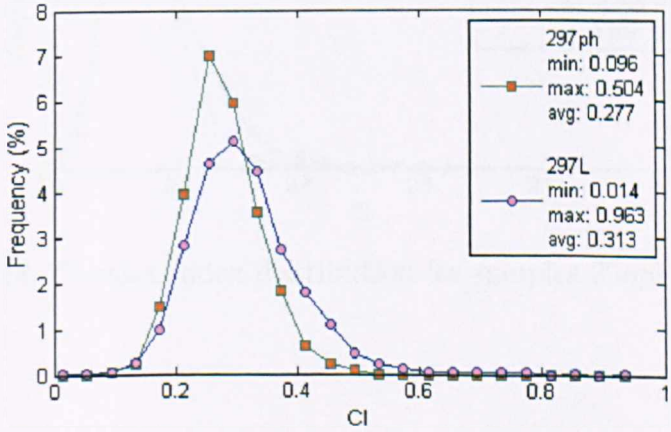

Figure 8.25: Contact index distribution for samples 297ph and 297L

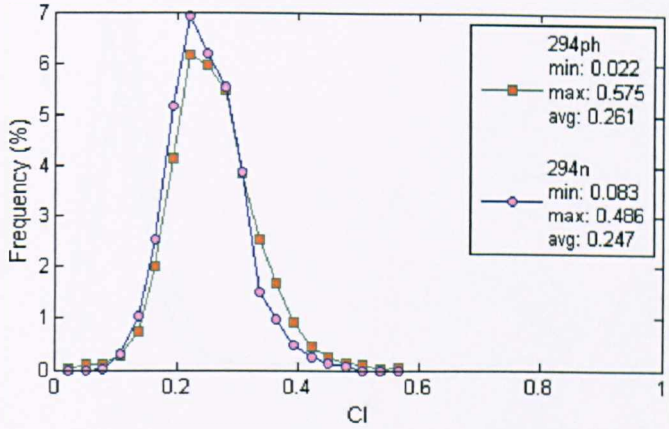

Figure 8.26: Contact index distribution for samples 294ph and 294L

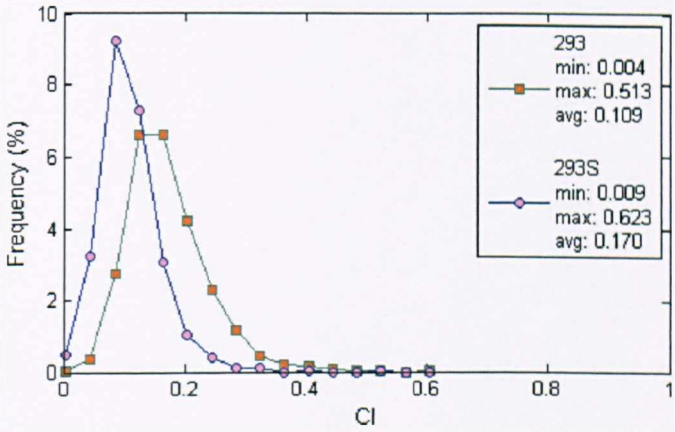

Figure 8.27: Contact index distribution for samples 293 and 293S

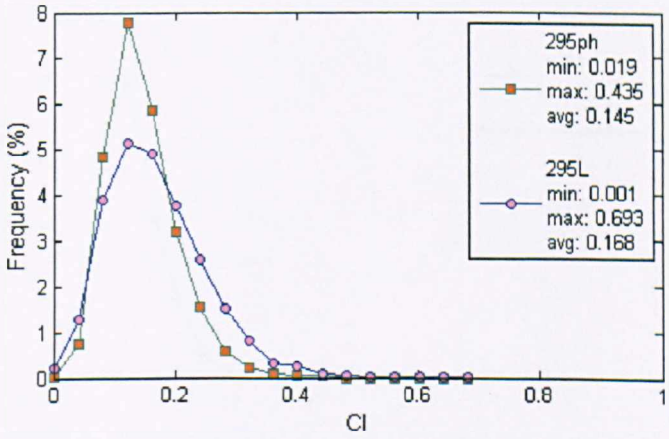

Figure 8.28: Contact index distribution for samples 295ph and 295L

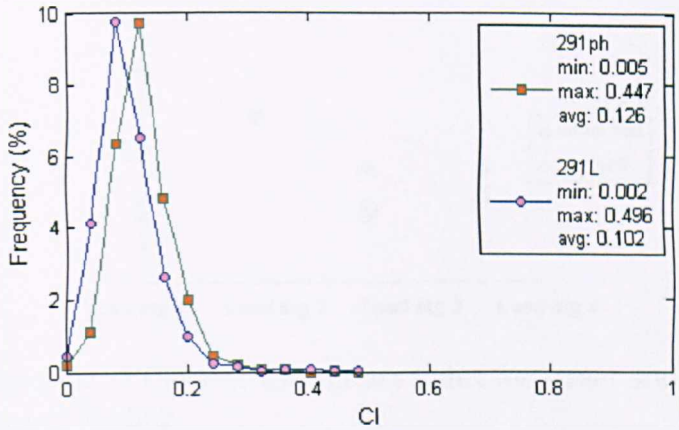

Figure 8.29: Contact index distribution for samples 291ph and 291L

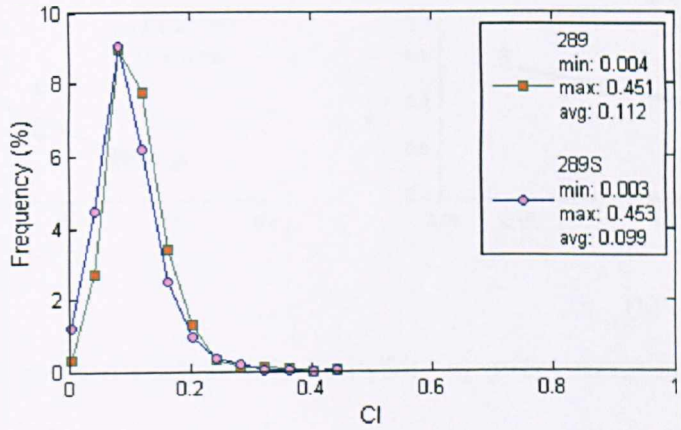

Figure 8.30: Contact index distribution for samples 289 and 289S

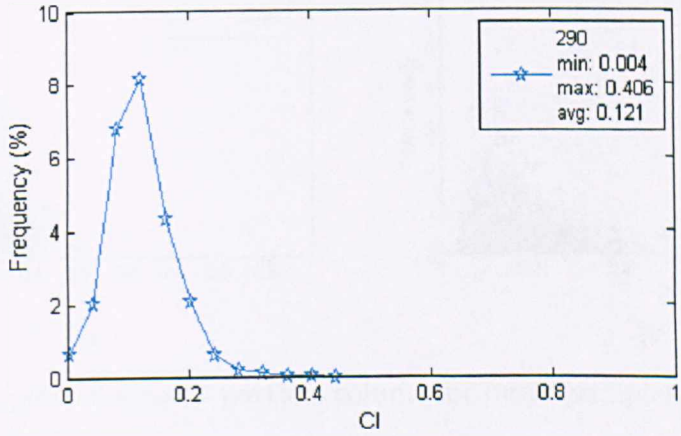

Figure 8.31: Contact index distribution for sample 290

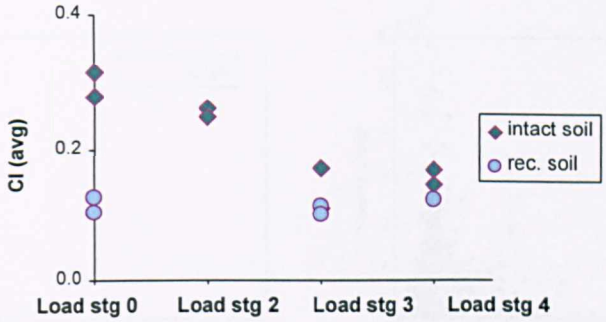

Figure 8.32: Evolution of the average contact index for intact and reconstituted soil at the four stages of loading

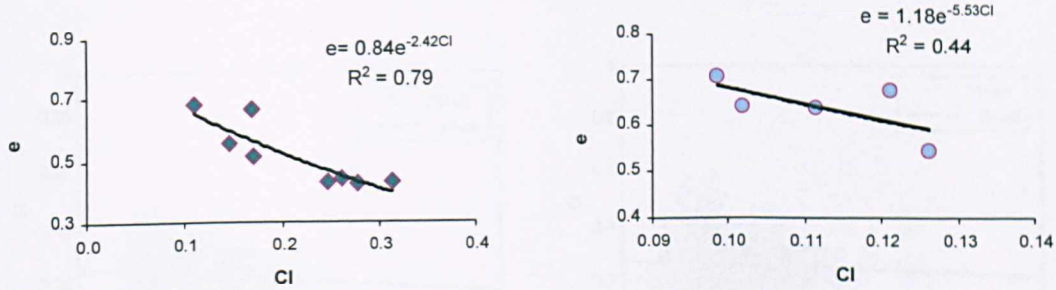

(a) (b)

Figure 8.33: CI plotted against void ratio for (a) intact samples (b) reconstituted samples

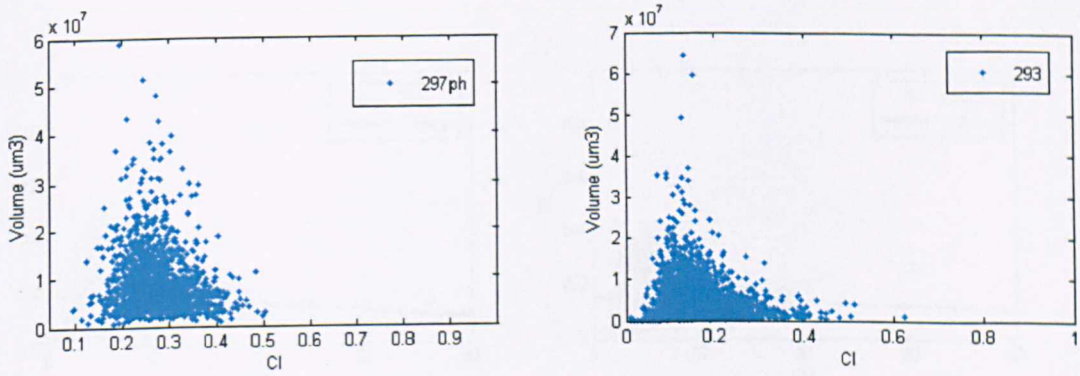

(a) (b)

Figure 8.34: CI plotted against particle volume for intact samples (a) 297ph and (b) 293

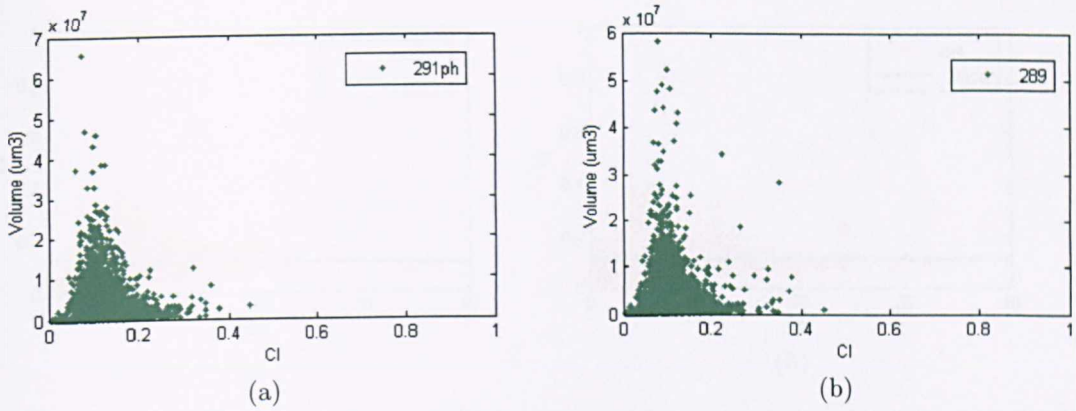

Figure 8.35: CI plotted against particle volume for reconstituted samples (a) 291 and (b) 289

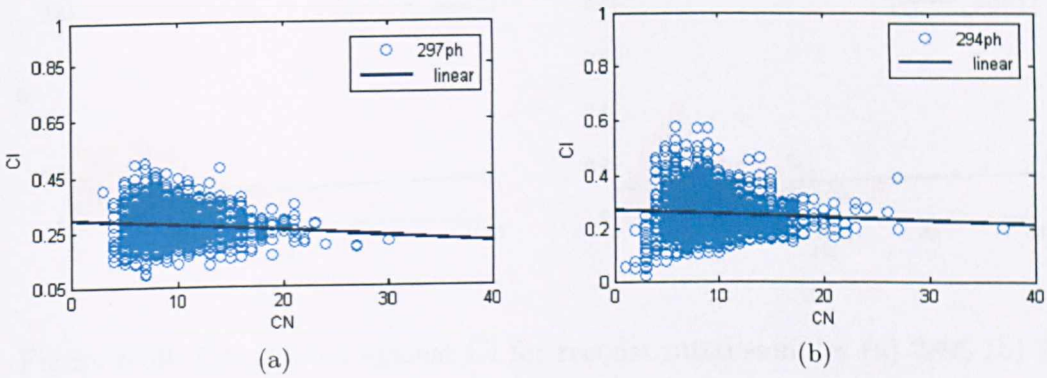

Figure 8.36: CN plotted against CI for intact samples (a) 297ph (b) 294ph

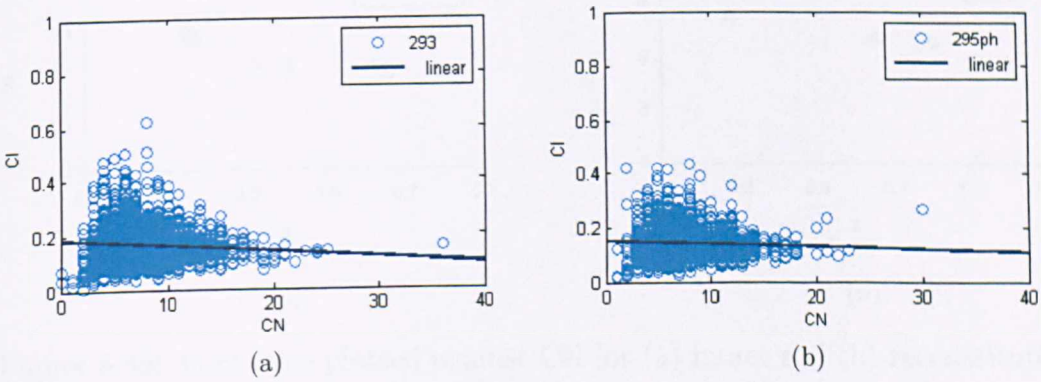

Figure 8.37: CN plotted against CI for intact samples (a) 293 (b) 295ph

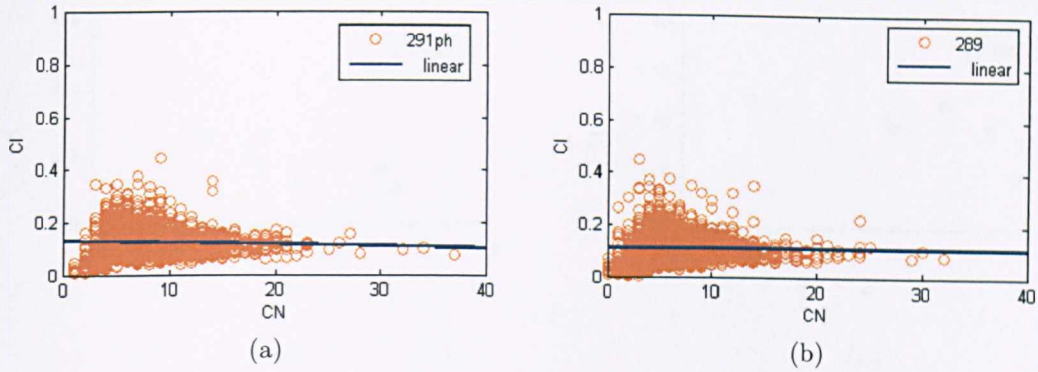

(a) (b)

Figure 8.38: CN plotted against CI for reconstituted samples (a) 291ph (b) 289

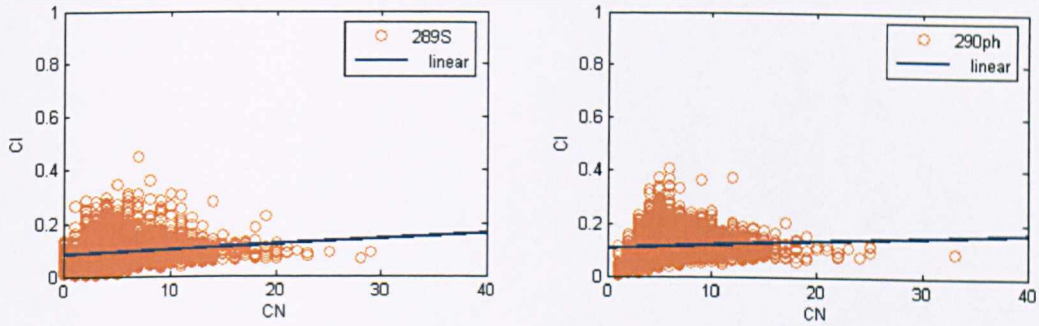

(a) (b)

Figure 8.39: CN plotted against CI for reconstituted samples (a) 289S (b) 290ph

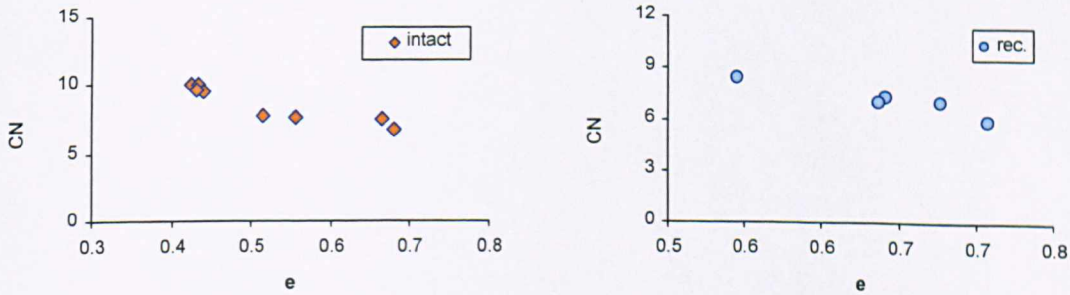

(a) (b)

Figure 8.40: Void ratio plotted against CN for (a) intact soil (b) reconstituted soil

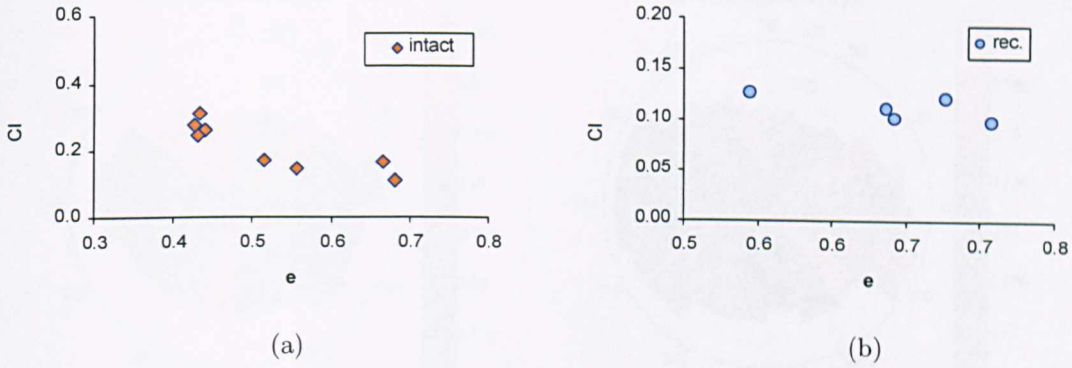

(a) (b)

Figure 8.41: Void ratio plotted against CI for (a) intact soil (b) reconstituted soil

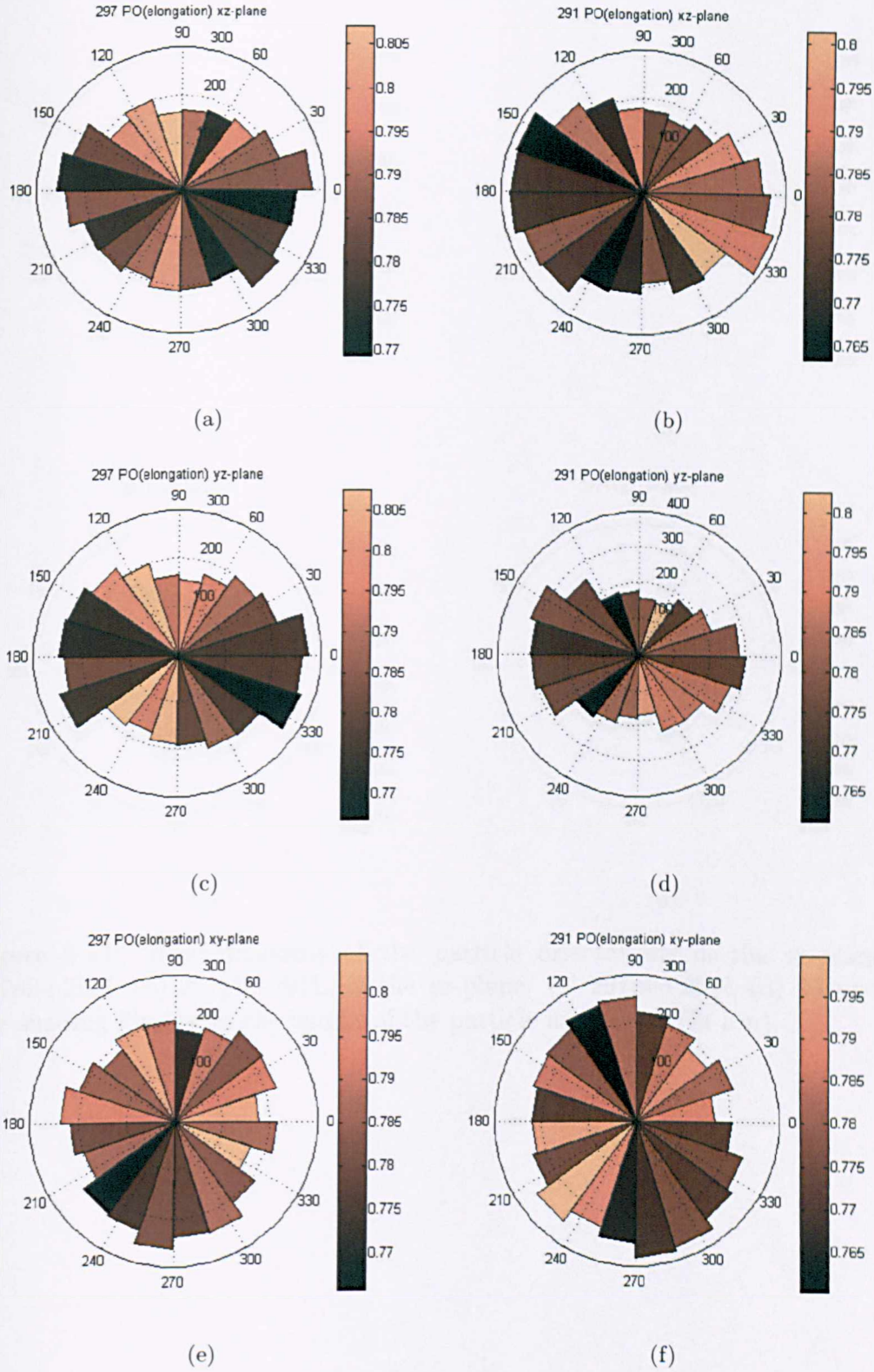

Figure 8.42: Rose diagrams of the particle orientations in the xz-plane: (a) 297ph+297L (b) 291ph+291L, in the yz-plane: (c) 297ph+297L (d) 291ph+291L, in the xy-plane: (e) 297ph+297L (f) 291ph+291L; the shading illustrates the elongation ratio

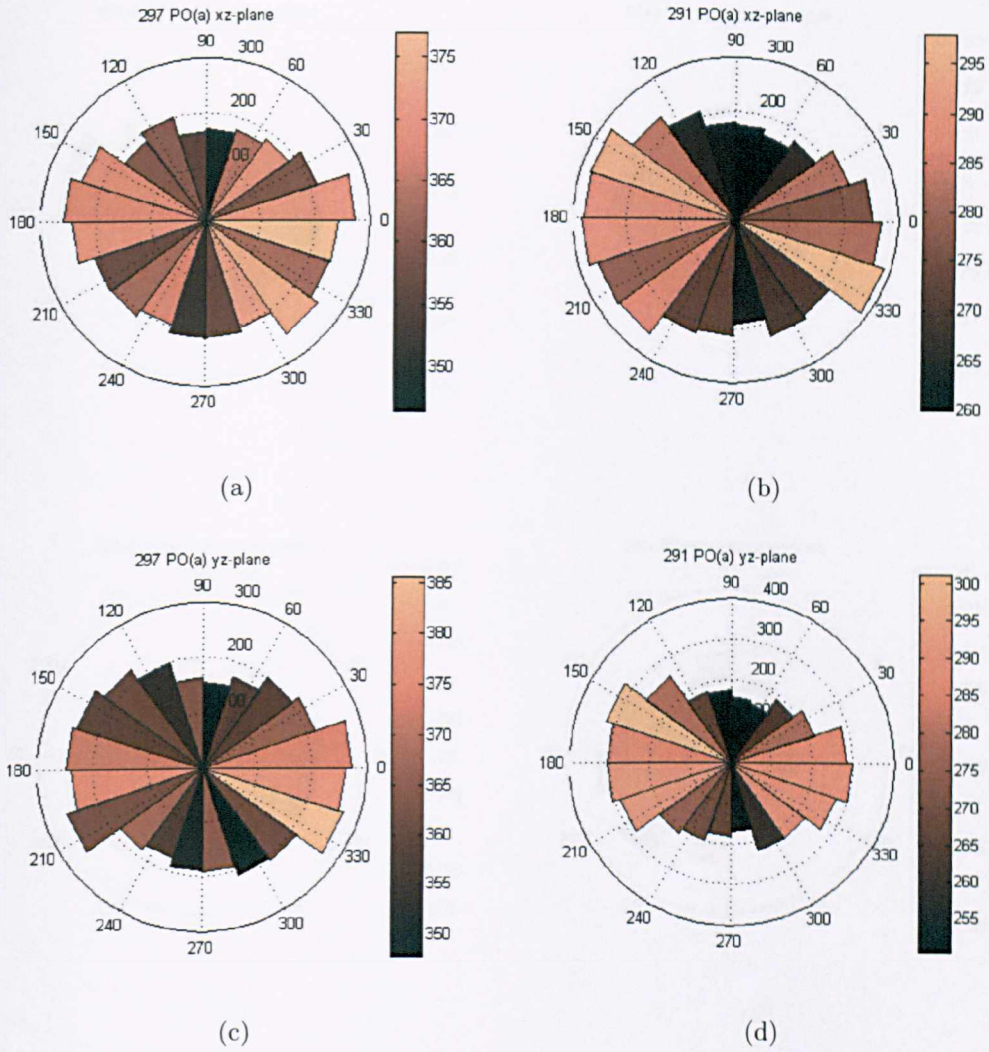

Figure 8.43: Rose diagrams of the particle orientations in the xz-plane: (a) 297ph+297L (b) 291ph+291L, in the yz-plane: (c) 297ph+297L (d) 291ph+291L; the shading illustrates the length of the particle major axis (in μm)

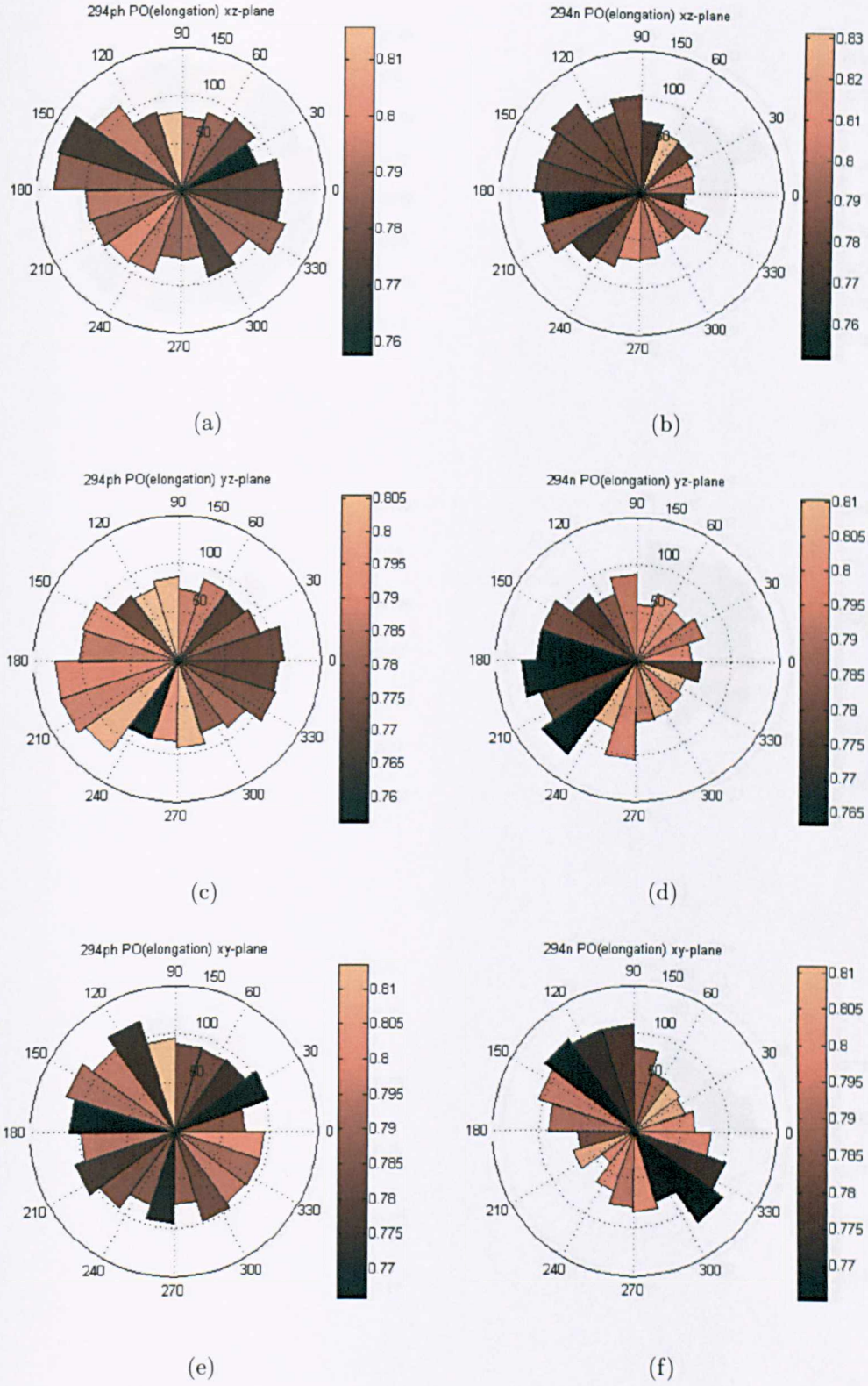

Figure 8.44: Rose diagrams of the particle orientations in the xz-plane: (a) 294ph (b) 294n, in the yz-plane: (c) 294ph (d) 294n, in the xy-plane: (e) 294ph (f) 294n; the shading illustrates the elongation ratio

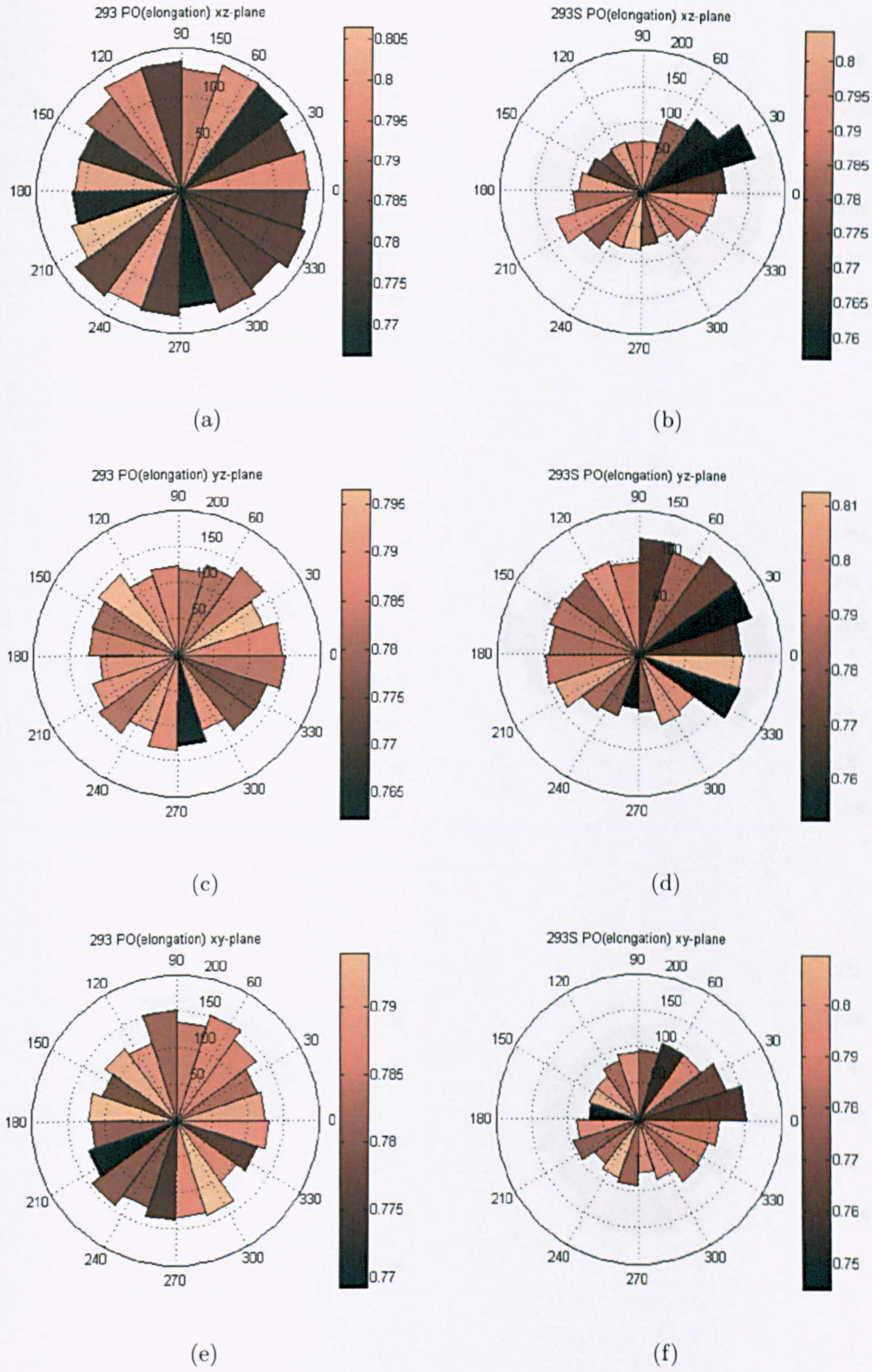

Figure 8.45: Rose diagrams of the particle orientations in the xz-plane: (a) 293 (b) 293S, in the yz-plane: (c) 293 (d) 293S, in the xy-plane: (e) 293 (f) 293S; the shading illustrates the elongation ratio

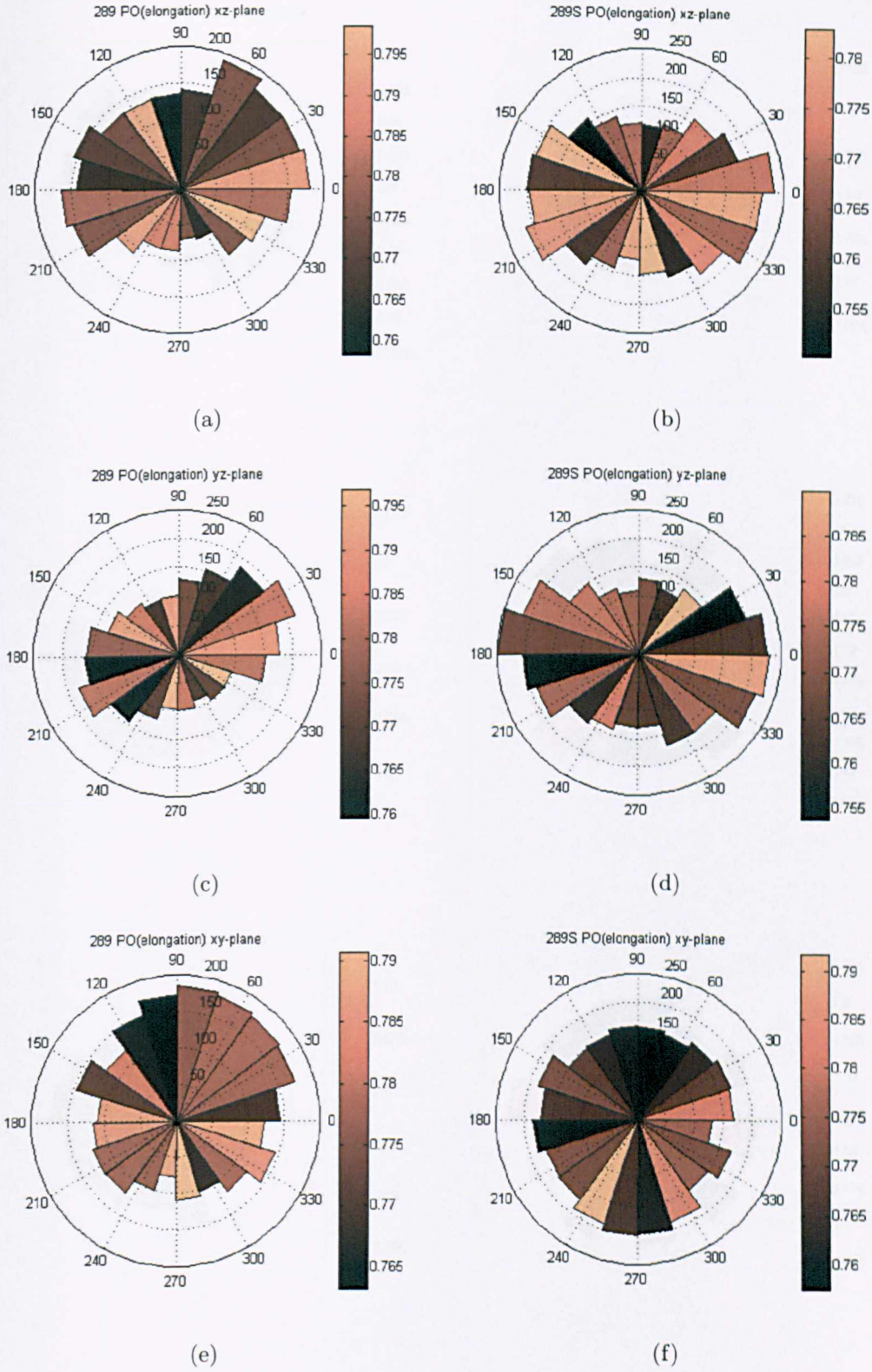

Figure 8.46: Rose diagrams of the particle orientations in the xz-plane: (a) 289 (b) 289S, in the yz-plane: (c) 289 (d) 289S, in the xy-plane: (e) 289 (f) 289S; the shading illustrates the elongation ratio

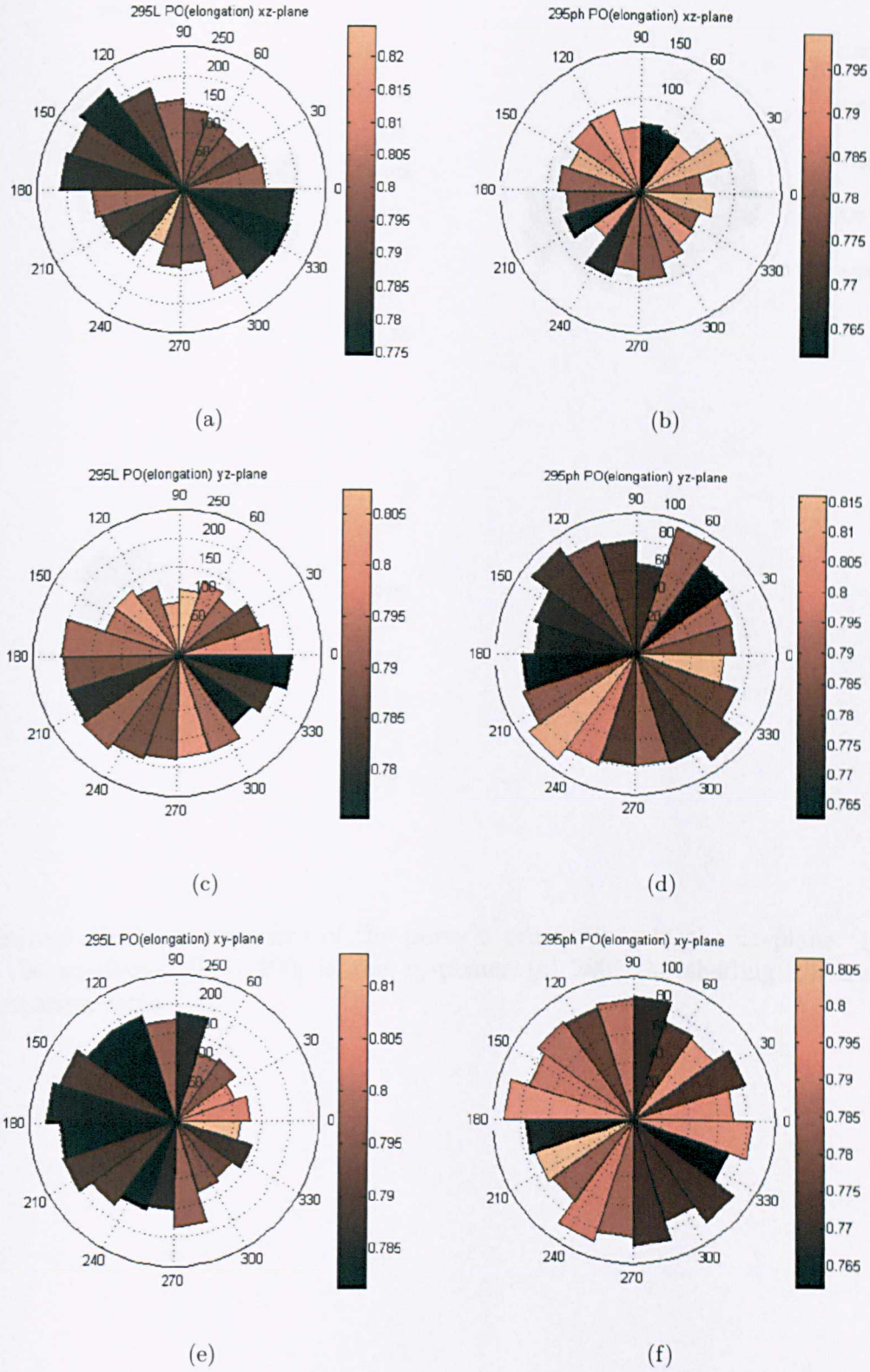

Figure 8.47: Rose diagrams of the particle orientations in the xz-plane: (a) 295ph (b) 295L, in the yz-plane: (c) 295ph (d) 295L, in the xy-plane: (e) 295ph (f) 295L; the shading illustrates the elongation ratio

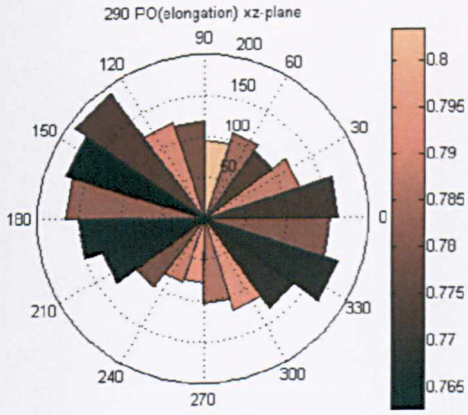

(a)

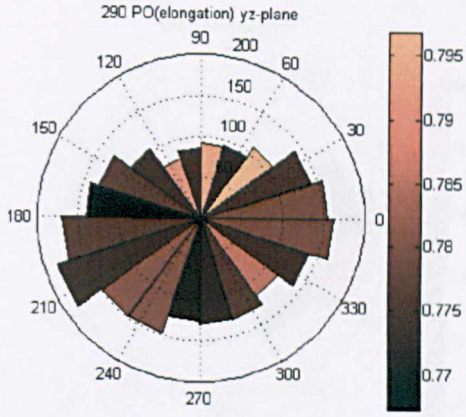

(b)

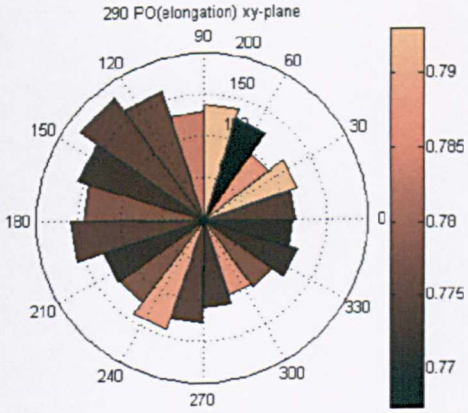

(c)

Figure 8.48: Rose diagrams of the particle orientations in the xz-plane: (a) 290, in the yz-plane: (bB) 290, in the xy-plane: (c) 290; the shading illustrates the elongation ratio

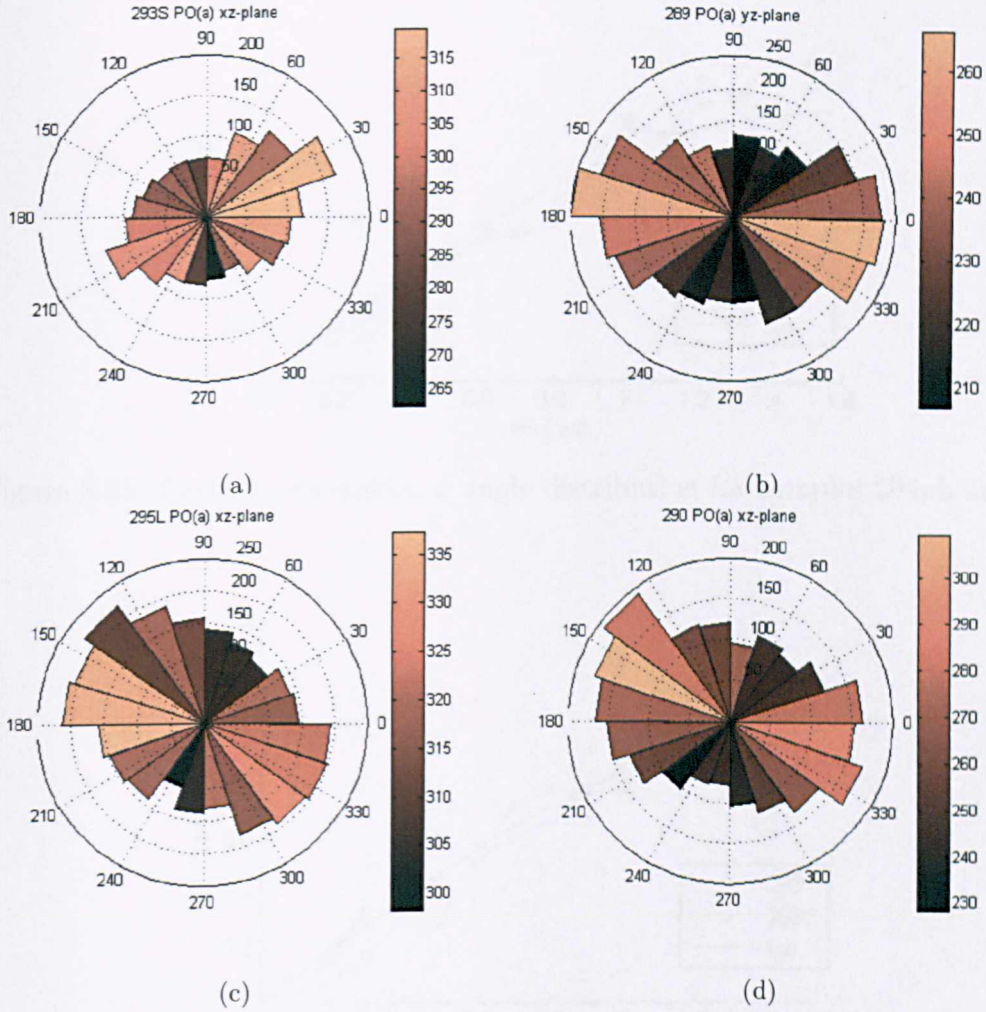

Figure 8.49: Rose diagrams of the particle orientation in one vertical plane (a) 293S (b) 289 (c) 295L (d) 290, the shading illustrates the length of the particle major axis (in μm)

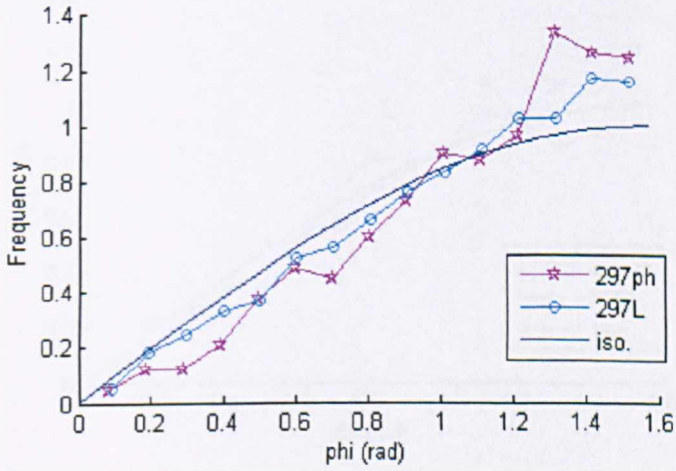

Figure 8.50: Particle orientation ϕ angle distribution for samples 297ph and 297L

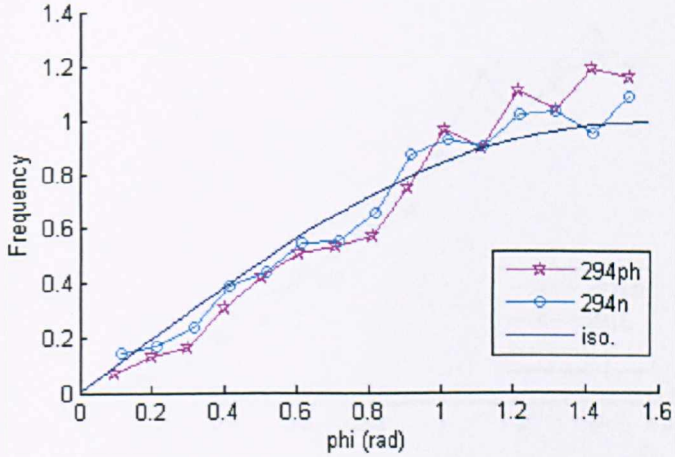

Figure 8.51: Particle orientation ϕ angle distribution for samples 294ph and 294n

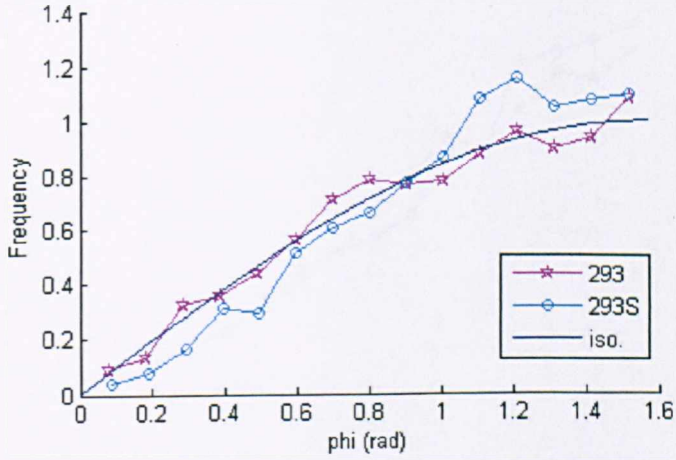

Figure 8.52: Particle orientation ϕ angle distribution for samples 293 and 293S

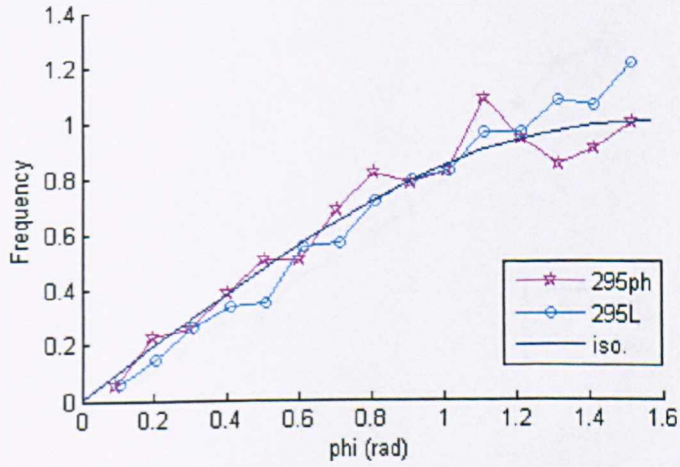

Figure 8.53: Particle orientation ϕ angle distribution for samples 295ph and 295L

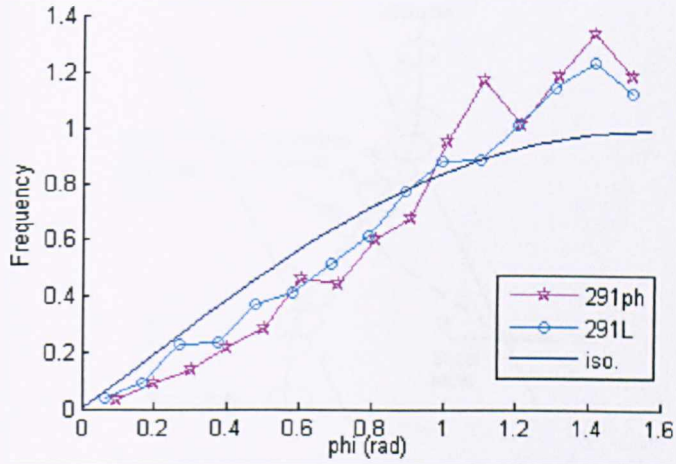

Figure 8.54: Particle orientation ϕ angle distribution for samples 291ph and 291L

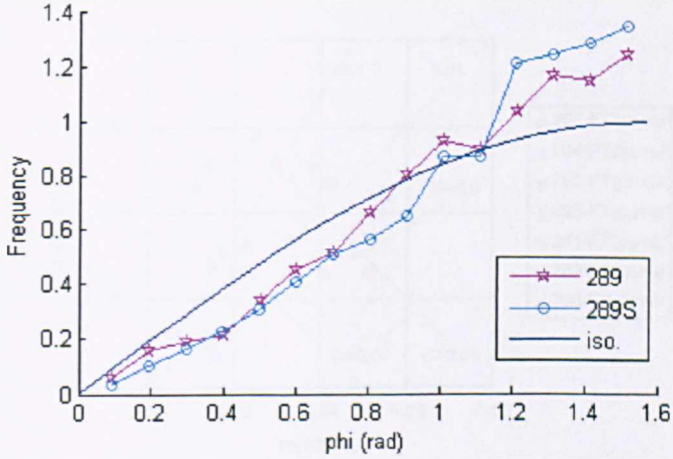

Figure 8.55: Particle orientation ϕ angle distribution for samples 289 and 289S

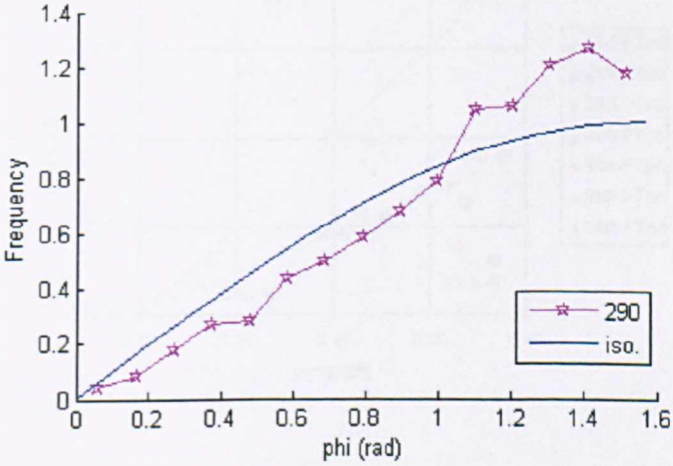

Figure 8.56: Particle orientation ϕ angle distribution for sample 290

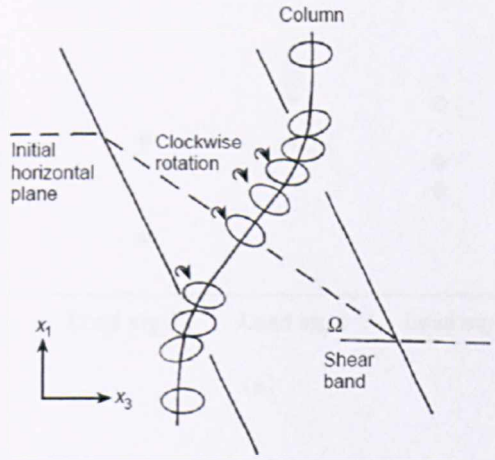

Figure 8.57: Particle rotation in a shear band (Oda and Kazama, 1998)

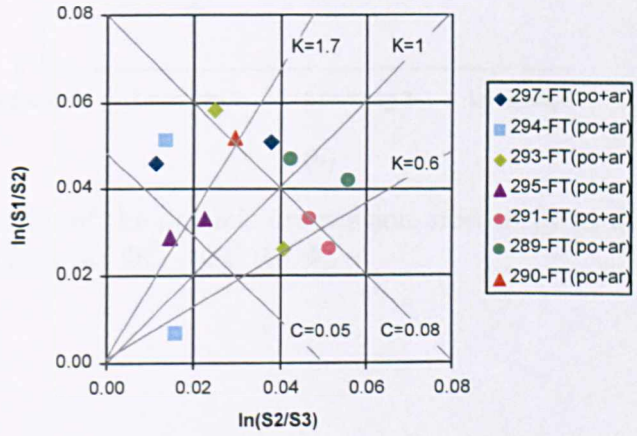

(a)

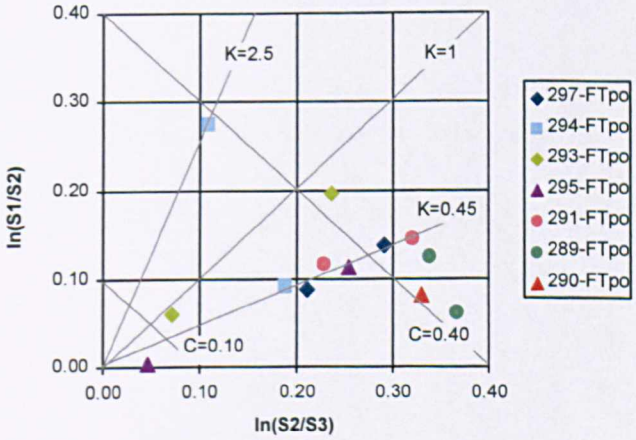

(b)

Figure 8.58: Eigenvalue ratios for particle orientation data using (a) Φ^P (b) Φ

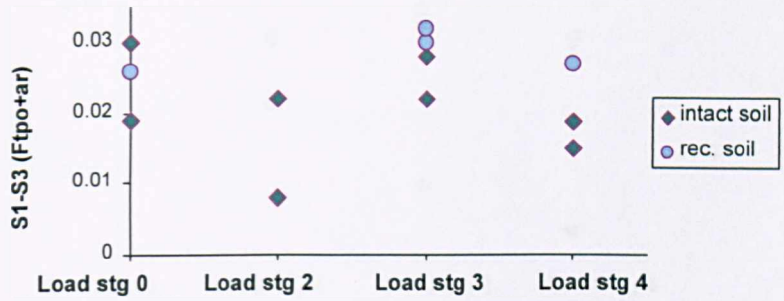

(a)

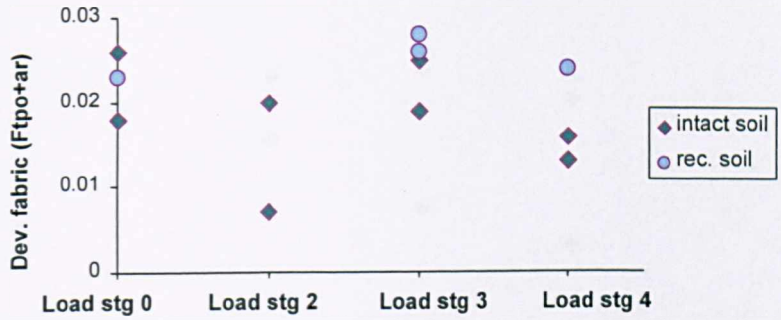

(b)

Figure 8.59: Evolution of the particle orientation anisotropy at different load stages using the formulations (a) $\Phi_1^P - \Phi_3^P$ (b) Φ_d^P

(a)

(b)

Figure 8.60: Evolution of the particle orientation anisotropy at different load stages using the formulations (a) $\Phi_1 - \Phi_3$ (b) Φ_d

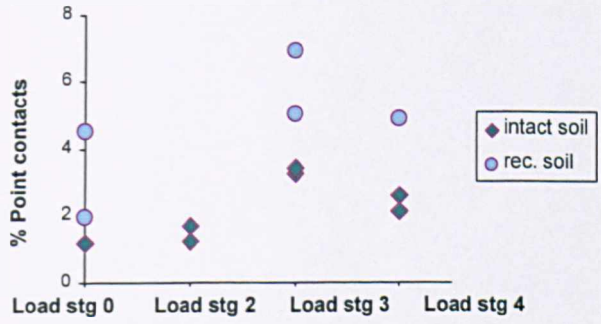

Figure 8.61: Percentage of point contacts at each load stage for intact and reconstituted samples

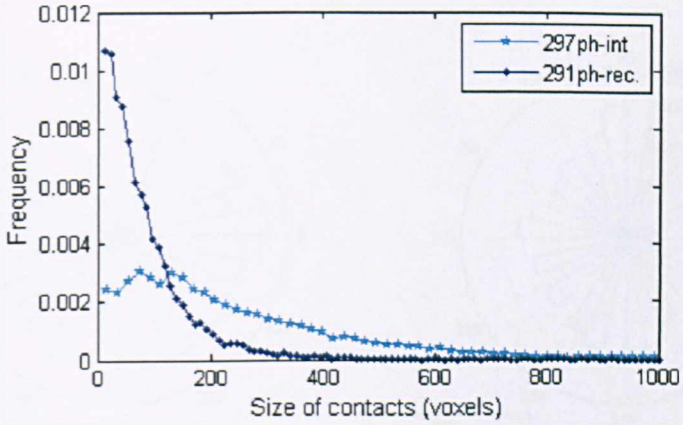

Figure 8.62: Contact size distribution of one intact sample (297ph) and one reconstituted sample (291ph)

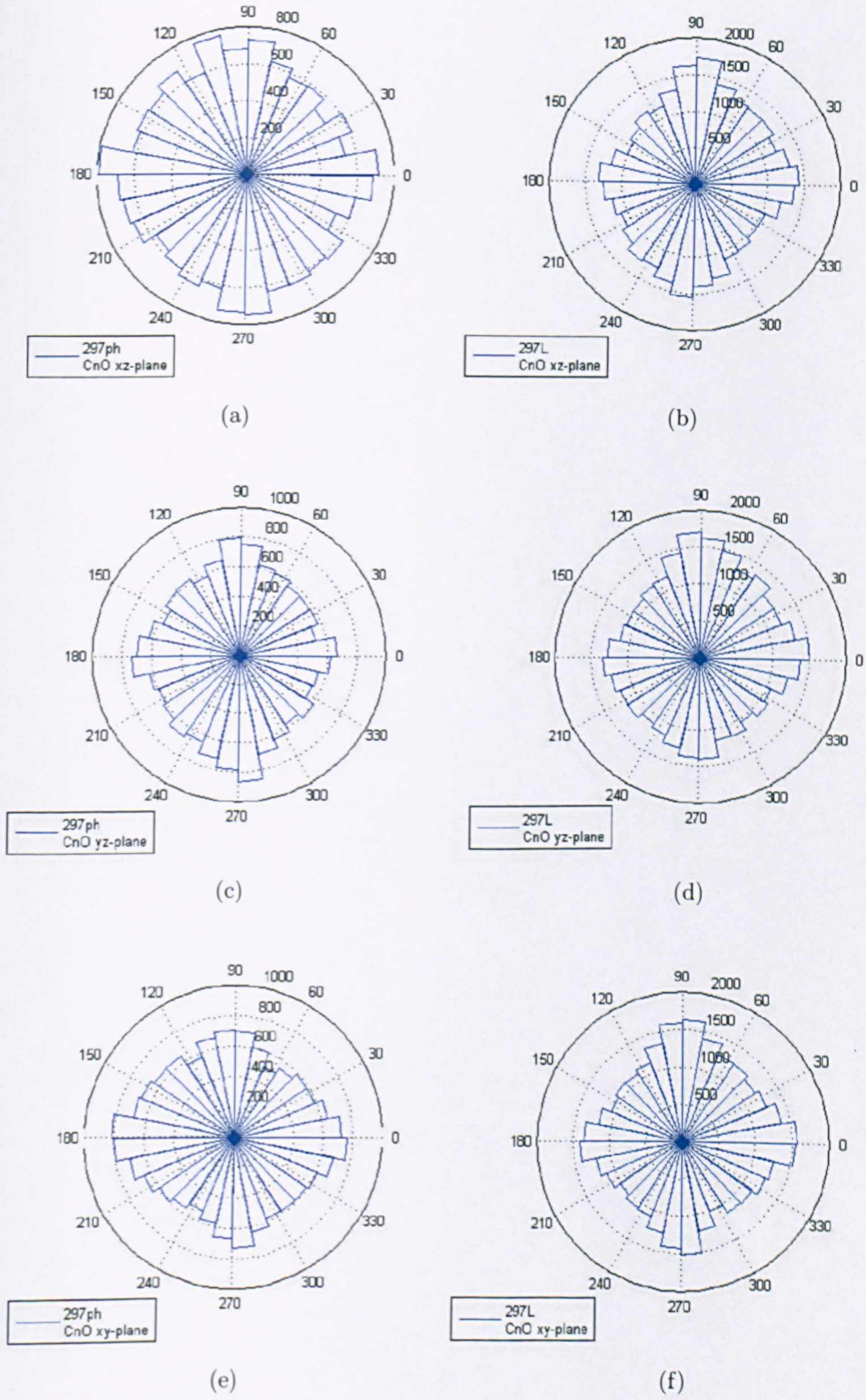

Figure 8.63: Rose diagrams of the contact normal orientation for the intact samples prior to loading, in the xz-plane: (a) 297ph (b) 297L, in the yz-plane: (c) 297ph (d) 297L, in the xy-plane: (e) 297ph (f) 297L

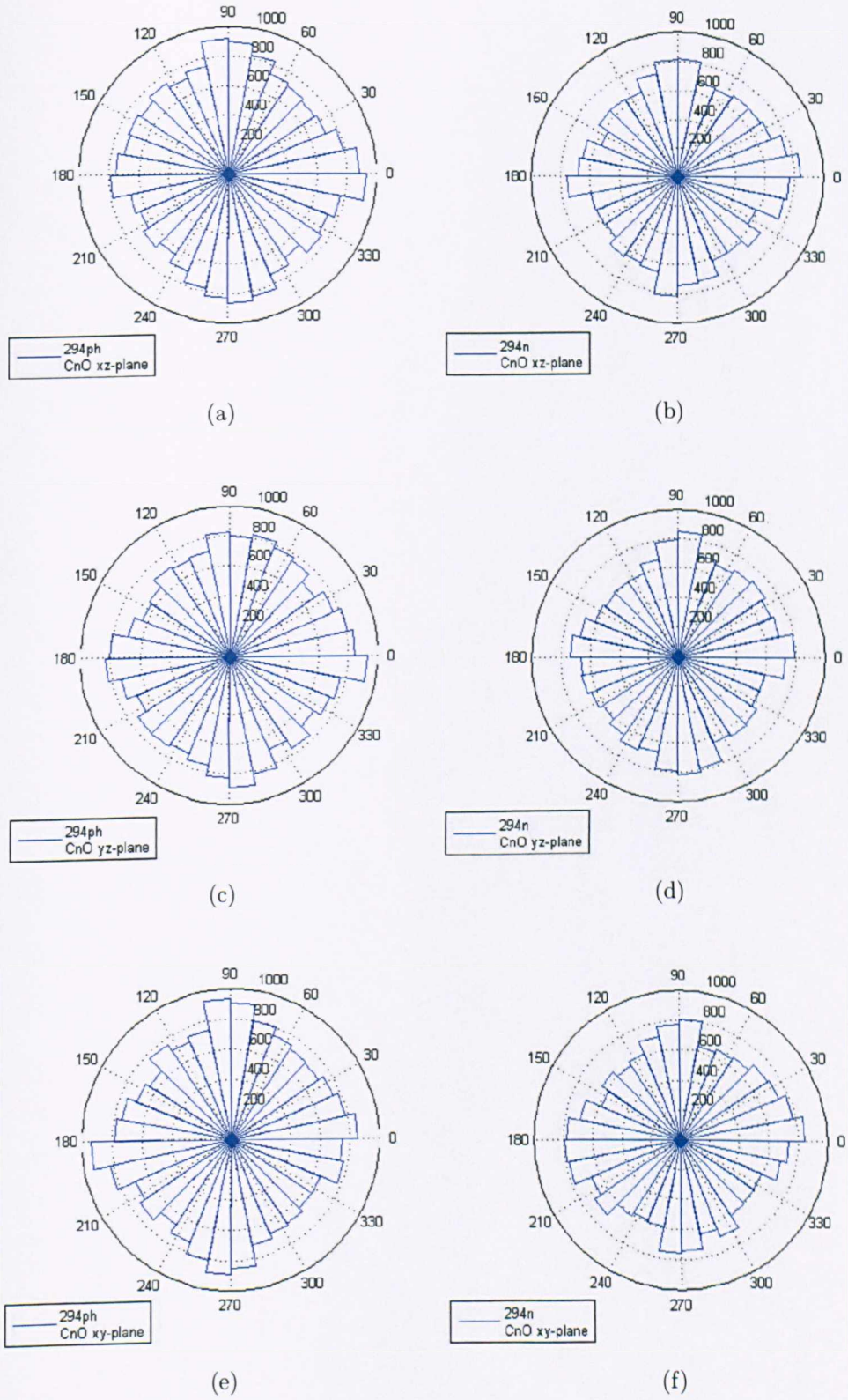

Figure 8.64: Rose diagrams of the contact normal orientation for the intact samples at load stage 2, in the xz-plane: (a) 294ph (b) 294n, in the yz-plane: (c) 294ph (d) 294n, in the xy-plane: (e) 294ph (f) 294n

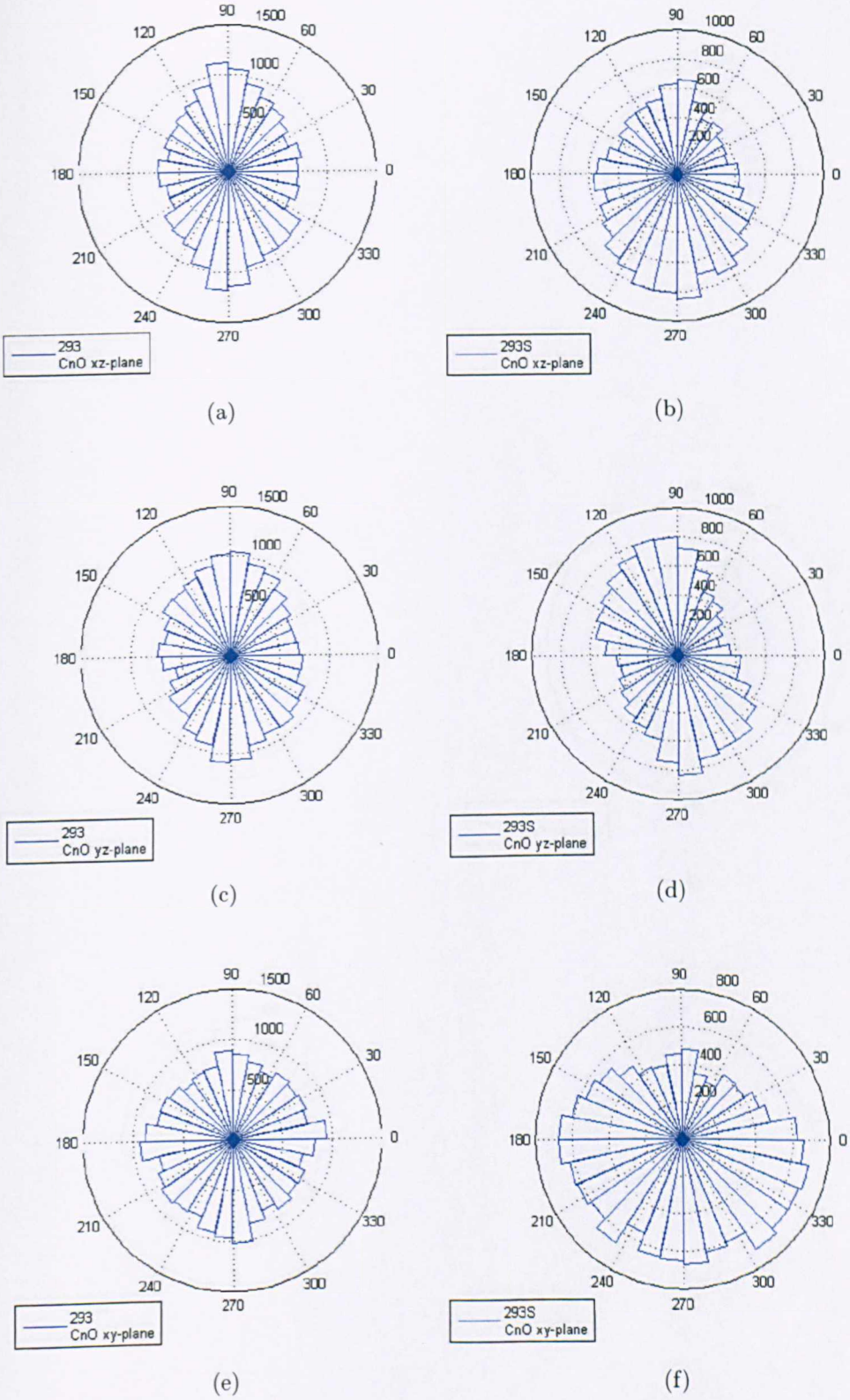

Figure 8.65: Rose diagrams of the contact normal orientation for the intact samples at load stage 3, in the xz-plane: (a) 293 (b) 293S, in the yz-plane: (c) 293 (d) 293S, in the xy-plane: (e) 293 (f) 293S

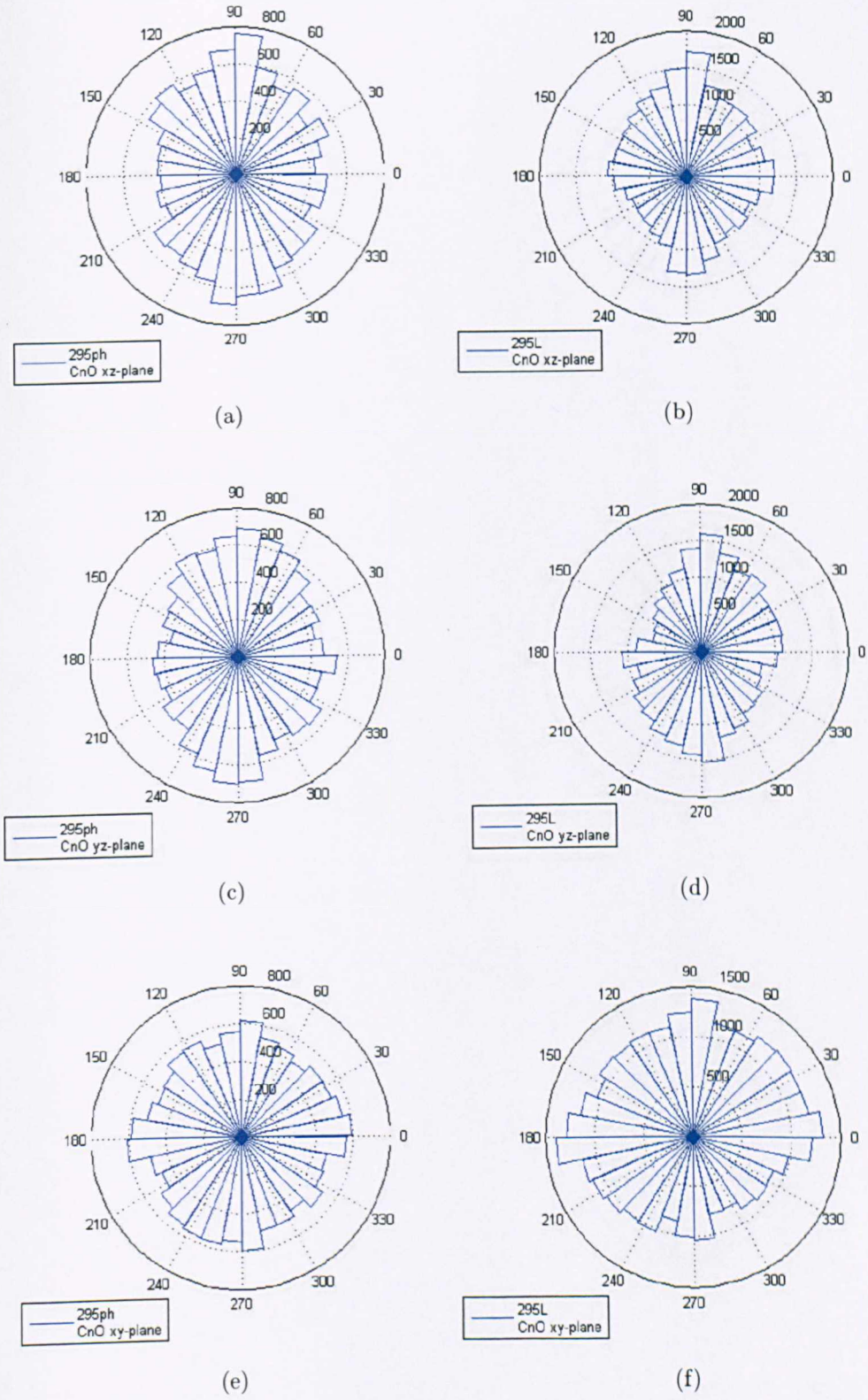

Figure 8.66: Rose diagrams of the contact normal orientation for the intact samples at load stage 4, in the xz-plane: (a) 295ph (b) 295L, in the yz-plane: (c) 295ph (d) 295L, in the xy-plane: (e) 295ph (f) 295L

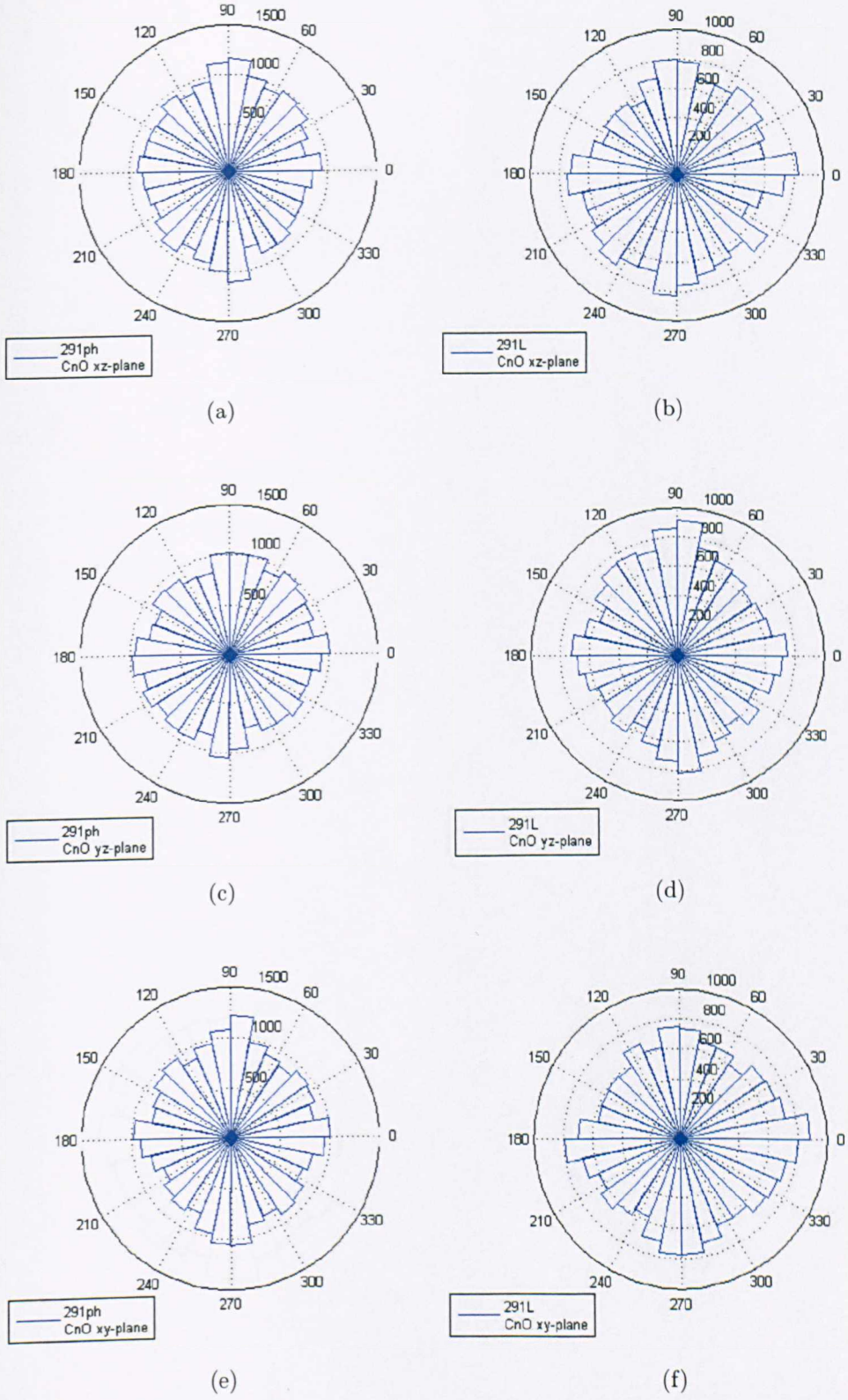

Figure 8.67: Rose diagrams of the contact normal orientation for the reconstituted samples prior to loading, in the xz-plane: (a) 291ph (b) 291L, in the yz-plane: (c) 291ph (d) 291L, in the xy-plane: (e) 291ph (f) 291L

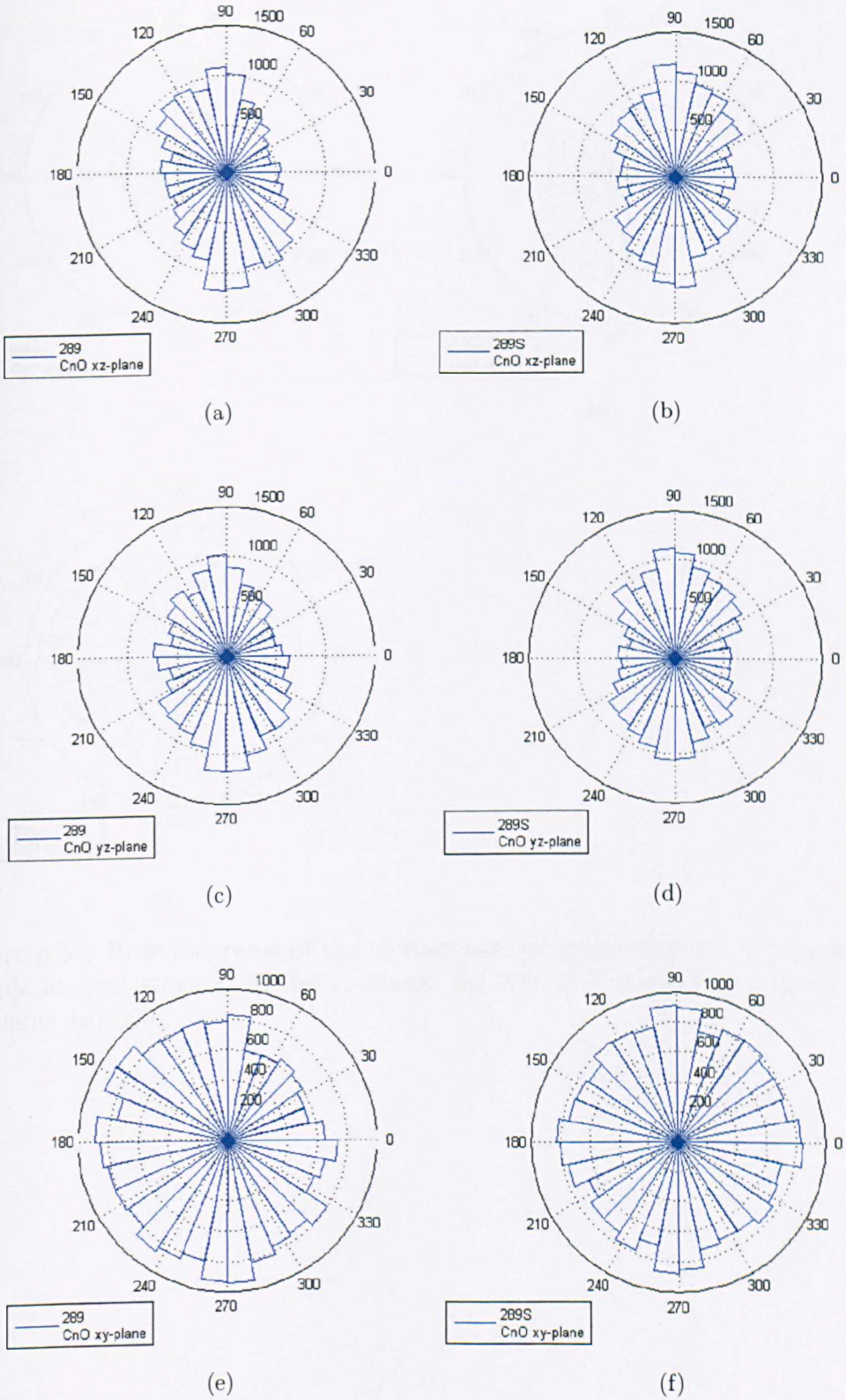

Figure 8.68: Rose diagrams of the contact normal orientation for the reconstituted samples at load stage3, in the xz-plane: (a) 289 (b) 289S, in the yz-plane: (c) 289 (d) 289S, in the xy-plane: (e) 289 (f) 289S

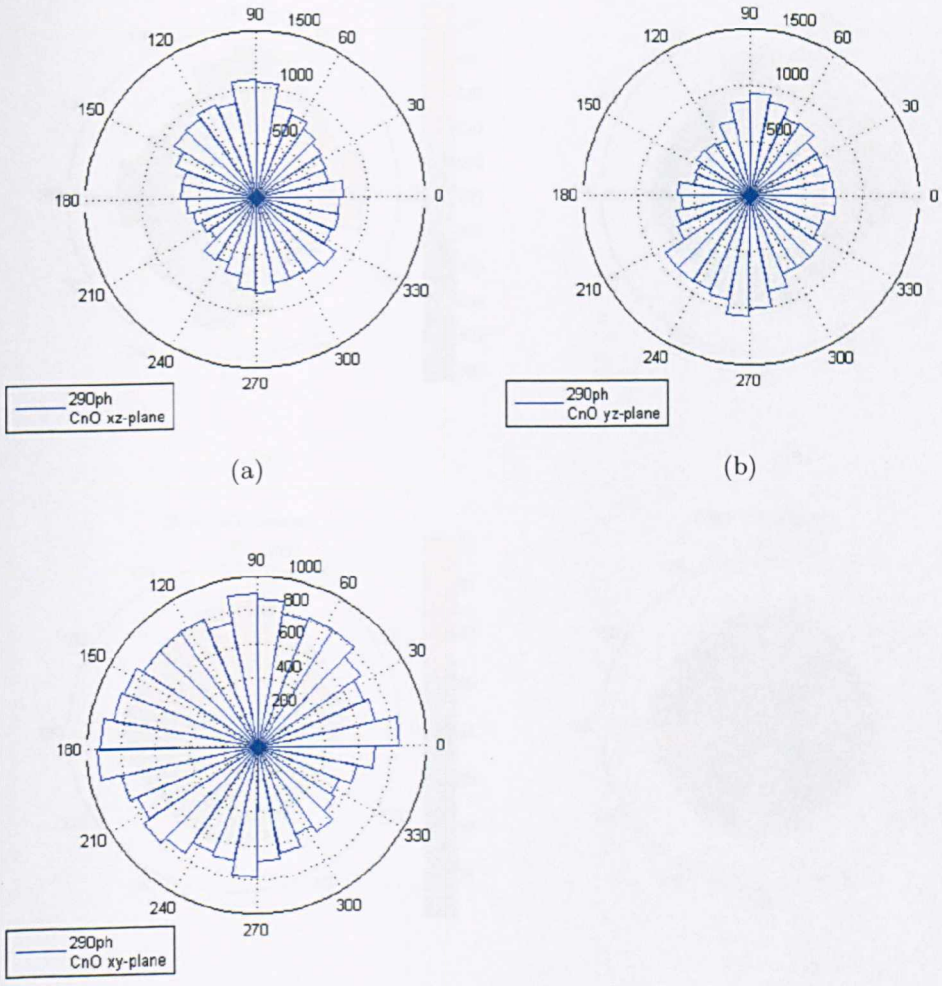

Figure 8.69: Rose diagrams of the contact normal orientation for the reconstituted sample at load stage 4, in the xz-plane: (a) 290, in the yz-plane: (b) 290, in the xy-plane: (e) 290

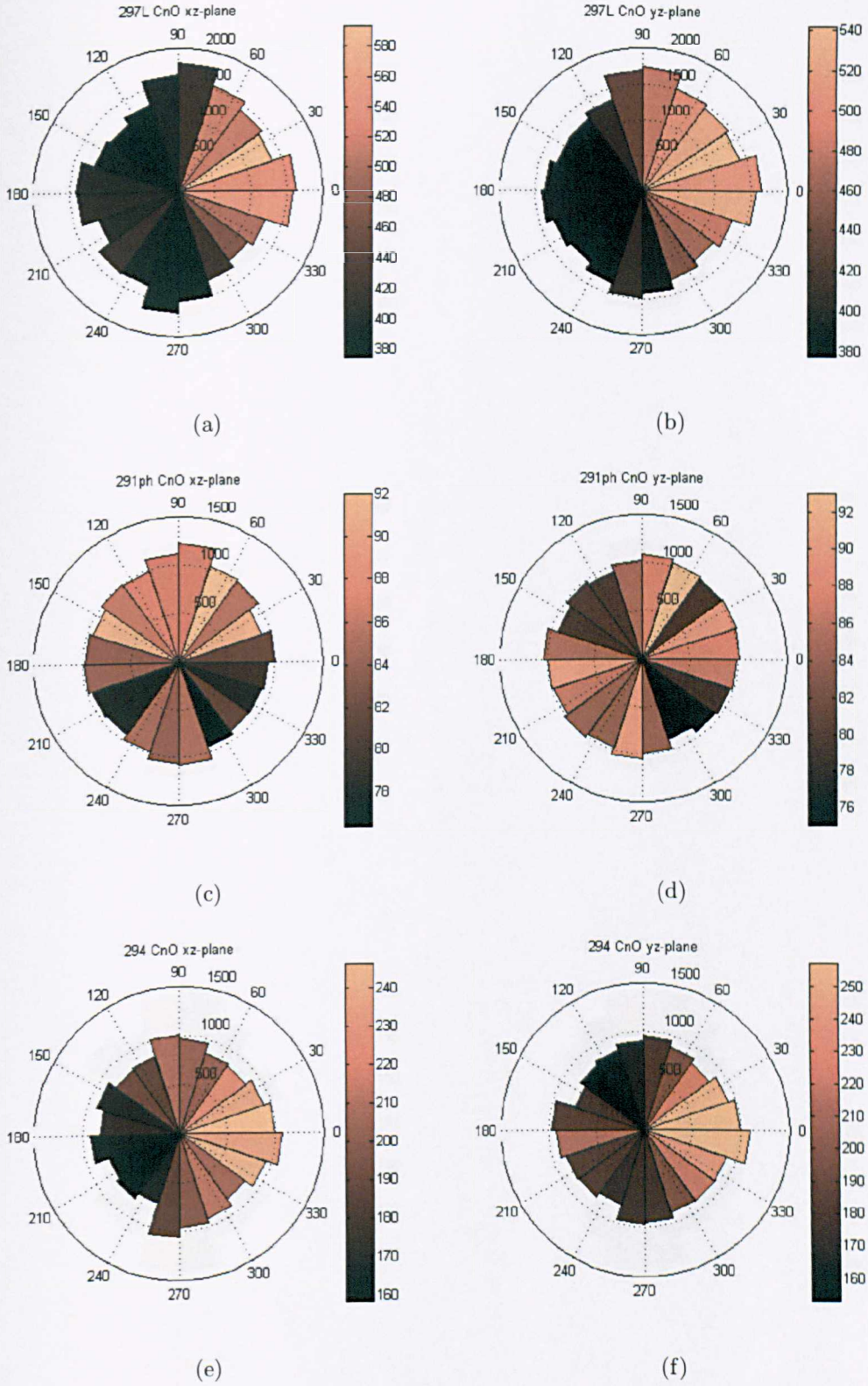

Figure 8.70: Rose diagrams of the contact normal orientation for intact and reconstituted sample at early load stages, in the vertical planes, (a)(b) 297L (c)(d) 291ph (e)(f) 294ph; the shading illustrates the size of the contact (in voxels)

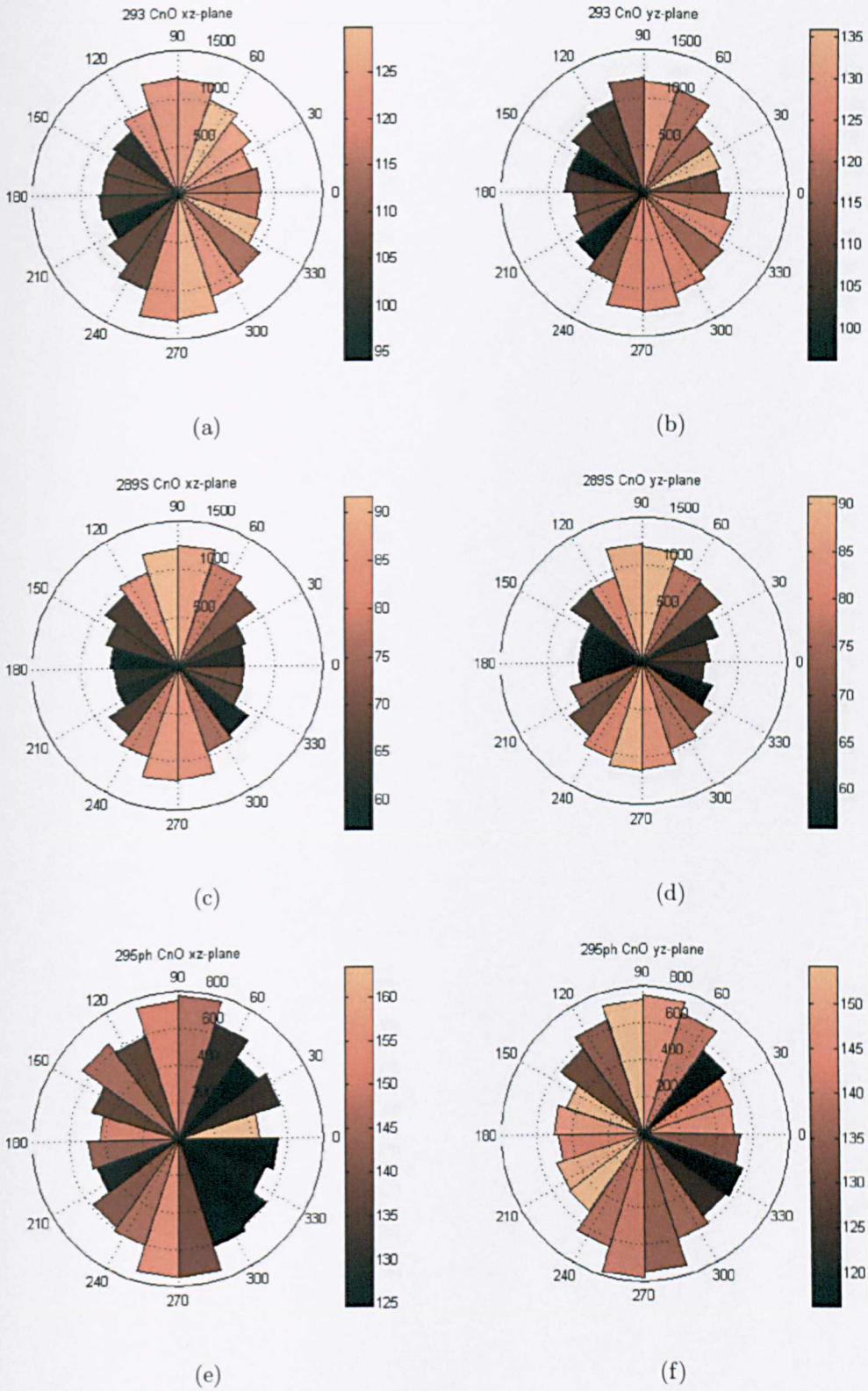

Figure 8.71: Rose diagrams of the contact normal orientation for the samples outside the shear band, in the vertical planes (a)(b) 293 (c)(d) 289S (e)(f) 295ph; the shading illustrates the size of the contact (in voxels)

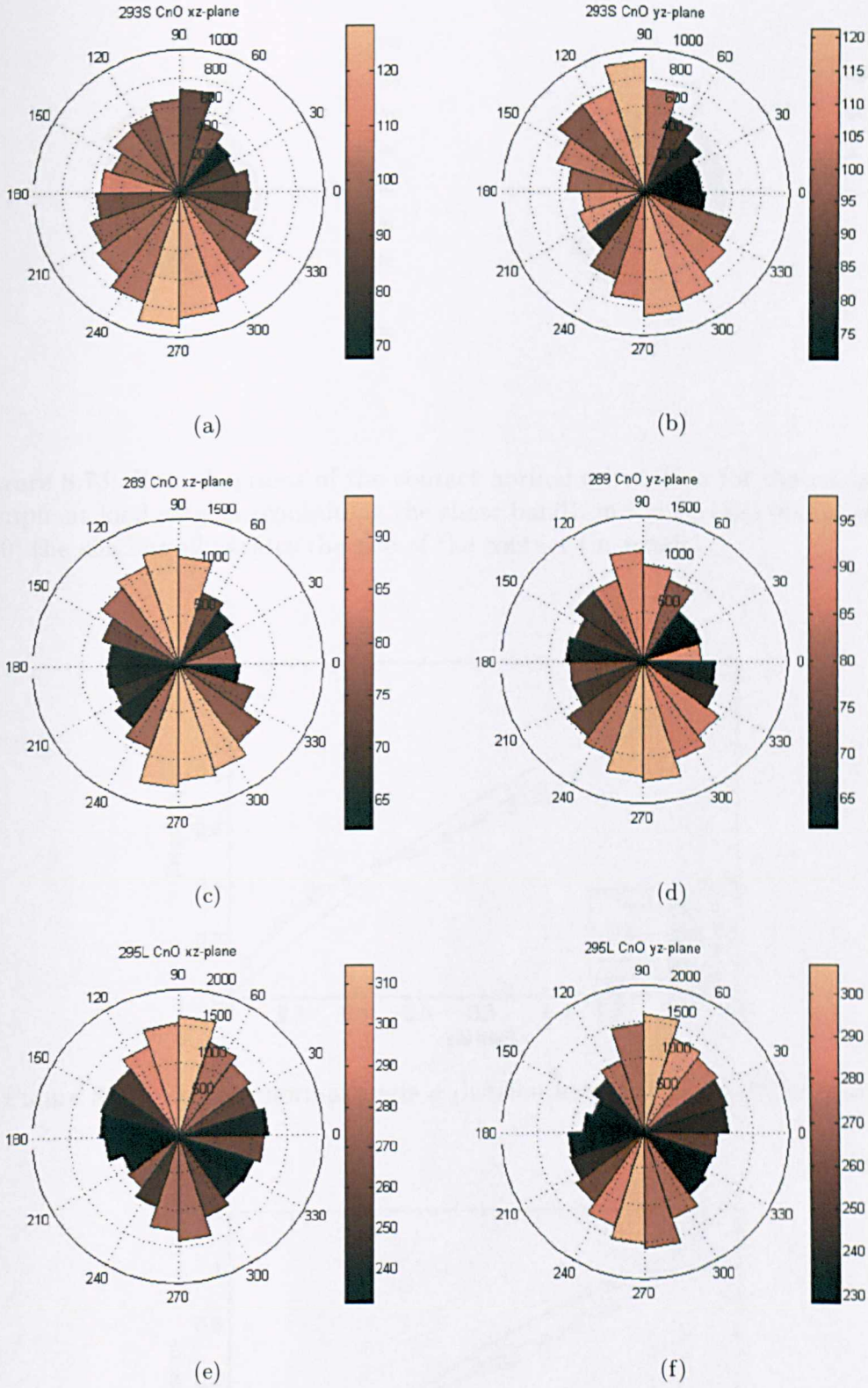

Figure 8.72: Rose diagrams of the contact normal orientation for the samples containing the shear band, in the vertical planes, (a)(b) 293S (c)(d) 289 (e)(f) 295L; the shading illustrates the size of the contact (in voxels)

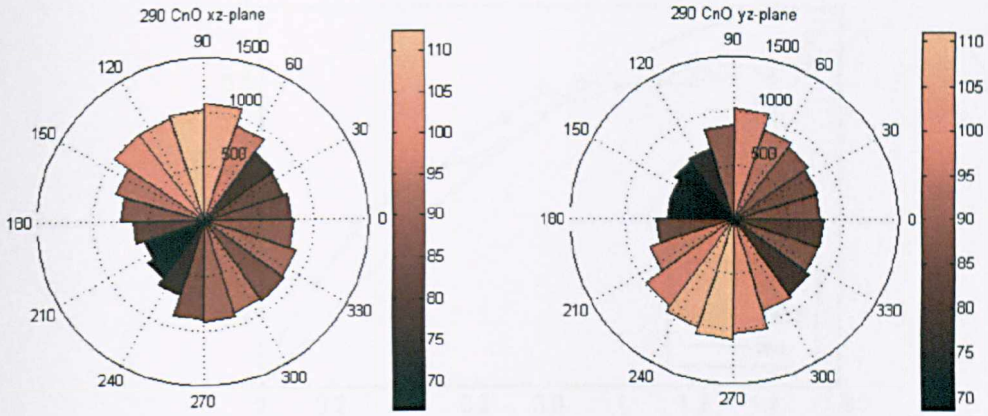

(a) (b)

Figure 8.73: Rose diagrams of the contact normal orientation for the reconstituted sample at load satge 4 (containing the shear band), in the vertical planes of sample 290; the shading illustrates the size of the contact (in voxels)

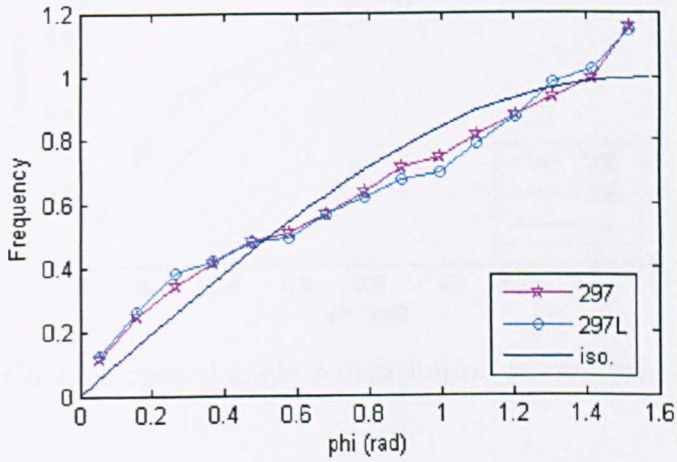

Figure 8.74: Contact normal angle ϕ distribution for samples 297ph and 297L

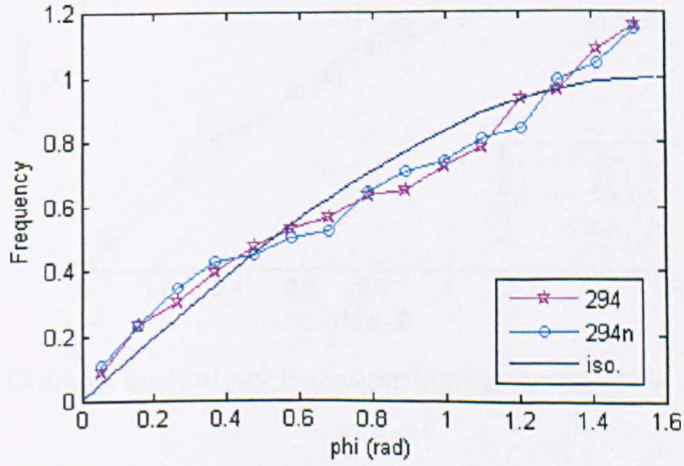

Figure 8.75: Contact normal angle ϕ distribution for samples 294ph and 294n

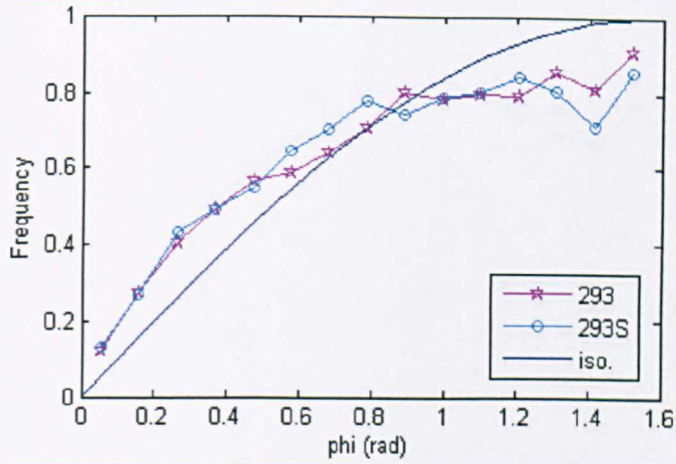

Figure 8.76: Contact normal angle ϕ distribution for samples 293 and 293S

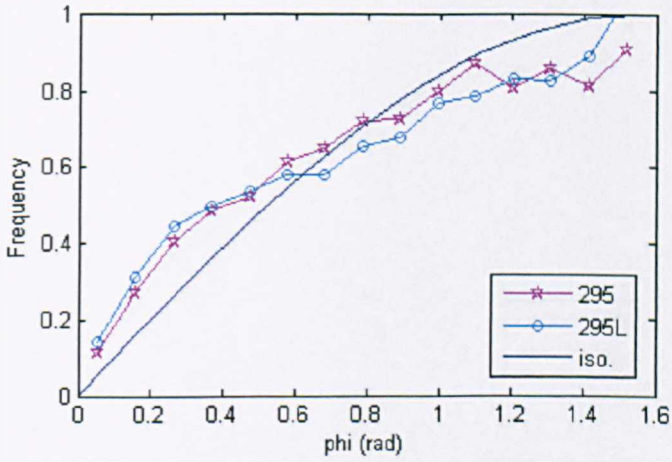

Figure 8.77: Contact normal angle ϕ distribution for samples 295ph and 295L

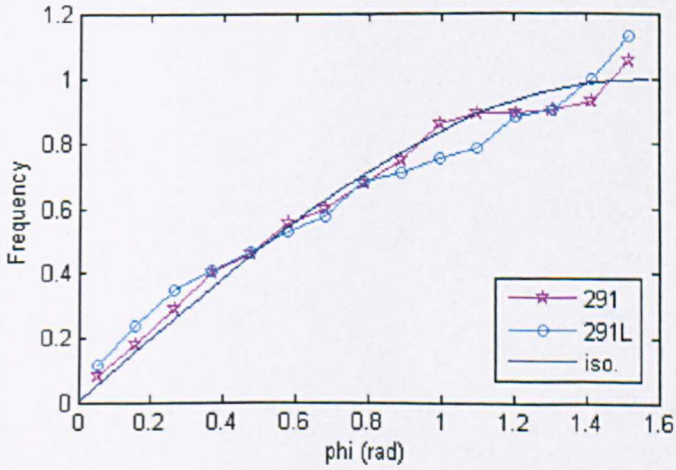

Figure 8.78: Contact normal angle ϕ distribution for samples 291ph and 291L

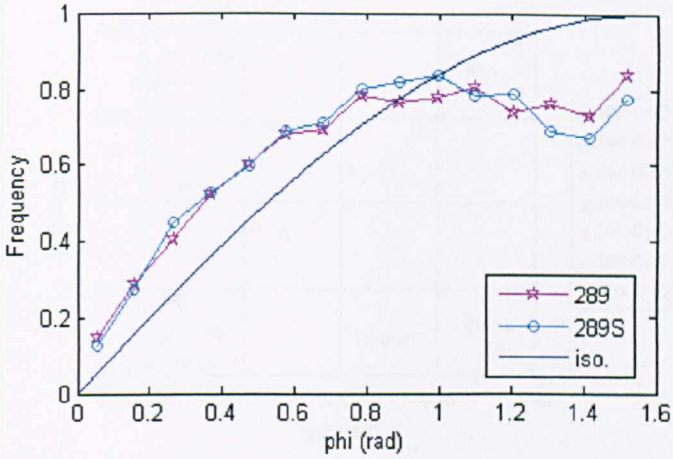

Figure 8.79: Contact normal angle ϕ distribution for samples 289 and 289S

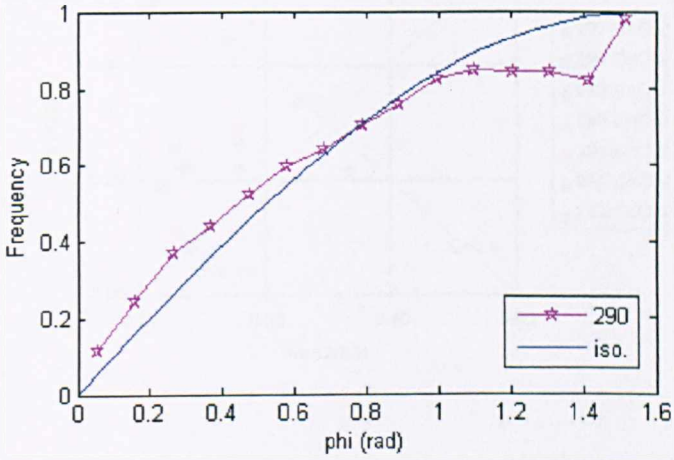

Figure 8.80: Contact normal angle ϕ distribution for samples 290

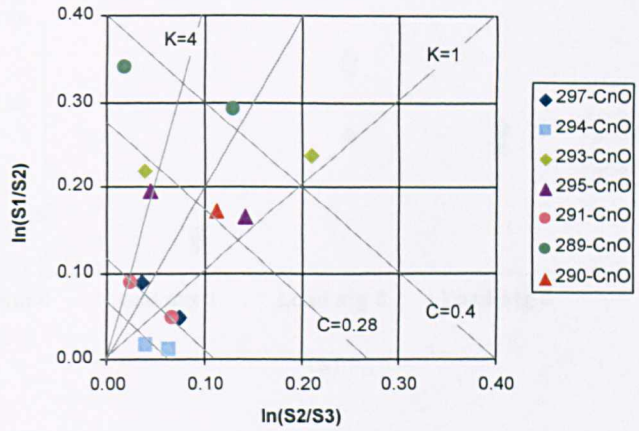

(a)

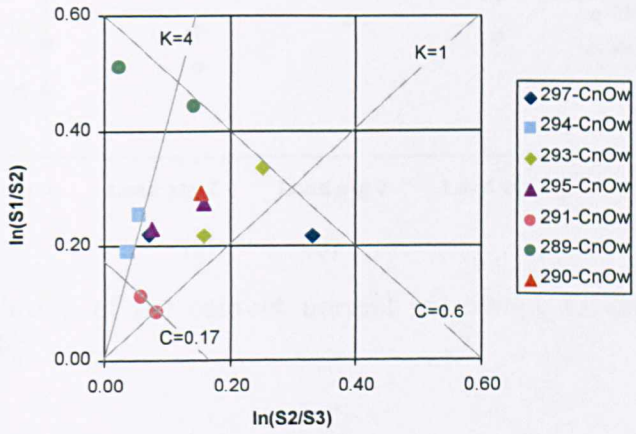

(b)

Figure 8.81: Eigenvalue ratios of the contact normal (CnO) data using (a) Φ (b) Φ^w

(a)

(b)

Figure 8.82: Evolution of the contact normal anisotropy at different load stages using (a) Φ_d (b) Φ_d^W

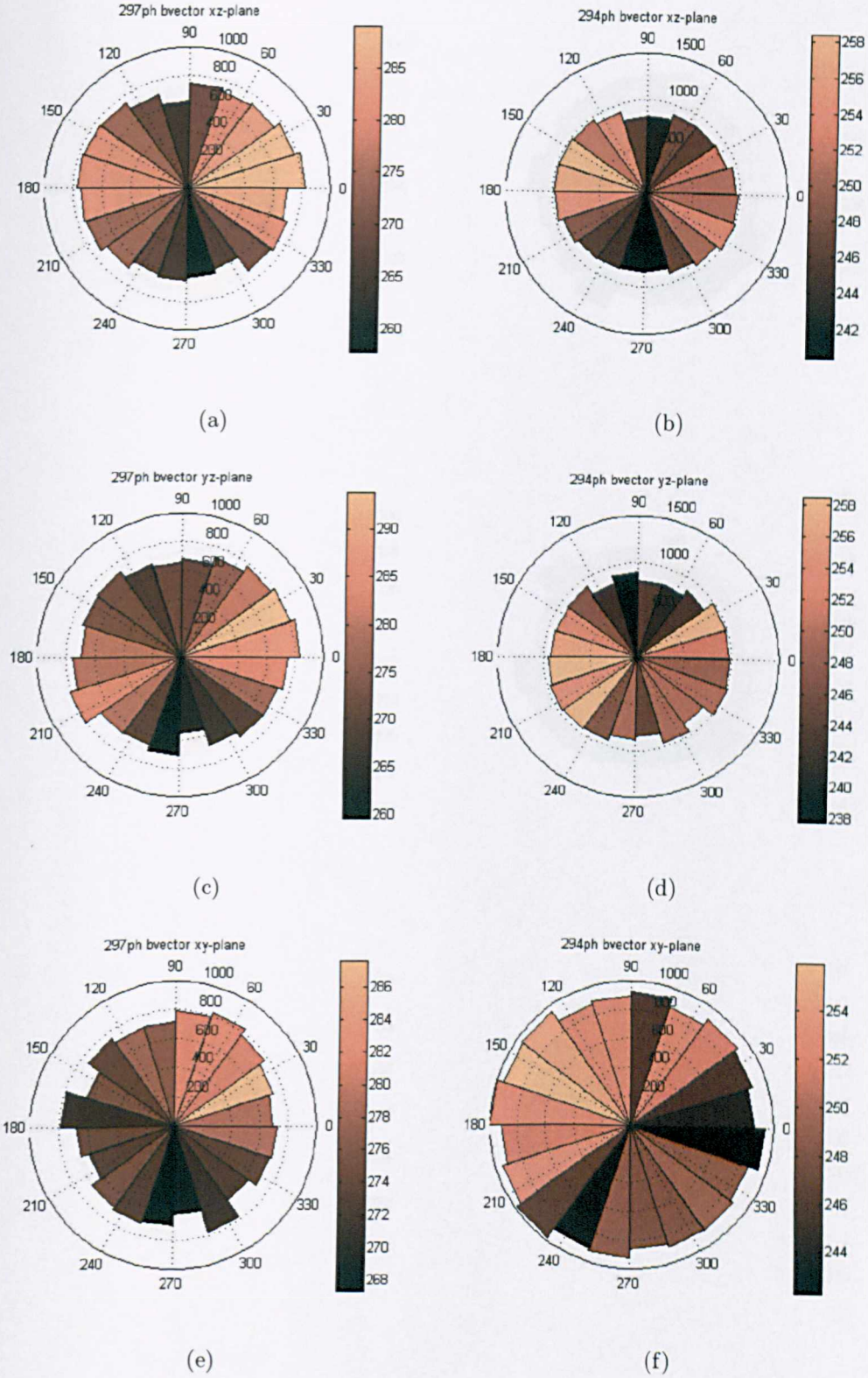

Figure 8.83: Rose diagrams of the branch vector orientation in the xz-plane: (a) 297ph (b) 294ph, in the yz-plane: (c) 297ph (d) 294ph, in the xy-plane: (e) 297ph (f) 294ph; the shading illustrates the branch vector length (in μm)

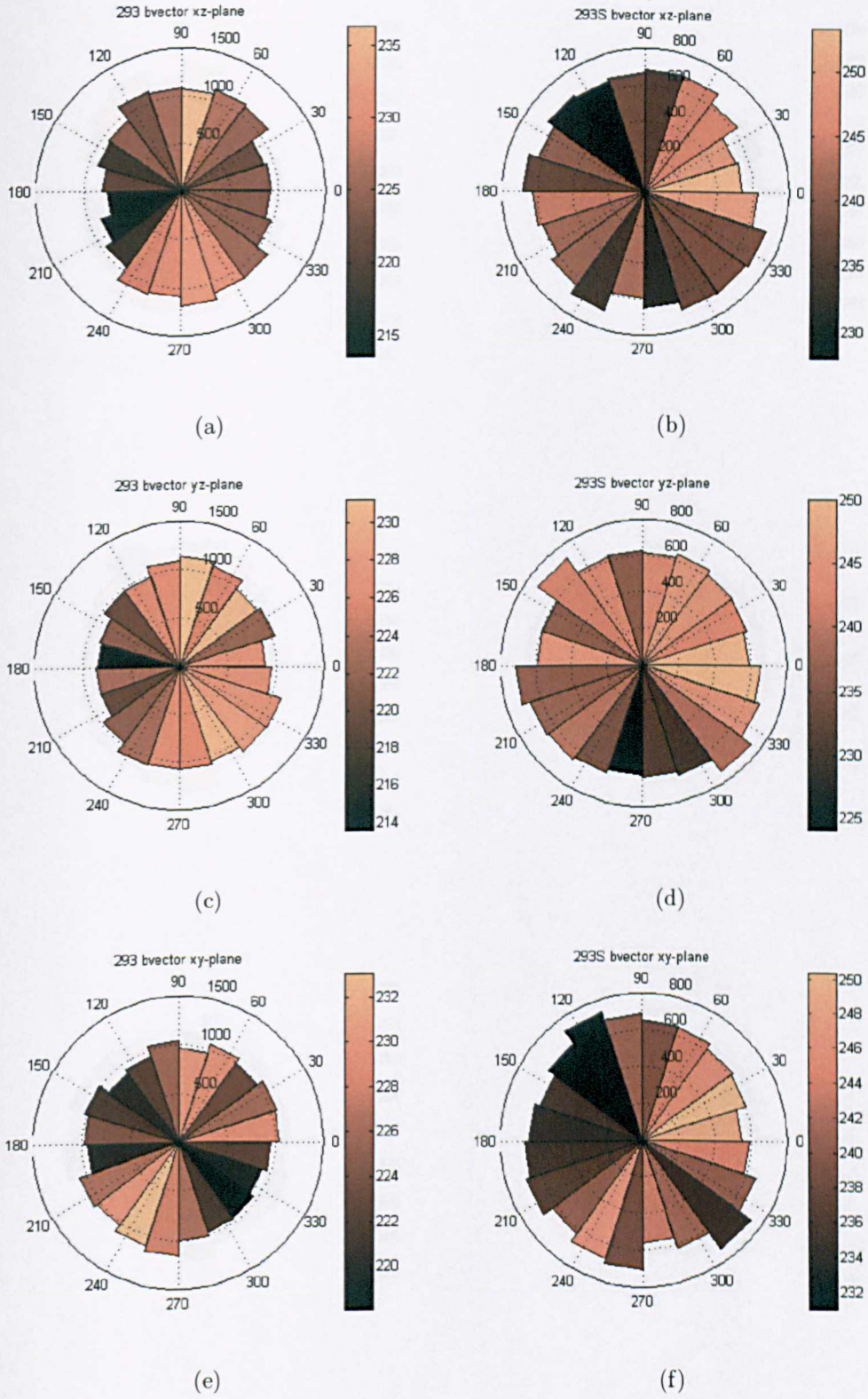

Figure 8.84: Rose diagrams of the branch vector orientation in the xz-plane: (a) 293 (b) 293S, in the yz-plane: (c) 293 (d)293S, in the xy-plane: (e) 293 (f) 293S; the shading illustrates the branch vector length (in μm)

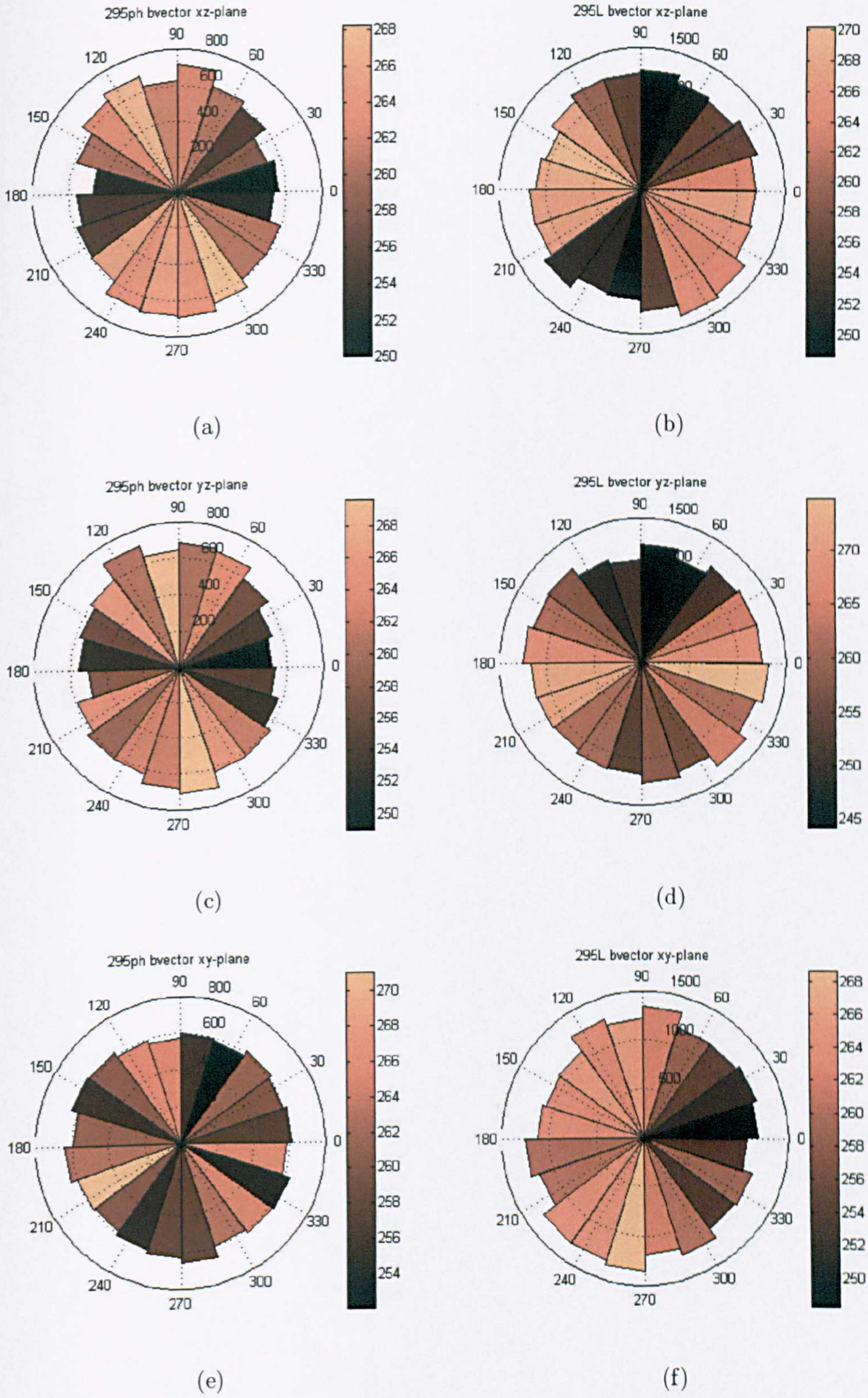

Figure 8.85: Rose diagrams of the branch vector orientation in the xz-plane: (a) 295ph (b) 295L, in the yz-plane: (c) 295ph (d) 295L, in the xy-plane: (e) 295ph (f) 295L; the shading illustrates the branch vector length (in μm)

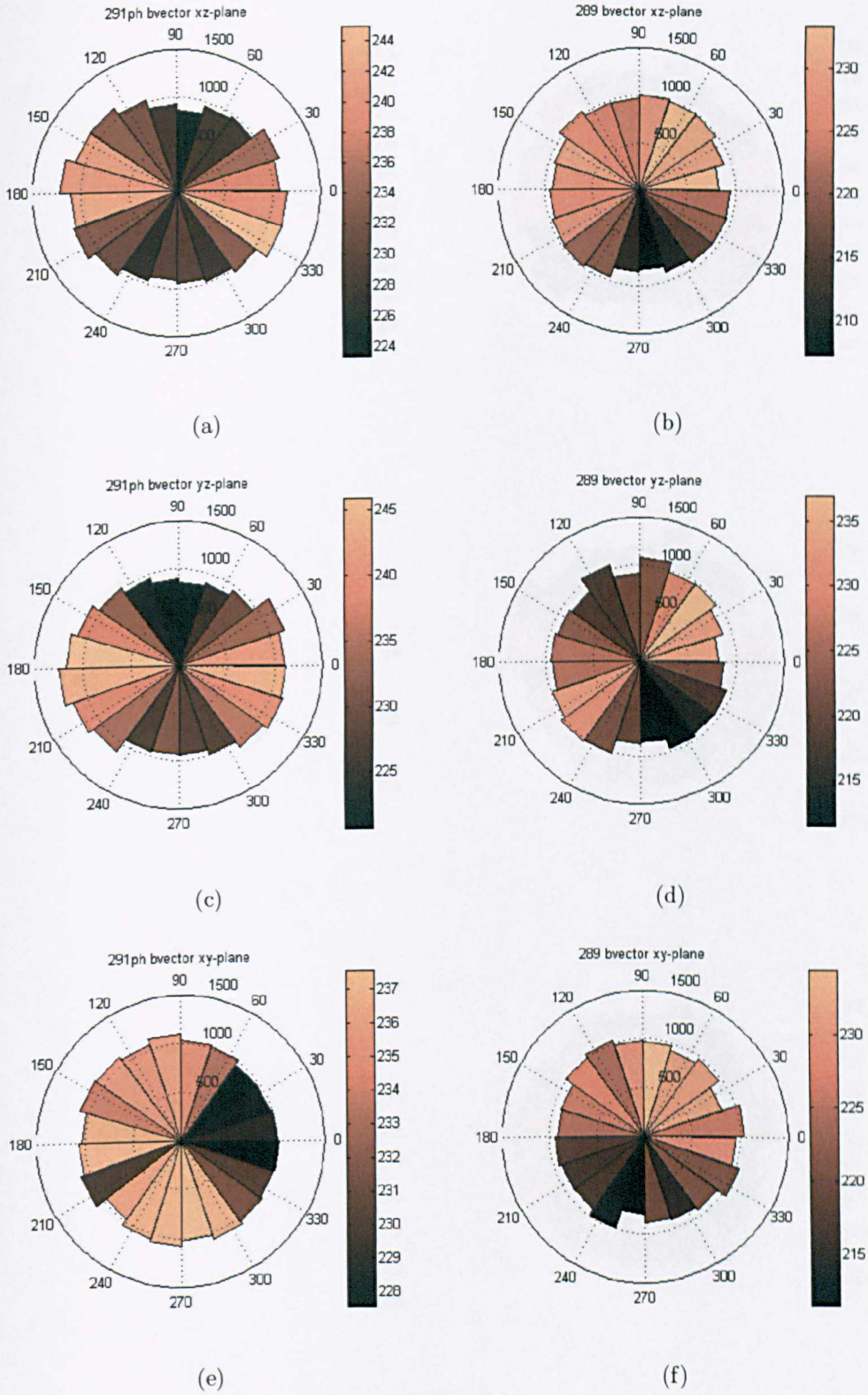

Figure 8.86: Rose diagrams of the branch vector orientation in the xz-plane: (a) 291ph (b) 289, in the yz-plane: (c) 291ph (d) 289, in the xy-plane: (e) 291ph (f) 289; the shading illustrates the branch vector length (in μm)

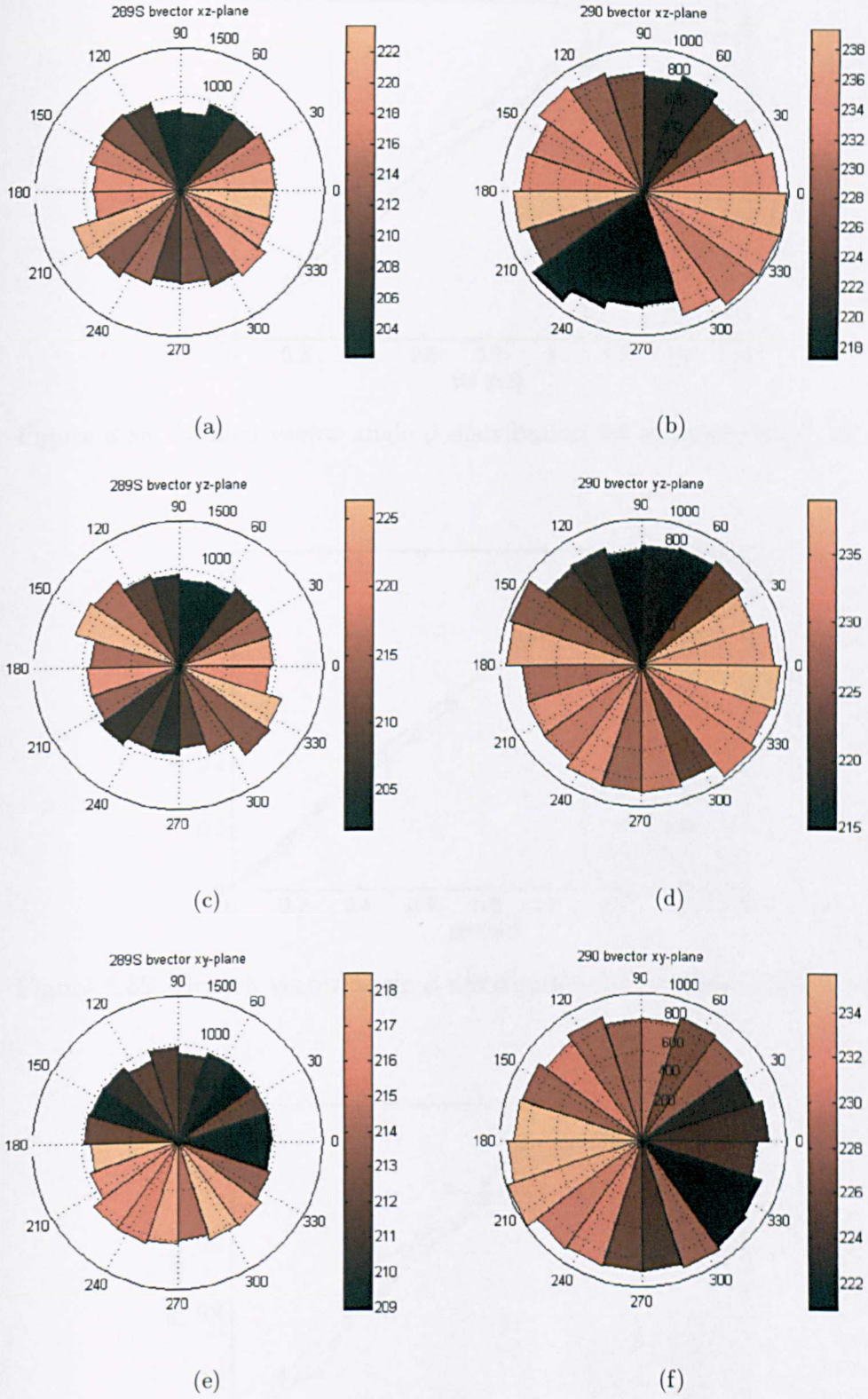

Figure 8.87: Rose diagrams of the branch vector orientation in the xz-plane: (a) 289S (b) 290, in the yz-plane: (c) 289S (d) 290, in the xy-plane: (e) 289S (f) 290; the shading illustrates the branch vector length (in μm)

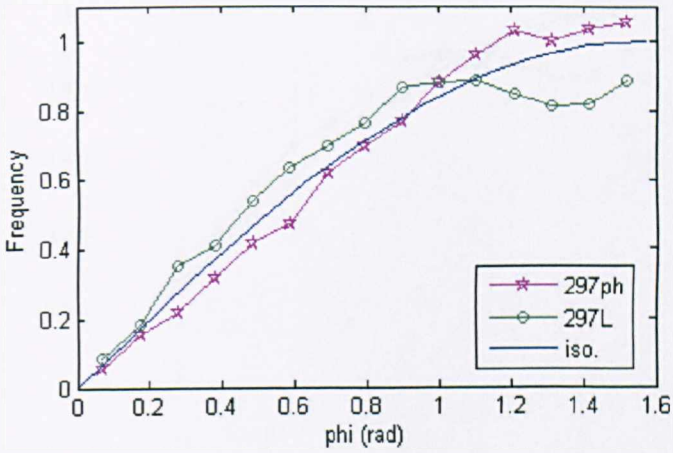

Figure 8.88: Branch vector angle ϕ distribution for samples 297ph and 297L

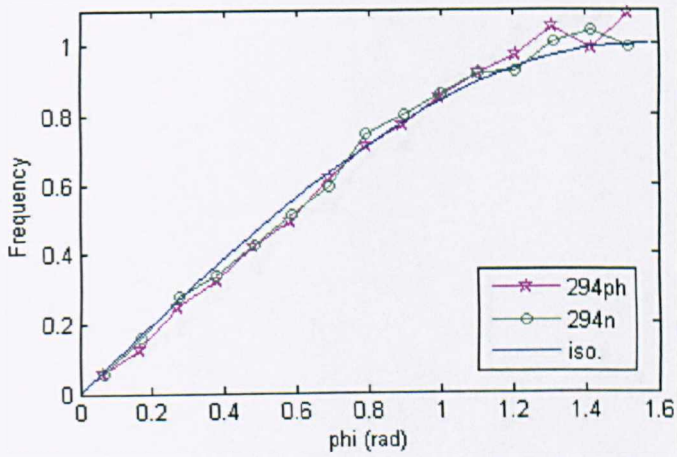

Figure 8.89: Branch vector angle ϕ distribution for samples 294ph and 294n

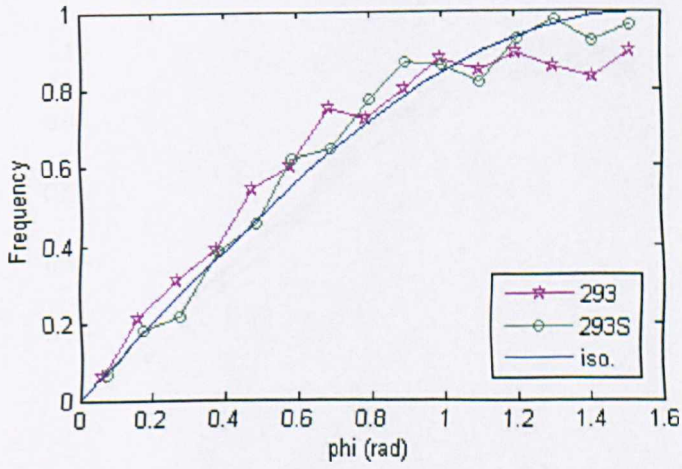

Figure 8.90: Branch vector angle ϕ distribution for samples 293 and 293S

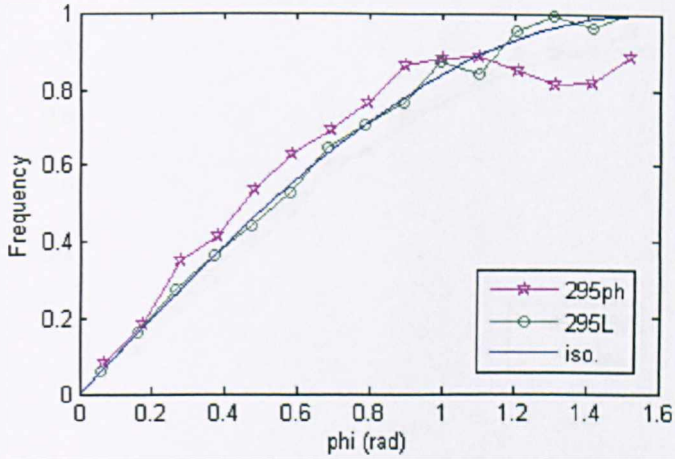

Figure 8.91: Branch vector angle ϕ distribution for samples 295ph and 295L

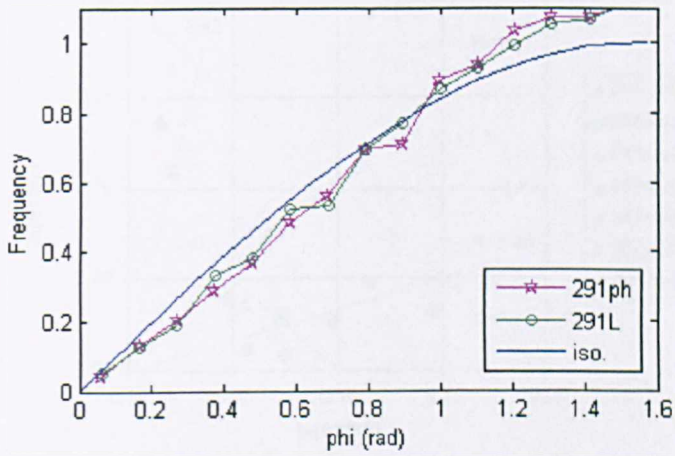

Figure 8.92: Branch vector angle ϕ distribution for samples 291ph and 291L

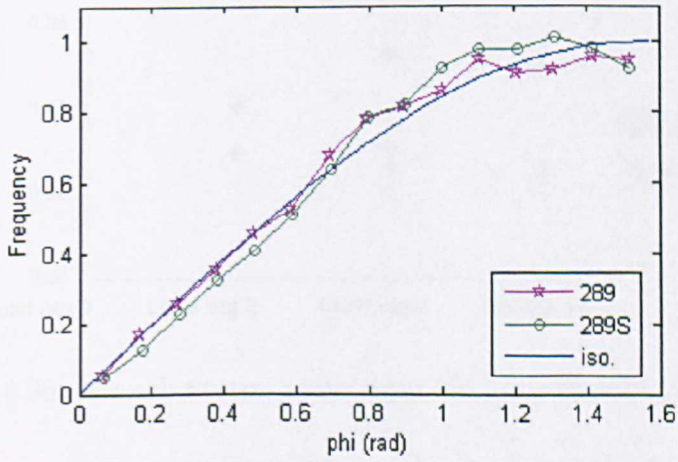

Figure 8.93: Branch vector angle ϕ distribution for samples 289 and 289S

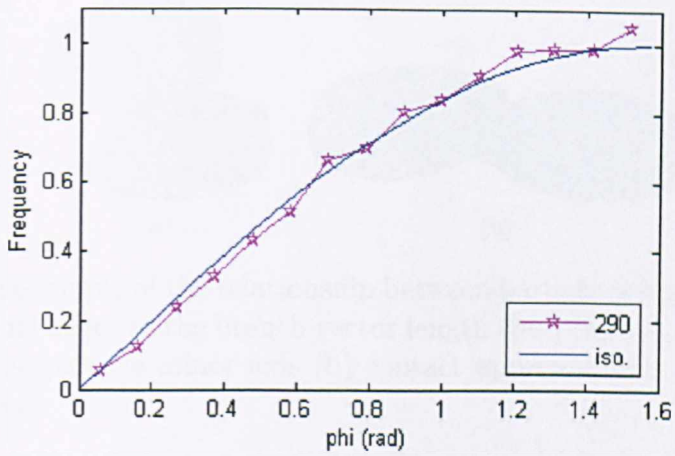

Figure 8.94: Branch vector angle ϕ distribution for sample 290

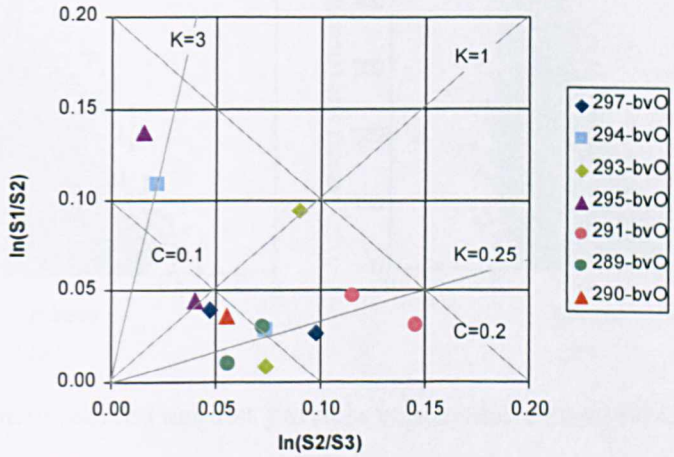

Figure 8.95: Eigenvalue ratios of the branch vector orientation (bvO) data

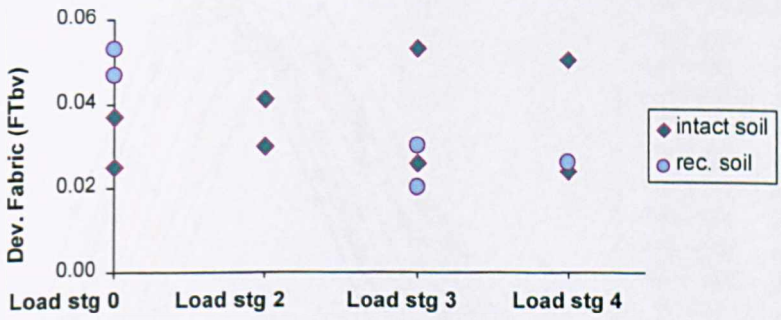

Figure 8.96: Branch vector anisotropy (Φ_d) at different load stages

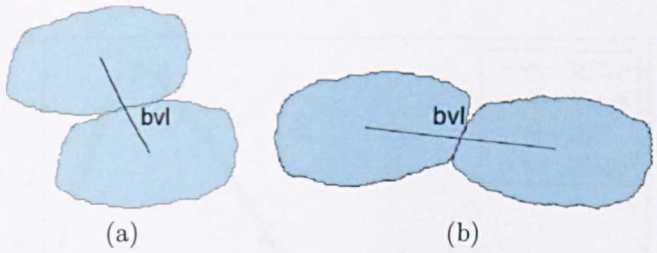

Figure 8.97: An example of the relationship between particle orientation and contact orientation and its effect to the branch vector length (bvl) (a) contact approximately orthogonal to the particle minor axis (b) contact approximately orthogonal to the particle major axis

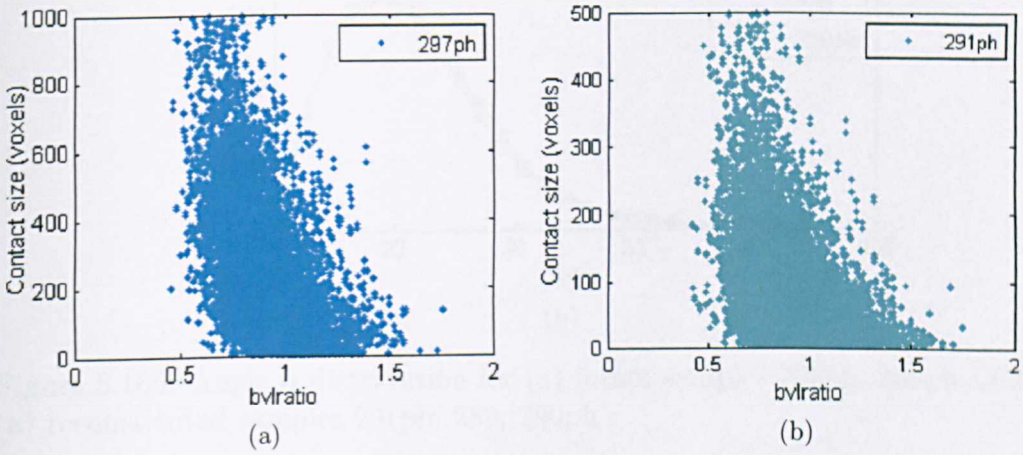

Figure 8.98: *bvlratio* plotted against particle volume for samples (a) 297ph (b) 291ph

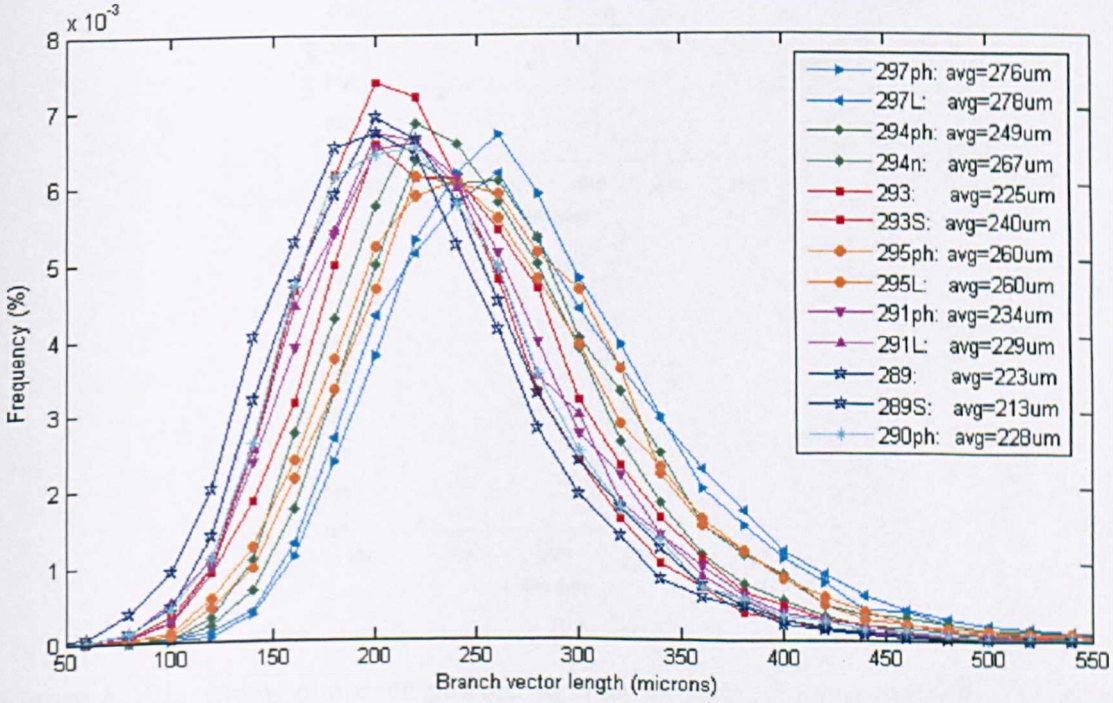

Figure 8.99: Branch vector length distribution for all samples

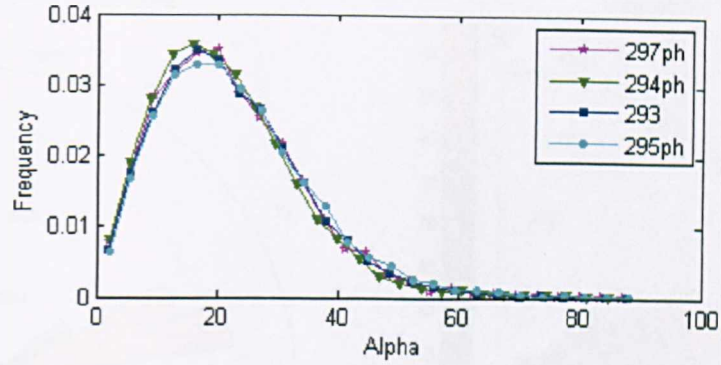

(a)

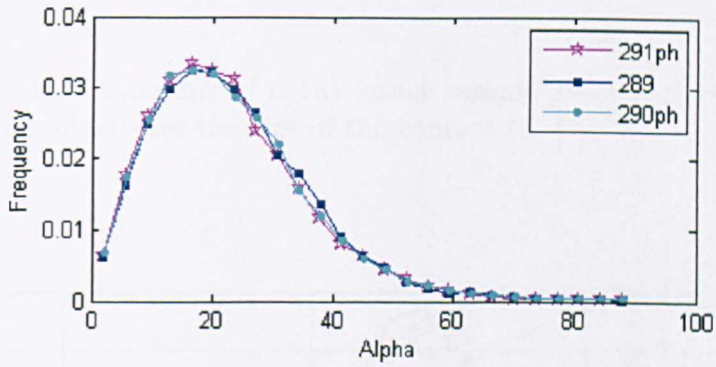

(b)

Figure 8.100: Angle α distribution for (a) intact samples 297ph, 294ph, 293, 295ph (a) reconstituted samples 291ph, 289, 290ph

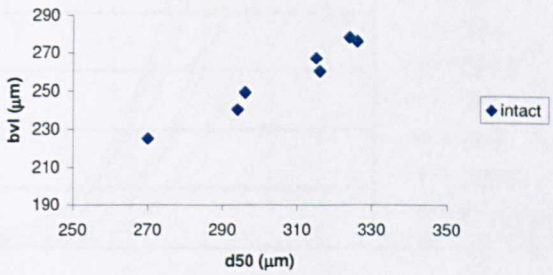

(a)

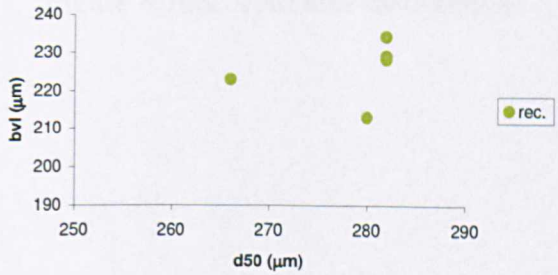

(b)

Figure 8.101: Mean diameter plotted against branch vector length for (a) intact samples (b) reconstituted samples

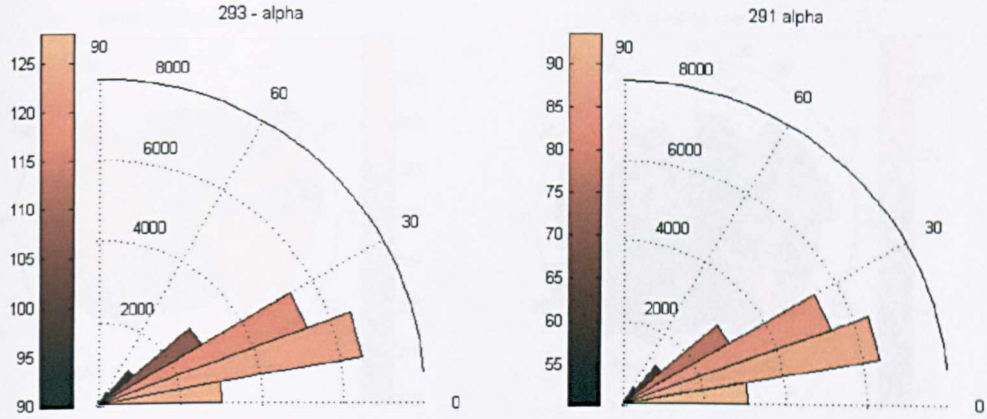

(a) (b)

Figure 8.102: Rose diagrams of α (a) intact sample 293 (b) reconstituted sample 289; the shading illustrates the size of the contact (in voxels)

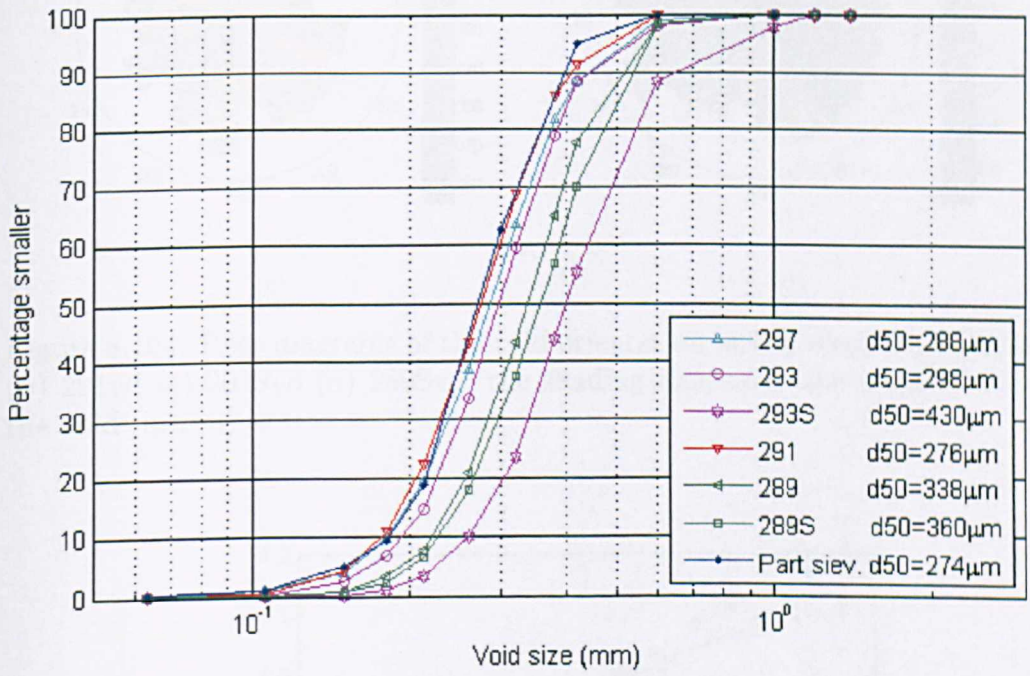

Figure 8.103: Void size distribution

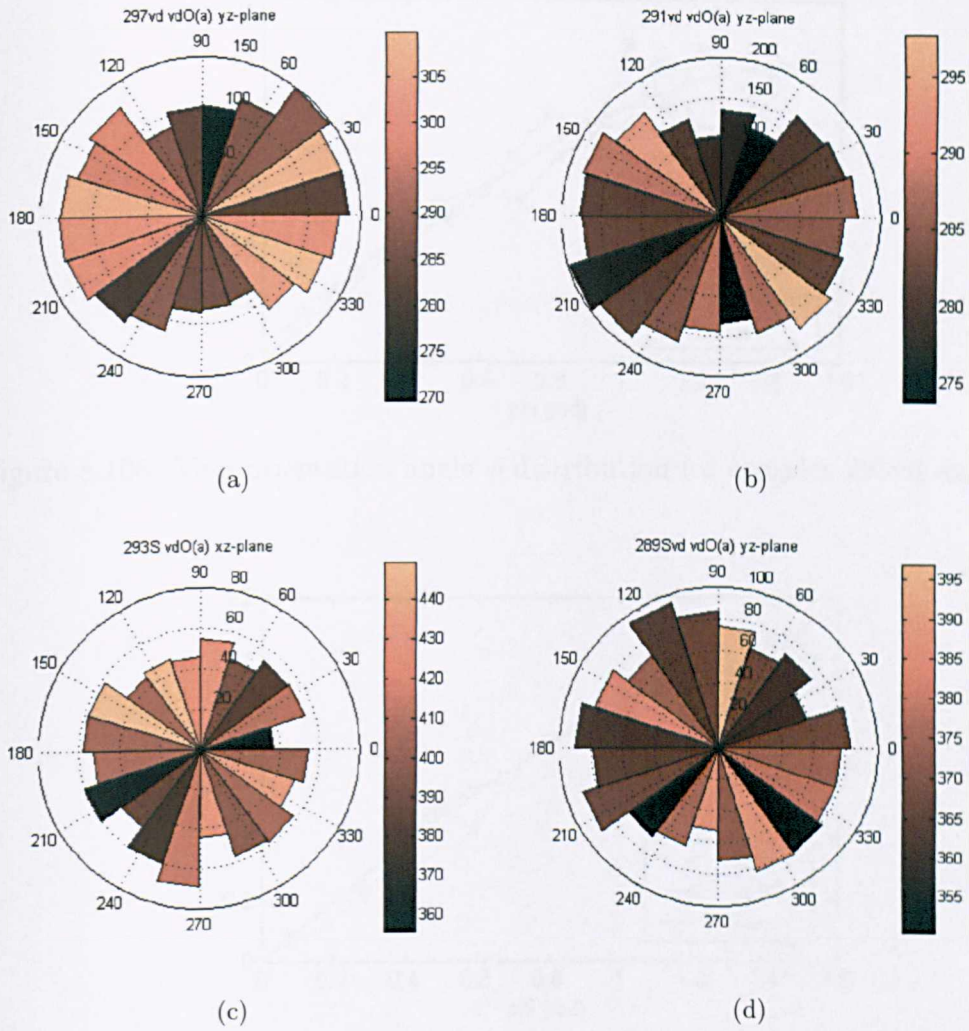

Figure 8.104: Rose diagrams of the void orientation in the vertical planes (a) 297vd (b) 291vd (c) 293Svd (d) 289Svd; the shading illustrates the major axis length of the void (in μm)

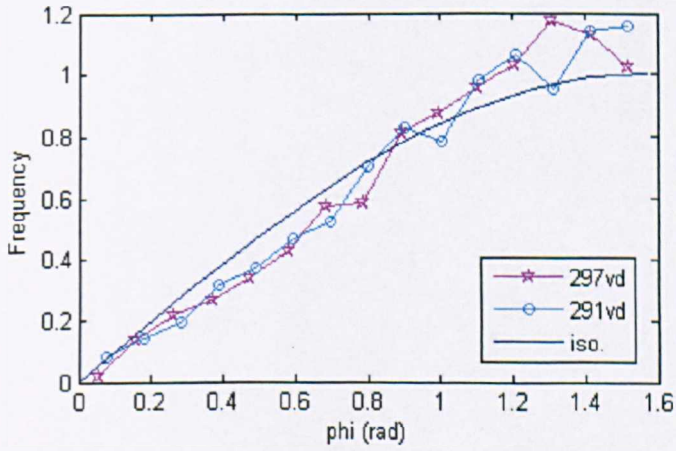

Figure 8.105: Void orientation angle ϕ distribution for samples 297vd and 291vd

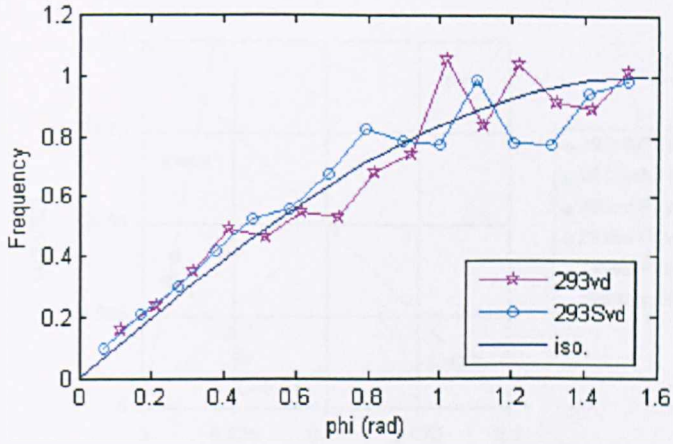

Figure 8.106: Void orientation angle ϕ distribution for samples 293vd and 293Svd

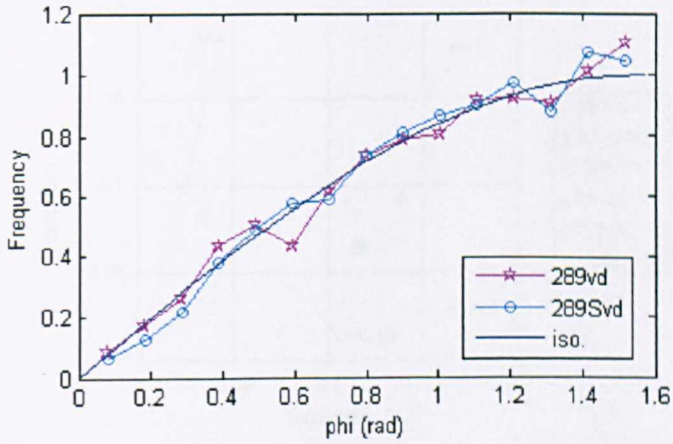

Figure 8.107: Void orientation angle ϕ distribution for samples 289vd and 289Svd

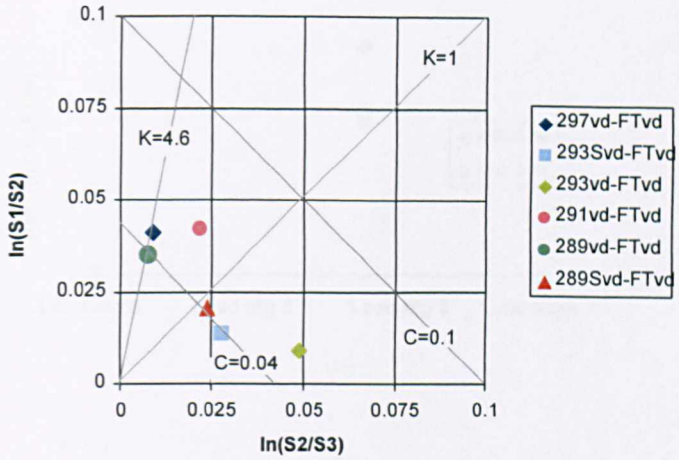

(a)

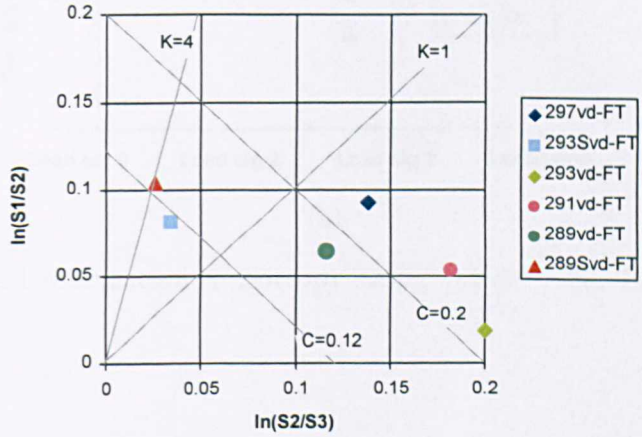

(b)

Figure 8.108: Eigenvalue ratios of the void orientation data using (a) Φ^{vd} (b) Φ

(a)

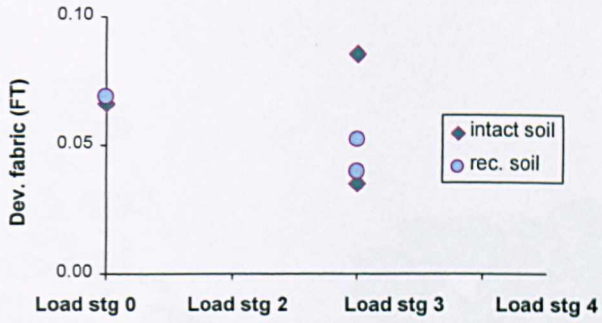

(b)

Figure 8.109: Void orientation anisotropy using (a) Φ^{vd} (b) Φ, at two stages of loading

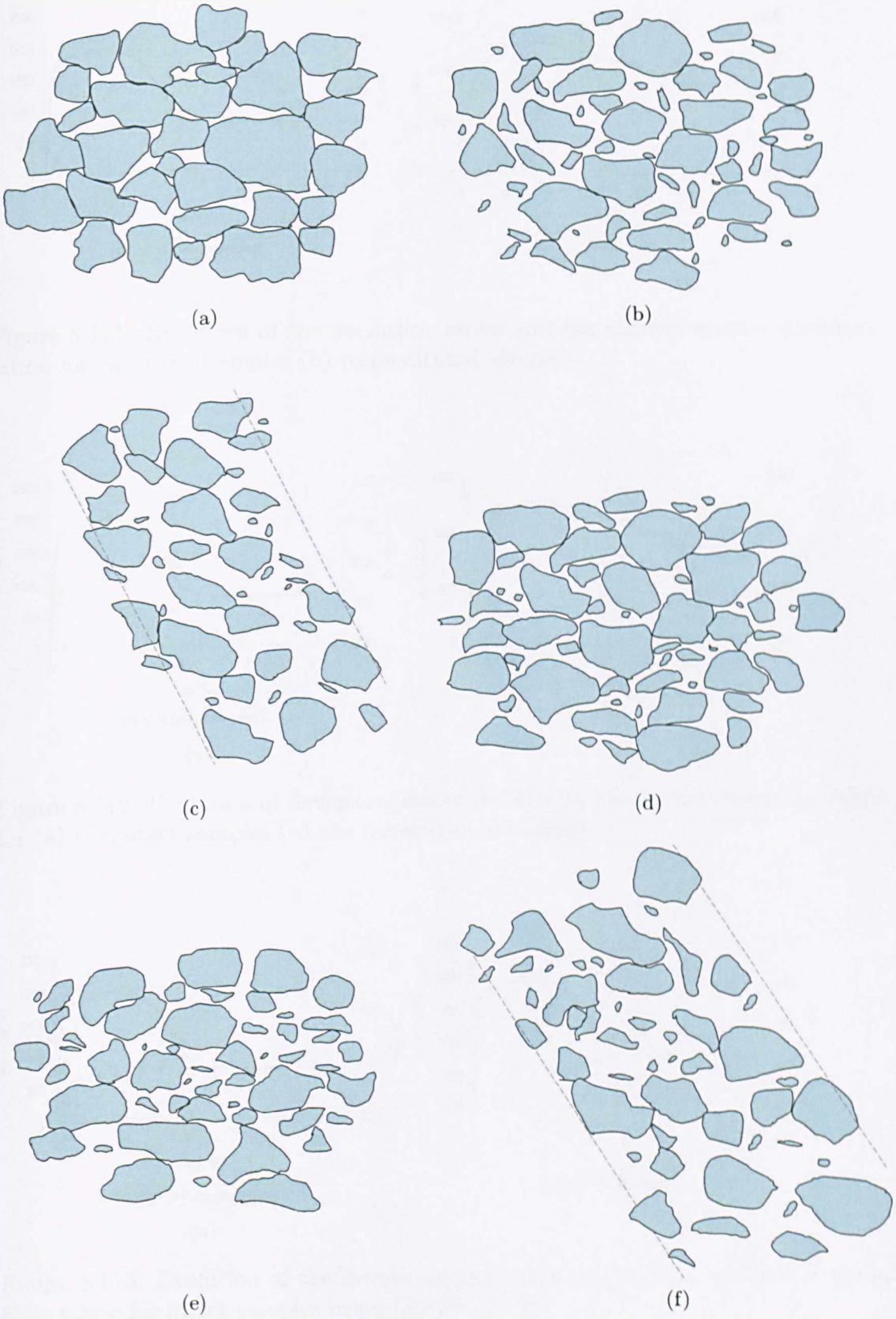

Figure 8.110: Schematic diagrams of the soil fabric (a) for the intact soil prior to loading (b) for the intact soil in the post-peak regime outside the shear band (c) for the intact soil in the post-peak regime inside the shear band, the dashed lines mark the limits of the shear band (d) for the reconstituted soil prior to loading (e) for the reconstituted soil in the post-peak regime outside the shear band (f) for the reconstituted soil in the post-peak regime inside the shear band

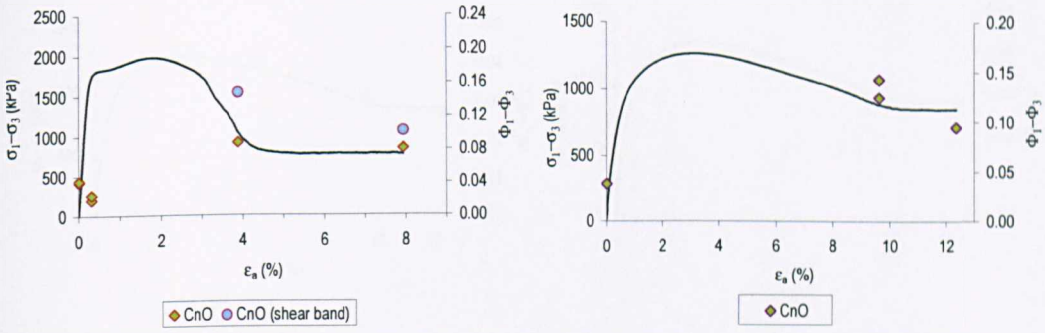

(a) (b)

Figure 8.111: Evolution of the deviatoric stress and the contact normal deviatoric fabric for (a) intact samples (b) reconstituted samples

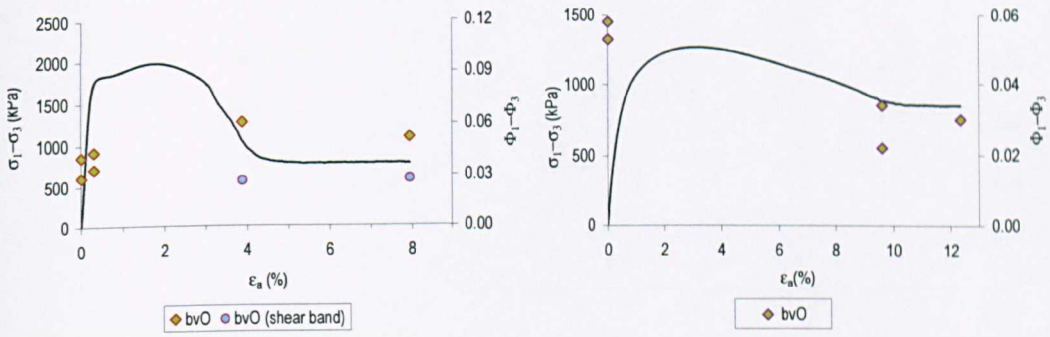

(a) (b)

Figure 8.112: Evolution of deviatoric stress and the branch vector deviatoric fabric for (a) the intact samples (b) the reconstituted samples

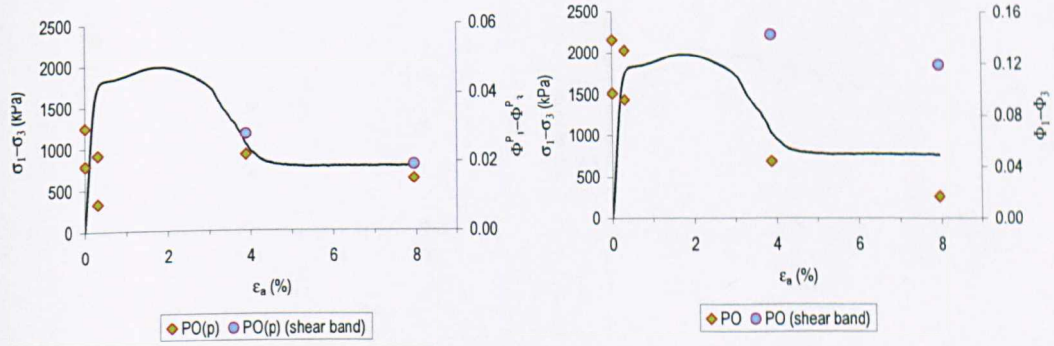

(a) (b)

Figure 8.113: Evolution of the deviatoric stress and the particle orientation deviatoric fabric for intact samples using (a) Φ^P (b) Φ

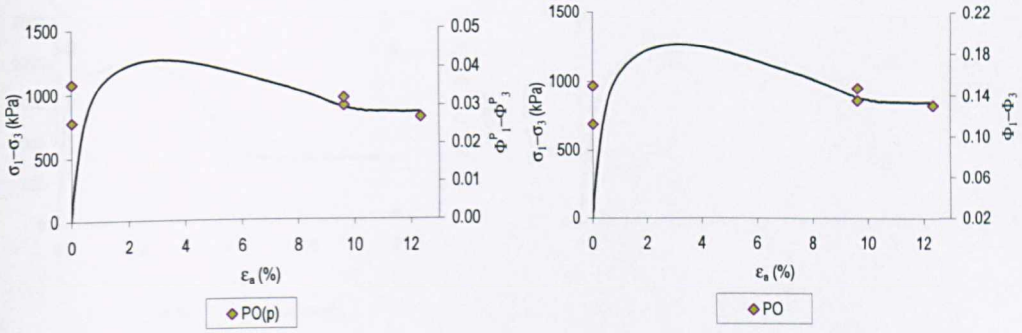

(a) (b)

Figure 8.114: Evolution of the deviatoric stress and particle orientation deviatoric fabric for reconstituted samples using (a) Φ^P (b) Φ

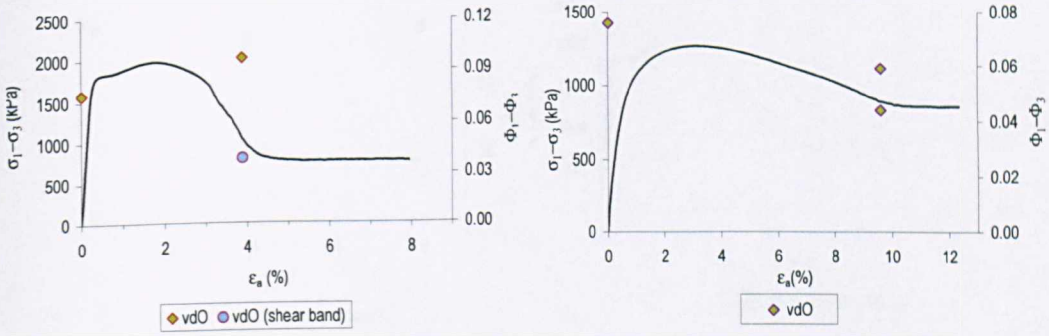

(a) (b)

Figure 8.115: Evolution of the deviatoric stress and void orientation deviatoric fabric for (a) intact samples (b) reconstituted samples

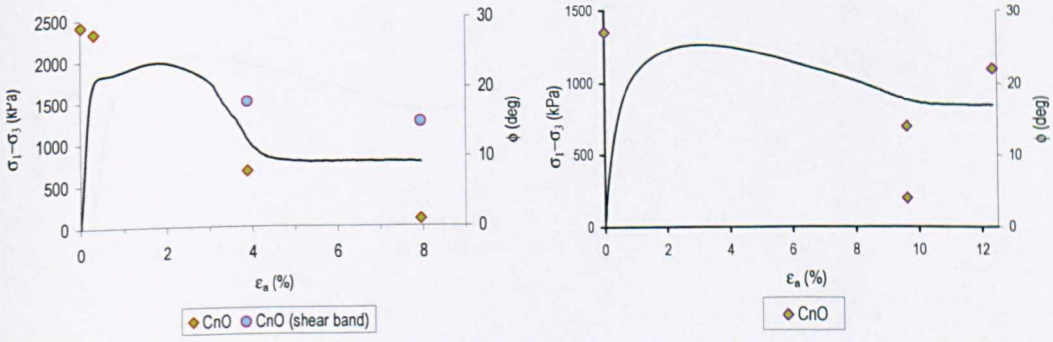

(a) (b)

Figure 8.116: Evolution of the deviatoric stress and the contact normal ϕ angle for (a) intact samples (b) reconstituted samples

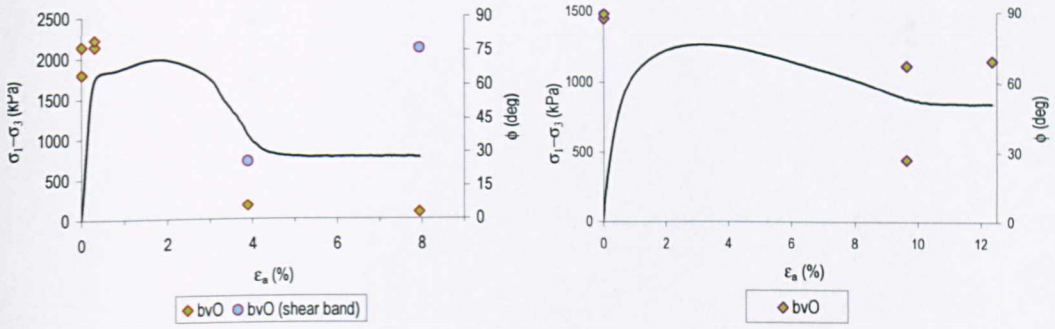

(a) (b)

Figure 8.117: Evolution of deviatoric stress and the branch vector ϕ angle for (a) intact samples (b) reconstituted samples

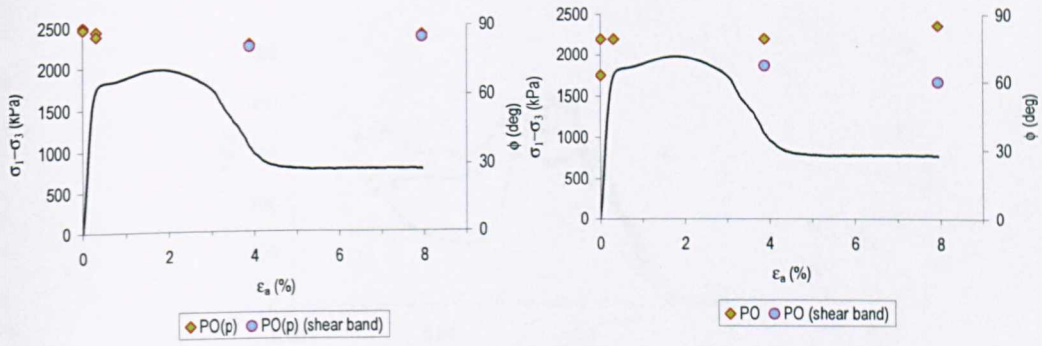

(a) (b)

Figure 8.118: Evolution of the deviatoric stress and the particle orientation ϕ angle for intact samples using (a) Φ^P (b) Φ

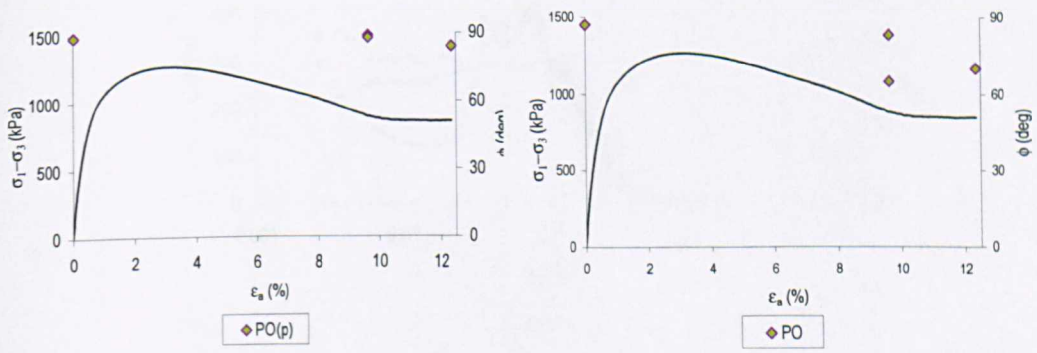

(a) (b)

Figure 8.119: Evolution of the deviatoric stress and the particle orientation ϕ angle for reconstituted samples using (a) Φ^P (b) Φ

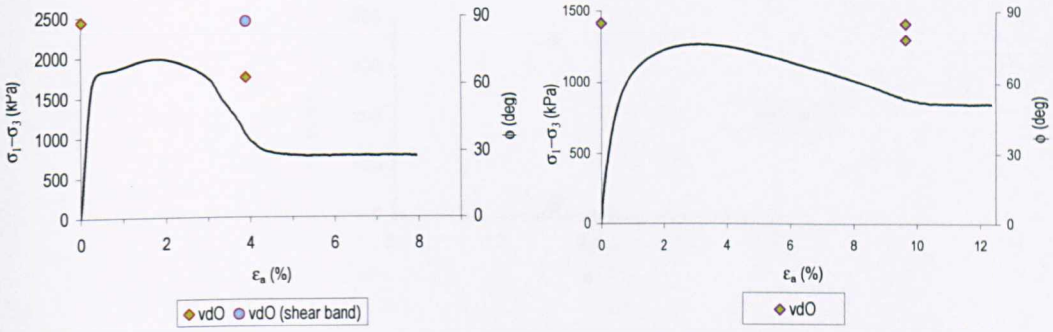

Figure 8.120: Evolution of deviatoric stress and the void orientation ϕ angle for (a) intact samples (b) reconstituted samples

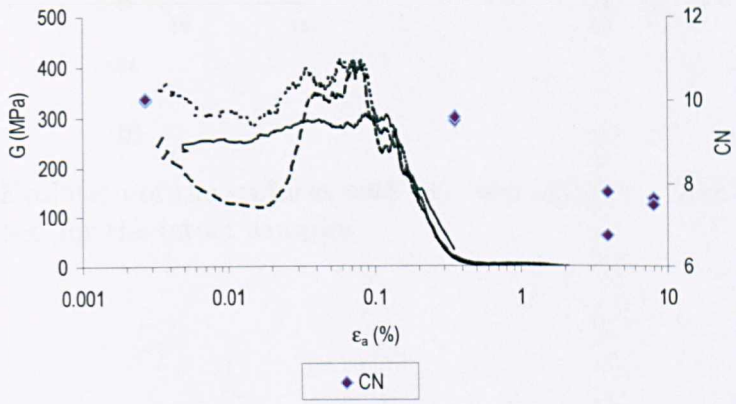

(a)

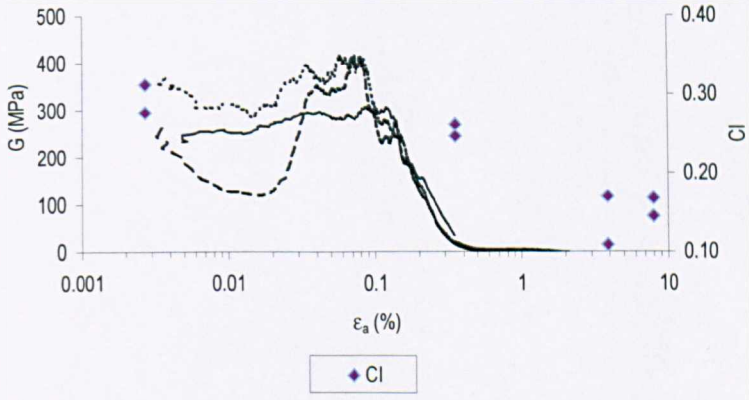

(b)

Figure 8.121: Evolution of stiffness and (a) CN (b) CI, for the intact samples

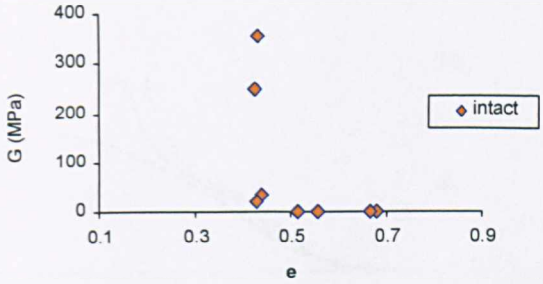

(a)

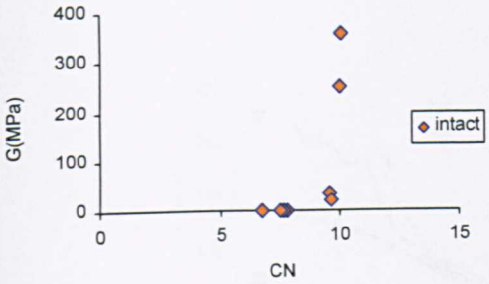

(b)

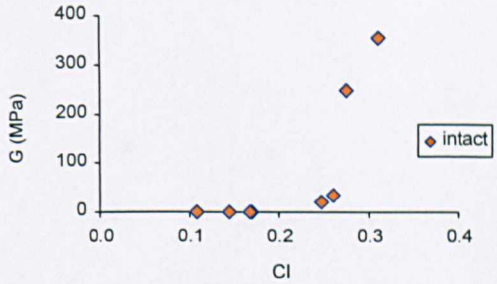

(c)

Figure 8.122: Evolution of the stiffness with (a) void ratio (b) coordination number (c) contact index, for the intact samples

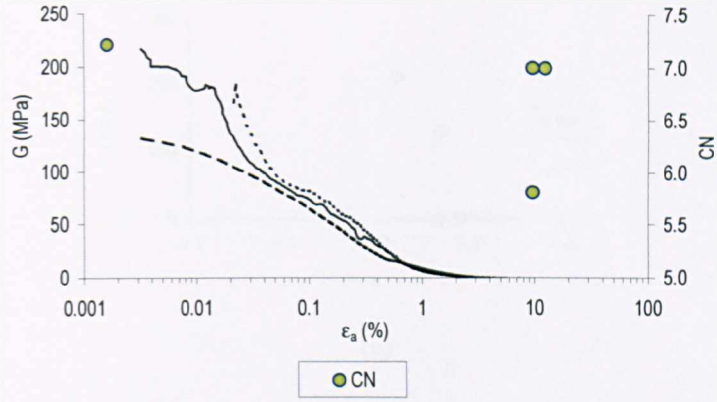

(a)

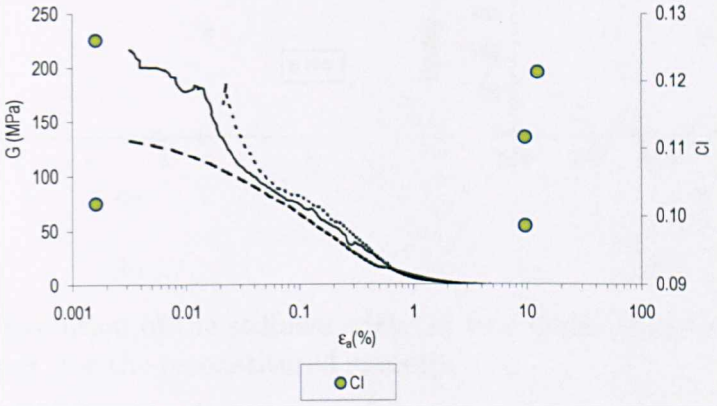

(b)

Figure 8.123: Evolution of stiffness and (a) CN (b) CI, for the reconstituted samples

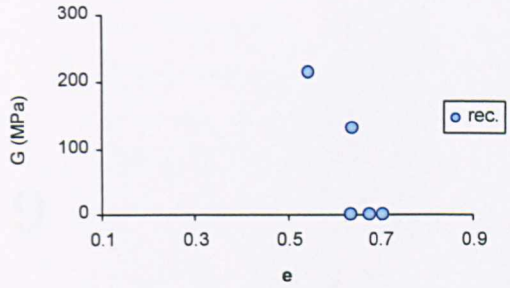

(a)

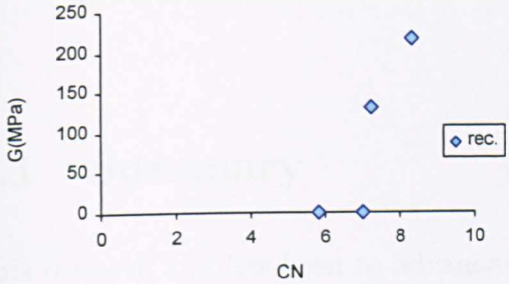

(b)

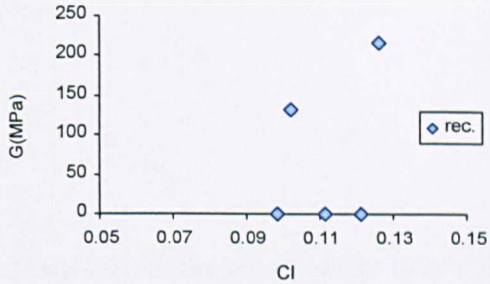

(c)

Figure 8.124: Evolution of the stiffness with (a) void ratio (b) coordination number (c) contact index, for the reconstituted samples

Chapter 9

Conclusions

9.1 Summary

This research aim has been to advance understanding of the micro-scale behaviour of natural sands by relating the behaviour of soil under loading to the changes in fabric. By exploiting recent developments in high-resolution computed-tomography (micro-CT), a unique micro-scale investigation of the material response was achieved and analysis techniques that had previously only been applied to physical analogue models and ideal DEM models could be used.

A natural locked sand with minimal cement content was chosen for the investigation. Owing to the particle interlocking, block samples of undisturbed material could be obtained. The intact and reconstituted specimens of this material exhibited different responses when subjected to shearing, as was documented in previous studies. The intact soil showed a significantly higher peak strength and higher dilation rates than the reconstituted soil. In addition, the initial shear stiffness of the intact material was higher and a more abrupt stiffness degradation was observed when compared with the reconstituted soil. The observations motivated consideration of this material in this research as it was hoped the differences in overall response could be scientifically explained by observation of the internal structure.

The reconstituted specimens were prepared to have densities that were close to those of the intact material, so the effect of fabric could be isolated. While the interlocked fabric could not be produced artificially, the change in soil gradings during reconstitution partially contributed to the high densities obtained for the reconstituted soil. In fact, the micro-scale investigation has shown that when the intact fabric is destroyed, some fractured grains disintegrate along pre-existing fissures into smaller fragments; these fragments filled the pore space between larger grains allowing higher densities to be achieved for the reconstituted specimens without developing a locked or similar structure that would be needed otherwise.

Following a number of trials, a system for resin impregnation of the sand specimens in the triaxial cell was achieved (prior to and after loading). The impregnation process required some modifications to be made to the original triaxial cell. The main challenges in the process were the high density of some specimens, the need to minimise the fabric disruption and the existence of a shear band in some cases. Cylindrical samples of approximately $5mm$ in diameter were cored from the impregnated triaxial specimens.

Micro-CT was used to obtain the 3D images for the measurement of the micro-scale quantities. A number of samples were imaged using different micro-CT laboratory systems to select the optimal scanning parameters and identify the necessary resolution and sample diameter. The image quality obtained in the initial scans was not satisfactory; these images exhibited some of the artefacts and shortcomings often associated with very high resolution images using laboratory sources. These shortcomings are related to the polychromatic nature of the source and the limited photon flux. Images obtained using synchrotron radiation do not exhibit most of these limitations and the higher image quality than can be obtained probably motivated the use of this type of radiation in other recent studies that have quantified sand fabric (Table 9.1). Access to synchrotron radiation sources is however limited; consequently the ability of laboratory sources to provide high quality images was explored in this study, as these are more likely to be adopted in geomechanics research.

The image quality and resolution required are both a function of the size of the features of interest in the images and the purpose of the investigation. Referring to Table 9.1, defining the resolution in soil mechanics studies as a function of d_{50} is important as it gives an indication of the level of detail of the features represented in the image. The resolution used in this research was $5\mu m$ (after 2×2×2 binning due to computational memory issues). This resolution was higher than that achieved in key earlier geotechnical studies (Table 9.1). These studies were, however, focused on the analysis of the particles. Where the contacts are also considered, as is the case of current investigation, higher resolutions are required to minimise the effect of the finite size of the voxels in the definition of the contacts. The final size of the samples and the optimised scanning parameters were based on a compromise between three main factors: image quality, time and cost of the process.

	Source type	Study type	$d_{50}(\mu m)$	Resolution	
Oda et al. (2004)	lab.	qualitative	206	$9\mu m$	$0.044d_{50}$
Al-Raoush (2007)	synchrotron	quantitative	325	$11.5\mu m$	$0.035d_{50}$
Hall et al. (2010)	synchrotron	quantitative	300	$14\mu m$	$0.047d_{50}$
Hasan and Alshibli (2010)	synchrotron	quantitative	160	$15\mu m$	$0.094d_{50}$
current study	lab.	quantitative	274	$5\mu m$	$0.018d_{50}$

Table 9.1: Comparison of the spatial resolution and source type used in some recent studies using high-resolution tomographic images of sand

As observed in the SEM images and in the optical microscope images of thin sections, Reigate sand exhibits non-convex grains with complex geometries, which together with the interlocked fabric have posed some challenges for the identification of the individual grains. In this research, the morphology and fabric quantification were carried out using specific algorithms developed for each measurement type and implemented in MATLAB. The development of this customised software had the advantage over the use of commercially available software packages, of being more flexible and requiring a thorough understanding of the process.

9.2 Key observations

This investigation has shown that, in the case of a highly fractured sand, the differences between the intact and reconstituted material are not limited to the geometrical arrangement of the grains but also to differences in the grading of the soil. The grading of the intact samples was seen to vary during loading as a result of the breakage of the fractured grains. This highlights the deficiency of standard laboratory techniques in measuring the PSD of an intact soil with fragile grains that are broken during reconstitution sieving. The fact that this phenomenon can only be measured using non-destructive techniques, is probably the reason why it was overlooked in previous studies of Reigate sand and other sands from the same strata. Cuccovillo and Coop (1999) found that the reconstituted soil seemed to have a different CSL to the intact in the $e : lnp'$ plane and this observation can possibly be related to the change in grading during reconstitution of the intact soil.

For the reconstituted samples, the particle size distribution (PSD) obtained using micro-CT data showed reasonable agreement with the sieve analysis and the size distribution using the QICPIC laser system. Due to computation limitations, the number of particles investigated using 3D micro-CT images cannot yet compete with the large number of particles used in sieve analysis or QICPIC analysis. However, the good agreement between the PSDs obtained for different micro-CT samples taken from the same triaxial specimen is an indicator that 3000 particles may be

enough to describe the PSD for this soil. Another soil type with a different grading might require a different number of particles to obtain representative data.

Measuring void ratio using micro-CT data has proven to be a good alternative to laboratory measurements that provide only global values and cannot easily differentiate between the material affected or not by the shear band. The comparison between the 3D and 2D void ratio values has demonstrated the subjectivity of the 2D measurements. It is proposed that when 2D analysis is carried out, using an average value obtained by considering numerous sections is likely to reduce the potential error.

The distribution of the particle orientations, in the initial state, for the intact soil showed a greater concentration around the horizontal plane, i.e., perpendicular to the direction of deposition. This finding was considered reasonable as no significant dip was observed in the soil strata and there were no obvious depositional features such as cross-bedding at the site. As shearing deformation progressed, the larger particles seemed to conserve their horizontal position (with the exception of the particles affected by the shear band movement where a deviation of approximately 30° from the horizontal plane was observed), while the more numerous smaller particles (the detached fragments) were orientated more randomly in less "stable" positions. The ability of the particle orientation fabric tensor, which accounts for the size and shape of the particles (as proposed by Oda et al., 1985) to capture quantitatively the greater influence that larger particles have in soil anisotropy was confirmed. The basic fabric tensor definition that considers only the particle major axis orientation did not permit this differentiation to be made. The particles in the reconstituted samples also exhibited an initial horizontal preferred orientation and this trend seemed to persist even after a critical state was apparently been reached (for the particles not affected by the shear band movement). The persistence of the fabric anisotropy in the soil outside the shear band is believed to be related to the localisation; after the shear plane forms the rest of the sample will hardly strain further and so never reaching a critical state.

Insights into contact geometries, not previously observed for natural sands, have been obtained. Sand particles are rarely smooth and convex and can lead to the formation of finite contact areas between particles. Moreover, contacts can be geometrically complex and each particle pair can have multiple contact regions that do not connect, i.e., a single contact area may not be simply connected and there can be parts of an area where the particles do not touch continuously. These observations raise doubts about the applicability, for real sands, of the fabric quantification approaches that are based on the representation of the contacts as points, as generally considered in DEM analysis. An example is the use of the coordination number, a metric that measures contact intensity, which takes into consideration only the number of contacts. A measure of the contact intensity that considers the contact

area, i.e., the contact index, was used. The contact index is defined to be the ratio of the contact area to the particle surface area and was shown to describe effectively the fabric of the intact material at different loading stages as well as to differentiate clearly between the fabric of the intact and reconstituted samples prior to loading.

The concentration of contact normals along the direction of the major principal stress, observed in the post-peak regime, is in agreement with the force chain theory postulated based on previous DEM and photoelastic studies. The deviation of the contact normal vectors from the vertical, found in the samples containing the shear band, can also be explained by the buckling of these force chains. An alternative version of the contact normal fabric tensor where each vector is weighted by the size of the associated contact was proposed.

The branch vector orientation data seemed insensitive to the evolution of fabric, seen using the other measures. However, scalar parameters such as branch vector length, the proposed parameter *bvlratio* and the angle between the contact normal and the branch vector were found to provide important information for the description of the arrangement of irregular grains.

The formation of large voids inside the shear band was confirmed, just as was observed by Oda and Kazama (1998) who made observations of 2D images of resin impregnated sand and also considered photoelastic rods. The analysis of the voids in terms of size and orientation can provide insight that cannot be obtained using the scalar void ratio index alone. The ambiguity associated with the partitioning of the individual voids in 3D images of real soil is probably the main constraint on the use of void space analysis to quantify the soil fabric.

The evolution of variables associated with the micro-mechanical process occurring at the particle scale, not previously achieved for triaxial experiments on real sand, was examined. While the data available in this study was limited, the potential to correlate the stress:strain response with the fabric orientational data and the stiffness with the scalar measures of the fabric was investigated. The results showed that for real sands the correlations may not be so clear as for the simple shapes used in DEM analyses. Samples from the same triaxial specimen showed different behaviour patterns depending on whether they were affected or not by the shear band. The correlations observed for the intact samples also differ from what was observed for the reconstituted samples. These observations highlight the fact that the simplifications and assumptions considered in DEM must be appreciated when developing conclusions about the relationship between the kinematics of the particle response and the overall stress-deformation behaviour of the material.

To conclude, this study is a small but essential step towards the development of a comprehensive understanding of the complex behaviour of granular materials. An analysis of more samples and consideration of more loading stages would have

allowed more conclusive observations to be made. Research into the fundamental particle scale mechanisms of soil that underlie the complexity of soil response remains a fascinating and yet largely unknown area of geotechnics.

9.3 Recommendations for future research

As highlighted in the above discussion, the research has confirmed the potential to use micro-CT to characterise the internal structure of soil and develop insight into particle scale soil mechanics. The experience gained in this investigation allows recommendations to be made for future research in this area.

Considering firstly particle morphology, the methodology presented here has great potential for 3D particle shape characterisation. However, because most previous studies of particle shape have been carried out using 2D images, few shape metrics or indices have been proposed in the literature for the 3D case. This is certainly an area where further research is needed, given the influence of particle shape on the engineering properties of granular soils as has been widely reported in the literature.

Where contact geometries are to be analysed, a higher voxel connectivity (e.g., 18-connectivity) should be considered so that the bias along the x, y and z axes observed in this study can be avoided. While it appears evident that using images with resolution lower than $5\mu m$ will produce a less accurate contact analysis, it would be interesting to investigate the effect of using higher resolutions and whether a more detailed examination would produce significantly better results and if this increase is accuracy would be worthwhile, given the increase in the computational cost of the analysis.

The branch vector length was not a sensitive measure to describe the evolution of the geometrical arrangement of the particles as shearing deformation progresses (for the reason stated above). Therefore it is suggested that vectors defined based on the concept of nearest neighbouring particles rather than contacting particles might be a better way to describe the phenomenon of dilation.

Tomographic images can be analysed as a 3D volume image or as a series of individual 2D images orientated along any of the three principal directions in the Cartesian coordinate system. This fact makes tomographic images well suited to comparing between 3D and 2D measurements of various micro-scale parameters for both morphology and fabric quantification, for example as was achieved in this study for the void ratio measurements.

Finally, future research considering additional loading stages is required, in particular at the peak deviatoric stress. This would produce more data and therefore it would permit a more comprehensive analysis of the evolution of the soil response

during shearing. While the interlocked fabric of Reigate sand provides a unique example of the gradual degradation of the initial fabric as shearing progresses, it would be interesting to apply the methodology proposed here to different sands. The main requirement for this application would be to use an image resolution able to resolve the smallest particles in the soil; which as discussed in Section 9.1 depends on the purpose of the analysis. An analysis based on the particle orientation requires a level of detail much lower than when for example particle surface is needed, for which, as shown in this study, less accurate measurements are likely to occur for particles defined by less than 2000 voxels.

References

Abdelaziz, T., C. D. Martin, and R. J. Chalaturnyk (2008). Characterization of Locked Sand from Northeastern Alberta. *Geotechnical Testing Journal 31(6)*, 480–489.

Abelev, A. V., S. K. Gutta, P. V. Lade, and J. A. Yamamuro (2007). Modeling cross anisotropy in granular materials. *J. Eng. Mech. 133(8)*, 919 - 932.

Al Asmar, R. (2006). Quantitative Measurements of The Fabric of Greensand. Master's thesis, Imperial College London.

Al-Raoush, R. (2007). Microstructure characterization of granular materials. *Physica A 377(2)*, 545–558.

Al-Raoush, R. and K. Alshibli (2006). Distribution of local void ratio in porous media systems from 3D X-ray microtomography images. *Physica A: Statistical Mechanics and its Applications 361*(2), 441–456.

Alshibli, K. and A. Reed (Eds.) (2010). *Proc. 3rd International Workshop on X-Ray CT for Geomaterials.* ISTE.

Alshibli, K. A. and M. I. Alsaleh (2004). Characterizing surface roughness and shape of sands using digital microscopy. *J. Comput. Civ. Engng. 18(1)*, 36 - 45.

Arthur, J. and B. Menzies (1972). Inherent anisotropy in a sand. *Géotechnique 22(1)*, 115–128.

Atwood, R. C., J. R. Jones, P. D. Lee, and L. L. Hench (2004). Analysis of pore interconnectivity in bioactive glass foams using X-ray microtomography. *Scripta Materialia 51*, 1029–1033.

Barreto, D. (2009). *Numerical and experimental investigation into the behaviour of granular materials under generalised stress states.* Ph. D. thesis, University of London.

Barreto, D., C. O'Sullivan, and L. Zdravkovic (2008). Specimen generation approaches for DEM simulations. In *International symposium on deformation characteristics of geomaterials.*

Barreto, D., C. O'Sullivan, and L. Zdravkovic (2009). Quantifying the evolution of soil fabric under different stress paths. In *Proc. 6th Inter. Conf. on Micromechanics of Granular Media*, pp. 181–184.

Barrett, H. and W. Swindell (1981). *Radiological Imaging; The Theory of Image Formation, Detection, and Processing.* Academic Press, New York.

Barrett, P. J. (1980). The shape of rock particles, a critical review. *Sedimentology 27*, 291–303.

Barton, M., S. Palmer, and Y. Wong (1986). A geological investigation of two Hampshire Tertiary Sand Beds: are they locked sands? *Quarterly Journal Engineering Geology 19*, 399–412.

Barton, M. E. (1993). Cohesive sands: The natural transition from sands to sandstones. In *Geotechnical Engineering of hard Soils-Soft Rocks Anagnostopoulos et al (eds) Balkema, Rotterdam.*

Beckmann, F. (2010). Micro- and Nanotomography using Synchrotron Radiation at DESY. In *High-resolution x-ray CT Symposium.*

Been, K. and M. G. Jefferies (1985). A state parameter for sands. *Géotechnique 35(2)*, 99 – 112.

Berg, R. (1986). *Reservoir Sandstones.* Prentice-Hall.

Beucher, S. and C. Lantuejoul (1979). Use of watersheds in contour detection. In *Proc. Int. Workshop Image Process. CCETT, Rennes, France.*

Bhandari, A. (2009). *The mechanics of an unbonded locked sand at low effective stresses.* Ph. D. thesis, University of Southampton.

Biarez, J. and K. Wiendieck (1963). La comparaison qualitative entre l'anisotropie mécanique et l'anisotropie de structure des milieux pulvérulents. *C.R. Acad. Sci. 256*, 1217–1220.

Bishop, A. and D. Henkel (1957). The measurement of soil properties in the triaxial tests. Technical report, Edward Arnold LTD, London.

Bishop, A. W. and L. D. Wesley (1975). A hydraulic apparatus for controlled stress path testing. *Géotechnique 25(4)*, 657–670.

Blyth, F. and M. de Freitas (1984). *A Geology for Engineers.* Arnold.

Borgefors, G. (1996). On digital distance transforms in three dimensions. *Computer Vision and Image Understanding 64(3)*, 368–376.

Bowman, E. T., K. Soga, and W. Drummond (2001). Particle shape characterisation using Fourier descriptor analysis. *Géotechnique 51(6)*, 545–554.

Brunke, O., S. Brockdorf, K. Drews, B. Müller, T. Donath, J. Herzen, and F. Felix Beckmann (2008). Comparison between X-ray tube based and synchrotron radiation based microCT. *Proc. of SPIE 7078*, 1–12.

Bésuelle, P., J. Desrues, and S. Raynaud (2000). Experimental characterisation of the localisation phenomenon inside a Vosges sandstone in a triaxial cell. *Int. J. Rock Mechanics Mining Sciences 37(8)*, 1223–1237.

Carrera, A. (2008). *Mechanical behaviour of Stava tailings.* Ph. D. thesis, Politecnico di Torino.

Casagrande, A. (1936). Characteristics of cohesionless soils affecting the stability of slopes and earth fills. *J. Boston Soc. Civil Engineers 23(1)*, 13–32.

Casagrande, A. and N. Carrillo (1944). Shear failure on anisotropic materials. *Proc. Boston. Soc. Of Civil Engineers 31*, 74–87.

Casey, R. (1961). The stratigraphical paleontology of the Lower Greensand. *Paleontology 3(4)*, 487–621.

Cates, J., R. Whitaker, and G. Jones (2005). Case study: an evaluation of user-assisted hierarchical watershed segmentation. *Medical Image Analysis 9*(6), 566–578. ITK - Open science - combining open data and open source software: Medical image analysis with the Insight Toolkit.

Cavarretta, I. (2009). *The influence of particle characteristics on the engineering behaviour of granular materials.* Ph. D. thesis, Imperial College London.

Chandler, R. (1966). The measurement of residual strength in triaxial compression. *Géotechnique 16(3)*, 181–186.

Chang, C. S. (1990). Packing Structure and Mechanical Properties of Granulates. *Journal of Engineering Mechanics 116 (5)*, 1077–1093.

Chang, C. S., S. S. Sundaram, and A. Misra (1989). Initial moduli of particulated mass with frictional contacts. *International Journal for Numerical and Analytical Methods in Geomechanics 13*(6), 629–644.

Cho, G. C., J. Dodds, and J. Santamarina (2006). Particle Shape Effects on Packing Density, Stiffness, and Strength: Natural and Crushed Sands. *J. Geotech. and Geoenvir. Engrg. 132(5)*, 591–602.

Christoffersen, J., M. Mehrabadi, and S. Nemat-Nasser (1981). A micromechanical description of granular material behavior. *Journal of Applied Mechanics 48 (2)*, 339–345.

Clayton, C., C. Abbireddy, and R. Schiebel (2009). A method of estimating the form of coarse particulates. *Géotechnique 59(6)*, 493–501.

Clayton, C., M. Xu, and A. Bloodworth (2006). A laboratory study of the development of earth pressures behind integral bridge abutments. *Géotechnique 56(8)*, 561–572.

Coop, M. R. (2005). On the mechanics of reconstituted and natural sands. In *Deformation characteristics of geomaterials. Recent investigations and prospects.*

Correa, C. and K.-L. Ma (2009). The Occlusion Spectrum for Volume Classification and Visualization. *IEEE Transactions on Visualization and Computer Graphics 15*, 1465–1472.

Craig, R. (2002). *Soil Mechanics.* Spon Press.

Cresswell, A., M. E. Barton, and R. Brown (1999). Determining the Maximum Density of Sands by Pluviation. *Geotechnical Testing Journal, 22(4)*, 324–328.

Cresswell, A. and W. Powrie (2004). Triaxial tests on an unbonded locked sand. *Géotechnique 54(2)*, 107–115.

Cresswell, A. W. (1999). *Sampling and strength testing an unbonded locked sand.* Ph. D. thesis, University of Southampton.

Cresswell, A. W. (2001). Block sampling and test sample preparation of locked sands. *Géotechnique 51(6)*, 567–570.

Cubrinovski, M. and K. Ishihara (2002). Maximum and minimum void ratio characteristics of sands. *Soils and Foundations 42(6)*, 65–78.

Cuccovillo, T. (1995). *Shear Behaviour And Stiffness Of Naturally Cemented Sands.* Ph. D. thesis, City University, London.

Cuccovillo, T. and M. Coop (1999). On the mechanics of structured sands. *Géotechnique 49 (6)*, 741–760.

Cuccovillo, T. and M. R. Coop (1997). Yielding and pre-failure deformation of structured sands. *Géotechnique 47(3)*, 491–508.

Cui, L. and C. O'Sullivan (2006). Exploring the macro and micro-scale response of an idealized granular material in the direct shear apparatus. *Géotechnique 56(7)*, 455–468.

Cundall, P. A. and O. D. L. Strack (1979). A discrete numerical model for granular assemblies. *Géotechnique 29(1)*, 47–65.

Curray, J. (1956). Analysis of two-dimensional orientation data. *J. Geol. 64*, 117–131.

Dafalias, Y., A. Papadimitriou, and X. S. Li (2004). Sand Plasticity Model Accounting for Inherent Fabric Anisotropy. *Journal of Engineering Mechanics 130(11)*, 1319 – 1333.

Danielsson, P. (1980). Euclidean Distance Mapping. *Comp. Graphics Image Process 14*, 227–248.

Davis, G. and J. Elliott (2006). Artefacts in X-ray microtomography of materials. *Materials Science and Technology 22(9)*, 1011–1018.

Davis, T., D. Gao, T. Gureyev, A. Stevenson, and S. Wilkins (1995). Phase-contrast imaging of weakly absorbing materials using hard x-rays. *Nature 373*, 595–598.

Deng, G. and L. Cahil (2002). An Adaptive Gaussian Filter For Noise Reduction and Edge Detection.

Desrues, J., P. Bésuelle, and H. Lewis (2007). Strain localization in geomaterials. *Geological Society, London, Special Publications 289*, 47–73.

Desrues, J., R. Chambon, M. Mokni, and F. Mazerolle (1996). Void Ratio evolution inside shear bands in triaxial sand specimens studies by computed tomography. *Géotechnique 46(3)*, 529–546.

Diamond (2010). http://www.diamond.ac.uk. (Last accessed November 2010).

Dines, H. G. and F. H. Edmunds (1933). *The Geology of the County around Reigate and Dorking.* Geological Survey of Great Britain.

Dittes, M. and J. Labuz (2002). Field and laboratory testing of St. Peter Sandstone. *Journal of Geotechnical and Geoenvironmental Engineering 128(5)*, 372–380.

Drescher, A. and G. Josselin De Jong (1972). Photoelastic verification of a mechanical model for the flow of a granular material. *J. Mech. Phys. Solids 20(5)*, 337–351.

Dusseault, M. B. and N. R. Morgensten (1979). Locked sands. *Q. J. Engng Geol. 12*, 117–131.

Feldkamp, L. A., L. C. Davis, and J. W. Kress (1984). Practical cone-beam algorithm. *J. Opt. Soc. Am. A 1*, 612–619.

Fernlund, J. M. (1998). The effect of particle form on sieve analysis: a test by image analysis. *Engineering Geology 50*, 111–124.

Fisher, R., S. Perkins, A. Walker, and E. Wolfart (2010). http://homepages.inf.ed.ac.uk/rbf/HIPR2. (Last accessed November 2010).

Fonseca, J. (2006). Image Analysis of Sand Using MATLAB. Master's thesis, Imperial College London.

Fonseca, J. and C. O'Sullivan (2008). A re-evaluation of the Fourier descriptor approach to quantifying sand particle geometry. In *Fourth International Symposium on Deformation Characteristics of Geomaterials.*

Fonseca, J., C. O'Sullivan, and M. Coop (2010). Quantitative Description of Grain Contacts in a Locked Sand. In *Proc. 3rd International Workshop on X-Ray CT for Geomaterials.*

Frost, J. and D.-J. Jang (2000). Evolution of sand microstructure during shear. *ASCE Journal of Geotechnical and Geoenvironmental Engineering 116*, 116–130.

Frydman, S., M. Talesnick, H. Nawatha, and K. Schwartz (2007). Stress-dilation of undisturbed sand samples in drained and undrained triaxial shear. *Soils and Foundations 47(1)*, 27–32.

Fu, Y. (2005). *Experimental Quantification and DEM Simulation of Micro-Macro Behaviors of Granular Materials Using X-ray Tomography Imaging.* Ph. D. thesis, Louisiana State University.

GE (2010). http://www.phoenix-xray.com. (Last accessed November 2010).

Gonzalez, R. C. and R. E. Woods (2008). *Digital Image Processing.* Prentice Hall.

Gossling, F. (1929). The geology of the country around Reigate. *Proceedings of the Geologists Association 40*, 197–259.

Goto, E. C., F. Tatsuoka, S. Shibuya, Y.-S. Kim, and T. Sato (1991). A Simple Gauge for Local Small Strain Measurements in the Laboratory. *Soils and Foundations 31(1)*, 169–180.

Guo, P. and X. Su (2007). Shear strength, interparticle locking, and dilatancy of granular materials. *Canadian Geotechnical Journal 44*, 579–591.

Gutierrez, G. (2007). *Influence of late cementation on the behaviour of reservoir sands.* Ph. D. thesis, University of London.

Hall, S., M. Bornert, J. Desrues, Y. Pannier, N. Lenoir, G. Viggiani, and B. P. (2010). Discrete and continuum analysis of localised deformation in sand using X-ray microCT and volumetric digital image correlation. *Géotechnique 60(5)*, 315–322.

Hanson (2007). Geological report.

Harkness, J. (2009). Potential particles for the modelling of interlocking media in three dimensions. *Int. J. Numer. Meth. Engng. 80*, 1573 – 1594.

Hasan, A. and K. Alshibli (2010). Experimental assessment of 3D particle-to-particle interaction within sheared sand using synchrotron microtomography. *Géotechnique 60(5)*, 369–379.

Hattab, M. and J.-M. Fleureau (2010). Experimental study of kaolin particle orientation mechanism. *Géotechnique 60(5)*, 323–331.

Hayakawaa, Y. and T. Oguch (2005). Evaluation of gravel sphericityand roundness based on surface-area measurement with a laser scanner. *Computers & Geosciences 31*, 735–741.

Hodson, E., D. Thayer, and C. Franklin (1981). Adaptive Gaussian Filtering and Local Frequency Estimates Using Local Curvature Analysis. *IEEE Trans. Acoust., Speech, Signal Processing Assp-29*, 854–859.

Holtz, R. and W. Kovacs (1981). *An Introduction to Geotechnical Engineering.* Prentice-Hall, Inc., Englewood Cliffs.

Howell, D. and R. P. Behringer (1999). Fluctuations in granular media. *Chaos 9 (3)*, 559–572.

Huffine, C. L. and C. F. Bonilla (1962). Particle-size effects in the compression of powders. *American Inst. Chem. Eng. J. 8(4)*, 490–493.

Ibanez, L., W. Schroeder, L. Ng, and J. Cates (2005). *The ITK software guide.* Clifton Park, NY, USA.

Ibrahim, A. A. and T. Kagawa (1991). Microscopic measurement of sand fabric from cyclic tests causing liquefaction. *Geotech. Testing J. 14(4)*, 371–382.

Iwashita, K. and M. Oda (2000). Micro deformation mechanism of shear banding process based on modified distinct element method. *Powder Technology 109*, 192–205.

Jang, D.-J. (1997). *Quantification of sand structure and its evolution during shearing using image analysis.* Ph. D. thesis, Georgia Institute of Technology.

Jang, D.-J., J. D. Frost, and J.-Y. Park (1999). Preparation of Epoxy Impregnated Sand Coupons for Image Analysis. *Geotechnical Testing Journal 22(2)*, 147–158.

Jardine, R. J., M. J. Symes, and J. B. Burland (1984). The Measurement of Soil Stiffness in the Triaxial Apparatus. *Géotechnique 34(4)*, 323–340.

Jolliffe, I. T. (2002). *Principal Component Analysis.* Springer-Verlag.

Joudi, A. (2008). A reassessment of standard laboratory sands. Master's thesis, Imperial College London.

Kak, A. and M. Slaney (2001). *Principles of Computerized Tomographic Imaging.* SIAM, New York.

Kanatani, K.-I. (1984). Distribution of directional data and fabric tensors. *International Journal of Engineering Science 22 (2)*, 149–164.

Kastner, J., B. Harrer, G. Requena, and O. Brunke (2010). A comparative study of high resolution cone beam X-ray tomography and synchrotron tomography applied to Fe- and Al-alloys. *NDT & E International 43*, 599–605.

Ketcham, R. and W. Carlson (2001). Acquisition, optimization and interpretation of X-ray computed tomographic imagery: applications to the geosciences. *Computers and Geosciences 27*, 381–400.

Klotz, E. and M. Coop (2002). On the Identification of Critical State Lines for Sands. *Geotechnical Testing Journal 25(3)*, 289–302.

Krumbein, W. and L. Sloss (1963). *Stratigraphy and Sedimentation.* W.H. Freeman, San Francisco.

Kuhn, M. (1999). Structured deformation in granular materials. *Mechanics of Materials 31*, 407–429.

Kuo, C.-Y. (1994). *Quantifying the fabric of granular materials and image analysis approach.* Ph. D. thesis, Georgia Institute of Technology.

Kuo, C.-Y., J. D. Frost, and J.-L. A. Chameau (1998). Image analysis determination of stereology based fabric tensors. *Géotechnique 48 (4)*, 515–525.

Kuwano, R. and R. J. Jardine (2002). On the applicability of cross-anisotropic elasticity to granular materials at very small strains. *Géotechnique 52(10)*, 727–749.

Larson, B. (2010). http://www.ndt-ed.org. (Last accessed November 2010).

Leroueil, S. and P. R. Vaughan (1990). The general and congruent effects of structure in natural soils and weak rocks. *Géotechnique 40(3)*, 467–488.

Li, X. and X. Li (2009). Micro-macro quantification of the internal structure of granular materials. *Journal of Engineering Mechanics 135 (7)*, 641–656.

Li, X., X. Li, and Z. Yang (2005). A fabric tensor for dilatancy of granular soil. In *Proc. of McMat2005.*

Lin, C. and J. Miller (2005). 3D characterization and analysis of particle shape using X-ray microtomography (XMT). *Powder Technology 154*(1), 61 – 69.

Maeda, K., K. Miura, and S. Toki (1995). Mechanical properties of elliptic microstructure formed in granular materials. *Soils and Foundations 35(2)*, 1–14.

Mangan, A. and R. Whitaker (1999). Partitioning 3D Surface Meshes Using Watershed Segmentation. *IEEE Transactions on Visualization and Computer Graphics 5*, 308–321.

Masad, E. and B. Muhunthan (2000). Three-dimensional characterization and simulation of anisotropic soil fabric. *Journal of Geotechnical and Geoenvironmental Engineering 126(3)*, 199–207.

Mimura, M. (2003). Characteristics of some Japanese natural sands, data from undisturbed frozen samples. Technical report, Disaster Prevention Research Institute of Kyoto University, Japan.

Mitchell, J. and K. Soga (2005). *Fundamentals of Soil Behavior.* John Wiley & Sons, Inc., NY.

Miura, K., K. Maeda, M. Furukawa, and S. Toki (1997). Physical characteristics of sand with different primary properties. *Soils and Foundations 37(3)*, 53–64.

Muhunthan, B., J. Chameau, and E. Masad (1996). Fabric effects on the yield behavior of soils. *Soils and Foundations 36(3)*, 85–97.

Muir Wood, D. (2008). Critical states and soil modelling. In *Fourth International Symposium on Deformation Characteristics of Geomaterials.*

Nave, C. R. (2010). http://hyperphysics.phy-astr.gsu.edu/hbase/hframe.html. (Last accessed November 2010).

Neuser, E. and A. Suppes (2007). nanoCT, Visualizing internal 3D structures with submicrometer resolution. In *DIR 2007 - Int. Symp. Digital industrial Radiology Computed Tomography.*

Ng, T.-T. (1999). Fabric Study of Granular Materials after Compaction. *Journal of Engineering Mechanics 125*(12), 1390–1394.

Ng, T.-T. (2001). Fabric Evolution of Ellipsoidal Arrays with Different Particle Shapes. *Journal of Engineering Mechanics 127*(10), 994–999.

Ng, T.-T. (2004). Macro- and micro-behaviors of granular materials under different sample preparation methods and stress paths. *International Journal of Solids and Structures 41*(21), 5871–5884. Granular Mechanics.

Ng, T.-T. (2009). Particle shape effect on macro- and micro-behaviors of monodisperse ellipsoids. *International Journal for Numerical and Analytical Methods in Geomechanics 33*(4), 511–527.

Ng, T.-T., D. Aube, and S. Altobelli (2002). Void distribution of sand specimens by MRI. In *Proc. 15th ASCE Eng. Mech. Conf.*

Nougier-Lehon, C., E. Vincens, and B. Cambou (2005). Structural changes in granular materials: the case of irregular polygonal particles. *International J. Solids and Structures 42(24-25)*, 6356–6375.

Nouguier-Lehon, C., B. Cambou, and E. Vincens (2003). Influence of particle shape and angularity on the behaviour of granular materials a numerical analysis. *Int. J. Numer. Anal. Meth. Geomech. 27*, 1207–1226.

Oda, M. (1972a). Deformation mechanism of sand in triaxial compression tests. *Soils and Foundations 12(4)*, 45–63.

Oda, M. (1972b). Initial fabric and their relations to mechanical properties of granular material. *Soil and Foundations 12(1)*, 17–36.

Oda, M. (1972c). The mechanism of fabric changes during compressional deformation of sand. *Soils and Foundations 12(2)*, 1–18.

Oda, M. (1977). Co-ordination number and its relation to shear strength of granular material. *Soils and Foundations 17(2)*, 29–42.

Oda, M. (1982). Fabric Tensor for discontinuous geological materials. *Soils and Foundations 22(4)*, 96–108.

Oda, M. and Iwashita (1999). *Mechanics of granular materials.* Balkema.

Oda, M. and H. Kazama (1998). Microstructure of shear bands and its relation to the mechanisms of dilatancy and failure of dense granular soils. *Géotechnique 48(4)*, 465–481.

Oda, M. and J. Konishi (1974). Microscopic deformation mechanism of granular material in simple shear. *Soils and Foundations 14(4)*, 25 – 38.

Oda, M., J. Konishi, and S. Nemat-Nasser (1980). Some experimentally based fundamental results on the mechanical behaviour of granular materials. *Géotechnique 30(4)*, 479–495.

Oda, M., J. Konishi, and S. Nemat-Nasser (1982). Experimental micromechanical evaluation of strength of granular materials Effects of particle rolling. *Mechanics of Materials 1*(4), 269–283.

Oda, M. and H. Nakayama (1989). Yield Function for Soil with Anisotropic Fabric. *Journal of Engineering Mechanics 115(1)*, 89–104.

Oda, M., S. Nemat-Nasser, and J. Konishi (1985). Stress induced anisotropy in granular masses. *Soils and Foundations 25(3)*, 85–97.

Oda, M., T. Takemura, and M. Takahashi (2004). Microstructure in shear band observed by microfocus X-ray computed tomography. *Géotechnique 54(8)*, 539–542.

Oh, W. and B. Lindquist (1999). Image Thresholding by Indicator kriging. *IEEE Transactions Pattern Analysis Machine Intelligence 21(7)*, 590–602.

Oldnall, N. (2010). http://www.e-radiography.net. (Last accessed November 2010).

O'Sullivan, C. (2010). *Particulate Discrete Element Modelling.* Taylor and Francis.

O'Sullivan, C., L. Cui, and S. O'Neil (2008). Discrete element analysis of the response of granular materials during cyclic loading. *Soils and Foundations 48(4)*, 511–530.

Otani, J., T. Mukunoki, and Y. Obara (2000). Application of X-ray CT method for characterization of failure in soils. *Soils and Foundations 40(2)*, 111–118.

Otsu, N. (1979). A threshold selection method from gray level histograms. *IEEE Trans. Systems, Man and Cybernetics 9*, 62–66.

Palmer, S. M. and M. E. Barton (1986). Avoiding microfabric disruption during the impregnation of friable, uncemented sands with dyed epoxy. *Journal of sedimentary petrology 56 (4)*, 556–557.

Palmer, S. M. and M. E. Barton (1987). Porosity reduction, microfabric and lithification in U. K. uncemented sands. *Diagenesis of sedimentary sequences. Geological Society Special Publication 36*, 29–40.

Peña, A., R. García-Rojo, and H. J. Herrmann (2007). Influence of particle shape on sheared dense granular media. *Granular Matter 9*, 279–291.

Qadimi, A. (2005). *The cyclic response of a carbonate sand through critical state soil mechanics.* Ph. D. thesis, Imperial College London.

Rechenmacher, A., S. Abedi, and O. Chupin (2010). Evolution of force chains in shear bands in sands. *Géotechnique 60(5)*, 343–351.

Reynolds, O. (1885). On the dilatancy of media composed of rigid particles in contact. *Philosophical Magazine 20*, 469–481.

Richards, N. P. and M. E. Barton (1999). The Folkestone Bed Sands: microfabric and strength. *Quarterly Journal of Engineering Geology 32*, 21–24.

Rivers, M. (2010). Potential and limitations of CT as a technology to study properties of geomaterials. In *Introduction to Computed Tomography (CT) and Neutron Tomography (NT) Short Course.*

Roscoe, K., A. Schofield, and C. Wroth (1958). On the yielding of soils. *Géotechnique 8(1)*, 22–52.

Rothenburg, L. and R. J. Bathurst (1989). Analytical study of induced anisotropy in idealized granular materials. *Géotechnique 39(4)*, 601–614.

Rothenburg, L. and R. J. Bathurst (1992). Micromechanical features of granular assemblies with planar elliptical particles. *Géotechnique 42 (1)*, 79–95.

Rothenburg, L. and N. Kruyt (2004). Critical state and evolution of coordination number in simulated granular materials. *International Journal of Solids and Structures 41*, 5763–5774.

Russ, J. C. (2007). *The Image Processing Handbook.* CRC Press.

Salaberger, D., B. Plank, J. Kastner, B. Harrer, G. Requena, H.-P. Degischer, and O. Brunke (2010). Comparative study of high resolution cone beam X-ray computed tomography methods and discussion of temperature influence on Nanotom stability. In *High-resolution x-ray CT Symposium.*

Santamarina, J. and G. Cho (2004). Soil Behavior: The Role of Particle Shape. In *Proc. Skempton Conf., London.*

Satake, M. (1982). Fabric tensor in granular materials. In *IUTAM Conference on Deformation and Failure of Granular Materials.*

Schofield, A. and C. Wroth (1968). *Critical State Soil Mechanics.* McGRaw Hill.

Sezgin, M. and B. Sankur (2004). Survey over image thresholding techniques and quantitative performance evaluation. *Journal of Electronic Imaging 13(1)*, 146–168.

Siever, R. (1959). Petrology and geochemistry of silica cementation in some Pennsylvania sandstones. *Silica in Sediments, Spec. Publ. Soc. econ. Palaeont. Miner., Tulsa 7*, 56–79.

Smith, S. W. (2010). http://www.dspguide.com/ch25/5.htm. (Last accessed November 2010).

Sorby, H. (1908). On the Application of Quantitative Methods to the Study of the Structure and History of Rocks. *Quarterly Journal of the Geological Society 64*, 171–233.

Stephenson, L. P., W. J. Plumley, and V. V. Palciauskas (1992). A model for sandstone compaction by grain interpenetration. *Journal of Sedimentary Research 62(1)*, 11–22.

Stock, S. (1999). X-ray microtomography of materials. *International Materials Reviews 44*, 141–164.

Stock, S. (2008). Recent advances in X-ray microtomography applied to materials. *International Materials Reviews 53(3)*, 129–181.

Summersgill, F. (2009). The use of particulate discrete element modelling to assess the vulnerability of soils to suffusion. Master's thesis, Imperial College London.

Taylor, M. A. (2002). Quantitative measures for shape and size of particles. *Powder Technology 124* (1-2), 94–100.

Thornton, C. (2000). Numerical simulations of deviatoric shear deformation of granular media. *Géotechnique 50(1)*, 43–53.

Thornton, C. and L. Zhang (2005). On the elastic response of granular media. In *Powders and Grains - García Rojo, Herrmann and McNamara (eds).*

Tordesillas, A. and S. Walsh (2002). Incorporating rolling resistance and contact anisotropy in micromechanical models of granular media. *Powder Technology 124*, 106–111.

Ventouras, K. and M. Coop (2009). On the behaviour of Thanet Sand: an example of an uncemented natural sand. *Géotechnique 59(9)*, 727–738.

Videla, A., C.-L. Lin, and J. D. Miller (2006). Watershed Functions Applied to a 3D Image Segmentation. Problem for the Analysis of Packed Particle Beds. *Part. Part. Syst. Charact. 23*, 237–245.

Viggiani, G. and S. Hall (2008). Full-field measurements, a new tool for laboratory experimental geomechanics. In *Fourth International Symposium on Deformation Characteristics of Geomaterials.*

Vincent, L. and P. Soille (1991). Watersheds in digital spaces: an efficient algorithm based on immersion simulations. *EEE Trans. Pattern Anal. Mach. Intell. 13(6)*, 583–598.

Wadell, H. (1932). Volume, shape and roundness of rock particles. *J. Geol. 40*, 443–451.

Wan, R. and P. Guo (2001). Effect of microstructure on undrained behaviour of sands. *Can. Geotech. J. 38*, 16–28.

Wan, R., P. Guo, and M. Al-Mamun (2005). Behaviour of Granular Materials in Relation to Their Fabric Dependencies. *Soils and Foundations 45(2)*, 77–86.

Wang, L., J.-Y. Park, and Y. Fu (2007). Representation of real particles for DEM simulation using X-ray tomography. *Construction and Building Materials 21*, 338–346.

Wang, L. B., J. D. Frost, and J. S. Lai (2001). Quantification of doublet vector distribution of granular materials. *Journal of engineering mechanics 127(7)*, 720–729.

Wang, Y. and C. Mok (2008). Mechanisms of Small-Strain Shear-Modulus Anisotropy in Soils. *Journal of Geotechnical and Geoenvironmental Engineering 134(10)*, 1516–153.

Wong, R. (2000). Shear Deformation of locked Sand in Triaxial Compression. *Geotechnical Testing Journal 23(2)*, 158–170.

Wong, R. C. K. (2003). Strain-induced anisotropy in fabric and hydraulic parameters of oil sand in triaxial compression. *Can. Geotech. J. 40(3)*, 489–500.

Woodcock, N. H. (1977). Specification of fabric shapes using an eigenvalue method. *Geological Society of America Bulletin 88(9)*, 1231–1236.

Wroth, C. P. and N. Bassett (1965). A stress-strain relationship for the shearing behaviour of sand. *Géotechnique 15(1)*, 32–56.

Yamamuro, J. and F. Wood (2004). Effect of depositional method on the undrained behavior and microstructure of sand with silt. *Soil Dynamics and Earthquake Engineering 24*, 751–760.

Yang, X. (2005). *Three-dimensional characterization of the inherent and induced sand microstructure.* Ph. D. thesis, Georgia Institute of Technology.

Yang, Z. X., X. S. Li, and J. Yang (2008). Quantifying and modelling fabric anisotropy of granular soils. *Géotechnique 58(4)*, 237 – 248.

Yimsiri, S. and K. Soga (2010). DEM analysis of soil fabric effects on behaviour of sand. *Géotechnique 60(6)*, 483–495.

Zdravkovic, L. and R. Jardine (1997). Some anisotropic stiffness characteristics of a silt under general stress conditions. *Géotechnique 47(3)*, 407–438.

Zingg, T. (1935). Beitrag zur Schotteranalyse. *Schweizer Mineralogische Petrographologische Mitteilungen 15*, 52–56.